A RESERVOIR CHARACTERIZATION OF ARAB-D SUPER-K AS A DISCRETE FRACTURE NETWORK FLOW SYSTEM, GHAWAR FIELD, SAUDI ARABIA

A DISSERTATION
SUBMITTED TO THE DEPARTMENT OF PETROLEUM ENGINEERING
AND THE COMMITTEE ON GRADUATE STUDIES
OF STANFORD UNIVERSITY
IN PARTIAL FULFILLMENT OF THE REQUIREMENTS
FOR THE DEGREE OF
DOCTOR OF PHILOSOPHY

Joe Voelker
December 8, 2004

I certify that I have read this dissertation and that, in my opinion, it is fully adequate in scope and quality as a dissertation for the degree of Doctor of Philosophy.

Dr. Jef Caers Principal Advisor

I certify that I have read this dissertation and that, in my opinion, it is fully adequate in scope and quality as a dissertation for the degree of Doctor of Philosophy.

Professor Andre G. Journel

I certify that I have read this dissertation and that, in my opinion, it is fully adequate in scope and quality as a dissertation for the degree of Doctor of Philosophy.

Professor Roland N. Horne

Approved for the University Committee on Graduate Studies.

Abstract

The Arab-D Formation of the Ghawar Field, Saudi Arabia, is the most prolific oil producing formation in the world, relative to both volume and productivity. Cumulative oil production from Ghawar, through 2003, exceeded 55 billion barrels, and maximum field production rate has exceeded 5.7 million barrels per day (under natural lift) - both worldwide industry records. Currently (2004), Ghawar alone provides one-half of Saudi Arabia's oil production, 15% of OPEC production, and 6% of world production.

An important hydraulic component of this carbonate formation, "super-k," provides for anomalously high, localized, fluid conductivity, and has to date eluded simple geologic characterization.

Spatial prediction of super-k occurrence is desired for placement of water injection and oil production wells, and for improved production forecasting. Premature oil well abandonment has become a problem for the operator, Saudi Aramco, due to the inability to mitigate the high injection water conductivity of super-k, and associated early water breakthrough at adjacent production wells.

Given the potentially deleterious effects of super-k, and the enormous volume of reserves that it impacts, the accurate characterization of super-k has profound implications.

This thesis provides a new model of Arab-D super-k, comprised primarily of interwell discrete fracture networks.

The model is used to predict production performance in an 11-well study area in the Hawiyah sector of the field. Four of the wells in the study area exhibit the effects of super-k.

The principal components of the thesis, the simulation of flow in large-scale, discrete fracture systems, preceded by the mapping of geocellular models to the flow simulation model, provide for a new general approach to modeling the flow effects these highly conductive systems. This approach is immediately applicable beyond Ghawar and super-k; in general, characterization of reservoirs which are severely affected by flow in large-scale fracture systems, most notably those oil or gas developments in which the accurate prediction of water encroachment is essential to well planning or determination of economic feasibility, may benefit from this model. The model is conducive to immediate industry application, due to two key elements.

First, sources, rather than discretization, are used to incorporate discrete fracture networks into the conventional, and commercial, finite difference flow simulator, without modification of the flow simulator code.

Second, a practical, stochastic discrete fracture network model serves as a tool for gradual deformation of the geocellular model in a history matching algorithm.

The source model offers several advantages over fracture discretization and dual porosity models, particularly for flow simulations performed as part of an optimization algorithm, as is the case in this thesis. Without the computational and gridding burdens of fracture discretization, or the inappropriate resolution of the dual grid, the source model provides a means by which discrete fracture flow simulation may be performed with conventional flow simulators, on coarse grids, using geocellular fracture models of fine resolution.

Implementation of the source model to simulate fracture flow has not been previously attempted in a history matching study of Arab-D super-k.

The discrete fracture network model serves as both, a means by which any geocellular fracture model may be mapped into the flow simulation model, and a means by which the geocellular fracture model may be perturbed for production history matching purposes. The model is stand-alone; it is independent of both the geocellular model and the source model, and thus may be easily incorporated into a history-matching workflow.

The super-k model was used successfully to predict production performance that is significantly affected by the presence of large-scale fracture systems, in the Ghawar

study area.

Acknowledgements

I thank Dr. Jef Caers, for guiding this thesis in the direction of my strengths, and managing, with superior effectiveness, an older student who required more than one "grandfather" waiver of the more modern, computing intensive prerequisites of our research group, The Stanford Center for Reservoir Forecasting (SCRF).

I thank Professor Andre Journel, for a four year tutelage that was rigorous, methodical, and professional; in a word, French. I thank him also for promoting a lively camaraderie in SCRF, both professional and social, through which enduring friendships were made.

I am grateful for financial support from the funding affiliates of SCRF. I am particularly indebted to Saudi Aramco, from which this project was obtained, and which further provided partial financial support for this work through its 2002 Out of Kingdom Study Program (project OOK-22/2002). I thank Jim Liu, our intermediary with Saudi Aramco, from whom the Ghawar study area data, original flow simulation model, and invaluable correspondence, was conveyed.

I am also grateful to The Research Partnership to Secure Energy for America, RPSEA. As a Spring 2004 Fellowship Award Recipient, my final academic year was entirely funded by this non-profit American consortium, that provides funding to applied research for diverse aspects of the safe, economic, and environmentally sensitive exploitation of natural gas reservoirs.

I thank the faculty of the Stanford Petroleum Engineering Department for their esteemed academic professionalism, and for directing partial funding of my research through the 2003 Henry J. Ramey, Jr. Fellowship Award.

Finally I express forever, my love and gratitude to my mother, Ririko, for her

deep love and devotion, and for her decision to marry a U.S. Airman, leave her home in Japan, and settle in the U.S., and to my father George, for his WWII and career military service, and for imparting a trait of independence and self-reliance that kept me afloat during this work.

Contents

List of Tables

List of Figures

Chapter 1

Summary and conclusions

The thesis describes a workflow to characterize, primarily through production history matching, a well production anomaly called "super-permeability," or "super-k," in the Arab-D Formation, in a small study area in the Ghawar Field, Saudi Arabia. Since a key element of super-k is composed of large-scale fracture networks, the thesis provides a general workflow for production history matching in reservoirs for which large scale fracture systems are important flow components.

The key chapters of the thesis, operational recommendations drawn from the thesis, and proposed extensions of the thesis, are summarized in this chapter.

1.1 Key chapters

Our history matching algorithm employs a conventional flow simulator to model discrete fracture networks, using sources, rather than discretization. The use of sources to model discrete fracture flow is without precedent in the reservoir engineering literature; only one reference in the groundwater hydrology literature describes a similar method. The source model is described in Chapter 7.

We hypothesize that super-k systems that are laterally extensive, for example those systems of greatest interest that enable premature breakthrough of injection water to adjacent producers, often in well spacing exceeding 1 km, are comprised predominantly of one or more discrete fracture networks, combined with a localized, thin,

high-permeability facies generally providing connections to the wells. An analysis of super-k mechanics, Chapter 6, shows the discrete fracture model to be plausible, and in fact, likely.

The history matching algorithm employs an object-based geologic model, and a conventional, commercial, finite difference flow simulator. Neither the use of discrete fracture network models, nor the explicit incorporation of these models into a conventional flow simulator, have been previously attempted to model super-k in the Ghawar Field. The tool we have developed to map *any discrete fracture network model*, explicitly into the flow simulation grid, DISCFRAC, is described in Chapter 9. A module of this type is essential in the use of sources to model fracture network flow, in that it provides for stochastic reservoir simulations, and subsequently a mapping mechanism to transfer the parameters to the flow simulator.

The source model's efficacy in modeling fracture flow is reviewed in Chapter 8, where fracture flow is described in the context of analytical studies from the engineering literature, and through numerical studies conducted as a course of the thesis work. The numerical studies provide a comparison of the conventional discretization method of modeling fracture flow, to the source model approach.

An extensive geology discussion is given in Chapter 4. The Ghawar depositional model provides, in part, a basis for an understanding of the principal reservoir mechanics of the field, and must be the underlying framework and foundation by which any appropriate fracture model will be constructed; therefore this chapter is quite detailed. Furthermore, this geologic formation may be the most important one ever deposited, relative to the oil industry at least, and so warrants a thorough discussion.

A comprehensive review of the Ghawar super-k technical literature is given in Chapter 5. The most exciting papers are currently being published, due to the completion of 3D seismic interpretation over various field regions (interpretation is continuing at the time of this writing). We include an extensive engineering analysis in the review, to both describe and analyze super-k models generated by Saudi Aramco, the nearly solitary public technical source of this literature, and to provide the reader with a comprehensive analysis of the fundamental reservoir mechanics of Ghawar. Almost thirty papers represent the entirety of the publicly known reservoir

engineering aspects of Ghawar, and of super-k. The majority of those publications are referenced in the literature review chapter, and the remainder elsewhere in the thesis.

Although the objective of this thesis was to develop a super-k, and large-scale fracture system, characterization workflow, a complete history matching study was not performed for the Ghawar study area. History matching is not currently useful, due to a lack of geologic data, most importantly, 3D seismic data. However, preliminary testing of the workflow was performed, using study area data. The results constitute sensitivity studies, rather than history matches. The sensitivity study demonstrates the capability of our algorithm, and is presented in Chapter 10. The workflow and corresponding algorithm constitute a history matching tool, that can be utilized in further work in which 3D seismic data may sufficiently constrain a fracture model.

1.2 Operational recommendations

Our results indicate a possible remediation of problems associated with super-k, based on two fundamental findings associated with the Ghawar waterflood, and characterized by simplicity and feasibility. Although not a principal objective of this thesis, these operational recommendations may prove substantive.

The first fundamental finding: the predominate, repeated waterflood pattern is that of line drive, specifically under long and thin, rectangular pattern boundaries. Second: Ghawar water injection wells are often inadvertently hydraulically fractured with unpropped fractures. We develop supporting bases for both of these conclusions, specifically in Chapter 5.

We conclude that these conditions exacerbate the problematic super-k condition, that of early water breakthrough. Our hypothesis for the structure of super-k, containing essential discrete fracture network components, naturally leads to a supposition that the two conditions stated above, are conducive to the formation of highly conductive pathways, consisting of hydraulic fractures at injection wells, connecting to natural discrete fracture systems, culminating in a network that may significantly affect production well performance, because it resides in a long, thin bounded region,

the tight waterflood pattern.

Remediation resides in the idea that the constricted waterflood pattern affords the possibility of controlling water breakthrough, both before and after the fact, through the selective shut down of offending water injection wells, or more desirably, through the cessation of water injection in those wells, at pressures above hydraulic fracture pressures. It is possible that the unpropped hydraulic fractures will be sufficiently constricted under lower injection pressures, to inhibit formation of an effective network. Evidence of such behavior is documented, and described in Chapter 5.

These remediation procedures may be worthy of pilot testing, as their cost appears minimal, relative to a potential substantial gain through the reduction of bypassed oil and water production.

1.3 Future work

The most immediate, and natural, extension of this thesis would emphasize construction of a detailed, static DFN geocellular model for the Ghawar study area, toward the objective of history matching study area production data, using the tools for perturbing the geocellular model, and simulating fracture flow, provided by this thesis. Construction of a detailed fracture system geocellular model involves research in data integration, most importantly the integration of fracture interpretations from 3D seismic data. Relative to the sparsity of other available static data, including well log, core, and well test data, seismic data is exhaustive, although with low resolution. The incumbent model uncertainty after integration of low resolution 3D seismic fracture data may be decreased with the incorporation of geomechanical models, constructed from higher resolution 3D seismic structure data.

Geomechanical models informed by 3D seismic structure data, and by seismic interpretation of major faults, may be used to generate rock stress maps informing the spatial distribution of fracture density, orientation, length, and vertical thickness. The application of these models may be crucial to further constraining a fracture geocellular model that is ill-informed of sub-seismic, though highly conductive and laterally extensive, fracture networks.

Perturbation of the static geocellular model may be performed by the algorithm developed in this thesis. Both facies parameter perturbation and fracture parameter perturbation may be performed. However, joint perturbation of either, facies and fracture parameters, or fracture parameters alone, cannot be accomplished in our algorithm. Facies parameters are perturbed independently of fracture parameters, and fracture parameters are perturbed independently of each other. Joint perturbation is desirable for those parameters that are strongly correlated, when sufficient data exists to verify such correlation. Given these desirable, yet probably rare, circumstances, joint perturbation serves to further constrain the geocellular model.

The source model may be further developed in future work, in two main areas, pertaining to accurate flow simulation of highly conductive, large-scale fracture systems. First, the model does not accurately reflect the flow process if vertical equilibrium flow within the fracture system is important. This process is significant in vertically extensive fractures under flow conditions in which gravity segregation occurs, thus inducing gravity segregation in the surrounding porous matrix. These flow conditions promote a bottom-up waterflood. The source model accurately predicts fracture flow in which flow is conducted without segregation, under conditions of thorough mixing of water and oil in the fracture system.

Accurate flow prediction by the source model in fracture systems may also be enhanced with improved computational performance. Although our sensitivity studies indicated reasonable flow simulation times for the study area case, nonetheless significant variation in CPU times were noted among the various fracture realizations, indicating differing convergence properties. Just as the introduction of horizontal wells into a flow simulation model changes its convergence properties, so does the introduction of fractures. The increase in CPU times inherent in these incorporations may prove to be problematic when applying the source model to fracture systems covering large regions, and in finely discretized flow simulation models. Methods developed to either improve the robustness of well (source) solutions under multiphase well flow, or methods to improve the Jacobian structure in the presence of complex well paths, will contribute to improved flow simulation behavior in modeling fracture flow using the source model.

Finally, advances in the analysis of well performance in the presence of discrete, conductive fracture systems, will benefit the interpretation of fracture location and properties from well tests. A plethora of analytical models exist for well response from hydraulic fractures; well response from conductive, discrete fractures that are isolated from the well is less understood. Two analytical models for the interpretation of well test response in the presence of discrete, conductive fractures and faults, are all that exist in the literature. Although the models are adequate, they are limited in application, applying to a small subset of possible cases. The improved prediction of isolated, discrete fracture properties from well test data will be valuable towards the fracture characterization problem, inherently beset with a severe, sparse data liability.

Chapter 2

Introduction

The characterization of fractured rock formations, specifically their fluid conductivity properties, has application in a variety of problems, most notably of late in contamination transport in fresh water aquifers, nuclear waste storage, and in hydrocarbon production, the topic of this thesis.

The most general hydrocarbon production problem is the determination of optimal well placement schemes, a task requiring accurate production forecasting under a given well development plan. Although it is not uncommon for a rather homogeneous characterization of the spatial distribution of reservoir storage and conductivity to suffice for an adequate production forecast, the occurrence of either of two particular geologic phenomena often invokes the requirement for a more detailed reservoir characterization. The phenomena are reservoir fracturing, and aquifer expansion. The combination of these two phenomena renders the task of rigorous characterization inescapable.

Rarely do the fracture systems in a reservoir not require consideration in generating production forecasts. Small scale, pervasive fractures, for example, may entirely define the conductivity of a reservoir. Large scale faults may be principal reservoir flow barriers, partitioning the reservoir into hydraulically isolated regions, each requiring a separate well development. The incremental development requirement has singularly cast many otherwise profitable developments as infeasible and therefore abandoned.

The expansion of an associated aquifer upon hydrocarbon depletion, or equivalently, the injection of water for secondary recovery, provokes the need for a detailed characterization, simply because a fluid that generates a revenue deficit is introduced into the productive region of the reservoir. The length of time before which a conductive region may bring water to a production well is a critical economic factor. Highly conductive regions, which benefit oil production, may provide detrimental pathways for water flow upon aquifer encroachment. Water flow in these pathways, accelerates arrival of water at the producing wells, and possibly circumvents the sweep of oil in significant volumes of reservoir rock. Mitigation of this problem is subsequent preferential placement of wells, in patterns designed to minimize the deleterious flow effects of these conduits.

By far the most potentially conductive elements of a formation are its laterally connected, discrete fracture systems, as permeability upper bounds of an extensive discrete fracture system may be orders of magnitude larger than that of porous media. The characterization of these local, high conductivity geologic elements, certainly present in all rock formations to some degree, is therefore critical, albeit extremely difficult, due to their illusive geometry.

Discrete fracture networks are infinitesimally thin, relative to reservoir size, and occur predominantly as approximately vertical planes. Therefore, direct sampling by vertical wells under conventionally large oil field areal spacing, is extremely rare, although sampling in horizontal wells may be substantial. In this case, borehole imaging data, core and log data, as well as drilling data (lost circulation), may correlate to discrete fractures. Otherwise, directly measured discrete fracture data from wells are generally too sparse.

Correlation of discrete fracture systems with seismic data is also difficult unless the fracture system generates significant vertical offset of bedding surfaces. Seismic data is, however, critical in that the detection of faults proves the existence of a sufficient condition for the occurrence of smaller scale fracture systems. Furthermore, detailed 3D definition of the reservoir structure aids in the generation of rock failure models, which may prove extremely beneficial toward the generation of a static fracture system model.

However, the most effective characterization data for discrete fracture systems are precisely those that bring their importance to bear, production data. Given that fracture systems influence this data through a physical process, namely flow in porous media, the data must necessarily be inverted to yield realizations of fracture system parameters. This is accomplished practically through an algorithm that calls for iterative simulations of a numerical implementation of the physical process, toward finding parameters that minimize the error between the field dynamic data and the computed data.

We have attempted to characterize a fracture dominated anomaly called "superpermeability," or super-k, in the Arab-D Formation, in a small study area in the Ghawar Field, Saudi Arabia, in which the operator, Saudi Aramco (SA), is attempting to resolve observed, massive, unmitigated hydraulic conductivity between injection and production wells separated often by more than 1 km.

Super-k has profound implications in reserves recovery in the field. Premature oil well abandonment has become a problem, due to the inability to predict the spatial distribution of super-k, which channels injection water preferentially to production wells. Super-k prediction would enable the placement of wells such that super-k is avoided, and would enable accurate production forecasts that incorporate the potentially profound effects of super-k.

The proposed super-k characterization method is new in that it explicitly incorporates a model for discrete fracture networks, and predicts the characteristics of the networks using a novel history matching algorithm.

Our model construction approach is founded on the philosophy that a reservoir model that is conditioned to all available data, is the most appropriate one to be used for the prediction of the spatial distribution of super-k, and for production forecasting.

The data are limited to static well log and well core measurements, and to dynamic well production data. The occurrence of super-k is indicated directly with a particular dynamic well production measurement, called flowmeter, and is also weakly correlated with thin, high permeability facies intervals at the wells, themselves correlated to static well log and core measurements.

Our reservoir characterization is accomplished through joint conditioning to well

flowmeter, well performance (well flow rates and pressures) and static data. We achieve joint conditioning through a combined fracture / facies model, in which the static data is honored with the facies model, and the dynamic data is honored predominantly with the fracture model. The dynamic conditioning is achieved through inversion, with a workflow that perturbs discrete fracture network parameters, optimizing the parameters under the minimization of the error between observed and simulated flowmeter response.

Our approach is practical in that a conventional commercial flow simulator suffices for the forward simulation in the workflow, because sources, rather than discretization, are used to model discrete fracture system flow. Furthermore, the use of sources is restricted to the forward simulation, and therefore our algorithm may be used with any discrete fracture or facies model.

2.1 Super-k characterization workflow

The objective of our workflow is the construction of a study area reservoir model that allows for the prediction of super-k spatial distribution, and generates production forecasts that incorporate the dynamic effects of super-k.

Generally, reservoir characterization requires a sound knowledge of reservoir engineering: the working familiarity of the fundamental aspects of the flow of fluids in the reservoir. A first order reservoir model is defined upon definition of the principal plumbing of the reservoir, which is quite often most informed by production data.

2.1.1 Establishing the fundamental reservoir model

The determination of the essential aspects of the super-k phenomenon, and the definition of a fundamental super-k model, are initial workflow components. We have approached this phase through both analytical and numerical routes. The analytical method was one in which fundamental fluid flow concepts were applied toward qualitatively describing the observed data (Chapter 6). Here, the "data" to be replicated were the primary, consistent observations that super-k flow behavior is correlated

strongly with intervals of abnormally high fluid flux, originating from thin zones (less than 20 ft). We have devised a simple, linear, layered flow model that includes a discrete fracture system. This model was constructed in an analytical, synthetic framework, but was constrained to the observed "data". No numerical models were constructed at this point in the workflow. Thus, the basic constituents of our reservoir model was determined: a discrete fracture network (DFN) of height necessarily less than the reservoir thickness (250 ft), which intersects a thin, high permeability layer, itself intersected by a well.

Verification of the fundamental model was accomplished in part, numerically, by a systematic inversion of dynamic data, in an exercise that showed what super-k was not: a facies-only construction (Chapter 6). A training image-based, stochastic simulation algorithm was used to generate multiple facies realizations, conditioned to static and conceptual facies spatial distribution data. No DFN models were included in these early reservoir models. Realizations were input into a flow simulator, and history matching of observed super-k behavior was attempted. Here, it is tacitly assumed that reservoir flow performance, and specifically super-k performance, may be adequately predicted by the knowledge inherent in the training image, and the static data (in this case facies data at the well as derived from well log interpretation and core analysis). The model failed in this prediction after exhausting attempts, thus verifying the need for an additional reservoir component, which we believe is the DFN.

We further employed a numerical model at an early stage in the workflow to address another super-k correlated observation, although not so common, that of time dependency (Appendix D). It has been observed that abnormally high flux from thin zones may decrease anomalously over time, through periods of relatively little apparent change in reservoir boundary conditions. Our approach was to discern the fundamental requirements such behavior imposed on flow, to determine if these characteristics existed in our super-k model, and if not, to decide if they warranted inclusion.

This behavior escaped our understanding in terms of simple analytical models, as, for example, relative permeability effects had been offered as a likely cause, so

we decided to perform numerical flow experiments on a 2D study area cross-section, reservoir model. This proved beneficial in that relative permeability manipulation proved ineffectual, and instead, simple water loading of DFNs through increasing water cuts of injection water, proved to be a plausible cause. We were therefore able to verify that our super-k model, of which DFNs are paramount, was capable of predicting yet another super-k observation.

2.1.2 Transition from the fundamental model to the final production forecasting model

The super-k model as it exists at the initial stages, following discovery through the application of flow concepts, is purely conceptual. The model must then be incorporated into the numerical reservoir model from which production forecasts will be made.

As the super-k conceptual model is composed of DFN and facies, our reservoir model is so composed (Sec. 10.2). Our DFN model is object-based and is combined with a training image-based facies model, which is constructed independently. Various DFN parameters may be perturbed in this model. The DFN model is described in Chapter 9.

Sensitivity studies, in which those attributes of the super-k model we suspect to be decisive, for example DFN length, density, and transmissibility, and DFN proximity to high permeability layers which connect to wells, comprise the next step of the workflow. The analysis is one in which the parameters are perturbed deterministically to gauge their effect on flow simulation results, in one or more wells, under the assumption that the production response in these selected wells are typical. Other DFN parameters are also tested to ensure that the set of key parameters is comprehensive.

The facies portion of the reservoir model is frozen as DFN parameters are perturbed, as we have concluded that, other than the thin facies serving as connections from the DFN to the well, flowmeter response is not sensitive to changes in the spatial distribution of facies, or in the facies petrophysical characteristics, and well pressure

and rate data are controlled principally by regional permeability means.

2.1.3 The general workflow

Our workflow is therefore initiated, and subsequently dominated, by a modeling approach that focuses on the reservoir flow process.

The workflow to construct a super-k predictive, production forecasting reservoir model consists of:

- Construction of a simple, conceptual super-k reservoir model, conditioned to a set of general, but consistently observed well conditions and production responses,
- Construction of a facies model, conditioned to well log and core data,
- Construction of an initial object-based DFN model,
- Combination of the facies and DFN model,
- Determination of key DFN parameters, through deterministic sensitivity studies
- History matching both flowmeter, and well pressure and rate response, in the study area wells, by minimizing the error in simulated and observed production response, through perturbation of key DFN parameters in a stochastic optimization process.

2.2 Thesis highlights

Two new findings were principal to the research summarized here, and deserve a cursory review at the outset.

2.2.1 The construction of a unique super-k model

First, a very concise and elementary mechanism for super-k has been clarified, based on well known flow models. It is the only published super-k model that offers a very

precise accounting of the most commonly observed characteristics of this phenomenon. The main attribute of this model is its simplicity; it is presented in Chapter 6.

The discussion of the model includes an observation that would not surprise any experienced reservoir modeler: super-k, if predicted accurately by this model, is constrained by almost no directly measured static data. Furthermore, the model requires the existence of possibly subseismic discrete fracture systems. Recently interpreted 3D seismic surveys, which we currently have no access to, may therefore not be relevant, except through providing boundary conditions, in the form of Arab-D structure and major fault definitions, for a geomechanical model. We conclude, in Chapter 6, "Therefore, unless the seismic data can predict fracture or fault systems which do not propagate vertically out of the Arab-D, static super-k data for this model will be sparse indeed, and composed mainly of horizontal well intersection data, and rock fracture mechanics model predictions. In regions developed with vertical wells, super-k data will be essentially non-existent. Unfortunately, horizontal wells have only recently been drilled at Ghawar, and in small, localized regions only, and lack of data informing rock fracture mechanics renders such modeling equally difficult." This is a fact, given our model, and We quote it up front because it testifies, in an extreme fashion, why reservoir engineering is unlike any other engineering discipline: we make predictions, from extremely sparse data, of extremely complex structures. Reservoir modeling is driven by hypotheses and assumptions, as our super-k model shows, having been derived without a shred of static data directly verifying the existence of a complete example of such a construction. This is true also, as will be shown, with every super-k model built since the first one[1], published in 1993 by our SA intermediary, Jim Liu.

Data sparsity is derived, as usual, from large well spacing, but is particularly aggravated in this case by geometry: vertical wells do not sample vertical faults and fractures. Well tests have confirmed them however, and recent 3D seismic has predicted faults. Our super-k is more elusive; our DFN geometry is probably subseismic, and our construction favors DFNs with small height, that do not intersect the well. Appealing as our model is regarding simplicity and coherence to observed data, it is in equal part difficult to sample directly. Fortunately, we will benefit from

an acceleration in the effort to characterize DFNs, or in the effort to quantify the flow aspects of these systems in the absence of characterization, as SA reservoir modelers are publicly unanimous (Chapter 5) that *faults and fracture systems are the primary flow elements at Ghawar.*

2.2.2 Another option for fracture flow simulation

Second, we have developed a very simple method of simulating flow in large scale fractures that transport fluids at high flux, over extended distances. We do not discretize them, either in a single or dual grid. We utilize the only remaining option - the very fundamental source term in the governing mass balance equation. This implementation is only the second in the industry, behind Seong Lee's[2] independent development in Chevron's *CHEARS* flow simulator, in 2001. We began the development of this model in 2002, and first presented it in 2003.[3]

Once the source term is disconnected from its traditional utilization in production or injection well models, they are seen to be geometrically unrestrained and accommodating of very fine-scales on coarse grids, and are bound realistically only by computational instability and lack of computation power. But so is discretization. A great appeal in the use of sources is that we can, and do, use a commercial flow simulator, *ECLIPSE,* in our history matching algorithm, which, as we will show in Chapter 5, is not done otherwise for fracture modeling at Ghawar. In fact, this research would not have been possible without a commercial flow simulator. The details of our use of sources is presented in Chapter 7. An analytical and numerical discussion of DFN flow and the use of sources to model it is presented in Chapter 8.

That our history matching algorithm uses a commercial flow simulator, is an advantage toward its acceptance as a bona fide industry tool, a trait in its development for which we have consistently strived. This effort was in part initiated with the transfer of the original *ECLIPSE* flow simulation model from SA (Sec. E.1), and our subsequent hesitation to convert it to a research flow simulator. This undoubtedly would have been ill-advised, since our source model is benefited greatly by the robust convergence properties of *ECLIPSE*'s state-of-the art well model.

The source model maintains the algorithm as industry-ready with another key advantage that discretization models cannot enjoy: we preclude the need for discretization upon the construction of each new reservoir realization. This is a necessity for fracture discretization, the crippling result of which is the imposition of an automatic gridding module, currently yet a research topic, as an element of the history matching algorithm.

Source representation of a DFN is necessarily of lower resolution than that afforded a discretization of the network. This fact does not in the least, however, render an unfavorable comparison, as the discussion in the previous section makes plain that any desire to define Ghawar DFNs at a scale warranting fine discretization, will remain wanting for a considerable period. Discretization is simply less viable under most circumstances, since a reasonably coarse fracture discretization is inferior to the source approach, as explained in Chapter 7, and the source model adequately predicts flow performance, relative to a fine discretization, as shown in Sec. 8.3.3.

Chapter 3

Ghawar Field and the study area

The Ghawar Field is shown in Fig. 3.1 and our study area in Fig. 3.2. The producing region, comprised of several fields, has been active for 65 years. The Ghawar Field, the largest in the region, and largest oil field in the world, has been producing since 1951, and provides half of Saudi Arabia's total oil production capacity.

The sectors of the field, partitioned for operational reasons, are: Ain Dar, Shedgum, Uthmaniyah, Hawiyah, and Haradh, from North to South. Each sector's enormity warrants their reference as "fields" in some of the technical literature. Nevertheless, the sectors are established as parts of a single hydraulic unit.

Our study area is located in the Hawiyah sector.

The Ghawar discovery well was drilled in 1948, in Ain Dar, a northern sector of the field, and subsequent field development proceeded from north to south. *Amazingly, Ghawar is still being developed, with the southern sector, Haradh, scheduled to be fully developed in 2010[4].*

The Ghawar reservoir is the Jurassic Arab-D, a shallow marine carbonate deposit. The field is a 230km-long, 3000km^2, anticlinal trap with a 1300 ft oil column, entirely carbonate with a thickness of 250 ft, sealed by an overlying impermeable anhydrite. A detailed description of Ghawar geology is given in Chapter 4. The Arab-D outcrops (Sec. 4.5) eastward in the Tuwaiq Mountains, near Riyadh, and in Riyadh, the Arab-D is the Riyadh Aquifer, a fresh water source for the city.

The Ghawar Field had produced in excess of 55 billion barrels of oil through 2003,

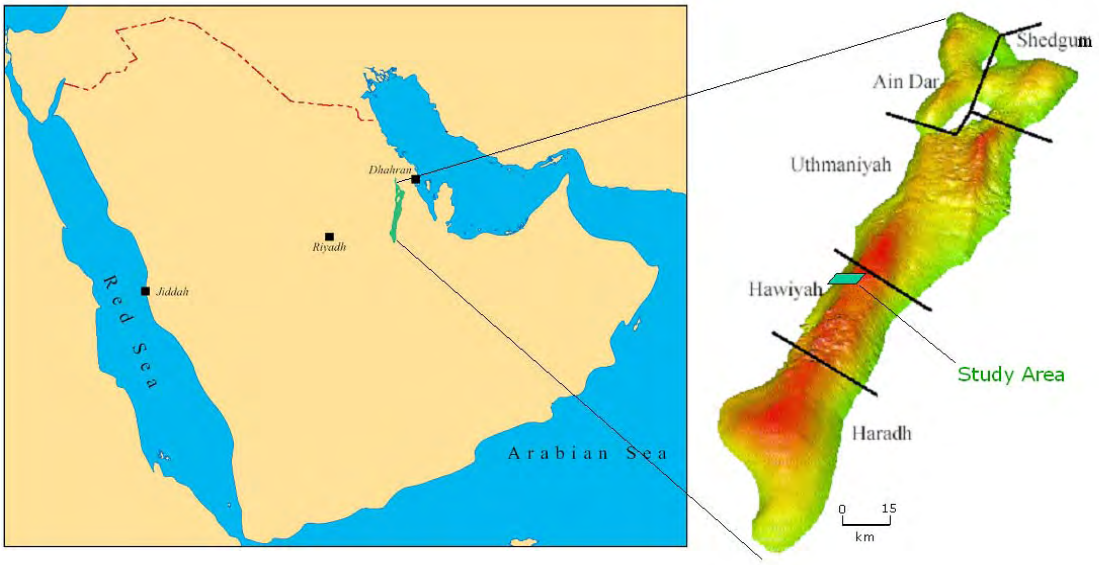

Fig. 3.1: Ghawar Field (Arab-D structure top) and study area location[5], [6]

with maximum production from the field exceeding 5.7 million BOPD (1981)[63], ranking it as the most prolific oil producing field in history. The maximum rate milestone is remarkable given that wells operate under natural lift. Individual well production has exceeded 25000 B/D.

Ghawar is normally pressured. Ghawar oil was discovered highly undersaturated, as low as 55% (p_{BP}/p_i), is moderate to low GOR, $32-36^o$ API gravity, and modeled as a black oil. Producing depths are found at 6350-7650 ft below sea level.

The field has been under secondary recovery, a peripheral water injection scheme providing effective reservoir pressure maintenance and oil sweep, since 1966, beginning with the Uthmaniyah sector. Seawater is the injection water source.

Typically, wells are vertical and completed open hole through the entire Arab-D. Acid washes are used to remove drilling damage, and to clear fines plugging in

water injection wells. Liners and selective perforation are installed in zonal isolation workovers. Horizontal wells have recently been drilled to develop the Uthmaniyah and southern-most Haradh sectors.

Reservoir performance essentially corresponds to that of a three-layer system, with the majority of reserves, pore volume, and flow transmissibility residing in an upper zone, above tighter zones having less pore volume and reserves. Fig. 5.1 presents permeability and porosity vertical distributions typical for the field, and indicates the vertically partitioned nature of the reservoir, as well as the prolific magnitudes of permeability and pore volume characteristic of the field.

The peripheral waterflood is achieving a bottom-up sweep of both reservoir layers, as vertical segregation of the injection water is enabled by sufficient vertical permeability.

The exception to the simple three-layer performance is incurred through the subject of this thesis, high transmissibility DFNs.

3.1 Ghawar reservoir flow simulation

The plethora of super giant fields in Saudi Arabia leaves no question as to the application there of state-of-the-art, multi million cell flow simulators toward the problem of reservoir characterization and production forecasting, with Ghawar being no exception. The concentration of application of massive computing power in this small region is staggering: flow simulation models of 500000 to 10 million cells, with an average of 1.5 million cells, are currently being used in the region, and a projected fifty such multi million cell models will be developed in the next three years[7].

Two such models, described in the literature, have been constructed for full field simulation at Ghawar. Both models are constructed using Saudi Aramco's proprietary flow simulator, POWERS, both employ parallel schemes, and are implemented either on PC clusters, or on a single main frame. One model,[7] a single-grid, 9.6 million cell model, comprises 17 layers, with an average cell size of $250m \times 250m \times 12ft$. This discretization is similar to the cell size of the flow simulation model used in the characterization of our small thesis study area, which is $3km \times 8km$ (cell size

$250m \times 250m \times 4ft$). The model requires only 6.5 hours computing time on 125 processors, for a full history simulation. Another model[8] employs a dual grid, each grid comprised of 2.57 million cells, and requires one day of computing time on 54 processors. This model also is comprised of 17 layers. Super-k is characterized in the fracture grid in this model, in a manner similar to smaller, sector models, described in detail in Sec. 5.4.

3.2 The thesis study area

The study area is located on the western flank of the Hawiyah sector, and adjoins the field's aquifer. It was selected by the operator for our study, and satisfies two main criteria: tractable size for the study , and prevalence of super-k production. It was desirable that the study area be small, with a reasonably small number of wells, given the complexity of the geology, the enigmatic nature of super-k, and the extensive production history to be matched.

The study area, comprising the region in white, is 8 km by 3 km by 250 ft thick. There are 11 wells in the study area, 9 producing wells and 2 water injection wells. The wells are drilled on approximately 1 km spacing, the typical spacing for the Ghawar Field.

Four wells in the study area, one injector and three producers, have been identified as having super-k zones, and are underlined in Fig. 3.2.

Three of the newest wells have little or no production history. The remaining 8 wells, having a significant amount of production data, are numbered in Fig. 3.2.

Production development in our study area began in 1974. Over 25 years of study area well performance history is available. Study area peripheral water injection began in 1976.

3.3 Study area data

SA provided us study area data including well log data from each study area well, core data from one well, 19 flowmeter surveys from various wells, and well performance

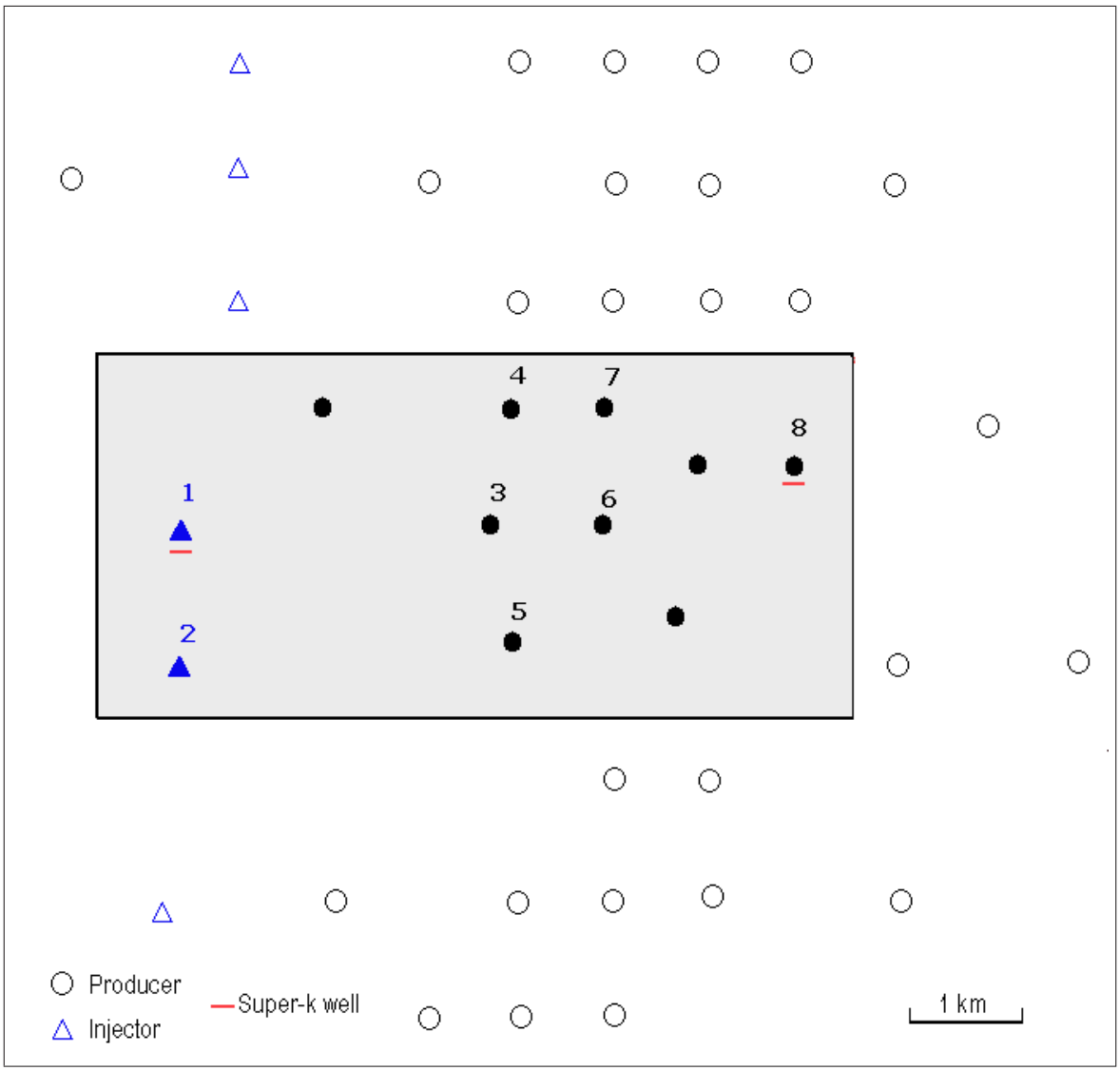

Fig. 3.2: Study area (gray rectangle) well locations

data from all wells. These data are combined as described in Chapter 10. Appendix E presents the data in detail. More specifically, well facies data was generated from a detailed interpretation of the porosity well logs. Also, global facies proportions were inferred for these results.

3.4 Study area reservoir simulation

SA also provided us with a full field Ghawar flow simulation model, which contained a local grid refinement comprised of our study area. This section provides a summary of the simulation of Ghawar study area reservoir performance, using the *ECLIPSE* simulator. The summary includes a description of the full Ghawar Field simulation, and reduction of the full field simulation to the study area only, by use of simulated boundary flux information.

3.4.1 Ghawar full field simulation

The full field simulation predicts 61 years of performance of the Ghawar Field and offset fields that are connected hydraulically, with production from 1996 wells. Ghawar production began in 1951. Peripheral water injection from 738 water injection wells assist aquifer support in the region. Water injection in the region began in 1956, with injection at Ghawar beginning in the mid-1960's. Performance predictions are constrained by quarterly measured hydrocarbon production rates, converted to total liquid reservoir rates, and quarterly measured well water injection rates. Bottomhole well pressures, well water cut, and well GOR are predicted by the simulator.

The full field simulator includes aquifer pressure support, and production from offset fields in communication with the Ghawar Field. Therefore, the discretized area is significantly larger than the producing area of the field. The discretized area is a 433 mile by 595 mile rectangle, with the 20 mile by 140 mile leg-shaped Ghawar Field residing within the larger rectangle. Fig. 3.3 is a map that shows the full discretized region of the full field simulator, with hydrocarbon accumulations shown in green. Ghawar is the elongated, leg-shaped field; the other hydrocarbon accumulations are in hydraulic communication with Ghawar, and thus their depletion rates affect Ghawar reservoir pressure. The remainder of the discretized area is aquifer.

The 2734 wells input into the simulator are developed as shown in Fig. 3.4. Some of the wells simulate production performance of fields offset to Ghawar. Also, edges of Ghawar are developed with peripheral water injection wells (blue). Two of these water injectors are located in the study area.

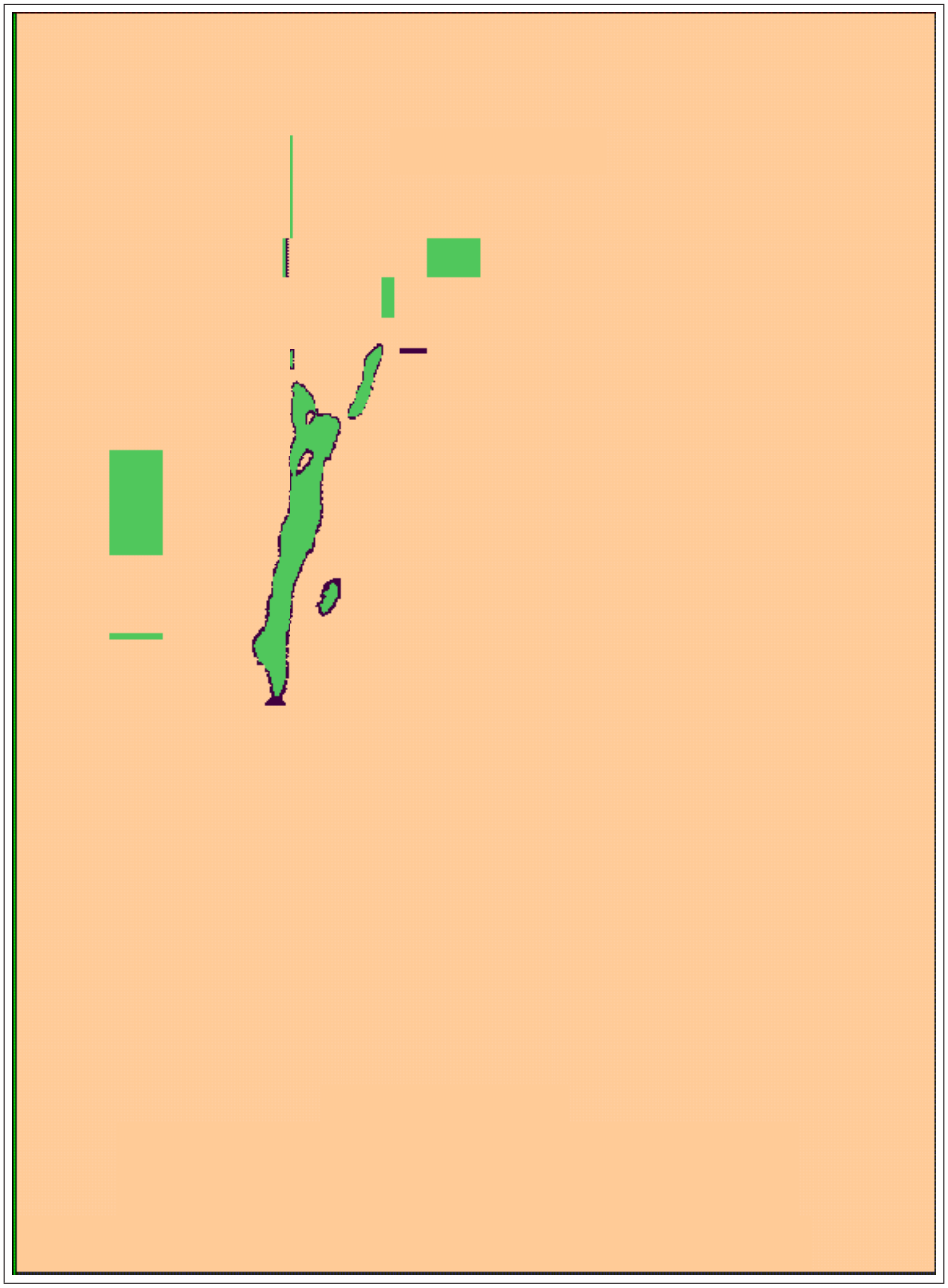

Fig. 3.3: Ghawar full field simulation area

The full field is discretized with a $125 \times 295 \times 1$ grid. Fig. 3.5 shows a part of the full grid. The white area within the outer rectangle is finely gridded with 115 grid lines in the X direction, and 285 grid lines in the Y direction. This finely

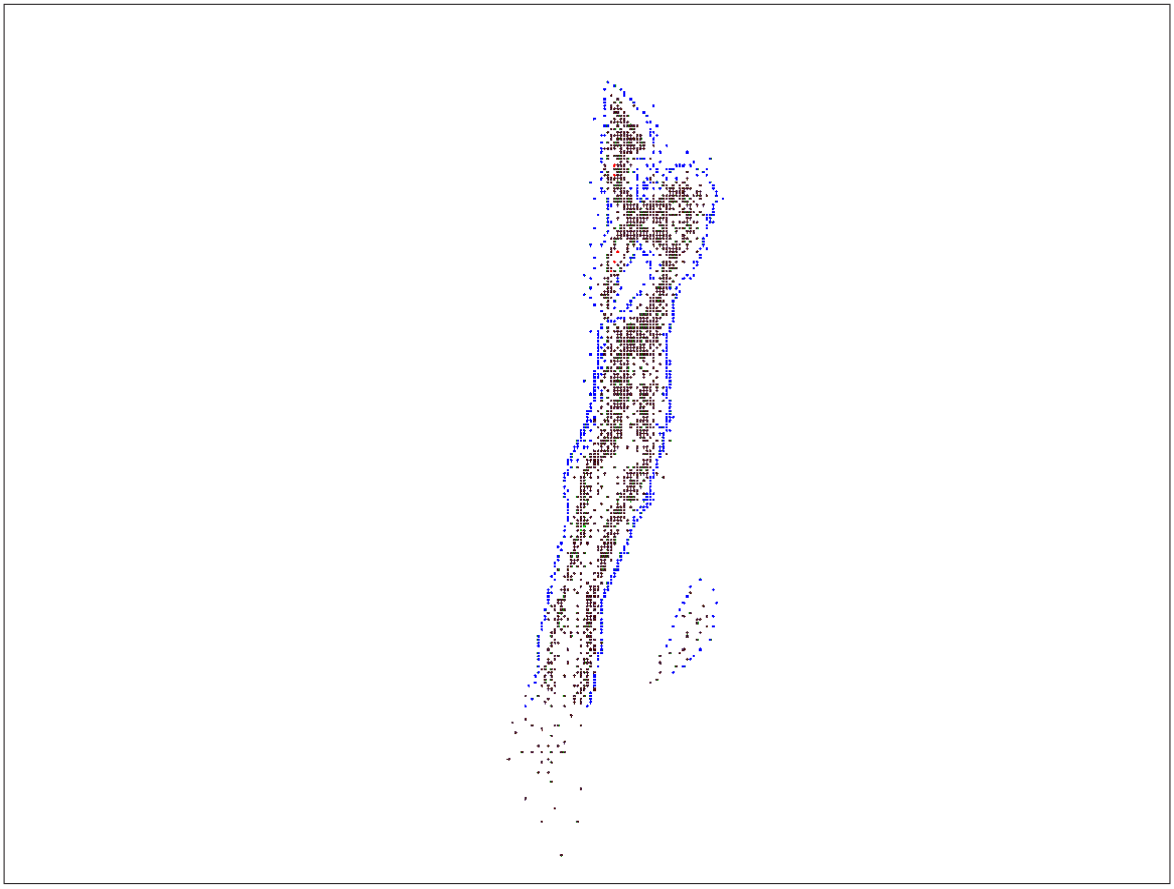

Fig. 3.4: January 2000 Ghawar well development (water injection wells in blue)

gridded area accommodates the Ghawar producing area, and is too intensely gridded to plot relative to the larger grid cell cells shown. Fig. 3.6 is a detailed plot of the finely gridded area containing the Ghawar producing area. The full grid is $697.5km \times 957.5km \times 250ft$.

The areal grid spacing in the fine grid region is 1 km. The finely gridded area containing Ghawar is 115×285 km. The study area is also indicated in Fig. 3.6 and is detailed in Fig. 3.7.

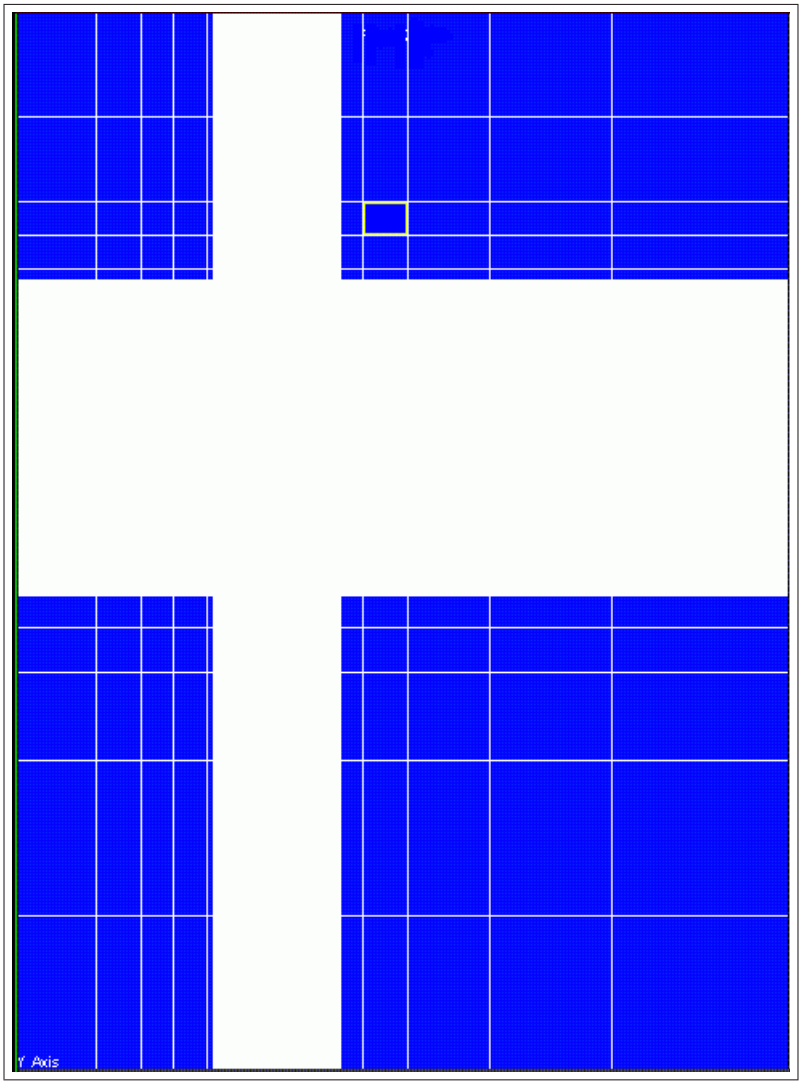

Fig. 3.5: Ghawar coarse grid

3.4.2 The study area

Fig. 3.7 shows the study area and the local grid refinement discretizing its area, in a water saturation map. The map is presented to indicate the location of the aquifer (blue) relative to the study area. The areal refinement replaces an 8×3 grid with a 32×12 grid. The discretization in the Z direction is increased from 1 layer to 180 layers. Production wells (black dots) and injection wells (white triangles) within the study area and in surrounding cells are also shown. Computation within the study

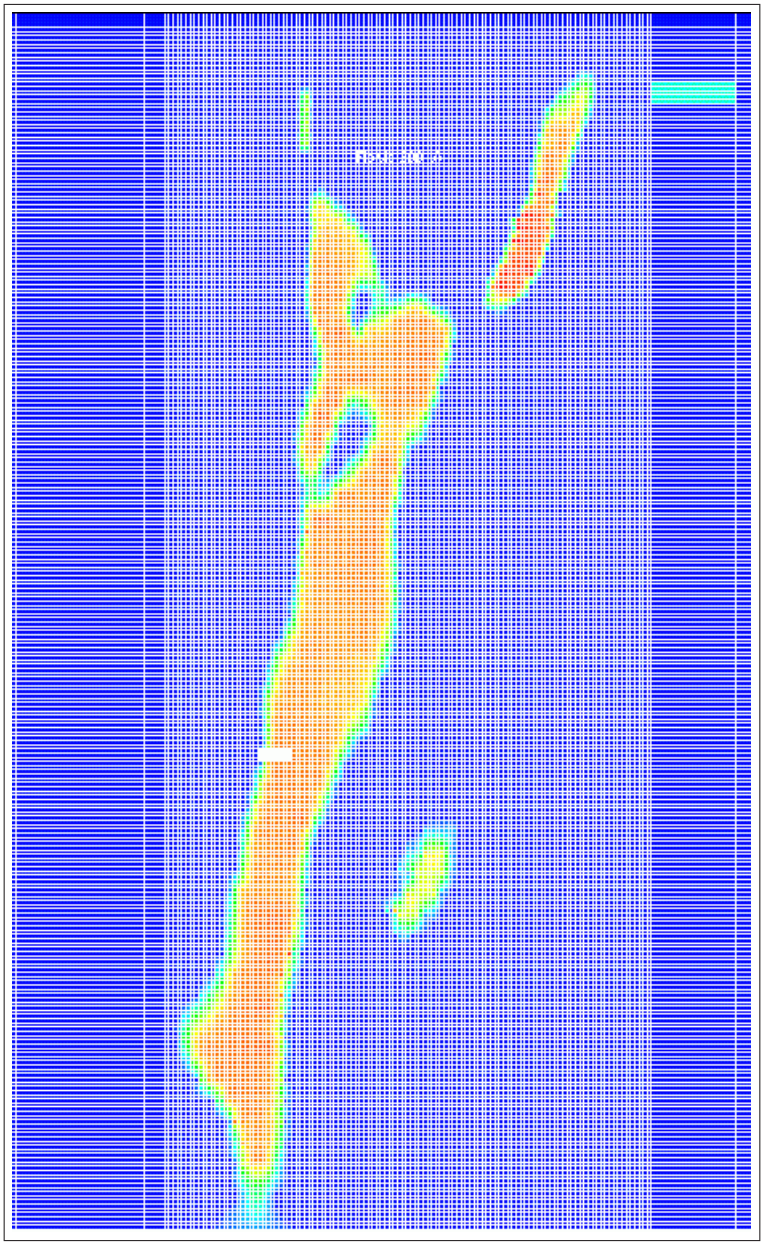

Fig. 3.6: Ghawar full field fine grid

area dominates the simulation, as there are 69120 cells in the study area local grid refinement, and 36851 cells in the coarser grid outside of the study area.

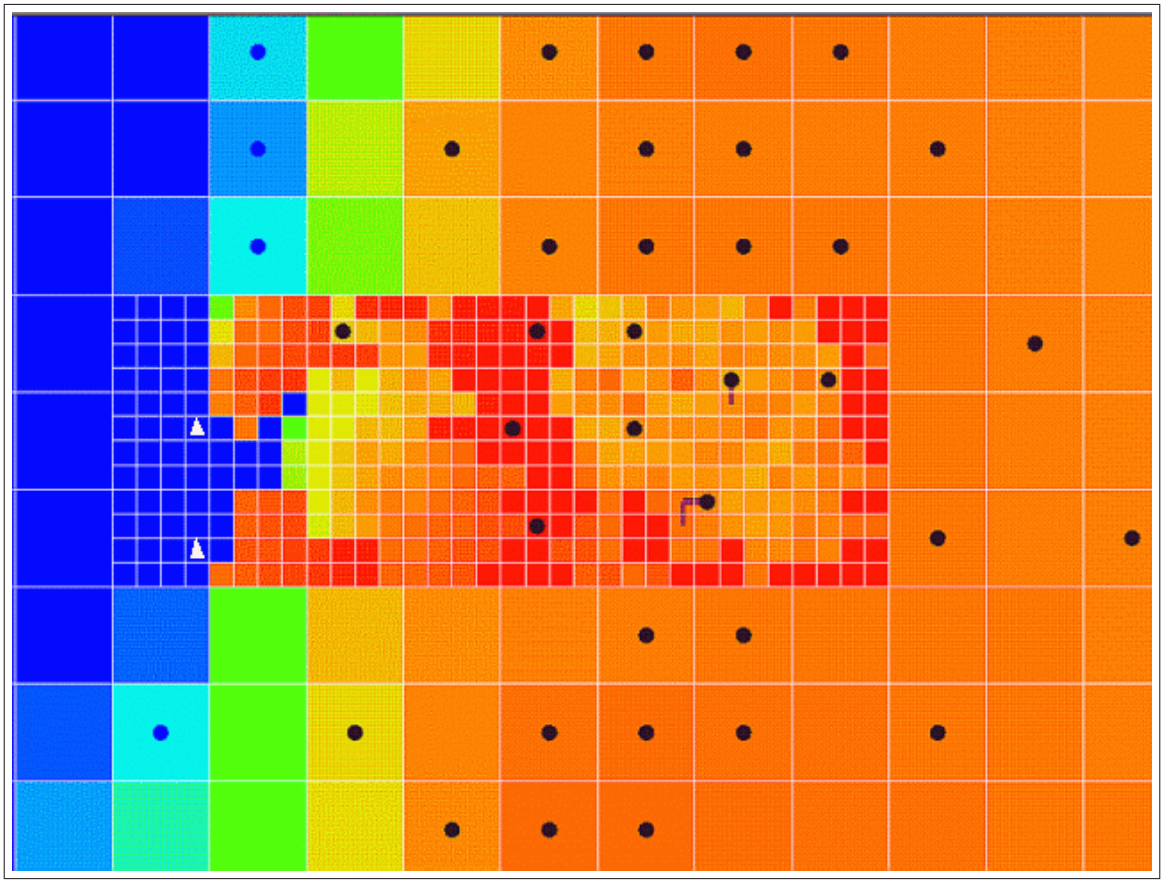

Fig. 3.7: Study area local grid refinement

3.4.3 Simulation runs

The full field simulation of 60 years of history takes approximately 4 hours of CPU time on a 1 GHz, 1 Gb processor. An attempt was made to decrease this runtime by employing the boundary flux option of *ECLIPSE*. This option writes the boundary flux history of the study area to a file which is then used in a subsequent, study area only, simulation. Unfortunately, the run time was not significantly reduced, indicative of the study area's domination of the simulation computation.

The run-time is significantly reduced, however, by the fact that production and injection within the study area did not commence until 1974. Therefore, a restart run beginning at that time is possible, under the assumption that study area reservoir characterization perturbations do not significantly affect the study area boundary flux

history before 1974. This assumption must of course be verified at some reasonable regularity during the course of this study. The combination of utilization of the boundary flux option and the restart option results in a CPU run time of 60 minutes.

3.5 Coarsening of the original model in Z

This study utilized reservoir models and flow simulation models which, like the original models transmitted from SA, and used in a precursor study[30], have the same grid sizes. However, the grid is coarser in the model used in this thesis, having been upscaled vertically to decrease flow simulation computation time. The global cell size is $1km \times 1km \times \tilde{}250ft$; the study area grid cell size is $250m \times 250m \times \tilde{}1.4ft$,

The coarsening of both reservoir and flow models from 180 to 60 layers was performed under the assumption that the loss of resolution accompanying the coarsening would not be detrimental to the modeling of the essential, geologic elements of the reservoir, those comprising super-k, to be described in Chapter 6. Coarsening both grids eliminates the need for upscaling from a fine reservoir grid, to a coarser flow simulation grid, as an element of the super-k characterization workflow.

Flow simulation time, as in many history matching algorithms, dominates the speed of the algorithm. Coarsening the flow simulation grid as described above reduces the flow simulation time by a factor of three. This represents a substantial reduction in time, at little to no expense in maintaining integrity of the geologic model.

Verification that the 60-layer model is equivalent to the 180-layer model is presented in Appendix G.

Chapter 4

Ghawar geology

The geological depositional model for Ghawar is a first order constraint on our Ghawar super-k model, and although we performed no work to further inform Ghawar sedimentary and structure modeling, the depositional model for Ghawar is well developed and accessible. Furthermore, it is anticipated that most readers will find the discussion enlightening, given the paramount importance of the field under discussion. This chapter presents a detailed description of Ghawar geology.

A caveat must be placed here: Ghawar DFN description, although certainly a component of Ghawar geology, is not presented here, simply because very little has been published on the topic. This is due to lack of data, although recently acquired seismic data, some of which is still being processed and interpreted as of this writing, is currently enabling the initiation of detailed Ghawar faulting models.

The hydrocarbon producing region of the Persian Gulf is perhaps the most geologically studied in the world. We have relied on both early and recent region-specific literature, and classic carbonate deposition literature, to gain an understanding of most aspects of the genesis and structure of this vast hydrocarbon system. The most important authors cited in this section include, J.L. Wilson[12],[16], a pioneer of carbonate stratigraphy who conducted extensive early studies in this region, and wrote a definitive AAPG Memoir chapter on the middle shelf environment (and graciously mailed me personal copies of a stratigraphic section of Mexico's Zuloaga Formation); F.O. Meyer[9],[18], formerly with SA, who has proposed recent depositional models of

the Ghawar Arab-D Formation; N. S. Alnaji[14], who wrote a very recent, comprehensive thesis on the geology of this hydrocarbon system; T.S. Albrandt[10], who led the publication of the U.S. Geological Survey's 2000 World Petroleum Assessment; R. Blakey[11], whose web site provided geographic paleontology predictions; and S. Boggs[13], whose textbook described elementary concepts of carbonate deposition and lithology.

4.1 Shelf deposit

The Ghawar Field structure is the largest of several giant anticlines, and the largest of approximately 100 oil fields, some of which are supergiants, associated with a vast, ancient continental shelf carbonate deposit, formed in a single, upper-Jurrasic, inland shallow sea. The deposition that occurred in this sea, at that moment in geologic time, has proved to be the most important in Earth history, accounting for 10% of known worldwide reserves, 290 billion BOE, equivalent to 2/3 of known U.S. reserves[10].

There are no modern depositional analogues, since recent worldwide sea level transgressions are not extensive, nor mature, enough to have developed but thin veneers of carbonate sediment, relative to ancient deposits which have accounted for hundreds of vertical kilometers of deposition, covering vast areas. The most pertinent modern analogue is in fact the only shallow inland sea in the world located in low enough latitudes and with clear enough water to permit carbonate deposition: the Persian (Arabian) Gulf, located only 50 km east of Ghawar. Although deposits in this analogue are not as thick as those of the ancient sea, the depositional processes and elements are similar[12],[13].

The Persian Gulf, as well as a scant few other modern deposits worldwide (West Florida Coast, Florida Bay, The Great Bahama Bank, and Belize / Yucatan), have been studied extensively, providing the only active depositional analogues for the otherwise voluminous ancient carbonate deposits which account for 25% of the geologic record, and one-third of the world's commercial hydrocarbon reservoirs[12],[13].

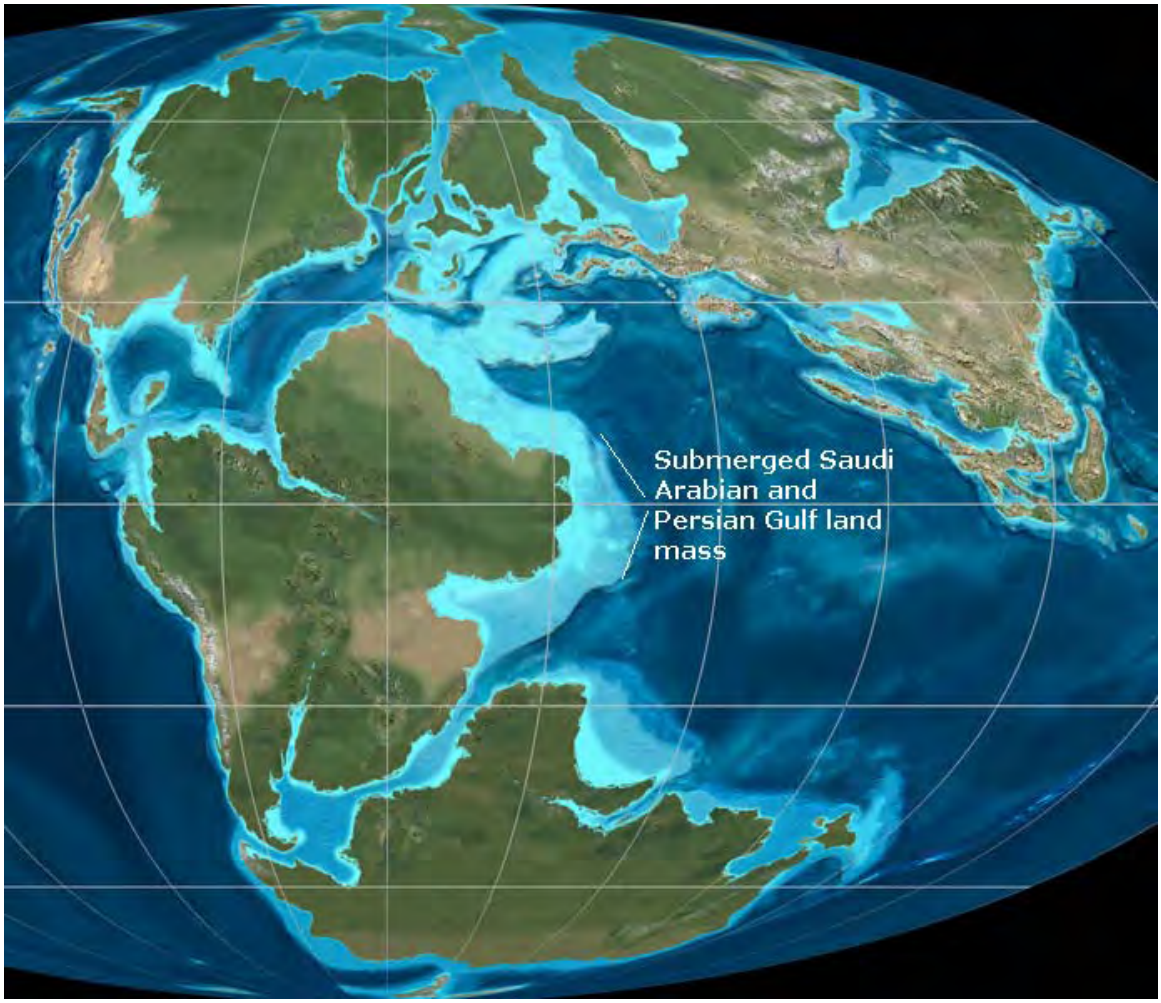

Fig. 4.1: Late Jurassic paleogeographic reconstruction[11]

The reservoir rock for this hydrocarbon system, the 500-800 ft-thick, purely carbonate, Arab Formation, was deposited near the west coast of the present-day Persian Gulf, when Saudi Arabia and the Persian Gulf were attached to Africa, and were shallowly submerged, in Late Jurassic time. The depositional area was the eastern coast of the Arabian Craton, then located at the equator. Fig. 4.1 is a predicted paleogeographic map for this time, and shows the great shallow sea covering Saudi Arabia, then a shelf between the Arabian Shield to the west, and the ancient, Tethys Ocean. Note the prediction of the widespread occurrence of shallow seas bordering many land

masses, the likes of which do not presently exist,[16].

The ancient sea remained until Late Tertiary, although frequent sea level fluctuations, which induced large areal advances and retreats due to the lack of slope on the wide shelf, left regions above sea level at certain periods. These areally extensive advances and retreats created important depositional environments in the generation of the hydrocarbon system that eventually hosted Ghawar.

4.2 Formation of the hydrocarbon system

This ancient shelf underlay a relatively quiet sea which was fairly restricted from circulation with the open ocean, probably due to its great breadth, and the associated cumulative friction effect. The shelf was comprised of, from landward to seaward, the inner shelf (water depths 0 to 10s of meters, and included the tidal and surf zones), the middle shelf (water depths of 10s to 100s of meters, shallow enough to be affected by storms), and the outer shelf, which borders the steep slope to the deep-marine basin. These three partitions are typical of many continental shelves, although this shelf was somewhat unique in that its restriction to the sea was comprised simply of its breadth, as opposed to restriction formed from discrete barriers or rims, such as barrier reefs. In fact, this depositional environment has almost no reef structures[16],[12],[14],[10].

The middle shelf was the environment of the most prolific deposition of reservoir rock, due to the optimum combination of high fluid energy, and availability of carbonate sediment. It was the pathway for currents, and was susceptible to fluid and sediment transport by storms. Its relatively shallow waters were hospitable to the majority of sunlight-seeking marine life, much of which became carbonate sediment. Therefore, the middle shelf was the depositional center for high volumes of coarse carbonate sediment, and so, the best reservoir rock.

Additionally, this shelf, early in its life, contained shallow, intra-shelf basins which formed an essential element of the hydrocarbon system: depositional areas of source rock. Landward of the inner shelf, sabkhas (salt flats) were also present. The occurrence of sabkhas is also essential in this system, as the depositional environment in which evaporite reservoir seals were formed. The occurrence of sabkhas indicates an

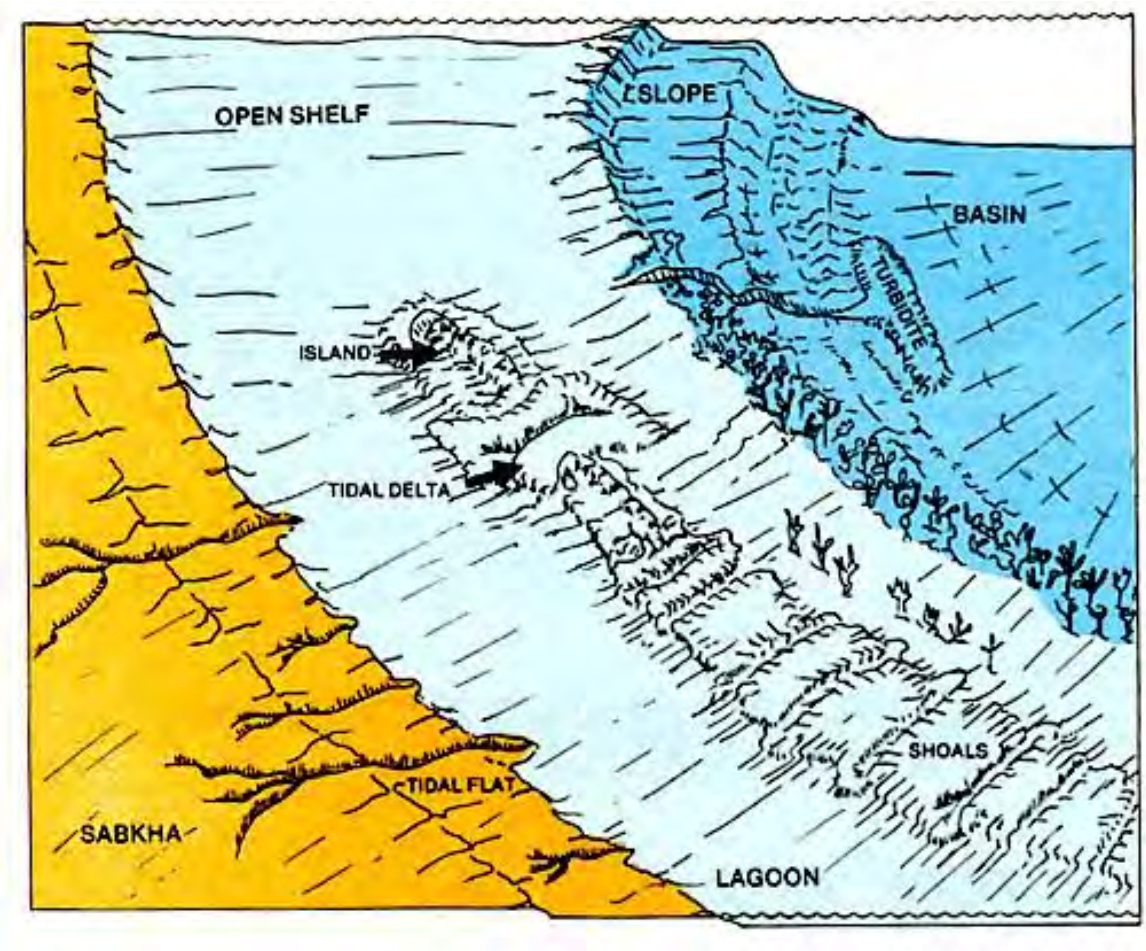

Fig. 4.2: Geometry of the marine shelf in Persian Gulf Late Jurassic[14]

arid climate, similar to that of the modern Persian Gulf. Fig. 4.2 is a diagram showing the principal elements of this shelf; not shown are the intrashellf basins[16],[14],[10].

The ideal reservoir-forming sequence of depositional processes that occurred here began with the formation of the three localized, shallow basins on the shelf, in Early Jurassic. Microscopic marine organisms settled to the bottom of the basins, which contained still waters relative to the higher energy conditions in shallower water outside of the basins. The bottom of the basins were starved of oxygen, so that biogenic ooze, formed from the deposit of the organisms, eventually transformed into thick source rock with total organic content of 4%-6%. Two main deposits, Tuwaiq Mountain and Hanifa Formations, laid down during Middle Jurassic, are the source

rock intervals for the system. These source intervals have thicknesses up to 150m, and 30m, respectively. Fig. 4.3 shows the location of these basins within the shelf, where it is noted that the Arabian Basin contains the source rock for the Ghawar Field, outlined as the elongate field contained entirely within the basin boundary[16],[14].

The basins were filled relatively quickly, with the source rock covered and preserved by shallow marine deposits. Following basin filling by Late Jurassic, the reservoirs of the hydrocarbon system were created by four major, and final, Jurassic sea level transgressions, or cycles. In general, a cycle is a shallowing upward deposit sequence, initiated by a sea level transgression. The cycle may be a full cycle, in which the transgression was large and stable enough to accommodate outer shelf sedimentation, up through sabkha sedimentation. Otherwise, the cycle may be composed of any subset of the full sequence, depending on the depth and longevity of the transgression.

These four transgressions resulted in the deposition of the Arab-D, -C, -B, and -A, in sequence. The magnitude of each successive transgression diminished, so that the initial transgression was the largest. Therefore, the oldest cycle, the Arab-D, became the most prolific reservoir. The sea made a full retreat from the region following these four major transgressions, before reappearing in Early Cretaceous to lay down more shelf sediment[16],[14],[15].

Each of these transgressions was comprised of a classic carbonate upward-shoaling (shallowing) sequence, in which the build-up rate of carbonate sediments continually exceeded sea level rise, thereby producing a shelf of continually shallower water (the common sedimentation process known as aggradation). The lowest cycle, the Arab-D, is comprised of a full cycle, whereas the later cycles, -C, -B, and -A, are partial cycles. That is, over a single geographic area, the inland sea depth shallowed sequentially, during Arab-D deposition, from that associated with the outer shelf, then to that of the middle shelf, to inner shelf, then to tidal flat, and finally to sabkha, all due simply to overwhelming carbonate build-up. The later cycles, -C, -B, and -A, were predominantly inner shelf deposits.

Each transgression cycle thus produced a vertical section of reservoir rock associated with the laterally varying shelf deposits, of which the middle shelf was most important, topped by an extensive evaporite deposit associated with the sabkha[16].

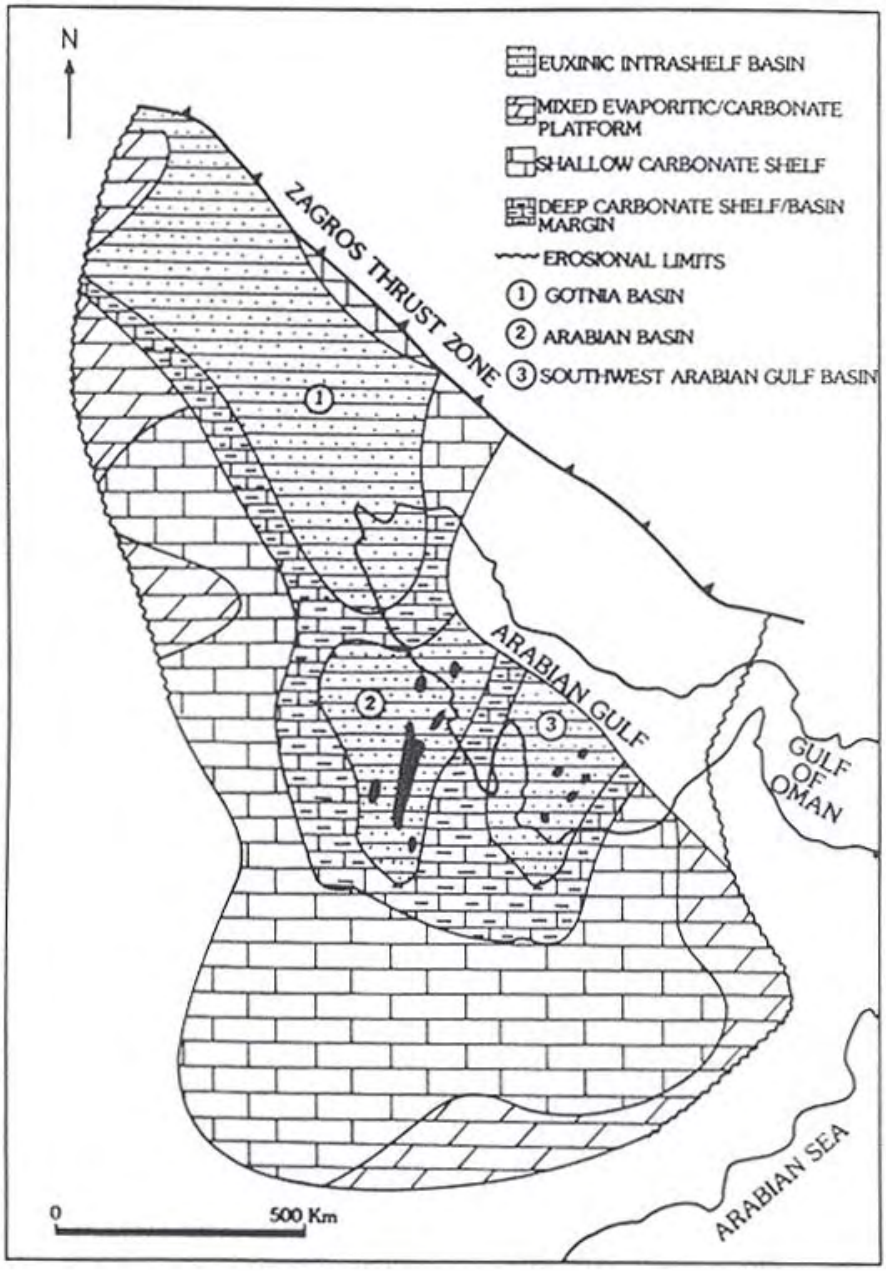

Fig. 4.3: Basins of Persian Gulf hydrocarbon system - source deposition[14], [19], [20]

The relative growth of shelf deposits eventually eclipsed the diminishing magnitudes of sea level transgression, leading to the formation of the remaining necessary hydrocarbon system component, the regional hydrocarbon seal. The inability of

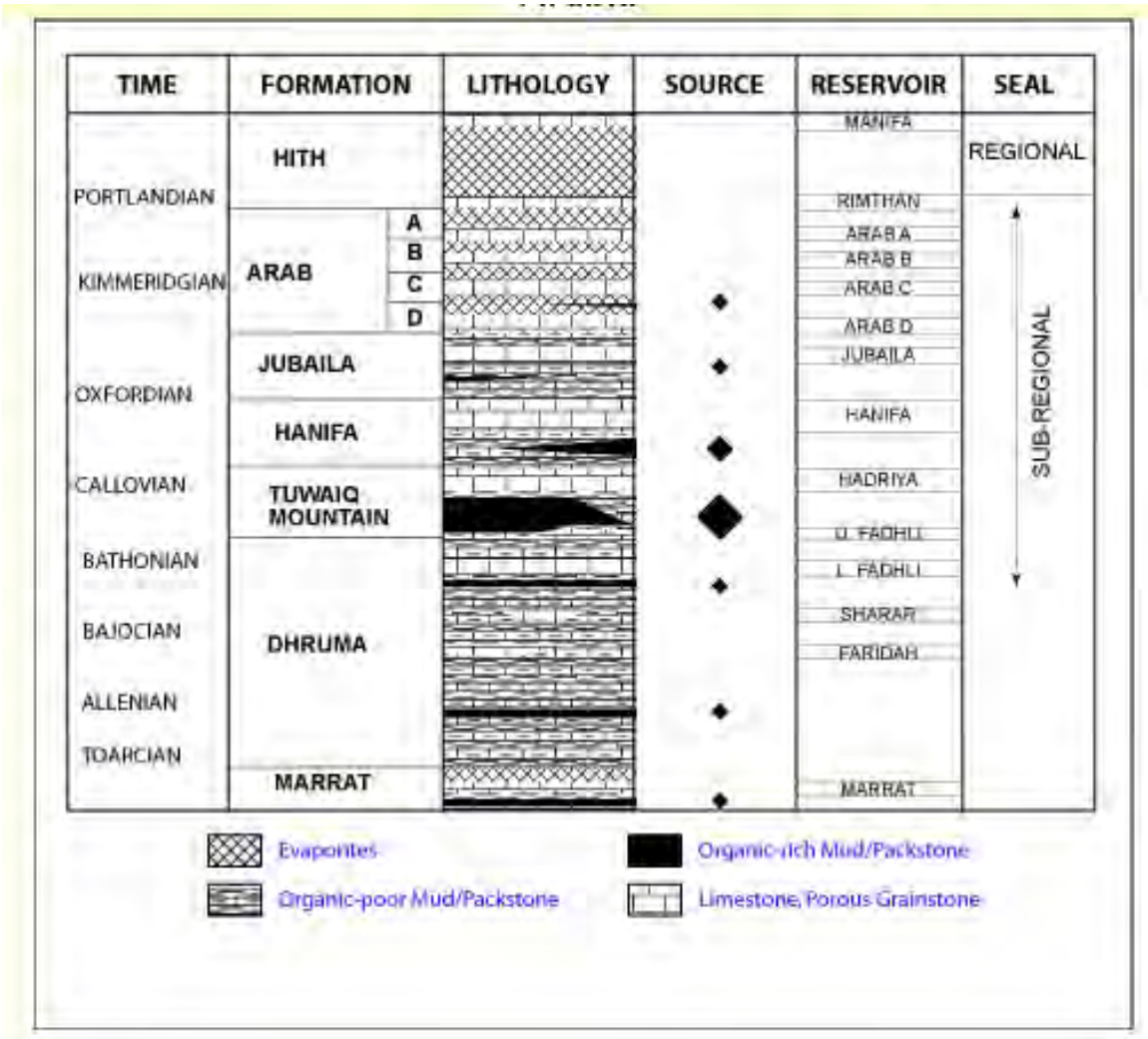

Fig. 4.4: Startigraphic column of the Persuian (Arabian) Gulf Hydrocarbon system[14], [21]

subsequent sea transgressions to flood the carbonate build-up, left the inland sea stranded, eventually producing a great sabkha, leaving a 150m thick, areally extensive gypsum, which eventually altered to an impermeable anhydrite, the Hith Formation[16].

Thus, the hydrocarbon system - source rock, reservoir rock, and cap rock were formed, later to be folded, by uplift of basement fault blocks, or by migrating salt domes, into predominantly anticlinal structural traps, in the Middle to Late Cretaceous. The Ghawar Field, as well as a number of other fields is located on the

predominantly north-south, 250 mile-long En Nala anticlinal axis, formed from basement fault block uplift. [14],[10].

Fig. 4.4 is a stratigraphic column showing the horizons described here, forming the elements of the hydrocarbon system.

The evaporite seals above each Arab cycle proved to serve as local hydrocarbon seals for each reservoir cycle, when, like the regional Hith Formation seal, they transformed by diagenesis to anhydrite. The principal seal for Ghawar is the anhydrite above the Arab-D, for example. Evidently, only the regional Hith anhydrite was effective at providing a global seal, as the deeper anhydrite layers, due to lack of areal continuity and faulting, allowed hydrocarbon migration to the upper-most Arab intervals, in various parts of the region[10].

The local sabkha evaporite seals provided an additional, most critical benefit, however, essentially preserving the great reservoir productivity for which Ghawar is also famous: they provided an impermeable barrier to early migrating waters, which would have precipitated pore-filling calcite in the most permeable reservoir grainstones, thereby decreasing the reservoir permeability from its present, darcy levels[17],[10]. Indeed, lack of cementing is indicated often by poor core recovery of many grainstone intervals at Ghawar[9].

The lowest interval, the Arab-D, became the most prolific reservoir of these four intervals, due to the relative thickness of its middle shelf facies, a depositional environment not as prominent in the later three cycles. The middle shelf environment is a site for the deposition of coarse grains, in high-energy structures such as shoals, beds, and channels, in a similar fashion to high-energy fluvial environments, and having similar sedimentary structures such as crossbedding. The diminishing magnitude of the later three transgressions produced depositions predominantly in the shallower inner shelf, such as tidal deposits, with lesser deposition in the middle shelf[16],[17],[10].

4.3 Arab lithology

The shelf into which the Arab Formation was deposited received virtually no terrigenous material. This shelf carbonate is rather typical, and predominantly composed of

aggregate particles (as are the majority of carbonate deposits, relative to crystalline precipitate formation), generally of skeletal elements of marine fossils, which become the coarser constituents, and of calcareous algae, which generally forms carbonate mud. Coarser particles are also derived from concretions of precipitate around a skeletal nucleus (ooids), or from calcareous fecal pellets (pelloids). Each of these three major coarse particle sources, skeletal fragments or whole skeletons, ooids, and pelloids, are present in the Arab Formation.

The particle size varies in this formation from silt to gravel, and therefore lithologies vary, in increasing grain size, from carbonate mudstone, to wackestone (carbonate mud supported, with some coarse grains), to packstone (coarse grain supported, with some mud), to grainstone (predominantly coarse grains, little to no mud). The coarser rocks, packstones and grainstones, form the most important elements of the Arab reservoirs.

Some of the Arab lithologies were chemically altered, through migration of foreign water, to dolomites. Both permeable crystalline dolomites (sucrosic), and dolomites in which porosity formed from leaching of fossils (vuggy), are important reservoir components in the Arab Formation[16],[14].

4.4 Arab-D depositional model

A close examination of the Arab-D finds much more complexity than suggested with a single, discrete, transgressive sea level event, as described above (Sec. 4.2). Within this transgression, over much of the region, occurred two principal subsequences, and within those, even smaller sequences of sea level fluctuation. Complexity is the rule in geologic formations, as a single formation may be deposited over a vast time span. The Arab-D, for example, was formed over a 5 - 10 million-year interval[9].

The two Arab-D subsequences are divided into five smaller zones, each representing significantly unique depositional transgressions. The upper subsequence is divided, from upper to lower, into zones 1, 2A, and 2B. The lower subsequence is composed of zones 3A and 3B. These zones were identified initially with major porosity pattern changes, and are the principal zonations of the Arab-D[9]. Fig. 4.5 and

Fig. 4.6 show the principal characteristics of the Arab-D zonation. With the exception of Anhydrite, all of the facies described in the "Facies" column of Fig. 4.5 are composed of various carbonate grain types and sizes, and therefore it is not important for the novice to be familiar with specific types. The most notable and informative information in Fig. 4.6 is the grain support (grain to mud ratio) column, which indicates increasing grain support to the left. This column also explicitly indicates dolomites (green)[9].

Fig. 4.6 indicates even finer resolution of heterogeneity than that represented by the five major zonations, showing 17 short intervals (black triangles), each representing a short cycle. These short cycles represent minor sea level fluctuations superimposed onto the two major transgressions. Even finer cycles exist, producing vertical repetitions on the order of feet and inches. The smallest of these cycles are proposed to have been deposited during storms[22].

The two larger sequences, having a boundary at the top of zone 3A, can be distinguished by a mean porosity shift, with the upper sequence (zones 1, 2A, and 2B) having a higher mean porosity than the lower sequence (zones 3A and 3B). The lower sequence represents outer, to middle, to near shelf depositions, with the short cycles indicating that the transition through the sequence was not monotonic, but varied with smaller sea level fluctuations. The upper sequence represents middle-shelf, up to sabkha depositions, again non monotonically due to small water depth fluctuations[9],[22].

The five zonations correspond to mean porosity groupings, resulting from association with a particular depositional environment in either of the two major upward shoaling sequences.

Zone 3B is the deep middle-shelf deposit of the first major Arab-D sea level transgression, and zone 3A is its shallower, middle-shelf deposit. The mean porosity increases from zone 3B to zone 3A, as expected since the shallower water deposit is a higher-energy environment. Zone 3B is also characterized, uniquely among the four other zones, by frequent layers of thin grain deposits. The grain deposits were most likely laid down by storms[9],[22].

The second major Arab-D transgression was similar in magnitude to the first,

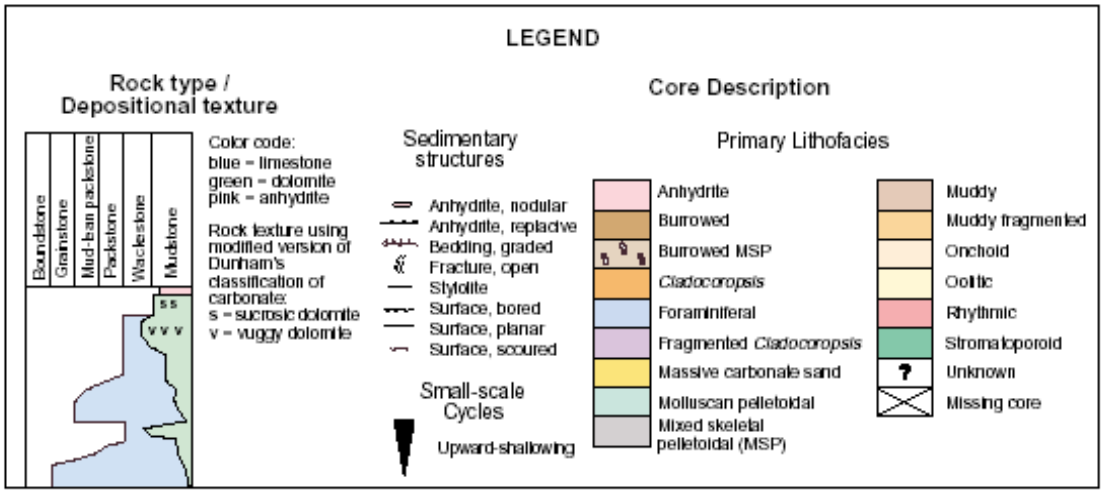

Fig. 4.5: Lithology and facies legend[9]

although with a lower volume of finer, deeper, sediments. Instead, this transgression hosted more, higher-energy middle-shelf deposits. The transgression was also long-lived enough to transition up to sabkha deposits. Zone 2B and 2A are middle shelf deposits, with zone 2A being a generally higher-energy environment, and therefore displaying a higher mean porosity. Zone 1 is an inner-shelf deposit, such as a tidal flat, with associated low mean porosity. This environment then transitions to a sabkha environment, in which the essentially zero porosity Arab-D anhydrite caprock was deposited[22].

Zones 2A and 2B are the most productive zones at Ghawar.

4.4.1 Detailed Arab-D architecture

The complexity of the Arab-D deposit is not restricted to vertical sequencing. Lateral variation of facies is prevalent, shown in a very coarse scale, in Fig. 4.7, a north-south cross section which also shows the relative thicknesses of the five major Arab-D zonations, and the Arab-D anhydrite, over the length of Ghawar[22]. Note that the productive, non-anhydrite intervals of the Arab-D, thin from north to south, as the anhydrite caprock thickens.

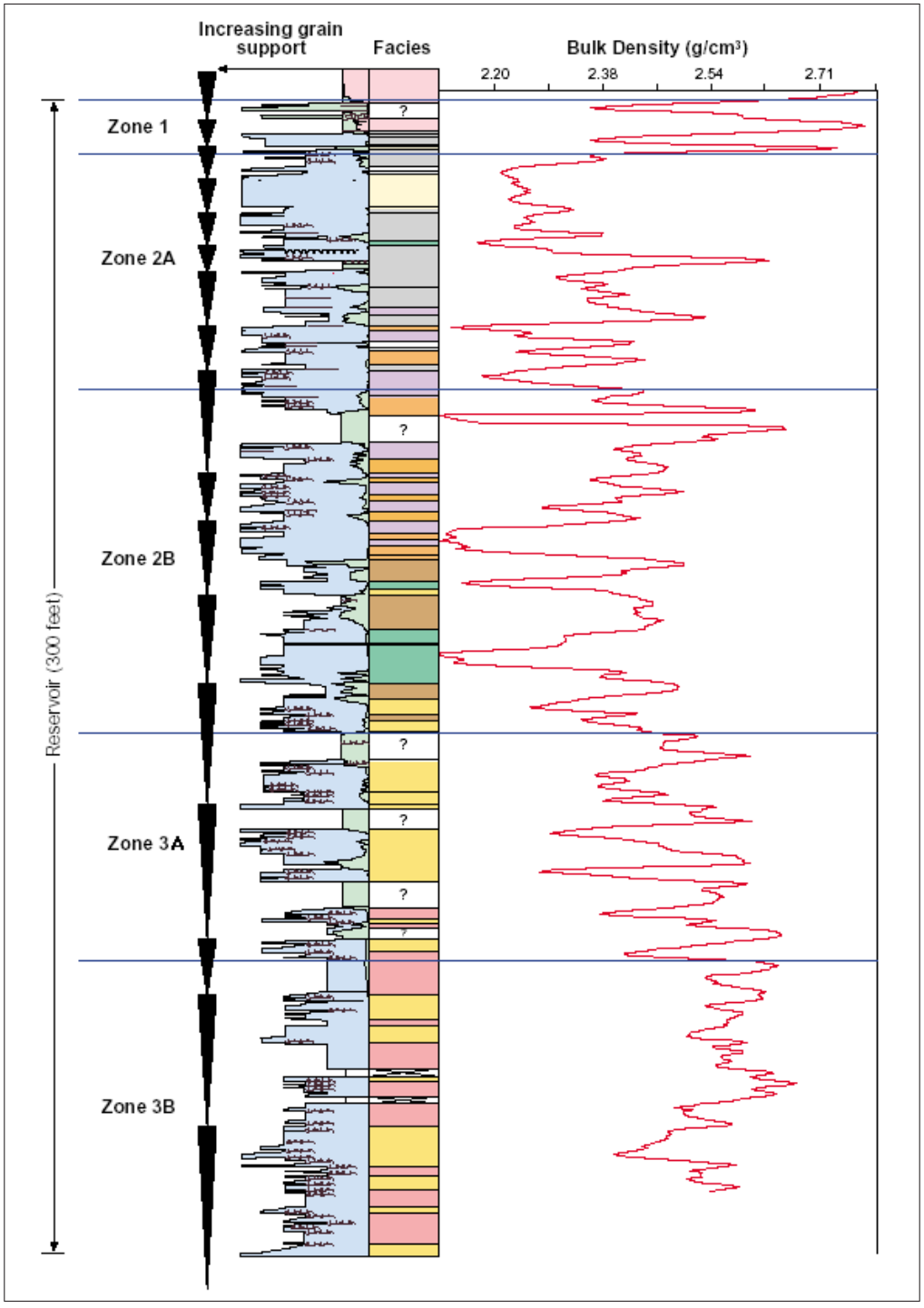

Fig. 4.6: Arab-D lithology, grain size, and density well log pattern[9]

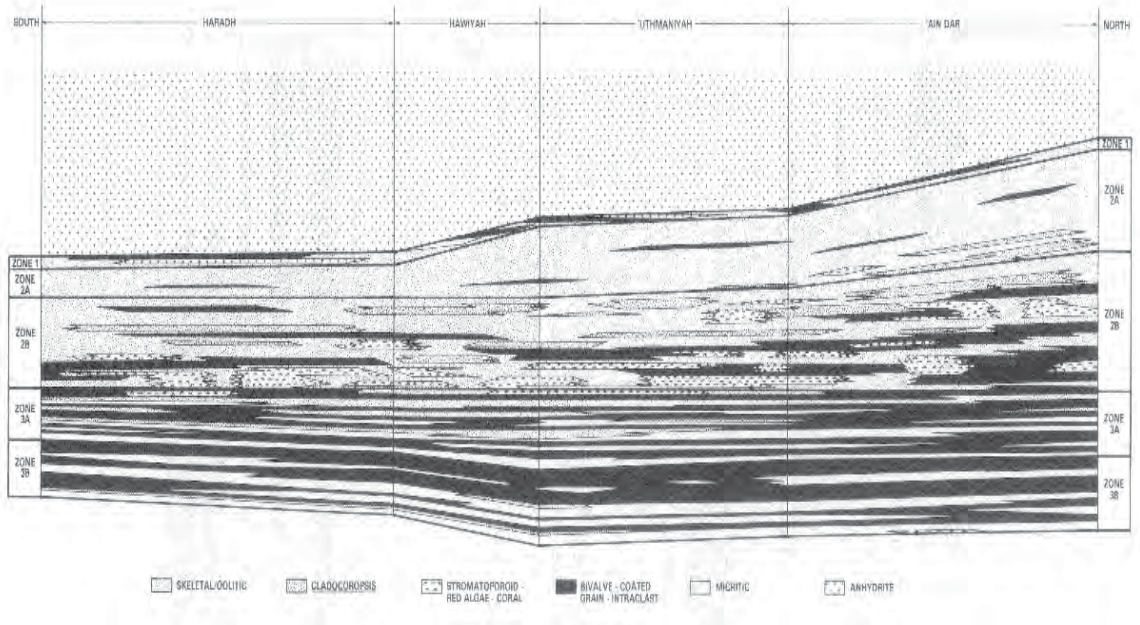

Fig. 4.7: North-south cross-section of Ghawar Arab-D[22]

The facies and grain size descriptions associated with depositional cycles, unfortunately reside at a scale that is too large to quantify important flow barriers needed for effective reservoir flow simulation.

A more detailed model for the Arab-D was proposed recently by Meyer and Price[18], who also later described specific super-k intervals in the Hawiyah sector, in which our study area is located, through an extensive stratigraphic and petrophysical study of super-k core data (Sec. 6.3.2)[9].

This depositional model proposes a more extensive, and complex, set of depositional processes than that which accounts for mere differentiation of grain size associated with the outer, middle, and inner shelf. The proposed processes produced unique geometries of deposits that provide principal controls on flow.

This Arab-D model requires only one major transgressive sea level event, rather than two. The authors propose that the shallow intershelf basins which eventually hosted the hydrocarbon system's source rock, were not entirely filled at the time of Arab-D deposition, as has been previously proposed. Therefore, the shelf base, rather than being topographically featureless, contained areas of depression toward which

shallow shelf sediments could gravitate.

The migration of grain sediments toward the basins, into deeper water, during a single sea level transgression, allows for the formation of the lower major sequence, zones 3A and 3B, previously hypothesized, as described earlier in this section, as having formed in a separate, conventional, earlier cycle.

Most importantly, permeable deposits in zones 3A and 3B, occur in laterally extensive (5 - 24 km) beds that are generally composed of mixtures of various grain types that are also present in the shallower shelf deposits, in zones 2A and 2B, albeit generally segregated by proximity to the shore.

The high-permeability beds in zone 3A are massive, although composed of a vertical series of layered, thin, grain beds up to 2.5 ft thick. Zone 3B also contains thin beds, but layered with thicker mudstones. Here, packages of multiple grain - mud pairs are 5 - 15 ft thick. These packages are referred to as "rhythmic" facies in the zone 3B interval of Fig. 4.5 and Fig. 4.6.

It is hypothesized that these permeable beds, in both zones 3A and 3B, are turbidites, derived from carbonate grains within the shallow shelf, and laid down by storms, very quickly, forming pods of thin grain beds covering a surprisingly large area. The major direction of transport was toward, and into, the intrashelf basins. Part of the turbidite lobe was deposited above the level which is affected by storms (storm base), and the remainder spilled onto the basin, in lower, quieter zones, which are otherwise dominated by finer-grained carbonate muds.

Thus, in this lower region, normal basin-wide deposition of mud, interrupted by sudden and widely distributed turbidite events, produced a laterally extensive, grain-mud layered system in zone 3B.

However, these repeated turbidite events created an aggregate series of purely grain beds, above the storm base, where mud deposition was scarce, to form the massive aggregate grain layers of zone 3A.

Both of these deposits are simply upper and lower components of the same turbidite deposit.

Therefore, the principal flow barriers occur in zone 3B, and are barriers to vertical flow. These barriers certainly exist, since the permeable beds alternate with the

impermeable mudstone.

Permeable deposits in the upper major sequence, particularly in zones 2B and 2A, on the other hand, are laid down as discrete, contiguous, lateral sets, in which the barriers to flow, if they exist, occur at the boundaries of contiguous bodies, and are therefore possible barriers to lateral flow. These deposits occurred from day-to-day processes that tended to transport sediment gradually, and shoreward. Further lateral discrimination in these upper zones was achieved simply by the varying water depth, which differentiated species of shelf organisms. Shelf organisms segregated themselves according to the water depth of their natural habitat. These organisms then became unique skeletal grain facies (see Fig. 4.8), which, except when washed basinward in a storm induced turbidity current, tended to form the local sediment.

The mechanism by which these laterally differentiated deposits, both the deposits of zone 3A and 3B, and the upper zone deposits, formed vertical sequences, is the well known and common depositional process of progradation, whereby the absence of a second sea level transgression precluded further upward carbonate build-up (aggradation) as the sedimentation reached the water surface, and the basin proximity then allowed the carbonate building to migrate instead, basinward. Thus, as the shelf built itself outwards, the deposits of shoreward environments overlaid those of deeper environments. This model is therefore heavily dependent on the hypothesis of the existence of the intershelf basins, as progradation would otherwise not be possible on the flat shelf of the traditional model.

Fig. 4.8 presents the essential components of the model. The upper diagram indicates various grain facies, each associated with a unique water depth and proximity to the shore. The names of the facies are not important, but their association with a particular shelf region is essential to sufficiently constrain the model. Note the lobe-shaped turbidite deposits at the deeper region of the shelf. The lower diagram displays a schematic of the turbidite deposit that migrates into an intershelf basin and thus forms an element of the lower major sequence, zones 3A and 3B. Note from the bottom diagram that over time these turbidites form frequent, thin beds which have a wedge-like cross section, and layering into the basin mudstone.

Although both the traditional model and this model generate the upward shallowing sequences observed in the Arab-D, the key depositional characteristics which favor this model are the lateral extent and thin sequencing of the turbidite lobes in zone 3A, not seen in typical coarse grain intervals of conventional shelf deposits, and the lithology of the turbidite intervals, each having a mixture of all the grain types deposited in the shallower shelf. The traditional model, which hypothesizes two sea level transgressions, attributes the grain-mud sequences of zone 3B to high frequency sea level fluctuations in a middle to outer shelf environment, whereby a brief sea level retreat would leave water depths conducive to middle shelf, grain deposition, and a subsequent small transgression would favor deeper, mud deposition.

4.5 Arab-D outcrop analogies

A potentially valuable set of data for the constraint of our super-k model is analogous outcrop data. A genuinely analogous Arab-D outcrop would help in the understanding of DFN geometries in this reservoir, and also the lithological preferences of these systems. Also, the areal extent of thin grainstone beds, which form the hydrodynamic connection from DFNs to wells, and generate super-k fluxes, is a critical parameter. In our model, these thin grainstone connections are not laterally extensive (see Sec. 6.3.2), and thus preclude the tendency for crossflow from DFNs, thus nullifying the super-k effect.

Models of our super-k elements, DFN structure and distribution, and thin grainstone areal extent, have not been sufficiently constrained from sparse, Arab-D subsurface sampling at Ghawar. It is important, therefore, that if an acceptable outcrop analogy exists, that it be analyzed sufficiently to determine if it may inform our principal super-k elements.

Although it is usually difficult to find an acceptable outcrop analogy for any reservoir under study, especially with consideration to fracture systems, given the complexity and uniqueness of depositional systems, and particularly of fracture systems, two outcrops have been cited as possible Arab-D equivalents.

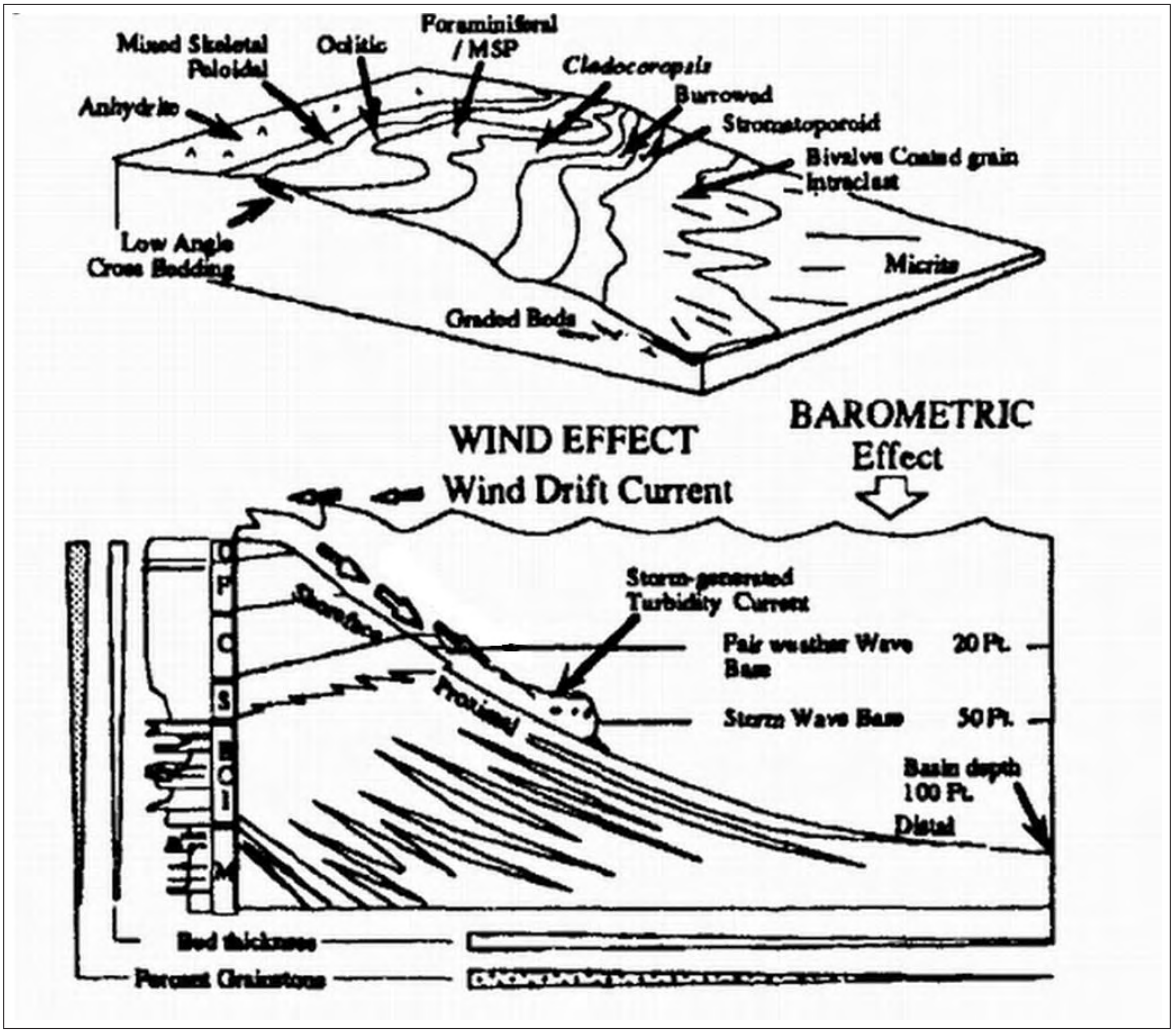

Fig. 4.8: The Arab-D model of Meyer and Price[18]

4.5.1 Arab-D outcrop

One of the possible analogues is the Arab-D itself, where it outcrops in the Tuwaiq Mountains of Central Saudi Arabia, in and near Riyadh, 200km west of Ghawar. All Saudi Arabia shelf deposits, including the Arab Formation, form a shallow monocline, dipping to the east at less than 1^o, extending to central Saudi Arabia. The monocline generally conforms to the surface of deposition, the Precambrian Arabian Shield, which is an igneous dome having an apex in the center of the Arabian peninsula. Some of the dip of the monocline may have also been generated by further uplift of

the Shield, following shelf deposition, however the region was otherwise tectonically very stable over most geologic history[15].

Upper Jurassic formations, such as the Tuwaiq Mountain Formation, the source rock for Ghawar, are steep cliffs in the north-south, 1000km Tuwaiq Mountain outcrop region, forming one of the major topographic features of the Arabian Peninsula. The Arab Formation forms a broad, undulating plain in this area, and is exposed in low, isolated hills, and in steep-walled, dry river beds (wadis). In Riyadh, the Arab-D is the Riyadh Aquifer, at 650ft depth, in which water and piezometric wells have been drilled and logged[24].

Meyer, *et al.*[23] analyzed the lithology and stratigraphy of the Arab-D outcrop in the Tuwaiq Mountains, but did not study, and made no mention, of DFNs. Lithologic comparisons between the outcrop, and the subsurface Arab-D at Ghawar, indicate zones 3A, 2B, 2A, and 1 are represented at the outcrop, and are generally similar to their subsurface equivalents except for significant outcrop thinning due to dissolution of the Arab Formation anhydrites. No structural comparisons were drawn against the Ghawar anticline. East-West lateral facies changes are consistent with the shore to basin shelf model. The lateral extent of individual facies varied from 100 - 500m in some grain intervals in zone 2B, and up to 2km for some thin (5ft thick), sheet-like grain beds in zone 2A. The lateral fluid flow continuity of these facies, was not surmised, nor was the structure and nature of potential fluid flow barriers, discussed[23].

Sharief, *et al.*[24] reported that fracturing was a common diagenetic feature of the Arab-D outcrops in their 5600 km^2 Tuwaiq Mountain study area, which contained Meyer's area as a subset, and also included the city of Riyadh. They also noted that the fractures, as well as intense local slumping, brecciation, and folding, were probably due to dissolution of the anhydrite beds of the Arab Formations. The brecciation, as well as leaching within the Arab Formations, is causing surface failure problems in Riyadh. Approximately 850ft of Arab and Hith anhydrite has dissolved into surface waters that have migrated through this bedrock. The fracturing of the Arab-D is due, largely, to the local deformation caused by anhydrite dissolution. This type of local, severe, deformation would not be present at Ghawar, since anhydrite

dissolution has not occurred there[24].

Further studies of the Arab outcrop have not been found, and therefore, currently, the pertinence of this analogue in informing super-k structure is not defined.

4.5.2 Smackover - Zuloaga

Another possible Arab-D equivalent is the prolific hydrocarbon-productive Smackover Formation of the northern coast of the Gulf of Mexico. The Smackover Formation outcrops as the Zuloaga Formation in Northeast Mexico[24],[16].

The Smackover Formation, like the Arab Formation, was deposited in Late Jurassic. Note in Fig. 4.1, that the southern coast of the U.S. landmass is inundated by an extensive coastal sea. Although this sea was not as large as the ancient Arabian sea that generated Ghawar, it nonetheless covered a broad shelf, and deposited a large volume of carbonate sediment, that was very similar to the Late Jurassic carbonate shelf sediments of Saudi Arabia. Fig. 4.9 is a regional paleogeographical reconstruction of the Late Jurassic, showing the arcuate inland sea of the northern Gulf of Mexico coast, which deposited a 100m stratum of shelf carbonates in a 30-80km wide belt, from Alabama, to Northeast Mexico[16].

The Smackover deposit is a single shelf cycle, identical to an Arab Formation cycle, except much thicker. Anhydrite caprock is present and effective at containing geopressured reservoirs[25] The carbonate grains are composed of more oolites than are the Arab grains.

Oivanki's[26] lithological description of the Zuloaga indicated a noted lack of fossil grain rock, and an abundance of oolitic grain facies. This disparity with the Arab-D, in which the grains are predominantly of fossil origin, may affect fracturing tendencies, if it is determined that oolitic carbonates have significantly different elastic rock properties than do fossil-grained rock.

Oivanki only studied the lithology of the outcrop, and proposed depositional environments for each major lithology, but did not measure areal facies extent, nor did he report on fracturing.

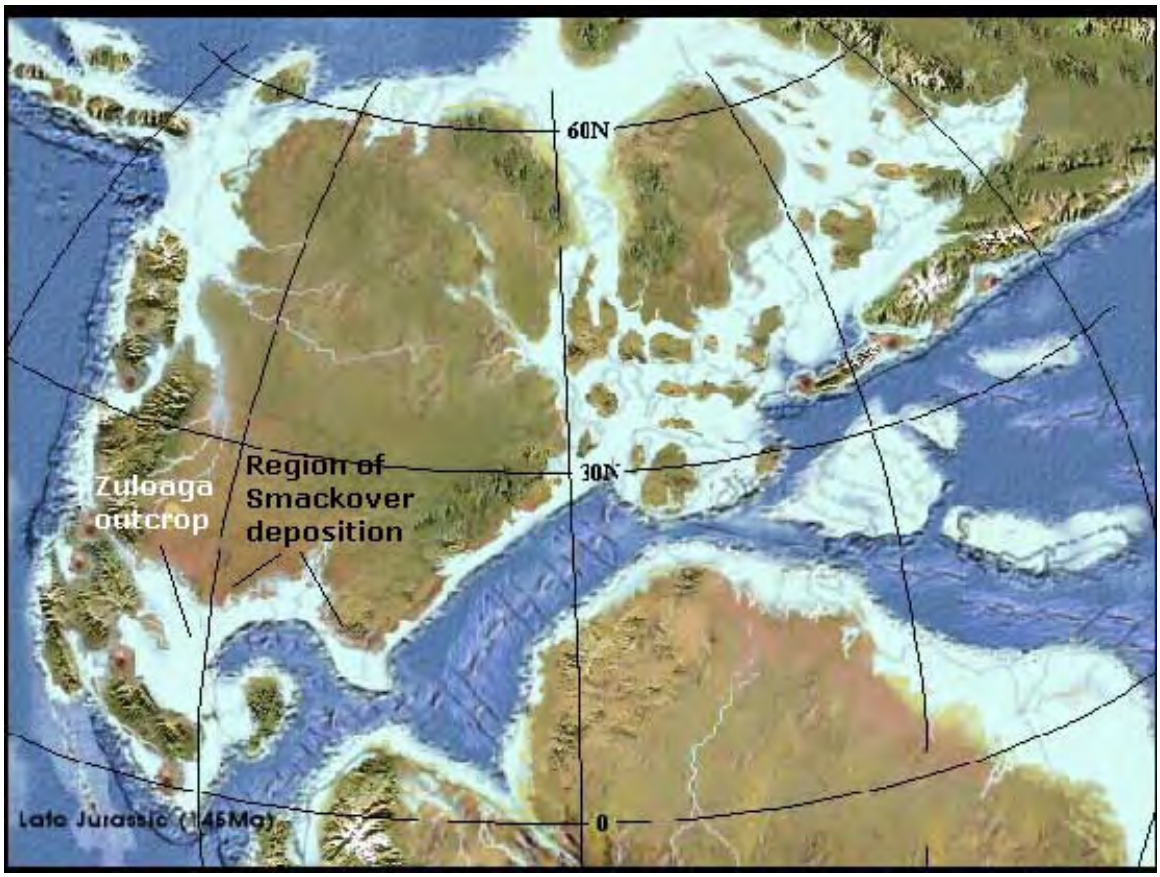

Fig. 4.9: North America Late Jurassic Paleography[11]

Wilson, et al.[27], Meyer and Ward[23], and Longoria[29], analyzed the stratigraphy and lithology of the outcrop. As neither rock fracture geometry nor facies architecture have, until recently, been an objective of studies of the outcrop, no mention is made of these characteristics in these studies.

Zuloaga field trip

Recent correspondence with current investigators[39] of this outcrop indicate an increase in interest in the fracture geometries of the Zuloaga. Reports and photographs of outcrop fracture systems are in transit. Based on further examination of these documents, and further discussion with the investigators, as well as with Prof. Atilla Aydin, Department of Geology, Stanford University, the quality of this analogue in

inferring fracture system geometries in the Arab-D, will be assessed. A favorable determination may result in a field trip to the outcrop, in which documentation of fracture system geometries will be emphasized. Tentatively, the investigators have offered to host the field trip.

Chapter 5

Background and literature review

The study of super-k is approximately 15 years old, and therefore, it is feasible to summarize the entirety of the pertinent reservoir engineering technical literature, comprising some 30 papers. The opportunity to present the complete corpus of a topic is rare indeed.

The general study of the effect of DFNs on well performance is also very limited. Despite a plethora of published research regarding the flux and pressure behavior of reservoirs with hydraulic fractures, that is, those fractures induced at the well for the purposes of well stimulation, there remains very little published on the effect of DFNs, which do not necessarily intersect the well, on well productivity. The whole of published research on the topic of a DFN that conducts fluid may be found, in fact, in three publications[40],[41],[42]. It may be noted that the topic is ripe for investigation, given the importance of DFNs in Ghawar and undoubtedly many other reservoirs, and the paucity of related research. The results of our work in this general topic are presented in Sec. 8.3.3.

The super-k literature may be classed simply by those which describe Ghawar super-k production responses, and those which attempt to simulate the flow in super-k. Unfortunately, there remains a conspicuous absence of super-k models which are consistent with Ghawar lithologic, facies, and DFN models. As will be shown, the predominant approaches to super-k modeling have remained strictly within the confines of high permeability layer or high permeability region models.

Ghawar super-k studies have been region specific, with three Ghawar sector regions spawning all of the studies. These sectors are Shedgum and Uthmaniyah, encompassing the middle and northern parts of the field, and Haradh, in the south.

A note concerning super-k nomenclature is warranted as a preface to the chapter. Much of the early super-k literature, that published prior to the acquisition of 3D seismic data, as well as horizontal well data, through which DFN systems were made evident, attributed the high flux magnitude to various high permeability facies, principally fossil grainstones or vuggy dolomites, and explicitly attached the moniker "stratiform super-k" to those facies in the specific instances where an anomalously high well flux was measured in them. The term "fracture super-k" was given to a high flux interval that was naturally fractured at the well. These terms were standard in the literature (curiously, no specific examples of fracture super-k is reported in the literature, suggesting a minimal occurrence in the field), and were bestowed void of having satisfied specific transmissibility or geometric criteria. We have adopted a very precise model of super-k, comprised of a series: one or more DFNs, and a thin, high permeability zone which intersects a well. Therefore, our application of the label "super-k" is quite different than that of standard usage, as we are invoking, at once, two discrete elements which must have specific characteristics (Chapter 6), rather than one, having ill-defined properties.

This chapter begins with a general discussion of topics related to Ghawar reservoir performance that most informs the study of super-k. This includes the Ghawar waterflood, the effective reservoir heterogeneities in the Arab-D, and the effect of super-k on overall field performance. Thereafter, performance studies are described, organized by Ghawar sector. All of the information presented here originates from the published literature. It is important to present a detailed review of the literature as well as analyses; unlike for broad research topics, the general readership will not be familiar with that which most pertains to an understanding of super-k, the particular reservoir mechanics of the field.

5.1 The Ghawar waterflood

Ghawar was discovered in 1948 normally pressured, although severely undersaturated. Initial average reservoir pressure exceeded 3200 *psia* at 6100 ft subsea. Ghawar oil bubble point pressure varies from approximately 1900 *psia* in the northernmost sector, Ain Dar, to 1700 *psia* in the southernmost Haradh sector[43]. First production occurred in 1951. The fact that a pressure maintenance program was not initiated until 1966 is testimony to the enormity of the field: 15 years of development and production, beginning in the north and proceeding south, occurred prior to significant depletion.

It was apparent that given Ghawar's enormous volume, the aquifer cannot possibly possess a correspondingly large enough volume, theoretically many multiples of the hydrocarbon volume, to affect a minimal pressure support. Therefore, aquifer support enhancement through water injection was chosen to arrest reservoir depletion pressure decline.

The Ghawar waterflood is primarily a pressure maintenance program, given the restriction of water injection wells to the hydrocarbon reservoir periphery, at the intersection of the original OWC with the top surface of the Arab-D, Zone 1, and given that the nearest producing wells are as far as 5 km updip.[44]

Initially, from 1966 to 1973, water injection at Ghawar was gravity fed. Pressured injection began in 1973. The original injection water was sourced from a saline aquifer (5000 *ppm* solids), from wells near Al-Hasa Oasis; seawater (56000 *ppm* solids), from the Persian Gulf, became the primary injection water source in 1978. Further evidence of the field size: production water handling facilities were not installed until 1979, 13 years after the start of water injection. The high productivity of the Arab-D is indicated with well injection rates approaching 100,000 B/D.

5.1.1 General reservoir performance under waterflood

Several references provide insight into the displacement process inferred to be occurring at Ghawar. Despite anomalous response incurred through the presence of DFNs, the principal process that seems to be evident is that of water injection under

essentially vertical equilibrium, segregated flow, in which the water-oil interface is essentially stable, and nearly horizontal (Sec. 5.4.1). The Arab-D reservoir, despite its cyclical depositional history (Chapter 4), apparently benefits from a relatively high level of isotropy, although not complete, but of sufficient magnitude to allow vertical equilibrium flow.

The lithologic and facies heterogeneities of the reservoir, however, play a significant role in the distribution of super-k (Chapter 6), and affect injection conformance, the vertical uniformity of waterflood front velocity in the reservoir. Nevertheless, regarding general waterflood performance, with super-k response noted as a conspicuous aberration, the Arab-D responds as a relatively isotropic three-layer system, rather than as a heavily stratified, no crossflow system.

The three layer nature of the Arab-D is seen in comparisons of permeability and porosity distributions among vertical zonations of the reservoir. A general summary is shown in Fig. 5.1, which presents core permeability, core and well log porosity, and core lithology from a well in the Uthmaniyah Sector.[45] The data were collected from 224 ft of core, in which 428 plug samples, obtained at 6 $in.$ intervals, were analyzed to obtain porosity and permeability measurements. Additionally, 153 irregularly spaced plugs were sampled for lithology descriptions.

The vertical zonation indicated, corresponds to the standard (Sec. 4.4), although some additional subsets are described which are specific to this well and generally not recognized, as lateral heterogeneity prevents field wide zonation of this precision.

The layered nature of the Arab-D is seen in the disparate permeability means of Zone 2A, 2B, and 3. The mean porosity does not vary significantly between the upper layers, however a significantly lower porosity mean characterizes Zone 3. Zone 2A is undoubtedly the most important layer, having a high pore volume and the highest permeability. Table 5.1 summarizes the data, by zone, and by major lithology. The lithology categories in Table 5.1 and in Fig. 5.1 are described in Sec. 4.3.

Recognition of the layered aspect of the Arab-D has provoked at least one major reservoir management initiative: the drilling of horizontal wells in Zone 3 to increase well productivity.[46],[51]

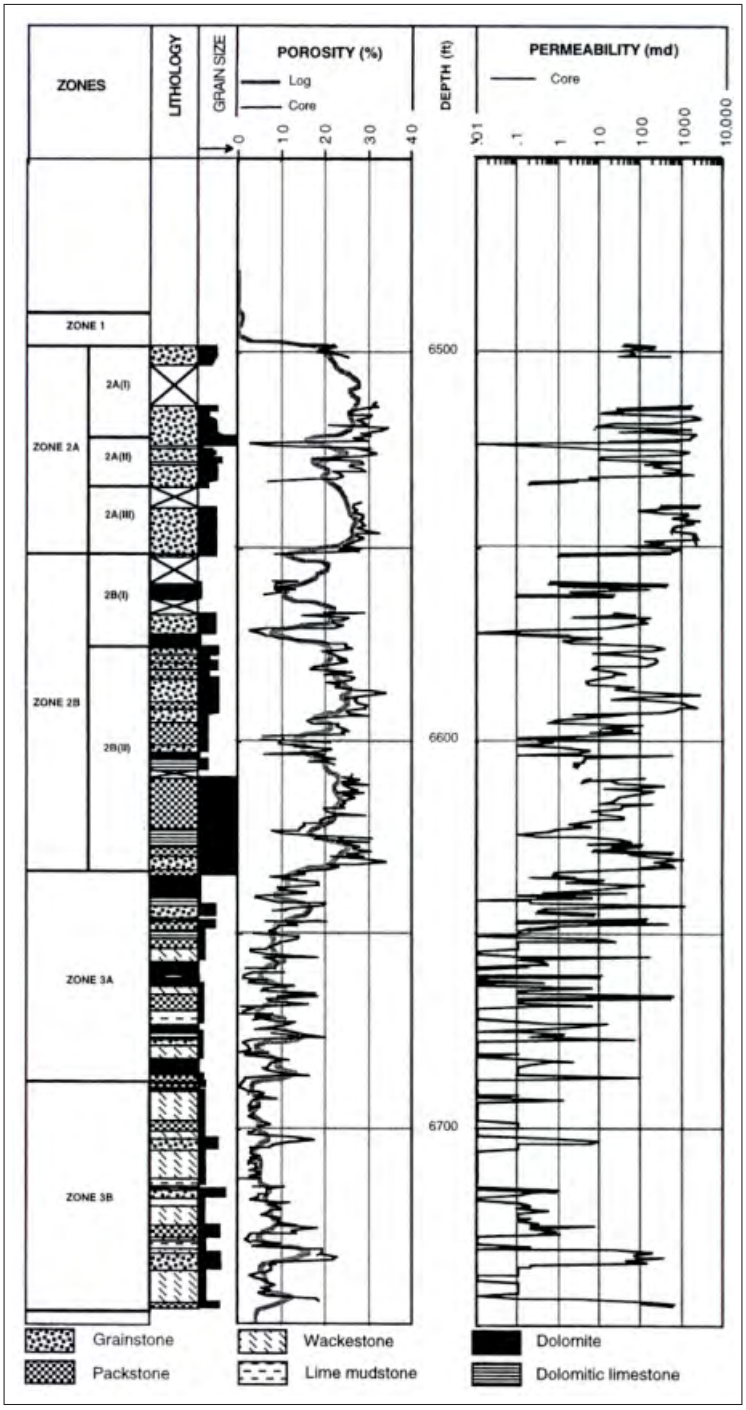

Fig. 5.1: Typical Arab-D permeability and porosity vertical distribution[45]

Table 5.1: Typical Arab-D permeability and porosity statistics[45]

	Total	2A(I)	2A(II)	2A(III)	2B(I)	2B(II)	3A	3B	Grain	Grain-Mud	Mud
Max ϕ %	34	34	31	32	29	34	21	22	32	29	19
Mean ϕ	15	26	23	27	14	22	9	7	26	16	9
Median ϕ	14	27	27	27	11	23	8	5	27	17	8
Max k md	2687	2687	1851	2547	444	2512	1077	621	2687	198	118
Mean k	179	645	383	1024	48	163	33	14	507	26	4
Median k	3	172	123	607	3	24	0.2	0.1	372	5	0.2

Conformance of injection water, which generally enters the entire openhole interval of the Arab-D, is certainly decreased by the contrast in mean permeability and porosity of the three layers. Since the flux over any gross layer is proportional to the mean permeability, it may be estimated that Zone 2A takes nine pore volumes of injected water for every two pore volumes taken by Zone 2B, and for every one pore volume taken by Zone 3, computed directly from the permeability and porosity values in Table 5.1. Zone 2 (A and B) will take approximately seven pore volumes of water for every pore volume taken in Zone 3.

Vertical equilibrium

Reports of the Shedgum[44] and Uthmaniyah[46] waterfloods indicate an effectively bottom-up sweep. Indeed, vertical equilibrium, segregated flow may be expected in the Arab-D, as the oil-water transition zone is short due to the high average permeability of the reservoir, and the gravity number, N_G, is most likely very low:

$$N_G = \frac{q_w \mu_w}{0.001127 \triangle \gamma d a k_v},$$

where q_w is the well water injection rate, B/D, μ_w is injection water viscosity, cp, $\triangle\gamma$ is the specific weight difference between oil and water, psi/ft, k_v is vertical permeability, md, d is the distance between injector and producer, and a is the distance between injectors, both in ft. N_G is essentially the ratio of the time required for water to travel the span of the reservoir thickness, under the force of gravity, to the time required to travel lateral length L under the viscous pressure drop. Gravity equilibrium is

favored when $N_G < 1$.

Given 1 km injector spacing, the injection rate corresponding to $N_G = 1$, is,

$$q_w = 1515 k_v \frac{d}{a}.$$

The ratio d/a may vary at Ghawar from 2/1, which corresponds to that of the closest injector/producer pairs in the field, to 17/1, corresponding to the farthest distance injection water will travel to a producer.

Consider a maximum well rate $q_w = 100000\ B/D$. Using the values of permeability and layer thicknesses from Table 5.1 and Fig. 5.1, the distribution of injection water rate into zones 2A, 2B, and 3, will be 75000, 20000, and 5000 B/D, resp. The range of values of k_v corresponding to these rates and the bounds on d/a specified above, are for each layer,

$$2A: \quad 3 < k_v < 25,$$

$$2B: \quad 0.8 < k_v < 7,$$

$$3: \quad 0.2 < k_v < 1.6,$$

Comparing the upper values of each range to the mean permeabilities given in Table 5.1, it is seen that a k_v/k ratio of 0.07 suffices to allow a balance between gravity and viscous forces in each layer, at a maximum water injection rate, where k is the lateral permeability. Larger values of k_v/k, and smaller injection rates q_w favor vertical equilibrium flow. So, vertical equilibrium is definitely plausible in each of the three Arab-D layers.

The waterflood at Shedgum has been shown to be in vertical equilibrium.[44] Furthermore, no evidence of three separate, field wide water-oil contacts at Shedgum has been reported, although local exceptions exist (Sec. 5.2.2). A deduction may be made, at the least, that Arab-D vertical permeability is significant at Shedgum, and that vertical heterogeneity is not significant, that is, there are few vertical permeability barriers in the reservoir that have significant lateral extent.

Lake[47] defines a criterion for vertical equilibrium as such,

$$\frac{d}{h}\left(\frac{k_v}{k}\right)^{0.5} > 10,$$

where h is the reservoir thickness. Thus, given the values for d specified above, $(2km < d < 17km)$, and the Arab-D thickness of 250 ft,

$$0.002 < \frac{k_v}{k} < 0.14.$$

Therefore, over the scale of 17 km, a k_v/k ratio of 0.002 suffices for the vertical equilibrium condition, and over 2 km, a ratio of 0.14 suffices. Ratios larger than these further favor vertical equilibrium.

The water-oil interface is stable under certain conditions, and if not, water will tend to underrun the oil, forming a curved interface, although vertical equilibrium governs flow in this case also. The tendency for instability of the water-oil interface is dependent on the mobility ratio, M,

$$M = \frac{k_v \mu_o}{k \mu_w},$$

and to a parameter related to N_G, G,

$$G = \frac{0.001127 \triangle \gamma k_v a h \sin\theta}{q_w \mu_w}.$$

where θ is the dip of the Arab-D, measured from horizontal. Stability of the interface occurs when $G > M - 1$. Thus, a favorable mobility ratio, $M < 1$, is sufficient to stabilize the interface. Given that k_v and k contrast is probably more significant than the viscosity contrast, the interface is most likely stable.

The dip of the oil-water interface, β, may be estimated by[47],

$$\frac{\tan\beta}{\tan\theta} = \frac{G - (M-1)}{G}.$$

Ghawar structure dip, θ, at the flanks, is approximately 15^o[5]. Given the layer rates corresponding to $q_w = 100000$ B/D, and the layer ranges of k_v, derived above for $N_G = 1$, the range of G for the layers is, assuming unity μ_o/μ_w,

$$0.001 < G < .01$$

Thus, for small k_v/k, as occurs in this example, given the large lateral permeability of the Arab-D, β may be much larger than θ. It has been shown[44], however, that the flood front is fairly horizontal, indicating that k_v is sufficiently large. Therefore, further evidence that vertical permeability barriers are not prevalent or effective in the Arab-D, may reside in the observation of a relatively flat waterflood interface.

Isotropy induced by DFNs The presence of vertical DFNs of high conductivity which intersect a large portion of the productive interval, favors vertical equilibrium flow, and may be a basis for the observed bottom up sweep of the Arab-D. A conductive DFN may have an extremely high k_v magnitude, and thus $N_G << 1$. Segregated flow within the DFN may induce such flow in the adjoining reservoir region (5.4.2). A high density of vertically extensive, conductive DFNs, therefore increases the degree of isotropy. Recent seismic data[5] indicates extensive faulting in the Arab-D. Faults resolved with seismic data may be of sufficiently large scale to penetrate a significant thickness of the Arab-D. Therefore, the degree of isotropy may be high in the densely faulted regions of the reservoir, favoring vertical equilibrium flow there.

5.1.2 Waterflood design and operation, and super-k

Ghawar waterflood design is principal in two respects with regard to super-k phenomenon. First, water injection well spacing is tight relative to distances to producing wells, and second, evidence is prevalent that water injection wells operate above reservoir fracture pressure.

Chapter 8 provides a description of the effect of a DFN on well performance, given various line drive pattern geometries of an injection well - production well pair. The numerical study indicates that DFN flow may profoundly affect well performance in long, thin line drive patterns, particularly if the DFN is in close proximity to either an injection or production well. It will be shown here that indeed these conditions exist at Ghawar, manifested through injection well spacing, and injection well hydraulic

fracturing.

Fig. 3.2 shows the injection and production well development in the region of the study area, in January, 2000. The injection well spacing, relative to the distance between injection wells and the nearest producing wells (black), is slightly less than 1:3. The relative injector/producer distance for the field, in general, varies from 1:2 to 1:6. Detailed, local maps, presenting an accurate distribution of wells, indicate ratios predominantly 1:8 in some regions(Sec. 5.4.2), and a maximum approaching 1:10.

The earliest paper in the super-k literature contains perhaps the most important data regarding the mechanics of super-k, that of measured stimulated well responses in Ghawar water injection wells, indicating hydraulic fracturing. Brown, *et al.*[48] analyzed pressure fall-off test data obtained in 1979 from all injection wells, approximately 110, in the Uthmaniyah sector. The average well skin factors computed from these tests, classed by region, were $-4.7 < s < -3.5$, without any mention of well stimulation programs or procedures. Later authors[49] indicated that the negative skin effect was attributable to the slightly acidic pH, 6.5, of the injection water, at that time sourced from a saline aquifer. This is highly doubtful, as negative skins of this magnitude correspond to an effective increase in well radius by a factor exceeding 100 (a factor e^{-s}). Furthermore, an acid of pH 6.5 corresponds, for example, to an HCl solution of 1.1×10^{-6} weight %. Therefore, it is highly unlikely the injection wells would attain such measured magnitudes of stimulation from a weak acidization effect. Hydraulic fracturing is a more plausible hypothesis for the large negative skin values.

Azeemuddin, *et al.*[50] reported fracture gradients computed from step rate tests in eight Ghawar injection wells. The locations of the wells were not reported. The fracture gradients varied from 0.6 to 0.7 psi/ft. Given an injection water gradient of 0.435 psi/ft, and an injection depth of 7000 ft, wellhead injection pressures of 1200 $psia$ to 1900 $psia$, minimum, correspond to formation fracture pressures.

Injection wellhead pressure data have not been reported, although bottomhole data are available. Of course, prior to the initiation of powered injection, in 1973, the wellhead injection pressure was zero $psig$, and thus it is doubtful that hydraulic

fracturing pressures were ever attained in injection wells. Correlation between the onset of powered injection and high negative skin effect in injection wells cannot be established because no skin data is available for the gravity feed injection period.

Nonetheless, powered injection appears to be a sufficient condition for high negative skins in injection wells, through analysis of step rate and pressure falloff tests. Fig. 5.2 displays well performance plots for a typical well in the eight well study of Azeemuddin.

It is noted most importantly, that the skin effect (center left plot) is initially negative, approximately -5, consistent with the findings of Brown.*[48]* The initial negative skin most likely associates with a hydraulic fracture, as justified above. Thereafter, the well is damaged, until 1992, when it is stimulated, to a -7 skin, and no longer indicates any tendency for damage. The positive skins of the interim period 1983-1991 are attributed to fines plugging, which was a documented field wide injectivity reduction phenomenon that prompted deliberate mitigation in 1984.[49]

Note, profoundly, that the final stimulation in well injectivity did not coincide with a stimulation treatment, as had previous decreases in skin, and that the final stimulation appears to be the most enduring. The previous, documented stimulation treatments were acidizations to remove fines plugging from contaminated injection water. The authors attribute the final stimulation to well hydraulic fracturing, concomitant with an increase in injection wellhead pressures, upon installation of high pressure injection well headers in the field beginning in 1989. Note that the increase in well productivity indicated in the center left plot, coincides with the increase in flowing bottomhole pressure, bottom left plot, which incidentally corresponds to a gradient of approximately 0.78 psi/ft, exceeding the formation fracture pressure gradient. It must be noted that a formal hydraulic fracturing procedure was not implemented on these wells, and in fact no mention of such operations exist in the literature.

The nature of the perm-thickness (kh) plot in Fig. 5.2 is indeed interesting, if not slightly perplexing. The increase in kh is associated with the final well stimulation, and the increase in injection pressure in 1992. Thus, a change in the reservoir *system* is indicated, with the new system comprised of a higher transmissibility. The authors

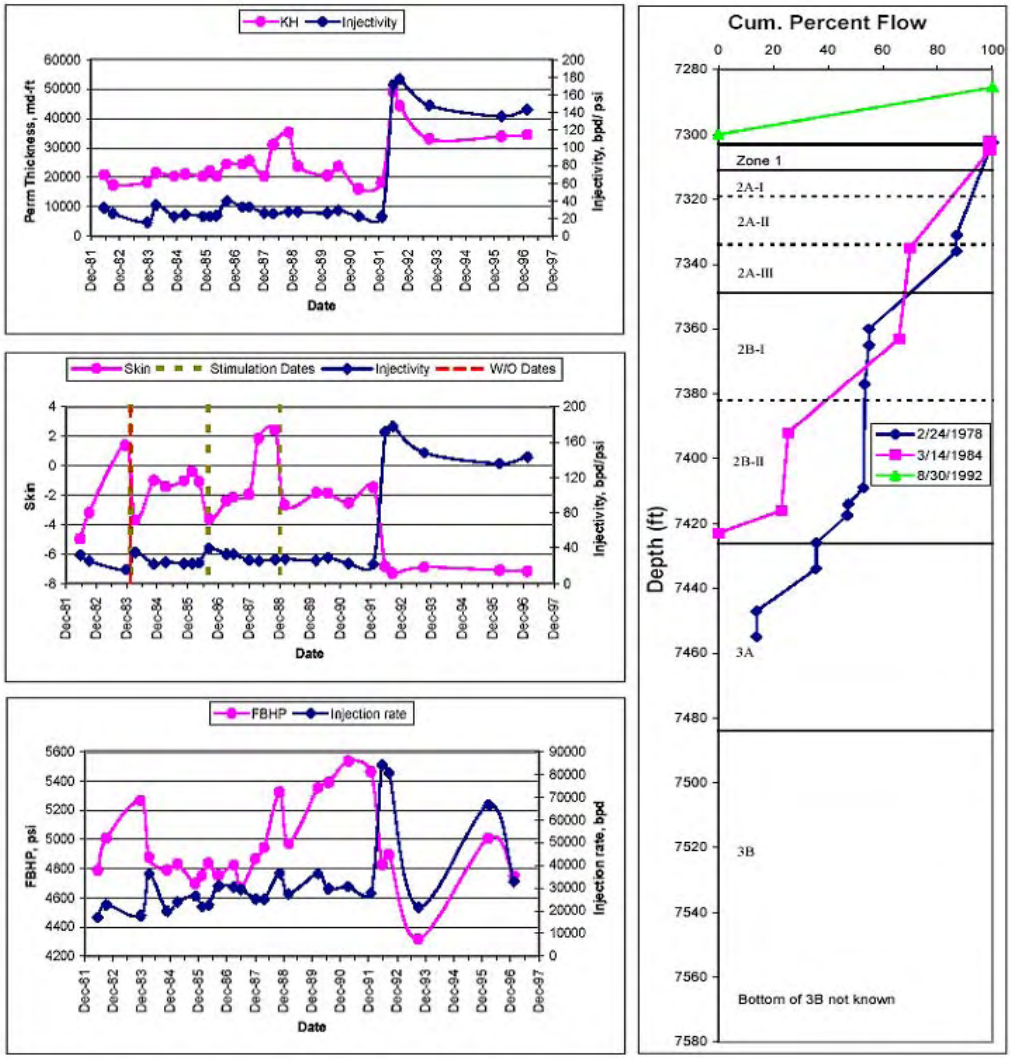

Fig. 5.2: Injection well performance example: pressure, injectivity, and flowmeter plots[50]

hypothesize, quite plausibly, that the system change is one associated with a linkage to a higher transmissibility region, via the hydraulic fracture. The flowmeter plot, right, corroborates their hypothesis, as the 1992 profile indicates 100% of injection water entering a 15 ft interval above Zone 1, compared to the injection interval indicated in prior surveys in 1978 and 1984, comprised of the Arab-D productive interval (note

that the Arab-D zonation of Saner and Sahin,[45] Fig. 5.1, is presented). The 1992 injection interval is essentially a non-productive interval. *Therefore, the stimulated, increased transmissibility well response of this period occurs in a thin, non-reservoir interval.* Thus, it is plausible, if not necessary, that the well is both fractured into the interval, *and* linked to a reservoir system having a transmissibility that exceeds the transmissibility of the entire Arab-D interval intersected by the well. It is not unusual that a fracture would form at the top of the producing interval, as that is the location of highest difference between injection and fracturing pressure in the open hole. It is noted that many occurrences of super-k have been reported in the top of Zone 2A, and that a slight depth correction to the 1992 flowmeter profile would place the high flux injection interval there.

The hydraulic fracture(s) created initially, yielding a -5 skin in 1982, occurred in one or more intervals in Zones 1,2 and 3, whereas the hydraulic fracture created in 1992 did not enter these zones, as inferred from the flowmeter plot, right.

A transmissibility increase may have also occurred initially, in 1982, due to the induced hydraulic fracturing of that period, although this cannot be confirmed without pre-injection performance data. Whether or not the initial hydraulic fracturing intersected a higher transmissibility system, the induced fracturing of 1992 evidently intersected a more prolific system.

The new transmissibility system could be either a high transmissibility facies region not intersected by the well, or a DFN system. The data favor the DFN system hypothesis. The permeability of the proposed facies region must exceed the mean well permeability by a factor 10, representing the ratio of the thicknesses of the pre-1992 injection interval to that of the 1992 interval. Furthermore, the facies region would have to be laterally extensive, since the increased kh persists into a steady state flow condition, evidenced by 6 years of history, 1992-1997.

Note also that the reservoir system, post 1992, does not appear to be a constant, but exhibits a decrease in kh, coincidental with a decrease in injection pressure and rate. We hypothesize a rate dependent kh resulting from the diminution of fracture apertures upon injection pressure reduction, such that fracture conductivities are reduced globally, or complete portions of the DFN system become inaccessible to

fluid flow at some threshold injection pressures. It is difficult to propose a model comprised of well linkage to a facies region, that would predict a rate dependent kh.

The significance of hydraulic fractures in water injection wells is profound, in that the proximity of DFNs to either producing wells or injection wells is a critical parameter of the super-k effect, as is demonstrated in Sec. 8.3.3. Although the distance from a DFN to a producing well is most probably non-zero, as Ghawar producing wells are not hydraulically fractured, and well data indicates no prevalence of natural DFN intersections to these wells, direct hydraulic links to DFNs from injection wells are possible through injection induced well fractures. Among the systems studied in Sec. 8.3.3, we investigate this specific system, composed of a DFN connected to an injection well, but not to a producing well.

5.2 Heterogeneity and anisotropy effects

Although the Arab-D performs in a gross sense as a bottom-up waterflood, spatial variation of facies and DFNs significantly affect specific well performance. The most problematic example, the subject of this thesis, is water breakthrough in thin, productive intervals. Another conspicuous example is the performance of horizontal wells which intersect DFNs, and subsequent local, high flux flow from the intersection interval, sometimes accompanied by immediate water breakthrough.

Generally, the complications in Ghawar well performance, attributable to reservoir heterogeneity and anisotropy, prevalent in the literature, may be reduced to two phenomenon: differential depletion, and water overriding oil. The super-k well response is an example of water overriding oil. Aspects of the important heterogeneity of the Arab-D, relative to flow, may be characterized by the production responses manifest in these two performance anomalies.

5.2.1 Differential depletion

Differential depletion is manifest in zone thieving, that is depleted intervals in wells that become sinks for production in the well, after it has exited other, productive

intervals, decreasing the total well production. The diversion of production, or *backflow*, is maximized during a well shut in, and has been observed in wells at Ghawar.

Thieving is not a recognized widespread problem currently at Ghawar, as thief zones do not appear to be common. However, thieving is a mature field bane, so its significance will increase. The reservoir heterogeneity informed by differential depletion is one not at all unexpected in the Arab-D. It simply indicates a region of the reservoir that is partially or completely hydraulically isolated, and is differentiated from the adjoining reservoir in its flow and storage properties. The implications of differential depletion, relative to heterogeneity can be analytically derived. The pressure depletion rate, R, of a bounded reservoir region may be related as such,

$$R \propto \frac{kh}{\mu}\left(\frac{1}{\phi c V}\right),$$

where the usual definitions apply, c is the system compressibility, and V is the bulk volume of the closed region. This expression, otherwise known as diffusivity, is simply the ratio of the productivity of the region, to it's producible fluid volume. Comparing the depletion rates, R_1 and R_2 of two bounded regions producing the same fluid type, the depletion ratio is,

$$\frac{R_1}{R_2} = \frac{k_1 h_1}{k_2 h_2}\left(\frac{\phi_2 V_2}{\phi_1 V_1}\right).$$

Furthermore, if the regions are of relatively constant thickness, such that $V = Ah$, then the equation is further simplified,

$$\frac{R_1}{R_2} = \frac{k_1}{k_2}\left(\frac{\phi_2 A_2}{\phi_1 A_1}\right),$$

Thus, differential depletion, $R_1/R_2 \neq 1$, occurs only in isolated regions having contrasting diffusivities. Practically, the production response incurred by differential depletion, backflow, is correlated only to important heterogeneities; extreme heterogeneities, $R_1 >> R_2$, or homogeneity, $R_1 = R_2$, do not elicit a significant backflow response. For example, an interval of extremely small volume, although depleting

quickly, is also repressured quickly, resulting in diminishing backflow rates. An interval of extremely low permeability depletes very slowly, but also backflows at a small rate. Both cases indicate reservoirs of little economic importance. Thus, problematic backflow indicates two or more important regions, differing in size, for example, or transmissibility.

The significance for the Arab-D is that backflow may help define the deposition heterogeneity, that may be, or will eventually become, significant to flow performance. The heterogeneity is manifest in isolated, but productive and voluminous facies.

A specific example[51] which has implications on the geometry of the thin, permeable facies associated with super-k, is that of an Uthmaniyah well which backflowed over 1000 B/D upon shut-in, into a thin interval located at the top of Zone 2A, a common stratigraphic location of super-k intervals (5.4.2). The interval is highly productive when the well is on production; however, it also necessarily has a significant areal extent. The reason is as follows. The zones of importance in this problem are the thin, permeable interval, and the remainder of Zone 2A and Zone 2B, together, as Zone 3 is low in productivity. The system may be effectively analyzed as composed of two layers, since the contrast between 2A and 2B is not significant, relative to that between the thin layer and the two combined. Let the thin layer be layer 1, and the combined zones be layer 2. The porosity contrast between these layers is not significant, so,

$$\frac{R_1}{R_2} = \frac{k_1}{k_2}\frac{A_2}{A_1}.$$

If $A_1 << A_2$, then the depletion ratio becomes very large, since $k_1 >> k_2$. A very large depletion ratio is not relevant, as explained above; this condition is contradicted by the existence of backflow. Thus, the thin layer must have a significant areal extent, relative to A_2, which spans the entire drainage area of the well, as zones 2A and 2B extend field wide. Furthermore, the condition $A_2 > A_1$ diminishes the depletion ratio, a condition also contradicting the observance of well backflow. The discussion in Sec. 5.2.2 provides further insight into the geometry of these thin, permeable intervals.

Thus, if the thin, high permeability layer in this well is characteristic of the type

that forms super-k, then it may be deduced that these layers have significant areal extent relative to the wells drainage area.

Another example of the manner in which differential depletion, or the lack of it, may correlate with reservoir heterogeneity is that associated with the three principal Arab-D layers. The depletion ratios for the 3 layer system is derived assuming A is constant over the layers, as they extend field wide. Therefore,

$$\frac{R_1}{R_2} = \frac{k_1}{k_2}\frac{\phi_2}{\phi_1}.$$

Using the mean values of k and ϕ in Table 5.1, it is concluded the depletion ratio is distributed as 9:2:1 among the three layers 2A:2B:3. Therefore, under the condition of complete isolation, from which the ratio expressions are derived, the average reservoir pressures following primary production in the Arab-D would have been distributed as 1:2:9, as the Arab-D was initially in hydrostatic equilibrium.

The actual reservoir pressures have, in fact, never exhibited such a distribution. In fact, the predominate distribution among the layers is one of persisting hydrostatic equilibrium: the pressures vary, generally, according to an oil or water density gradient, only, and differential depletion is minor.[46] Thus, the zones cannot be effectively isolated field wide. In fact, we may conclude both, that a sufficient degree of isotropy exists in the Arab-D (5.1.1), and a sufficient degree of vertical homogeneity presides, that is, the boundaries between layers are not vertical flow barriers.

5.2.2 Water overriding oil

Although vertical equilibrium may pertain in general, well performance suggests local exceptions, where vertical water saturation and phase production discontinuities have been measured. The subject of this thesis, early water breakthrough in thin zones connected to DFNs, concerns one peculiar model of water override.

Another model for local water override may be derived from the vertical equilibrium model, applied to a layered system in which layer boundaries are vertical flow barriers. Fig. 5.3 is a schematic diagram illustrating the effect of such a model as it may apply to the three layered Arab-D, showing relative locations of the water-oil

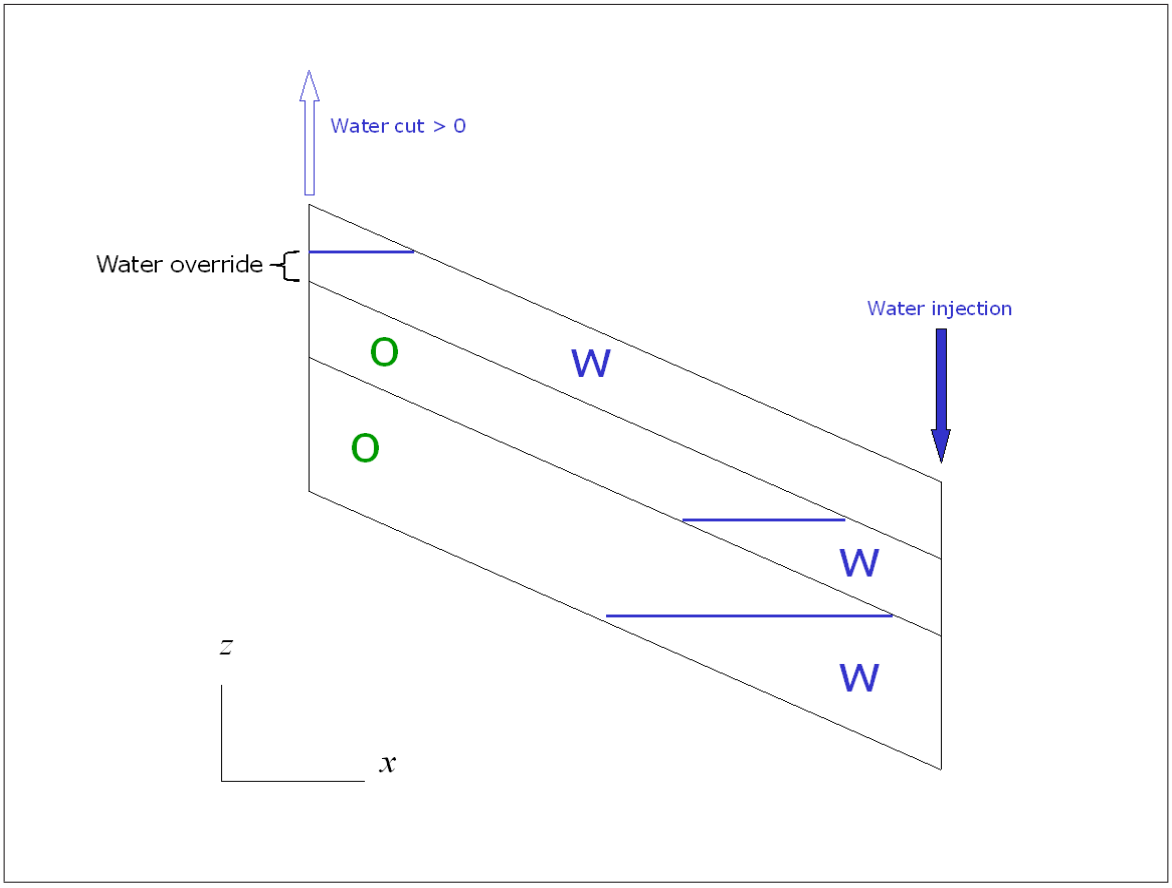

Fig. 5.3: Vertical equilibrium flooding under vertical heterogeneity

contacts under the assumption of the existence of vertical flow barriers. It is evident this model predicts water override at the producing point of the reservoir. However, it has not been established that such a condition exists in the Arab-D, that is, three principal field wide oil-water interfaces. The instances of water override reported are local only.[46],[51]

The observed local water overrides are equivalent to the super-k phenomenon, although possibly without abnormally high interval flux characteristic of super-k. Characterization of the reservoir heterogeneity associated with this production response is therefore important.

These overrides are associated with water production from high permeability, thin intervals, generally restricted to two locations: the top and bottom of Zone 2B. Many

reported occurrences of super-k also coincide with these depths. The occurrence of overrides and super-k in these strata may be explained in the frequency of occurrence of dolomites there, possessing the unique combined qualities of high permeability, and bounding surfaces that are relatively impervious to vertical flow. Fig. 4.6 indicates the occurrence of perhaps the thickest intervals of dolomite at the layer boundaries of Zone 2B. Fig. 5.1 also shows the presence of two dolomite intervals at the top and bottom of Zone 2B.

Sec. 6.3.2 provides a detailed description of super-k lithofacies, indicating that sucrosic and vuggy dolomites account for many reported super-k intervals. The dolomite intervals are not predominantly high permeability, however, as can be seen in Fig. 5.1, where the dolomite intervals under discussion have low permeability.

Therefore, these dolomite strata may assume a lateral variation in permeability: it is highly permeable in regions where it is vuggy or sucrosic, and very tight otherwise. The lateral heterogeneity of these dolomite strata may, in fact, provide a model for the characteristic geometry inferred (Sec. 5.2.1) for the associated thin, permeable super-k intervals: the lateral extent of a vuggy or sucrosic region may define the boundaries of the thin permeable bed associated with our super-k model.

The anisotropy of these intervals has not been explained. It may arise from the nature of the vugs, which are formed from the post dolomitization leaching of a stick-like coral that branches preferentially in the horizontal, rather than the vertical. Lateral connectivity of the vugs may therefore by greater than vertical. One example[51] cited a 10 ft dolomite bed that produced at high rates (the interval loaded the well with water), and was found to have two 6 in thick intervals of darcy permeability. Thus, the restricted vertical permeability of very productive dolomite beds may be explained by vertical heterogeneity within the bed.

Nevertheless, the role these high permeability, bounded dolomite layers may serve in accounting for local water override is demonstrated in Fig. 5.4. Here, the arrival of the oil-water interface at the down dip end of the dolomite bed is followed by a high flux of water through the bed and into the producing well. The bounded surfaces prevent crossflow from the adjacent oil saturated reservoir, and ensures a maximum water cut through the bed and, unfortunately, at the well, sometimes loading the well

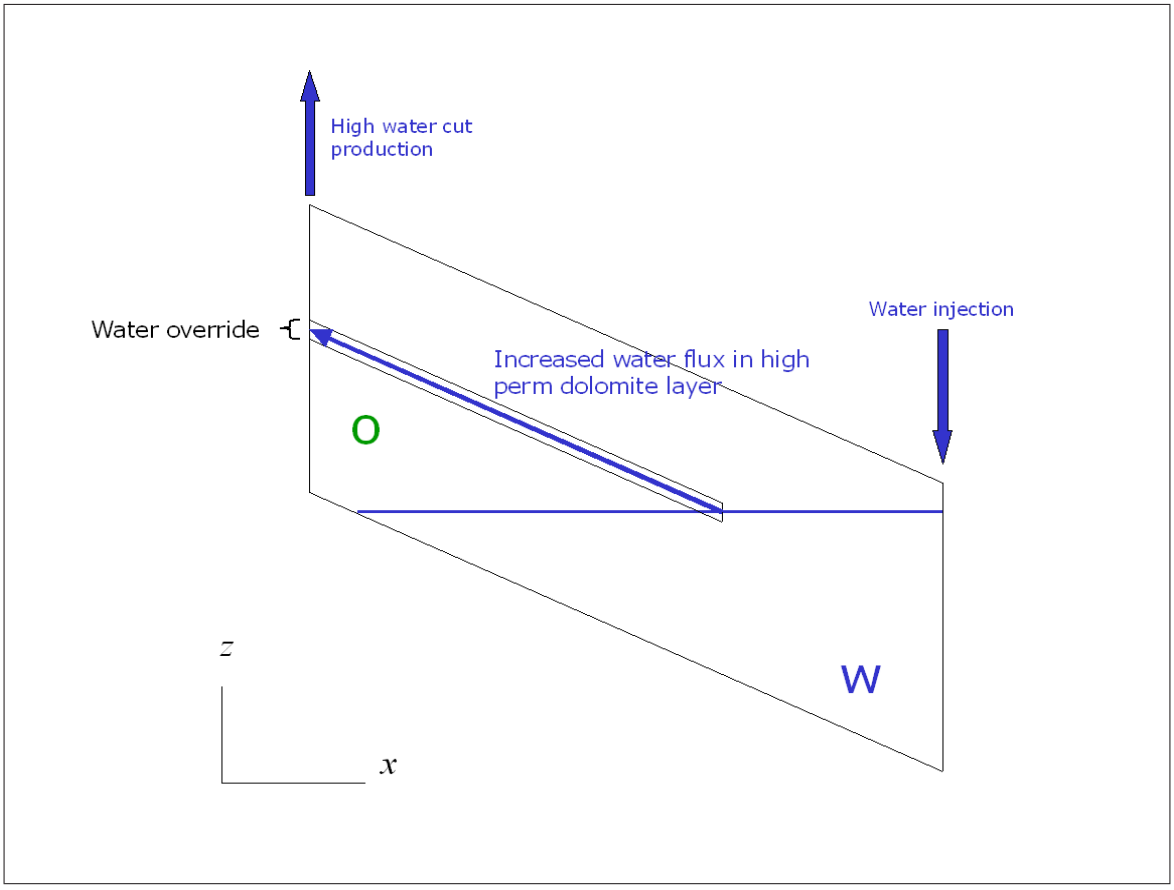

Fig. 5.4: Water override due to high permeability, bounded dolomite bed

sufficiently to kill it.[51]

It is demonstrated in Chapter 6 that this is similar to the mechanism we are hypothesizing for super-k, with the exception that our super-k model includes a vertical DFN connecting to the bed, providing a highly conductive conduit from the region of water injection wells. The conductive bed, in our model, may be viewed as the traditional "stratiform super-k" model.

The characterization of these dolomite beds through well pressure testing has been reported[51]. A vertical interference test was conducted in an Uthmaniyah well in which water production from a 10 ft dolomite interval at the top of Zone 2B had loaded up the well. Core analysis indicated two high permeability (> 1 $darcy$) streaks, each only 6 in thick, within the dolomite interval. The objective of the test

was to determine the vertical permeability through the dolomite bed, and its geometry. The test was conducted following a workover in which a liner was run through the water producing interval, isolating it. The well was then perforated above and below the offending interval. The interference test consisted of pressure measurement in the lower interval, while producing the upper interval. The pressure response at the upper perforations was also recorded; the two perforations were isolated from each other in the well.

The test was a 12 hour isochronal, preceded by a 48 hour flow. Fig. 5.5 presents the test results. The profiles (top) correspond to the rate from the upper perforations, and the pressure response at the lower perforations. The profiles represent the end of the 48 hour flow, and two, 12 hour shut-in and flow periods, followed by a final shut-in. It is seen that the pressure response was directly correlated to the production impulse, indicating vertical communication between the upper and lower perforations; however, a vertical flow barrier was also indicated*: note the 200 minute lag between impulse and response, attributed to a vertical permeability barrier of limited lateral extent.*

The pressure response at the upper perforations during the 48 hour flow is presented in Fig. 5.5, lower plot. The response indicates a dual permeability system, with a factor four increase in permeability demonstrated at 200 minutes. Subsequent 3D radial simulation generated a model that history matched all the data, from both the upper and lower perforations. The model consisted of a vertical barrier between the two perforations, extending 400 ft radially from the well, and a high permeability region at 500 ft. The geometry of the region was not specified in the report, but the pressure response at the upper perforations suggest the region must be areally extensive. The authors hypothesized the region to be a conductive fault; we show, in Sec. 8.3.3, that a response indicating a four-fold productivity gain may be realized in a rectangular drainage pattern containing a DFN. 3D seismic of the area containing the well indeed shows the presence of faults near the well. Also, an offset well exhibited a similar pressure response upon test.

It was not reported if the thin dolomite interval produced at super-k magnitude

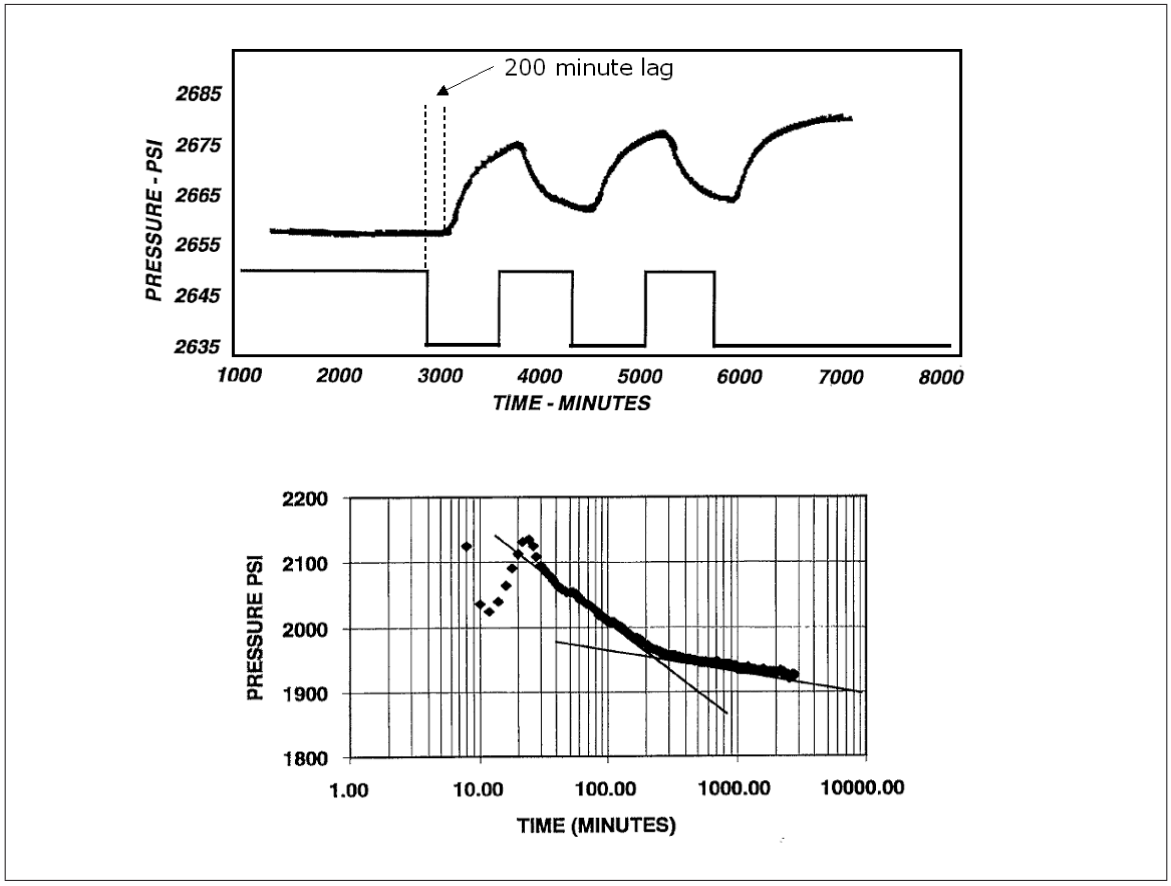

Fig. 5.5: Pressure and rate profiles, top, extended drawdown pressure response, bottom

flux values, prior to the workover; nevertheless, this example demonstrates that a conjunction of thin, permeable beds of limited areal extent, and DFNs, have significantly affected well production performance.

Rate dependent water cut

A final example of water override is that of rate dependent water cut.[51] A well in the Uthmaniyah Sector was found to have a thin interval at the top of Zone 2A, producing 90% of the well total production rate. An oil-water contact intersected the well 70 ft below the interval. The well produced 11500 $BOPD$ at 30% water cut. The well rate was reduced to 8000 $BOPD$ at which it ceased producing water. A flowmeter measurement taken at both rates indicated no change in flow profile of either water

or oil. Water cut rate dependence can only be predicted with a water coning model. However, the complete cessation of water production at a non-zero well rate cannot be predicted by a conventional coning model, but one in which the cone height suffers no hysteresis. This may occur in a DFN, where capillary forces may be very small relative to gravity forces. Therefore, a plausible hypothesis offered by the authors is coning within a DFN that is located away from the well, and that intersects the thin, high permeability layer. Further evidence of this model is seen in the very interesting result that the intersection of the oil-water contact with adjacent wells occurs 40 ft above that in the subject well. It appears the flux of water through the flow network defined by the DFN, thin bed, and well, is sufficient to induce a significant, local draw down of the oil-water contact.

5.3 Is super-k good or bad?

The published literature presents some specific cases of the ill effect of thin, permeable beds that dominate the performance of some wells at Ghawar, as described above. These intervals, however, are also critical to the prolific oil productivity of some wells in the field. The prevalence of either of these classes of wells determines the field wide impact of these intervals.

The fundamental difference between the two classes of wells is simply manifest in the hydraulic relationship between the thin high permeability layer, and injection water. Indeed, under primary production, during which water movement was insignificant at Ghawar, the positive impact of any high permeability region is not questioned.

Therefore, a comparison of the mechanisms by which injection water may contact the high permeability intervals, to those mechanisms which keep the water at bay, can inform the question of the value of these intervals.

The high permeability intervals are kept water free for the longest period under the condition of a bottom-up sweep by injection water, as the thin, permeable intervals are generally located at the tops of zones 2A and 2B. The observation that, in general, precisely this type of sweep is occurring at Ghawar(Sec. 5.1.1), favors the intervals.

The opposite extreme occurs if the intervals are laterally extensive such that both production and injection wells are intersected by them, or if one or more DFNs intersect the intervals at such an orientation as to facilitate the flow of injection water to the interval. The first condition has not been verified in the literature, and in fact contradicts the prevailing facies distribution model for the Arab-D (Chapter 4). The second condition, however, may be prevalent. The existence of faults and discrete fracture systems have been confirmed throughout the field.[5] Furthermore, the high conductivity of these systems has been accepted as prevalent,[1],[52],[46],[51] and the orientation of the fracture systems, although becoming better defined with seismic studies currently being conducted over much of the field, may be practically irrelevant, as coning within a DFN has been demonstrated, as cited in the previous section. Thus, under this condition, a DFN of any orientation, and any appreciable length, for that matter, that has a sufficient vertical thickness to connect a permeable interval intersected by a well, to a region of high water fractional flow, located at a greater depth, may contribute to high water cut at the well. Thus, the existence of DFNs in the Arab-D favors, and may in fact determine completely, the detrimental effects of the high permeability intervals.

Note that we have adopted, in the title of this section, the traditional parlance for super-k, as describing only the thin, permeable interval. It must be made clear that our model of super-k consists of the combination, thin conductive interval and DFN. Therefore, under our definition, it is concluded definitely that super-k is bad: under waterflood conditions, DFNs provide conduits for water flow, and the conductive intervals provide connections from DFNs to producing wells.

Al-Ajmi, *et al.*[54] presented the results of a study of well productivity for 450 wells (over half of the total) in the Uthmaniyah Sector, that clarifies which of the two classes of wells, those favorably disposed to thin, conductive intervals, and those rendered non-productive by them, prevails.

The authors computed interval flux magnitudes from flowmeter surveys from all wells, and selected the maximum interval flux to represent each well. This statistic is a general indication of the existence of thin, high permeability intervals in the well. High values of flux may indicate the presence of such intervals. They also

computed the mean oil rate for each well, computed over the period following water breakthrough for each well (acronym MORABT). This statistic is obviously directly related to the mean water cut of the well. Generally, a high mean water cut, and corresponding low mean oil rate, may be associated with a well in which the water production increased dramatically, and therefore may indicate wells associated with permeable intervals hydraulically connected to DFNs.

Fig. 5.6 is a map of the maximum interval flux values for each Uthmaniyah well, using bubble indicators, blue, where the size of the bubble is proportional to the flux. The indicators are placed on a MORABT map, in color, where low rates are green, and high rates are white. Both of these maps are placed on the Arab-D structure contour map.

Generally, as expected, the MORABT map is correlated well with the Arab-D structure, as wells low on the structure have been producing under flooded conditions for relatively longer periods of time. The MORABT map is therefore directly related to the movement of the waterflood front. The regions where MORABT does not correlate well with structure, however, indicate wells which have unusually high water cuts, and therefore possibly contain a high density of DFNs which are effectively conducting water to wells. One such region, outlined by the rectangle, has been the subject of perhaps the greatest number of super-k studies in the field, and is known to be heavily faulted and deformed (Sec. 5.4.2). Note that this region contains some large interval flux magnitudes, although the most anomalous MORABT area within the region does not contain large flux magnitudes. This may indicate that the density of DFNs is such that the role of thin permeable intervals in conducting water to the wells is lessened: the proximity of DFNs to wells enables intervals of moderate permeability to conduct water to wells.

Note that the density of large flux magnitudes is highest at the structure crest. This is a fortuitous result indeed, as it affords high productivity wells to produce for the maximum period of water-free production. The critical question is then obvious: what is the density of DFNs at the crest? If the density is high, then future anomalously high mean water cuts are to be expected at the crest following water breakthrough. As the majority of these wells' productivity may be derived from thin

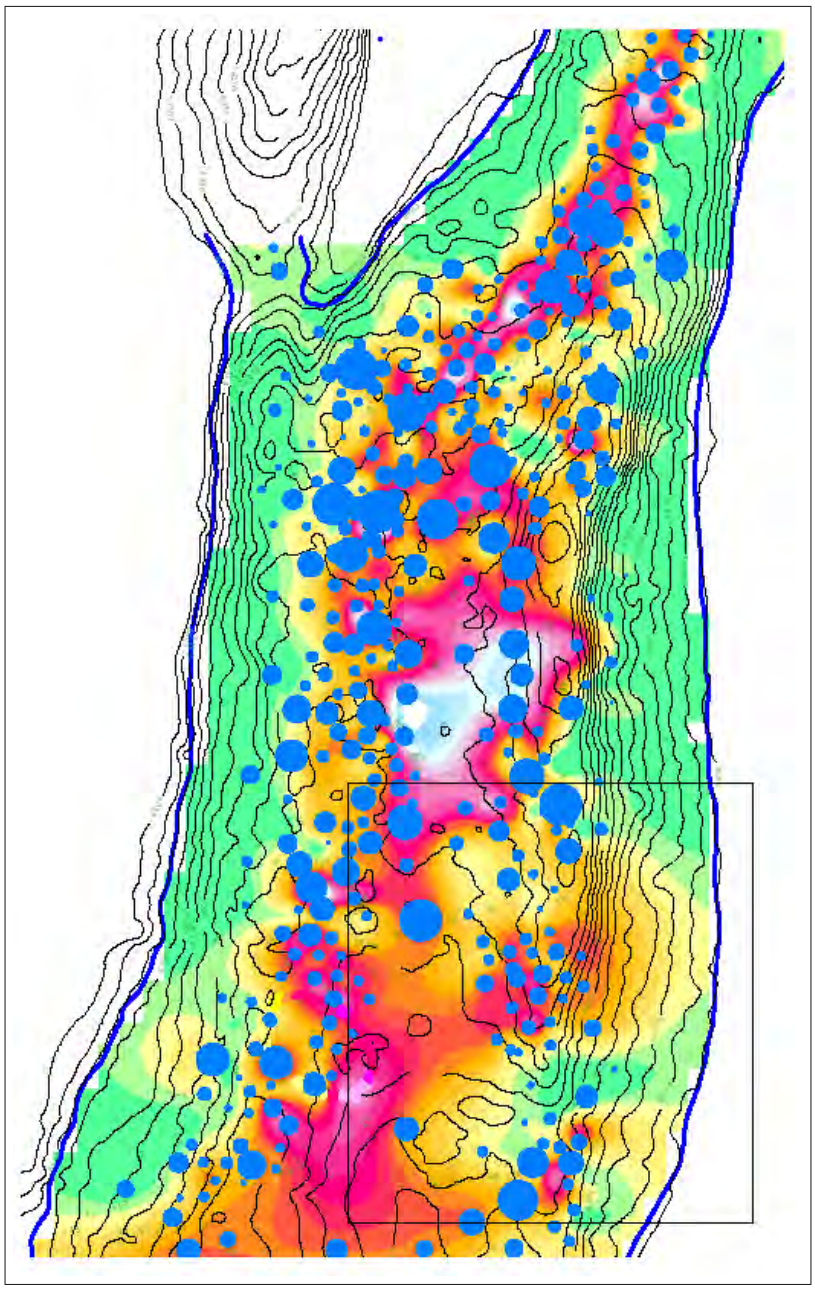

Fig. 5.6: Maximum interval flux (bubble), MORABT (color), and structure (contour)[54]

intervals, isolation of these intervals to reduce water production may also severely reduce the wells' oil rate. In fact, isolation workovers which have been conducted on wells with precisely this problem, suffer with low oil rates. Fig. 5.7 shows the results

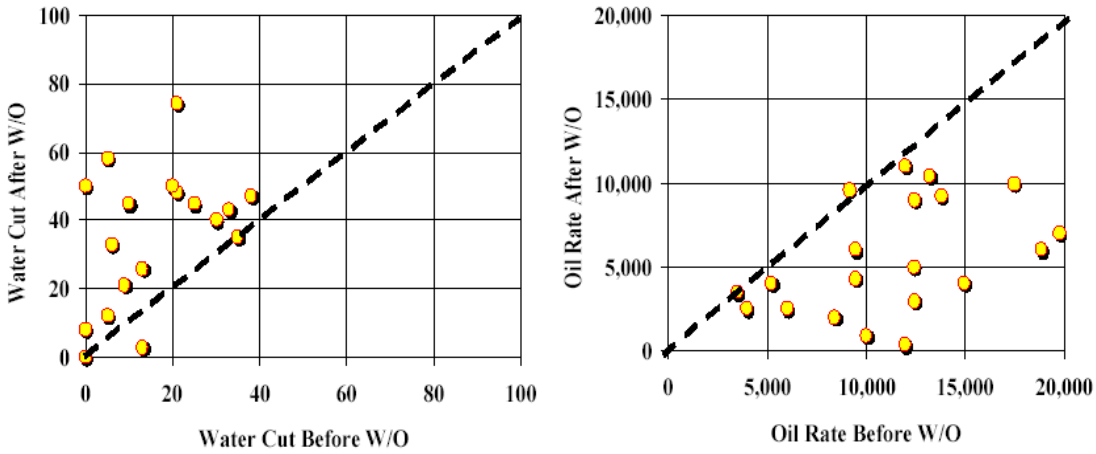

Fig. 5.7: The effect of workovers (W/O) to isolate super-k, oil rate and water cut[54]

of such isolation workovers for 25 Uthmaniyah wells. Evidently, isolation of these thin intervals was a detriment to these wells, as both a reduction in oil rate, *and* an increase in water cut ensued. The isolations in these examples were performed to increase the recovery from the reminder of the productive interval in the wells. The post-workover high water cuts simply indicated the higher water fractional flow in the remaining interval, which were not realized prior to the workovers, while the thin intervals, which possessed lower water fractional flow, were dominating production. Reperforation of the thin intervals has been reported, bringing the well back to pre-workover producing rates.

If, on the other hand, the density of DFNs is low at the crest, then future production, characterized by high oil rate, with gradually increasing water cut, may be expected.

The proportion of wells which have thus far produced from thin, high permeability intervals with low mean water cuts, is apparently higher than those in which the intervals incur anomalously high water cuts. Fig. 5.8 presents the correlation between MORABT and maximum interval flux for all Uthmaniyah wells, in which a positive correlation is indicated.

The future maintenance of this positive correlation is not certain, as it may be dependent on the density of DFNs at the Arab-D crest. This question is a very

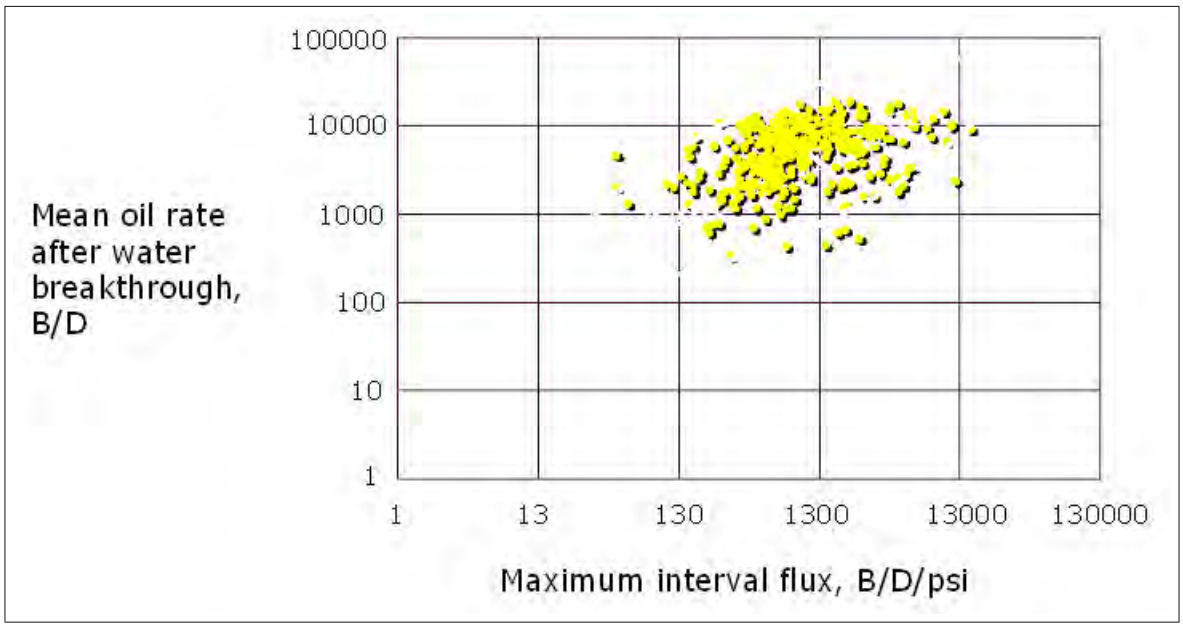

Fig. 5.8: Correlation betwen AORABT and maximum interval flux[54]

serious one, given the density of high flux magnitudes at the crest, and the associated potential for high water cut production if the thin intervals possessing these flux values are intersected by DFNs.

5.4 Performance studies

Further insight into the reservoir performance of the Arab-D may be culled from history matching studies in which areas in specific Ghawar sectors are emphasized. Super-k modeling was recognized early as essential components of these studies. Indeed, the inadequacy of a general full field reservoir model to capture region specific super-k behavior, prompted a new generation of reservoir models designed to gain understanding of the super-k phenomenon. The first of these was constructed for history matching studies in the Shedgum Sector.

5.4.1 Shedgum

Although the first reference[55] to super-k occurs in publication of a study of the Uthmaniyah Sector, the first model[1] of super-k originated from a study in the Shedgum Sector. Also, an early study[44] of the waterflood performance in Shedgum was the first to report the subsequently well established tendency, within the Arab-D productive interval at Ghawar, with some notable exceptions like super-k, toward vertical equilibrium (segregated, oil above water) flow.

The first super-k model

Liu, *et al.*[1] devised the first reservoir model which incorporated the recognition of a separate flow system manifested as super-k. They constructed independent permeability maps for each layer of a 17-layer Arab-D model, by linearly combining super-k and non super-k permeability maps. The coefficients of the linear combination were indicator expectations derived from indicator kriging on binary, super-k / non super-k maps. The indicator data was derived from well test data, from which super-k threshold values were determined. The objective of their study was to construct an initial permeability map, from which history matching would proceed.

The 17-layer model is derived from the sequence stratigraphy defined by Meyer, *et al.[9];* the sequence is shown (inverted triangles) in a type log in Fig. 4.6.

The details of the construction of their permeability model are as follows:

1. Computation of layer transmissibility, kh_i, for each layer i at each tested well in Shedgum from the combination of transient pressure test and flowmeter data: transient pressure test data was used to conventionally compute a total well transmissibility, kh_{well}, and the flowmeter test was used to distribute kh_{well} among the 17 layers, generating each kh_i.

2. Super-k indicator maps were then constructed for each layer. First, the super-k threshold value, kh_i^{sk}, was determined for each layer, using cumulative distribution plots of kh_i/kh_{well}. A single distribution plot was constructed for each layer, using the kh_i data derived from all tested wells, per step 1. Fig. 5.9 is a

schematic example of such a cumulative distribution plot. Data from all tested wells and a given layer, i, are used to construct the distribution. Note that the maximum value of kh_i/kh_{well} is necessarily less than 1, as the plot includes data from only a single layer. The value of kh_i^{sk} is determined as the point at which a significant change in slope of the distribution curve occurs. This change of slope was evident on most of the layer cumulative distribution plots. Locations at which kh_i/kh_{well} exceed the threshold are given super-k indicator values of 1, for the layer i. The remaining data locations are assigned an indicator value of 0. This procedure is repeated for every layer.

3. Separate super-k maps, kh_{SK} and non super-k maps, kh_{NSK}, were constructed for each layer, independently, by kriging kh_i data. The layer super-k map was generated using kh_i data from only those locations assigned a super-k indicator value of 1. The non super-k map for the layer was generated with the remaining kh_i data.

4. Finally, the combined kh_i map was constructed by applying probabilities, p, derived from indicator kriging maps, to the separate super-k and non super-k kh_i maps:

$$kh_i(u) = (p)kh_{SK}(u,i) + (1-p)kh_{NSK}(u,i)$$

for a location u, where p is the indicator expectation derived from the super-k indicator kriging map for layer i.

Although it may be commented that this model is too smooth to characterize DFN flow, nonetheless, it represents a systematic incorporation of super-k transmissibility on a layer basis, and set a precedent for such incorporation in all reservoir models that followed.

The Shedgum Leak Area

Fracture systems were suspected early as significant elements of flow in Shedgum, by the advent of the "Shedgum Leak." Wells in a local, approximately 30-well area on the

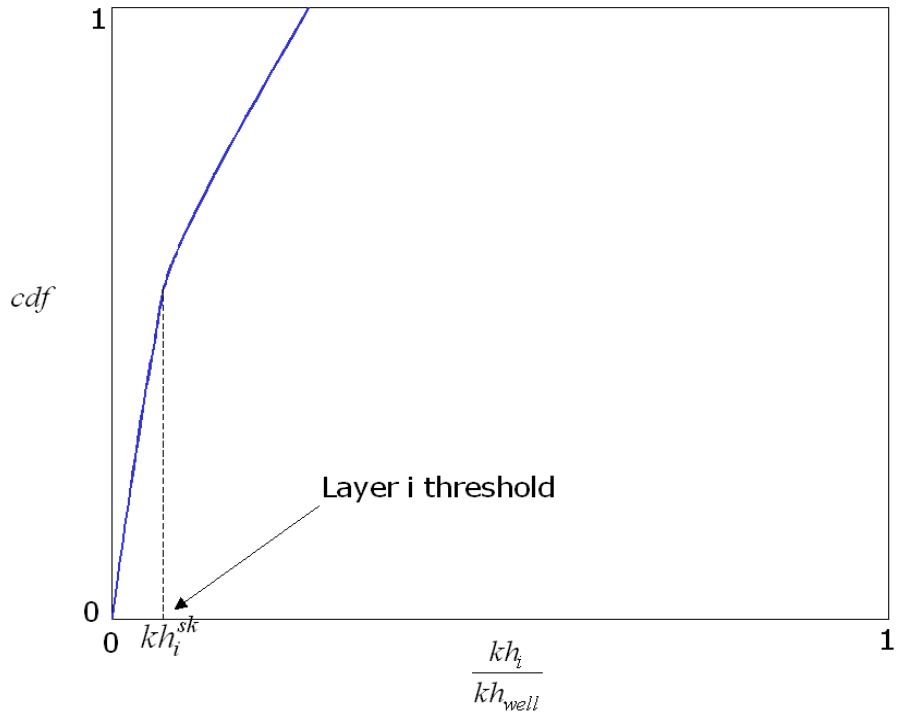

Fig. 5.9: Determination of layer i threshold for super-k indicator variable

crest of the structure in Shedgum had begun producing water, prior to waterflooding. It is now hypothesized that the water is sourced in the Jubaila and Hanifa Formations, located below the Arab-D, and conducted through a system of vertical DFNs. The fracture system recently provided the first opportunity for the application of transient well pressure analyses[56] to the problem of DFN detection in Ghawar. The authors present well pressure analysis from 23 wells in the Leak Area, citing responses of DFNs intersecting producing wells, in three cases, and an additional three cases of non-intersecting DFNs. The conventional infinite conductivity fractured well model was used to match responses for those wells intersecting DFNs. The model of Abbaszadeh and Cinco-Ley[41] matched well response for non-intersecting DFNs. This model is

discussed in detail in Chapter 8.

5.4.2 Uthmaniyah

The peripheral waterflood in Uthmaniyah exhibited the earliest anomalous production response, prompting the earliest published study of Ghawar waterflood problems, and super-k[55]. Fig. 5.10 is an Arab-D structure map that also presents injection and production well distributions, and the location of the waterflood front in 1990. The front preferentially extends locally in a small region. Note also the tight spacing of injection wells, relative to distances to producing wells. The ratio of these distances is approximately 1:8 over much of the row of injectors.

The structure map in Fig. 5.10 is derived from well data only, and indicates little structural deformity. A revised map[5], updated with recently interpreted 3D seismic data, suggests a much greater degree of deformation. The new structure maps, presented in Fig. 5.11, give an indication of Uthmaniyah's proclivity to anomalous flow behavior. It is seen that northeastern Uthmaniyah is perhaps the most deformed region of the Ghawar anticline, and is replete with faults, some of which are delineated in the map in Fig. 5.11.

The anomalous flood front

Moore[55] reported superficial flood front velocities $v = 15\ ft/day$ over an 8 km span on the Uthmaniyah flood front. Flood front velocities in the range $67 < v < 130$ ft/day were reported for the Haradh Sector[59], over a distance of several kilometers. Effective permeabilities allowing these magnitudes of velocity are very large. Indeed, Darcy's law allows an estimation,

$$u = 7.324 \times 10^{-5} \frac{k}{\mu} \nabla p$$

where k is in darcys, and u is in $ft/\sec$. Assuming a porosity $\phi = 0.20$, appropriate for the main Arab-D producing interval (Table 5.1), yields $u = v\phi = 3.0\ ft/day$. Then, assuming $\mu = 1\ cp$,

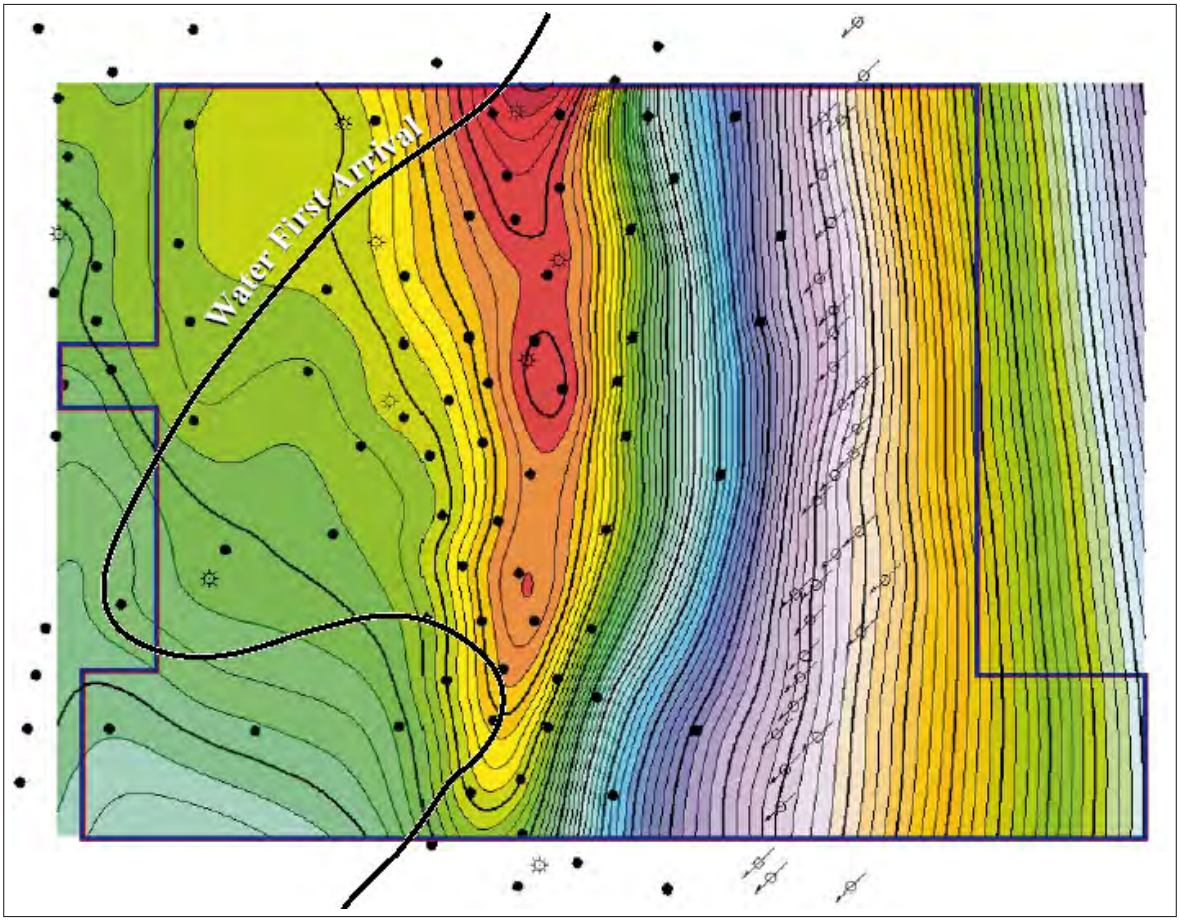

Fig. 5.10: Well spacing in the Uthmaniyah anamolous waterflood performance area[5]

$$k\nabla p = 0.48.$$

Fig. 5.12 presents a plot of the permeability corresponding to the observed flood front velocity as a function of the pressure drop over the 8 km span. Isobaric data[44] from the Shedgum Sector indicate a pressure drop of several hundred psi would not be unusual over this distance. A pressure drop in the range of 500 to 1000 psi, for example, corresponds to a permeability range of 12 to 25 $darcies$, effective over the entire 8 km distance. The Haradh flood front velocity indicates mean permeabilities of several times that computed in this example, over a distance of several kilometers.

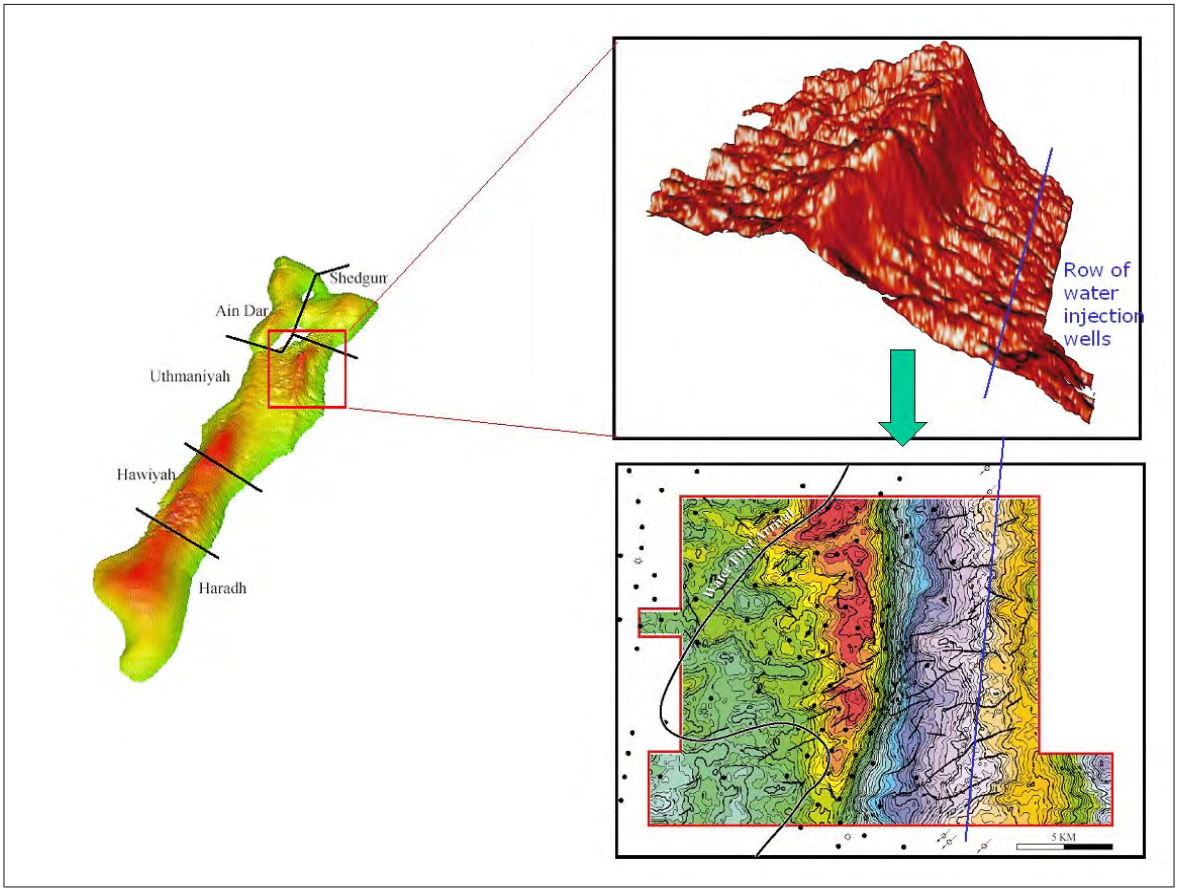

Fig. 5.11: Uthmaniyah anamolous waterflood performance area[5], [6]

General super-k observations

Moore[55] initially reported several observations, subsequently common in the super-k literature, that present insight into the modeling of super-k. Super-k almost always occurs in thin intervals, $5 - 15\ ft$, and very often is associated with *low porosity* facies, as measured at the well. He reported flux magnitudes, associated with super-k intervals, of approximately 1500 $B/D/ft$.

Super-k is most often associated with the two principal producing zones in the Arab-D, Zone 2A and Zone 2B, and very often occur in thin intervals at the top of either zone. Vuggy and sucrosic dolomite, and skeletal limestone are facies most often associated with super-k.

Core derived permeability measurements from super-k intervals rarely exceed 2 to

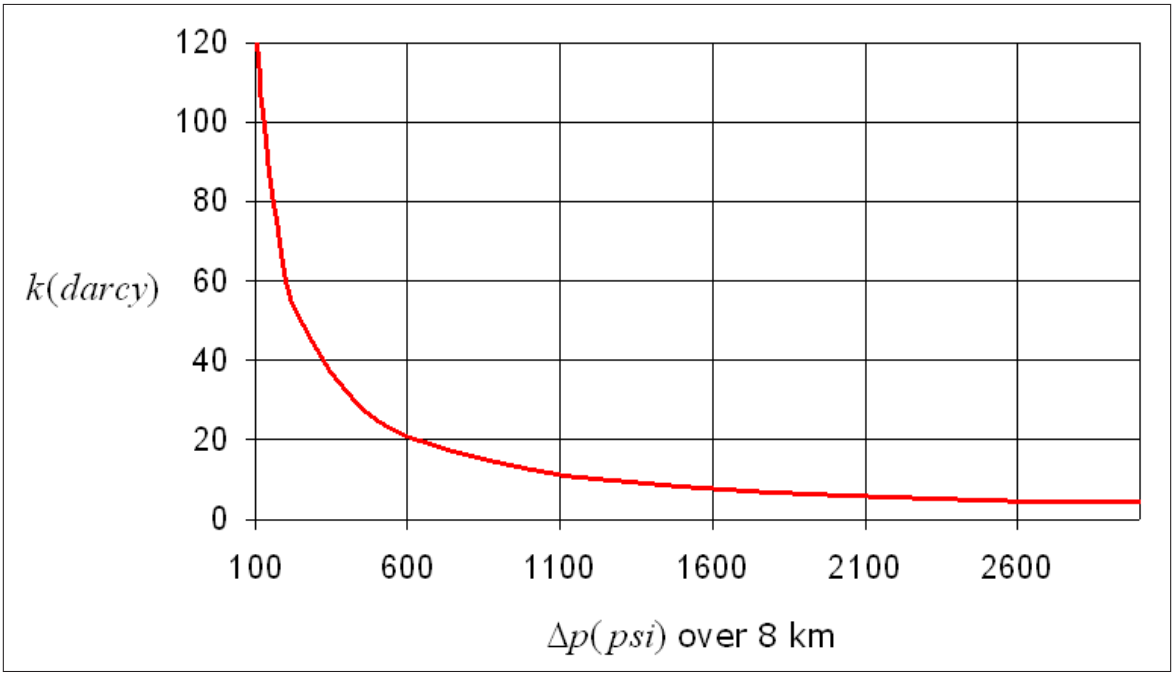

Fig. 5.12: Permeability corresponding to Darcy velocity of 3 ft/day

3 *darcies* (Table 5.1), and super-k associated rock properties may exhibit significant variation over the distance of the well spacing, typically 1 km.

Our hypothesis of the mechanics of super-k, which relates these observations, are presented in Chapter 6.

DFN characterization in Uthmaniyah

Although DFNs had been suspected early as important super-k elements, the advent of 3D seismic acquisition and the drilling of horizontal wells has clarified their role in the Uthmaniyah Sector. The Ghawar structure, as defined previously by only well data to be a gentle and smooth anticline, has now been clarified by seismic as much more significantly deformed, possessing local regions of severe curvature, and most importantly, pervasive large scale fracturing.[5],[46]. The conductivity of the fracture systems has been well established, furthermore, by data obtained in horizontal wells, which include, most importantly, complete lost circulation while drilling, and immediate water production.[56],[46] The realization of the presence of

large scale fracturing has also brought well pressure analyses to bear on the problem of DFN characterization[56],[46], although a dearth in the development of analytical models in which a large scale fracture is near to, but does not intersect the well (only two published models currently exist[41],[40]), hampers analysis. This topic is explored further in Chapter 8.

Uthmaniyah flow simulation models

The first published Ghawar flow simulation results[52] give specific indications of DFN flow at Uthmaniyah, although DFNs were not formally incorporated. The authors explicitly state, however, that super-k is the "main conduit" for the transport of injection water.

The authors history matched production in the anomalous flood region described above, using a locally refined discretization, decreasing the dimension of the square, 1 km, full field coarse grid, to 1/3 km. They modified the 17-layer, full field model, to 15 layers within the local refinement, in order to accommodate a thin layer designated to simulate observed super-k flux.

Fig. 5.13 is their history matched permeability model for the designated super-k layer, in which very high permeabilities are distributed in areally thin, long, discrete regions. The authors acknowledge the 250 *darcy* region to be fracture related, and in fact incorporate linear relative permeability curves (as in Fig. D.6) over the entire layer, "where conventional concepts of flow in porous media are not thought to apply."

The authors report an updated model[53], in which recently interpreted 3D seismic data (Fig. 5.11) was incorporated. The authors explicitly state the need for the incorporation of DFNs, given their clear presence as indicated by the seismic data, and are the first to attempt to incorporate DFN flow characteristics into a flow simulation model. The model was not significantly altered, however; it is not clear from the paper, but it appears certain high permeability regions from the previous model of the super-k layer, were simply isotropically vertically extended, although the depths to which they were extended were not reported. Their history matched super-k layer permeability distribution appears to be identical to their previous model; only the maximum permeability is modified, from 250 *darcies*, to 50 *darcies*, indicating

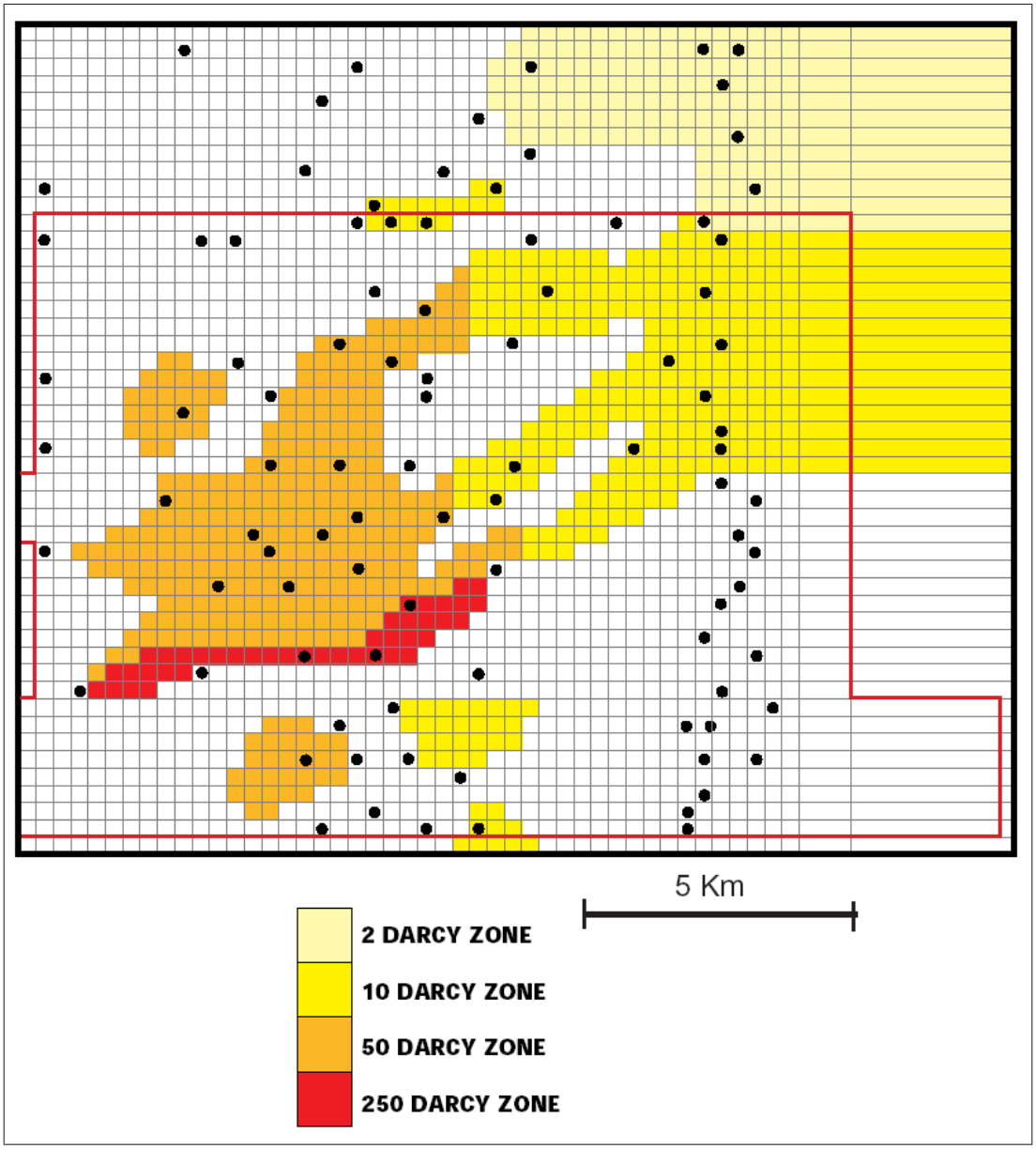

Fig. 5.13: Uthmaniyah history matched model of Valle, et al.[52]

the vertical extension effectively increased the transmissibility of the modeled high permeability regions.

Fine scale parallel, and dual grid models Recent approaches[57],[58] to the incorporation of DFNs into flow simulation models has involved the utilization of

massive computing power, and the development of fine grid, parallelized single grid, and dual porosity, dual permeability (DPDP) models.

A full sector, 2.54 million cell flow simulation model has been used to forecast Uthmaniyah production[57]. The model discretizes DFNs, the spatial distribution of which were interpreted from 3D seismic data. The model includes approximately 30 years of production history from all 800 Uthmaniyah wells, and is discretized as $256 \times 148 \times 67$ layers. The grid sizes vary, with the finest at 20×100 m. The model is derived from a geologic model which possessed 134 layers, with an individual cell size 250 m. DFNs were not incorporated into the geologic model, but in a separate model of DFNs only, constructed from the seismic data. The details of construction of either model were not reported.

Fig. 5.14 presents a summary of the grid, where it is seen that a finely gridded sub-area in the center of the grid contains an orthogonal set of the finest grid cells, used to simulate DFN flow. This sub-area encompasses the area of anomalous waterflood performance.

The authors assigned one of the 67 layers to model a thin, high permeability zone, of limited areal extent, shown in Fig. 5.14, bottom, in green. This set of grid cells was assigned a permeability of 70 *darcies*. The three linear traces within the green area are the DFNs chosen to be modeled, using the fine grid cells. These cells were initially assigned a permeability of 10 *darcies*. The rationale behind assigning a lower permeability to DFNs than to the strata was not reported, nor was the final history matched DFN permeability. Also, both the high permeability strata and DFN cells were assigned linear relative permeability functions. Although linear functions are standard for DFNs, no reason was given as to their application to a rock layer. The vertical extent of the DFNs were also not described. The authors present adequate water production history match results from seven wells. They report CPU times averaging 4 hours.

Dual grid model The current approach to modeling the flow effect of DFNs in the Arab-D is through dual grid models, the first published version[58] of which exemplifies the many difficulties encountered in representing DFNs in flow models.

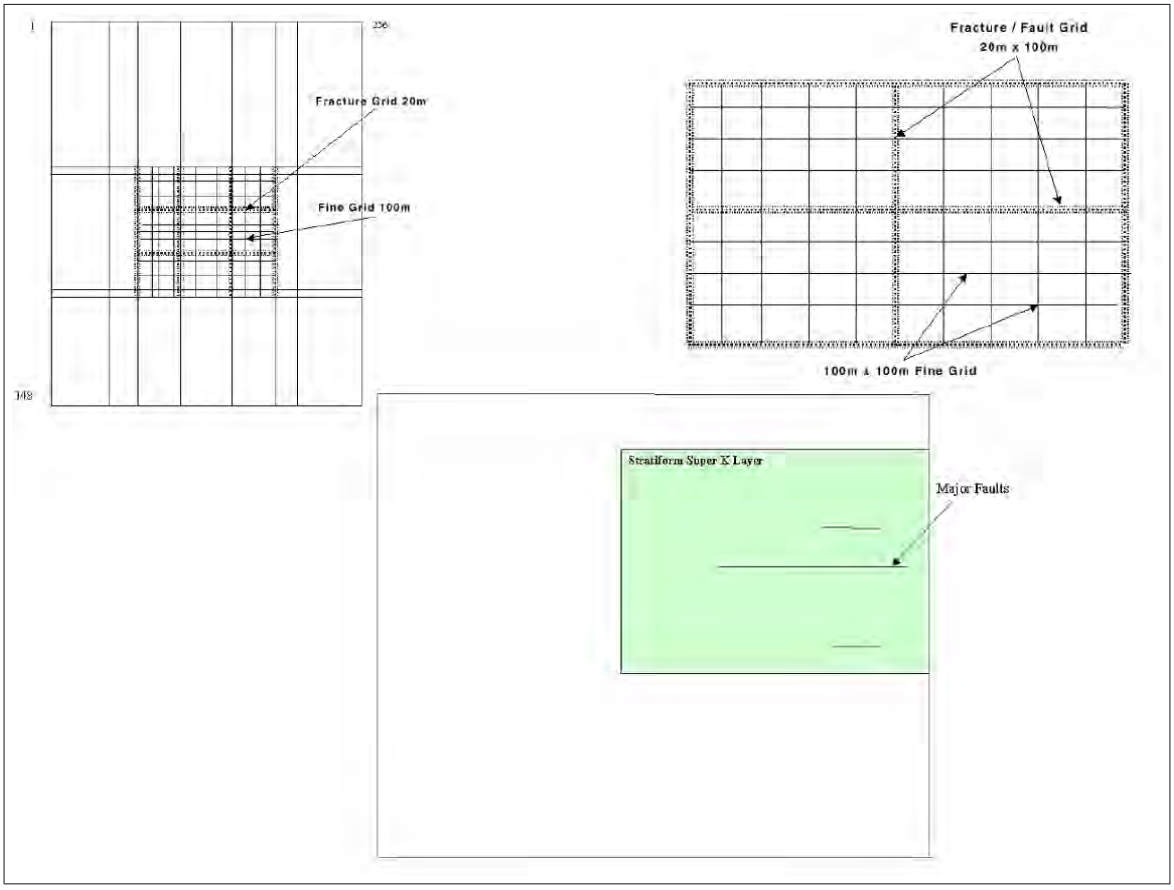

Fig. 5.14: Uthmaniyah history matched model of Dogru, et al.[57]

The model is a full field, 17-layer model, with a local grid refinement used to model a portion of the Uthmaniyah Sector, chosen for history matching, north of the study area emphasized in the prior discussion of this section. The study area location is shown in Fig. 5.15, upper left. The local grid refinement is comprised of 18 layers, and a grid cell size of 1000 m.

The authors construct the model under the premise that the principal Arab-D flow components are DFNs, thin permeable strata, and the remaining rock volume, referred to as "background." Their approach is to combine the first two elements into the fracture grid, and the third into the matrix grid.

The geologic model of high permeability strata is a kriging map, derived from well log porosity, transformed to permeability using a core derived $\phi - k$ regression.

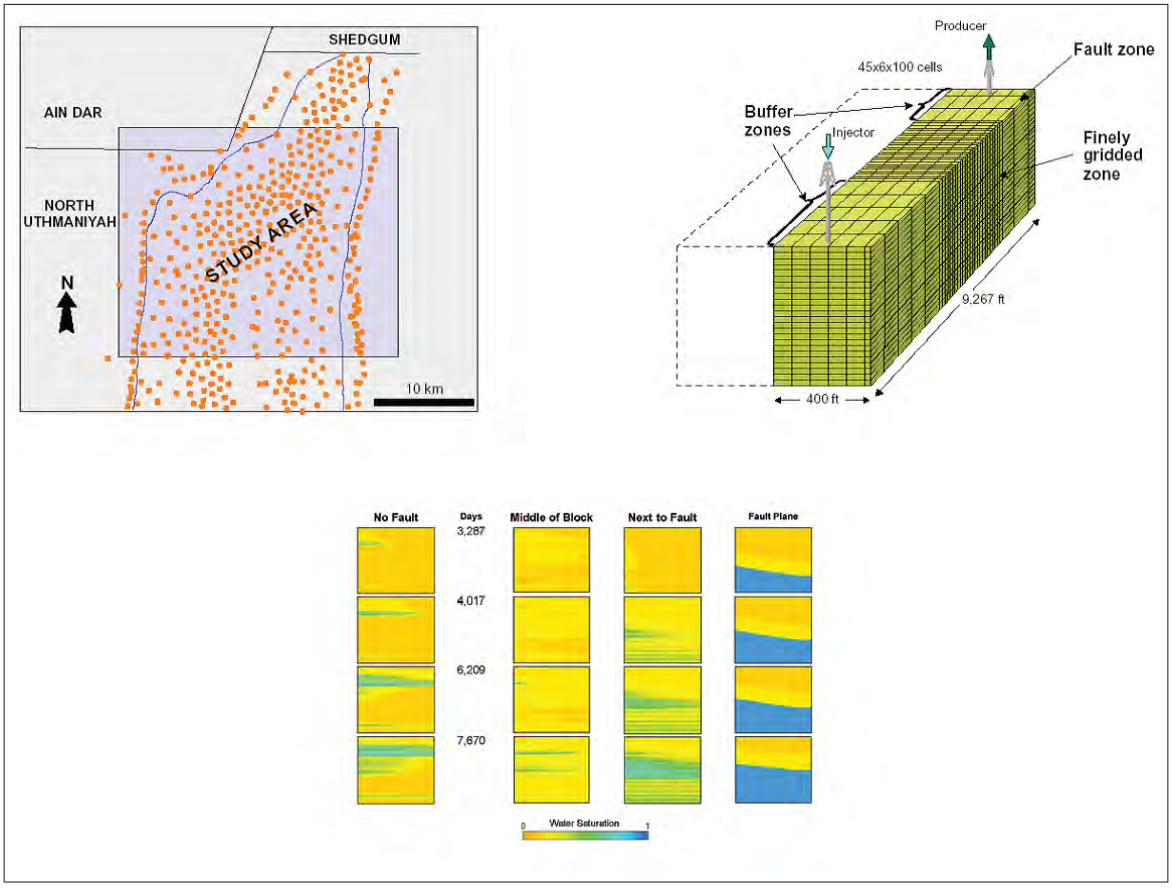

Fig. 5.15: Uthmaniyah history matching study of Phelps, et al.[58]

Only permeabilities above a threshold value are kriged for this model. Permeability values below the threshold value are used to construct the background permeability model, which is also a kriging map. The background permeability is frozen during the history match. History matched values of either of these permeability models are not reported, although $\phi - k$ correlation plots presented in the paper indicate permeabilities not exceeding a few *darcies*.

The DFN geologic model is derived from DFN lineament maps interpreted from 3D seismic data, and incorporates DFN density and length. An index related to these parameters was derived and mapped. Although the details of construction of the maps was not reported, an example map included in their paper reveals a smooth, kriging-like distribution.

The two permeability models are combined to populate the fracture grid with permeability k_f, through the following linear combination,

$$k_f = k + \alpha I$$

where k is obtained from the high permeability strata kriging model, I is obtained from the DFN index model, and α is a coefficient, which becomes the most important history matching parameter, according to the authors. k_f and k are anisotropic, although the determination of the anisotropy is not described. During the history matching process, k is frozen, and the anisotropy of k_f is a history matching parameter. Also, it was indicated that local updating of I occurred during the history match, "in conjunction with geological advice." Eventual history matched values of k_f ranged from 25 to 55 *darcies*.

Relative permeability functions for the fracture grid are derived from a combination of those associated with the high permeability strata, and the DFNs. The DFN relative permeability functions are linear. The relative contribution of either type of function is controlled by α, although the precise method of combination is not described.

The transfer function σ, for the dual grid model is,

$$\sigma = 4\left(\frac{1}{l_x^2} + \frac{1}{l_y^2} + \frac{k_x}{k_z}\rho^2\right)$$

where l_x and l_y are characteristic lengths of the background rock geometry, the origin of which is not described by the authors, k_x and k_z are background lateral and vertical permeabilities, and ρ is the proportion of the high permeability strata. The derivation of this transfer function is not described by the authors. The pertinence of the various parameters comprising σ is ambiguous, and as a result, it becomes yet another history matching parameter which is rather arbitrarily manipulated. The authors present adequate history matches of well block pressure and water cut for two wells. CPU times were not reported.

It is evident from the description above that the parameters associated with the DFN permeability model, and the transmissibility between DFNs and the surrounding

rock, alone control the history matching algorithm.

Vertical equilibrium induced by DFNs These authors presented an interesting, separate, single grid model to study the flow in and near a DFN, shown in Fig. 5.15, upper right. The model consists of 100 layers, with a high degree of vertical heterogeneity. A high permeability slice, having a high degree of isotropy, located on the right side of the model, represents a DFN. Water is injected and displaces oil. Results from the study are shown in Fig. 5.15, bottom, where it is seen that vertical equilibrium is established in the DFN, and that relative to the case having no DFN, lower layers are preferentially swept.

Results from the full field model in the study area could not confirm these results: the DPDP model would not converge for $k_v > 0.05\ md$ in the fracture grid. The authors therefore used k_v values less than $0.05\ md$. Given the history matched fracture grid lateral permeability range $25 < k_f < 55\ darcies$, the associated k_v/k_f range $2 \times 10^{-6} < k_{v/}/k_f < 4 \times 10^{-6}$ cannot support vertical equilibrium flow, evident from the water saturation maps presented in the paper, Fig. 5.16. These are four vertical slices from the fracture grid water saturation map at a point in time. The vertical phase segregation shown is due to layering, not gravity.

5.4.3 Haradh

Water injection at the Haradh Sector was initiated in 1995. The northern one-third of the Haradh Sector has been developed; the middle third is currently being drilled (2004)[62]. Complete Haradh development is projected in 2010[4]. The delay in development, in conjunction with an engineering rigor demanded by a nearly four-fold decrease in reservoir permeability compared to that in the sectors in the northern portion of the field, has prompted the application of modern development and modeling paradigms in this sector. For example, horizontal wells, exclusively, are being drilled in the middle third portion of the sector, in Zones 2A and 2B only, to exploit the relatively high permeability in these zones, and a projected bottom-up waterflood displacement[62]. This contrasts the scheme in the Uthmaniyah Sector in which some horizontal wells are drilled in Zone 3, to both increase well productivity

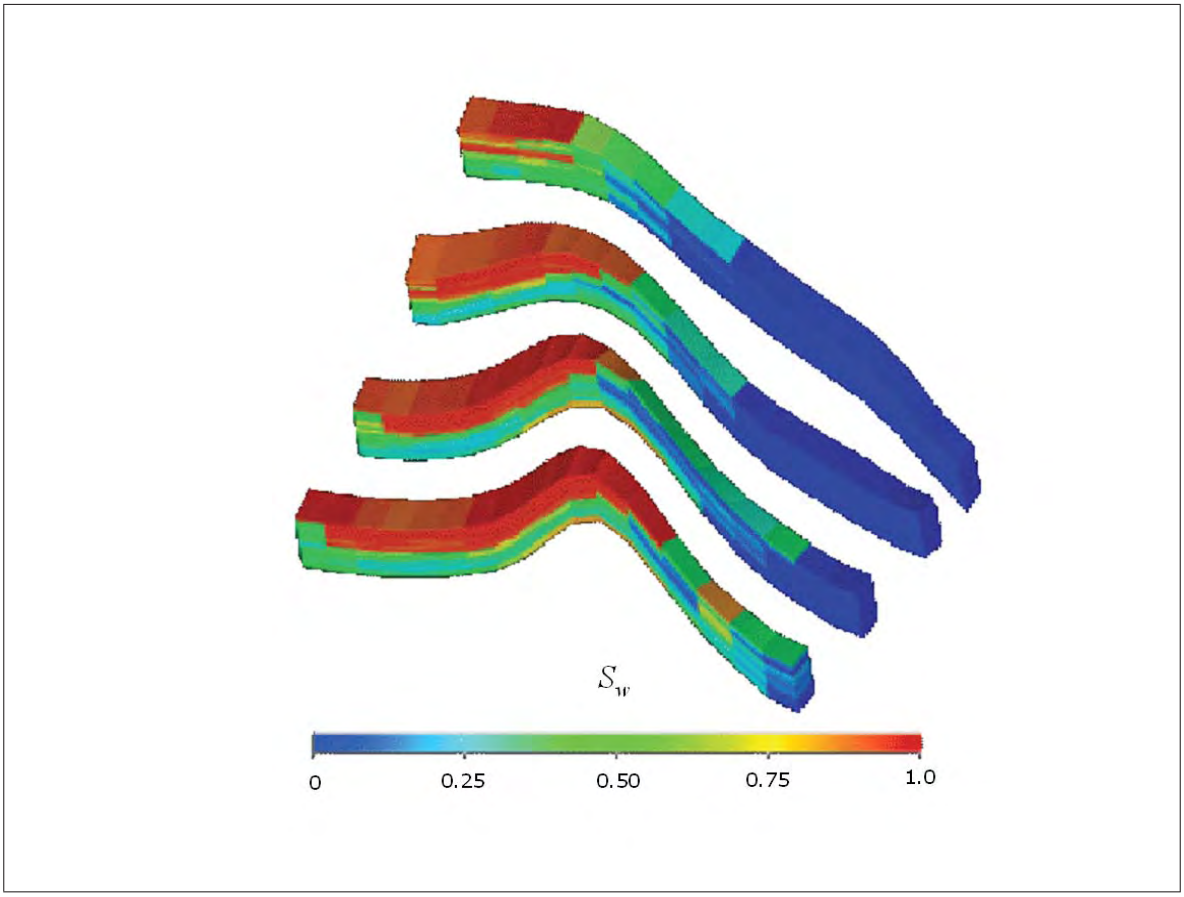

Fig. 5.16: Flood movement in the fracture grid of the DPDP model of Phelps, et al.[58]

in these lower permeability regions. Furthermore, the horizontal wells are placed parallel to predominant fracture system azimuths, to avoid intersection.

Reservoir characterization studies have benefitted from the incorporation of recently obtained 3D seismic data, and powerful flow simulation models. These studies emphasize the importance of DFN flow, given the relatively lower reservoir permeability, and the realization, from experience in the developed norther sectors, that DFNs are primary reservoir flow components. The published Haradh Sector studies are described in this section.

All published Haradh studies described reservoir characterizations in two study areas, shown in Fig. 5.17. An erratic flood front has been observed in Haradh, as in the northern sectors; a portion of the front, coinciding with the northern Haradh

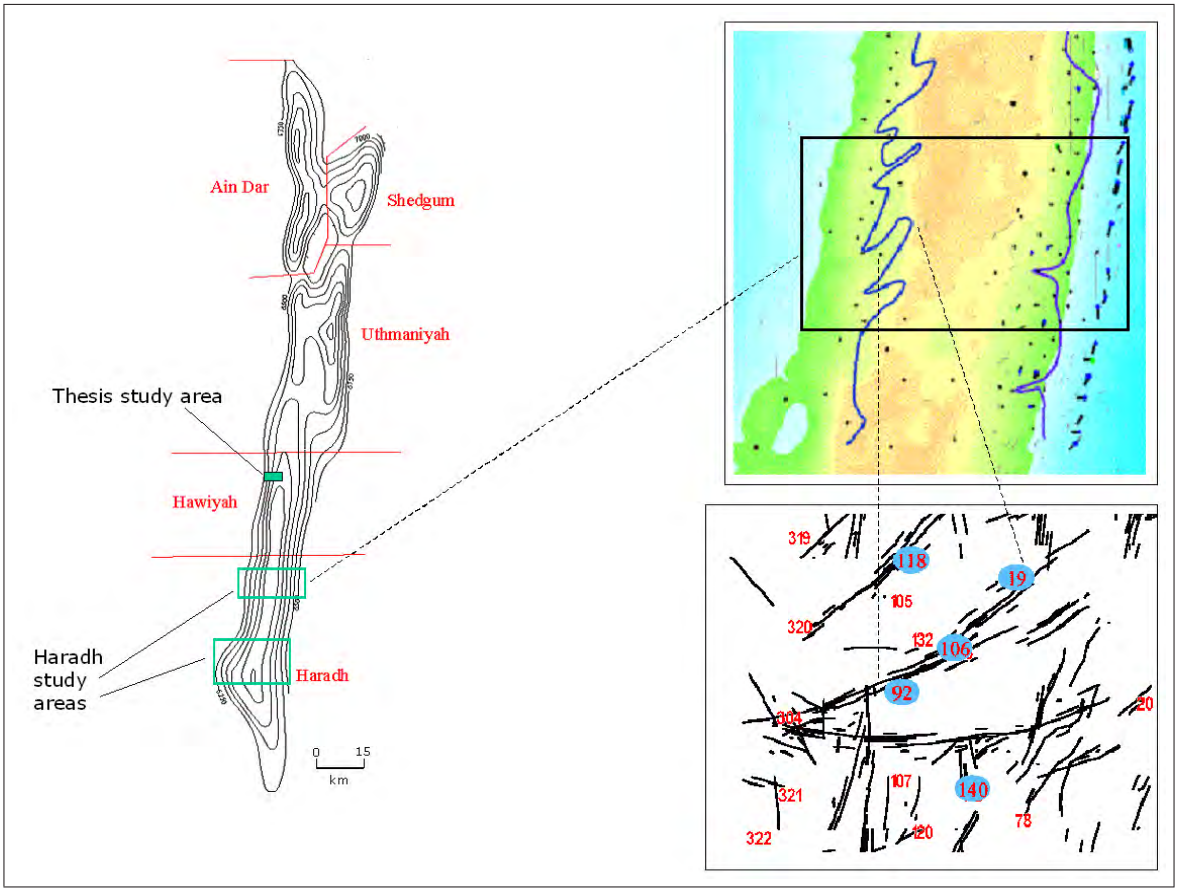

Fig. 5.17: Haradh study areas, anomalous flood front, fracture lineations[4],[63],[43]

study area is shown in Fig. 5.17, upper right. Correlation between fracture delineation maps, generated from detailed 3D seismic structure interpretation, and the flood front map has been indicated. An example of the correlation is shown in the lower right of Fig. 5.17. Here, wells in which anomalous water breakthrough has occurred, indicated in blue, coincide with predicted DFNs, while adjacent wells, in red, remain dry.

Incorporation of static DFN models

The specific generation of the type of fracture system map shown in Fig. 5.17, lower right, has unfortunately not been described in the petroleum literature. This may be due to the relative infancy of fracture modeling at Ghawar. Indeed, the principal

source of data for these models, 3D seismic interpretation, is available only in the northern third of the sector, as acquisition and interpretation are being undertaken currently in the remaining two-thirds.

The scant reporting indicates that fracture systems are modeled from prediction of major faults from 3D seismic interpretation, and from "curvature analysis" applied to detailed structure models, which are also generated from 3D seismic data. The fracture maps are integral to the spatial distribution of permeability in Haradh flow simulation models, and thus the basis for their generation is extremely important.

Fig. 5.18 presents a fracture system realization, the objects of which are represented as white lineaments, placed on the Haradh structure map. The three portions of the sector are also indicated. A detail of the middle section is presented in Fig. 5.20. The fracture lineament map is a stochastic realization of an object-based fractal process[61], using major lineaments derived from curvature analysis of 3D seismic interpretation as "data." The realization of the fracture system distribution in the middle region, indicates three distinct sets of azimuths.

Hard DFN data are rare, although more available in Haradh than in the other sectors, given the prevalence of horizontals wells. Fig. 5.19 presents examples in which lost circulation intervals recorded during horizontal well drilling, as well as borehole image logs, both of which record direct measurements of the occurrence of DFNs, and additionally, with the image logs, DFN azimuth and dip, are combined with 3D seismic lineament maps to generate static DFN models.

As this thesis does not address the generation of such fracture system maps, the interpretation of such maps in terms of DFNs is still open. Each lineament may be interpreted as a separate DFN, for example. Or, a density threshold may define the amalgamation of a set of lineaments into a single DFN. An example of a thresholding technique is presented here.

The transfer of the lineament map to the flow simulation model is demonstrated in the two figures, right, in Fig. 5.20. Here, the lineament map is overlain on the flow simulation grid, composed of $250m \; x \; 250m$ cells. The grid in this case is the fracture grid of a dual grid flow simulator. Fig. 5.21 demonstrates the subsequent discretization method, in which interblock transmissibilities between two adjacent

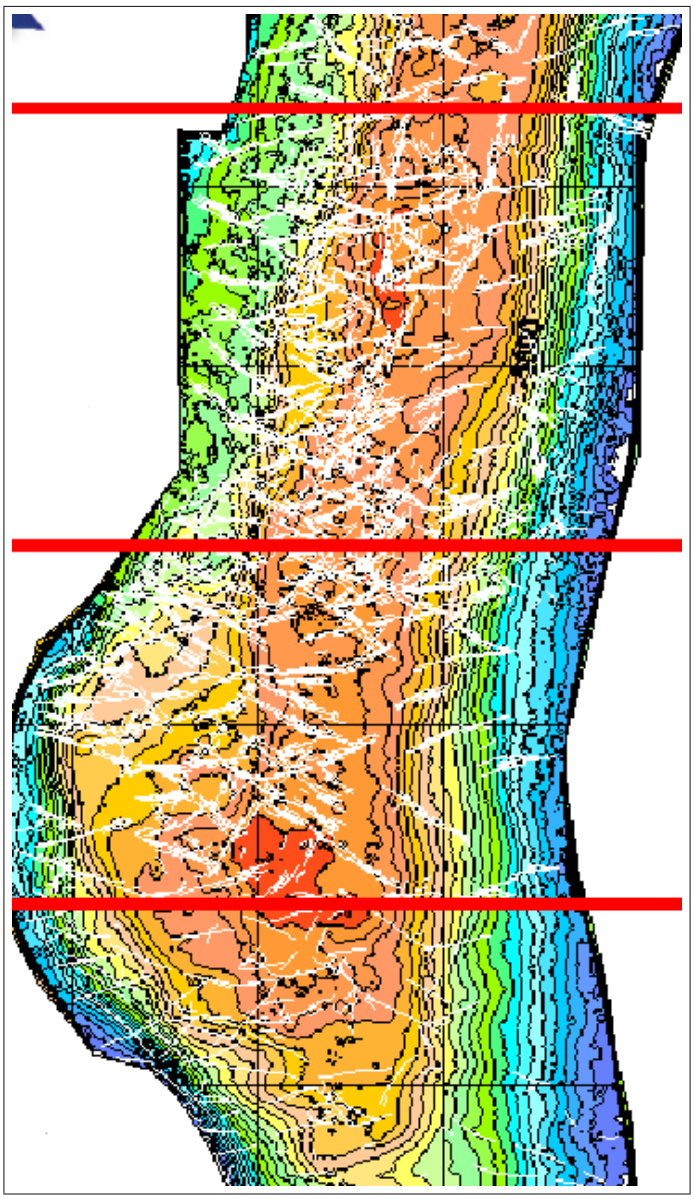

Fig. 5.18: Haradh fracture system realization and structure map[60]

blocks are derived from lineament lengths traversed through the blocks. Here, $kfrac \cdot efrac$ is the fracture transmissibility, which is generally an arbitrary history matching parameter, as neither $kfrac$, the permeability of a lineament, nor $efrac$, the aperture of the lineament, are ever measured, and $\triangle Z$ is the grid block vertical thickness. A range of $30 < kfrac \cdot efrac < 200\ darcy \cdot ft$ is quoted in various Haradh studies.

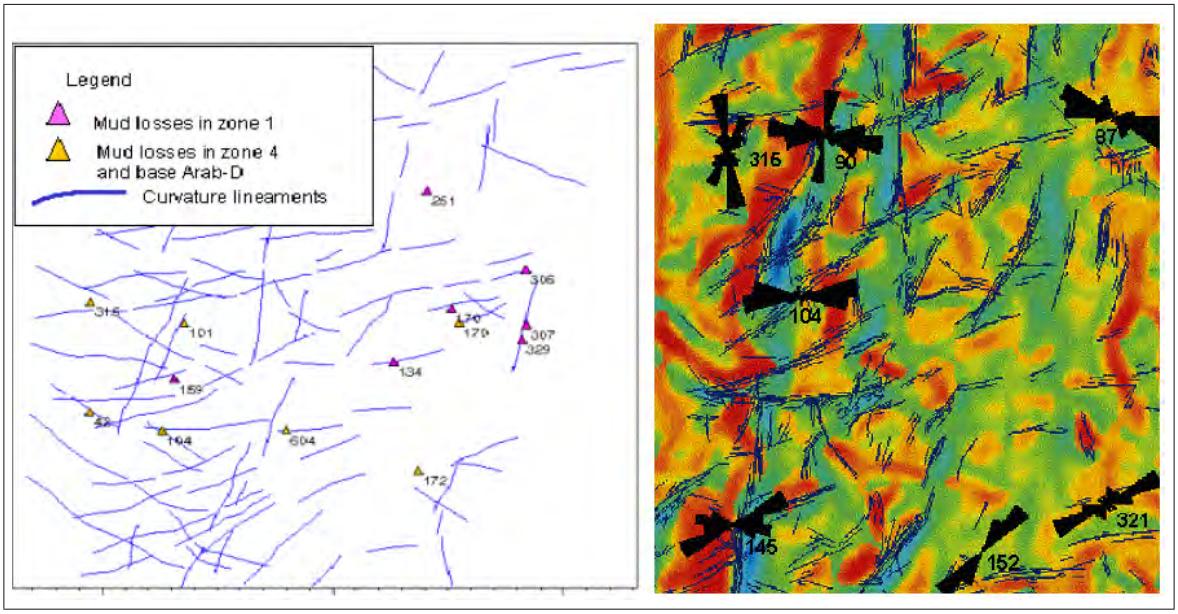

Fig. 5.19: Haradh well lost circulation data, left, and image log data, right[4]

Thresholding is demonstrated in Fig. 5.20, using cumulative lengths per grid block. The top right figure shows that individual fracture grid blocks over which the sum of fracture lineament lengths exceed $150m$, are subject to the transmissibility calculation detailed in Fig. 5.21. Fracture grid blocks failing the threshold are null in the fracture grid. In this case, the matrix grid of the dual grid model controls flow at these failed locations. The black nodes are those blocks which originally contained lineaments, but failed the thresholding. The lower right discretization in Fig. 5.20 presents the results of a $250m$ thresholding.

Flow in the fracture grid, therefore, is controlled by interblock transmissibilities, not permeability. Flow in the matrix grid is controlled by permeability, derived from a geologic model.

The importance of the fracture systems on flow is demonstrated in one study[59] with a synthetic model, the results of which are shown in Fig. 5.22. The authors extracted a model from the western half of the northern study area, comprised of an area 2 km wide (north -south direction). This represents a width to length ratio of approximately 1:5. The authors indicate both a fine scale single grid model and coarse dual grid model used in the study. The objective of the study is to

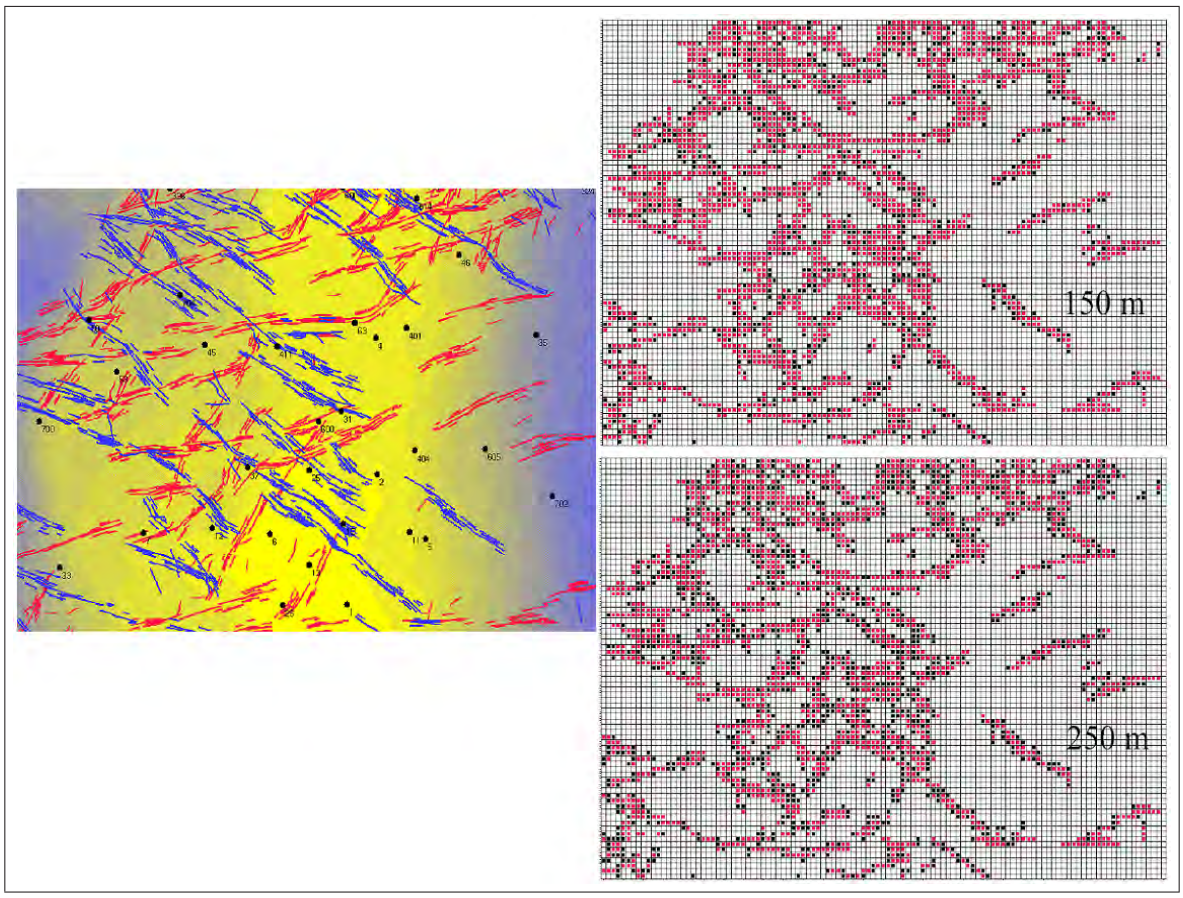

Fig. 5.20: Fracture mapping and discretization [4]

ascertain the relative importance of three flow elements under boundary conditions in which water is injected in the down-dip, western end of the model, and oil and water are produced at the updip, eastern end of the model. The flow components analyzed are: matrix permeability, thin, high permeability layers, and DFNs. The results of four cases are presented in Fig. 5.22 : a model comprised of only of a matrix permeability, a model having both a matrix permeability model and a thin, permeable layer (labeled "SK", or super-k, consistent with the accepted nomenclature), both in the form of a single grid and dual grid discretization, and finally, a combined matrix permeability model and DFN model. There are many aspects left unexplained by the authors concerning this study, such as the areal extent of the thin, permeable layer, the dimensions of the DFN, and which model, single grid or dual grid, is used

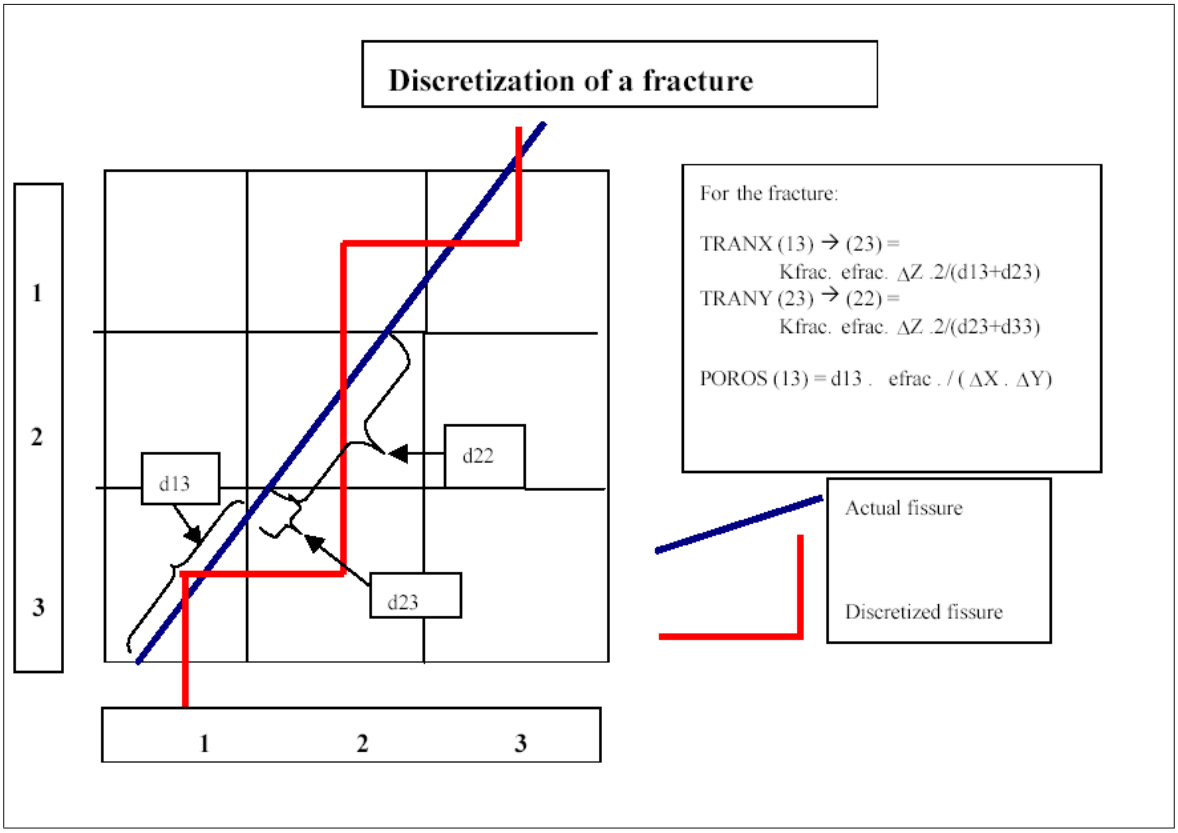

Fig. 5.21: Fracture discretization [59]

for the DFN case. Nevertheless, one important conclusion may be derived: a DFN model can generate early water breakthrough simulation results.

Dual grid and single grid flow simulation studies

Dual grid flow simulation models have been used in reservoir characterization studies at Haradh, most specifically to optimize development of horizontal wells, through models developed in both the northern and southern study areas. These models were constructed as described in the previous section, using 3D seismic derived fracture lineament maps.

The northern area was modeled with a 46000 cell dual grid simulator, consisting of 13 layers, with $250m \; x \; 250m$ cells. The authors reported an adequate history match of two study area wells. The model was used to predict optimal layer placement of

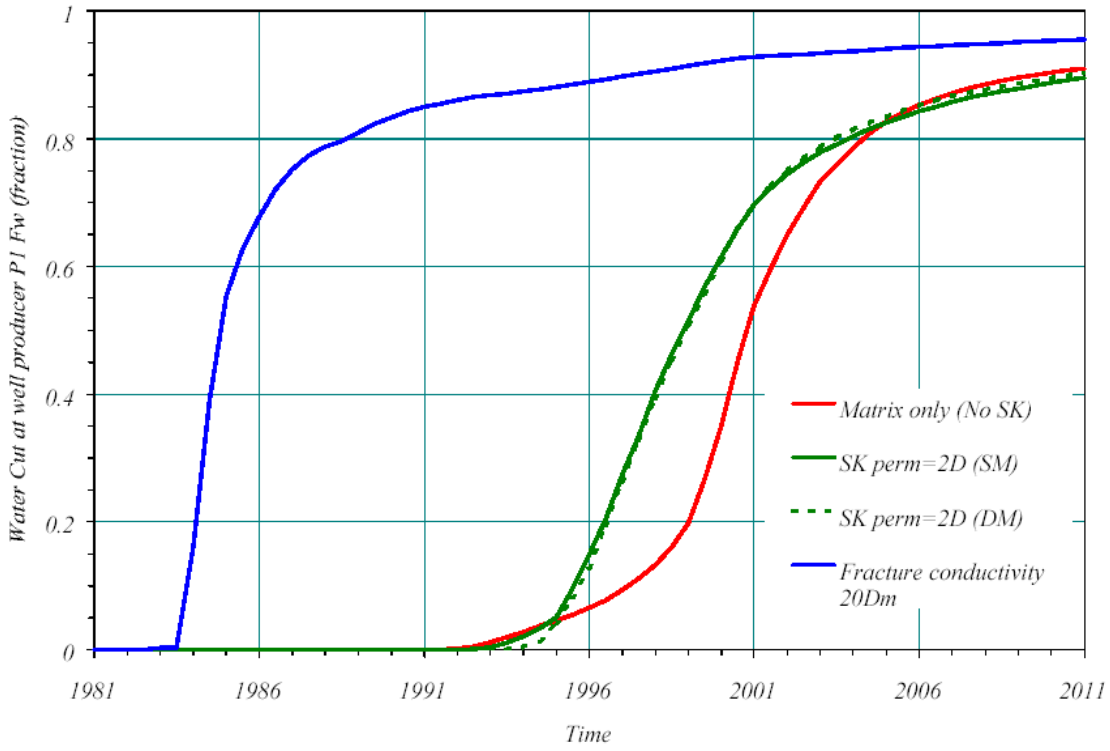

Fig. 5.22: Synthetic flow simulation comparative study[59]

horizontal wells; it was concluded that Zones 2A and 2B were the layers in which horizontal wells, if oriented such that DFNs were minimally intersected, would maximize oil recovery and oil production rate[62]. This result reflected the bottom-up water displacement predicted by the model.

Another model[60], constructed to characterize the southern study area, was comprised of 50000 cells, 15 layers, and the same cell size as the northern study area model. This model was used to ascertain the sensitivity of the production forecast under a horizontal well development restricted to Zones 2A and 2B, to various reservoir parameters. The parameters included DFN transmissibility and connectivity, and the permeability of thin, high-flux intervals observed in well flowmeter surveys. The range of investigation for DFN transmissibility was presented in the previous section, as was the idea of thresholding cumulative lineament lengths in constructing DFNs of various degrees of connectivity. The permeability of thin, high-flux layers

varied from 500 *md* to 5 *darcies*.

The sensitivity study concluded that forecasted production from horizontal wells drilled at the top of the reservoir, in Zone 2, if oriented such that they do not intersect DFNs, benefit from high DFN transmissibility and connectivity, and high permeability in the thin, high-flux intervals. This reflects, again, the predicted bottom-up waterflood displacement, which minimizes lateral water channeling through high conductivity reservoir regions.

A single grid model[64] was constructed for the northern study area, in which DFNs, derived from 3D seismic predicted lineament maps, were incorporated through modification of grid block permeability and relative permeability. The permeability k_b intersected by fracture lineaments was computed as,

$$k_b = k_m + \frac{k_f n_f d_f}{d_b}$$

where k_m is the cell matrix permeability, k_f is the fracture permeability, n_f is the number of lineaments intersection the cell, d_f is the fracture lineament aperture, and d_b is the cell length (square cells). Unfortunately, neither the magnitudes, nor the origins of any of the elements of the second, right side term, is provided by the authors. The relative permeability function for each grid block is a combination of a linear function, representing the DFN, and the matrix relative permeability function. The authors offer no history matching examples, and do not indicate any use of the model as a predictive tool.

Unresolved matters

Two principal difficulties are noted from a review of the published Haradh studies:

- A glaring omission in the literature describing the incorporation of DFNs into the models, is a description of the projected vertical dimensions of the lineaments, and the corresponding number of flow simulation layers intersected by the fracture systems. The omission implies all layers are intersected, or as logically, only the uppermost layer. No reports of the sensitivity of production forecasts to this parameter was found in the literature.

- The problem of computational convergence plagued these models when a high level of isotropy is incorporated into the DFN characterization in both the dual grid and single grid approaches. Specifications of the level of anisotropy required for convergence, that is, to attain practical timestep lengths and therefore reasonable computation durations, was not given. If the practical computational level of anisotropy is similar to that of the Uthmaniyah models, $2 \times 10^{-6} < k_{v/}/k_f < 4 \times 10^{-6}$, then vertical equilibrium in the DFNs cannot be attained in simulation, and therefore the contribution DFNs make toward vertical equilibrium in the reservoir, cannot be deduced through flow simulation. Therefore, if vertical equilibrium, that is, a bottom-up waterflood displacement, is observed in the flow simulation models, then it must be attributed solely to isotropy in grid blocks which are not intersected by DFNs.

- No assessment of uncertainty in the DFN models has ever been reported. Although the Haradh static DFN model is stochastic, the use of the model to estimate DFN model uncertainty, or even cursory, qualitative discussions as to the possible sources of uncertainty in the static models, has not, unfortunately, been provided in the published literature.

Chapter 6

The flow mechanics of super-k

A heuristic, simple super-k model is developed in this chapter. The model is a tractable one, in that it can be practically incorporated into both a geostatistical reservoir model, and a reservoir flow simulation model, utilizing tools presented in Chapter 7 and Chapter 9. Furthermore, the model is supported by both analytical and numerical studies of flow and pressure behavior of its most important component, the DFN. These studies are described in Chapter 8.

The heuristic model is based upon simple flow models, which clarify the flow process involved in inducing the anomalous flow signature of super-k. It is shown that the combination of a few simple flow concepts, suffices toward a plausible description of super-k mechanics.

6.1 A precise definition of super-k

SA defines super-k as intervals in which the liquid flux, injection or production, exceeds 500 $B/D/ft$, and which account for more than 50% of the total well flow. The definition is limited to observed flux because super-k has historically eluded more precise description or prediction, either geologically or hydraulically.

We believe the benchmark flux, and higher, may be further clarified as a flux that cannot be predicted by conventional radial influx performance models; this characteristic of the flux provides for the superlative of the moniker. This approach then

prompts us to offer a precise analytical super-k model, which we have done, using elementary flow models.

A demonstration of the more technical description of super-k, as a well interval in which the flux defies conventional influx performance description, is presented in Fig. 6.1, Fig. 6.2, and Fig. 6.3. These data are taken from five wells from a study[65] in the Haradh Sector, in which flowmeter data was used to distribute total well transmissibility, derived from well pressure transient tests, over the producing interval of a well. The data are presented here as cumulative transmissibility, kh, generating a profile of increasing transmissibility from the bottom of the interval to the top, with the uppermost point corresponding to the total well transmissibility. This profile is referred to as the "reference profile," in the plots. The data are presented as such because the imposition of a vertically constant pressure gradient, as well as a constant skin effect, over the producing interval, will yield a flow profile of identical shape.

The accompanying profile in each plot is that corresponding to cumulative transmissibility derived from core-measured permeability.

The flux over the producing interval, expressed as $B/D/ft$, is proportional to the slope, $\frac{dkh}{dh}$. Inconsistencies between the two profiles may be interpreted as due to differences in flux at one or more intervals in the well, if the flux were computed from the transmissibility profiles. Super-k may be understood as present in those intervals in which flux inconsistencies are demonstrated, with the observed flux exceeding the flux computed from core permeability. The implication of the discrepancy is the failure of either, or both, of the assumptions of constant pressure gradient, or constant skin effect, over the producing interval.

The classic signature of Ghawar super-k is flux inconsistency over discrete, thin intervals; indeed, the signature is apparent in these plots, in thin intervals over which the reference curve flattens appreciably, relative to the core permeability-derived curve. It is not known if the actual flux generated in these wells surpassed the official SA threshold definition of 500 $B/D/ft$. It is apparent, however, the 50% flow contribution threshold is met in some of the thin intervals in these particular wells.

It will be shown in this chapter that the discrepancy in flux lies most probably, in

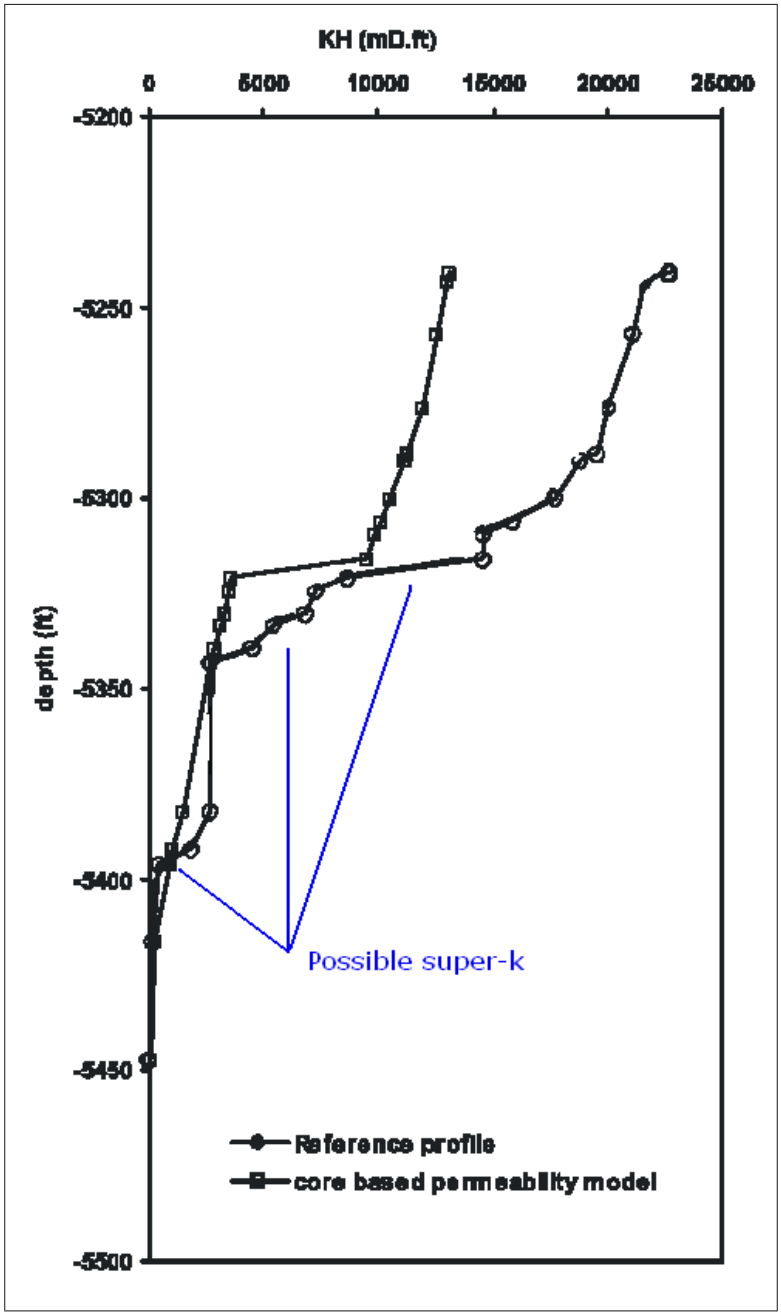

Fig. 6.1: Cumulative transmissibility from core and flowmeter data[65]

the case of Ghawar wells, in the constant pressure gradient assumption, as preferential interval stimulation, or damage, has not been imposed, or observed, in the openhole completions of Ghawar wells, in either injection wells or producing wells. Therefore,

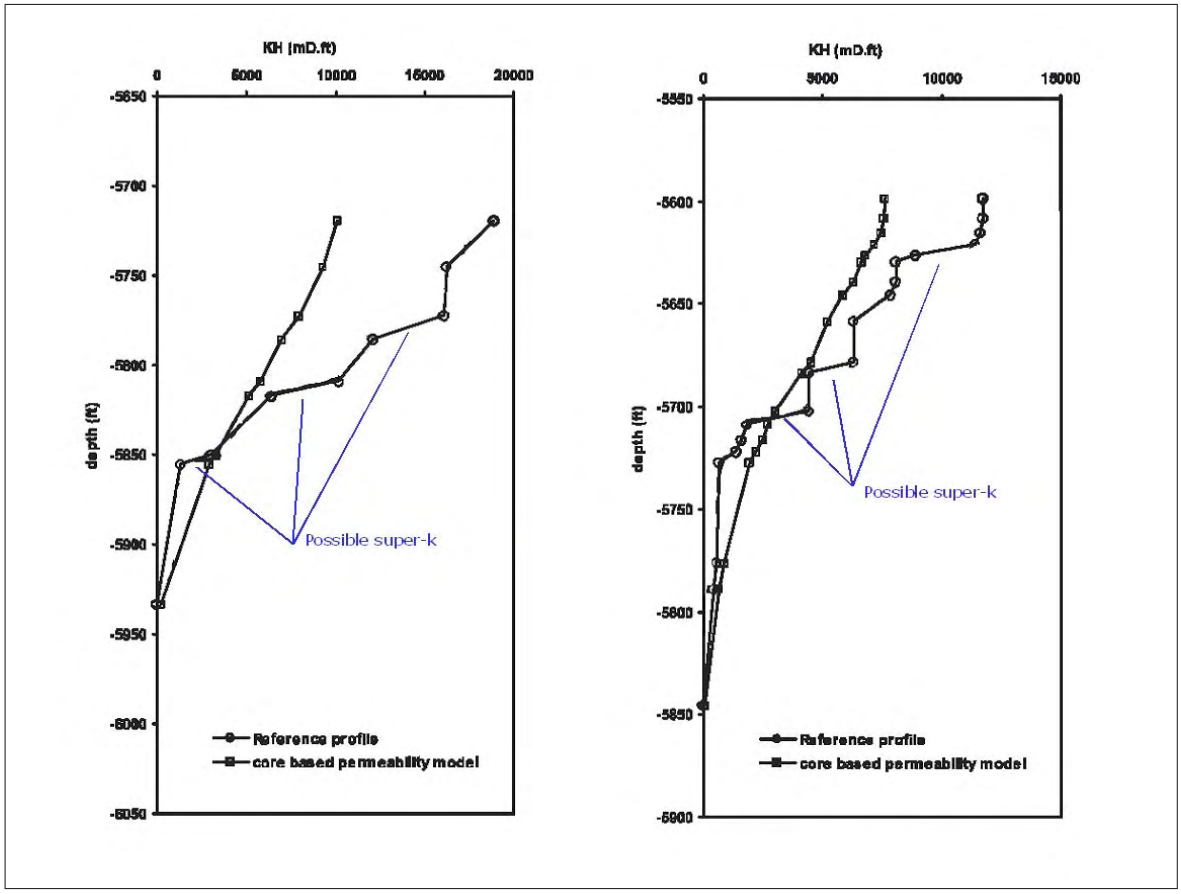

Fig. 6.2: Cumulative transmissibility from core and flowmeter data[65]

the implication of heterogeneity, which follows from nulling the constant pressure gradient assumption, provides insight into the flow mechanics of super-k.

6.2 Influx performance of super-k

Super-k structures are, potentially, secondary recovery (water injection) management problems, and therefore objects requiring prediction. Some instances of production well abandonment have been attributed to super-k. High water cut at producing wells that are hydraulically connected to injection wells through super-k structures, has been mitigated historically by production well abandonment. Super-k structures thieve so effectively as to sometimes prevent zonal isolation by cement squeezing.

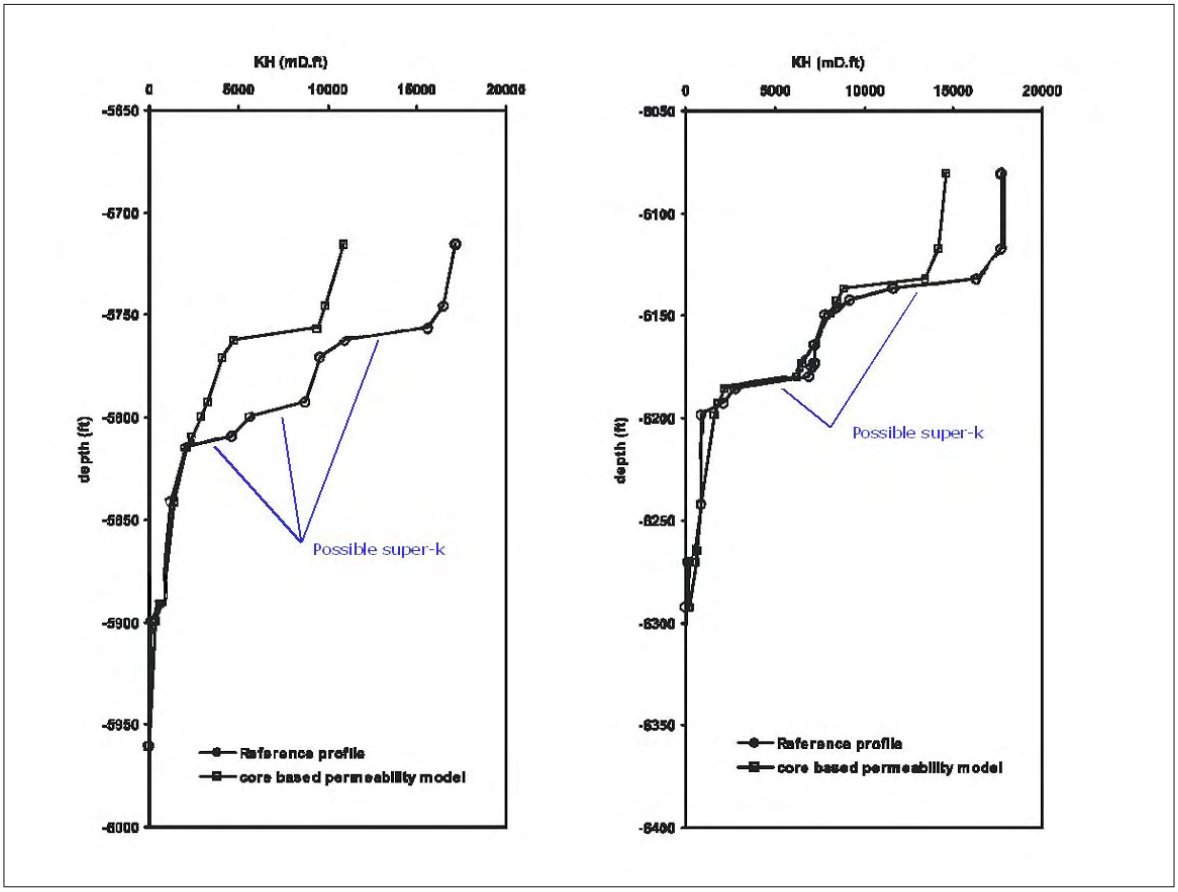

Fig. 6.3: Cumulative transmissibility from core and flowmeter data[65]

Super-k, however, contributes to primary recovery efficiency in "dry areas", those areas defined by the operator as not having been effectively repressurized or swept by injection water. Here, super-k may provide high conductivity conduits from high storage, high permeability facies units, to producing wells.

Super-k zones were named such because production rates from the zones exceeded that predicted by conventional influx performance. Fig. 6.4 shows the distribution of maximum flux values (FI_Rate) for 450 wells in the Uthmaniyah sector. A majority of the wells have intervals of maximum flux which exceed the 500 $B/D/FT$ (log value of 2.7) super-k benchmark, a large proportion exceed 1000 $B/D/FT$ (log value of 3), and some flux values exceed 10000 $B/D/FT$ (log value of 4).

The significance of these levels of flux can be seen with a simple steady state radial

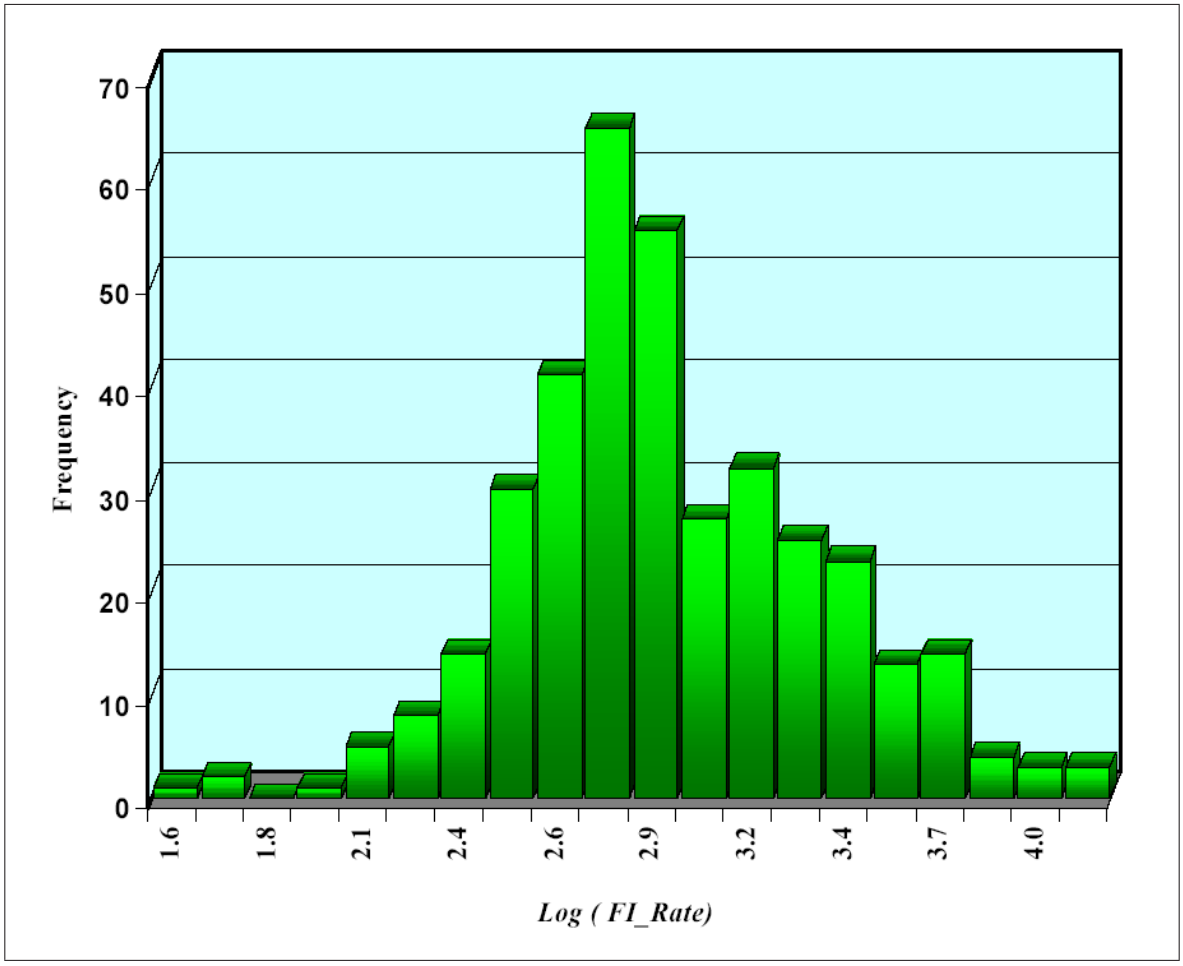

Fig. 6.4: Maximum well flux in 450 Uthmaniyah wells[54]

flow model:

$$\frac{q}{h} = \frac{0.00708k(p_r - p_w)}{\mu B_o(\ln r_e/r_w - 0.5 + s)}$$

where p_r is the average reservoir pressure in the well's drainage radius. Substituting appropriate values, and a minimum and maximum stimulation effect of $s = 0$ and $s = -4$,

$$2(B/D/FT)/(psi \cdot darcy) < \frac{q}{h} < 4(B/D/FT)/(psi \cdot darcy),$$

that is, the flux varies between 2 and 4 $B/D/FT$ for each psi drawdown and each

darcy of permeability.

The literature (Chapter 5) indicates producing wells are acidized to remove drilling damage, and moderate stimulation may be incurred[55],[52]. Skin values in producing wells are not widely reported, although moderate skins of the magnitude -2 are evident from reported improvements in productivity index[55],[46]. It is not believed that large negative skins are obtained on Ghawar producing wells. However, the literature reports[48],[50] large magnitude stimulation of water injection wells, with skin values approaching -7. These stimulation results are discussed more fully in Sec. 5.1.2.

Ghawar wells operate on natural flow, and must have a wellhead flowing pressure capable of producing against a separator pressure of several hundred psia. A wellhead pressure of 750 $psia$, for example, for 4900 B/D production, against a 320 $psia$ separator pressure, was described in one publication[55]. Typical liquid producing rates may be higher, with rates above 10000 B/D not uncommon[55]. Maximum reservoir pressure does not exceed 3000 $psia$, and is currently several hundred psi less in the majority of the reservoir. Assuming an oil gradient of 0.31 psi/ft and an interval depth of 7000 ft, the drawdown at the reservoir, at 750 $psia$ wellhead pressure, is 80 psi, maximum. This is a reasonable guess, as much lower drawdowns, for much higher rates, have been reported. A 21 psi drawdown for a flux of 600 $B/D/FT$ is an example[71]. Thus, at an 80 psi drawdown,

$$160(B/D/FT)/darcy < \frac{q}{h} < 320(B/D/FT)/darcy,$$

Therefore, several $darcies$ of permeability may be required to produce the benchmark flux of 500 $B/D/FT$, and permeabilities approaching many 10's of $darcies$ are required to produce the highest flux values, given an undamaged or stimulated well. If the well is damaged, then even higher permeabilities are required. Arab-D core measured permeabilities of magnitudes exceeding 2-3 $darcies$ are rarely reported. Thus, many measured flux values greatly exceed those predicted by this conventional radial flow analysis.

However, Ghawar water injection pressure gradients may reach magnitudes of 0.55 to 0.8 psi/ft,[50] thus enabling water injection pressure drops into the reservoir of

1000 *psi* to 3000 *psi*. The maximum range of undamaged or stimulated fluxes in this case would then be,

$$2000(B/D/FT)/darcy < \frac{q}{h} < 12000(B/D/FT)/darcy,$$

Thus, super-k flux magnitudes are reached in water injection wells in intervals having permeabilities significantly less than a darcy, assuming undamaged or stimulated intervals. If the interval is damaged, then the permeability requirement will be higher. This suggests super-k occurrence will be preferential to water injection wells, and indeed this is the case, at least in one of the sectors in which the published data is available to evaluate such a phenomenon (see Sec. 6.3.2).

6.3 Requirements for "stratiform" super-k

The technical literature has adopted the moniker "stratiform" super-k for the predominantly thin intervals in which super-k flux magnitudes are observed. Stratiform super-k is regarded as a facies-only super-k structure, in which permeabilities of enormous magnitudes, as described in Sec. 6.2, exist in a single, laterally extensive facies, and provide the requisite conductivity required for super-k magnitude influx. A facies possessing a permeability of 77 D, extending over an area of 1.2 km, for example, was modeled in a recently published production well test analysis[71]. This zone produced 600 $B/D/FT$ with a 20 psi drawdown.

There is no conclusive data in the literature, however, of the existence of such a facies. Although laterally extensive facies surely exist in the reservoir, and some of these have core measured permeabilities in the 2-3 darcy range (Table 5.1), no facies of multiple 10's of *darcies* has been reported. It is evident from published core slab photos that vugs in some facies have sufficient cross sectional areas to host enormous permeabilities. However, no published data suggests any facies at Ghawar may have a connected network of vugs extending distances of kilometer scale.

We hypothesize, therefore, that the high conductivities associated with super-k flux is derived from DFNs. We explore further in this section, however, the evidence against stratiform super-k, as a sole mechanism for super-k flow.

6.3.1 Carmen-Kozeny computed grain diameters

A rendering of a *pore* geometry, corresponding to rock of magnitude 10s of *darcies*, may be made with the Carmen-Kozeny equation, which relates the permeability of a porous rock, having constant grain size, to the grain diameter:

$$k = \frac{1.0 \times 10^6}{72\tau} \left[\frac{\phi^3}{(1-\phi)^2} \right] D^2,$$

where k is the permeability in *darcies*, τ is the pore geometry tortuosity ($\tau = (L_T/L)^2$, the square of the ratio of the length of the tortuous pore path, to the superficial linear path length), ϕ is the rock porosity, and D is the grain diameter, in millimeters.

If the referenced rock of 77 *darcies*, for example, possesses a 25% porosity, and a tortuosity of 5 (not atypical), then the grain size of this rock is 1 millimeter. Thus, permeabilities of these magnitudes correspond to very unusual rock indeed, in that enormous, vug scale, pore sizes must form connected networks in pods exceeding one kilometer in diameter.

6.3.2 Lithofacies of super-k in the Hawiyah Arab-D

Two general facies dominate the literature as apparently capable of rendering permeabilities of this magnitude, over adequate lateral extent, as stratiform super-k: skeletal, oolitic, or pelloidal grainstones, and sucrosic or vuggy dolomites. An extensive core study of super-k intervals[9] reveals, in part, the difficulty in substantiating the stratiform super-k model. Fig. 6.5 presents the distribution of wells which possess super-k intervals, in the Hawiyah sector, in which our study area is located. The possible significance of the plethora of super-k occurrences in zones 2A and 2B, is discussed in Sec. 6.5. Here, 88 wells, both producers and injectors, have known super-k intervals.

Note the high relative frequency of super-k wells on the flanks of the sector, at the productive boundary of the field, where peripheral water injection wells are located. As discussed in Sec. 6.2, this observation is expected, given the high injection pressures

in these wells, relative to the significantly lower drawdown pressures at producing wells.

Seventeen of these wells were cored. Core analyses from eight of these wells are published[9], and we will reproduce summaries of a few of these here, demonstrating the conspicuous lack of core permeability magnitudes discussed in the previous sections. The eight wells are labeled with letters A through H in Fig. 6.5.

Well A, Fig. 6.6, contains a Zone 2B super-k interval of skeletal grainstone in which thin section photomicrographs show, at left, a cross section of a complete skeleton called *Cladocoropsis,* and right, fragments of the skeleton. The facies, lithology, and grain support legend is found in Fig. 4.5. In both photomicrographs, the *Cladocoropsis* is in white, other skeletal grains are brown, and pore space is blue. *Cladocoropsis* was a coral or sponge-like organism composed of thin branches, each several centimeters long and a few millimeters in diameter. The fossil of this particular animal is associated with more super-k grainstone intervals than any other organism. It is found within super-k intervals, both whole and fragmented, in grainstones, as in Fig. 6.6, and as ghosts, where it is leached out whole, leaving only vugs, in dolomites. Fig. 6.7 presents two core slabs of whole *Cladocoropsis* in a mud supported limestone, left, and fragmented *Cladocoropsis* grainstone, right. The mud supported rock is presented to display the geometry of the *Cladocoropsis*, although such a matrix supported rock would never conduct a super-k magnitude flux. However, a dolomitized version of this rock, in which whole *Cladocoropsis* skeletons have been leached, and are in high enough proportion to form a connected network, have been documented as perhaps the most prolific super-k intervals[9],[55],[71].

Note the core measured permeability in Fig. 6.6, in the super-k interval, of between 120 mD and 450 mD, despite millimeter scale pores, and pores within the Cladocoropsis skeleton itself. This permeability range is definitely not capable of the benchmark super-k flux of 500 $B/D/FT$, under typical drawdowns. The most logical explanation for the "depressed" permeability is lack of pore connectivity.

Well B is a water injection well with several Zone 2B super-k intervals. It is a prolific injector, having a 42000 B/D injection rate during flowmeter testing. The

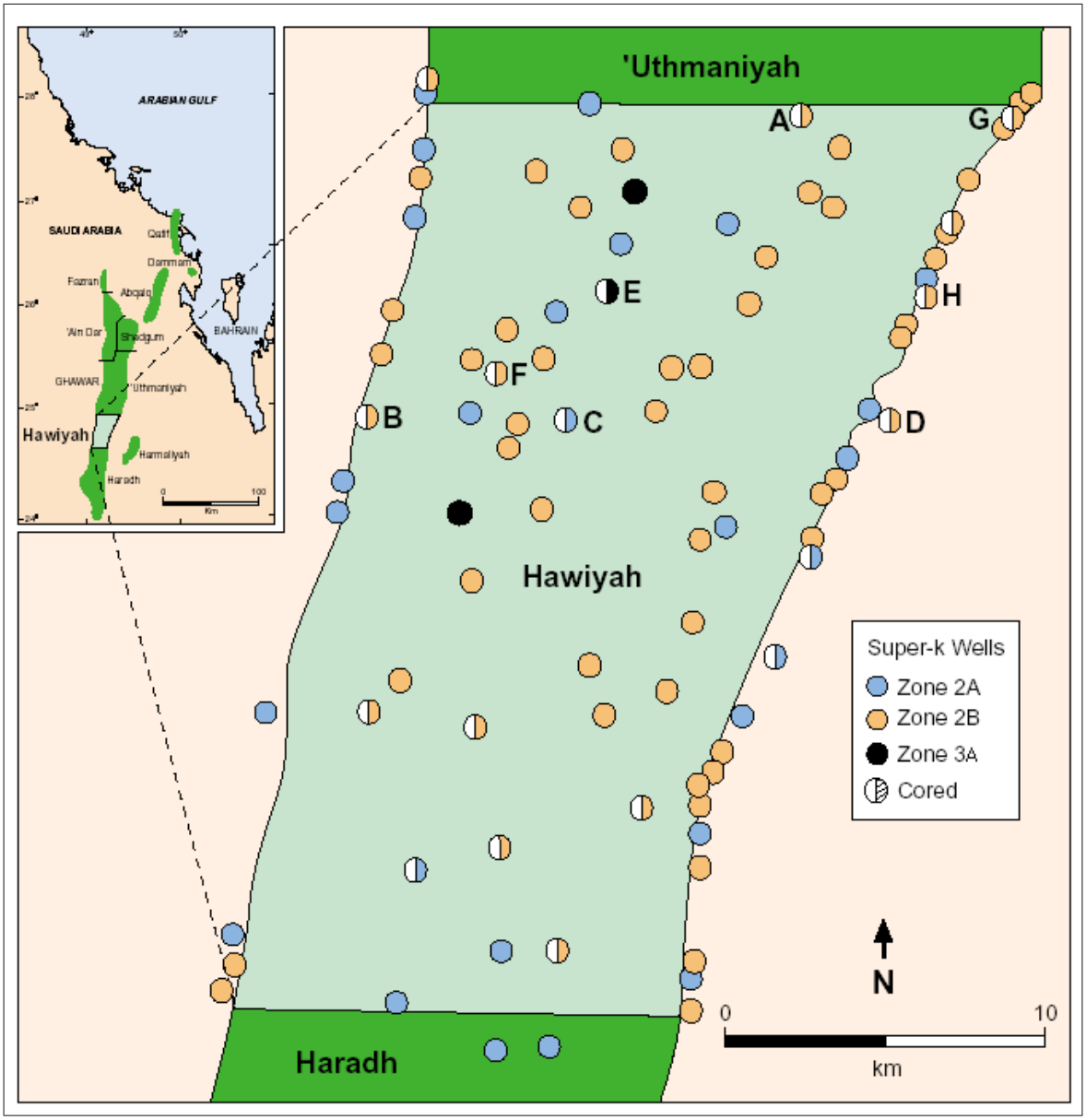

Fig. 6.5: Areal and zonal distribution of super-k[9]

super-k zones in this well are labeled A through F, and took the following injection fluxes during the flowmeter test: A, -500 B/D/FT, B, -705 B/D/FT, C, -1905 B/D/FT, D, -2540 B/D/FT, E, -930 B/D/FT, and F, -680 B/D/FT.

As indicated in Sec. 6.2, these flux values are reasonable, given the high injection pressures of Ghawar water injection wells, although the low permeabilities of super-k

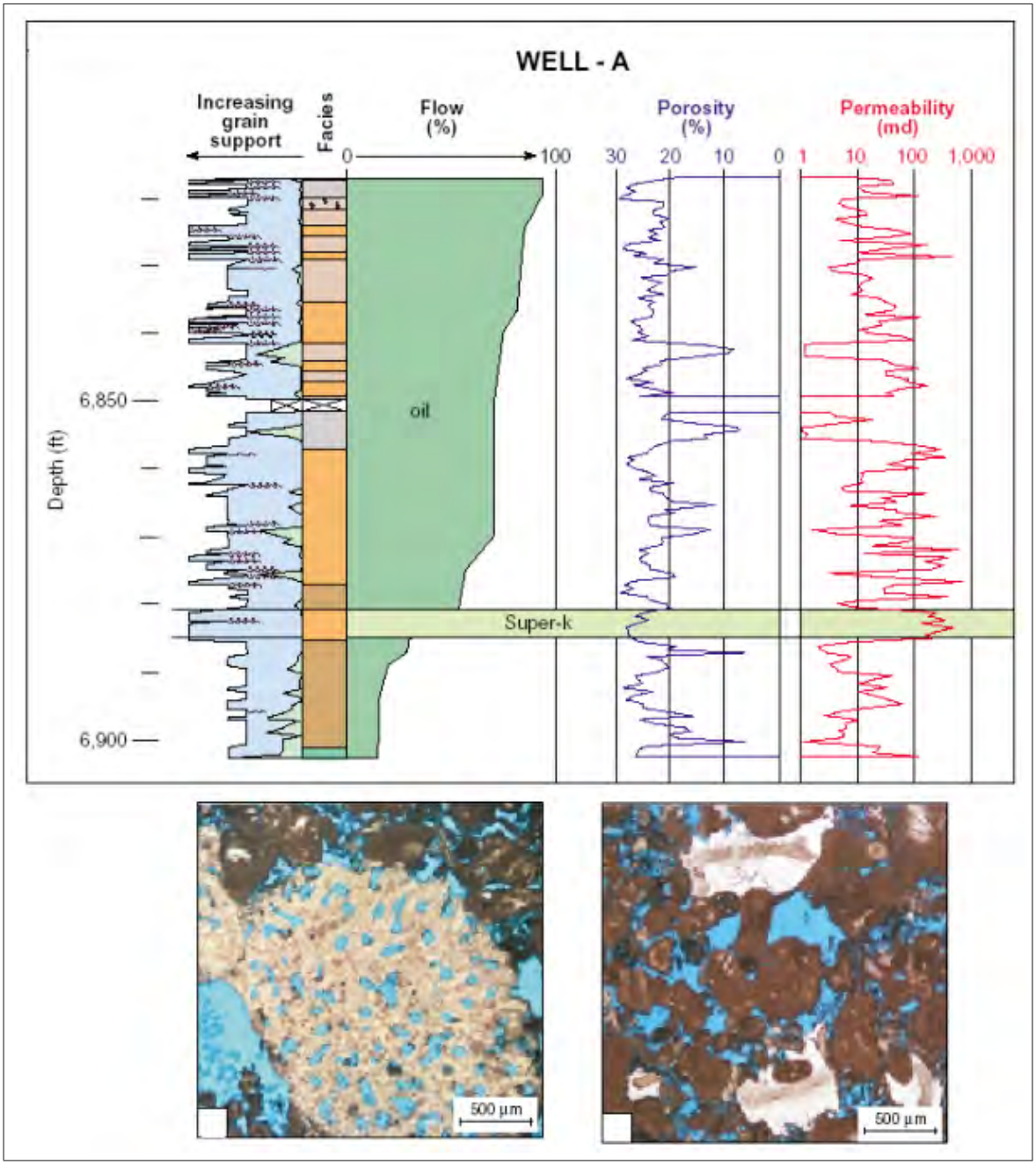

Fig. 6.6: Core analysis summary and thin sections from super-k interval of Well A[9]

zones A and F suggest these intervals are stimulated. It has been suggested[50] that Ghawar injection pressures often exceed reservoir fracture pressures, and that injection induced hydraulic fractures are formed. These fractures may be extensive.

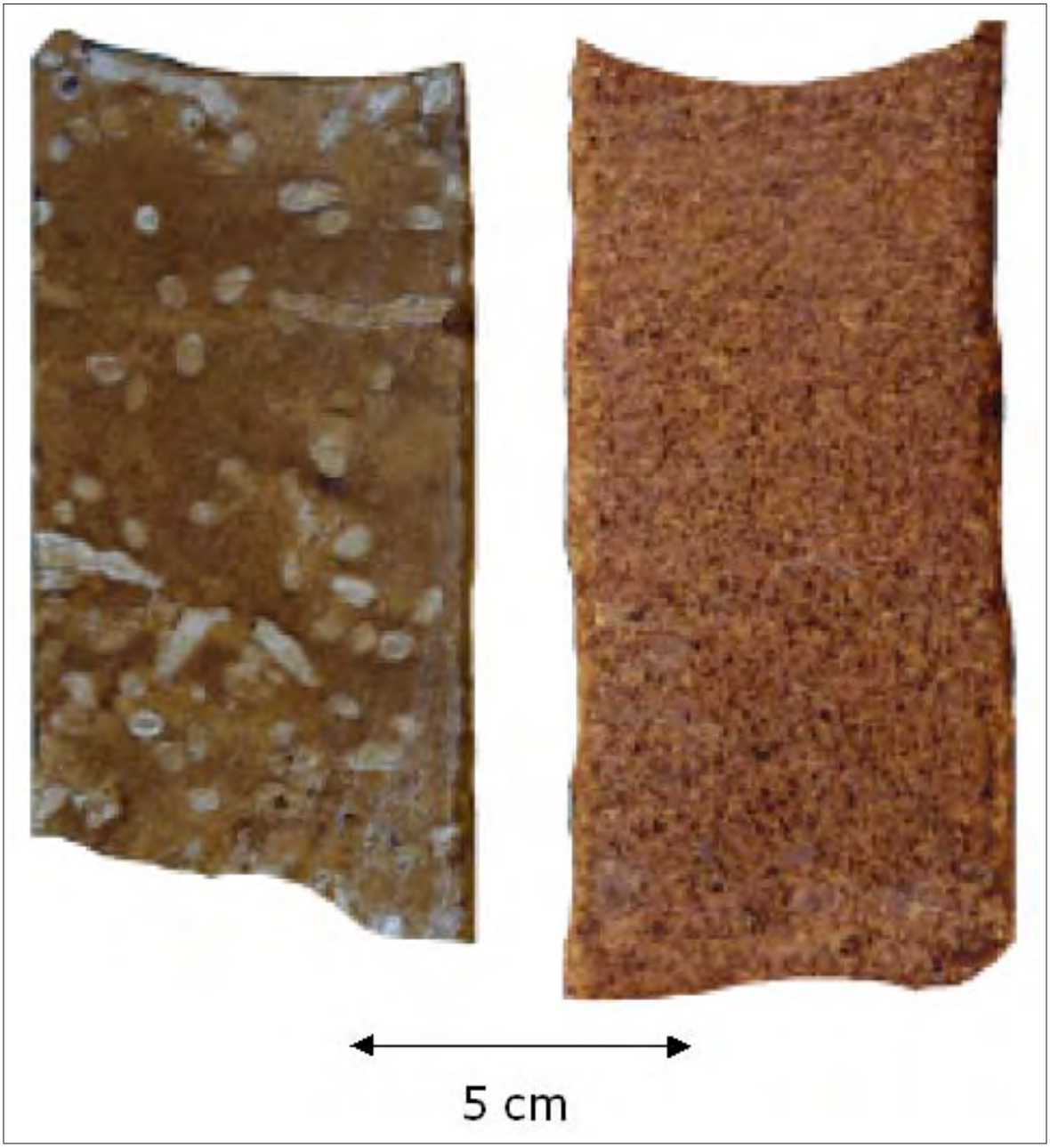

Fig. 6.7: Core slabs of Cladocoropsis limestone [66]

Otherwise, influx performance as predicted by the simple stratiform super-k model is consistent with observed flux magnitudes in this well. However, there are inconsistencies in the measured data which the simple model cannot reconcile.

Note that the highest flux interval, D, is almost a factor of four times more productive than the B interval, although the permeability of the B interval is higher. If this discrepancy is not due to skin effect differences, then it may be concluded that a simple radial influx performance model cannot predict the observed data. This matter is addressed further in Sec. 6.4.

Although the thin section micrographs show the *Cladocoropsis* facies corresponding to the highest flux interval, D, the remaining super-k intervals in this well also include oolitic grainstone facies, and mixed skeletal, pelloidal facies.

The highest super-k permeability was recorded in another water injection well, Well D, which is summarized in Fig. 6.9. The super-k interval here is a vuggy dolomite, in which the vugs attain diameters of several millimeters. An example of a large vug is shown in the thin section photomicrograph in Fig. 6.9. The core permeability of this zone was 2.7 D. The flux of this super-k zone was measured at 9000 B/D/FT. Nearly 60% of the total well production exits from the 2 ft super-k interval. As with Well B, the radial flow model seems to predict the flux magnitude adequately, given high injection pressures.

A final example, showing plainly the failure of the homogeneous radial flow model in predicting super-k flux, is presented in Fig. 6.10. Well F is a producing well with a Zone 2B super-k interval. This 4 ft interval possesses a flux of 5843 B/D/FT and accounts for 84% of the total well production. Incredibly, most of the interval is a tight dolomite, a thin section of which is shown in Fig. 6.10, on the right. The average permeability of the interval is 120mD, with a maximum 700 mD occurring at the top of the interval. This maximum permeability corresponds to a vuggy and sucrosic dolomite, shown in the thin section on the left in Fig. 6.10. Clearly, these permeabilities do not support the observed flux, even in the case of stimulation (Sec. 6.2).

6.3.3 Summary

We have attempted to indicate here that despite core-measured permeabilities of prolific magnitudes, the various lithologies and facies that have been correlated to

super-k intervals of the Arab-D nonetheless are not characterized with the magnitude of permeability observed in well response and flood front velocities. The following sections present analyses which support a super-k construction, incorporating DFNs, that provides for the observed prolific magnitudes of super-k flow capacity.

6.4 Multi layer analysis

Super-k is enigmatic only in its specific geological manifestations, which may be many, and not in its basic mechanics, which are easily understood using basic flow models.

We have shown that one principal difficulty encountered with facies models which do not include DFNs is that associated simply with radial flow; this is demonstrated in Appendix F, in which significant variations in a facies model, generates insignificant perturbations in simulated well performance (well pressure and well total rates) results. Appendix F describes our history matching attempts using training image-based facies models, and a probability perturbation algorithm.[74]

Our attempts to history match specifically flowmeter data that exhibited super-k flow behavior, using only a facies model, were not successful. In fact, several facies models, predecessors to the models that incorporate DFNs, to be described in Chapter 10, were used, unsuccessfully, in an attempt to form high conductivity networks, and therefore to replicate super-k flow behavior.

The common result of the facies model flow simulations was that abnormally high zonal flow rates, measured in a flowmeter survey, could not be reproduced under the conditions in which the facies models were constrained to facies data at the well, derived from well log analyses. Thus, despite the spatial perturbation of facies having very large permeabilities in the facies model, the well constraint predominantly controlled inflow performance. Unfortunately, measured Arab-D inflow performance is not controlled by facies properties at the wells in super-k zones.

These results may be explained vaguely as resulting from radial flow, which is the predominant regime in facies only models. We will show in the next section that models which induce a predominance of linear flow, those incorporating highly conductive DFNs, are more appropriate in predicting super-k behavior.

Radial flow dictates that the highest radial pressure gradients occur nearest the well. Therefore, permeabilities of facies away from the well, even when made unreasonably high, have a limited effect in increasing flow capacity in facies constrained intervals at wells. If facies are constrained at the well, as they are in this study, then the constraints largely determine the flow at the well, and therefore the simulated flowmeter response.

Therefore, even facies models that are successful at generating extensive, high-permeability, flow networks, and successful at constraining the networks to thin intervals at the wells, fail in generating super-k flow behavior. Even if unreasonably high permeabilities are allowed to become a part of the network, the facies constraint at wells, and the assignment of measured, or reasonable, permeabilities to those facies, renders the components of the simulated network, away from the well, as relatively unimportant.

Fig. 6.11 and Fig. 6.12 show examples of this result. The plots present flowmeter flux data and simulation results, over the vertical producing interval of the well, represented on a flow simulation vertical axis scale, in units of simulation grid vertical block number.

Fig. 6.11 presents flow simulation and history matching results, for one of the flowmeter tests, that of the water injection well located on the west end of the study area (Fig. 3.2), using a facies only model. This is a modest example of super-k. Much larger discrepancies between computed and measured inflow performance exist, including that of a producing well in our study area (Chapter 10).

In this case, a training image-based, binary facies model is used. The facies components consist of a high permeability facies, in green ("grainstone"), having permeability $k_1 = 2000\ md$, and a lower permeability background component, with permeability $k_2 = 300\ md$, in blue. Fig. 6.12 presents the same history matching attempt using a facies model which includes a third, very high permeability facies called "super-k bed." The third component is given a permeability of 5000 md. This model is described in detail in Sec. 10.2.

Both figures present flow simulation results for 15 realizations of each model. The realizations differ in the spatial distribution of facies, perturbed with the probability

perturbation method.[74] Compared to the flowmeter simulation results, in blue, are the measured flowmeter data, red. The simulation results and data are plotted as BPD/ft, vs. vertical well block number (z). The interval of interest is that from 50 to 52, having a measured flux of approximately $2000 BPD/ft$. This interval is constrained to grainstone, while the lowest flow interval, at z = 33 to 43, is constrained to background facies.

Here, the ratio of flux from the highest flow interval to that of the lowest flow interval, $\frac{q_1}{h_1}/\frac{q_2}{h_2}$, is computed for the simulated results, with the outcome, for both models,

$$\left(\frac{\frac{q_1}{h_1}}{\frac{q_2}{h_2}}\right)_{simulated} < 5.$$

The value of the measured ratio is,

$$\left(\frac{q_1}{h_1}/\frac{q_2}{h_2}\right)_{measured} = 7.2.$$

This result was unchanged even for cases in which the third component permeability was assigned 10 *darcies*; essentially the third facies cannot significantly affect a layer's well performance in a predominantly radial flow regime.

6.4.1 The DFN and linear flow

The results above imply that a facies only model, under the conditions of radial flow, is not appropriate in predicting large interval flux magnitudes as measured in flowmeter tests. It follows that the appropriate model be that which is not dominated by radially convergent flow: the linear flow model. We discuss this concept in the next section.

It is also useful to hypothesize that the condition of radial flow is incurred by a facies only model. If that can be accepted, then it follows that linear flow may be induced by a different reservoir model. Indeed, both of these ideas may be supported, and the latter is further developed in this chapter and in Chapter 8.

The reservoir model we have adopted is one that includes a DFN. The efficacy of the DFN to induce linear flow in the reservoir is rooted in the well known paradigm of hydraulic fractures generated at the well for stimulation purposes, in which convergent flow is displaced from the well, to the fracture extremities, and the linear flow through the fracture is the dominant regime. The potentially very large permeability within the fracture is fully exploited in this model. It will be shown in Chapter 8 that this paradigm is also applicable in the case of natural DFNs that are isolated from the well.

Fig. 6.13 illustrates the ability of reservoir models per se to induce a specific flow regime. The case presented at the top of the figure represents a facies only model, with a high permeability facies, in red, located away from the well, in green. It was shown in the previous section that the facies, no matter how conductive, does not significantly alter the radial flow regime, under which permeability nearest the well, outlined in blue, dominates well performance.

The second model, in the middle of the figure, represents the hydraulic fracture case, with the fracture shown in red. Here, convergent flow occurs at the fracture extremities, outlined in blue; the majority of the total system flow, under even modest fracture conductivity conditions, enters the fracture endpoints. The flow proceeds to the well linearly to the well, through the fracture, exploiting its relatively higher conductivity. Linear flow therefore dominates the system in the region intersected by the fracture.

The third schematic in the figure is essentially the model we propose, and further develop and analyze in this thesis. The isolated DFN, in red, will be shown to behave much like the hydraulic fracture, in that convergent flow occurs at the DFN remote endpoint, linear flow exploits the fracture conductivity, divergent flow exits the near DFN endpoint, and predominantly linear flow proceeds from the DFN to the well. As with the hydraulic fracture, modest DFN conductivities promote nearly all of the system flow to occur through the DFN. Thus, half of the reservoir system, on the right side of the well, over the length intersected by the DFN, is dominated by linear flow.

The facies-only model is lacking from other important aspects of conductivity and

geometry. Permeabilities characteristic of DFNs which are moderately conductive, may be enormous, especially in the Ghawar field. The ratio of fracture permeability to reservoir matrix permeability, k_f/k, depends on the DFN geometry, but the range $1000 < k_f/k < 100000$ is not atypical. Given Ghawar mean reservoir permeabilities in the $100s$ md, equivalent facies permeabilities of $100s$ $darcies$ would be required if a highly conductive facies were proposed to replace the DFN component. Furthermore, the facies must maintain the high permeability over an appreciable distance: in the case of Ghawar, from 1 to 10 km. A DFN, by definition, possesses both lateral extent and high conductivity. Very few, if any, real, geologic facies models can satisfy these conditions.

Note that the DFN model may be equivalently represented as two sources, red dots, which are hydraulically connected, as shown in the bottom of Fig. 6.13. This is particularly applicable in the case of an infinite conductivity DFN, as will be shown in Chapter 8. We show in that chapter that the reservoir pressure and flux distribution generated by this source model is practically identical to that of the DFN model, in all cases of reasonable DFN conductivity.

6.4.2 A layered, linear flow model

Consider a two-layer, two-facies linear flow model, in which the layers share common boundary conditions. Fig. 6.14 presents a schematic flowmeter plot showing layered production from the model, along with the calculated linear flows. The ratio of flux between two intervals is governed by permeability and pressure gradient:

$$\frac{\frac{q_1}{h_1}}{\frac{q_2}{h_2}} = \frac{k_1 \left(\frac{\partial p}{\partial l}\right)_1}{k_2 \left(\frac{\partial p}{\partial l}\right)_2}.$$

Here, skin $s = 0$. Note that measured ratios could easily be predicted without constraints on well skin. However, we assume here that skin is known, and that measured skin cannot predict measured inflow performance of super-k. The basis for a skin-induced super-k effect has never been proposed in the Ghawar technical literature (Chapter 5), as well stimulation is not emphasized in Ghawar wells.

Let the flux from layer 1 represent the higher flux. The maximum value for

the ratio is achieved with a layered model, similar to that depicted in Fig. 6.15, but with only two layers. In this linear model, the pressure gradients in all layers are necessarily equal, so,

$$\left(\frac{\frac{q_1}{h_1}}{\frac{q_2}{h_2}}\right)_{\max} = \left(\frac{k_1}{k_2}\right),$$

It should be noted that this maximum ratio is a reliable maximum, in that if boundary conditions dictate that the pressure gradients are different in the two layers, then the differential favors the low flux layer, since differential depletion performance in this system is dictated by the ratio $\frac{k_1}{k_2}$. Therefore, assuming equal initial layer pressures, if differential depletion has occurred, so that the layer boundary conditions (layer average pressures) are unequal, then layer 1 will be more depleted than layer 2. Thus,

$$\left(\frac{\partial p}{\partial l}\right)_1 < \left(\frac{\partial p}{\partial l}\right)_2,$$

and so,

$$\frac{\frac{q_1}{h_1}}{\frac{q_2}{h_2}} < \left(\frac{\frac{q_1}{h_1}}{\frac{q_2}{h_2}}\right)_{\max}.$$

Given the permeabilities of the binary model example above,

$$\frac{k_1}{k_2} = 6.7.$$

Any departure in the binary facies distribution from the layered model, as shown in Fig. 6.15, bottom figure, for example, will result in a ratio *lower* than the maximum, since fluxes will be computed with harmonic averaging of permeabilities. Thus, for any binary, non-layered reservoir model, having permeabilities from the example model,

$$\frac{\frac{q_1}{h_1}}{\frac{q_2}{h_2}} < \left(\frac{\frac{q_1}{h_1}}{\frac{q_2}{h_2}}\right)_{\max} = 6.7.$$

The fact that the measured ratio, 7.2, exceeds the maximum, suggests the inadequacy of the binary facies model, and necessitates at least a third major facies, or other major flow component.

This is demonstrated readily with a 3 component model. Let the 2-layer, binary model be modified such that a third facies, with permeability k_3, is added to each layer, away from the well. That is, the well is conditioned to the original binary facies set, and the third facies is not sampled at the well. So, the facies with permeabilities $k_1$and k_2 remain connected to the well. The ratio of layer fluxes is now,

$$\left(\frac{\frac{q_1}{h_1}}{\frac{q_2}{h_2}}\right) = \quad \left(\frac{k_1}{k_2}\right)\left(\frac{\alpha k_2 + k_3}{\beta k_1 + k_3}\right)\left(\frac{\beta+1}{\alpha+1}\right),$$

due to harmonic averaging of permeabilities (series flow is introduced with the third facies), where α is the ratio of proportion of the the third facies to that of the original facies in layer 2, and β is the ratio of proportions in layer 1. For example, if the third facies is 90% of layer 2, then $\alpha = 9$. If the third facies is 10% of layer 1, then $\beta = \frac{1}{9}$.

The effect of the third facies is seen in extreme examples. If k_3 is much smaller than the lower permeability, say k_2, such that $k_3 << k_2$, then,

$$\left(\frac{\frac{q_1}{h_1}}{\frac{q_2}{h_2}}\right) \simeq \quad \frac{\alpha}{\beta}\left(\frac{\beta+1}{\alpha+1}\right),$$

so that an ultra-low permeability third facies dominates the system simply by proportions. Thus, a high proportion, α, of the third, low permeability facies in layer 2, coupled with a very low proportion, β, in layer 1, may produce abnormally high flux ratios, no matter the permeabilities measured in the layers at the well. A low permeability third facies would also generate low absolute values of layer fluxes, however, and so would be distinguished from super-k behavior, which is characterized by abnormally *high* fluxes.

If k_3 is much larger than the higher permeability, say k_1, such that $k_3 >> k_1$, then,

$$\left(\frac{\frac{q_1}{h_1}}{\frac{q_2}{h_2}}\right) \simeq \frac{k_1}{k_2}\left(\frac{\beta+1}{\alpha+1}\right),$$

and the system is again controlled by the proportions of facies three, with a proportion, β, in layer one, relative to α in layer two, potentially increasing the flux ratio. The high permeability of layer three also increases the flux rates.

Taking extreme α and β, if β is very large, and α is very small, then,

$$\left(\frac{\frac{q_1}{h_1}}{\frac{q_2}{h_2}}\right) \simeq \frac{k_3}{k_2}.$$

If β is very small, and α is very large, then,

$$\left(\frac{\frac{q_1}{h_1}}{\frac{q_2}{h_2}}\right) \simeq \frac{k_1}{k_3}.$$

Interestingly, if $\beta = \alpha$, then,

$$\left(\frac{\frac{q_1}{h_1}}{\frac{q_2}{h_2}}\right) < \frac{k_1}{k_2},$$

so that a uniform distribution of the third facies decreases the flux ratio, no matter the value of k_3.

Fig. 6.12 presents flow simulation results for the non-layered facies model, with the third facies permeability, $k_3 = 5000\ md$. Here,

$$\frac{k_3}{k_2} = 16.7.$$

$$\frac{k_1}{k_3} = 0.4,$$

The simulated flux ratio, 5, evidently places α and β at equivalent levels. Indeed, the third facies proportion, 0.18, is a global proportion, and has no spatial correlation. It was further confirmed that the permeability level of the third element does not affect the match.

6.4.3 Super-k, thin layers, and DFNs

These results demonstrate that facies distribution away from the well may be important. Note that a linear flow model is used; although radial flow will diminish the effect of a third facies away from the well, the following principal conclusion still applies: super-k flow behavior is caused by a medium, facies or otherwise, which has the following characteristics,

- it is unsampled at the well,
- it has higher conductivity than that of facies sampled at the well,
- it occurs in preferentially higher proportion in the dominant, high-flux layer.

A further, profound, fact is that super-k, almost exclusively, occurs in thin, less than 20 ft, zones. Fig. 6.16 shows the distribution of the interval thicknesses corresponding to the maximum flux intervals of the 450 wells presented in Fig. 6.4. The interval mean of 5 ft is consistent with the vast majority of reported super-k interval thicknesses.

Thus, a plausible geologic construction of super-k must account for its prevalence in such zones, its high conductivity, and for the lack of sampling at the well.

A facies model of super-k simply cannot satisfy these three criteria at once. However, a DFN model readily accommodates these conditions.

DFNs are potentially very conductive, and have been confirmed so at Ghawar (Chapter 5). Furthermore, vertical fracture systems are rarely sampled by vertical wells, which are predominant at Ghawar. Recent horizontal wells, however, often intersect fracture systems, and the data from these intersections have confirmed that Ghawar fracture systems are both prevalent, and predominantly vertical.

Finally, the occurrence in thin layers is essential to the super-k DFN model. The requirement that the high-conductivity element occur in preferentially higher proportions in a layer, is satisfied as a result of the geometry of the thin layer. Indeed, a DFN of any height, intersecting a set of layers, will, with favorable probability, intersect the thinner layers of the set, in their entirety, and the thicker layers only

partially. Thus, DFN conductivity occurs in greater proportion in thin layers, than in thicker layers. Fig. 6.17 is a schematic diagram of the various effects resulting from the intersection of a DFN and a thin, conductive layer. The schematic flowmeter diagrams, which are plotted in the conventional format of vertical producing interval on the ordinate, and cumulative flux ($B/D/ft$) contribution on the abscissa, indicate that a DFN large enough to fully intersect both a thin, high permeability layer, and an adjacent, thick, lower permeability layer, will not appreciably affect the relative response between the two layers, compared to that of no DFN. That is, the relative contribution of the layers will not significantly change, as was concluded in Sec. 6.4.2. However, the magnitude of the flux from both layers will increase.

A DFN that penetrates the thin layer fully, but the adjacent, thick layer only partially, will alter the productivities of the layers such that the flowmeter profile will measure a relative increase in the thin layer flux. Additionally, the absolute layer flux magnitudes will increase, although not equally.

The analysis above shows that if the DFN encompasses the entire height of the producing interval, that super-k behavior is not predicted. Therefore, our model applies to DFNs with heights shorter than that of the producing interval, 250 ft, for example, for the Arab-D. Large scale faults seen in Ghawar 3D seismic probably would not account for super-k behavior, as these structures may cut the entire Arab-D interval. *Therefore, unless the seismic data can predict fracture or fault systems which do not propagate vertically out of the Arab-D, static super-k data for this model will be sparse indeed, and composed mainly of horizontal well intersection data, and rock fracture mechanics model predictions. In regions developed with vertical wells, super-k data will be essentially non-existent. Unfortunately, horizontal wells have only recently been drilled at Ghawar, and in small, localized regions only, and lack of data informing rock fracture mechanics renders such modeling equally difficult.*

6.4.4 The role of impermeable bounding layers

Impermeable layers or surfaces bounding the thin, high permeability super-k layer, above and below, have been noted[9],[46]. The role of these impermeable boundaries

are probably minor in the context of our super-k model, although theoretically they maintain a high flux in the thin layer by preventing crossflow out of the layer.

This is demonstrated schematically in Fig. 6.18, where a very conductive DFN fully penetrates a thin, high permeability layer, but only partially penetrates an adjacent, thicker, lower permeability layer. There then exists the pressure profile shown in the thin layer (green diagram, vertically exaggerated), and two pressure profiles in the adjacent layer. We assume constant boundary conditions over the layers. The pressure profiles describe the pressure drop from a point in the layers having pressure p_e, and the flowing well pressure, p_w. The influence of the DFN on pressure distribution is discussed in Chapter 8.

It is seen that pressures may be higher in the intervals intersected by the DFN, than in adjacent layers, simply due to the preferential productivity enhancement that DFNs provide to the intersected intervals, relative to adjacent, unaffected intervals.

Assume here that the layers are fairly isotropic. Note in Fig. 6.18 that complete crossflow exists from the thin layer to the adjacent layer where both are penetrated by the DFN, simply due to the high conductivity of the DFN. Thus, a pressure equilibrium is maintained between the thin layer and the top of the adjacent layer, where it is penetrated by the DFN.

However, pressure equilibrium does not exist between the top of the adjacent layer and the bottom of that layer. Thus, crossflow is induced between the top and bottom of the adjacent, thicker, layer, promoting the pressure profile indicated by the dashed curve. This modified pressure profile crossflow then induces crossflow from the thin layer to the adjacent layer, in the region not penetrated by the DFN. Any crossflow which actually occurs out of the thin layer reduces its flux into the well, and therefore reduces its super-k effect, as shown in the flowmeter profile schematic. Therefore, if the surface between the thin layer and the adjacent layer is impermeable, the super-k effect is maximized. Crossflow from the thin layer, however, does not necessarily nullify a super-k flux, but only diminishes it.

The limiting case of a thin DFN which only penetrates the thin zone, results in the entire adjacent zone having the bottom pressure profile exhibited in Fig. 6.18, and thus induces a maximum differential pressure across the layer boundary. If an

impermeable layer or surface does not exist between the two layers, then crossflow is maximized, and super-k flux from the thin layer into the well is minimized. If, however, an impermeable surface or layer does exist between the two layers in this case, then the super-k effect on the flowmeter profile is maximized, as the thin layer's productivity is preferentially enhanced, the adjacent layer's productivity does not benefit from the DFN, and no crossflow occurs from the thin zone.

6.5 Correlation of super-k, facies, and lithology

Fig. 6.5 indicates a predominance of Hawiyah super-k intervals in Zone 2A and Zone 2B. Zone 2B contains 67% of Hawiyah super-k wells, and Zone 2A contains 27%. The remainder, 6%, are found in Zone 3A. In fact, this correlation seems to hold in the remainder of Ghawar also. Fig. 6.19 presents the distribution of maximum interval transmissibility in Uthmaniyah wells, discussed previously (Sec. 6.2). The author analyzed the zonal distribution of wells in which the highest flux interval met or exceeded the benchmark flux of 500 $B/D/FT$, indicated in blue in the histogram. The pie chart indicates the predominance of these super-k intervals in Zone 2A and Zone 2B.

The possible significance of super-k abundance in Zone 2B and Zone 2A, relative to our super-k DFN model, is the prevalence of two necessary lithologies: one which is prone to fracture, to form the DFNs, and another which provides thin, high-permeability intervals, that serve as connections to wells.

It is likely that Arab-D fracturing occurs preferentially in the most brittle lithologies, which are probably mudstones and dolomites. Dolomites are most densely distributed in zones 2A, 2B and 3A. Mudstones are most prevalent in zone 3B. Thin, high permeable intervals occur most frequently in zones 2A, 2B and 3B. Thus, zones 2A, 2B and 3B seem to be optimally constructed, relative to the other zones, to contain our super-k model.

The lack of super-k in zone 3B (Fig. 6.5) may be due to two characteristics that distinguish it from zones 2A and 2B. First, mudstone is much more prevalent than dolomite in Zone 3B. Therefore, if dolomite fails preferentially to mudstone, then

DFNs may form more readily in the dolomite intervals.

Second, the mudstones occur in packages in which they are layered with alternating, thin, turbidite grain deposits (Sec. 4.4.1). The dolomites in zone 2B are thicker, and occur as single units that are not layered. Therefore, DFNs developing in the dolomites may have greater vertical thickness, and are therefore more productive. High productivity is the key contribution of the DFN to super-k structure.

A third unique characteristic of zone 3B that may prevent super-k formation is the geometry of the grain-mud layers. Our super-k model is a simple series model, in which the high-conductivity DFN connects, in series, to a thin, high-permeability interval, at the well. A thin interval is necessary, as explained in Sec. 6.2, because thin intervals benefit more from DFNs than do thicker, adjacent zones. The layers in Zone 3B are all relatively thin. So, a DFN may likely intersect the whole thickness of many of these zones, as in Fig. 6.17, and thus not differentially increase the productivity of any single zone. Thus, although flux magnitudes are increased by the DFN, they are increased for many zones, not just one, and thus no single zone exhibits an abnormally high flux characteristic.

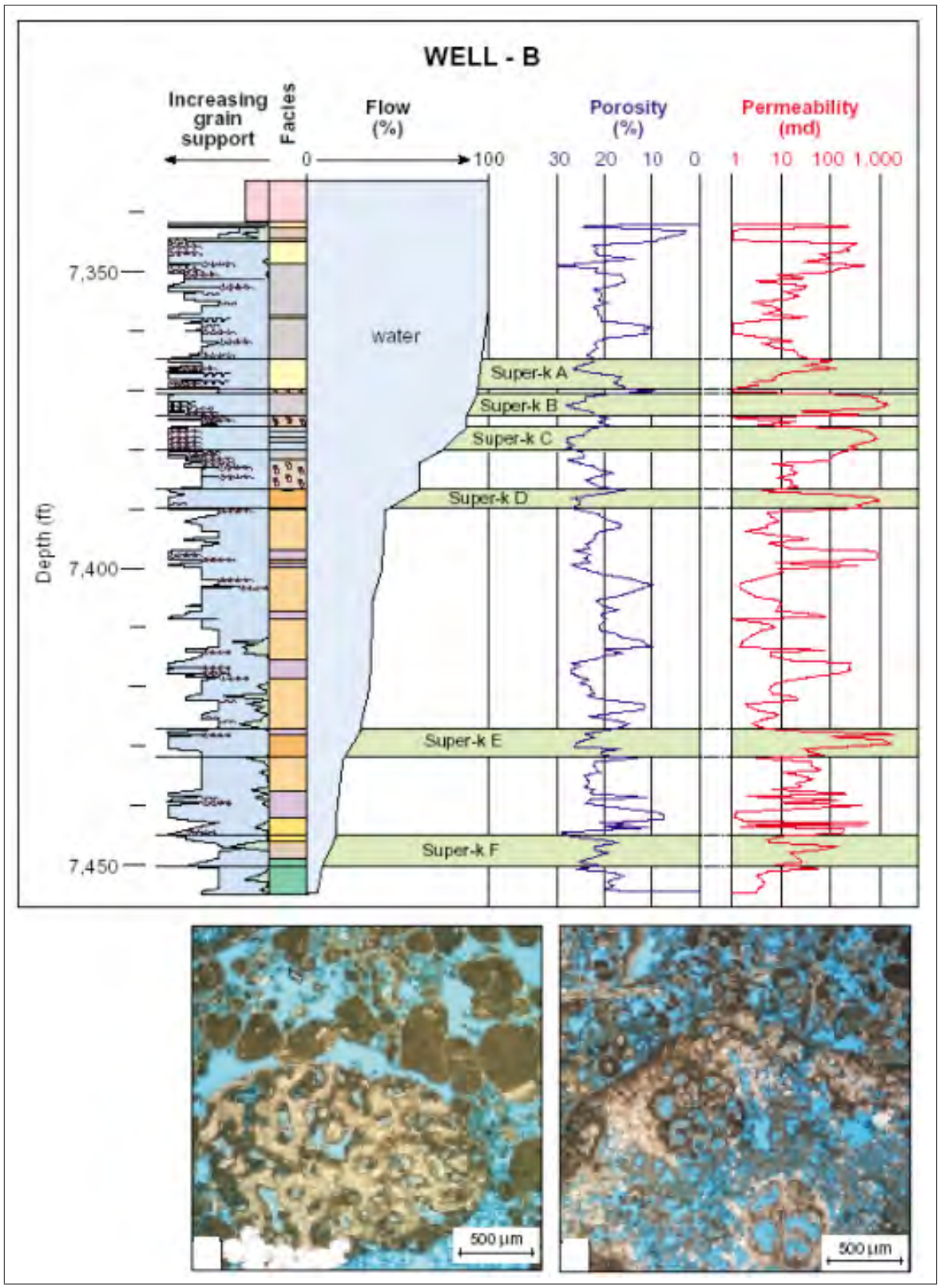

Fig. 6.8: Core analysis summary and thin sections from super-k interval of Well B[9]

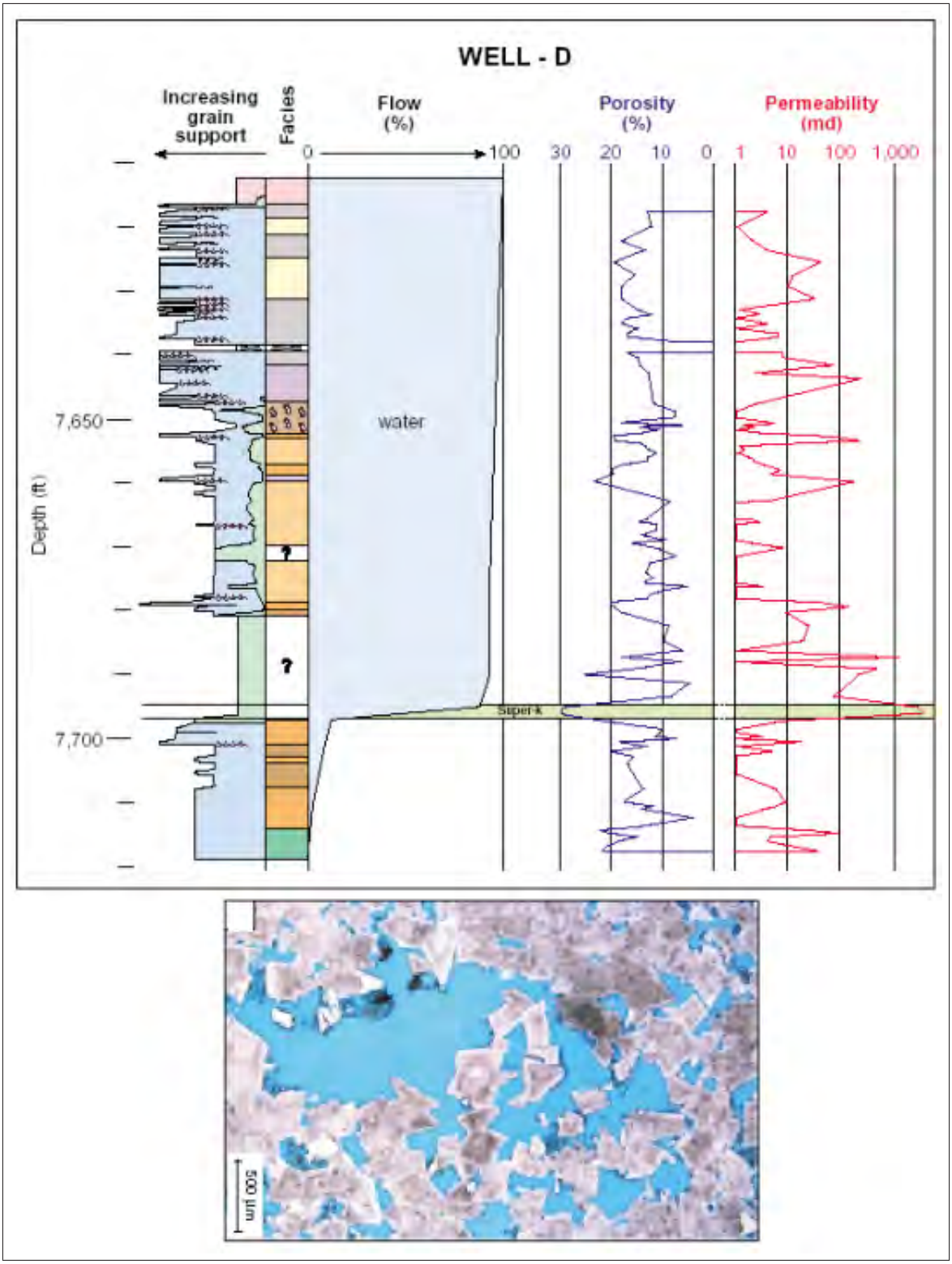

Fig. 6.9: Core analysis summary and thin sections from super-k interval of Well D[9]

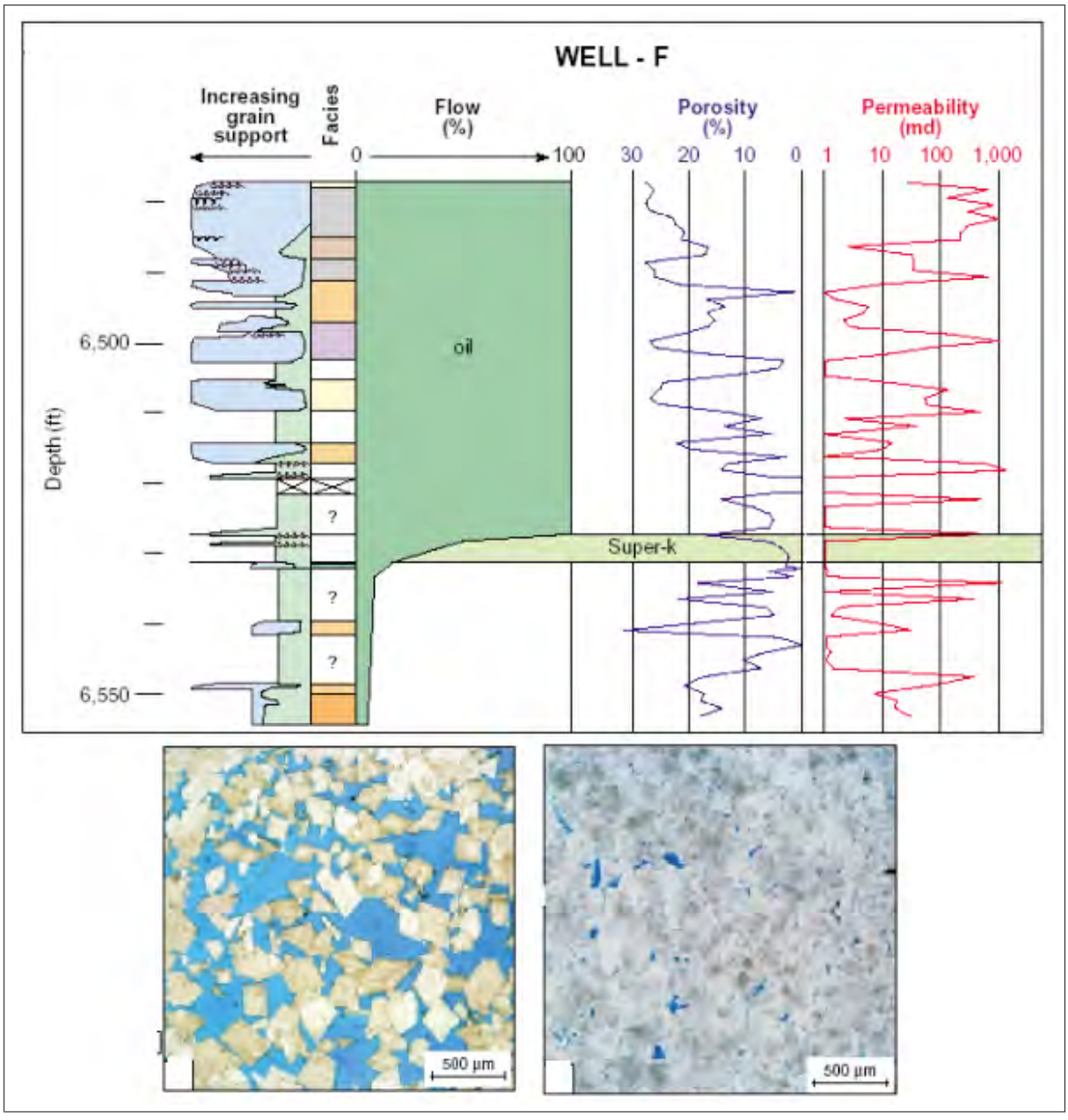

Fig. 6.10: Core analysis summary and thin sections from super-k interval of Well F[9]

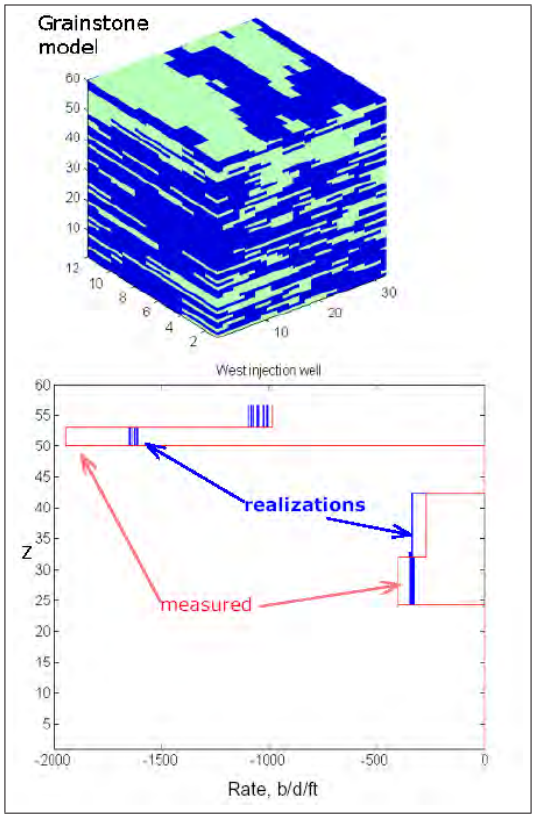

Fig. 6.11: Grainstone-only realizations

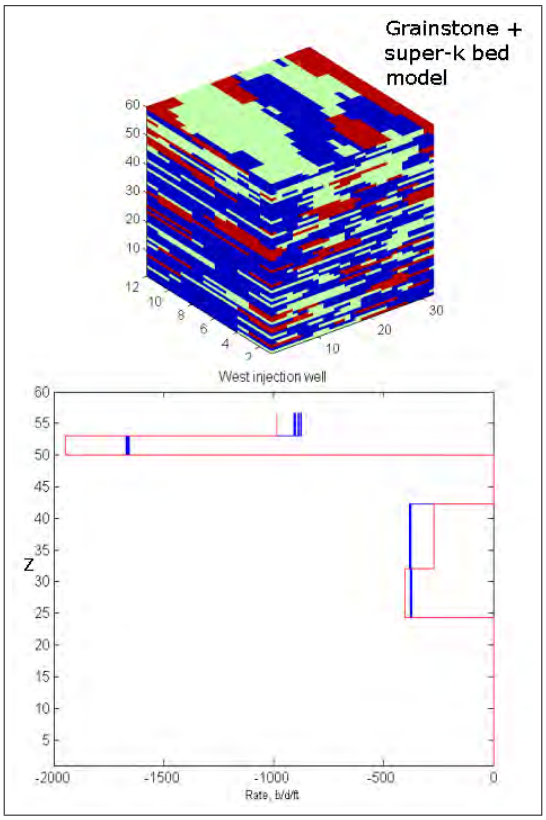

Fig. 6.12: Grainstone + super-k realizations

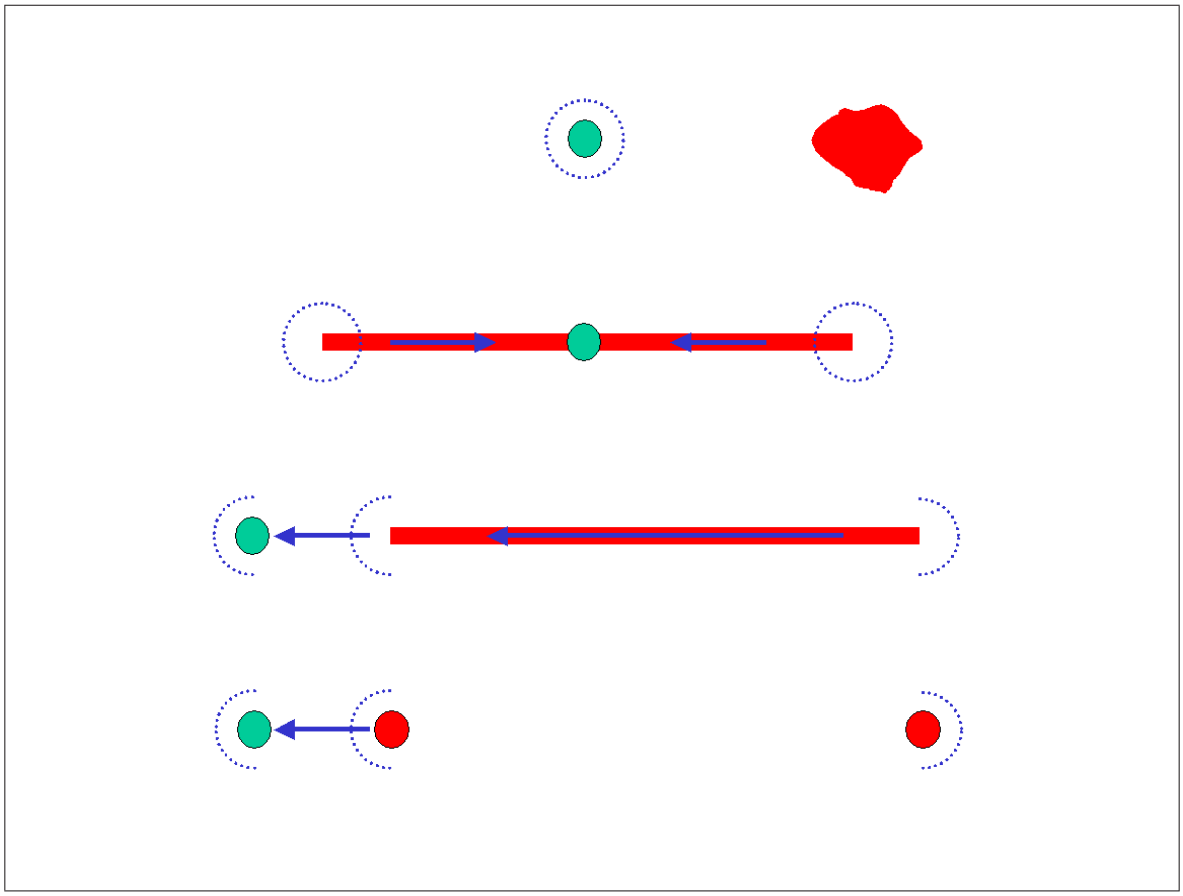

Fig. 6.13: Flow geometries under various reservoir models

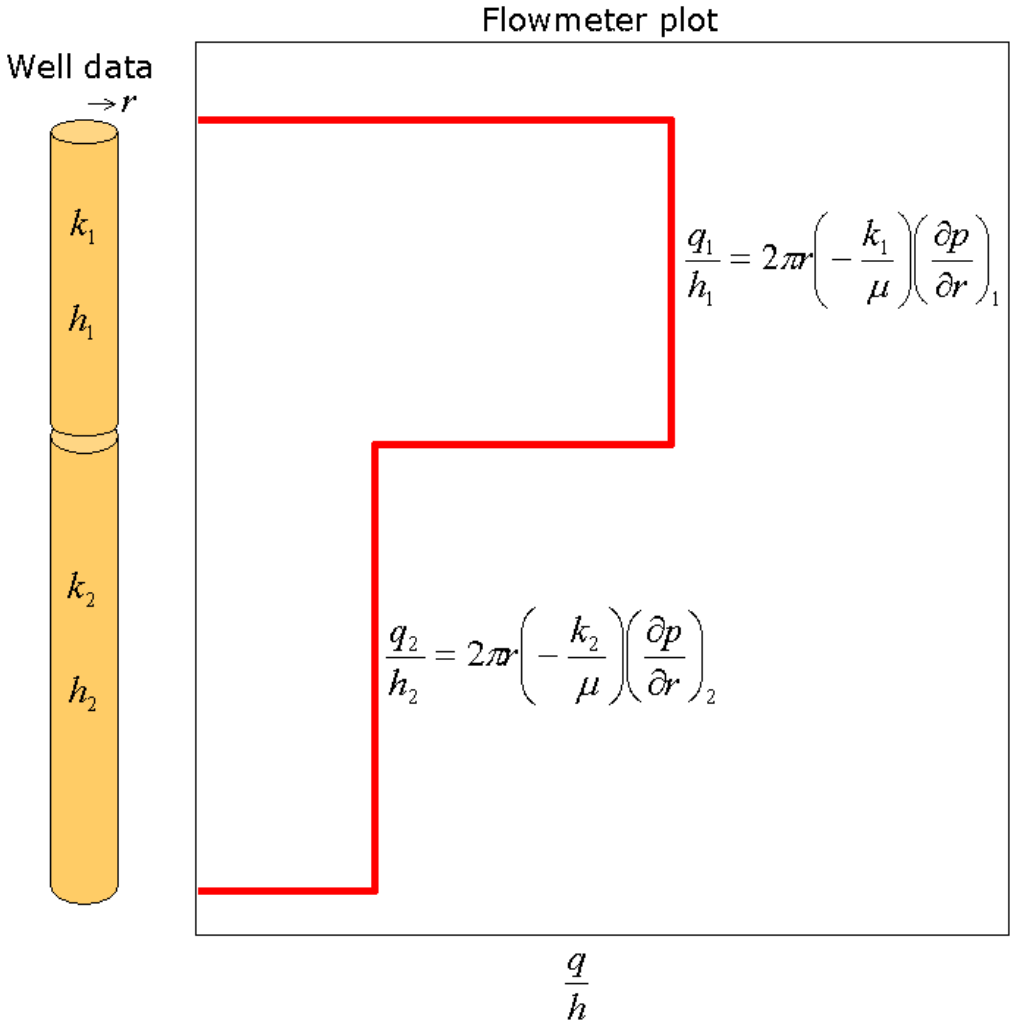

Fig. 6.14: Analysis of flowmeter data under radial, steady state flow

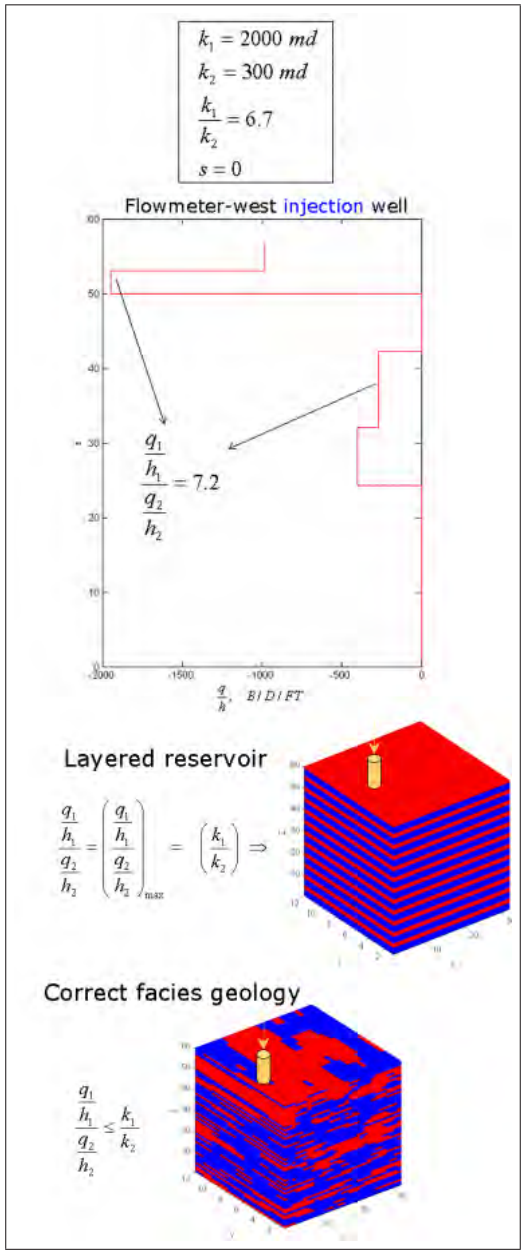

Fig. 6.15: Flow capacity of facies only model

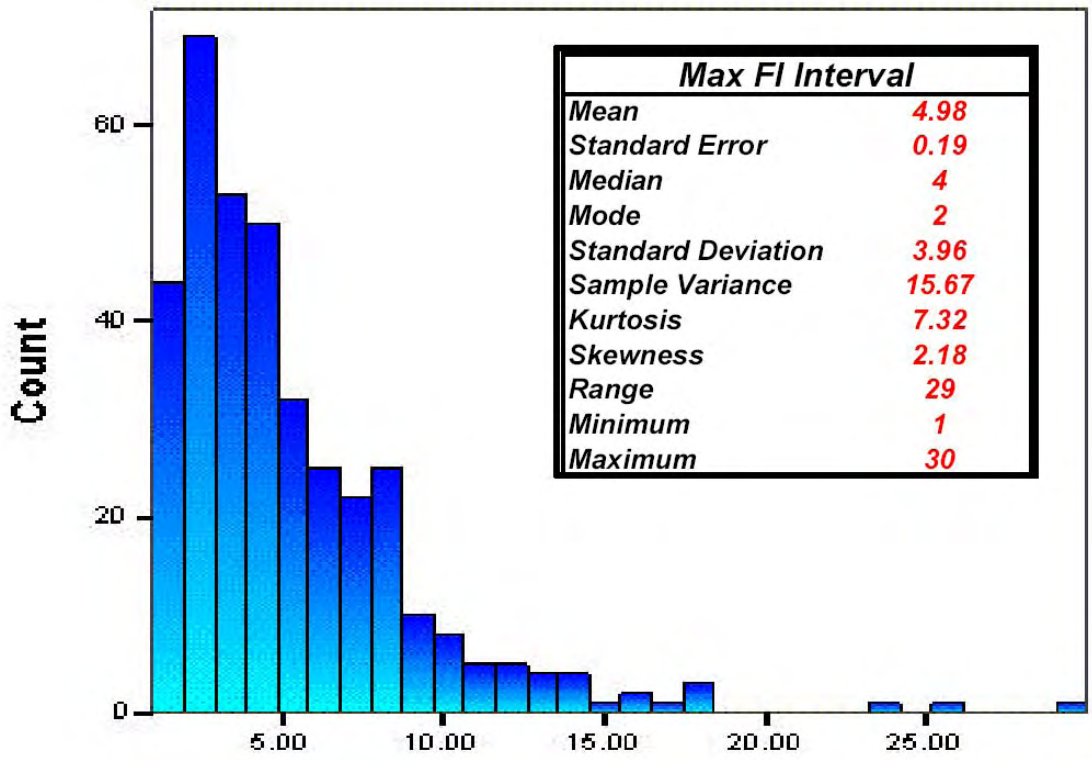

Fig. 6.16: Maximum well flux interval thickness (ft) in 450 Uthmaniyah wells[54]

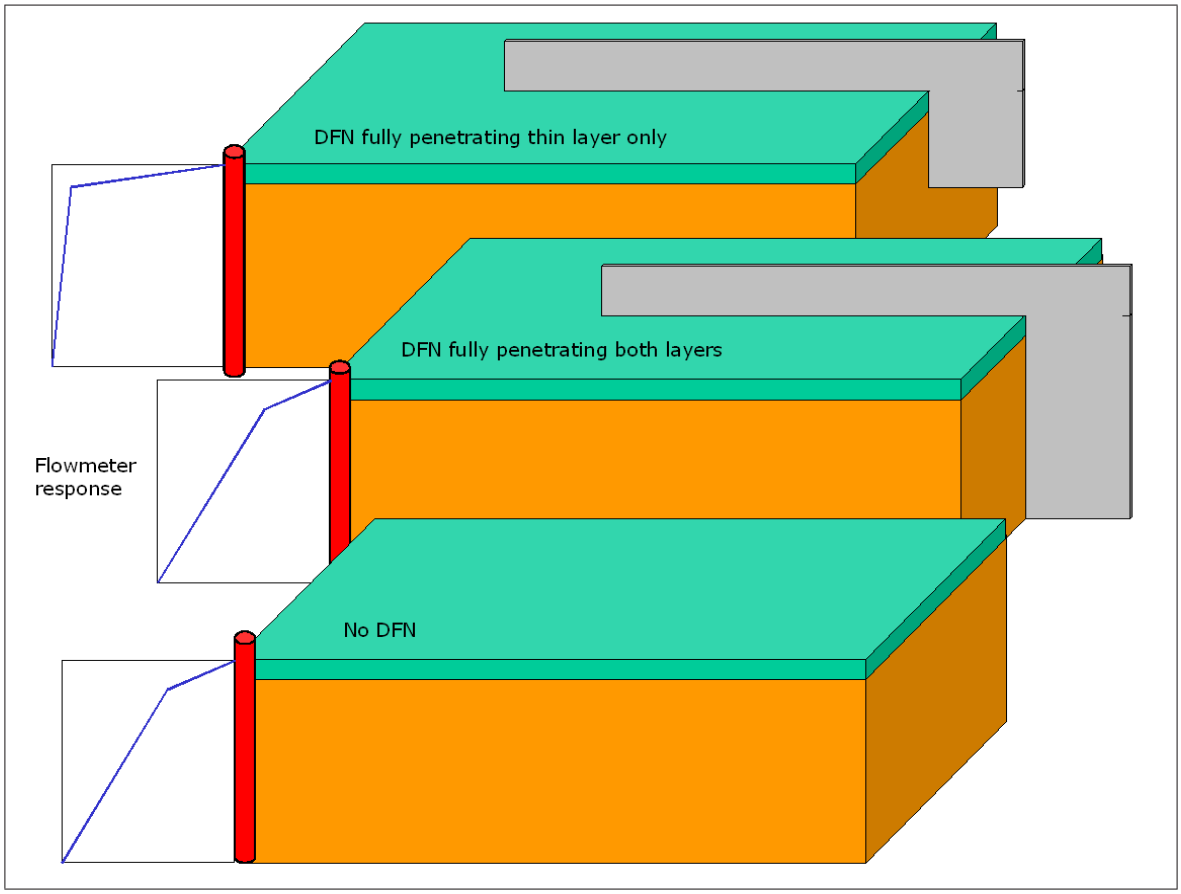

Fig. 6.17: Flowmeter response under various DFN associations

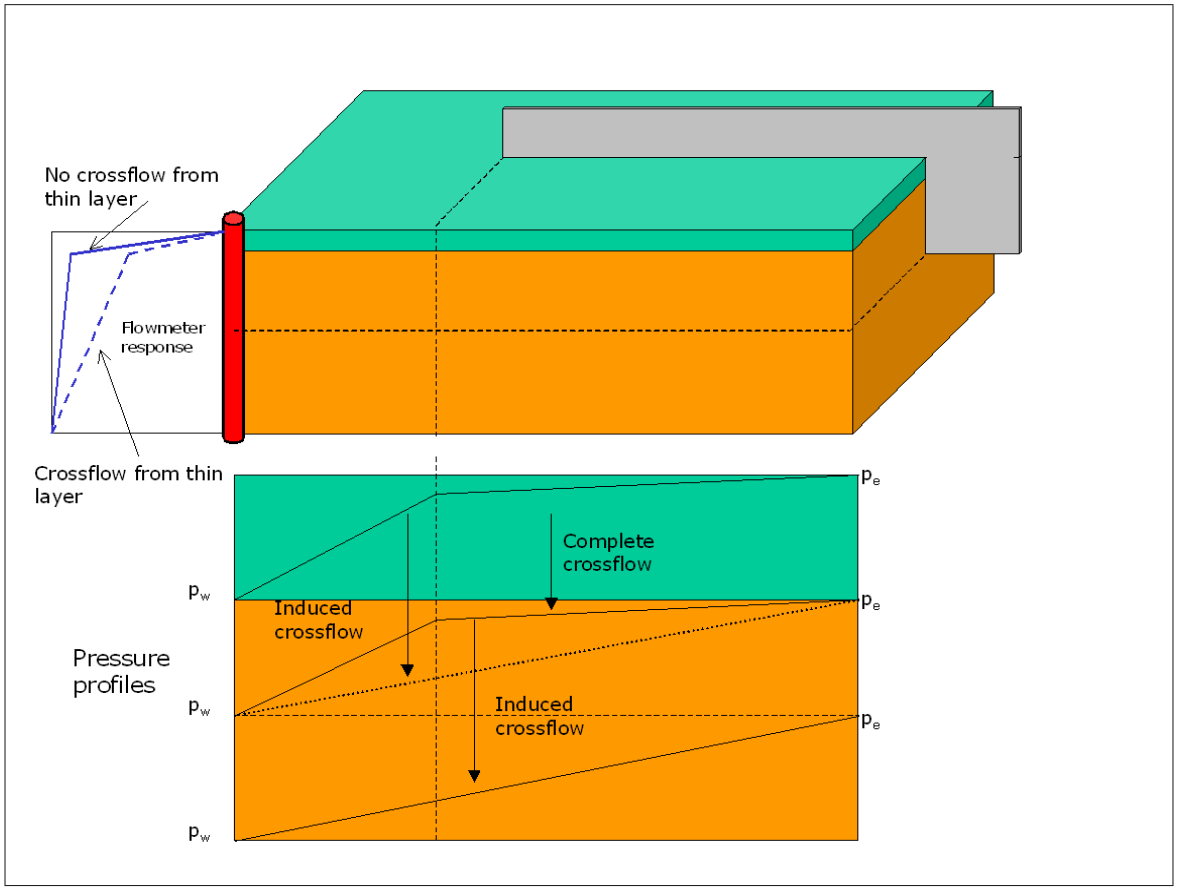

Fig. 6.18: Crossflow from thin layer to adjacent layer in the presence of a DFN

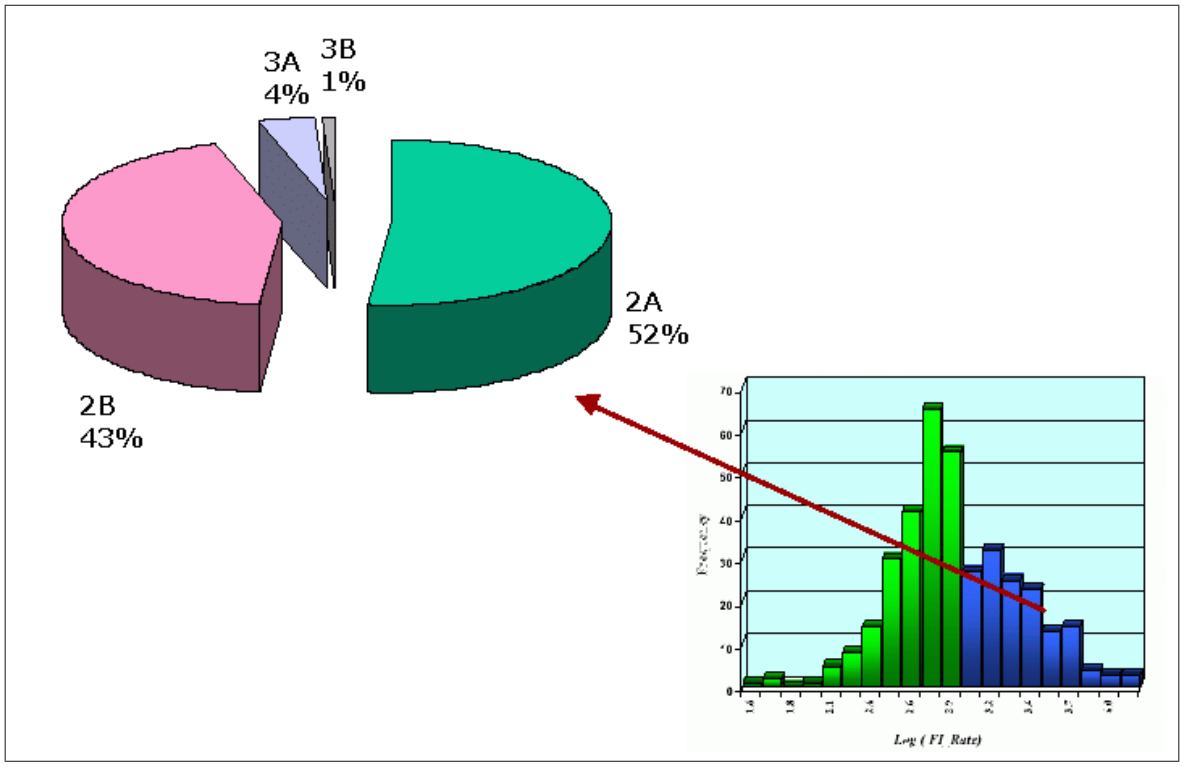

Fig. 6.19: The zonal distribution of super-k intervals in Uthmaniyah wells[54]

Chapter 7

The DFN flow simulation source model

The petroleum literature is nearly void of reports of the use of sources to model DFN flow; it includes one reference[73], which is a derivative of this thesis. The groundwater hydrology literature contains one reference: Lee, et al.[2] used sources to model "long fractures," those with lengths greater than grid block dimensions. Independently, they found, most importantly, that generally only DFN endpoints require sources, corroborating our principal result. Interestingly, the authors are oilfield researchers, and in fact, their research has resulted in the incorporation of the source model for DFN flow into ChevronTexaco's in- house flow simulator, *CHEARS*. Currently, there are no published examples of the use of this *CHEARS* module in a practical application.

The discrete form of the source model, is simply the conventional well model in a finite difference flow simulator; and thus the simple association is made, DFN $\Longrightarrow$ well.

The reasons for the delay in the industry use of sources to model DFN flow are not evident, since, under certain conditions, the use of the conventional source model is appropriate, as we will demonstrate in this thesis. Furthermore, the availability of the source model in all conventional reservoir flow simulators prompts, at least, a cursory trial, given the alternative of discretizing fractures, or adopting a dual grid, which was

designed for fracture systems described more appropriately with a continuum model. Those researchers designing optimization algorithms which process multiple reservoir realizations, and therefore requiring an automatic gridding routine to accommodate varying DFN discretizations, must currently seek alternatives, of which sources should be primary, since automatic gridding routines are currently available only in research code.

The apparent rarity of in-situ DFN problems (as opposed to hydraulically induced for well stimulation), as well as the prevailing and overwhelming lack of data to sufficiently constrain DFN reservoir models, a severe obstacle hindering this history matching study, may explain the dearth in the literature. While the latter consideration is probably largely responsible, the former should not be, as fractured rock most certainly prevails in many reservoirs, particularly carbonate, and the continuum model, as seen clearly in surface outcrops of the gamut of sedimentary deposits, is not always more appropriate than the discrete model. However, the lack of data may render the problem practically unsolvable, and thereby perhaps contribute to a tendency to ignore the treatment of DFNs in most history matching problems.

Nonetheless, despite the lack of feasibility in the face of sparse data, explicit modeling of flow in DFNs is, in some cases, imposed by necessity, as in the case of performance prediction in reservoirs affected by super-k. Although no single geologic model of super-k has emerged as preeminent at Ghawar, the role of DFNs, provided sufficient geologic constraint does not nullify the probability of their existence, certainly must be considered as likely objects which can possess both the necessary high magnitudes of conductivity which characterize super-k, and significant lateral extent. The latter quality, required to resolve observed, massive, unmitigated hydraulic conductivity between injection and production wells under large spacing, is especially important. It has been difficult to propose an alternative *facies* super-k model, laterally extensive, connected, with uniformly high permeability, in a highly heterogeneous facies deposition, as in the upward shoaling shelf deposition that is Ghawar. The difficulties of the facies model was discussed in Sec. 6.4 and is also detailed in Appendix F.

The association of DFNs with injection wells operating at high pressures, is also

compelling, in that, fracture pore pressures most certainly are over-predicted in fractured rock, and in-situ, disconnected DFNs are susceptible to connection under conditions of injection at abnormally high pressure (Sec. 5.1.2). Although the very high matrix permeability at the Ghawar study area might decrease this tendency, very high conductivities in the fractures may prevail instead. Indeed, the fact that mineral precipitation has not diminished the matrix permeability at the Ghawar study area to below darcy levels, may suggest that fracture permeability enjoys the same lack of diminution.

Given that it may be necessary to treat DFNs as a significant component of a flow simulation model, whether or not this may be the case at the Ghawar study area, we present a general development of one option for doing so. The source model is discussed and developed with a combination of analytical, elementary proposals for a practical implementation, used in the history matching study. Otherwise, conditions under which they are not valid are presented. Our intention is that a working model, applicable not only to reservoirs like Ghawar, but more generally, be proposed.

A final introductory remark may be warranted regarding the incorporation of the source model as a DFN flow model. It has been our experience that those introduced to the idea, initially conclude that a proxy intended for conventional wells is being applied to DFNs. However, the source model is not a construct that is peculiar to oil and gas reservoir flow simulators. It is more fundamental: a source function in the governing mass balance equation. That a DFN may be treated as a source function, a spatial distribution of mass flux densities not described by the flux term in the governing equation, is believable, if not evident.

The source function is not restricted; it may assume any geometry, for example a surface, as with fractures, or a curve, as with wells. The geometry will affect the computational performance of the simulator; however, no other restriction is imposed by commercial simulators on the spatial geometry of the source function.

The fact that these sources are hydraulically constrained is the peculiar aspect to reservoir engineering. Wells and fractures are a hydraulic continuum, whereas sources in a general mass balance process need not be.

A similarly non-intuitive idea is that of modeling flow in wells, not with sources,

but with blocks. The lack of computational feasibility does not detract from the efficacy of modeling wells by discretizing them. The reason sources are used instead is that the hydraulic constraint in wells just happens to be amenable to an analytical treatment, and the reason for this is that, at its simplest, it is a simple function of one parameter, depth. Extending the analytical constraint to include flow is not difficult, as the flow properties of the well are typically very homogeneous, and can be known very precisely. The analytical treatment eliminates the requirement of discretization. Fracture flow networks are definitely not as homogeneous as wells, and their flow properties cannot be known precisely. However, it is reasonable to propose that DFNs that are so conductive as to significantly affect reservoir flow performance, may approach a homogeneity in flow properties that may afford an analytical treatment. Therefore, the use of sources for fracture flow modeling, although not as efficacious as for well modeling, may be, under some conditions, fundamentally more appropriate than discretization. Discretization, however, is the more appropriate approach for the class of fracture systems that is described as a continuum, that is, composed of small scale, pervasive fractures, rather than the large scale, discrete variety. The dual grid approach was invented for precisely this model. However, the conventional well model is implemented within the dual grid framework without modification. Therefore, the source method may be used in mixed fracture systems, those in which both small scale and large scale fractures must be modeled, by straightforward incorporation into a dual grid model.

The developers of *ECLIPSE*, the flow simulator used in this study, and most other successful commercial simulators, have coupled the sources to their hydraulic constraints very effectively. Given that the hydraulic constraint in DFNs is identical to that of production and injection wells, only the flow geometries are different, the addition of a DFN flow module would not represent a coding development requiring new paradigms. As evidenced in this study, if the hydraulic constraint is simplified to that of static equilibrium only, no further coding development is required at all - the flow simulator may be used without modification. Furthermore, if the hydraulic flow constraint is also imposed, and may be described using a pipe friction pressure gradient model, again the flow simulator may be used without modification.

Nonetheless, it may be argued that a separate, at least in name, module within a commercial flow simulator, is desired for fracture flow modeling using sources, as ChevronTexaco has done in *CHEARS*. The justifications may be:

1. The availability of a modeling tool will encourage the incorporation of DFNs into flow simulators, when appropriate,

2. A friction pressure gradient model applicable to fracture flow geometries will provide for more straightforward application than a pipe flow model,

3. A connection location and transmissibility input paradigm which conforms to planar geometries would provide a more natural user interface.

We hope to promote at least some contemplation of incorporation of the source model to DFN flow simulation in commercial reservoir simulators. That currently, no feasible flow simulation approach exists for DFNs, and that any DFN reservoir model, no matter how well-conditioned, is useless to a reservoir engineer if it cannot be practically incorporated into a flow simulator, conveys a definite need for the source model to be examined as a feasible approach.

7.1 The use of sources to model DFN flow

Conventional flow simulation of DFNs lays significant obstacles within a history matching algorithm. Two conventional methods are discretization of DFNs, and the dual porosity model.

The advantages and disadvantages of these two models, with respect to their inclusion in a history matching algorithm, are shown in Fig. 7.1.

Included also in Fig. 7.1 is a list of pros and cons for the method used in this study, the conventional well model, or more appropriately, the use of sources.

The source model is implemented in a "dumpflood" manner. That is, the "well" is not produced at the surface, but instead is open only to backflow between the source connections. A mapping algorithm, described in Chapter 9, is used to place source

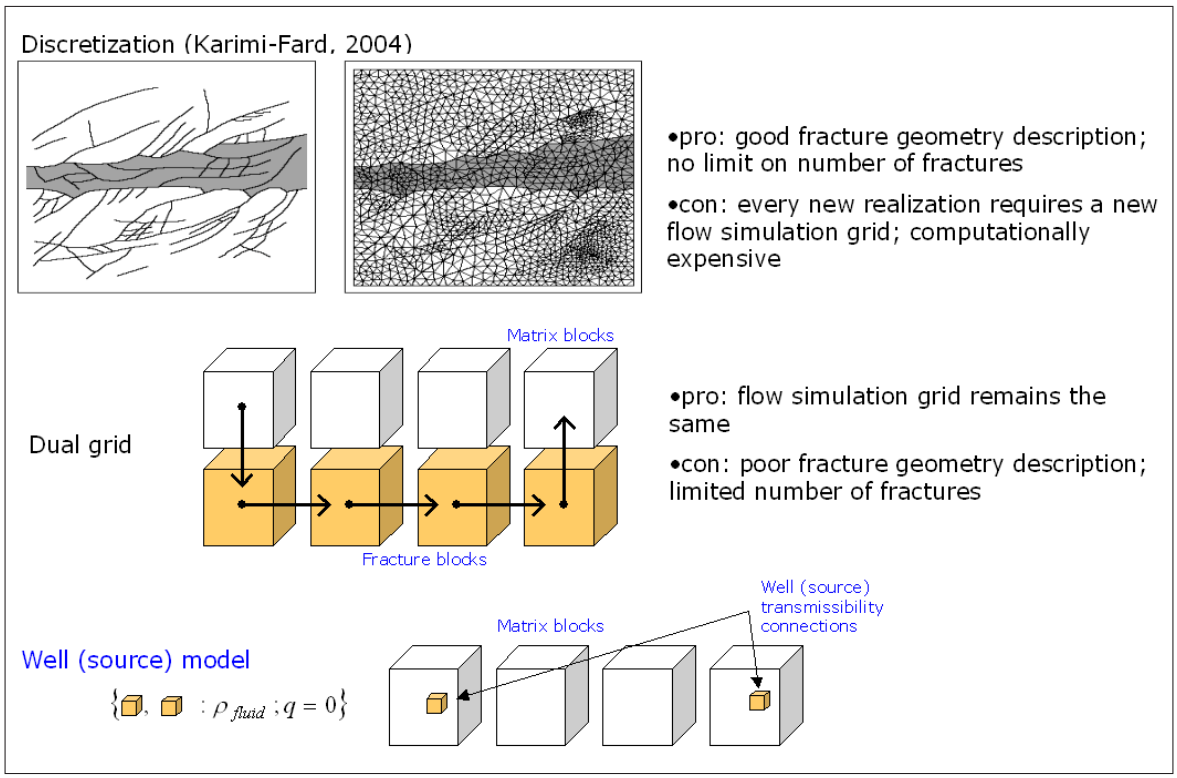

Fig. 7.1: Comparison of flow simulation methods for discrete fractures

connections in flow simulation blocks intersected by the DFN, provided a model for the networks exists.

A discretized DFN model, given that very fine blocks may be used to define the DFNs, may resolve the geometries of the networks very well, although at a severe cost of simulation convergence performance, even if unstructured grids are used, simply because of the severe contrast in volumes between the coarse and fine blocks. This cost currently renders discretization as generally not feasible for this use. Additionally, every realization of a DFN model, upon which the flow simulation grid is built, requires a new flow simulation grid. Thus, any history matching algorithm employing optimization methods, which must, by necessity, run numerous flow simulations, will require an automatic gridding module as part of the algorithm.

The dual grid model was developed to simulate flow through fracture systems more appropriately defined by a continuum model, and therefore is generally not suitable for application to DFNs. A dual grid may be used to model DFNs, by selectively

assigning high permeabilities, in the fracture grid, to those blocks which contain DFNs. However, practical models are coarse, and so the resolution of DFN geometries is poor. Finely discretized dual grids, if computationally practical, nonetheless cannot approximate the resolution afforded by the source model, as the number and density of sources which can be accommodated by any flow simulation grid, no matter how coarse, is theoretically unlimited.

7.1.1 The conventional flow simulation source model

The conventional source model, in the context of DFN modeling, is represented simply as a set, S^w, of connection transmissibilities, T_j^w, constrained to be in hydrostatic equilibrium, and constrained to a zero net source volume flux,

$$S^w = \left\{ T_1^w, T_2^w, ..., T_j^w : \rho_{fluid}; q = 0 \right\},$$

where w is a DFN name, and j is the block being connected. The condition that the connections are in hydrostatic equilibrium is represented by ρ_{fluid}, the density of the source fluid. The net source volume flux, q, is constrained to zero, as both a realistic condition, and a necessary one, since conventional source models do not allow accumulation.

Another, more general, way of describing S^w is as a set of sources, with each source j having a strength represented by T_j^w, and with a unique name, w, given to indicate that members of the set are governed by the same constraints.

This set is shown pictorially in Fig. 7.2, where the source term $\tilde{q}$ is represented as a set, $S^w = DFN$, consisting of green cubes, with the hydrostatic and net flux constraints included.

A further constraint of the set may be added, that is, a function which maps rate and location within the DFN, to DFN friction pressure gradient. This constraint comprises advanced well features in most commercial simulators, including *ECLIPSE.*

The friction gradient function is not considered in this thesis. However, it is recognized that DFN friction pressure gradient is not insignificant relative to matrix flow pressure gradient, in many instances. We assume it is negligible in our study

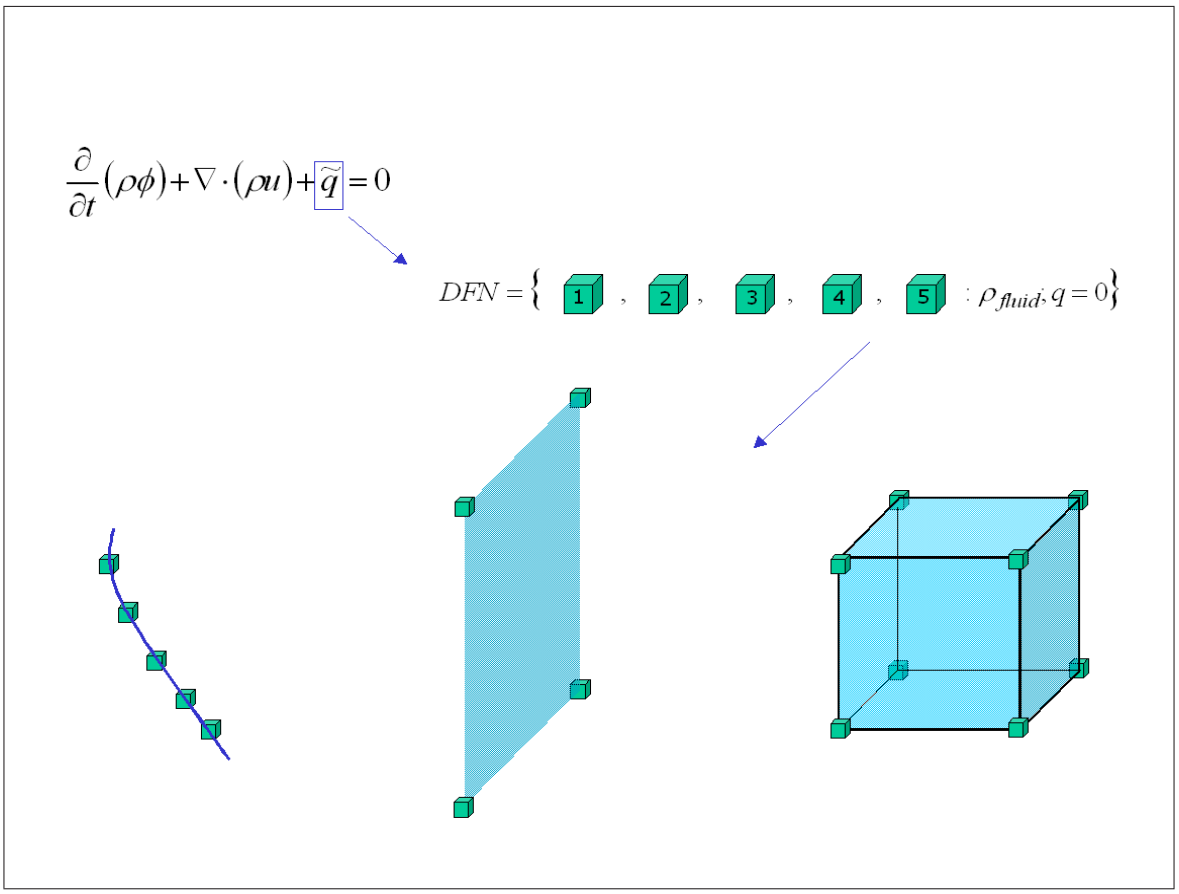

Fig. 7.2: Representation of a DFN with a set of sources

area, currently, while reserving the prospect of incorporating the friction gradient function, using *ECLIPSE*'s pipe friction model, in future work.

The simplicity of representing the DFN as the set S^w is symbolic of the simplicity in which it is implemented in all conventional flow simulators. Advantages afforded the use of the source model are primarily:

- ease of implementation: adding DFNs is as straightforward as adding wells,
- invariance of the flow simulation grid: no updating of the flow simulation coarse block discretization is required with a new DFN model realization,
- the geometry of sources is not constrained: the sources in S^w may lie along a curve, as in a production or injection well, in a plane, as in a DFN plane, in

multiply oriented and connected planes, or any other geometry in 3D, as shown in Fig. 7.2. Another example of the lack of geometric constraint is seen in Fig. 7.1. Note that for representation of the DFN by source transmissibility connections, only two connections are used, although the apparent flow path of the network includes four blocks. Although connections in the intermediate blocks may be desired under some conditions, they are not required in order for the source model to deliver fluid from one block with a connection to the other. There are conditions in which omission of intermediate connections does not introduce significant error in predicting the effect of flow in the DFN on reservoir performance. These conditions are discussed in Sec. 7.3, and in Sec. 8.3.3.

- there is no limit on the total number of sets S^{α}, and multiple sets S^{α} may occupy a single grid block: any number of DFNs may be introduced, and multiple networks, none of which are directly connected hydraulically, may occupy a single grid block, just as there is no limit on the number of producing wells which may by input into a flow simulator, and multiple producing wells may occupy one block. Of course, there are computational limits on the numbers of sets S^{α}.

- The transmissibility of connections are controlled by the user input, and may be different from the transmissibility as may be computed from flow geometry and the block transmissibility. This ability is available in all commercial flow simulators, to incorporate, for instance, skin effect in production wells, and is desirable due to the variability of DFN connection transmissibility due to complex, small scale fracture geometries, as in transmissibility increases resulting from brecciation.

- generality: the source model approach may be used with any DFN reservoir model. The only requirement is that the DFN model be enabled to be mapped onto the flow simulation grid

The last point is emphasized: the source model does not require the specific

static DFN models constructed in Chapter 9, or any other specific model, but instead requires only that an algorithm be incorporated which maps a static DFN model (an object-based or pixel-based fracture map) onto flow simulation block locations, as transmissibility connections. One such model is presented in Chapter 9. The source model approach, therefore, does not limit the choice among DFN reservoir models.

Chapter 9 describes a gridless, 3D, object-based, stochastic 3D static model of DFNs. This model also performs the mapping of source connections to a flow simulation grid, given a DFN realization, the flow simulation grid, and the location of production and injection wells. The model places connections in simulation blocks at key points along the DFN, including those near production or injection wells, near other DFNs, at DFN intersections, and at DFN terminals. The model also establishes intersecting DFNs as hydraulically connected, given an intersection criterion. Currently, the model provides the mapping of connections in the *ECLIPSE* format.

The advantages remaining for the discretized fracture model, not found in the source model, are: multiple, varied, transmissibility connections to a single coarse grid block from multiple fracture grid blocks, and simulation of the viscous flow process through the fracture. However, if a well friction model is incorporated into the source model, although not done in this study, the latter advantage is eliminated. The principal drawback of the discretized fracture model, the requisite generation of a new flow simulation grid for every reservoir model realization, may render the remaining advantage over the source model as minor.

An important disadvantage, currently, of the source model is that its incorporation into a DFN model is new; the flow simulation solution convergence behavior may be problematic, as was discussed in a previous report[3].

Fig. 7.3 further compares the fracture models, with respect to the steady state fracture liquid flow rate, q_{frac}, and the dimension of the Jacobian matrix, $\dim J$, of the solution system.

The flexibility of the source model with respect to controlling transmissibilities is shown in the calculation of q_{frac}. The transmissibility terms, T^m(matrix transmissibility), and T^{mf}(matrix-fracture transfer function), are controlled through the

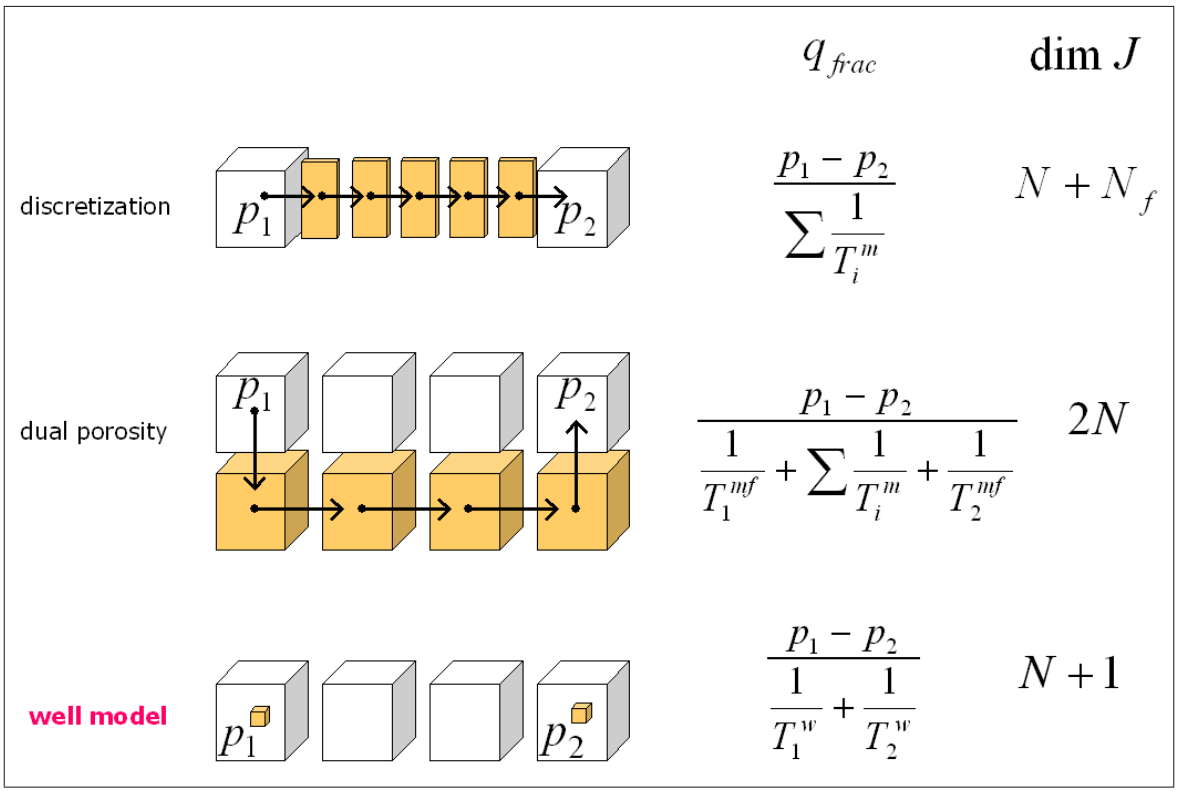

Fig. 7.3: Comparison of flow simulation methods for discrete fractures

permeabilities and geometries of the blocks defining the DFN, in both the discretization and dual porosity models. The number of these transmissibility terms in the flow calculation is determined by the number of blocks defining the DFN.

The transmissibility governing q_{frac} in the source model, however, are controlled by the terms T^w, the source connection transmissibility, which is controlled directly by the user. Furthermore, the number of terms, for any one DFN, can be as few as two. Therefore, control over q_{frac} is independent of the permeabilities and geometries of the blocks; the reservoir DFN model may be independent of the facies model, and no change in the facies model is required to add DFNs and simulate DFN flow. Also, the DFN definition may be as simple as manipulating two transmissibility terms.

The dimension of the Jacobian matrix, $\dim J$, determines, in large part, the CPU cost of the flow simulation. The Jacobian matrix is increased in size directly by the number of additional DFN blocks, N_f, added to the original coarse grid, having N

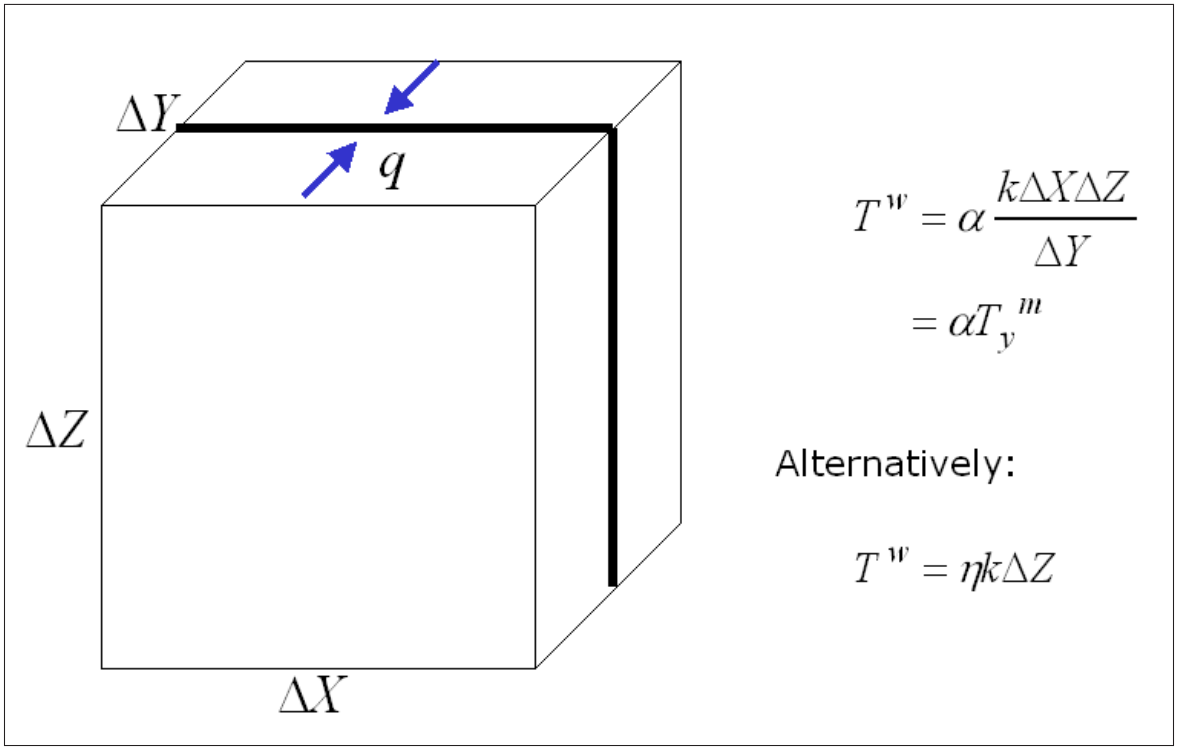

Fig. 7.4: DFN connection transmissibility relations

blocks, for the discretization method. The dual porosity model, by definition, requires a $2N$ dimensional Jacobian matrix.

The dimension of the Jacobian matrix is increased only by the number of DFNs added to the reservoir model, for the source model approach. Thus, if one DFN is added to the reservoir model, as shown in Fig. 7.3 , for example, then $\dim J$ is increased only by one, no matter how many DFN connections are included in the single DFN. The typical band structure of the matrix will be changed, however, possibly having an adverse effect on the linear solution convergence behavior, although this effect on total CPU time may be minor compared to that of significantly increasing the size of the matrix.

7.1.2 Fracture connection transmissibility

The simplest treatment of the source connection transmissibility, T^w, is to derive it relative to the matrix transmissibility, T^m, as shown in Fig. 7.4, which presents the

case in which the DFN is oriented in the x direction.

Here, T_y^m is the matrix transmissibility in the y direction, and α is a scalar function of DFN conductivity. The connection transmissibility of a DFN oriented in the y direction would be a function of α and T_x^m, the matrix block transmissibility in the x direction. A DFN of arbitrary orientation would have a connection transmissibility that would be a combination of these two orthogonal transmissibilities.

Alternatively, the geometry of the block in the x and y directions could be aggregated into a scalar function η, which also is dependent on DFN conductivity. This formulation, which proves to be very advantageous, and the function η, is discussed in detail in Sec. 8.3.3.

7.1.3 Source connection transmissibility in *ECLIPSE*

The *ECLIPSE* keyword WPIMULT allows for direct user manipulation, and algorithmic manipulation during parameter deformation, of the DFN connection transmissibility. Although the following construction is not the only one which enables transmissibility to be modified, it has proven useful. *ECLIPSE* allows the specification of a vertical or horizontal well, the transmissibilities of which are defined uniquely. The following allows for use of either, although for reasons unknown, the vertical well option causes less convergence problems.

The source connection transmissibility, T_w, may be defined as,

$$T_w = WPIMULT \left[2\pi \frac{kh}{\ln(r_o/r_w) + S} \right]$$

where $WPIMULT$ is a multiplication factor.

The expression is simplified by the following assumptions,

$$\begin{aligned} r_o &= e \ (the \exp onential) \\ r_w &= 1 \\ S &= 0 \end{aligned}$$

Then,

$$T_w = WPIMULT\,(2\pi kh)$$

Now let the transmissibility, T_f, for flow into a vertical, X direction (for example), DFN, from a grid block of dimension DX, DY, DZ, be defined as,

$$T_f = \alpha \frac{kDZDX}{DY}$$

where k is the block permeability, and η is a scalar (see Sec. 8.3.3).

Let $T_w = T_f$. Then,

$$WPIMULT == \alpha \frac{DZDX}{2\pi hDY}$$

If a vertical well is used, $h = DZ$, so the corresponding multiplication factor, $WPIMULT_V$, is,

$$WPIMULT_V = \alpha \frac{DX}{2\pi DY}$$

Similarly, if a horizontal well in the X direction is used, $h = DX$, so the corresponding multiplication factor, $WPIMULT_H$, is,

$$WPIMULT_H = \alpha \frac{DZ}{2\pi DY}$$

The alternative version of T_f, presented in Fig. 7.4, yields $WPIMULT$ of,

$$WPIMULT = \frac{\eta}{2\pi}$$

DFNs may be input into *ECLIPSE* using these formulations. That is, they may be specified by $r_o = e$, $r_w = 1$, and $S = 0$ under the COMPDAT keyword, along with a WPIMULT keyword, followed by the appropriate value, either $WPIMULT_V$, $WPIMULT_H$, or $WPIMULT$. The export, to an *ECLIPSE* data input file, of all appropriate keywords, including WPIMULT and COMPDAT are performed automatically by the algorithm described in Chapter 9.

7.2 DFNs and the connections used to describe them

A limitation of the source model is inherited from it's one dimensional simplicity: it cannot simulate the effects of gravity segregation and capillary flow in the DFN. Notwithstanding this limitation, the source model captures the essential elements to describe simple DFN flow:

- connection transmissibility,
- hydrostatic continuity,
- viscous friction drop in the DFN through the appropriate selection of a well friction model.

The last aspect of DFN flow is not utilized in this study. It is assumed here that viscous pressure drop in the DFN is insignificant, relative to that from, and into, the connections.

It must be emphasized that the use of the source model to simulate fracture flow is more appropriately applied to a fracture *flow network,* the DFN. A fracture flow network may be comprised of one fracture, but more commonly the network is comprised of multiple fractures in hydrostatic equilibrium, often culminating in geometries of considerable lateral or vertical extent.

A fracture flow network may assume a geometry that a single fracture may not, as for example that generated by intersecting fractures, or that developed over large distances, comprised of many fractures arranged en echelon.

The modeling of individual fractures is undesirable for the purposes of reservoir simulation, given that the flow characteristics of fractures often are determined at scales much larger than that accommodating individual fractures. The conductivity of fractures only becomes important, in its effect on reservoir performance, when many individual fractures amalgamate into a flow conduit that extends a distance appreciable relative to well spacing.

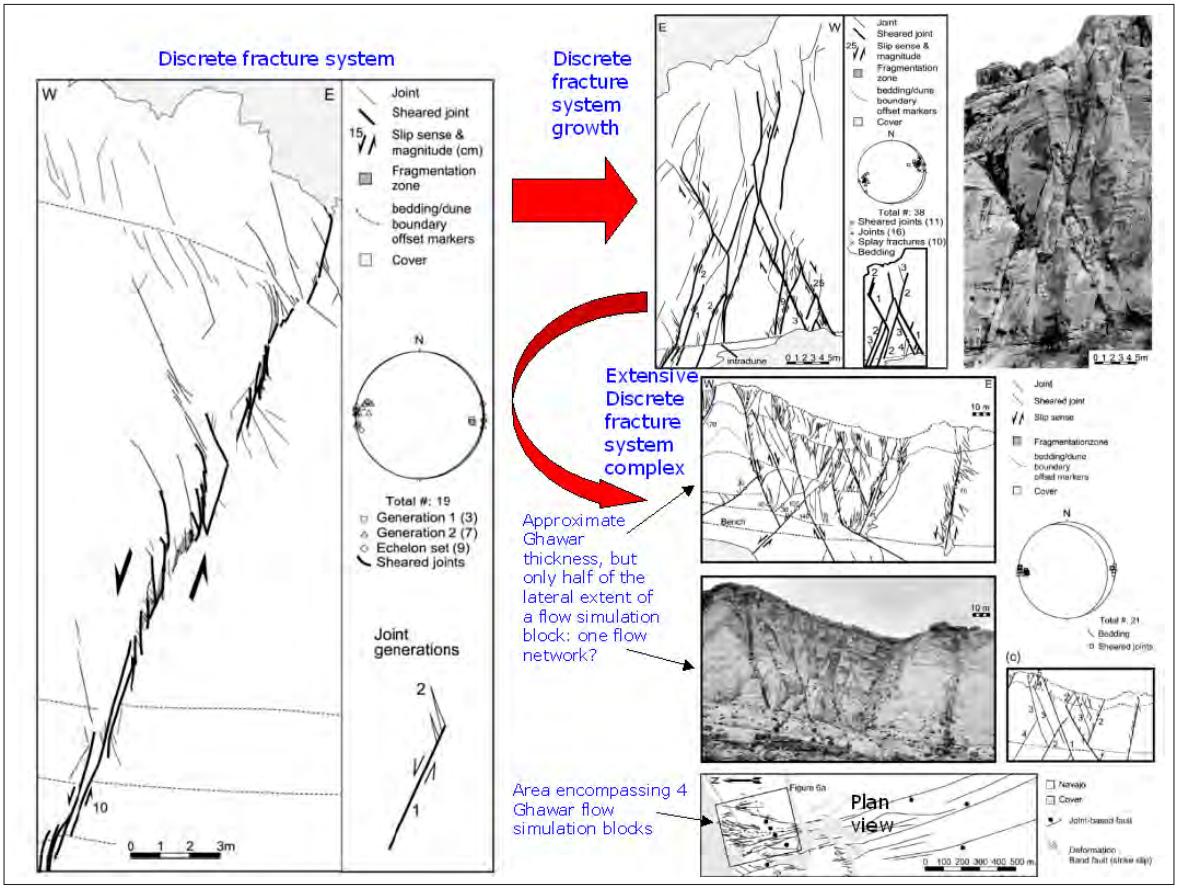

Fig. 7.5: Hierarchy of fracture flow network development[33]

7.2.1 Representation of the fracture flow network

A fracture flow network is the apex of a hierarchical system beginning with en echelon *individual joint* planes, which are in turn associated with other *fracture system* components, including oblique joints, dissolution or compression bands, crushed rock shear regions, brecciated zones, and even faulted zones, in turn forming *discrete fracture system groups and complexes,* some parts of which form an effective flow conduit, the *DFN*. Thus, the DFN is actually a subset of the intersecting fracture system complex, since not all components may contribute effectively to the conduit. This hierarchy is firmly established by the scale encompassed within a typical coarse flow simulation block, as in that of this study, measuring 250m x 250m x 4ft.

Fig. 7.5 presents the elements of the DFN hierarchy, as observed in field data[33].

Individual joints are seen to comprise only a part of a complex fracture system, which could alone form an isolated DFN. Intersecting fracture systems, forming groups and more extensive complexes, may form one or more networks. The complex may become very extensive, yet be entirely contained within the scale of a single column of flow simulation grid blocks.

A practical DFN model cannot generate components of the network, only the culminating network itself. However, in the absence of observed fracture distribution maps, or perhaps fracture density maps derived from seismic interpretation, this model is necessarily constrained by those data which inform the formation of the fracture system, that is, bed lithology and geometry, and the history of stress orientation and magnitude. In other words, although the DFN model is updated in a history matching algorithm by production data, its generation is reliant heavily on geologic data. Often, as in the case of this study, that geologic data is very sparse.

The DFN model described in Chapter 9, generates realizations of DFNs represented as isolated or intersecting planes. A DFN in this model, despite actually being comprised of a complex fracture system, or a series of intersecting fracture systems, is assumed to have a gross geometry which is planar in the least, as with an isolated fracture system, or at most complex, comprised of intersecting planes, as for intersecting fracture systems.

7.2.2 Terminal connections

Given the emphasis on flow, it is further desirable to limit the number of source connections that are mapped to the simulation grid, as circumstances may dictate that only a few key connections are pertinent. Furthermore, a large number of low-flux connections, unnecessarily burdens computation, while not contributing significantly to the resulting effect of the DFN flow.

The flow at the terminal regions of the DFN, for example, are often the most important to flow, and therefore most relevant to the flow simulation (Chapter 8). The terminal locations, by definition, are regions of maximum transfer flux to the

matrix. Indeed, a prolific fracture flow network is developed only where transmissibility connections conduct fluid at high rates to the matrix. Geologic features such as fracture complexes, even those in hydrostatic equilibrium, are effectively nulled if the transmissibility between the fracture and the matrix is not appreciable at two or more connections. The *flow network* is defined by the connections of highest fracture-matrix transmissibility, separated by the greatest distances, and yet defining the basic skeleton of the network. The DFN model generates realizations of objects assumed to have such favorable terminal connections.

Fig. 7.6 presents 2D and 3D examples, showing the geometry of a realization of a static DFN model, as, for instance, corresponding to that of the model described in Chapter 9, and its corresponding mapping of terminal connections, represented as squares or cubes. Each connection is contained in a flow simulation grid block. Fig. 7.6 also includes fracture intersection connections, to be described in Sec. 7.2.3. The connections are colored uniquely according to the DFN set in which they belong, that is, the flow network in which hydrostatic equilibrium is assumed. Note that in the case (bottom figure) for which a DFN possesses a vertical thickness that encompasses more than one flow simulation grid block, the entire column of grid blocks, intersected by the DFN end regions, is populated with connections.

High DFN matrix transfer flux at terminal connections may arise from a number of conditions, including high matrix or connection transmissibility, low friction pressure drop, and large reservoir pressure drop over the regions containing the network. Each of these conditions require specific DFN properties. The existence of these properties, unfortunately, are highly uncertain, in that they are rarely measured directly and extremely difficult to infer because of a lack of data. The proposition of their existence is highly dependent on a geologic fracture mechanics model based on data informing the given lithology under the given stress history of the reservoir, and data informing the diagenetic history of the reservoir . This data is commonly very sparse, if not nonexistent, and therefore these critical fracture properties are very uncertain.

Nevertheless, an examination of these high flux conditions is useful for an elementary understanding of high-conductivity DFNs.

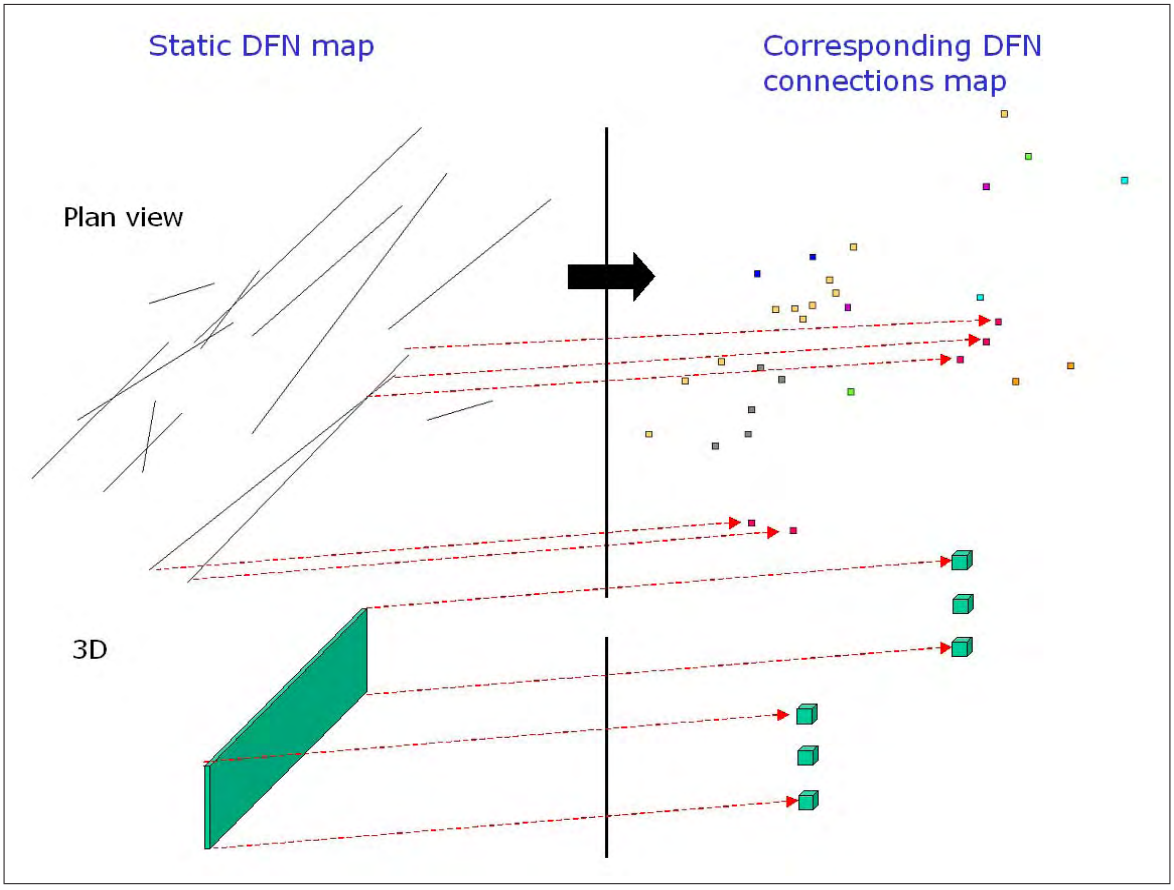

Fig. 7.6: Mapping transmisibility connections from a static DFN model

High matrix transmissibility at a terminal source will result when the DFN terminates in a high permeability facies. Also, the imposition of high source transmissibility may be warranted, due to brecciation, for example, at the terminal source. The source will conduct high fluid fluxes at these connections. The probability of existence of DFNs in a given lithology, as well as the tendency of a specific lithology for brecciation, is, again, a determination by application of fracture mechanics to the given reservoir.

Fracture geometries which enable low friction pressure drop flow, relative to the pressure drop associated with viscous flow through the matrix, enable high pressure drops across terminal connections, and therefore high fluid fluxes. This condition results from DFNs in which permeability is very high relative to permeability outside

the DFN, in the non-fractured rock. Fracturing does not necessarily imply high conductivity, as many mechanisms leading to fracturing also diminish, rather than increase, rock permeability. Therefore, it is appropriate to discern, as much as is possible, whether conditions leading to fracture in any specific case are amenable to high-conductivity DFNs.

DFNs which have sufficient lateral extent to breach regions of significantly differing pressure regimes, such as, for example, one which spans the reservoir between an injection and production well, may experience large DFN matrix flux, due to the pressure drop in the matrix at the terminal connections. The existence of this condition, unlike the two previously discussed, is determined more readily, as it depends on well locations and matrix permeability, and therefore is a reservoir engineering determination.

7.2.3 Intersection connections

When individual DFNs intersect, they may or may not form a unique hydrostatic flow unit, due to the complexity of the fracture systems and that of the intersection region. However, when they form a network in equilibrium, the intersection region may be important in that the connection transmissibility may be enhanced or diminished there. Also, the overall geometry of the DFN may be better defined with a connection at the intersection region, especially for DFNs with significantly different azimuths and plunge. Therefore, transmissibility connections are placed at all effective DFN intersections. An intersection is determined to be effective, or not, in a stochastic manner, as explained in Appendix G.

7.2.4 Near-well and near-neighbor connections

Points in the network that are near well blocks may also be critical, because these are regions where fluid flux in the reservoir is large. Furthermore, the influence of DFNs is highest when they are near wells.

Finally, points in the network that are near neighboring, networks are important for the following reason: geologically, DFN systems are complex failure regions,

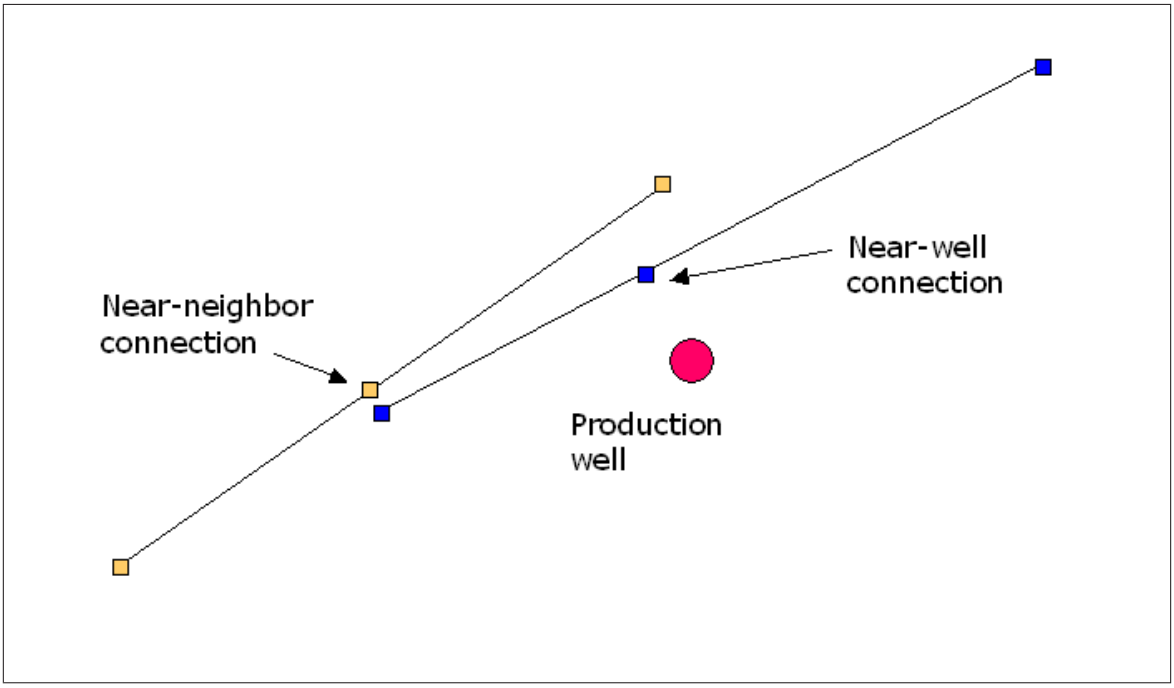

Fig. 7.7: Near-neighber and near-well connections

often not confined to narrow and restricted geometries, as may be individual fractures. Fracture systems in close proximity to each other may possess damage zones which overlap, although without the development of conductivity to allow substantial inter-fracture flow, but nevertheless possibly inducing higher fracture-matrix transmissibility than existed in the undamaged rock. Fig. 7.7 shows an example of the placement of these type of connections.

7.2.5 Conditioning DFNs to super-k flow intervals

The previous sections describe the placement of source connections, including those near production or injection wells. Given that the objective of the study is flowmeter data history matching through DFN characterization, it follows that intervals in which super-k has been observed, are intervals which may be influenced by DFNs. Therefore, flow network location is conditioned to these intervals. The DFN model described in Chapter 9, performs this conditioning.

This is demonstrated in Fig. 7.8. Here, at an injection well for example, super-k

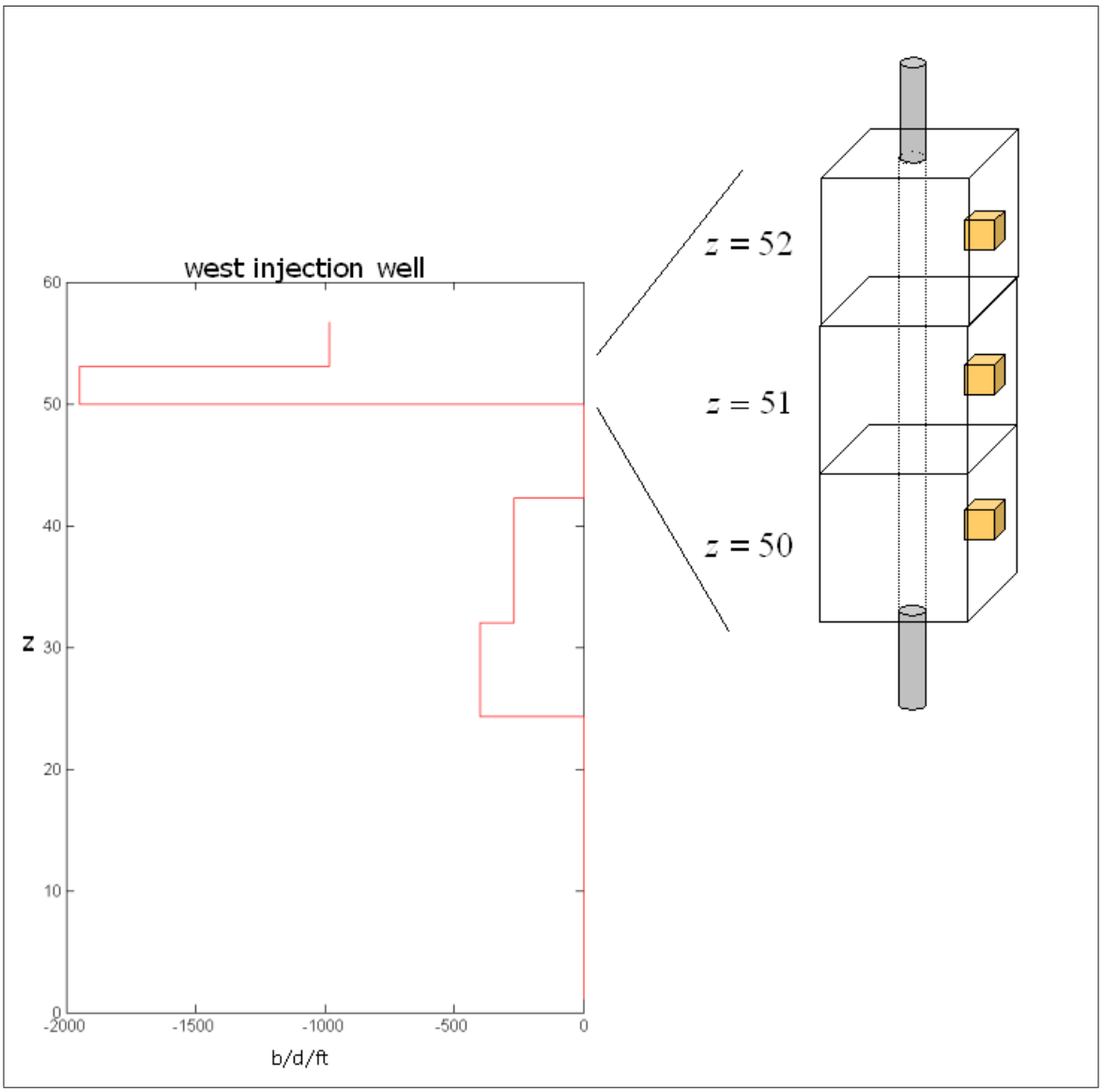

Fig. 7.8: Placement of source connections at well blocks

injection flow is observed at well blocks z = 50, 51, and 52, where z is the vertical dimension of the reservoir modeling grid, and in the particular case of the Ghawar study area, also the dimension of the flow simulation grid (total 60 vertical blocks). The yellow cubes represent DFN connections conditioned to those three well blocks.

The implication of this placement of DFN connections at the well blocks is not well stimulation. That is, the fracture is not being simulated as connecting directly

with the injection wellbore, as would a well stimulation hydraulic fracture. The implication is that the fracture is near the well, and more precisely, that it is near the Peaceman[34] radius, r_o, of the well,

$$r_o = 0.208\Delta x$$

where Δx is the lateral length of the well block. The distance r_o is approximately 160 ft in the flow simulation grid of this study.

Note that the conventional well model precludes the intersection of two wells. Wells may share a common block, but may not share a common connection. Therefore, a fracture may not directly intersect an injection or producing well in this model. Indeed, fractures are difficult to observe at wells, and no substantiation exists for assuming that super-k networks connect directly to wellbores via DFNs, with any significant frequency.

7.3 Analytical considerations for source application

It is readily shown that the source model, if used with currently available friction pressure drop capability, and with transmissibility connections placed at all coarse blocks intersected by the DFN, has only the following shortcomings, when compared to discretizing the DFN:

1. It is not appropriately applied when multiphase effects are important in the fracture,

2. It cannot appropriately model flow in which gravity segregation effects are significant and important in DFNs,

3. It is difficult to apply in fractures having highly variable permeability, where very fine discretization must be constructed to capture the heterogeneity, and the resulting fracture/matrix transmissibility variation cannot be easily predicted and then resolved with a single source transmissibility.

4. It may not be appropriately applied to cases in which accumulation in the fracture is significant, relative to that in the matrix. However, since DFN systems comprise a miniscule volume relative to the pore volume of the matrix, for any commercial reservoir, this condition is irrelevant and will not be discussed further.

The source model may be used, however, in a flow simulator in which DFNs are discretized, to account for the conditions above. It can then model specifically networks in which the above can be ignored. Similarly, the source model may be used within a dual grid model, to simulate flow in abnormally conductive networks, in which the above conditions are not important.

If the source model is restricted to usage in conditions other than those enumerated above, it is conceptually equivalent to fracture discretization, assuming the following:

1. The friction pressure drop facility can be calibrated to the pressure drop due to viscous flow through the fracture,

2. The source transmissibility can be calibrated to the fracture/matrix transmissibility

The equivalence between the source model and the discretized model is established because well flow friction models can indeed be calibrated to Darcy flow models, given adequate homogeneity and isotropy in flow properties, and source transmissibility functions can certainly be adequately calibrated to inter-block transmissibility functions, again under adequate homogeneity and isotropy.

7.3.1 Multiphase effects

Capillary and relative permeability effects in the fracture are important only in that their magnitudes are large when the DFN is not significantly more conductive than the surrounding matrix, a condition that is not of great interest.

Alone, capillarity is not important because the critical reservoir processes it controls, displacement and ultimate recovery, is not important in the fracture, due to its miniscule reservoir volume.

Nevertheless, the implication of large capillarity, to fracture conductivity can be seen in the capillary number, N_{cap},

$$N_{cap} = \frac{u\mu}{\gamma}$$

where u is the total volumetric flux, the Darcy velocity, μ is the mean viscosity of the liquids, and γ is the interfacial tension between the liquids, and more importantly, by examining the relative permeability function in the fracture.

It may be safely assumed that if N_{cap} is large enough in the matrix that capillary effects are insignificant relative to viscous effects, then capillary effects may be ignored in the fracture as well. However, often this is not the case, as capillary effects are commonly very important in the matrix. The difference between the capillary number in the fracture, and the capillary number in the matrix, can be assumed to lie in u. So, when the capillary number is small in both the matrix and the fracture, it simply expresses that u in the fracture is not significantly larger than in the matrix, a condition which may arise if the fractures are not appreciably more permeable than that of the matrix. In this case, the DFNs may not strongly affect reservoir performance over large scales, as that spanning adjacent well pairs.

Similarly, that highly non-linear relative permeability curves persist from the matrix to the fracture, suggests liquid-solid interaction is important in the fracture, nullifying significantly high conductivity flow. These fractures are not important in this study.

7.3.2 Gravity effect

Discussions of vertical equilibrium flow in 5.1.1 and 5.4.2 indicate that the ability to model gravity segregation within a DFN may be desirable if it is suspected that such behavior induces like behavior in the reservoir matrix.

As presented previously, although in a different form (5.1.1), the tendency toward gravity segregation in the DFN or reservoir matrix may be examined with the gravity number, N_g,

$$N_g = \frac{k_h}{\Delta\gamma k_v}\frac{H}{L}\nabla p$$

where $\Delta\gamma$ is the phase weight density difference, k_h is horizontal permeability, k_v is vertical permeability, H is the vertical thickness of the DFN or reservoir, and L is the predominant length over which viscous flow occurs. A low magnitude N_g is conducive to vertical equilibrium flow.

Evidently, a difference between the gravity number in the reservoir matrix and that in the DFN will be determined by the difference in the ratio $\frac{k_h H}{k_v L}$. Thus, highly conductive DFNs, in which isotropy is likely, will have a greater tendency for segregated flow than will a typical reservoir matrix, in which isotropy is rare. Therefore, if reservoir matrix vertical equilibrium can be induced only by that in a DFN, as has been indicated (5.4.2), then accounting for this behavior is important. However, if the reservoir matrix flow tends toward vertical equilibrium intrinsically, then this DFN behavior is not important. Furthermore, vertically thin DFNs, which will have a relatively higher tendency toward vertical equilibrium, become less important in inducing such in the reservoir matrix, as their limited geometry becomes prohibitive.

Gravity segregation in a DFN is also important when attempting to history match a flow rate profile along the vertical thickness of the DFN, for example when the DFN affects a production well which has been surveyed with a flowmeter. Then, the profile over the interval affected by the DFN, assuming its vertical resolution is adequate, cannot be resolved precisely if segregation is ignored.

Typically, this precision in flowmeter history matching is not required. Indeed, it is most important to discern the affected interval from unaffected intervals, rather than predicting the local flow profile over the affected interval. Specifically in the case of this study, super-k flow generally occurs over small vertical intervals. The flow usually contrasts sharply with the flow outside of the affected interval. Therefore, the variation of flow within the affected interval is not important, and often cannot be resolved by the flowmeter.

Finally, gravity segregation is not important with respect to recovery within the DFN, since the volume within a DFN is negligible.

7.3.3 Highly heterogeneous DFN permeability

This last condition under which the source model is not appropriate, is rarely considered, simply because a DFN cannot be resolved to such a fine scale that would justify the application of any heterogeneity in flow parameters within the simulated network. There currently exists no measurement paradigm that would enable the acquisition of variation in fracture flow properties such as permeability and fracture aperture, for fractures that cannot be directly measured. Indeed, commonly fracture description is very uncertain at the largest scales, with the objective in characterizing them being to capture the large scale flow effects. If, on the other hand, the DFNs are very precisely characterized, including the properties within the networks, then perhaps DFN discretization is warranted.

A flow regime which may be induced by heterogeneous DFN permeability, channeling, in which portions of the DFN are completely void of fluid transport, and the fluid follows a highly tortuous path through the DFN, cannot be modeled using sources, unless the effective conductivity of the DFN is approximated under the channeling condition.

7.3.4 The simplified source model

It is imperative that flow simulation models be optimized as much as possible with regard to speed and accuracy, when the model is used in a history matching algorithm. This is due to the need for numerous flow simulations in the optimization algorithm.

The complete source model, in which all possible connections are included, that is, all blocks which are intersected by the DFN are given transmissibility connections to the network, and in which a friction model is utilized to compute viscous pressure drop within the network, although accurate in its description of flow through the network, may become computationally burdensome.

The computational load is especially severe with irregular geometry, and large numbers, of transmissibility connections. This is due to the diminution of uniformity of the structure of the Jacobian matrix, brought about by the connections. This problem will not be elaborated on more in this thesis, except to say that, fortunately,

the prominence of horizontal wells has prompted work to improve the performance of unconventional well models in flow simulators, and that any computational gains made will greatly benefit the use of sources to model DFN flow.

Therefore, it is advantageous to discern those conditions in which a simpler source model may be used.

One such simple source model, currently being used in this study, employs the following modifications to the complete model:

1. Flux in the DFN is assumed to vary linearly with pressure gradient,

2. Flux through terminal regions, near production and injection wells, and near other DFNs, are assumed much greater than at other regions in the network.

The source model resulting from these assumptions, therefore does not employ a friction model to describe viscous flow pressure drop within the fracture, and does not place transmissibility connections anywhere in the network, except in those blocks at the terminus, near production and injection wells, and near other networks.

Ignoring nonlinear viscous flow pressure drop

A nonlinear pressure drop function of flux in the DFN is caused by turbulence, and so ignoring the non-linearity implies the flow in the network to be laminar. Expressed as a backpressure relation, the assumption is equivalent to specifying a backpressure exponent, n, close to 1:

$$q = (\Delta p)^n \ ; \ n \tilde{=} 1$$

The pressure drop due to laminar flow may be modeled with transmissibility connections alone, without an additional, friction pressure drop constraint.

Constructing DFN transmissibilities

When flow in the network is laminar, and the pressure drop is described as the viscous pressure drop through a possibly heterogeneous permeability distribution within

the DFN, the network may be modeled with as few as two source transmissibility connections, each located at the terminal points of the network. We demonstrate this here, by assuming the DFN permeability distribution is represented as a discrete set, such as that defined by a fine scale discretization of the DFN.

Fig. 7.3 presented the linear flux relation between two matrix blocks, for three DFN modeling techniques: discretization, dual grid, and source. Equating the flow terms from the discretization model and the source models,

$$\frac{1}{T_1^w} + \frac{1}{T_2^w} = \sum \frac{1}{T_i^m}$$

This relation may be viewed as a calibration of the DFN source model transmissibilities, T_1^w and T_2^w, with the discretized model fracture block transmissibilities, T_i^m. Here, only two connection transmissibilities, T_1^w and T_2^w, are being used to characterize the DFN for the source model, as discussed in detail in Chapter 8.

Fig. 7.9 demonstrates the elements involved in this calibration, for the case in which a fracture connects a region near an injection well, and a region near a producing well. A fracture flow pressure curve, assuming high conductivity (relatively flat pressure gradient), and linear flow, is shown. This fracture pressure curve is assumed to be that which would be generated by the discretized fracture model. Also, the source model flow pressure curve, which is flat, as expected for the exclusion of a friction pressure drop model, is presented. A coarse reservoir flow simulation grid is shown at the top of the figure, in which an injection well and producing well are placed. Also, two source model connections are placed in the well blocks.

Results similar to that in Fig. 7.9, for actual flow simulation models,are described in detail in Chapter 8.

The transmissibility of the coarse reservoir simulation grid blocks are not considered here; the transmissibilities, T_i^m, are those of the fine scale blocks of the discretized fracture model, which is not shown in the figure.

The calibration of T_i^m is practically achieved by production history matching, and therefore may become a critical history matching parameter. The calibration generally cannot be accomplished directly, since permeability variation data in DFNs is rarely directly measured.

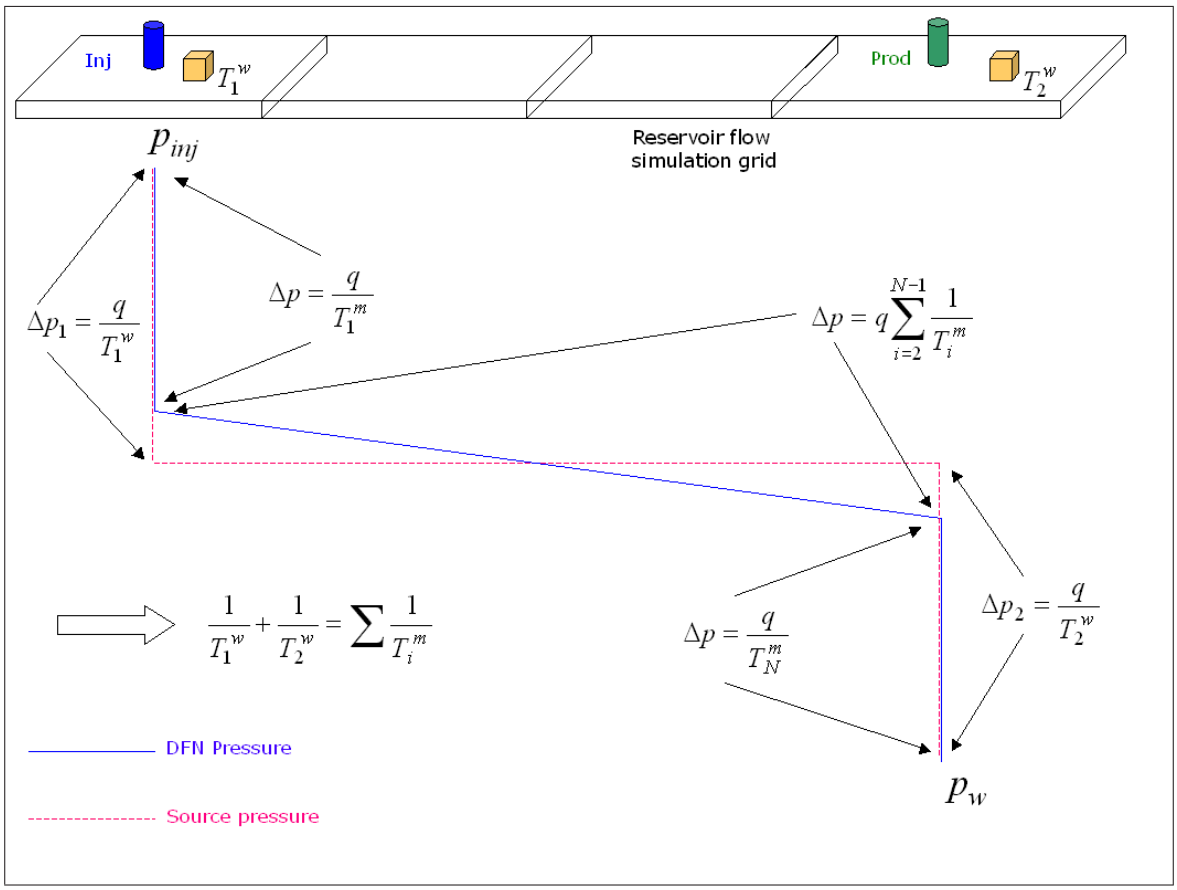

Fig. 7.9: Calibration of source transmissibilities

The assumption of laminar flow in the DFN precludes the requirement of a turbulent friction pressure drop model in the network. Many commercial flow simulators, however, like *ECLIPSE*, contain turbulent flow friction models, otherwise known as pipe friction models. These models may be used directly in the source model, if turbulence is suspected as important in DFN flow.

Ignoring low-flux connections

Convergent flow around injection and production wells largely determines the pressure distribution in reservoirs, which generally is characterized by relatively small gradients over most of the reservoir volume, and much larger gradients in a small volume containing the well. This follows from the logarithmic pressure distribution generated

by radial flow.

It may be assumed that flow in highly conductive DFNs are likely not to be radial, given the linear, planar geometry of the network, but rather, linear. Under this assumption, the linear flow equations in Fig. 7.3 are appropriate.

Given that highly conductive DFNs will also have relatively flat flow pressure gradients, then the question of whether or not fracture regions which are not near well blocks may have large fluxes depends on:

1. The coarseness of the flow simulation grid,

2. The magnitude of the difference between the source transmissibilities at the terminal regions of the DFN.

Fig. 7.10 shows the significance of coarse flow simulation grids, with regard to resolving reservoir pressure near wells. The grid shown at the top of Fig. 7.10 is similar to the grid spacing of the Ghawar study area flow simulator, relative to well spacing in the study area (250 m grid spacing and 1 km well spacing). The reservoir pressure curve represents that which would exist without isotropy (without crossflow between reservoir and DFN) and thus indicates the maximum difference in pressure profiles between the two.

Note that the majority of pressure change due to the injection well is enclosed in the well block, and that the pressure gradient in the adjacent block is relatively flat. Indeed, assuming that the well block pressure, p_1, may be computed as the Peaceman pressure[34], occurring at a radius from the center of the injection well, $r_o = 0.208\Delta x$, then simple radial flow in a homogenous reservoir dictates that the pressure of the adjacent block, p_2, is such that,

$$\frac{p_1 - p_2}{p_1 - p_{mid}} \tilde{=} 0.8$$

for this particular reservoir flow simulation grid spacing, where p_{mid} is the reservoir pressure at the midpoint between the injection well and production well, computed from the radial flow equation. Generally the following holds, again from the radial flow equation in a homogeneous reservoir, for a flow simulation grid which has a grid

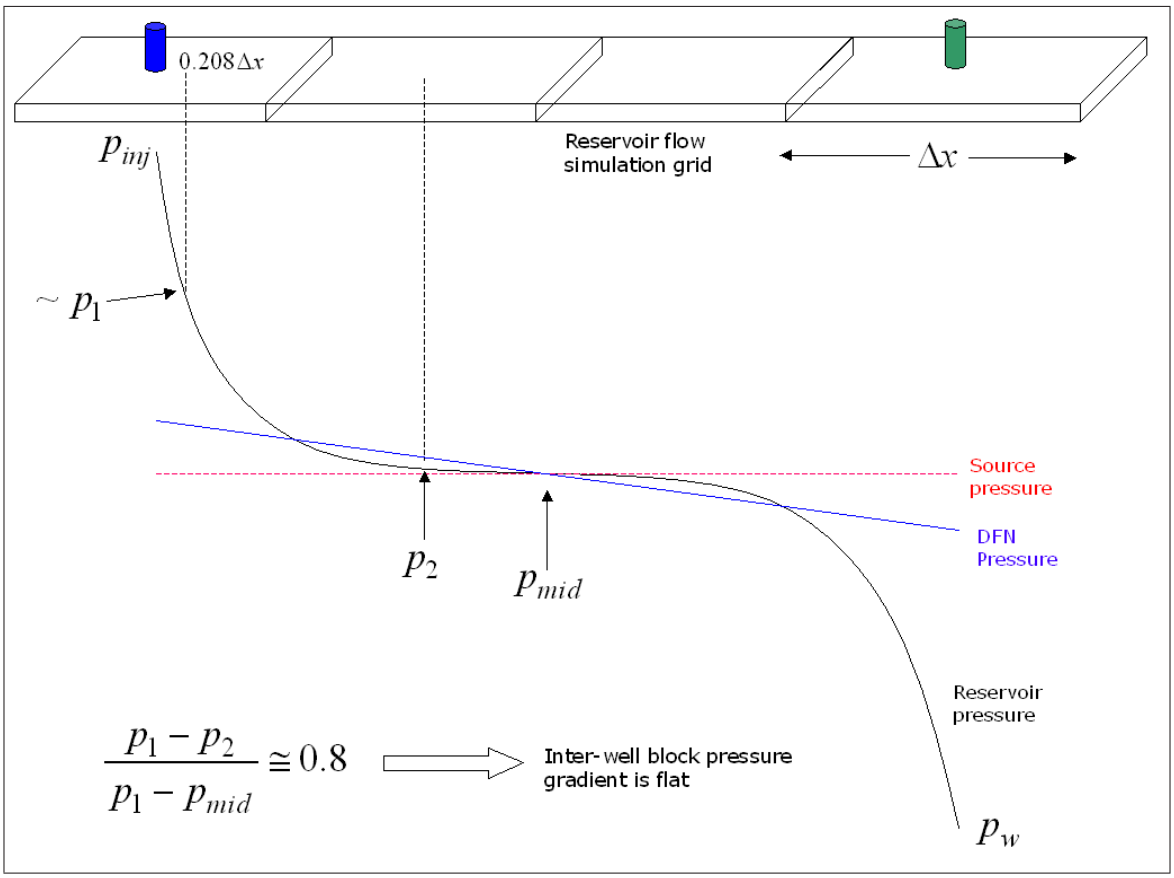

Fig. 7.10: DFN and source pressure compared to reservoir pressure

density of N blocks between wells, where N includes the well blocks, ($N = 4$ in this example):

$$\frac{p_1 - p_2}{p_1 - p_{mid}} = \frac{1.57}{\ln[(N-1)/2] + 1.57}$$

Note in Fig. 7.10 that both the fracture pressure curve and the source pressure curve intersect the inflection point of the reservoir pressure curve. This condition, the flat fracture pressure gradient, and the coarse grid, all combine to generate small differences between the fracture pressure and the reservoir block pressures. Thus, under these conditions, liquid flow between the fracture and these inter-well matrix blocks is limited.

This set of conditions, which has been observed in published numerical simulations[2],

and demonstrated in Sec. 8.3.3, warrants the exclusion of source transmissibility connections in the inter-well reservoir blocks.

The symmetry of the pressure profiles in Fig. 7.10 is due to the transmissibilities between the matrix and fracture, or the source transmissibilities, at the terminal points, being equal, in this example. The equations presented in Fig. 7.9 show how these conditions arise. The ratio of Δp_1 and Δp_2 is,

$$\frac{\Delta p_1}{\Delta p_2} = \frac{T_2^w}{T_1^w}.$$

Thus if T_1^w and T_2^w differ, then the DFN pressure in the source model, p_f, will be displaced from the block pressures of intermediate blocks, an example of which is shown in Fig. 7.11.

The scenario generating p_f in this case is one in which T_1^w is larger than T_2^w. Thus, liquid in the fracture, when entering blocks 2 and 3, for example, will tend to exit the fracture, into these two blocks, with flux magnitudes that are proportional to $(p_f - p_2)$ and $(p_f - p_3)$.

These conditions may require a source transmissibility connection be placed in blocks 2 and 3, depending on the magnitude of the source model pressure, p_f ; however, it may be shown that often this is not required. For instance, very large differences in source connection transmissibilities may result in the irrelevance of the DFN. This is seen in the flow equation for the DFN,

$$q = \frac{\Delta p}{\frac{1}{T_1^w} + \frac{1}{T_2^w}}$$

If either T_1^w or T_2^w is small, then q may be small enough that the effect of the DFN on reservoir performance is negligible.

As another example, assuming differences in fracture geometry between the terminal points of the network may be neglected, source connection transmissibility differences generally arise from differences in the permeability of the rock at the terminal points. A heterogeneous permeability distribution may result in large differences in the permeabilities of the terminal regions. However, this heterogeneity also affects the reservoir pressure gradient, and in a fashion which diminishes the effect of the heterogeneity on the source connection transmissibilities, as shown in Fig. 7.12.

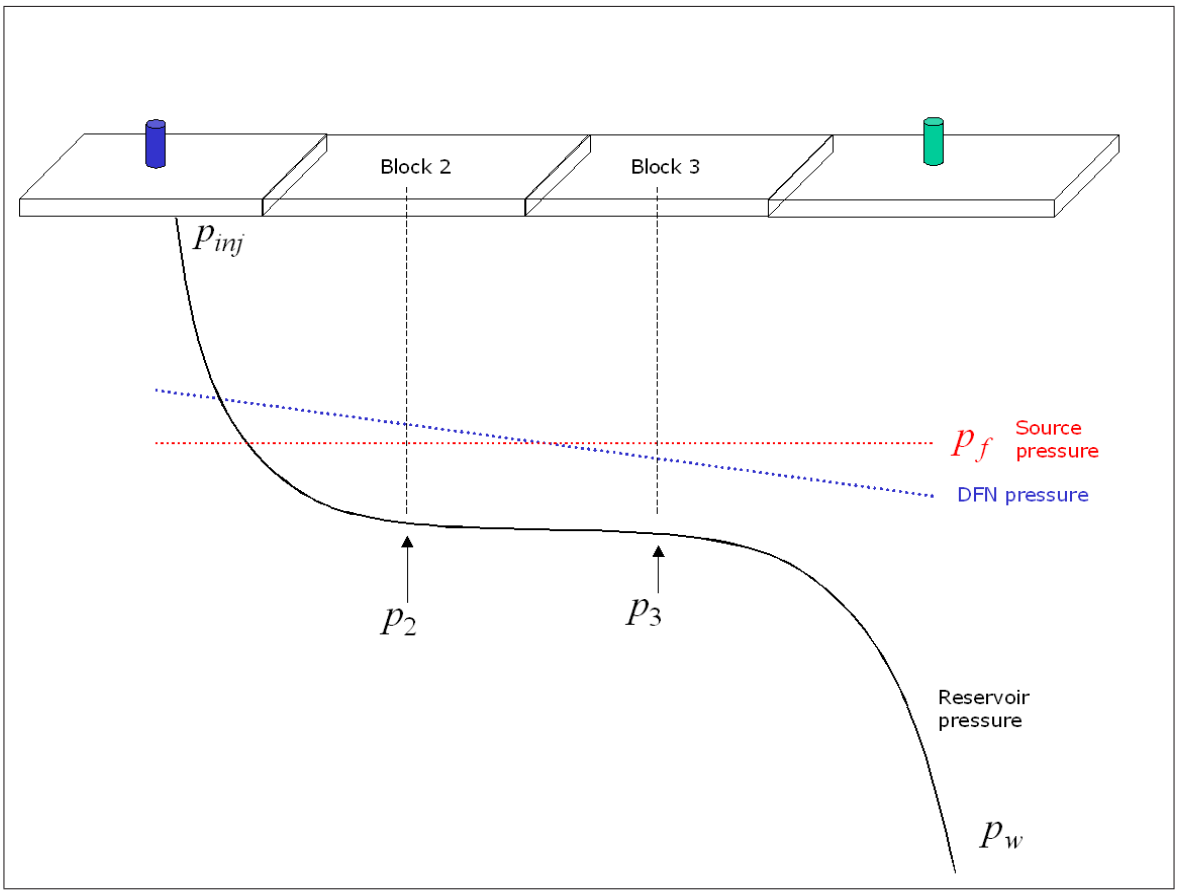

Fig. 7.11: The effect of unequal source transmissibilities

Here, permeability heterogeneity, for example, higher permeability near the injection well, result in *both*, source connection transmissibility increase at the injection well block, and reservoir transmissibility increase near the injection well. Since permeability regions near the wells significantly affect the reservoir pressure gradient, the reservoir pressure curve may be shifted significantly, as is the fracture pressure curve. Thus, pressure differences between the fracture and the reservoir at inter-well block regions tend to be ameliorated, as shown in Fig. 7.12.

Similarly, lower permeability near the injection well will cause both fractures and reservoir curves to shift downward, again decreasing the pressure difference between the two.

Therefore, if significant source connection transmissibility differences arise at the

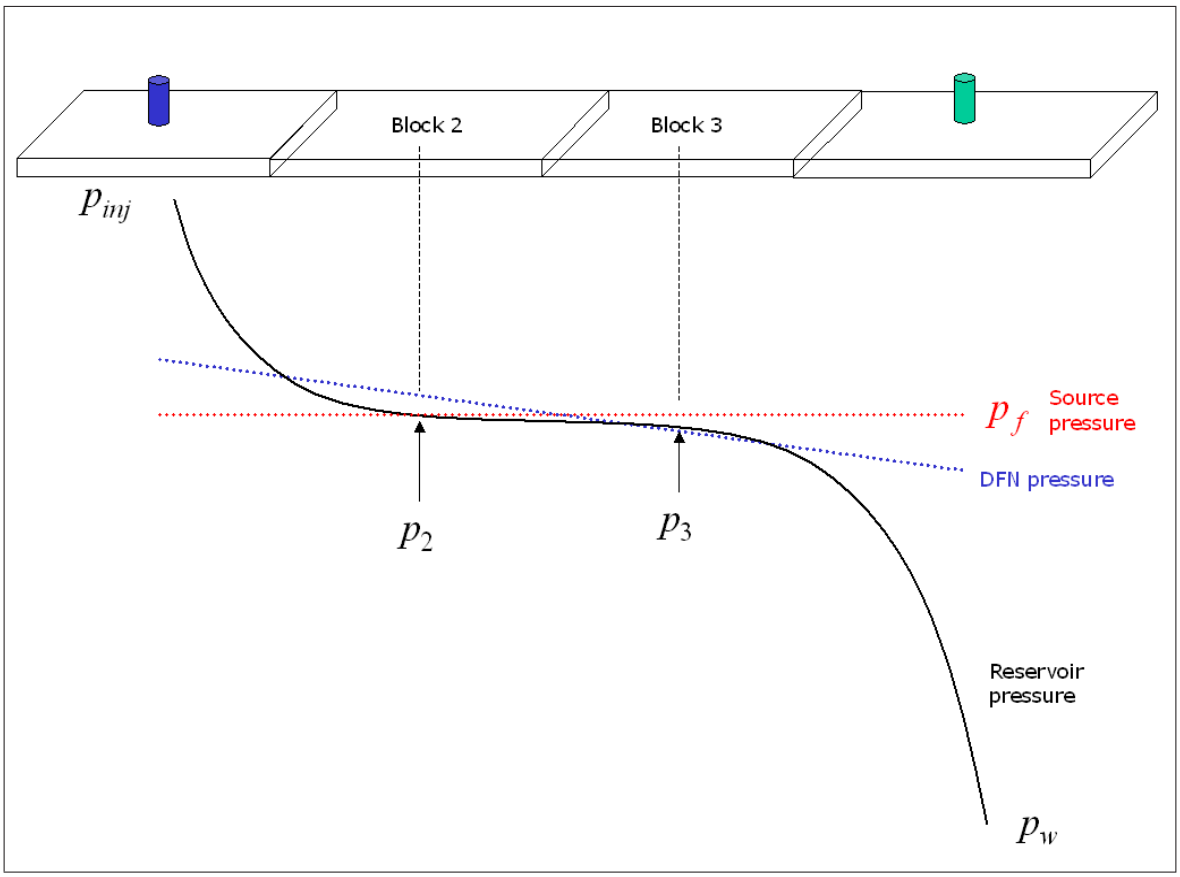

Fig. 7.12: The effect of heterogeneity in permeability

terminal regions, due to heterogeneity in reservoir permeability, the omission of source transmissibility connections at inter-well blocks may not introduce significant error.

7.4 Summary

This chapter has provided the motivation and development of the source model as a DFN flow simulation model. Appendix B describes the computational behavior of the actual implementation of this DFN modeling method to our study area.

The source model has been shown, in this chapter, and in Chapter 8, as a well founded, and practical discrete model. The analytical basis for it's use as a DFN model, stems from its inclusion as a fundamental term in the governing process relation, completely independent from a flux treatment. It's implementation benefits

from decades of development of the conventional well model in finite difference simulators. The source model has proven in our study to be viable, and in light of the profound obstacles preventing the practical application of finely gridded and dual grid models, the source model warrants future research, and invites further, immediate practical application.

Chapter 8

The mechanics of DFN flow

Our super-k model is comprised primarily of one or more DFNs. Adequate modeling of the DFN is therefore essential. Modeling requires an elementary knowledge of DFN flow mechanics, which may be comprised of two parts: knowledge of the fluid flux distribution within the DFN, and of the pressure distribution in the reservoir as influenced by the DFN.

We will begin with an elementary linear model which shows qualitatively, though very clearly, the flux and pressure distributions expected from DFN flow. We will then present some analytical results, found in the literature, which verify the elementary model.

8.1 An elementary linear model

The basic flow mechanics of the DFN may be seen with a linear model as shown in Fig. 8.1. Here, an infinite conductivity vertical DFN, that is, a DFN within which flow occurs with a zero pressure gradient, is embedded in a homogeneous matrix. The perspective is plan view.

The first case we consider is simple linear flow under constant boundary conditions p_1 on the right, and p_2 on the left. No flow normal to the the DFN plane occurs. Also, flow normal to the extensions of the DFN plane to the boundary, as shown, does not occur. The pressure distributions within the DFN and outside of the DFN are

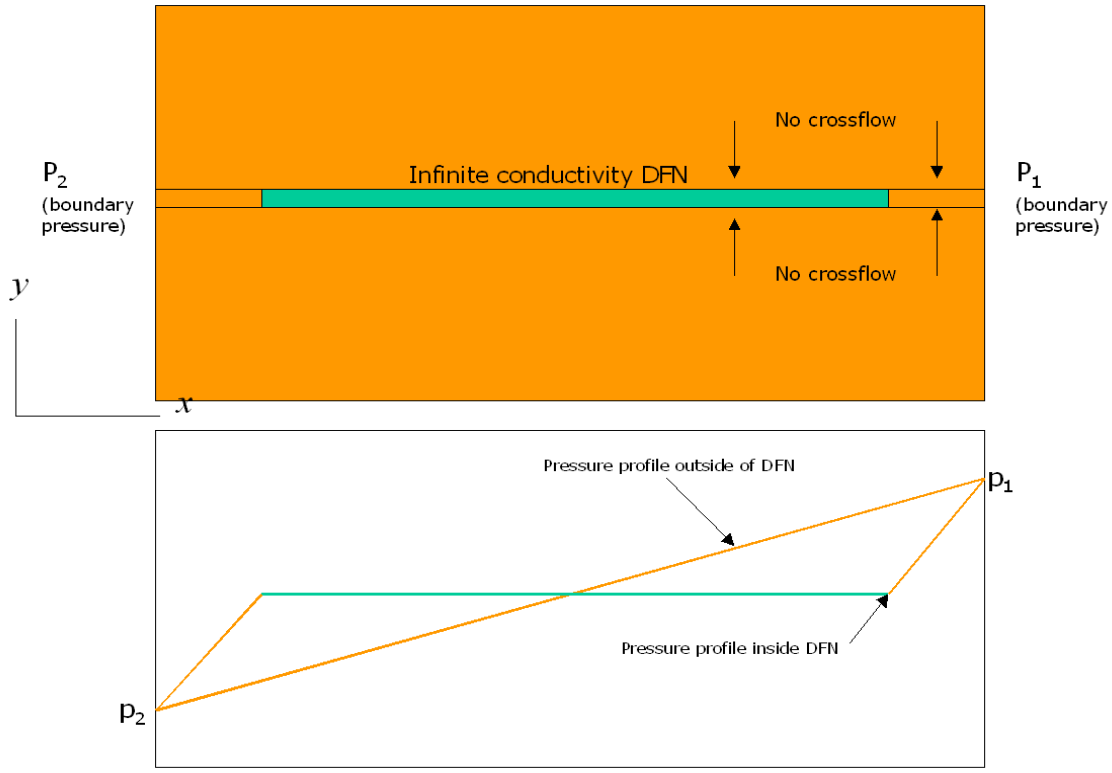

Fig. 8.1: Plan view of pressure distribution of an infinite conductivity DFN, no crossflow

shown. Note that no pressure drop occurs in the DFN, and that fluid flux through the DFN is significantly larger than fluid flux outside the DFN, as indicated by the steep pressure gradients at the DFN endpoints.

It is evident from the pressure distributions that if crossflow were to occur, it would have a direction into the DFN, over its right half, and out of the DFN over its left half. Furthermore, the crossflow flux would be maximum at the DFN end-points, and would diminish to zero at the DFN mid-point, as well as at the constant pressure boundaries.

We next examine the case in which complete crossflow occurs between the DFN and the matrix: the reservoir is everywhere isotropic. Fig. 8.2, bottom, presents the steady state pressure distribution of such a model, compared to that of the no crossflow model, top. Note the isopotential lines are parallel when no crossflow

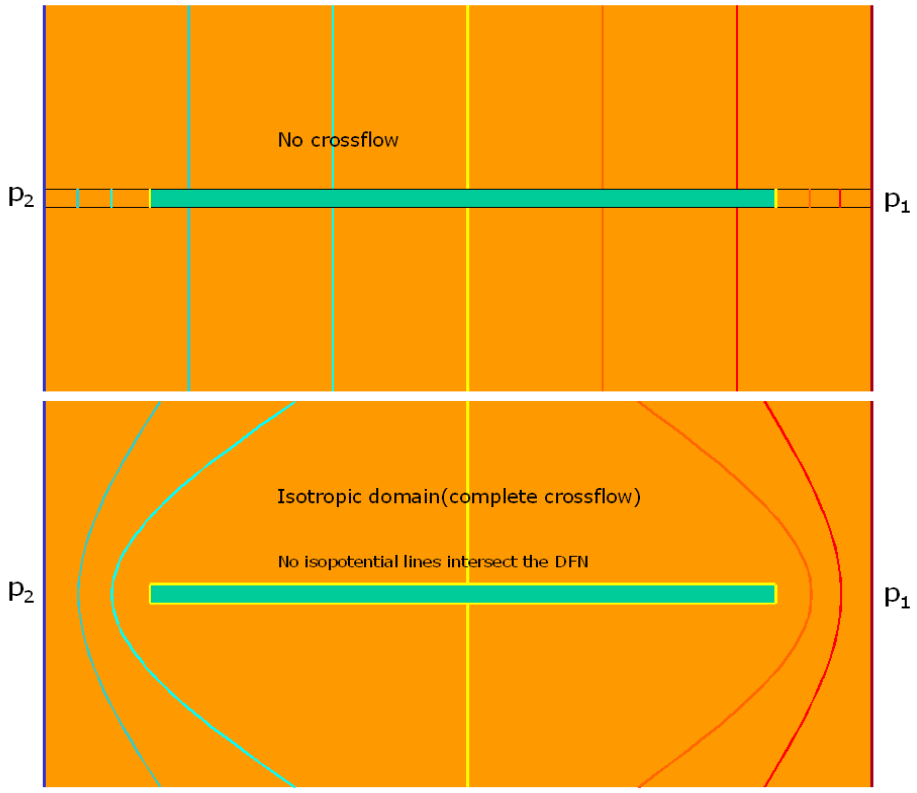

Fig. 8.2: The pressure distribution in and around an infinite conductivity DFN, isotropic case

occurs, and that they are discontinuous over the DFN.

The crossflow case imposes continuity of isopotential lines, by definition. Furthermore, the infinite conductivity of the DFN prevents any intersection of isopotential lines and the DFN, since no pressure drop occurs within the DFN.

The principal result of the combination of infinite conductivity and isotropy, is that isopotential lines are compressed at the ends of the DFN, but are separated in the region away from the DFN ends. Thus, pressure gradients are maximized at the ends.

Fig. 8.3 indicates schematically the pressure surface for the crossflow model. Only half of the model is shown, by symmetry.

The pressure distribution can no longer be represented by only two profiles, as in Fig. 8.1; instead, the pressure surface is represented with six vertical slices, numbered

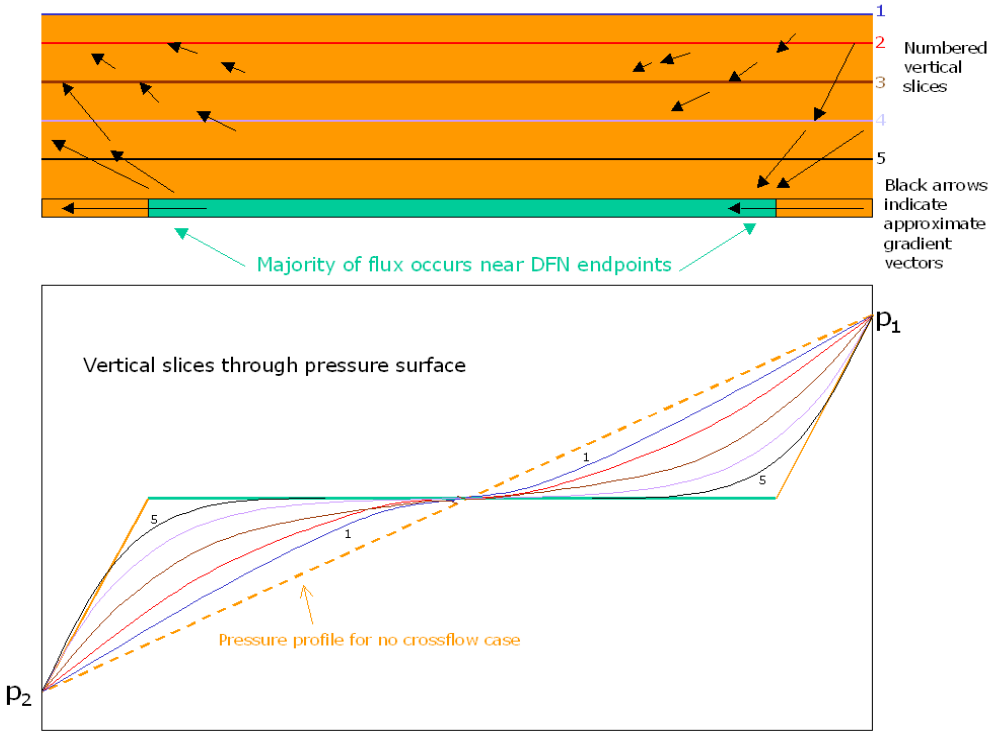

Fig. 8.3: Pressure surface and streamlines around an infinite conductivity DFN, isotropic case

1 through 5, and a sixth profile through the DFN.

It is evident from the profile slices that the largest gradients occur near the DFN ends and that they are directed to the DFN. Thus, the majority of the flux in the DFN enters and exits at the ends. Furthermore, gradients diminish to zero toward the center of the DFN.

Note also that near the DFN, but away from the ends, the pressure surface is relatively flat, approaching that of the flat profile within the DFN (see Sec. 6.4.4).

This result may be modified in a straightforward manner for the case of a finite conductivity DFN. Finite conductivity necessitates a nonzero pressure gradient within the DFN, and thus isopotential lines must intersect the DFN, as shown in Fig. 8.4. The upper diagram displays the approximate pressure distribution for a finite conductivity DFN, for which the dimensionless conductivity, F_{CD}, is defined,

$$F_{CD} = \frac{k_f w_f}{k L_f}$$

where k_f is the DFN permeability, w_f is the DFN aperture, k is the matrix permeability, and L_f is the DFN length. F_{CD} is a familiar characterization parameter for hydraulic fractures, induced at the well for well stimulation purposes. It may be interpreted as a comparison between the reservoir permeability, and a weighted DFN permeability, where the weighting factor is dependent on DFN geometry: the factor is increased with increased aperture, and decreased with increased length.

The lower diagram presents the pressure distribution for a finite conductivity DFN, where F_{CD} is less than that represented in the upper diagram. This figure demonstrates the evolution of the pressure distribution with differing degrees of DFN conductivity.

Experimental studies using electromagnetic models have confirmed the above heuristic demonstration of the compression of isopotential lines in the presence of highly conductive reservoir regions. Fig. 8.5 is a result from one study[67], in which an electrically conductive thin copper blade is placed in an aqueous solution containing a point source anode and a circular boundary cathode, modeling the steady state pressure distribution of a single well, circular reservoir containing a DFN. The measured isopotential lines in this electromagnetic model, left, match the expected, heuristic distribution, right, as shown. The copper blade is placed at an arbitrary angle relative to the radii emanating from the anode, in this example.

8.2 Analysis of DFN flow

This section presents analytical results existing in the petroleum literature, that quantify the previous section's heuristic development. Three publications represent the entirety of those describing analytical models addressing well response in the presence of remote DFNs, those that do not intersect the well. Two of these, by Cinco-Ley, *et al.*,[40] and Abbaszadeh and Cinco-Ley[41], are drawn upon heavily in this discussion. The third[42] provided a minor extension of the other two papers.

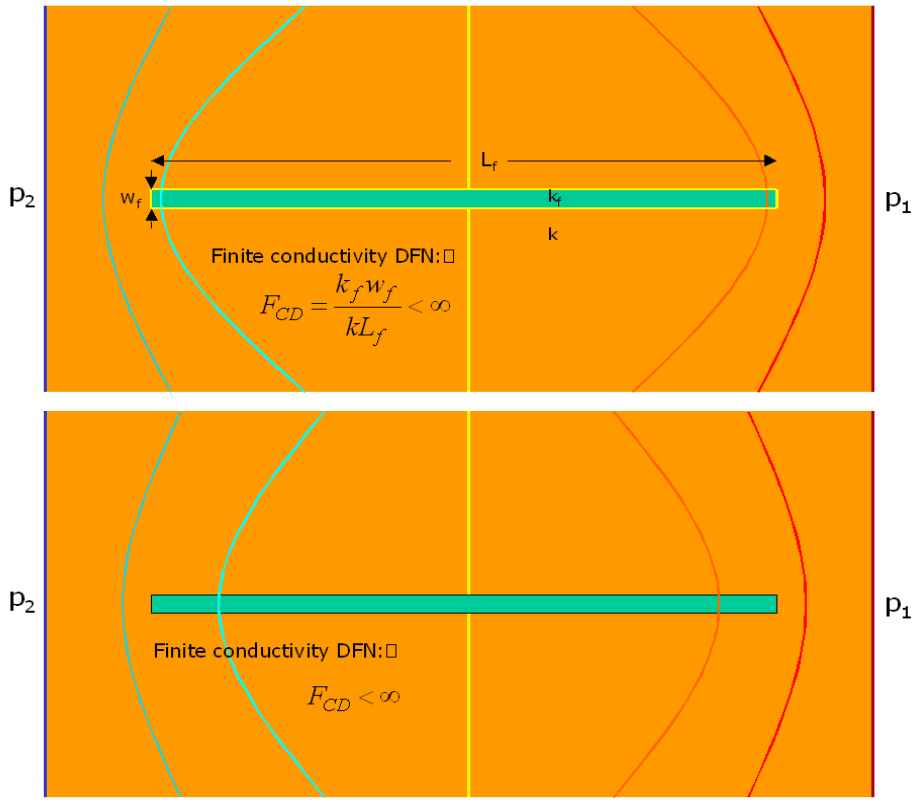

Fig. 8.4: Pressure distribution around finite conductivity DFNs

The analysis of flow in DFNs which intersect the well, hydraulic fractures, generated at the well for stimulation purposes, are plentiful in the literature. Some fundamental analytical results may be extended from hydraulic fracture models to that of remote DFNs, and thus some of these established models are applied here.

Further research on the flow in DFNs which do not intersect wells, is sorely needed, and will be supplemented in part with some numerical results presented in this chapter (Sec. 8.3.3); however, the topic will remain largely unexplored and open for further work.

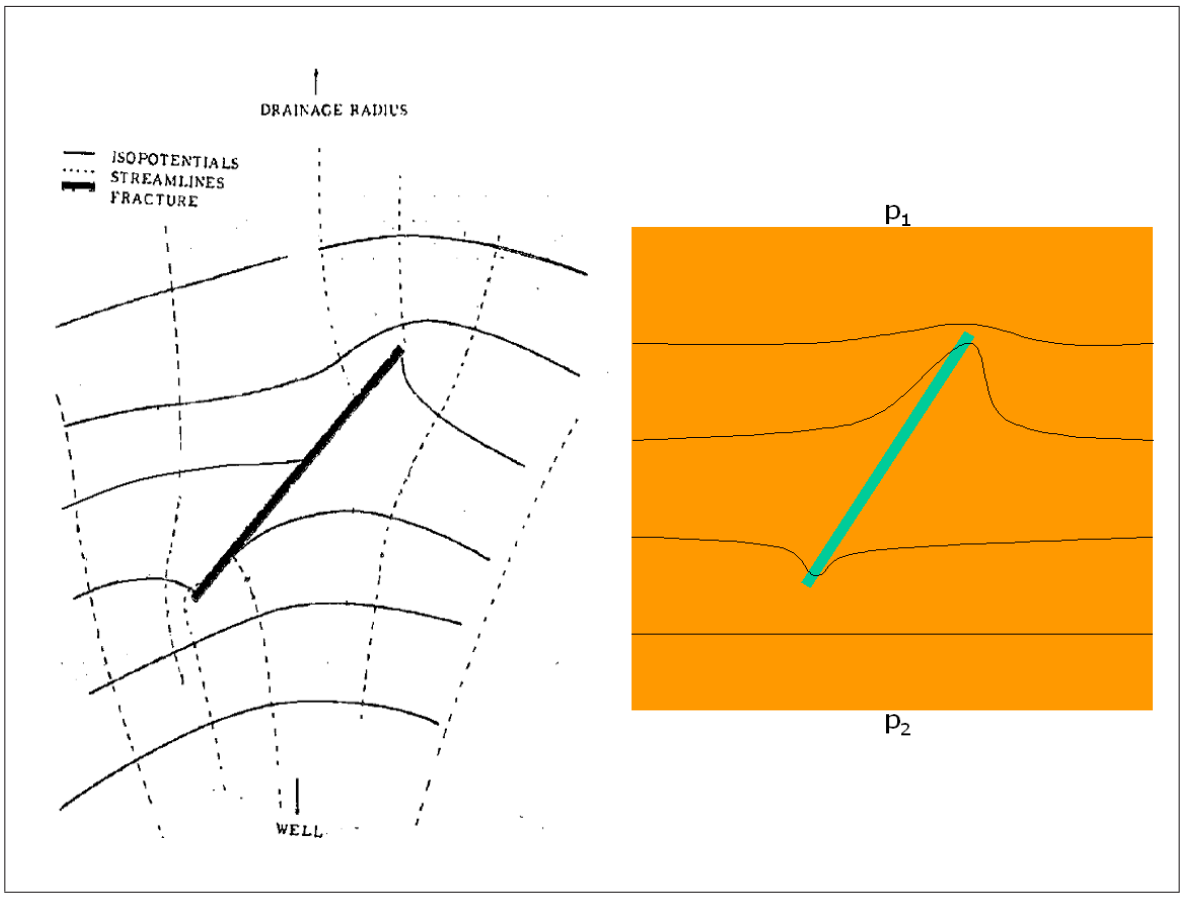

Fig. 8.5: Electric analogy of isopotential distribution about a non-radial DFN[67]

8.2.1 Infinite conductivity DFN of finite length

Rigorous analysis has confirmed that the important, linear, observation of Sec. 8.1, that flux is highest at the ends of DFNs, prevails in radial flow systems. Fig. 8.6 shows the results of an analytical derivation[40] of the late-time flux distribution, that is, after long times when little change in reservoir response occurs, in an infinite conductivity DFN located near, but not intersecting, a producing well, in an infinite, 2D, reservoir. This result is a solution of the diffusivity equation through the application of uniform flux source functions[69] to a discretization of the DFN, under the constraint of uniform pressure in the DFN, thus simulating infinite conductivity, in a slightly compressible system. Solutions to the diffusivity equation are applicable to Ghawar, given its predominantly liquid comprised system.

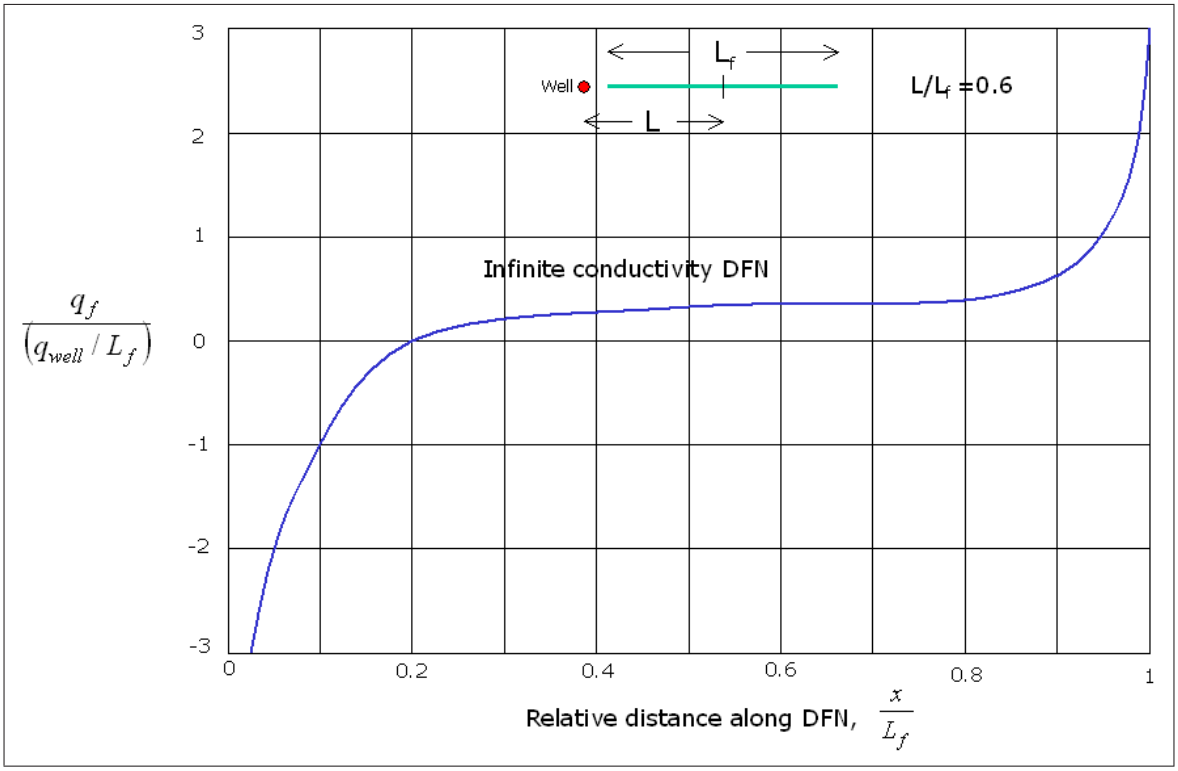

Fig. 8.6: The flux distribution in an infinite conductivity DFN near a producing well[40]

Here, q_f is the DFN flux, in units of volumetric rate per unit length, as a function of position along the DFN, and q_{well} is the volumetric rate at the well. The DFN lies on a radial of the well, and is located at a distance equal to 10% of the DFN length ($L/L_f = 0.6$, where L is the distance from the well to the DFN center, and L_f is the DFN length). q_f is positive away from the well, where liquid enters the DFN, and negative near the well, where liquid exits the DFN and flows to the well. Note that the majority of the DFN flux, positive or negative, occurs within 20% of the DFN length on each end.

8.2.2 Finite conductivity DFN

Quantification of DFN flow in the form of a single parameter, F_{CD}, is most useful when the pressure and flux characteristics associated with specific values of the parameter are known. An example is presented in Fig. 8.7, where pressure drop in the DFN

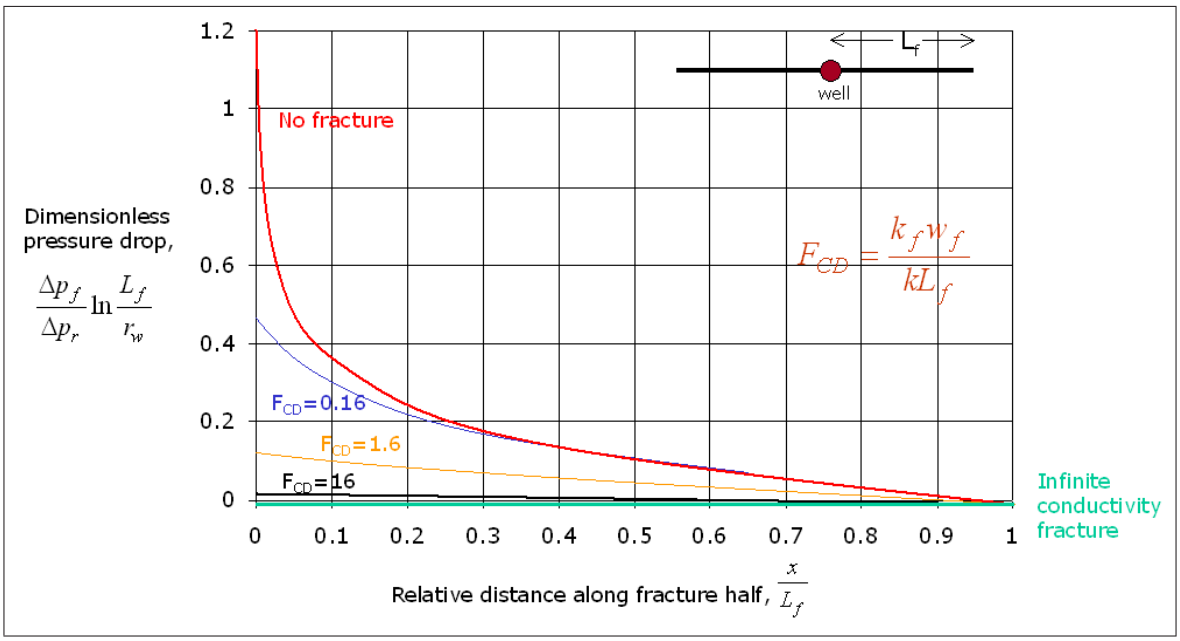

Fig. 8.7: Relative pressure drop in a finite conductivity DFN[68]

is quantified as a function of F_{CD}. These results were derived from an analysis[68] in which steady state pressure distribution within a DFN intersecting a well was computed; they are solutions of the 2D Laplace equation, by Fourier series, in a system with two homogeneous, isotropic, regions: the DFN, and the remainder of a bounded, circular reservoir.

The abscissa is the relative distance along the DFN half-length, as the solution is symmetric relative to the well. The ordinate is the relative pressure drop, from that at the endpoint of the DFN. Δp_r is the pressure drop in the reservoir with no DFN present, and is the result of steady state radial flow. Δp_f is the pressure drop within the DFN. Note the ratio $\Delta p_f/\Delta p$, depends on the position along the DFN, the dimensionless conductivity F_{CD}, and the term $\ln(L_f/r_w)$, where r_w is the well radius. This latter term is practically $1 < \ln(L_f/r_w) < 10$, and thus the relative pressure drops are lower than the values read directly from the ordinate.

The significance of these results is manifest in the very low DFN pressure drop for essentially $F_{CD} > 2$, for which the pressure drop is less than 10% that under radial flow with no DFN present. An order magnitude higher value of F_{CD}, say $F_{CD} > 20$,

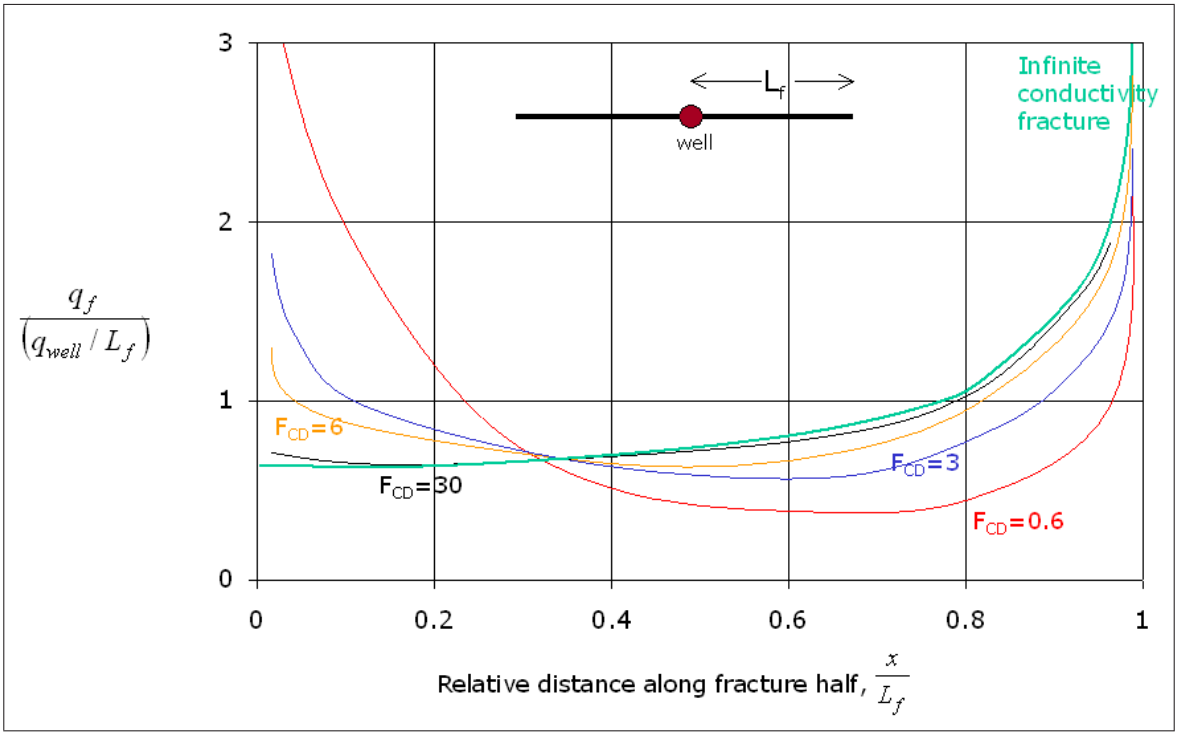

Fig. 8.8: Flux in a finite conductivity DFN[70]

is equivalent to infinite conductivity, that is, no pressure drop in the DFN.

This conclusion is obtained also in the analysis[70] of the DFN flux distribution, Fig. 8.8. These results were obtained by simultaneous solution of the diffusivity equation (including source terms) applied to both the DFN and separately, the remainder of an infinite 2D reservoir. The analytical solution was derived using Green's and source functions[69], and computed using a discrete method.

The flux distributions shown are at late time. Note, similarly to the result in Fig. 8.7, that $F_{CD} = 30$ behaves equivalently to an infinite conductivity DFN, that is, a significant portion of the total flux occurs near the end of the DFN.

The extension of these results, in which the finite conductivity DFN intersects the well, to the isolated finite conductivity DFN, is straightforward, using Fig. 8.6 as a guide. Clearly, decreasing magnitudes of conductivity diminish the flow rate within the DFN, and thus the flux over the length of the DFN. The limit, at $F_{CD} = 0$, requires flux to be constant and zero at all points on the DFN. Thus, the transition

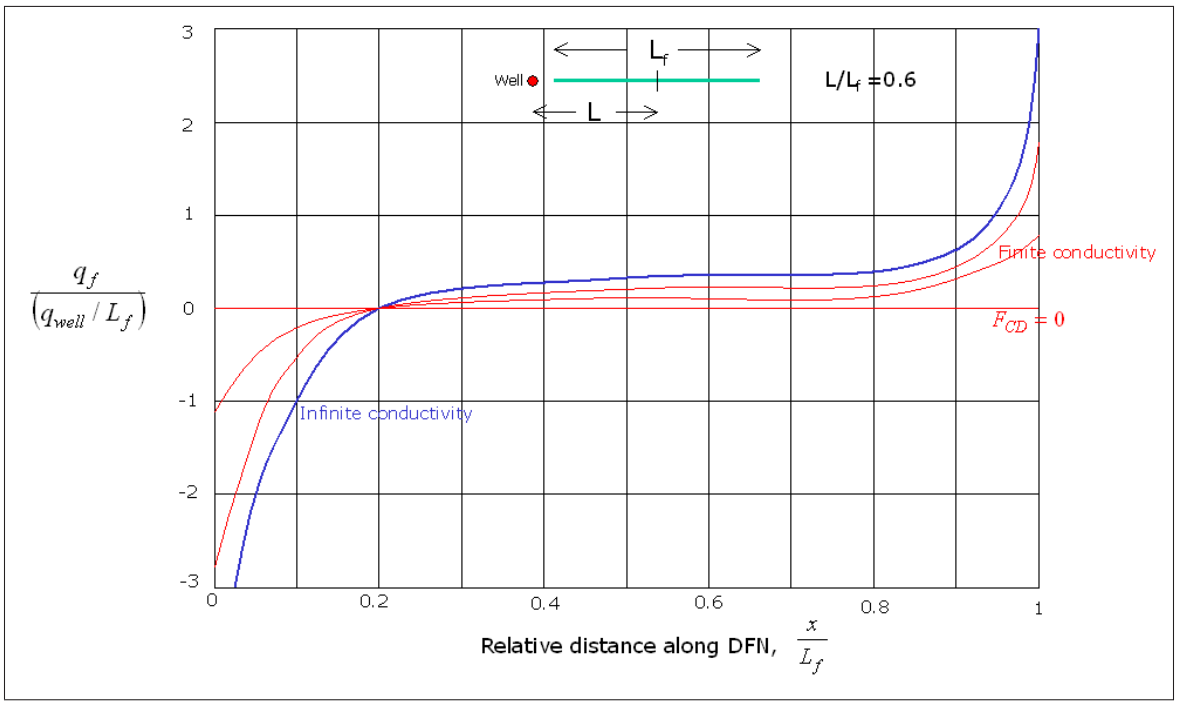

Fig. 8.9: Estimted flux profile in a finite conductivity DFN[40]

from infinite conductivity to the limit should be continuous, and similar to that shown in Fig. 8.9. Note that in the transition toward the limit, the proportion of flux entering and exiting the DFN ends decreases.

The occurrence of finite or infinite conductivity in real reservoirs may be addressed, at least in the case of the Ghawar Field, by computing F_{CD} for various geometries of open mode fracture systems. Open mode fractures have not been confirmed at Ghawar, although seismic data indicating normal faulting has appeared in the literature[5]. These faults appear to be nearly vertical. Nonetheless, the DFNs associated with the deformation of the Ghawar structure are documented as very conductive, so it may be useful to examine the conductivities associated with open mode fracture systems, as these produce the most conductive DFNs, and the determination of dimensionless conductivity is straightforward.

An additional comment is warranted, as DFNs differ from hydraulic fractures in a significant respect: rarely are hydraulic fractures not propped, and thus the upper bound of permeability within the fracture is generally not that corresponding to a

void aperture. However, DFNs may have void apertures, if they are open mode and void of breccia or precipitate.

The permeability of an open mode DFN of aperture w_f is, assuming laminar flow,

$$k_f = 8.4 \times 10^4 w_f^2,$$

where k_f is in *darcies*, and w_f is in mm. Substituting into the relation for F_{CD},

$$F_{CD} = \frac{0.084 w_f^3}{k L_f},$$

or,

$$F_{CD} k L_f = 0.084 w_f^3.$$

where k is the reservoir permeability, in *darcies*, and L_f is the DFN length, in km. Fig. 8.10 is a plot of this relation. A DFN of length 1 km, for example, in a reservoir of permeability 1 *darcy*, having an aperture $w_f = 6\ mm$, has a dimensionless conductivity $F_{CD} \simeq 20$. Note that lower magnitudes of k yield larger values of F_{CD}; shorter DFN lengths also result in larger conductivities.

Thus, open mode DFNs of relatively small aperture may readily achieve magnitudes of F_{CD} large enough to behave as approaching infinite conductivity.

8.3 Well performance in the presence of a DFN

The relevance of a DFN, relative to reservoir flow, is determined by a solitary consideration: its effect on well performance. We describe and analyze this affect on two aspects of well performance: well pressure response, which is important in determining DFN characteristics through well transient pressure testing, and well productivity. These discussions involve the review of analytical work of other investigators, actual well tests from Ghawar, and original numerical studies.

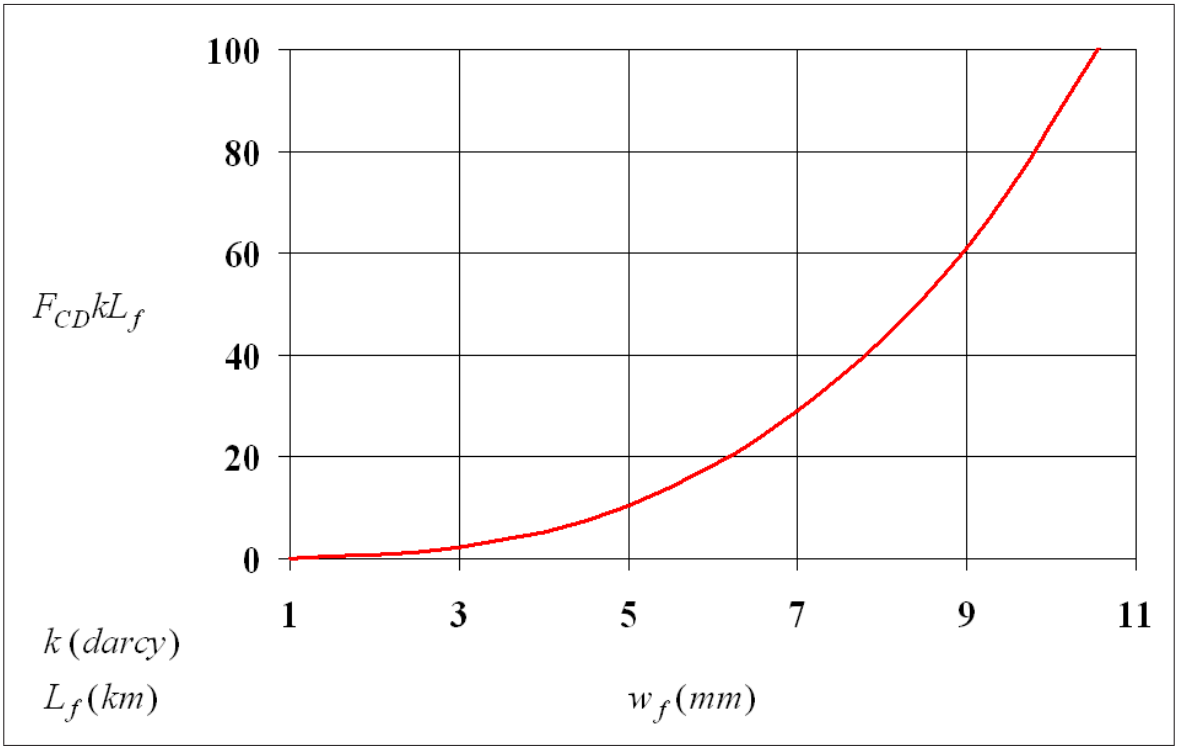

Fig. 8.10: Derivation of dimensionless conductivity in an open mode DFN

8.3.1 DFN pressure analysis

The first analytical study[40] of the well response in the presence of a DFN not intersecting a well, has shown that the productivity of a single well in a reservoir containing an infinite conductivity DFN of finite length, is related to the length of the DFN relative to its distance from the well, and to its orientation relative to the radial flow geometry of the well. Fig. 8.11 presents the main results from the study, the analytical formulation and solution of which are described in the previous section. Note that the effect on well performance is essentially one of well stimulation, represented by a shift of the dimensionless pressure, p_D, solution curves, to the right. The pressure response indicates a negative skin effect, which diminishes with decreasing ratios of L/L_f, and with DFNs oriented transversely at increasing angles, α, with the well radii. A DFN located such that $L/L_f = 0.6$, oriented orthogonally with the radii, for example, has no effect on well productivity, as no significant shift in the p_D curve occurs. A similar null effect is realized from a radially oriented DFN, separated

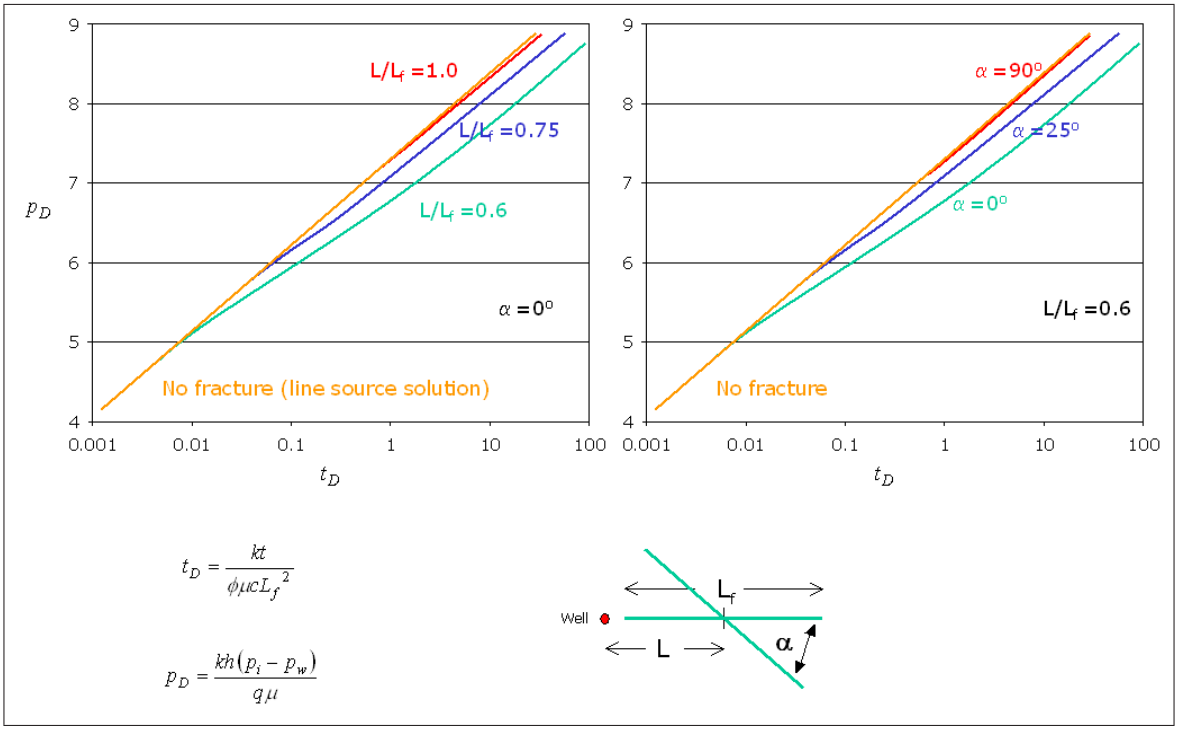

Fig. 8.11: Well pressure solution for a proximal infinite conductivity DFN[40]

from the well, a distance exceeding its length.

The response is similar to that of a dual porosity system, although the difference between the two models are distinct: the dual porosity response is essentially controlled by the small scale fracture system permeability, and the "stimulation" effect is generated by the pore volume of the tight matrix, whereas the DFN model response is controlled by the permeability of the matrix, with the stimulation effect wrought by the DFN.

The stimulation effect is seen to be minor, in the cases cited by the author. The skin factor associated with the case of $L/L_f = 0.6$, and $\alpha = 0$, for example, is -0.65. This stimulation effect increases significantly, however, with decreasing DFN distance from the well. Indeed, hydraulic fractures have generated prolific increases in well productivity, as can be understood with the steady state radial flow equation with apparent wellbore radius derived from an infinite conductivity DFN:

$$\frac{PI_f}{PI} = \frac{\ln(r_e/r_w)}{\ln(2r_e/L_f)}$$

where PI_f and PI are productivity indices with and without a hydraulic fracture, respectively, and r_e is the reservoir radius. The relation above assumes a DFN of length $2L_f$ intersects the well symmetrically, and so overpredicts the productivity increase of the asymmetric intersection of a DFN of length L_f. Nonetheless, a significant productivity increase would be expected relative that of the isolated DFN (Sec. 8.3.3). Fig. 8.12 is a plot of this relation, in which it is seen that significant productivity gains may be realized by DFNs of modest length, connected to the well. The productivity gain is reflected also in the skin effect, which may also be large:

$$s = -\ln(\frac{L_f}{2r_w})$$

with skin factors approaching -7 measured regularly in practice.

The results of the analytical model presented here for well response in the presence of a finite length, infinite conductivity DFN, preceded the development and widespread use of the pressure derivative, and diagnostic identification of bilinear and linear flow regimes associated with fractured wells. Therefore, no identification of these regimes associated with DFN flow was presented (the model used by the author did not account for flow within the DFN, regardless, so that bilinear flow could not have been identified).

The orthogonally placed DFN is investigated further in a more recent study[41], in which the well pressure response, and DFN flux distribution, was analytically derived for a finite conductivity DFN of infinite length. Fig. 8.13 summarizes the results of the study. The diagram at right presents the problem modeled: a well located in an infinite reservoir, containing an infinitely long DFN which separates the reservoir into two half-spaces, one of which contains the well. The model consists of three parts: the right-side reservoir, from which the flux into the DFN is represented as q_{fR}; the left-side reservoir in which the corresponding flux exiting from the DFN is q_{fL}; and the DFN, within which flow is divergence free, owing to the small volume, and linear, along the long axis of the DFN. The governing model in both reservoirs is

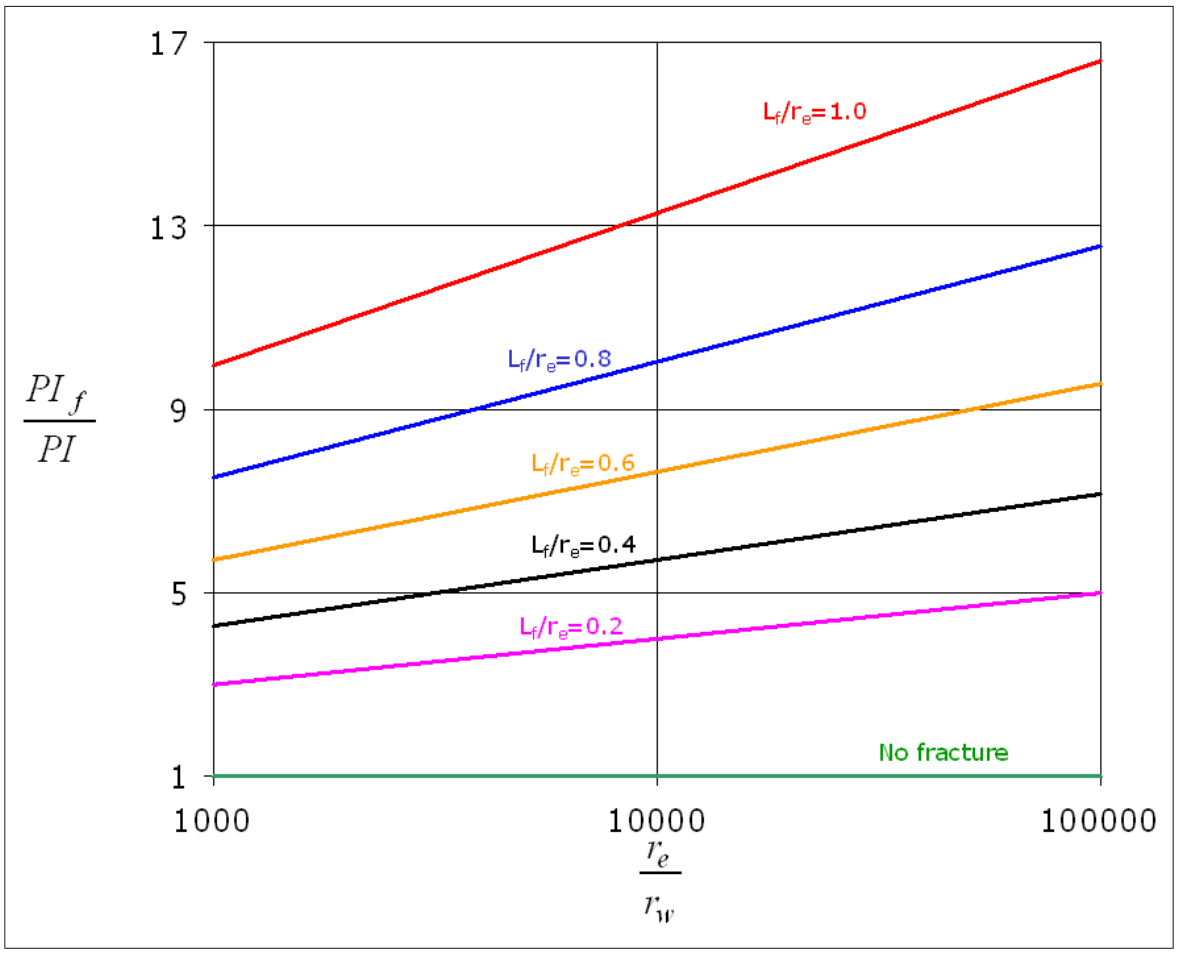

Fig. 8.12: Well productivity gain from infinite conductivity DFN

the diffusivity equation, but with source terms at the DFN, and Poisson's equation in the DFN. The governing equations are coupled and solved discretely using Green's and source functions[69].

The lower figure is the computed dimensionless well pressure and derivative response for constant rate production, for various values of F_{CD}. The dimensionless variables are defined in the usual way, except for t_{Df} :

$$p_{wD} = \frac{2\pi kh}{q_w \mu}(p_i - p_w)$$

$$t_{Df} = \frac{kt}{\phi \mu c d_f^2}$$

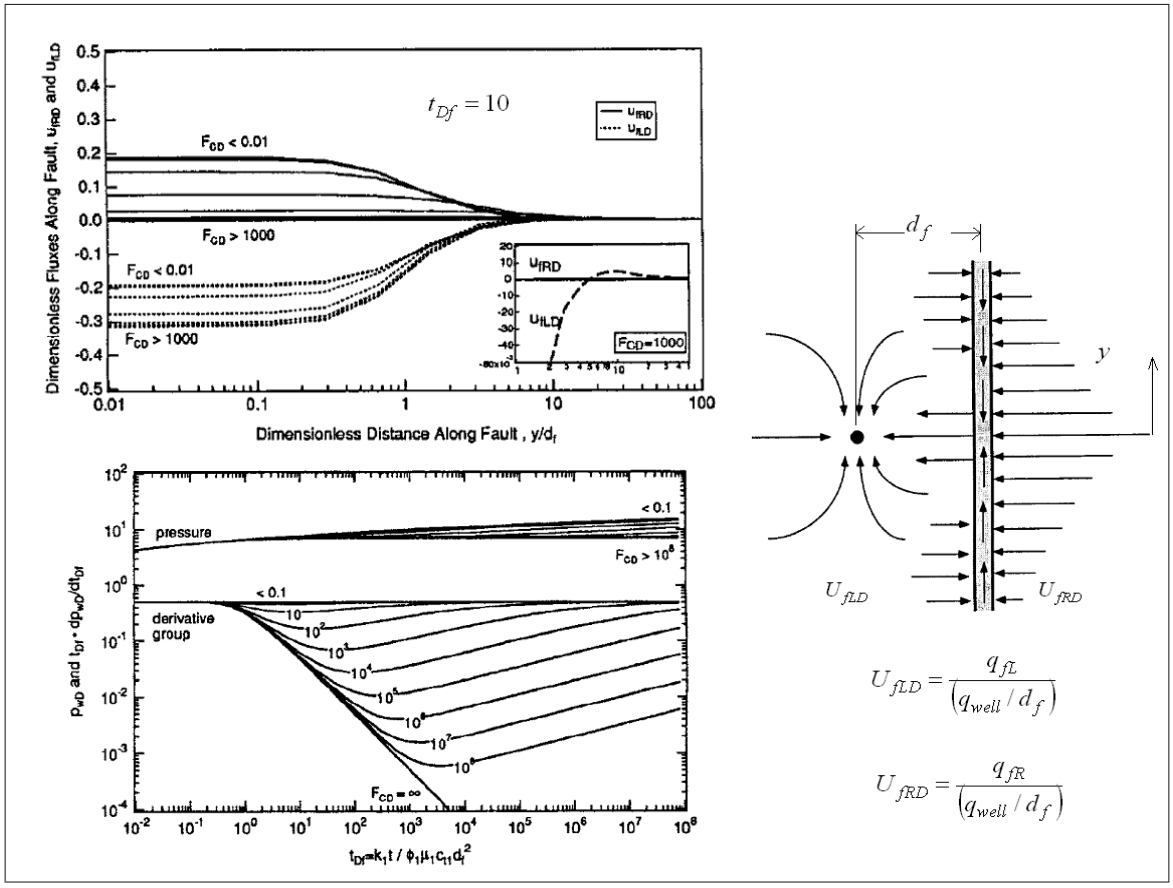

Fig. 8.13: Flux and pressure behavior of a finite conductivity DFN of infinite length[41]

where k is the permeability of both reservoir half-spaces.

Note first, most evident in the cases of moderate to low values of F_{CD}, two radial flow responses, separated by a dip in the derivative, equivalent to the response indicated in Fig. 8.11. The transition, or dip, in the derivative response follows a negative unit slope, especially for the cases of high F_{CD}, and in the limit, an infinite conductivity DFN generates a constant pressure boundary response.

A maximum productivity index increase of less than a factor three, corresponding to the infinite conductivity case, is indicated by the spread of the pressure responses at late time.

Note also the quarter-slope of the derivative curve, most evident in cases having high values of F_{CD}. The quarter slope is not, however, present on the pressure

response, so that the interpretation of bilinear flow, attributed to the quarter-slope in hydraulic fracture well response, is an open question. No half-slope, linear flow regime is indicated in either the derivative or the pressure prediction.

The upper diagram is the computed flux distribution along the DFN, at an early time, $t_{Df} = 10$. DFNs having low dimensionless conductivity essentially do not influence well response, as the flux from the right side is balanced by the flux exiting to the left side and to the well. This case is induced, for example when $k_f \simeq k$, that is, no DFN. A low dimensionless conductivity does not represent a barrier, as the model does not address flow transverse to the DFN.

Cases of increased dimensionless conductivity generate increasing DFN flow, at the expense of decreasing flux from the right side reservoir, such that, in the limit of infinite conductivity, the flux from the right side reservoir approaches zero. Effectively, therefore, the DFN acts as a barrier, as the right side reservoir does not contribute to the well production, and only the left side reservoir is drained. Note in the inset plot, that a slight positive flux is indicated from the left side reservoir into the DFN, at this early time. The flux distribution at late times would undoubtedly indicate higher positive flux magnitudes from the left side reservoir, with a high proportion of the flow entering the DFN, away from the well, flowing in the DFN toward the well, and exiting the DFN at the region nearest the well.

8.3.2 Well performance field tests

The application of well pressure testing to detect the presence and effect of DFNs at Ghawar began relatively recently (1998), and therefore few reports exist in the literature. These reports are reviewed in this section.

The earliest reference to a DFN response on well test is in the study[46] described in Sec. 5.2.2, in which a well test model predicted an inter-layer barrier of limited extent, and a very high permeability region, hypothesized to be one or more DFNs, at a distance from the well, and which effectively nulled the barrier in that proximity (Fig. 5.5) A build-up test was subsequently conducted on the well, the pressure measurements of which are presented in Fig. 8.14. Despite the anomalous, severe

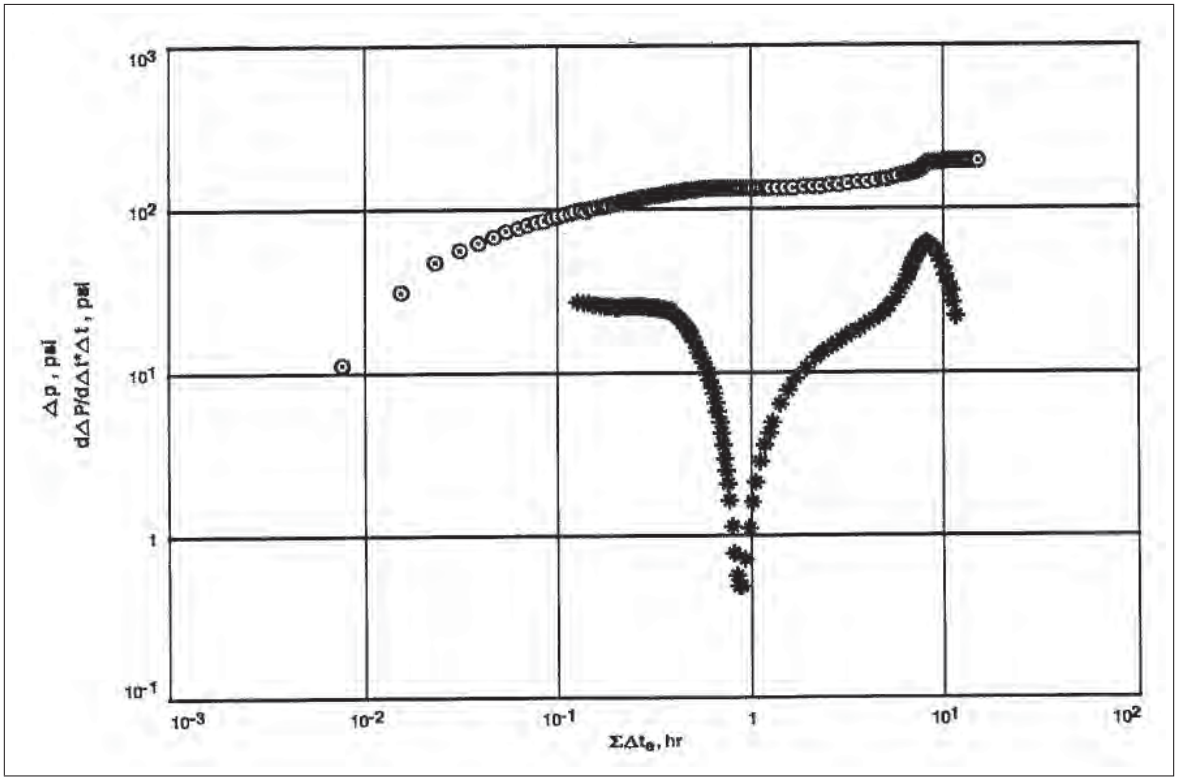

Fig. 8.14: Pressure and derivative response in Uthmaniyah well[46]

dip, and severe peak, in the derivative curve, it appears as if two radial flow periods are indicated, one before the severe dip, and one before the severe peak. The final drop-off is expected derivative response in a build-up test. The authors interpreted the response as due to that of a finite conductivity DFN, although they presented no specific history matching results.

A build-up test conducted in a north Haradh well indicates a possible intersection with an infinite conductivity DFN[4]. The test measurements are presented in Fig. 8.15. The axes are conventional dimensionless pressure and derivative on the ordinate, and dimensionless time on the abscissa; they are omitted because the magnitudes of the curve values are irrelevant to our discussion - only the curve shapes are important. Note that bilinear flow (quarter slope) is predicted. No other data, such as flowmeter, image log, or lost circulation during drilling, was reported in the reference. Also, the well angle was not reported.

Pressure tests reported from some Shedgum wells show evidence of both DFN

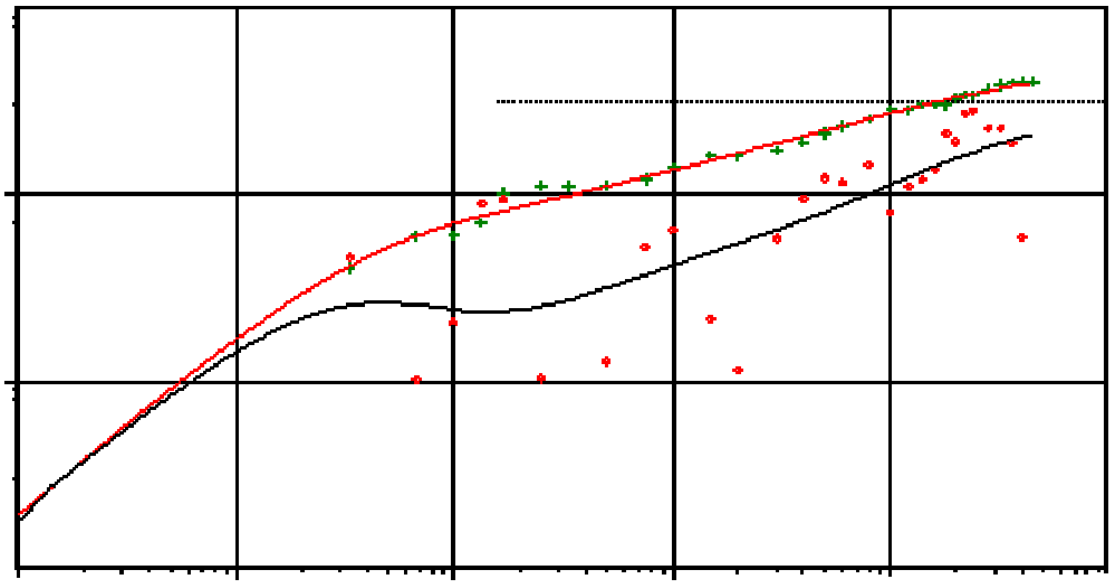

Fig. 8.15: Pressure and derivative response in northern Haradh well[4]

intersections with wells, and remote DFNs[56]. Fig. 8.16 presents build-up pressure measurements in three Shedgum vertical wells. Flowmeter profiles indicate very high flux in the intervals tested here, and caliper logs indicate large washouts in these intervals. The test pressure and derivative responses indicate bilinear (quarter-slope) flow, and each case was adequately modeled with a finite conductivity DFN intersecting the well.

Fig. 8.17 presents pressure measurements and derivatives for build-up tests in two wells. The data in the upper plot was taken from the well represented in the lower plot in Fig. 8.16, after the indicated intersecting DFN had been isolated from the well by casing, upon workover. The data in the upper plot possibly indicates the DFN continues to affect well performance, although it is no longer connected directly to the well.

The lower left plot of build-up data was taken from a well in which a hypothesized DFN, located remotely from the well, affects the well's performance. Note the extended radial flow period, contrasting that expected from the model presented in Fig. 8.13, lower left, occurring prior to the characteristic dip in the derivative.

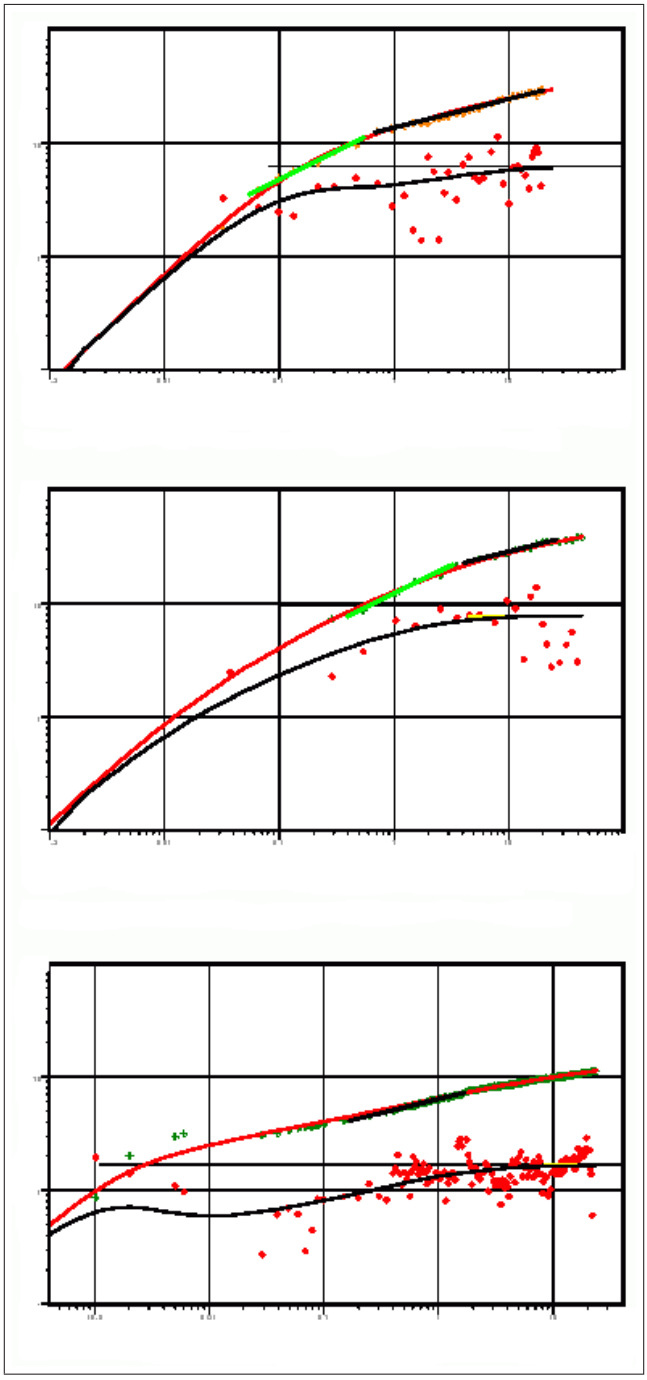

Fig. 8.16: Pressure and derivative response in Shedgum wells[56]

The derivative curves of a model[41] which may history match this well response is presented on the lower right, Fig. 8.17. The model includes a damage skin effect,

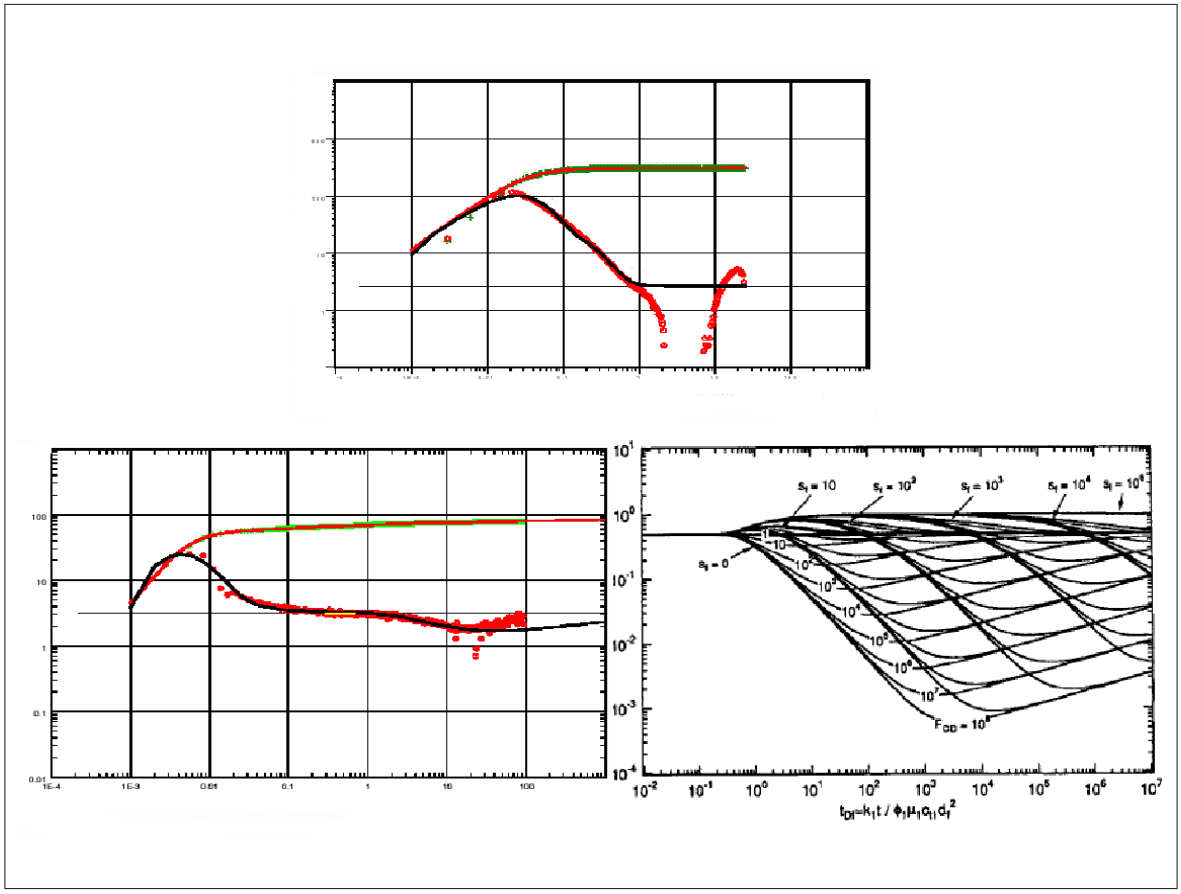

Fig. 8.17: Pressure and derivative response in Shedgum wells;[56] DFN with skin;[41]

associated with the DFN. The skin effect is modeled by thin, altered permeability zones adjoining the two DFN boundaries. Note, particularly for those cases of large skin effect, the doubling of the derivative, characteristic of the well response in the presence of a linear boundary. The higher the skin effect, the more extended the radial flow period having the doubled derivative, before the dip in the derivative, indicating a stimulated well response, as described in the previous section (Fig. 8.11, Fig. 8.13). The data from the well does not indicate a doubled derivative, although storage may have masked the initial radial flow period, existing prior to the doubling of the derivative, that is, the radial flow response prior to the linear barrier response.

The final examples[71] consist of build-up tests in three wells, locations unknown, in which the pressure and derivative response were interpreted exclusive of DFN

models. Fig. 8.18 presents the data from these wells. The upper plot was modeled with a 20 ft thick, radial composite model, consisting of an inner, 2000 ft radius reservoir of permeability 77 *darcies*, and an outer reservoir which has a permeability that is reduced by a factor six, relative to that of the inner reservoir. Flowmeter data confirmed that 80% of the well's rate of 15100 B/D (with only 21 psi drawdown) exited from the 20 ft interval, located at the top of Zone 2A.

The data presented in the lower right plot, from a second well, was modeled with a 13-layer model, also radial composite with an inner, 2000 ft radius reservoir. A 2 ft layer within the inner reservoir model was given a permeability of 70 *darcies*. Both lost core and complete loss of circulation while drilling, occurred at the 2 ft interval, located, as in the first well, at the top of Zone 2A. The red and black curves coincident with the pressure and derivative data are the model predictions.

The data presented in the lower left plot was taken from a well which produced a test rate of 12400 B/D, with just 94 psi drawdown, in which a 20 ft interval, located at the bottom of Zone 2B, dominated production. The model used to history match this response consisted of a 20 ft thick radial reservoir of permeability 6 *darcies*.

The models used to match well response in these three cases may be considered unusual considering the magnitudes of permeabilities required in the dominant, thin, intervals in the wells. Given core measured permeabilities do not exceed a few *darcies* in the Arab-D, it may be feasible instead to model the response in these wells using DFN models. Indeed, a quarter-slope derivative response is present in two of these tests, upper, and lower right, both of which required $\sim$ 70 *darcy* magnitude permeabilities to match performance , with non-DFN models. Note also the negative unit derivative slope in the lower right plot, which is indicated in the predicted response of the analytical model presented in Fig. 8.13. Although the data in these two wells do not readily match the response predicted by the analytical models shown in Fig. 8.13 and Fig. 8.17, the quarter-slope, bilinear flow response, as well as the derivative negative unit slope evident in the data, invites a history matching attempt with a DFN model. The attempt was not made in this thesis work.

Well response indicating the presence of DFNs was also documented in four

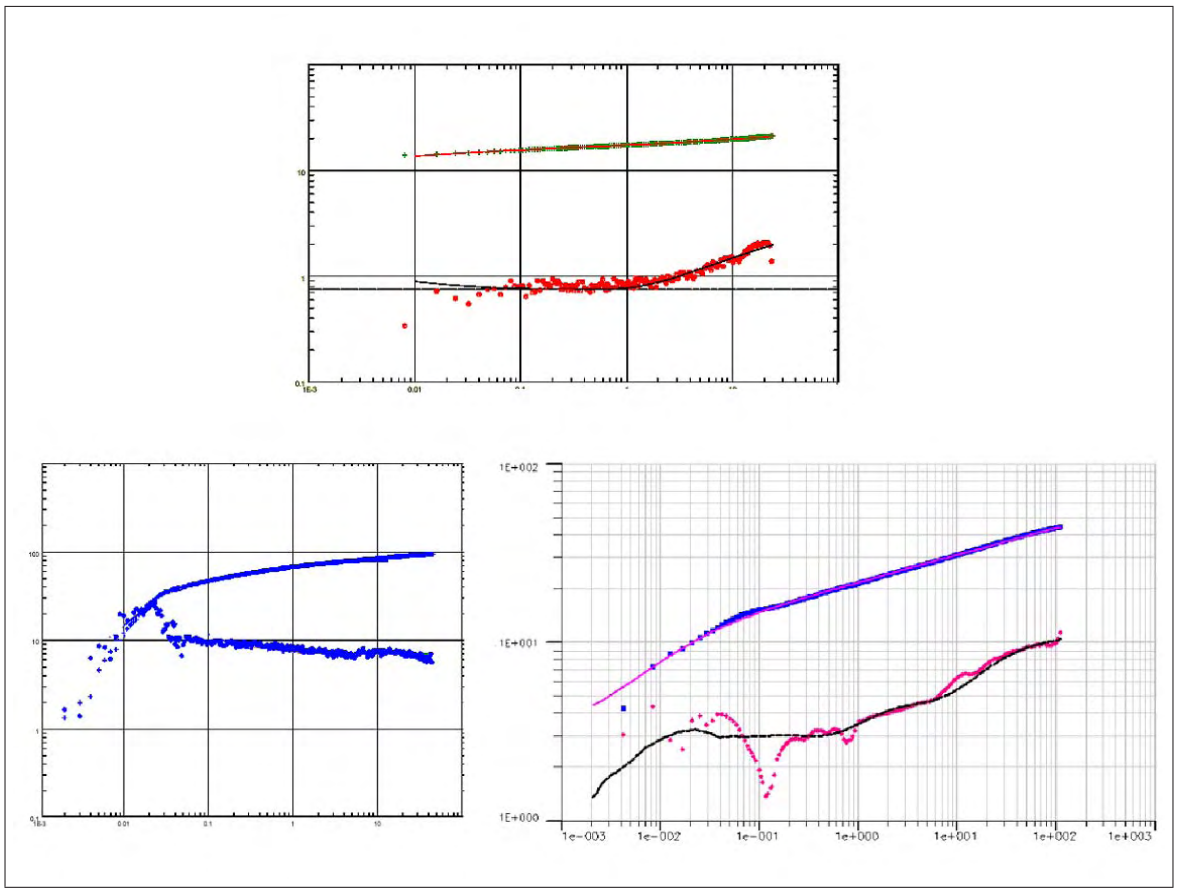

Fig. 8.18: Pressure and derivative response in three wells[71]

wells[6], locations not reported, in which intersecting, as well as remote, DFNs were predicted.

Fig. 8.19 is a deviated well pressure and derivative build-up response indicating quarter slope, bilinear flow, characteristic of a DFN intersecting the well. A flowmeter survey conducted in the well indicated 96% of the total well flow exited from an 8 ft interval, which coincided with a fracture zone measured with a borehole image log. The black and red curves result from an infinite conductivity DFN model prediction. The Arab-D zone in which the DFN was measured was not reported, although well logs indicate the DFN occurs in a zone of low porosity.

Fig. 8.20 presents pressure and derivative build-up response in three wells for which both intersecting and remote DFNs were predicted. The data presented in the

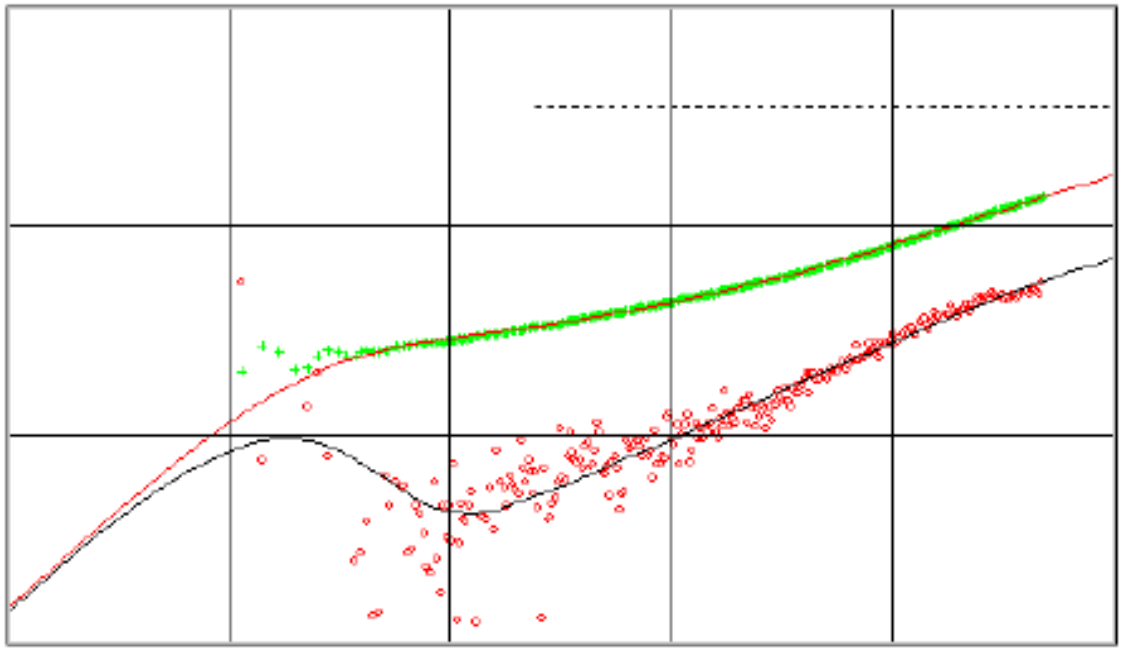

Fig. 8.19: Pressure and derivative response in a well intersecting a DFN[6]

lower right plot was measured in a deviated well. The labels on the plot indicate the radial, transition, and bilinear flow regimes predicted by the remote DFN analytical model (Fig. 8.13). 3D seismic data supports this model, as the region is indicated to be heavily faulted.

The upper plot of data is matched with a combination intersecting DFN and remote DFN. The intersecting DFN is predicted for the early, quarter-slope, bilinear flow data (labeled "fracture behavior"). Later, a transition through negative unit derivative slope, followed by another bilinear flow period is evident (labeled "conductive fault behavior"). Both regimes are predicted with finite conductivity DFNs, one intersecting the well, inducing the early response, and another remotely placed from the well, causing the later response. This well experienced premature water breakthrough, and flowmeter data indicates 80% of the total well flow is derived from the fracture zone. Major faults near the well are predicted by 3D seismic data.

The plot of data in the lower left was also modeled with a combination intersecting and remote DFN. Two derivative quarter-slope, bilinear flow periods are evident,

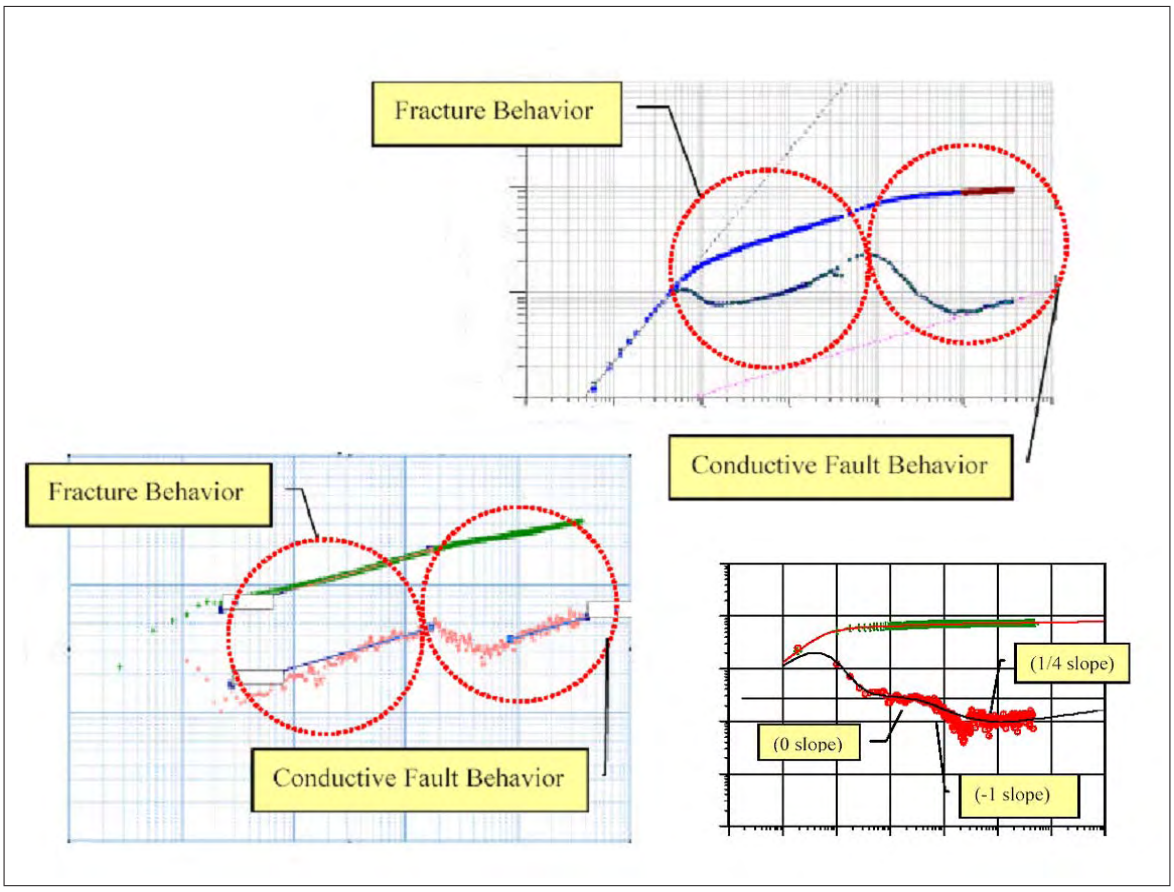

Fig. 8.20: Pressure and derivative response in intersecting and remote DFNs[6]

separated by a negative unit slope transition period. Oddly, this well was vertical. The well produced 18700 B/D on test, the majority of which exited from a 3 ft interval at the top of Zone 2A. The authors chose to model this well's response numerically, using a thin, high permeability layer, connected to a vertical DFN. The authors referred to the high permeability layer as representing a *horizontal* DFN. The thin layer permeability required to match the data was 43 *darcies*. The abnormally high permeability given to the thin layer is certainly suggestive of DFN magnitude conductivity; however, this model is the only one published in which a horizontal DFN was acknowledged as a viable model. As with the other three wells analyzed in this study, 3D seismic data predicted heavy faulting in the well region.

The existence of horizontal DFNs in the Arab-D has otherwise not been confirmed,

although a recent outcrop study describes horizontal DFN formation from the shearing of stylolites.[38].

The recent advent of horizontal well drilling at Ghawar has permitted more frequent sampling of DFN data, due to the greater occurrence of intersections between wells and DFNs. Fig. 8.21 presents horizontal well pressure and derivative data from two production wells, and a water injection well, indicating both intersections of DFNs, and the existence of remote DFNs[72].

The authors attribute the build-up response of the upper left plot to a DFN intersection with the well, a model of which matches the data very well, as shown. They note both a half-slope, linear flow response, and later, a quarter-slope, bilinear response. The authors, do not explain the occurrence of the half-slope response in the derivative, with no accompanying half-slope response in the pressure data, however. Bilinear flow is indicated, though, in both the derivative and the pressure data, supporting their interpretation.

A clear quarter-slope region is indicated in the derivative data of the upper right plot, representing data from a fall-off test in a horizontal injection well. Relative to the analytical model presented in Fig. 8.13, it appears a DFN, not intersecting the well, may be influencing well response. The authors, however, successfully match the data with a non-DFN model, the primary attribute of which is a varying permeability distribution. The permeability increases from the well location, near the aquifer, toward the crest.

The final well response example is interesting indeed, presented in the lower plot. The data was obtained from a build up test in a horizontal lateral, extended from a well that confirmed a full column of oil in the Arab-D. The lateral was drilled at the top of the Arab-D. The lateral length was initially designed at 1500 ft, but the well lost complete circulation at 890 ft and was terminated there. The well experienced water breakthrough upon first production, despite the full oil column in the region. Furthermore, late build-up pressures *declined* with time.

This seemingly complex set of conditions was modeled by the authors with a correspondingly complex model, consisting of a remote DFN, placed parallel to the lateral, and an injection well placed opposite the DFN. The history match was very

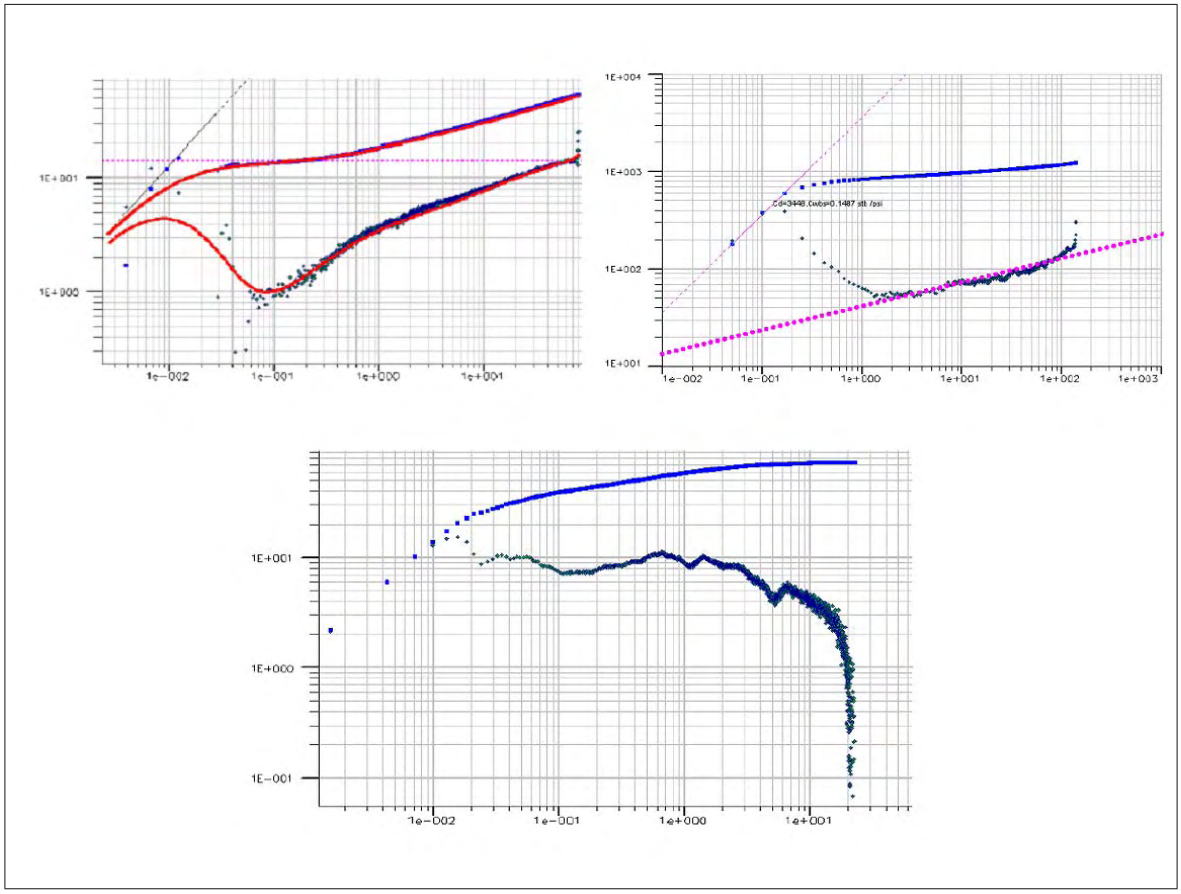

Fig. 8.21: Response in horizontal wells intersecting, and near DFNs[72]

good. The quality of the late pressure decline match was not reported, however, and is not shown in the plot. The authors also did not verify the existence of the injection well.

The water breakthrough upon first production is suggestive of the presence of a highly conductive DFN, and in fact, a derivative quarter-slope, bilinear flow period is indicated in the data, following the shallow dip, as shown. A plausible model may consist of a remote DFN that is hydraulically connected to remote injection well. The late pressure decline, however, is difficult to model, although implies well interference, possible exacerbated by the high conductivity of the DFN. The late, steep derivative decline is not attributable to the anomalous pressure decline, but is a typical late build-up response.

8.3.3 Numerical studies of the effect of DFN flow

We have quantified the flow and pressure behavior of DFNs, through synthetic numerical flow models, for some elementary steady state cases, designed to gain a fundamental and rigorous understanding of both the effect of DFNs on the flow performance of a single reservoir layer, and the ability of the source model to predict this effect. The results of this numerical study may be summarized as follows:

- Layer performance is affected by DFN flow according to the location of the DFN and its geometry, the geometry of the reservoir, and the dimensionless conductivity, F_{CD}, of the DFN;
- The source model accurately predicts steady state DFN flow and its effect on well performance;
- The source strength, or connection transmissibility, of a DFN, is a simple, linear function (heuristically derived) of F_{CD}, in modeling steady state flow;
- The representation of a DFN with only endpoint sources provides a reasonable approximation to the behavior predicted by a finely discretized DFN model.

8.3.4 Model description

Given the specific application for which this thesis was prepared, our flow models are designed to inform the steady state reservoir mechanics for water injection / oil production well pairs, under a line drive pattern, the predominant condition for which super-k is effective at Ghawar.

The objective of the modeling is to discern the pertinent flow parameters under these conditions, in a reservoir that contains a DFN. The models predict the effect of geometry, both of the DFN, and of the line-drive pattern, and of the dimensionless conductivity of the DFN, which we assume, as has become accepted, characterizes completely the flux and pressure distribution within the DFN. We affirm this particular finding in this numerical study.

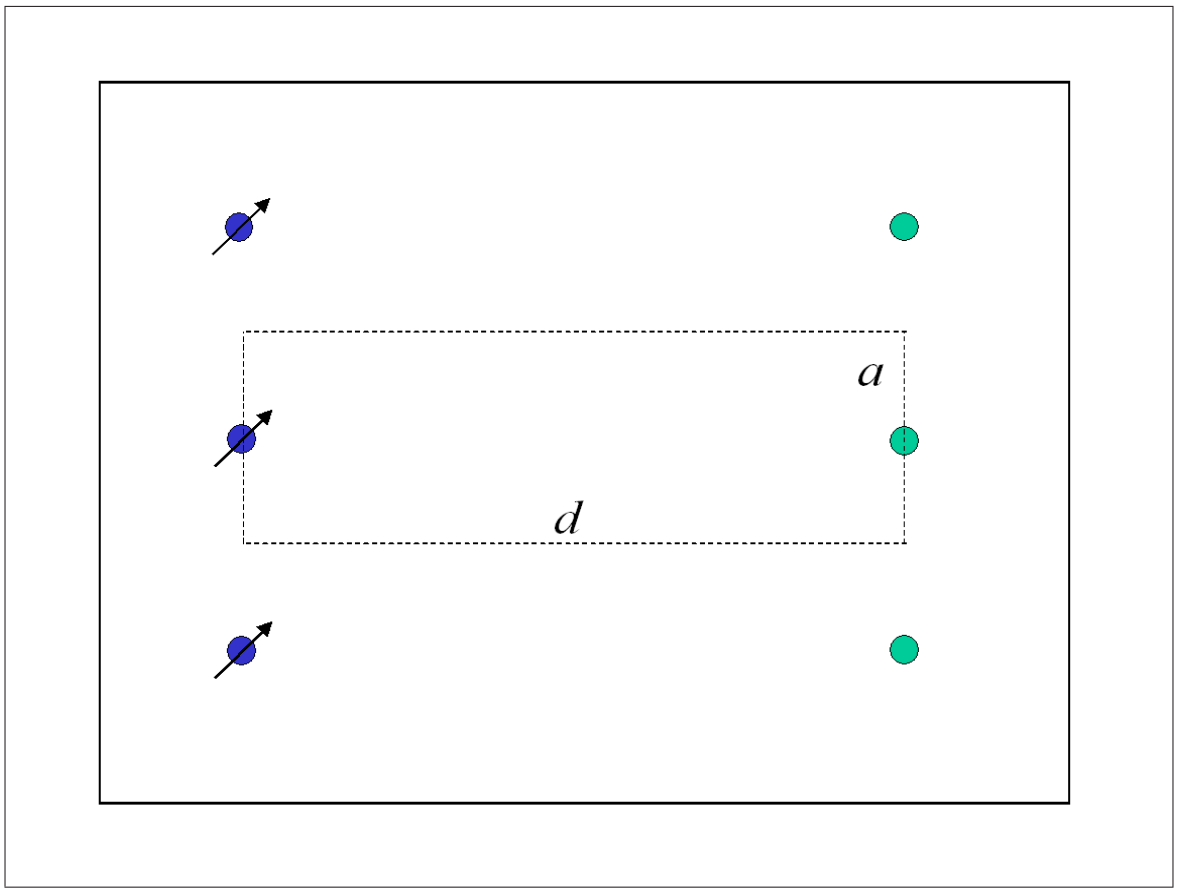

Fig. 8.22: Line drive pattern geometry

A key characteristic of the Ghawar peripheral waterflood is the prevalence of long and thin line drive patterns. The pattern geometry, which is approximated as a rectangle, as shown in Fig. 8.22, may be characterized simply as the ratio of pattern rectangle length to width, d/a, as shown. This ratio generally has the range $2 < d/a < 10$ at Ghawar, with high values of the ratio predominant. The ratio in our study area is 3 to 4, as seen in Fig. 3.2, although it is generally higher in the remainder of the field as described in Sec. 5.1.2, and in Sec. 5.4.2.

The flow models are 2D rectangular and horizontal, and contain an injection / production well pair, both operating under constant well pressure boundary conditions, located at the ends of the rectangle. The model permeability is isotropic and homogeneous; the porosity is also homogeneous. Fig. 8.23 is a schematic of the

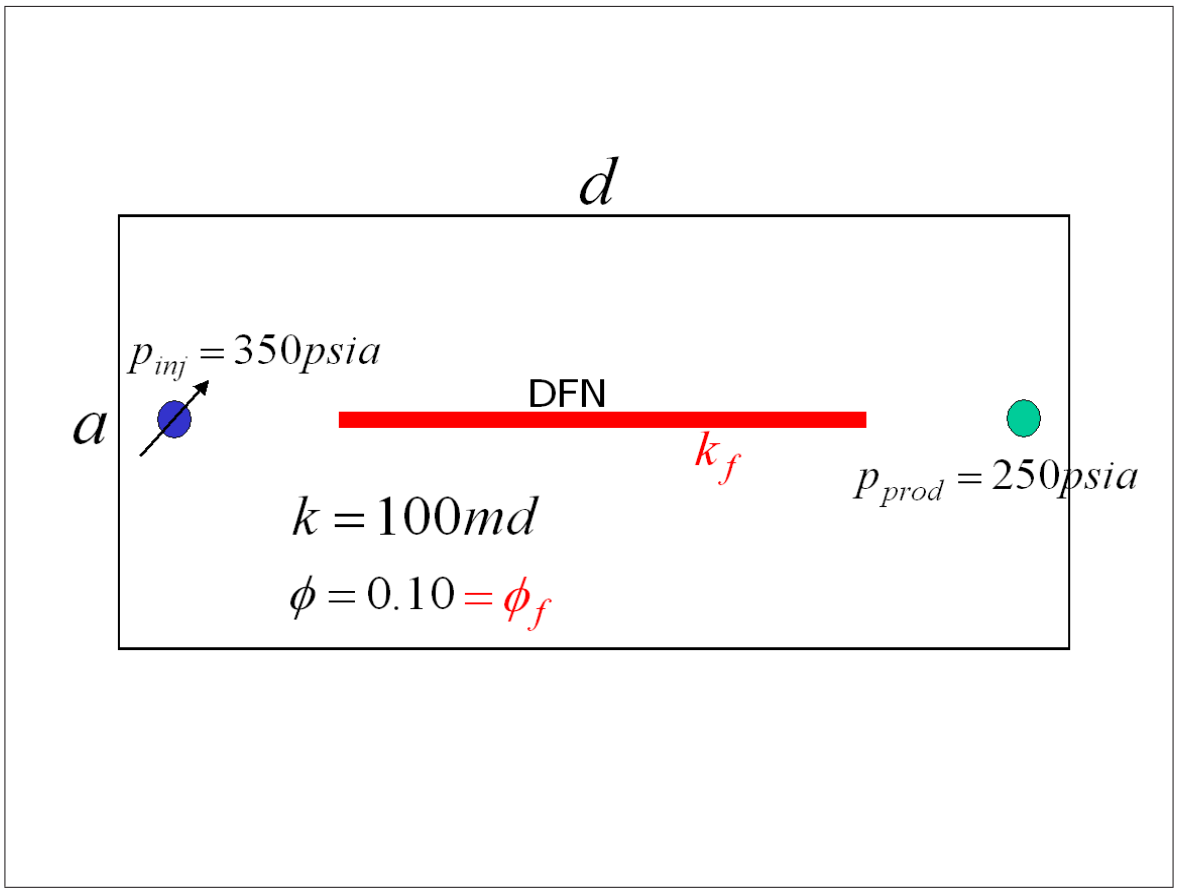

Fig. 8.23: General synthetic model description

model, and presents the model parameters.

The models contain a single DFN, located between the wells, and lying entirely on the straight line between them, as shown in Fig. 8.23. The permeability of the DFN is k_f.

Two versions of the numerical model were constructed: one in which the DFN is represented as a reservoir discretization, the other in which it is represented as a set of sources. Fig. 8.24 presents the differences in the construction of the two models. The areas outlined in green comprise regions in which the two models differ; otherwise, the models are identical.

The discretized DFN version, top, contains a set of blocks adjacent to the DFN which are thinner in the y direction by a factor of 2, relative to the remaining grid, to

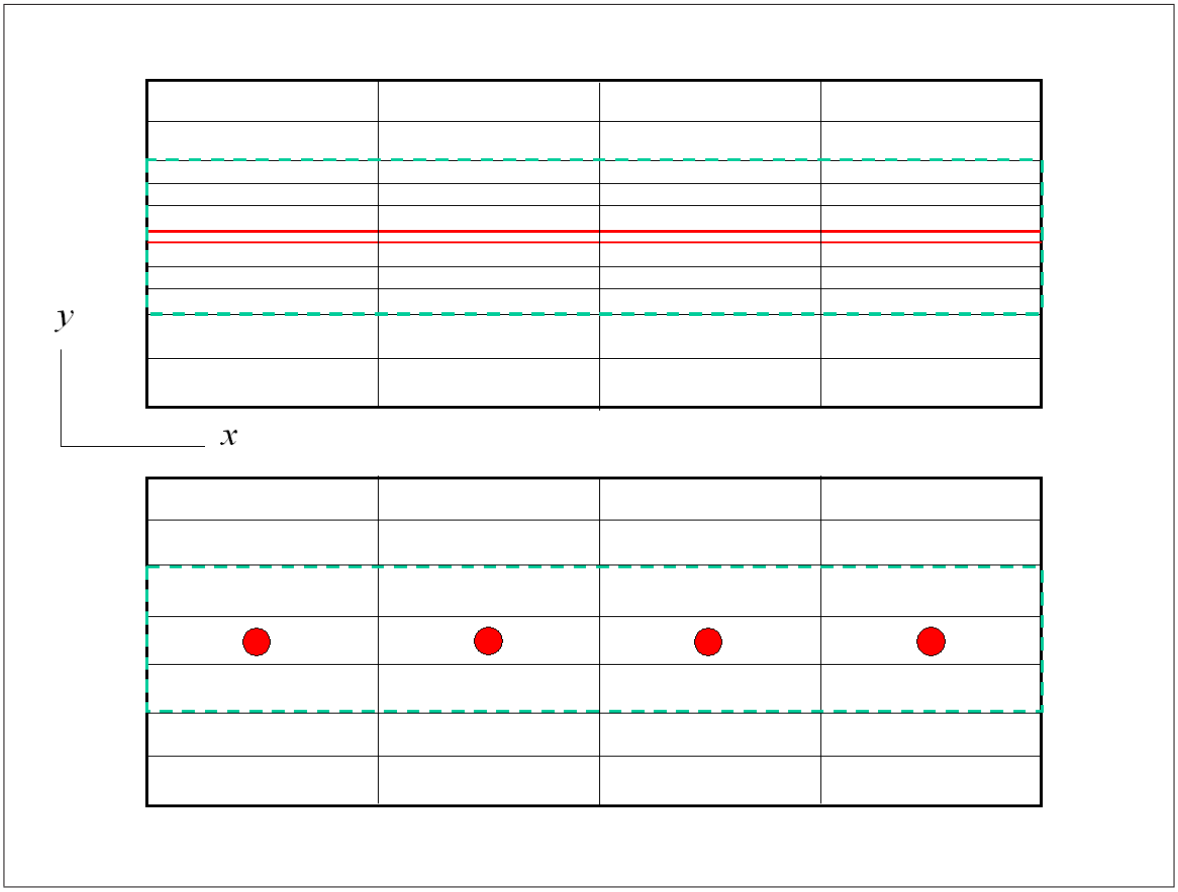

Fig. 8.24: DFN models: discretized, top, sources, bottom

alleviate potential convergence difficulties. The DFN, outlined in red, is represented as a set of blocks which are thinner in the y direction by a factor of 10. Neither the adjacent blocks nor the DFN blocks are finer in the x direction: the grid is modified only in the y direction.

The dimensions of this grid is 101×105, with the larger y dimension accommodating the thinner blocks and the DFN blocks.

The source DFN version, bottom, has a dimension 101×101, with a uniform grid block geometry. The geometry is identical to that of the first version, top, in the region outside of the green area. The DFN is represented as set of sources, shown as red dots.

The DFN grid blocks in the upper diagram represent additional pore volume

not contained in the source model; this additional volume, approximately 0.1%, is insignificant, since the problems we are investigating in this study are steady state.

The wells are located at the extreme ends of the models. The injection well is placed at $x = 1$, and the production well at $x = 101$. Both wells are located on the horizontal center line of the models, which is also colinear with the DFN.

Several models were constructed, with the following parameters made variable:

- the ratio d/a,
- DFN location,
- DFN length,
- DFN F_{CD},
- the number of sources representing the DFN.

8.3.5 Performance of the source model

An important characteristic of the waterflood is the prevalence of hydraulically fractured water injection wells, as described in Sec. 5.1.2. If an injection well hydraulic fracture intersects with reservoir DFNs, a single, highly conductive hydraulic unit may form which connects directly to the injection well. We therefore investigated two general types of DFNs: those which connect directly to the water injection well, and those which do not. We refer to these DFN types as "connected," and "isolated," respectively.

The source strengths, or connection transmissibilities, are, as described in Chapter 7, the principal components of the source model, along with the source locations. As we are using these sources to model DFN flow, it is desirable to calibrate source connection transmissibilities to one or more parameters which characterize the behavior of the DFN. We found a heuristic, although very successful calibration, based on an analytical approach.

The discrete transmissibility, T_{DFN}, for flow into a vertical, planar DFN, from a simulation grid block, may be expressed as,

$$T_{DFN} = \eta k DZ,$$

where k is the block permeability, DZ is the vertical block dimensions, and η is a scalar, presumably a function of DFN characteristics, and of the water injection pattern geometry. The conversion of this expression for DFN transmissibility into a source connection transmissibility is detailed in Sec. 7.1.3, with the result,

$$WPIMULT = \frac{\eta}{2\pi},$$

where $WPIMULT_V$ is a multiplier used in the *ECLIPSE* simulator input file to describe a source connection transmissibility.

This study concludes that the following heuristic relations for η apply:

$$\eta = \begin{cases} \pi F_{CD}, \ connected \\ \frac{\pi}{10} F_{CD}, \ isolated \end{cases}$$

These were found by trial and error. The result is in agreement with established findings from the analysis of hydraulic fractures, however, in that F_{CD} dictates the flow performance of the DFN of a given length.

Furthermore, it was found that $F_{CD} = 100$ is the practical limit for a DFN, as $F_{CD} > 100$ does not effectively change the flow behavior of the DFN. The DFN effectively achieves infinite conductivity at this value. So, a maximum value, $\eta_{\max}$, is established,

$$\eta_{\max} = \begin{cases} 100\pi, \ connected \\ 10\pi, \ isolated \end{cases}$$

The value $\eta_{\max}$ is particularly significant, as infinite conductivity DFNs have the maximum effect on well performance, and must therefore be considered appropriately applicable in reservoirs for which production performance has been deemed as significantly affected by DFNs. Indeed, it is not an unreasonable paradigm that employs $\eta_{\max}$ exclusively in the modeling of DFNs, as the mere incorporation of DFNs into the reservoir model implies they are conductive enough to affect well performance.

Some insight into the heuristic relation for η can be obtained by examining the relation for source transmissibility, T_w, generally employed in conventional flow simulators:

$$T_w = WPIMULT \left[2\pi \frac{kh}{\ln(r_o/r_w)} \right]$$

where the terms were previously defined in Sec. 7.1.3, and a zero skin effect is assumed. Calibrating the DFN transmissibility amounts to equating T_{DFN} and T_w.Thus, the appearance of π in the heuristic relation is explained. Further, substituting η (the connected DFN expression, for example) into the expression for T_{DFN},

$$\begin{aligned} T_{DFN} &= \pi F_{CD} k DZ \\ &= \pi \frac{k_f w_f}{k L_f} k DZ, \end{aligned}$$

it is seen that the T_{DFN} is dependent on DFN permeability and geometry, and the vertical dimension of the simulation grid block in which the connection is placed. The analogy with the relation for T_w, for the flow capacity terms, kh and kDZ, and the well (DFN) geometry terms, $k_f w_f / kL_f$, and $1/\ln(r_o/r_w)$, is evident.

An explanation for the factor 1/10 associated with η for isolated DFNs is not evident. It is noted that he factor is equivalent to imposing a damage skin on the DFN. Also, the flow geometry for the connected DFN may be different than that for the isolated DFN, for the endpoint nearest the well. Since T_{DFN} must completely account for the effects of flow geometry in the source model, perhaps the factor 1/10 indicates a less efficient flow geometry at the entry point of an isolated DFN, relative to that of a connected DFN.

Application to the modeling of hydraulic fractures

We will show in the following section that the source model adequately predicts the well stimulation effect of a DFN that directly intersects an injection well. These results imply that the source model may be used to predict the well stimulation effect of a hydraulically fractured well, using the relation for η given in the previous

section, at least under steady state flow conditions. Transient flow response was not investigated, as it is not relevant for our purposes in this thesis.

Conventionally, the well stimulation effect of a hydraulic fracture is modeled with a large negative skin applied to the well connection transmissibility, although this procedure is problematic in modeling long, infinite conductivity fractures which induce very large negative skin effects, in which the effective wellbore radius exceeds the Peaceman radius.[34] An alternative procedure is to discretize the fracture. We believe the source model is also a viable alternative, with the advantages of ease of application in any conventional flow simulator, and the avoidance of discretization.

Source model results: connected DFN

Verification of the conclusions given in the previous sections are presented here. The most important result is that which presents both, the effect of a connected DFN on well performance, and the ability of the source model to predict the effect. These results are shown in Fig. 8.25 and Fig. 8.26. Here the productivity gain, PI/PI_0, of the well productivity, PI, in the presence of the DFN, relative to the well productivity, PI_0, with no DFN, is plotted against the ratio L_{DFN}/L_0 where L_{DFN} is the length of the DFN, and L_0 is the distance between wells. The DFN intersects the injection well, and extends from the injection well toward the producing well, without intersecting the producing well. Fig. 8.25 are results for $d/a = 2$, and Fig. 8.26 are results for $d/a = 10$, essentially the two extremes of line drive pattern geometry in the field.

Several cases for each pattern geometry are presented, corresponding to various values of F_{CD}. Each F_{CD} case is represented with results from both, the model in which the DFN is discretized (solid curves), and that in which the DFN is represented by sources (dashed curves).

The source model is applied such that a DFN source is placed in *all* grid blocks intersected by the DFN.

Note that the agreement between these two models, for each F_{CD}, and for each pattern geometry, is very good, verifying the source model, and more specifically, both the relation for η and for T_{DFN}.

Note also that the productivity gain may be substantial in both of these pattern

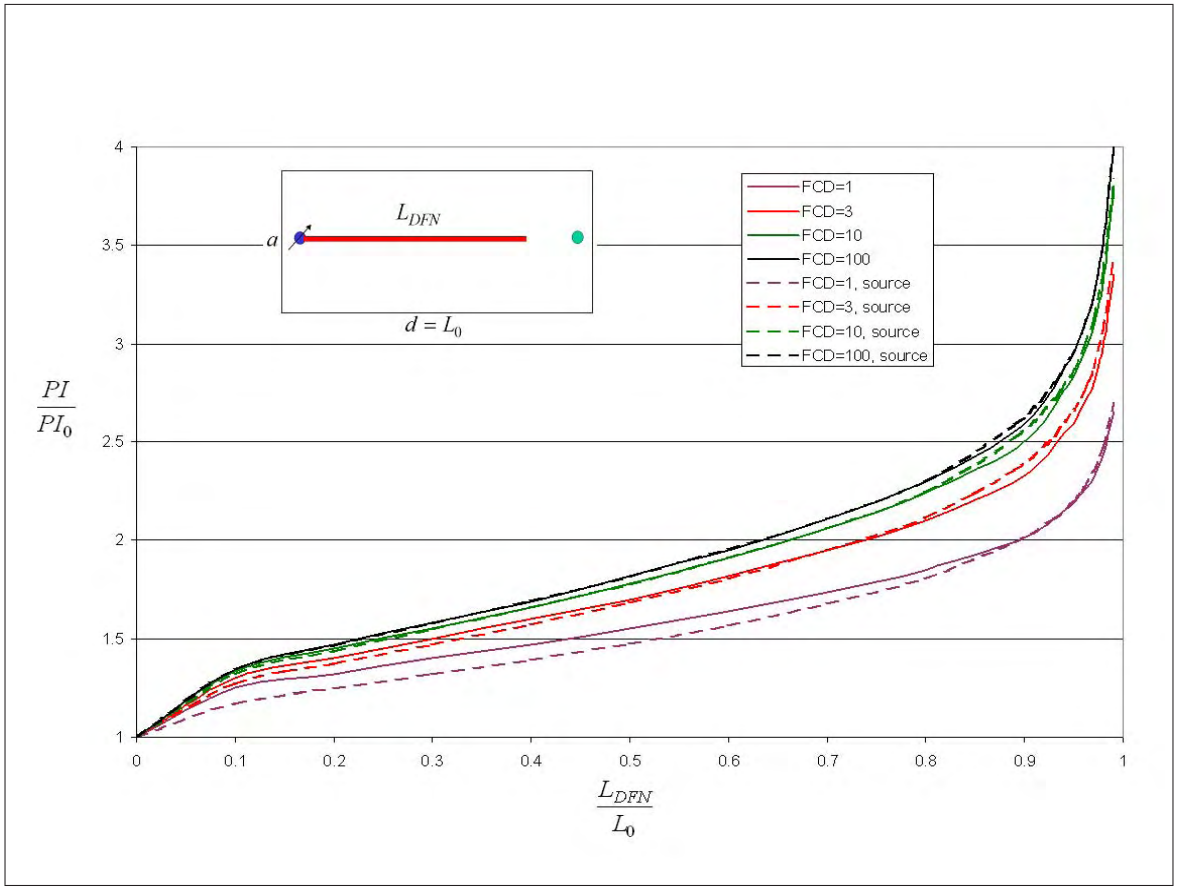

Fig. 8.25: PI gain from connected DFN flow, d/a=2

geometries, for long DFNs, particularly so for the case $d/a = 10$. Here the productivity gain approaches a factor of 10. This result verifies the ability of a single DFN to substantially increase well productivity, including those cases in which DFNs have finite dimensionless conductivities.

The intersection of the DFN is achieved, in the discretization case, by completing the injection well in a DFN grid block. This provides a direct connection from the DFN to the injection well. Such a direct connection is not made, however, with the source model. Instead, a DFN source is placed in the injection well block, and both the source connection transmissibility and that of the injection well are made equal to T_{DFN}. Thus, two connections occupy the injection well well block: the injection well connection, and the DFN connection. These two connections are

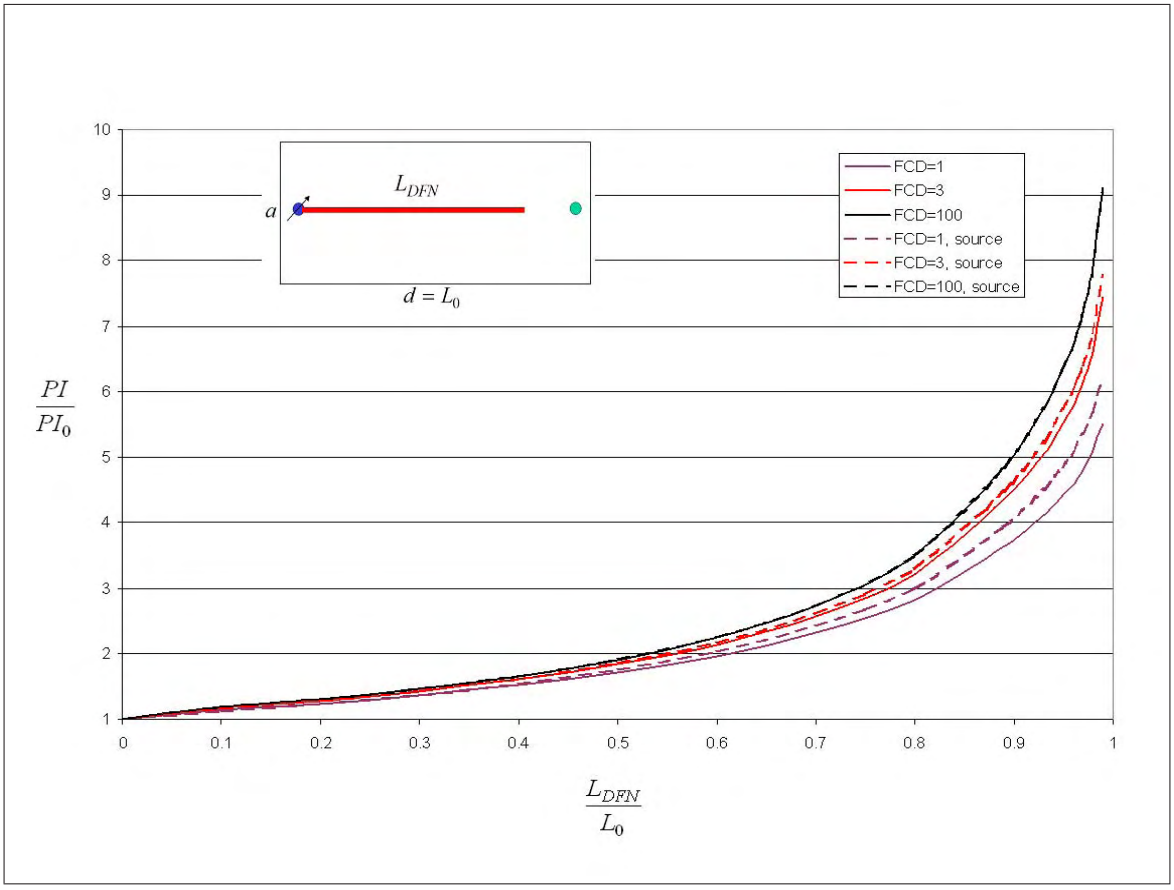

Fig. 8.26: PI gain from connected DFN flow, d/a=10

separate, in that they belong to two unique sets of sources, each having different rate or pressure constraints. The two connections do, however, have identical source strengths. This differs from the DFN discretization case, in which the injection well connection transmissibility is determined from conventional well transmissibility parameters, such as wellbore radius and skin factor.

The effect of assigning T_{DFN} to the injection well connection is to stimulate the injection well, as if, for example, it had been hydraulically fractured, with the fracture possessing the same F_{CD} as that of the natural DFN it intersects. This procedure is therefore consistent with the field observation that injection wells are stimulated, due to injection pressures exceeding formation fracture pressures (Sec. 5.1.2).

An alternative DFN source model might consist simply of extending the injection

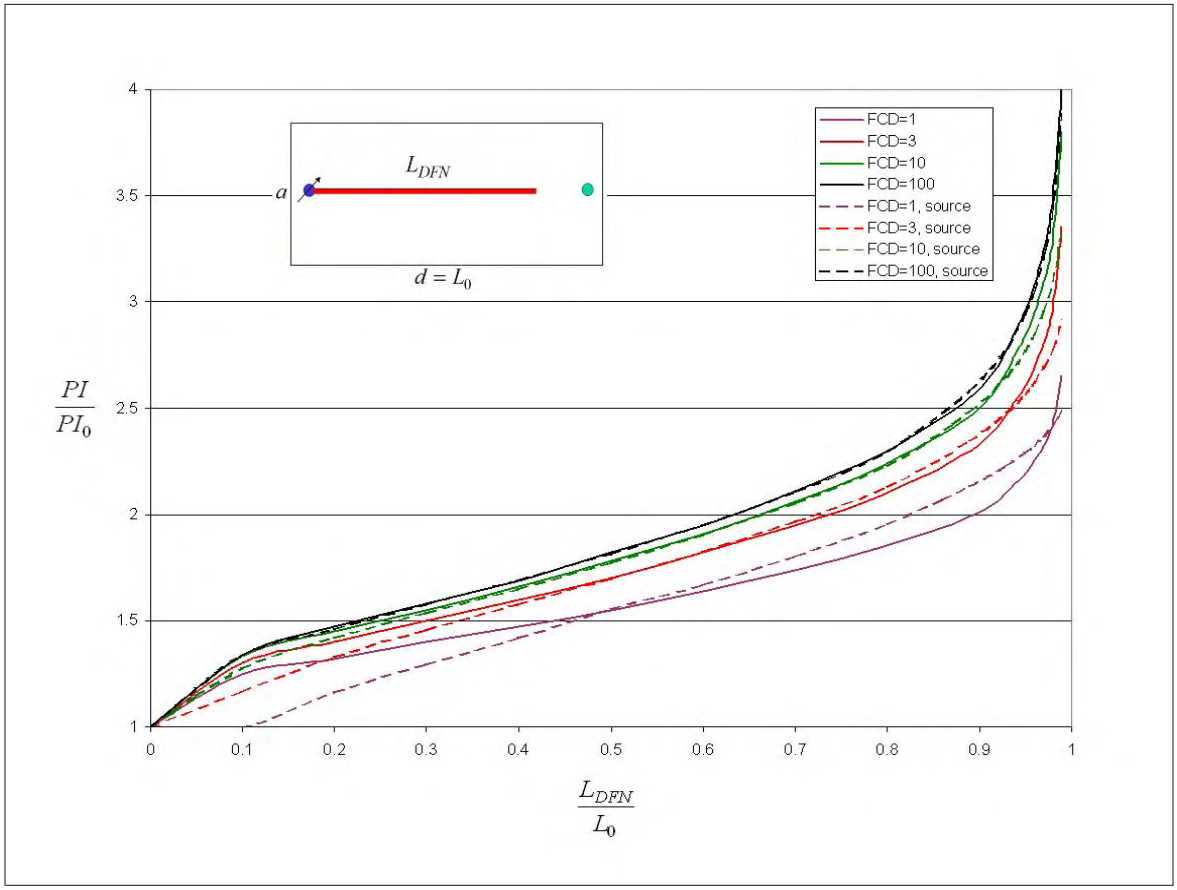

Fig. 8.27: Connected DFN source model as an extension of the injection well, d/a=2

well, by placing injection well connections along a path that is coincidental with the DFN. The connections would have transmissibilities of T_{DFN}, in those blocks which are intersected by the DFN. This model is equivalent to that of a horizontal lateral of length L_{DFN}, branching from the injection well, and following a path that is coincidental with the DFN. This model was constructed, although the agreement with the discretization results was not as satisfactory as those associated with a separate DFN source model, as can be seen in Fig. 8.27. Note that the injection well extension model generates curve shapes which are much less similar to those of the discretization models, relative to the similarity of curve shapes generated by the separate source models.

Another important result, from which our source model benefits, is that which

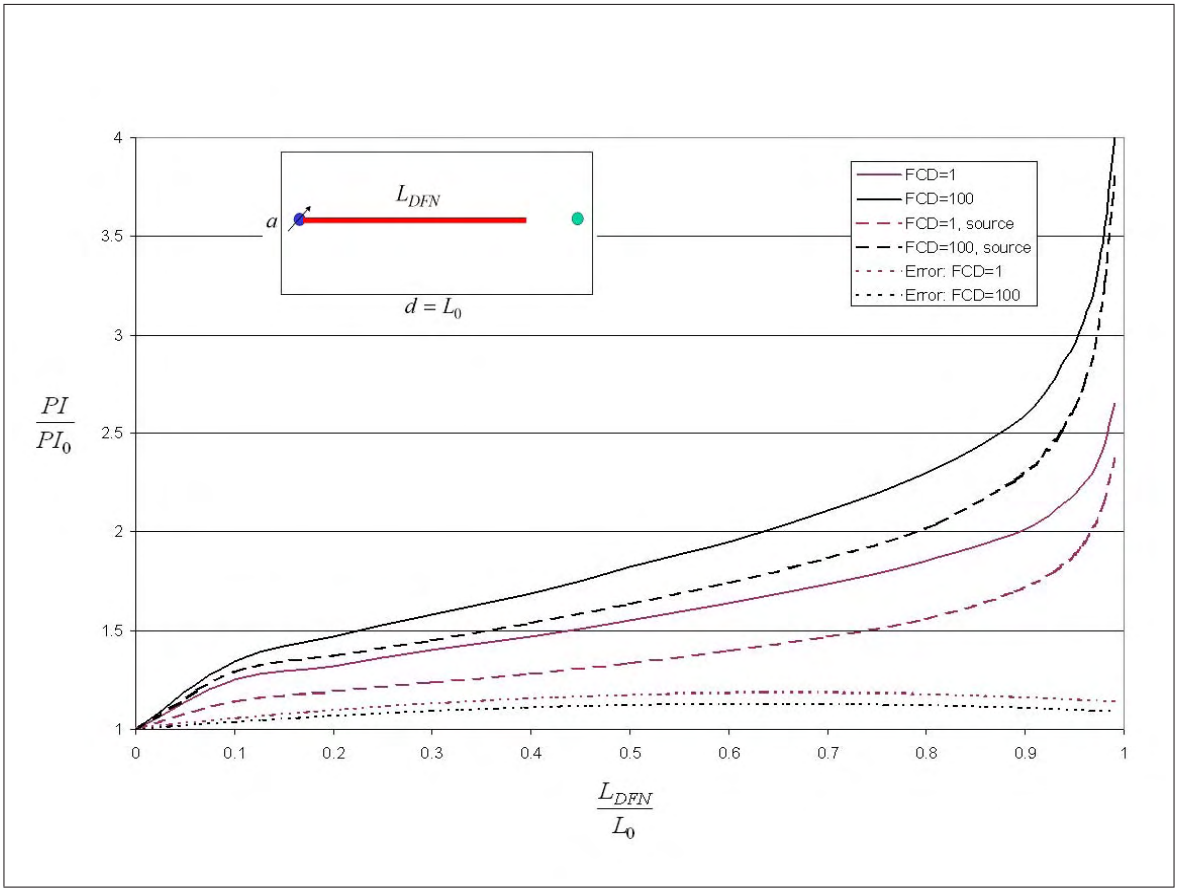

Fig. 8.28: Connected DFN source model using only two sources, d/a=2

demonstrates the efficacy of utilizing only DFN endpoint sources, rather than all possible DFN sources. These results are presented, for these two pattern geometries, in Fig. 8.28 and Fig. 8.29.

The plots are similar to those two previously presented, with the addition of curves which show the error between the source and discretization models, expressed as the ratio of the discrete model productivity gain, to that of the source model. Note, that although there is a larger discrepancy between the discrete and source models, when only two sources are used, the errors remain modest, particularly for the case $d/a = 10$. The largest error, 19%, occurs in the case $d/a = 2$, $F_{CD} = 1$. The errors in the case $d/a = 10$ are insignificant.

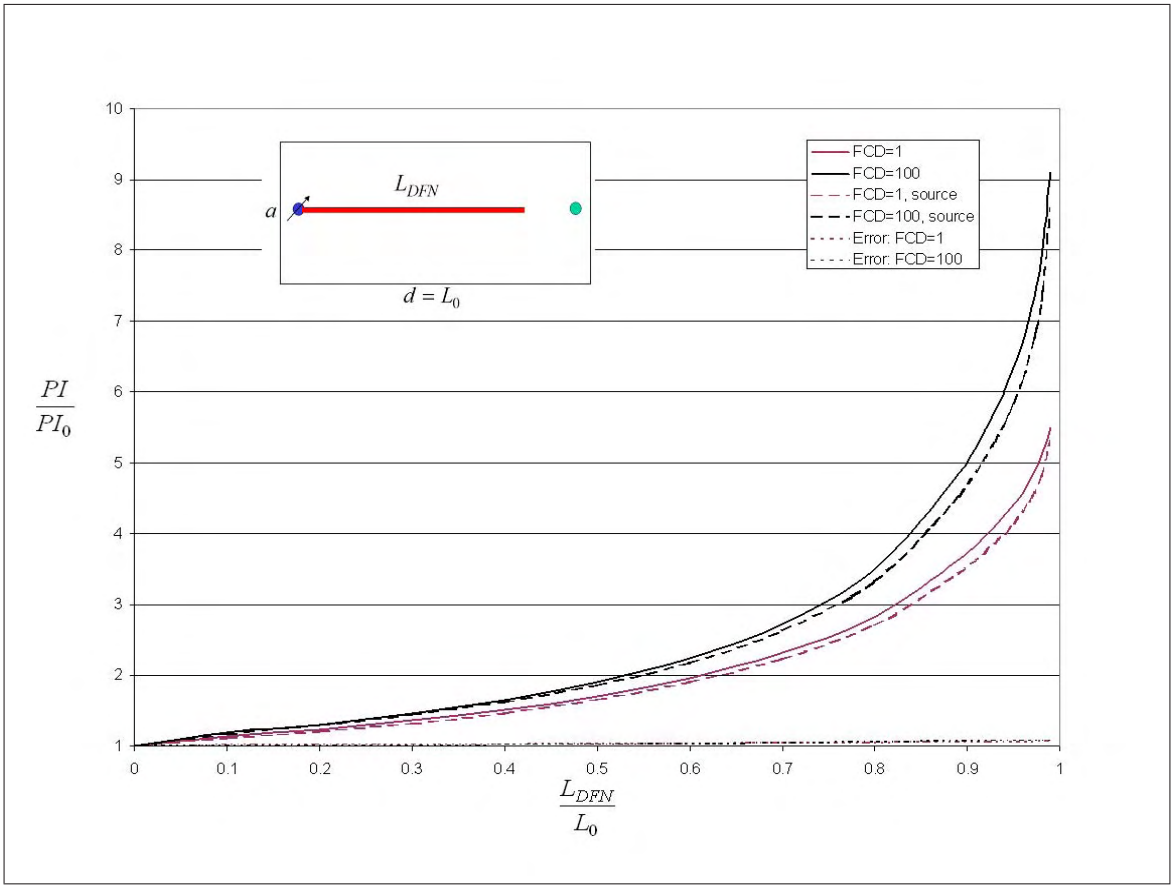

Fig. 8.29: Connected DFN source model using only two sources, d/a=10

It is important to note that the prediction of the two-source model may be improved by simply optimizing the value of η, or equivalently, T_{DFN}, rather than using the heuristic relation. However, this cannot be done in the case of $F_{CD} \geqslant 100$, as increases in the value of T_{DFN} for these cases, do not significantly modify the DFN flow performance. This is demonstrated in Fig. 8.30, where an increase in T_{DFN} by a factor of 3 modifies the $F_{CD} = 1$ curve, but the $F_{CD} = 100$ curve cannot be modified appreciably, under any increase in T_{DFN}. However, it is seen that errors associated with infinite conductivity DFNs are modest: the use of endpoint sources is viable for these cases.

Note the modified source curve for $F_{CD} = 1$ overpredicts productivity gain at large DFN lengths; the result here does not suggest the modified curve is optimum, but

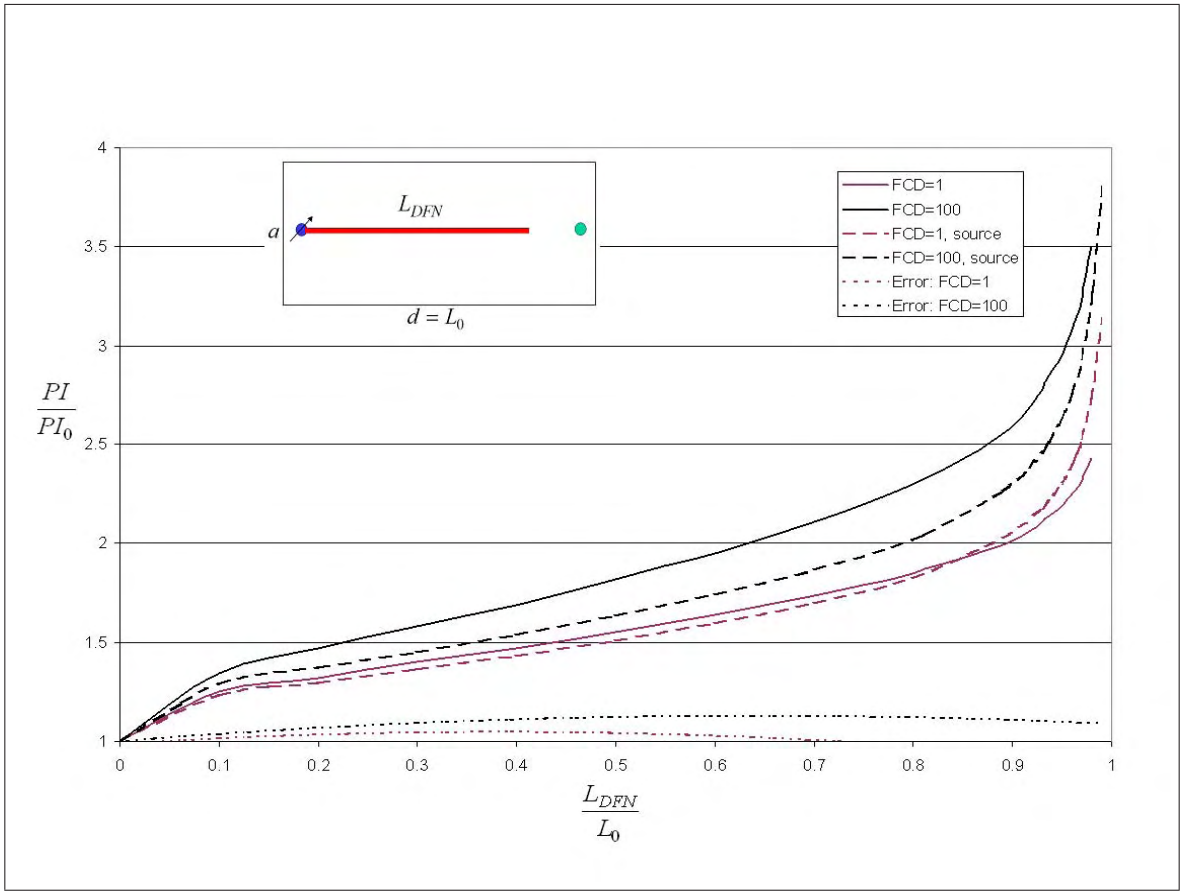

Fig. 8.30: Connected DFN source model using only two sources, d/a=2, modified case

merely demonstrates that for DFNs of lower dimensionless conductivity, optimization may be performed. However, infinite conductivity DFNs cannot be modified in such a way to increase productivity gains. Thus, $\eta_{\max}$ is applicable to DFN source sets consisting of two sources only, as well as sets containing more than two sources.

Source model results: isolated DFN

A similar analysis was performed for isolated DFNs. Here, the DFN is centered at the midway point between wells, and its length is varied such that its geometry remains symmetric relative to the wells, as in Fig. 8.23. The effect of an isolated DFN on well performance, and the ability of the source model to predict the effect, are shown in Fig. 8.31 and Fig. 8.32, for the two pattern geometries $d/a = 2$, and

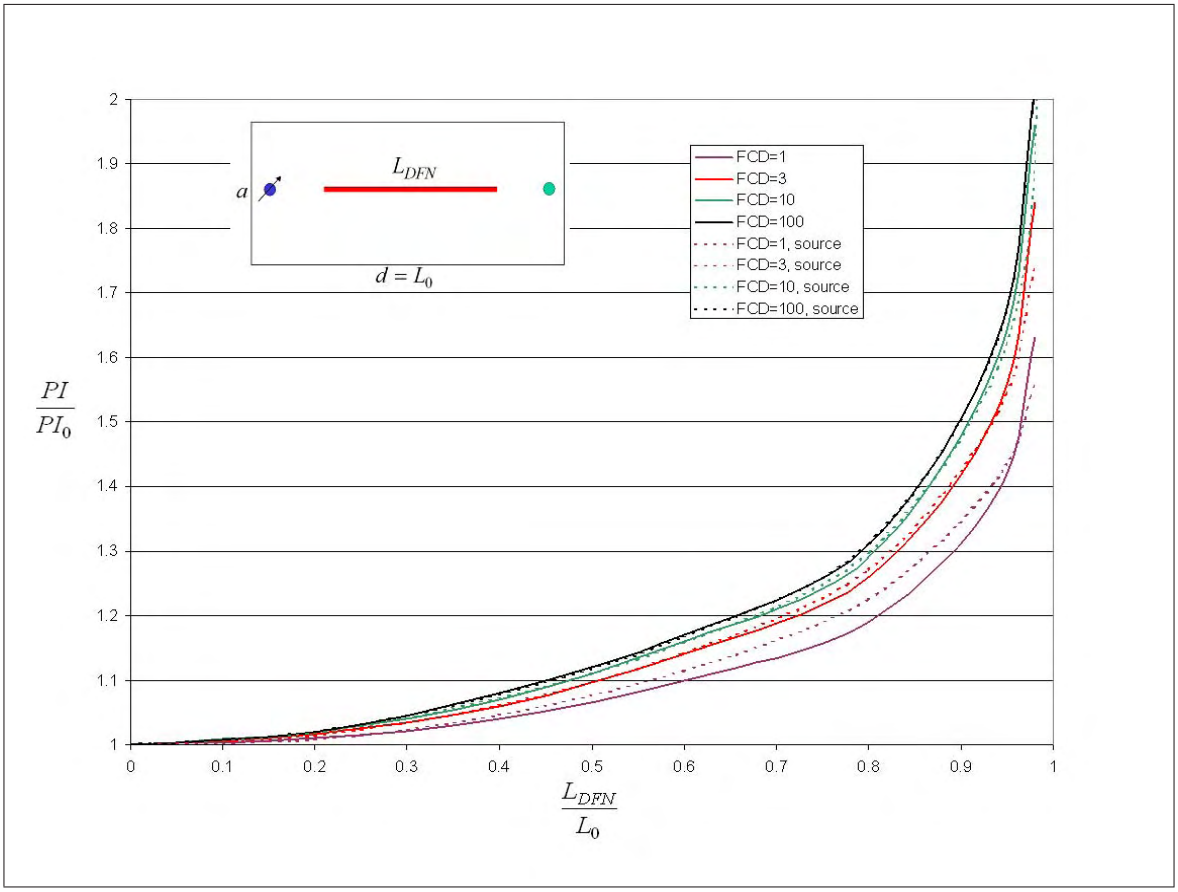

Fig. 8.31: PI gain from isolated DFN flow, d/a=2

$d/a = 10$.

As the DFNs do not connect with the injection well, no modification of the injection well connection transmissibility is performed; the connection transmissibility is as computed from conventional well transmissibility parameters.

As for the connected DFN case, several cases for each pattern geometry are presented, corresponding to various values of F_{CD}. Each F_{CD} case is represented with results from both the discretized DFN model, and the DFN source model. Sources are applied in all grid blocks intersected by the DFN. Note that the agreement between these two models is very good, verifying the source model for these isolated DFNs.

Note that the productivity gains are not as substantial as for the connected DFNs,

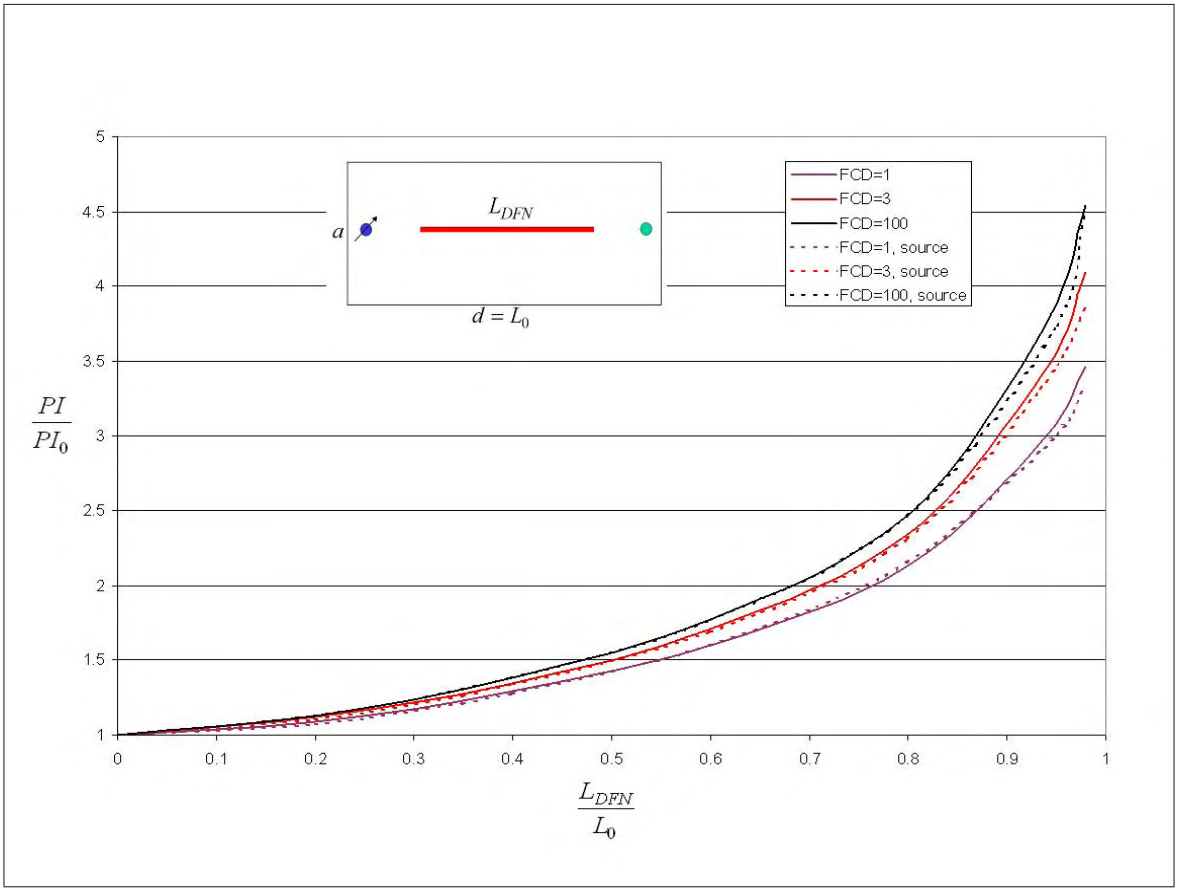

Fig. 8.32: PI gain from isolated DFN flow, d/a=10

which provide approximately twice that presented in these results.

The efficacy of the application of only endpoint sources, is indicated in Fig. 8.33 and Fig. 8.34. The errors associated with omitting all but endpoint sources for the finite conductivity DFNs may be substantial, whereas, as in the case with connected DFNs, the errors associated with infinite conductivity DFNs are modest to insignificant. Furthermore, as seen Fig. 8.35 and Fig. 8.36, the discrepancies incurred in the $F_{CD} = 1$ case, with the two-source model are alleviated by increases in T_{DFN}, by a factor of 7, in both pattern geometries.

As in the case of the connected DFN, isolated DFNs of $F_{CD} \geqslant 100$ cannot be significantly modified, although the errors associated with these cases are small.

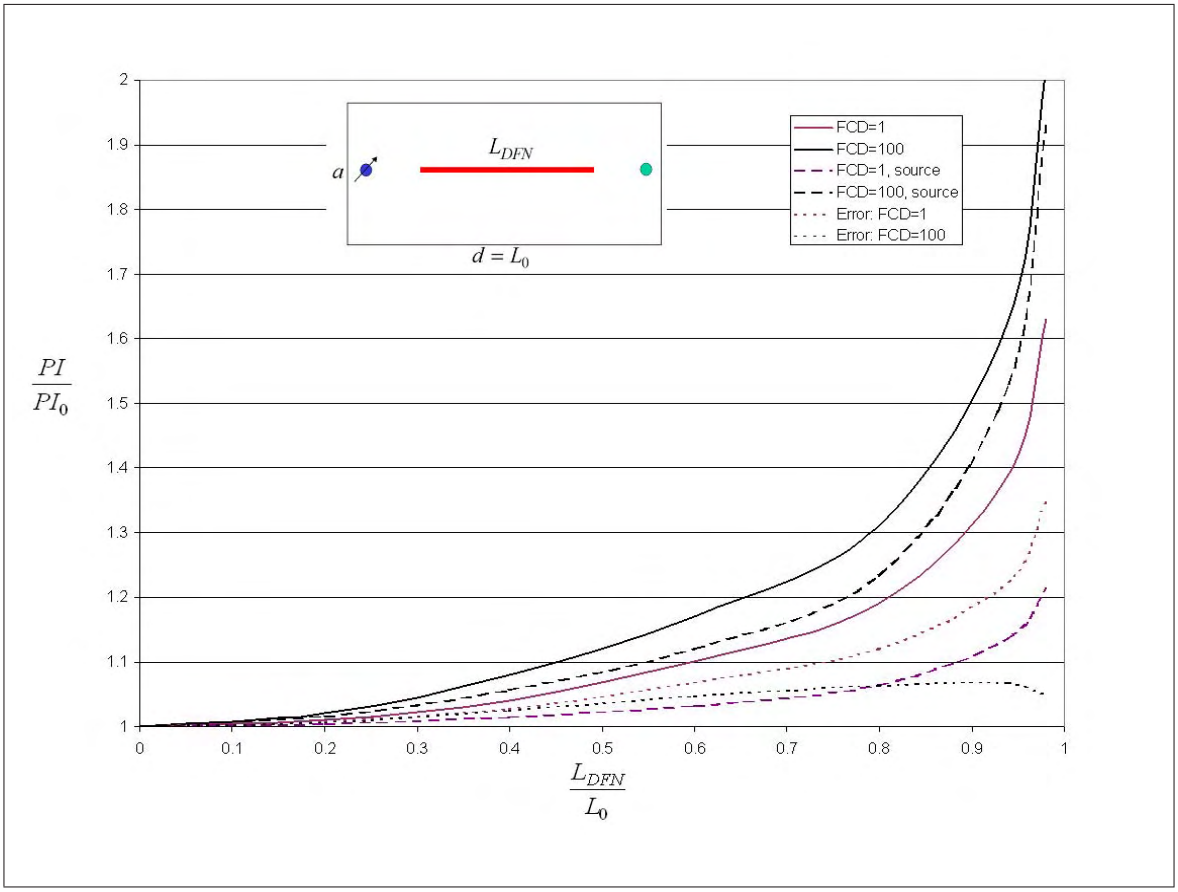

Fig. 8.33: Isolated DFN source model using only two sources, d/a=2

Flux and pressure distribution - connected DFN

The success of the source model in predicting the effect of DFN flow on steady state well performance suggests that prediction of DFN steady state flux and pressure distributions is also good, and indeed this is the case, as the flux and pressure distribution plots, presented in this section, show. The ability of the source model to replicate the flux distribution must be established in verifying its legitimacy as a viable DFN flow model.

Fig. 8.37 and Fig. 8.38 present the flux distribution of the connected DFN, as defined by the source and discretized models. Here, the flux is approximated by flow rate, q, from a DFN grid block, or a DFN source, and is plotted in the flux ratio q/q_t, where q_t is the steady state total flow rate injected and produced in the model.

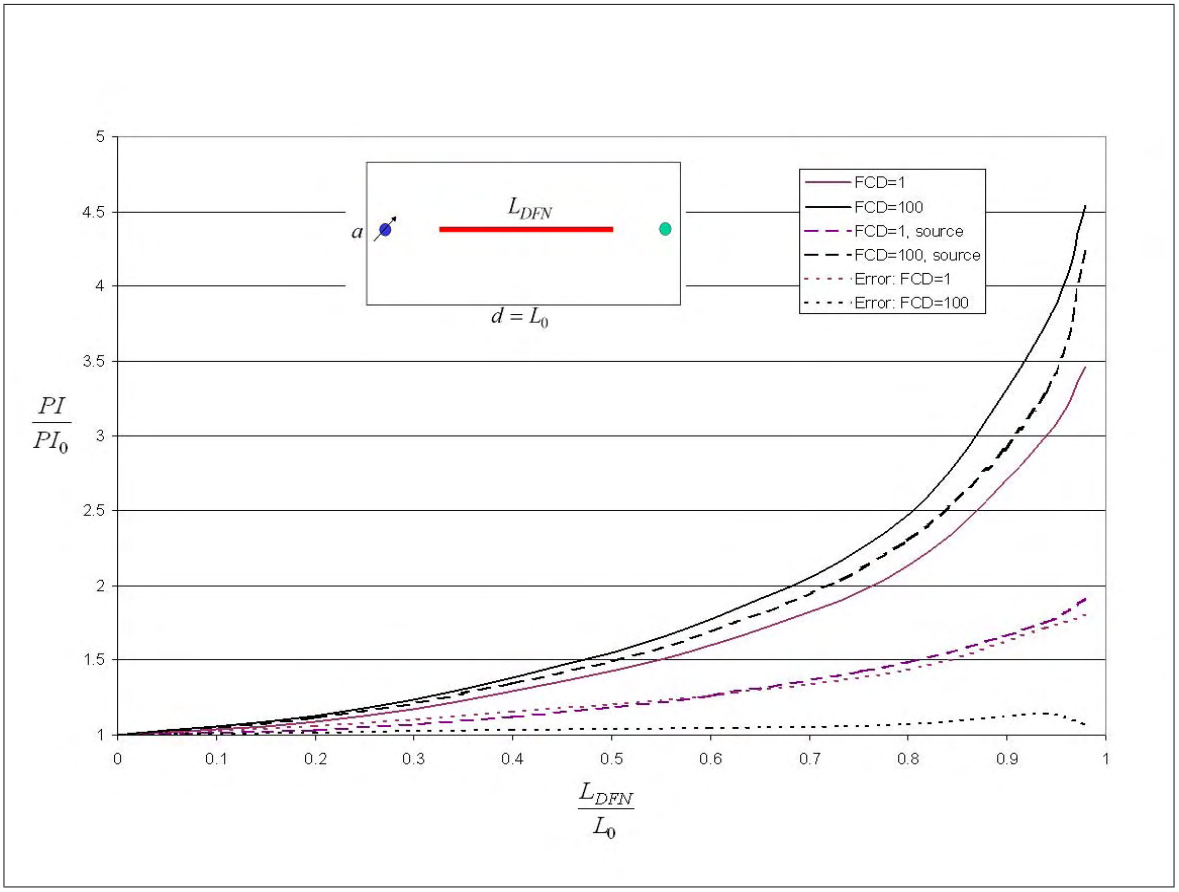

Fig. 8.34: Isolated DFN source model using only two sources, d/a=10

A positive flux indicates a net flow *into* the DFN. The flux ratio is plotted against L_{DFN}, presented in grid block units.

The two cases $F_{CD} = 1$ and $F_{CD} = 100$ are shown, for various DFN lengths. The pattern geometry is that of $d/a = 2$.

The proportion of the total rate, q_t, which passes through the DFN is also presented, in the figure legends, as the parameter P. This parameter indicates the relative importance of the DFN to the total flow system, and therefore is generally correlated to the DFN's effect on well performance, discussed in the previous sections.

Note that the DFN conducts practically all of the fluid flowing in the system, in all cases, as indicated by P. The flux distribution is asymmetric, with nearly 100% of the total flux entering the endpoint of the DFN at the injection well, but exiting

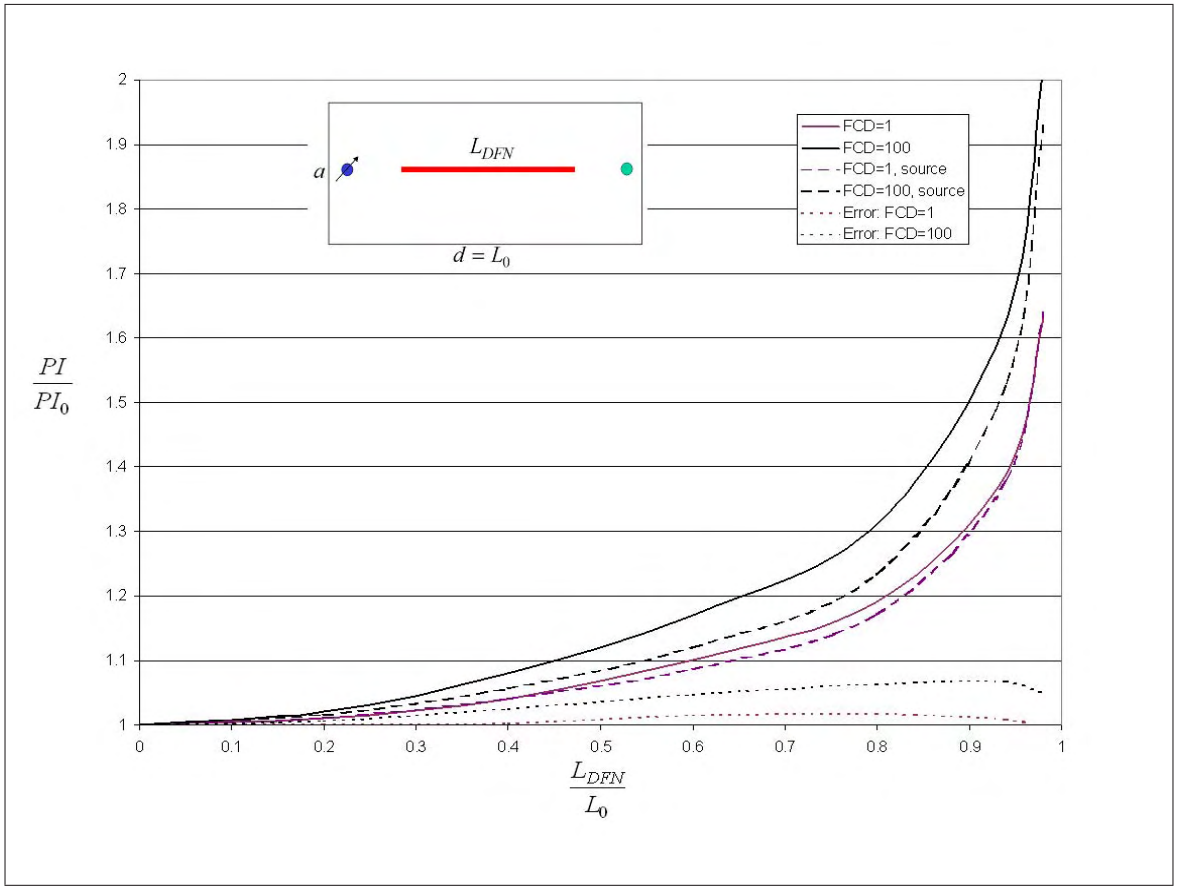

Fig. 8.35: Isolated DFN source model using only two sources, d/a=2, modified case

nearly all of the DFN blocks, although the majority of the DFN flow exits the blocks closest to the producing well. The DFN flow for $F_{CD} = 1$ is interesting in that a significant amount of flux exits blocks near the injection well, as predicted by the discrete model. The source model, however, does not predict this behavior.

Sources are placed at all grid blocks intersected by the DFN. Comparison between the source and discrete models indicates good agreement in general, with the match between the cases $F_{CD} = 100$ essentially exact. The parameters P are also equivalent in the two models.

Fig. 8.39 and Fig. 8.40 present the pressure distributions for the two cases discussed above. These plots present the pressure distributions both within the DFN, and outside the DFN, along its axis. Thus, reservoir pressure gradients induced by

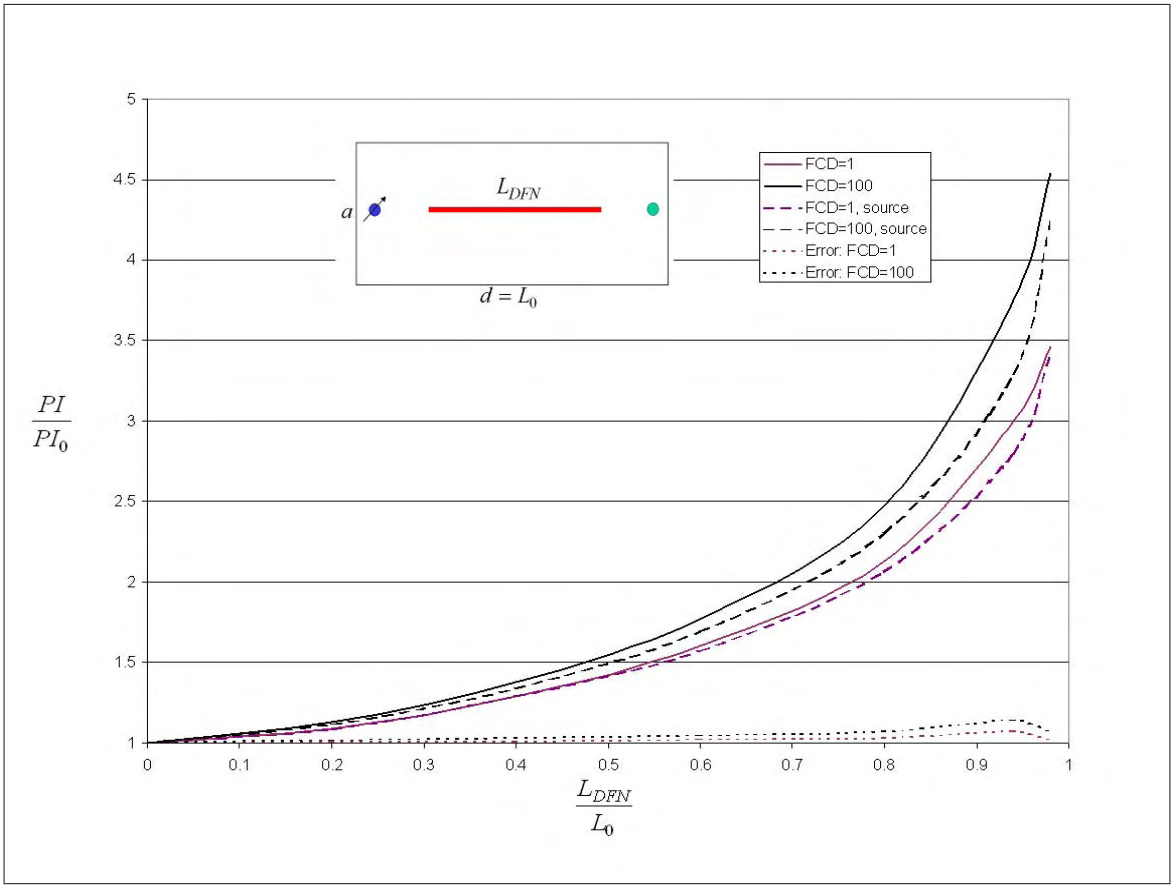

Fig. 8.36: Isolated DFN source model using only two sources, d/a=10, modified case

the DFN, for each model, may be compared.

Fig. 8.39 shows the distribution for the lower conductivity DFN, for various lengths. Note, by definition, the zero pressure gradient within the source model. This is seen also in Fig. 8.40, in the source model, and essentially also in the discrete model, which generates an insignificant gradient within the DFN.

Importantly, the two models generate equivalent reservoir pressure gradients outside the DFN, explaining the good agreement between the productivity gains predicted by the two models. The gradient, as well as the pressures, are nearly exact for the infinite conductivity case.

Fig. 8.41 through Fig. 8.44 present results for the same cases as in the previous four plots, for the pattern geometry $d/a = 10$.

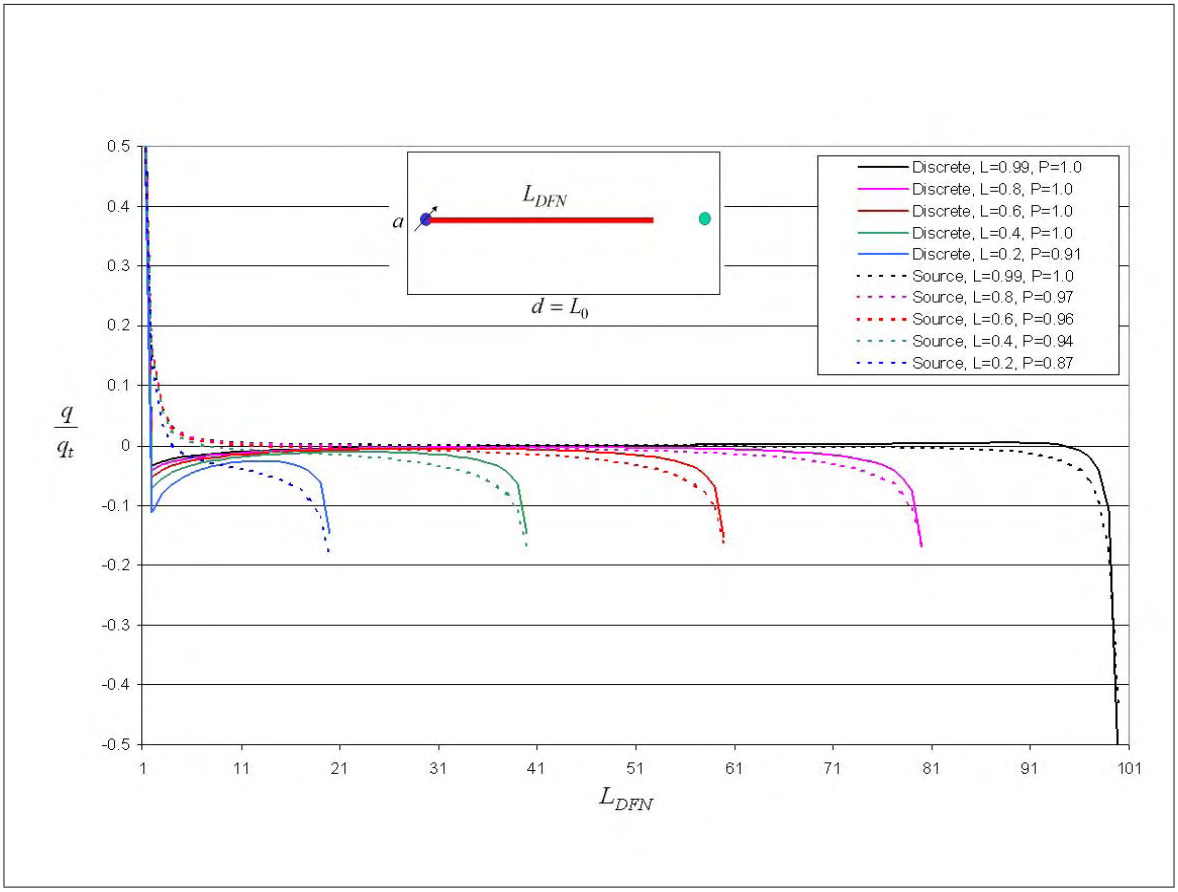

Fig. 8.37: Flux distribution for connected DFN, FCD=1, d/a=2

Note that the thinner pattern geometry promotes greater flux symmetry in the DFN, and indicates a greater dominance of the DFN endpoints in controlling the flux distribution, providing a basis for the greater success of the endpoint sources in modeling DFN flow in this pattern, relative to the wider pattern (see Fig. 8.28 and Fig. 8.29). The agreement between the two models, as with the wider pattern, particularly for $F_{CD} = 100$, is very good, for both flux and pressure distributions.

Flux and pressure distribution - isolated DFN

The flux distribution within the isolated DFNs for the discrete and source models are presented in the eight plots, Fig. 8.45 through Fig. 8.52. The first four plots present the flux and pressure distribution results of both models for the pattern $d/a = 2$, and

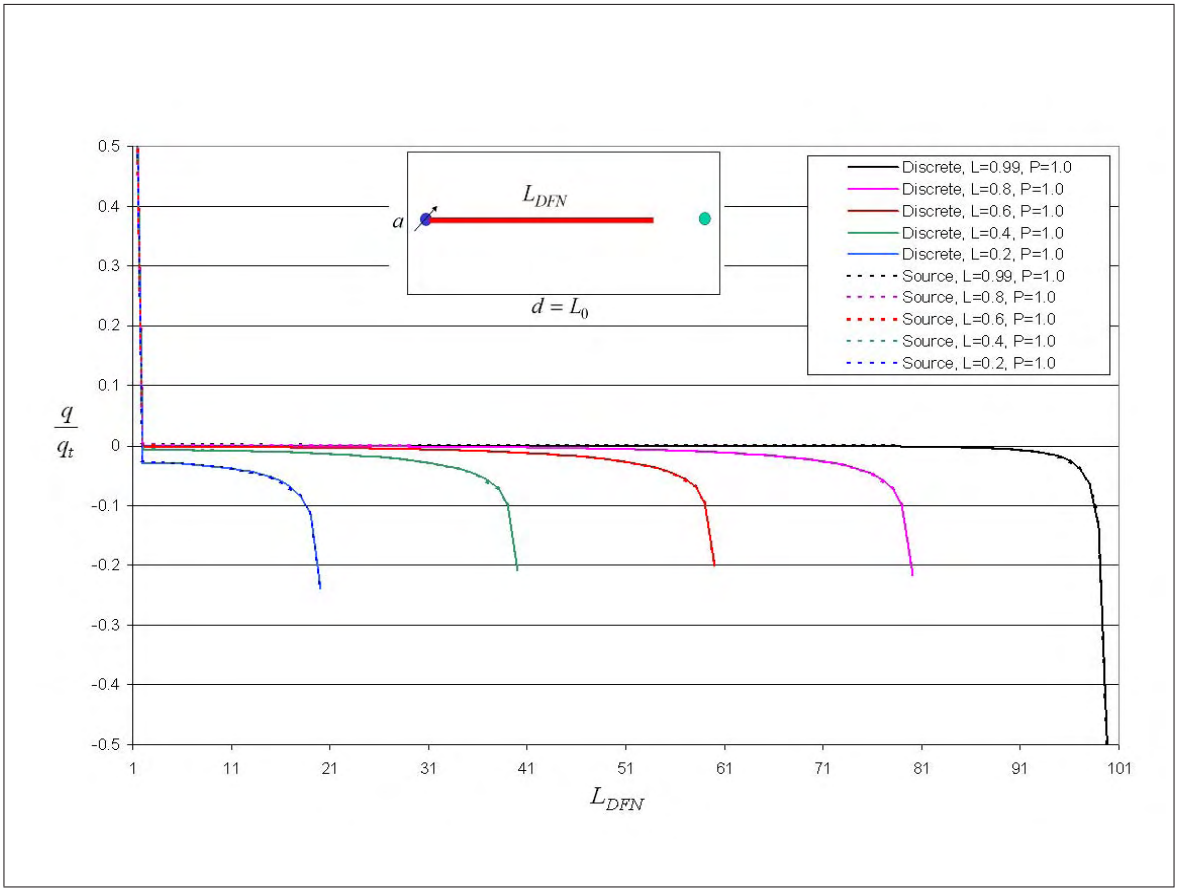

Fig. 8.38: Fflux distribution for connected DFN, FCD=100, d/a=2

the last four plots, for the geometry $d/a = 10$.

As with the connected DFN results, the agreement between the source and discrete models is good, and for all cases $F_{CD} = 100$, the model results are essentially identical. The thinner pattern generally accommodates less discrepancy for the case $F_{CD} = 1$, as was true for the connected DFN.

The isolated DFNs generated the most flux discrepancies between the two models, of all the cases investigated in this numerical study, for $F_{CD} = 1$, as is shown in Fig. 8.45 and Fig. 8.49. The source model underpredicts the flux contribution of the DFN endpoints, and overpredicts that for the nodes near the DFN center. The discrepancy does not affect the prediction capability of the source model for productivity gain, as seen in Fig. 8.31 and Fig. 8.32. However, the prediction shortcomings

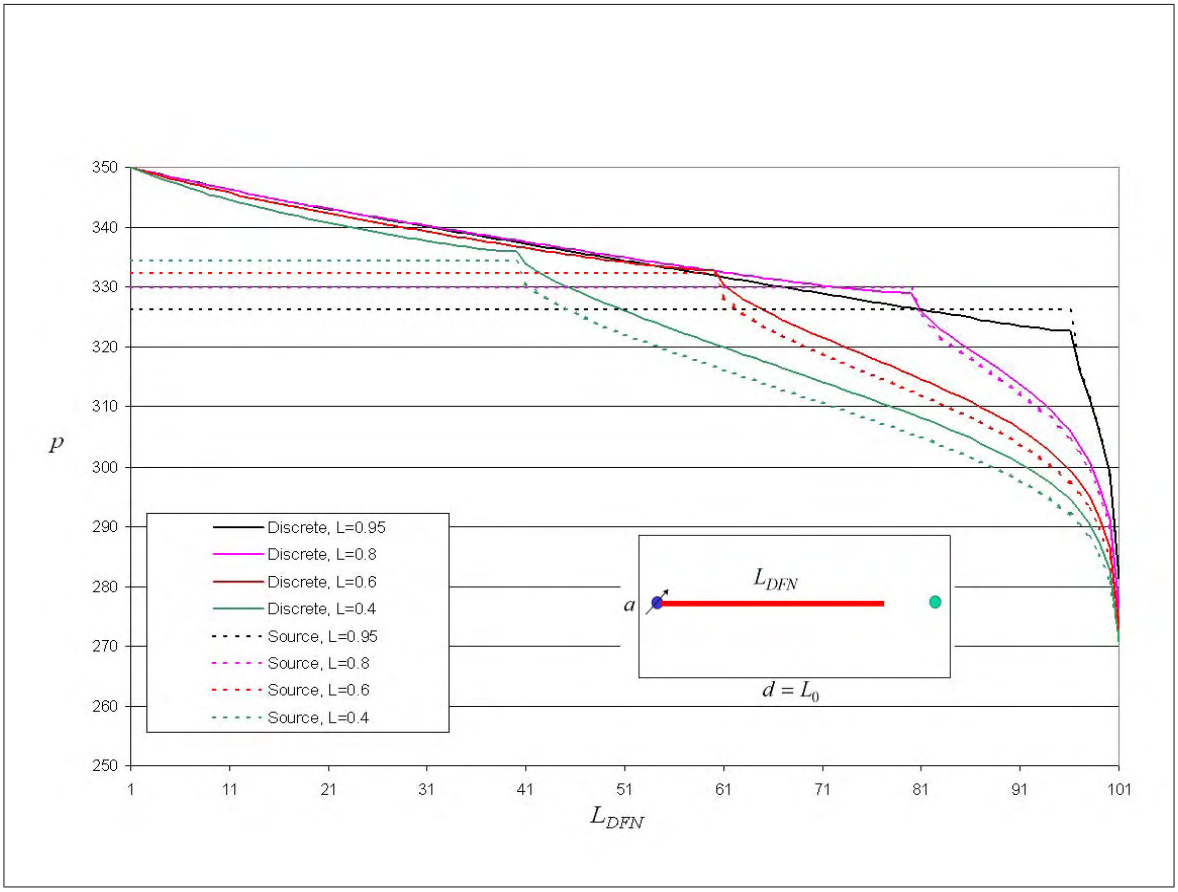

Fig. 8.39: Pressure distribution for connected DFN, FCD=1, d/a=2

of the use of endpoint sources in isolated DFNs, as seen in Fig. 8.33 and Fig. 8.34, are clarified with these discrepancies. However, as indicated previously, the modest productivity gain induced by DFNs of $F_{CD} = 1$, leaves little relevance to the inaccuracy displayed by the source model for these cases.

Note the thinner pattern induces proportionally larger contributions form the DFN endpoints, similarly to the result from the connected DFN, promoting the efficacy of the endpoint source approach when utilizing the source model.

Flux and pressure distribution for the endpoint source model

The final set of results presented here elaborate on the performance of the endpoint source model: that which is constructed with only two sources at the endpoints.

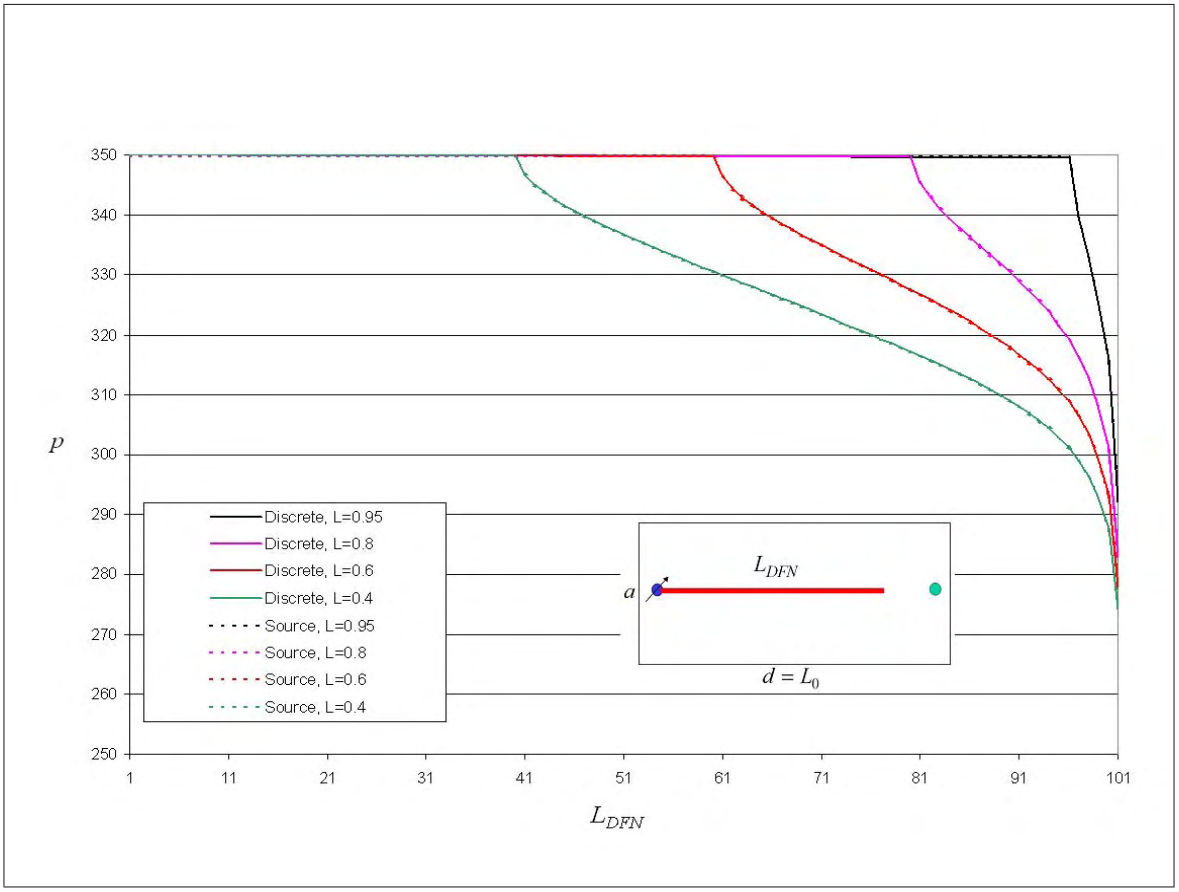

Fig. 8.40: Pressure distribution for connected DFN, FCD=100, d/a=2

It is essential to clarify the circumstances for which representing a DFN with only endpoint sources, is valid. It was concluded in 8.3.5 and 8.3.5 that the endpoint model predicts productivity gain well, in general, although significant discrepancies were found for isolated DFNs of low conductivity. Despite the apparent irrelevance of these types of DFNs, as they incur small gains in well productivity, nevertheless the analysis of their behavior, relative to that of the more successful endpoint DFN models, is insightful.

Fig. 8.53 through Fig. 8.60 present the pressure and flux distributions within the DFN and of the reservoir outside of the DFN, along its axis, compared to that of the discrete model. Connected DFN results are first presented, in Fig. 8.53 through Fig. 8.56, for $F_{CD} = 1$ and $F_{CD} = 100$ cases, and pattern geometries $d/a = 1$ and

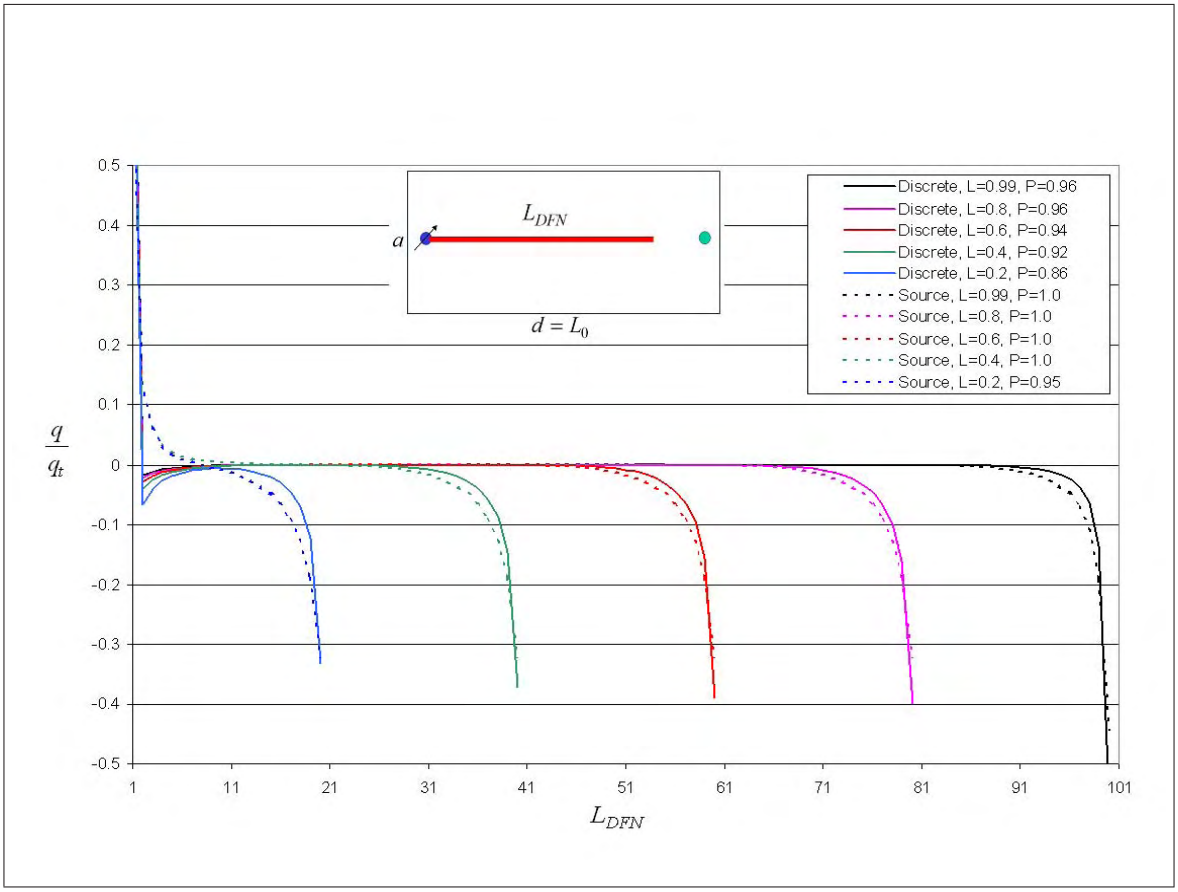

Fig. 8.41: Flux distribution for connected DFN, FCD=1, d/a=10

$d/a = 10$, as have been presented previously. The final four plots, Fig. 8.57 through Fig. 8.60, are similar cases for the isolated DFN.

The flux comparison of these two models is represented by the values of P , the proportion of the total system flow rate that enters the DFN, included in the legend, as this value equals the endpoint model flux:: that entering the DFN at one endpoint must equal that exiting the other endpoint. The value of P for the discrete model is also presented in the legends, for comparison. The flux distribution for the discrete model DFNs have been presented, although the comparison between the values of P suffice in these presentations for our purposes.

The agreement between both pressure and pressure gradient is very good in general, as shown, with a couple of exceptions. First, Fig. 8.53 and Fig. 8.54, connected

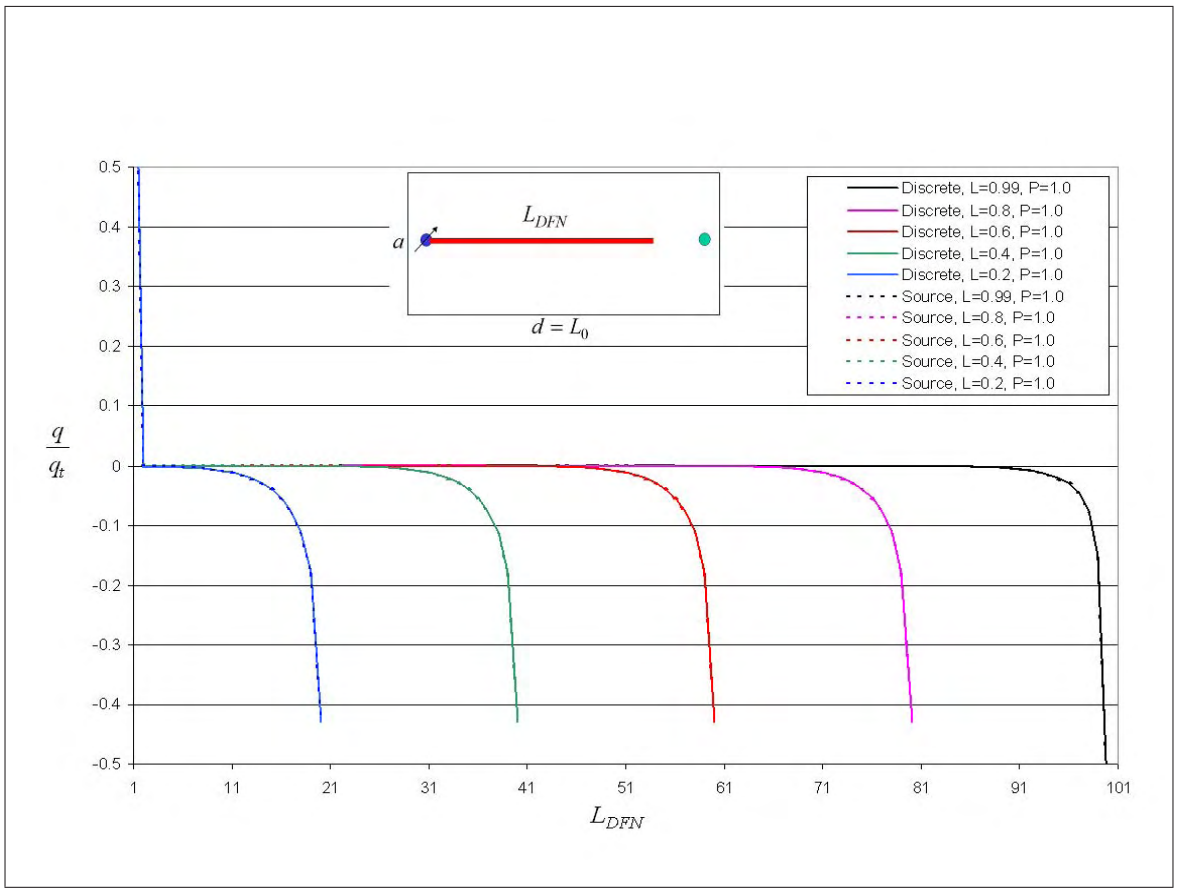

Fig. 8.42: Flux distribution for connected DFN, FCD=100, d/a=10

DFN results within the pattern $d/a = 2$, for the cases $F_{CD} = 1$ and $F_{CD} = 100$, respectively, indicate a pressure discrepancy between the two models, although with consistent pressure gradients. The productivity gain from the two models agree well (Fig. 8.25), a result corroborated by the gradient agreement. Note that the source model gradient is very steep at the source location: the lack of sources at locations other than the endpoints, is compensated by a higher flux in the reservoir near the solitary source.

Note that discrepancies also exist in the values of pressure P between the two models, for the case $F_{CD} = 1$, although the productivity gain error is much less substantial (Fig. 8.25) For example, the discrepancy in P for the case $L_{DFN} = 0.4$ is 40%, although the error in productivity gain is much smaller, ˜7%. This apparent

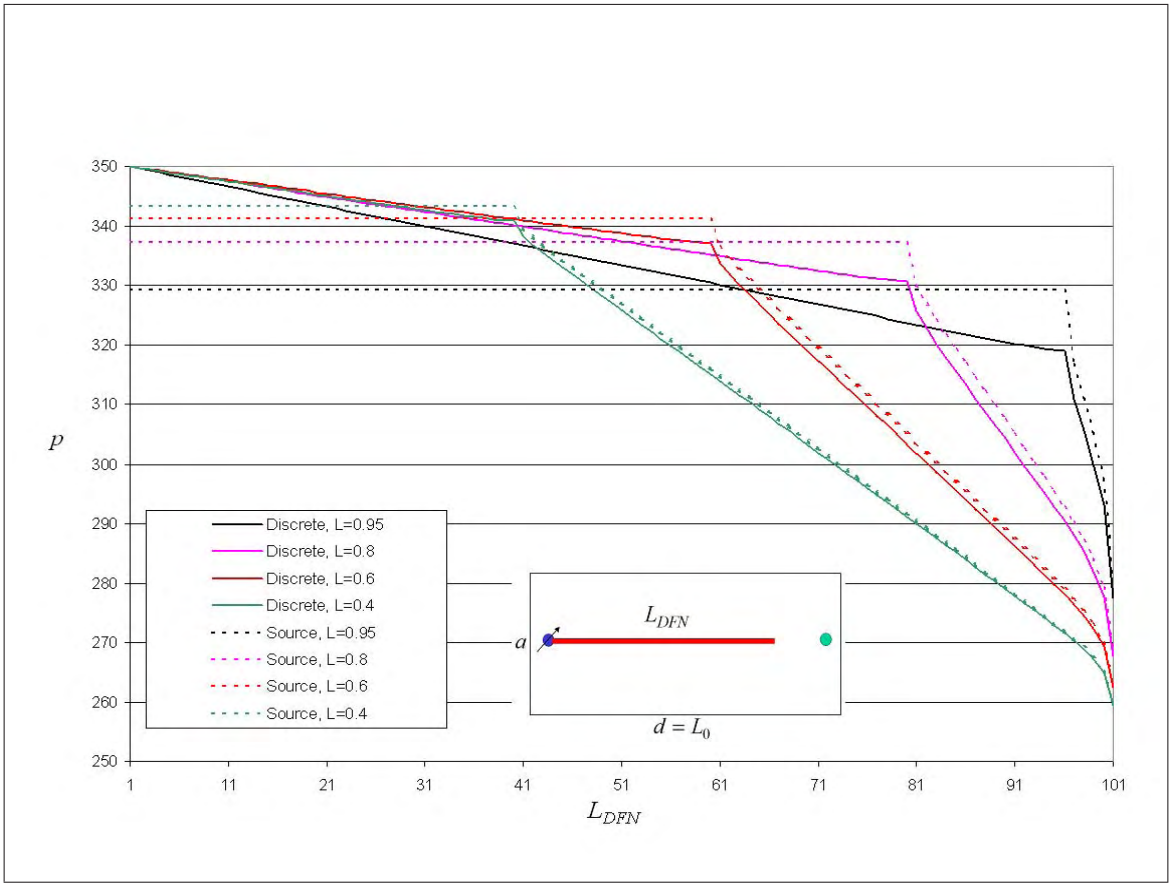

Fig. 8.43: Pressure distribution for connected DFN, FCD=1, d/a=10

inconsistency is resolved by the effect of the low conductivity of the DFN. It's relative importance in the flow system is nominal; fluid flow preferentially directed into it does not substantially increase the system productivity, and thus productivity gain is not well correlated with P.

The other discrepancy is seen in Fig. 8.59, a case that generated the largest error in predicted productivity gain, as seen in Fig. 8.34. This is the isolated DFN of $F_{CD} = 1$, in the pattern $d/a = 10$. Note that the pressure gradient in the reservoir for the endpoint model is significantly lower than that predicted by the discrete model, behavior consistent with the lower productivity gain predicted by the endpoint model. This discrepancy is generated also in the pattern $d/a = 2$, although with less severity. The large discrepancy associated with low conductivity, isolated DFNs in the pattern

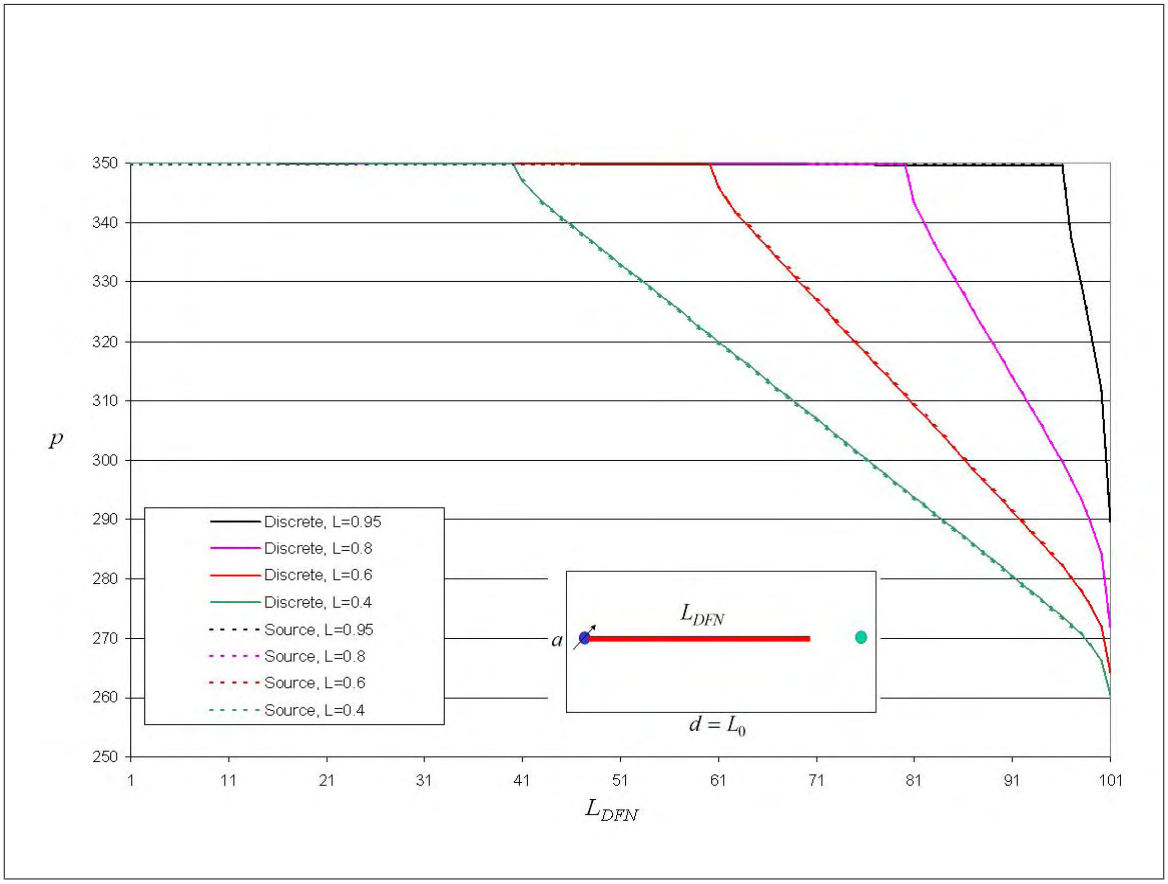

Fig. 8.44: Pressure distribution for connected DFN, FCD=100, d/a=10

$d/a = 10$, is also observed in Fig. 8.45 and Fig. 8.49. Note that the source model, using all available sources, is proportionally less predictive of flux distribution in the thin pattern than in the wider pattern. The flux and pressure discrepancies in the thin pattern indicate that the inadequacy of the endpoint source model in modeling low conductivity, isolated DFNs is emphasized in patterns for which this type of DFN approaches significance, that is, thin patterns. Fig. 8.32 indicates, however, that the general source model, in which all available sources are used, predicts isolated DFN productivity gain well in the thin pattern. Furthermore, it must be recalled, that in the case of a low conductivity DFN, the source transmissibility may be increased to achieve the desired productivity gain.

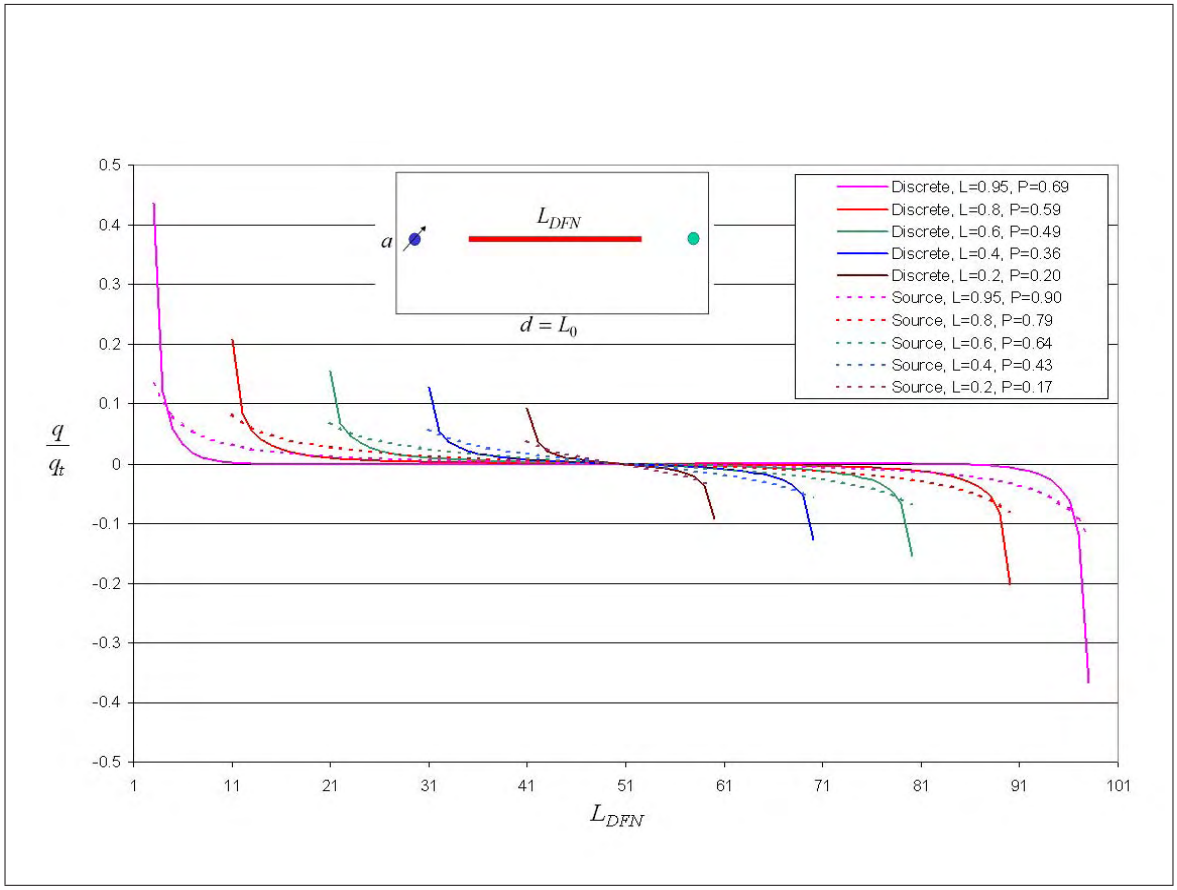

Fig. 8.45: Flux distribution for isolated DFN, FCD=1, d/a=2

Summary

The efficacy of the source model to predict steady state flow performance for a waterflood pattern containing a DFN is proven in this section. Furthermore, the approximation of DFN flow performance with endpoint sources is shown to be adequate, incurring only modest errors for finite conductivity DFNs, and insignificant errors for infinite conductivity DFNs.

The calibration of the source transmissibility, by defining it as a simple function of F_{CD} and a/d, renders a viable DFN source model, with possible extension to the modeling of hydraulic fractures in wells.

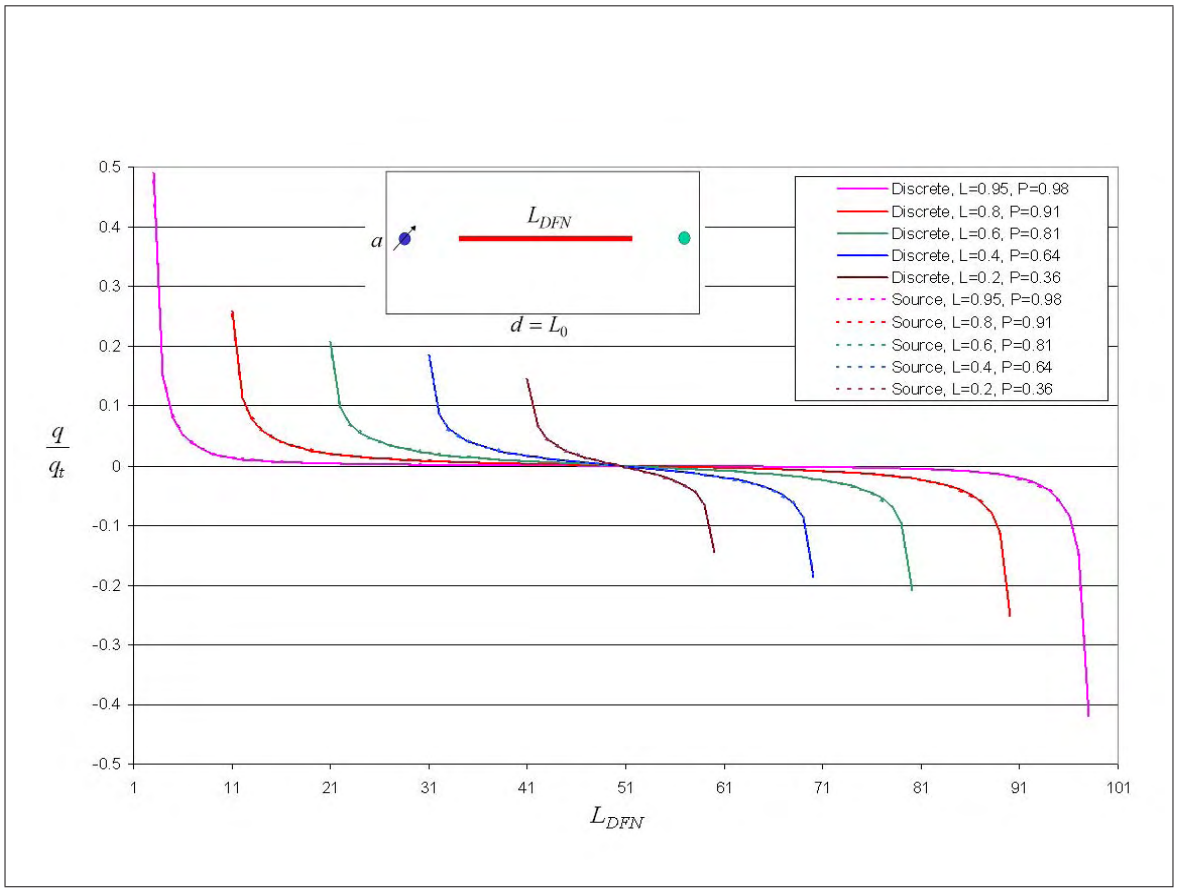

Fig. 8.46: Flux distribution for isolated DFN, FCD=100, d/a=2

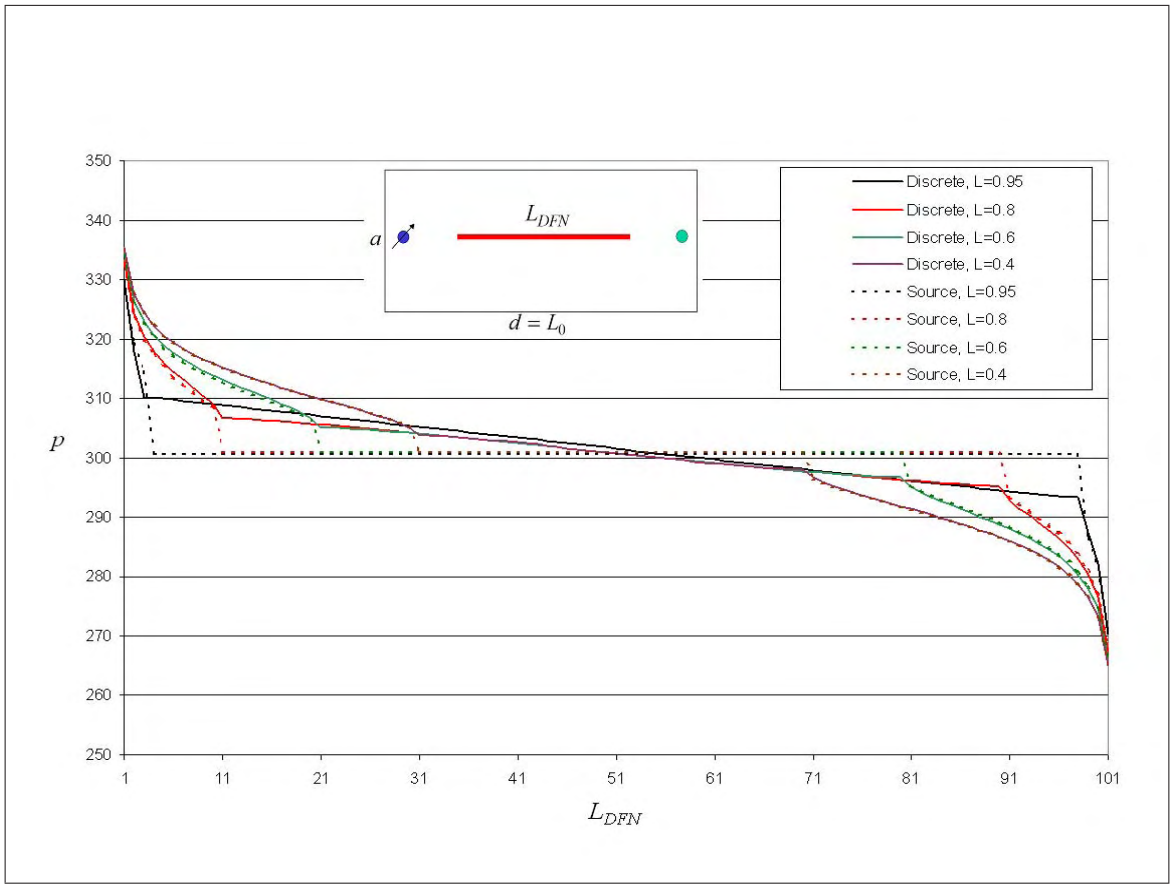

Fig. 8.47: Pressure distribution for isolated DFN, FCD=1, d/a=2

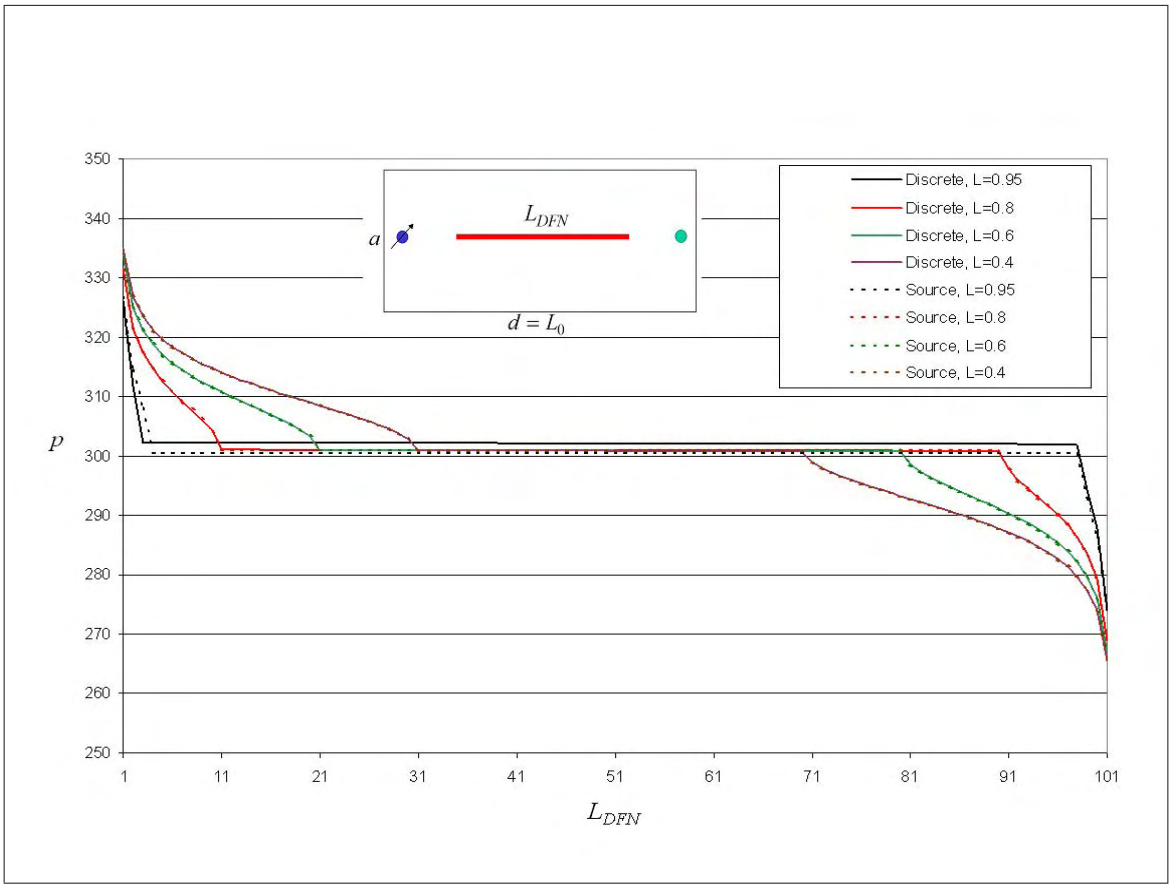

Fig. 8.48: Pressure distribution for isolated DFN, FCD=100, d/a=2

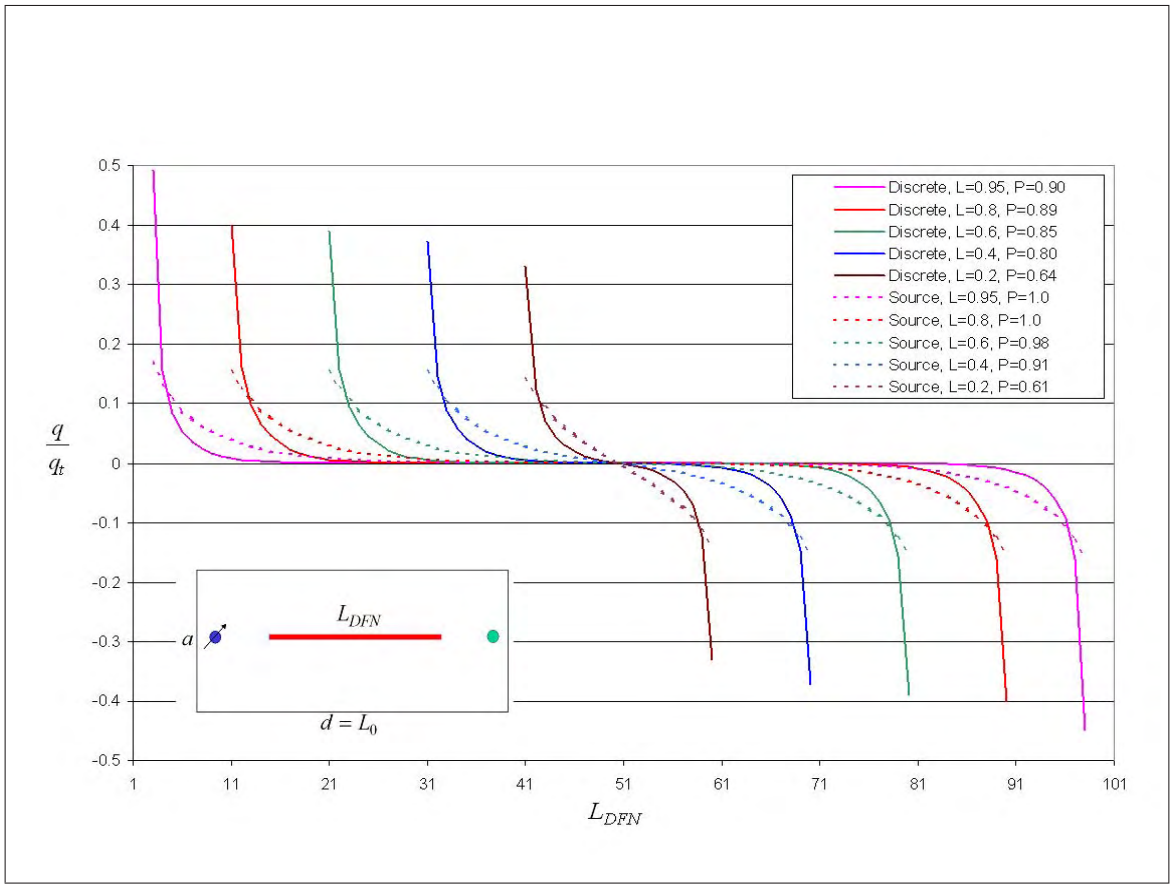

Fig. 8.49: Flux distribution for isolated DFN, FCD=1, d/a=10

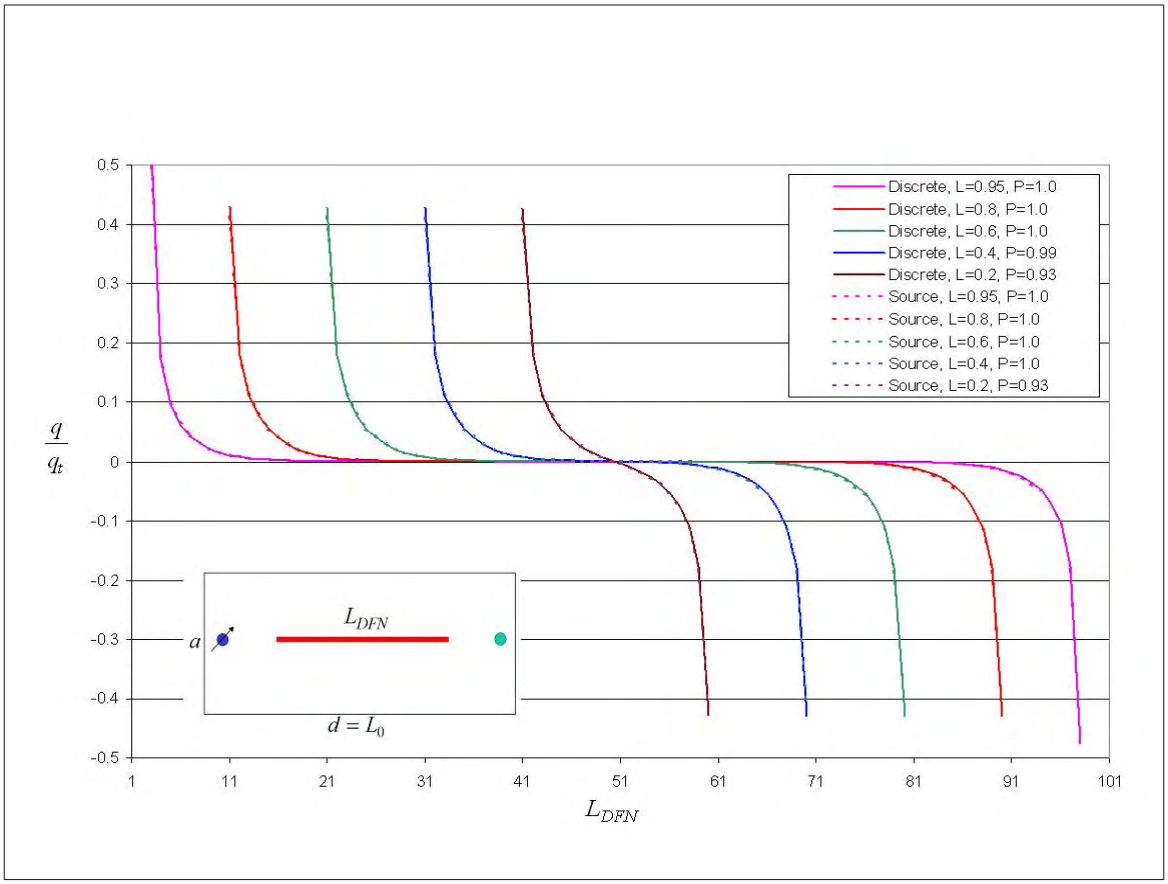

Fig. 8.50: Flux distribution for isolated DFN, FCD=100, d/a=10

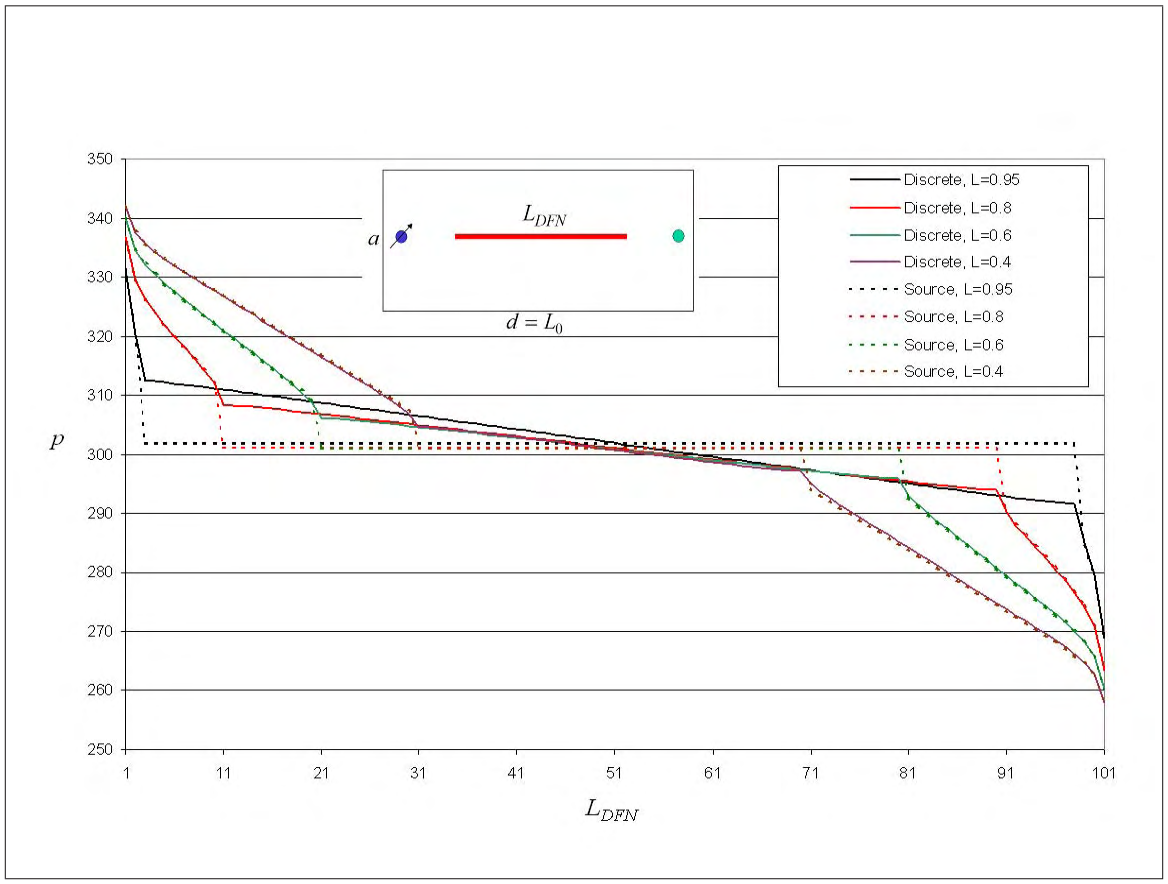

Fig. 8.51: Pressure distribution for isolated DFN, FCD=1, d/a=10

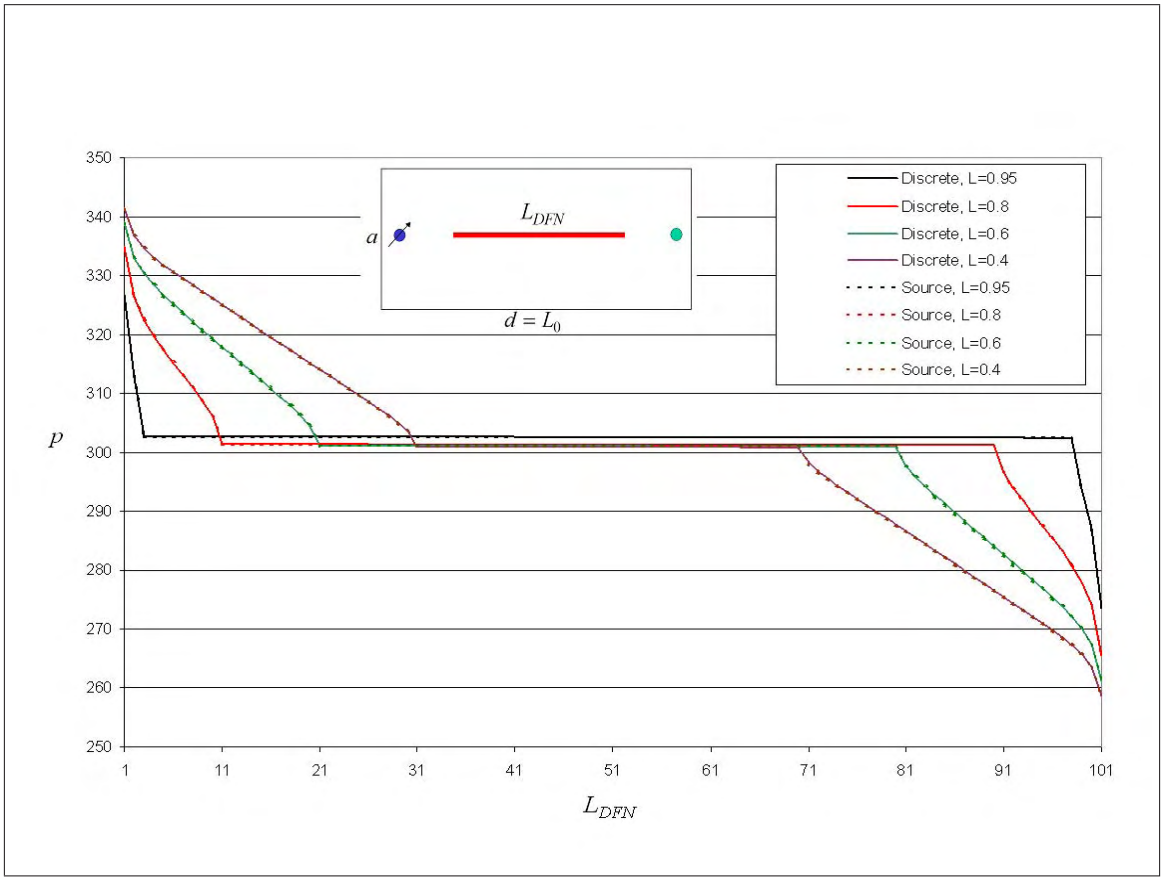

Fig. 8.52: Pressure distribution for isolated DFN, FCD=100, d/a=10

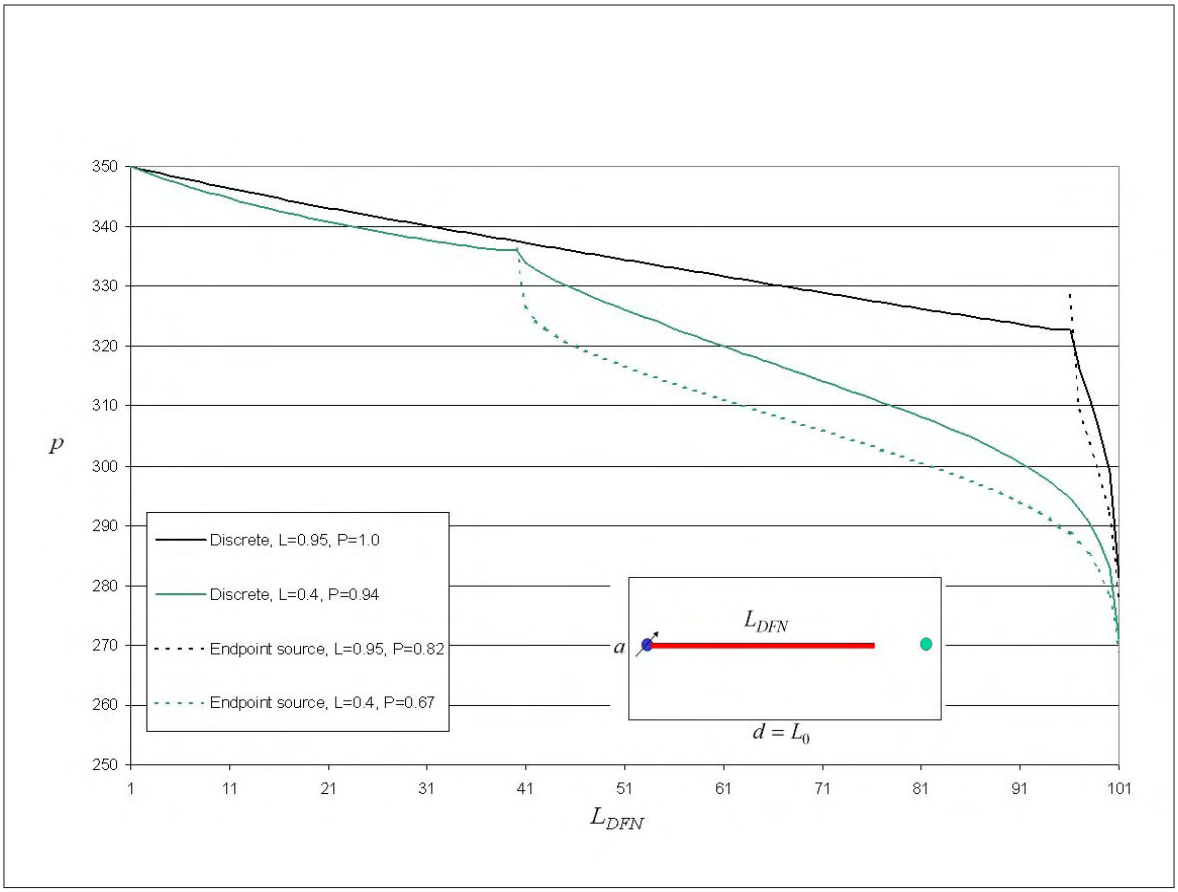

Fig. 8.53: Pressure distribution for connected endpoint DFN, FCD=1, d/a=2

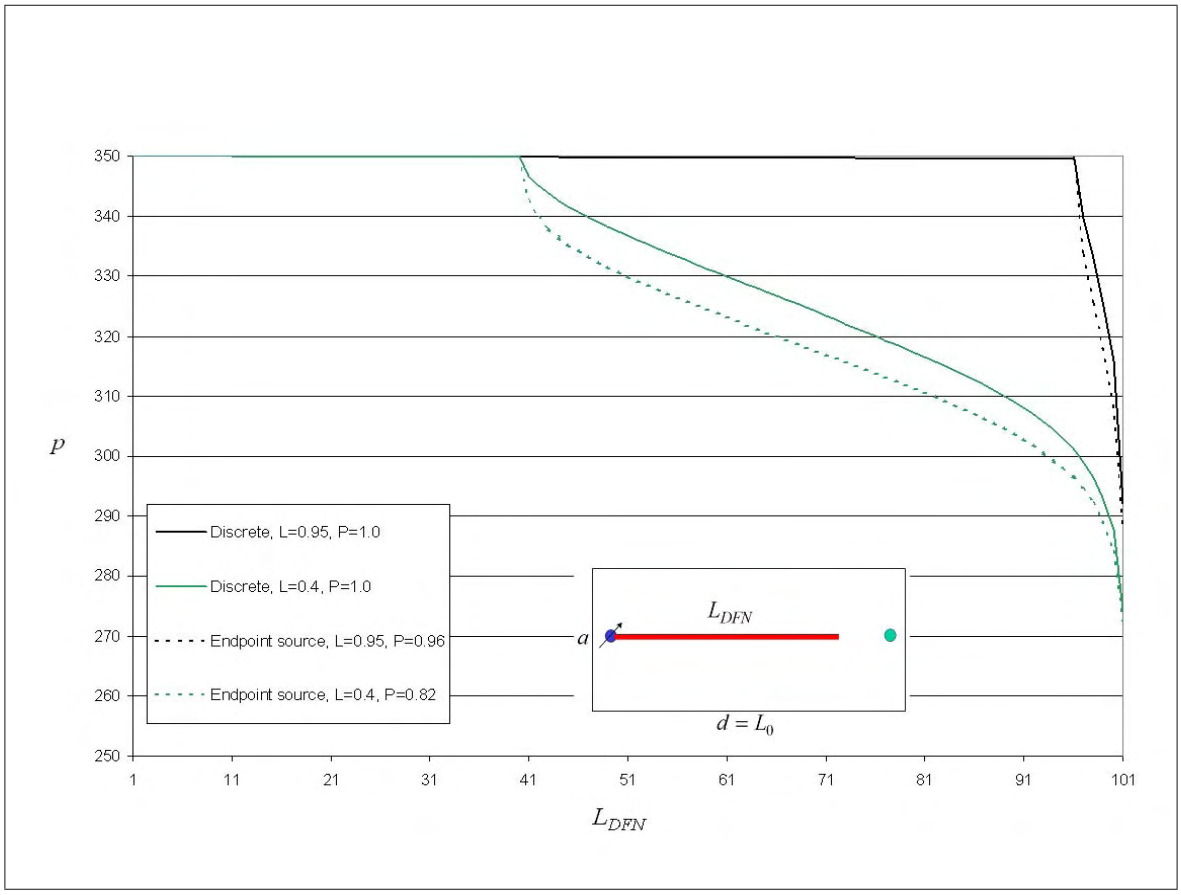

Fig. 8.54: Pressure distribution for connected endpoint DFN, FCD=100, d/a=2

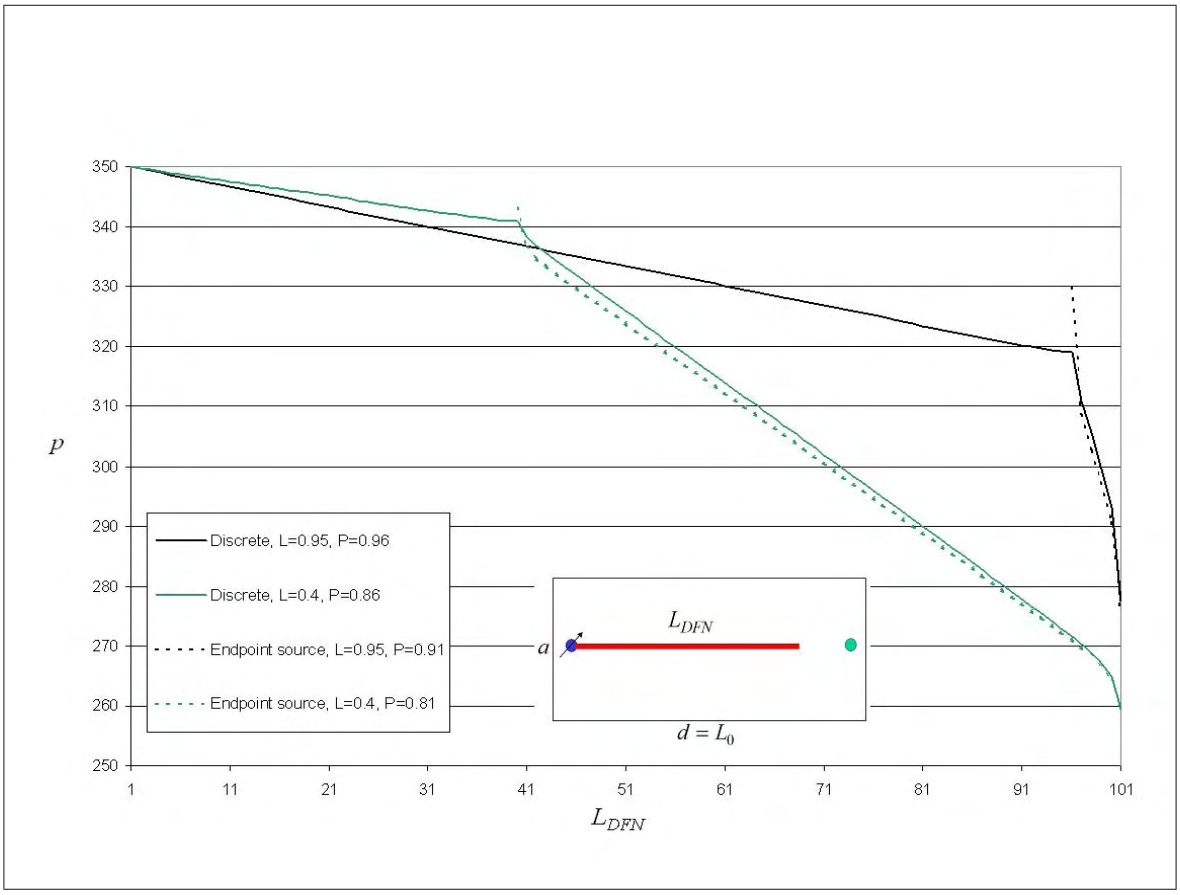

Fig. 8.55: Pressure distribution for connected endpoint DFN, FCD=1, d/a=10

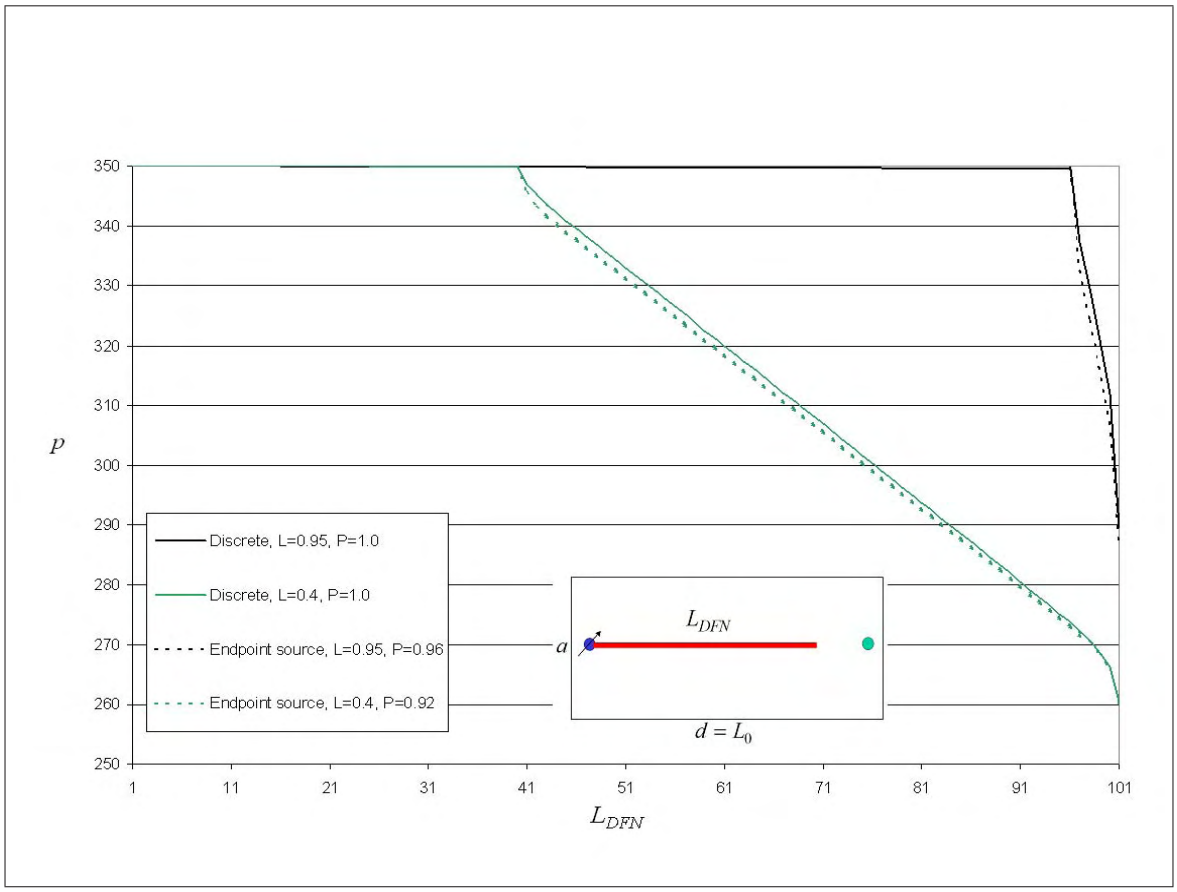

Fig. 8.56: Pressure distribution for connected endpoint DFN, FCD=100, d/a=10

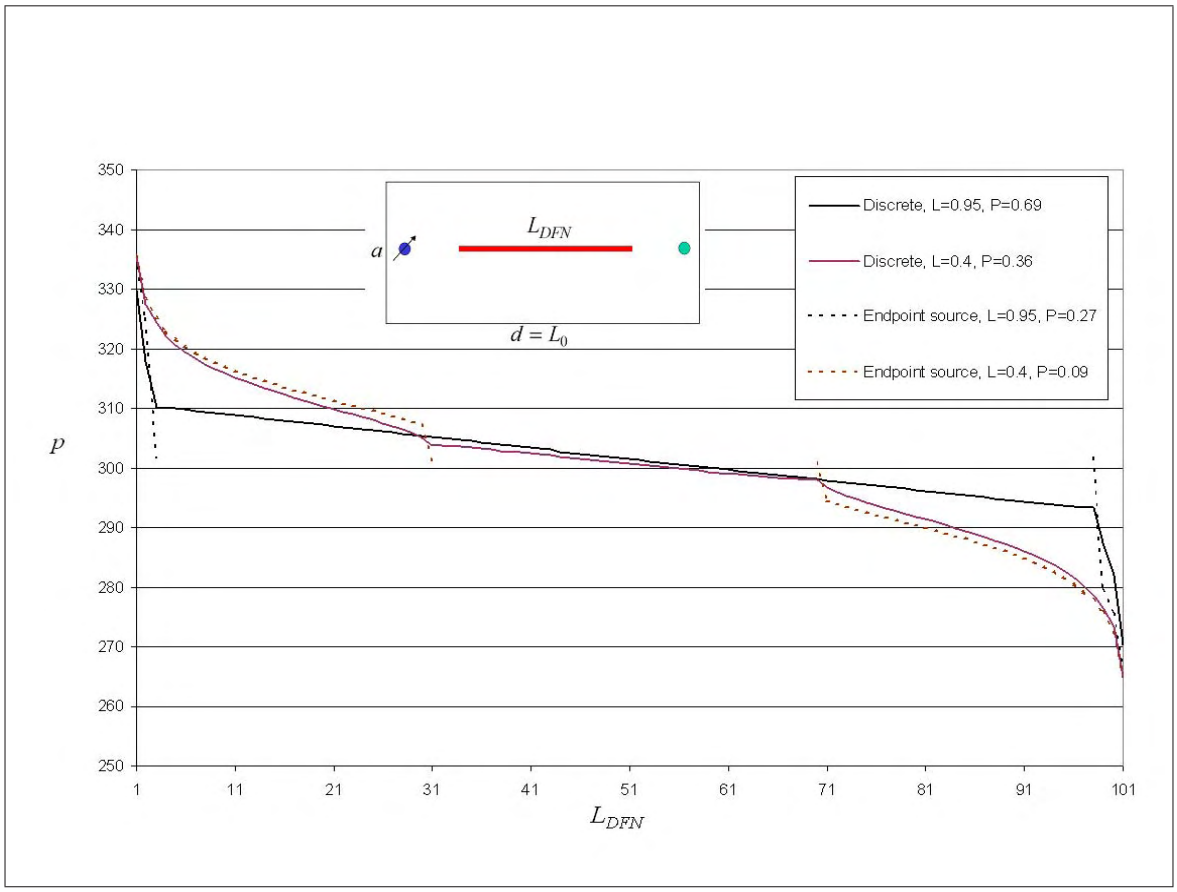

Fig. 8.57: Pressure distribution for isolated endpoint DFN, FCD=1, d/a=2

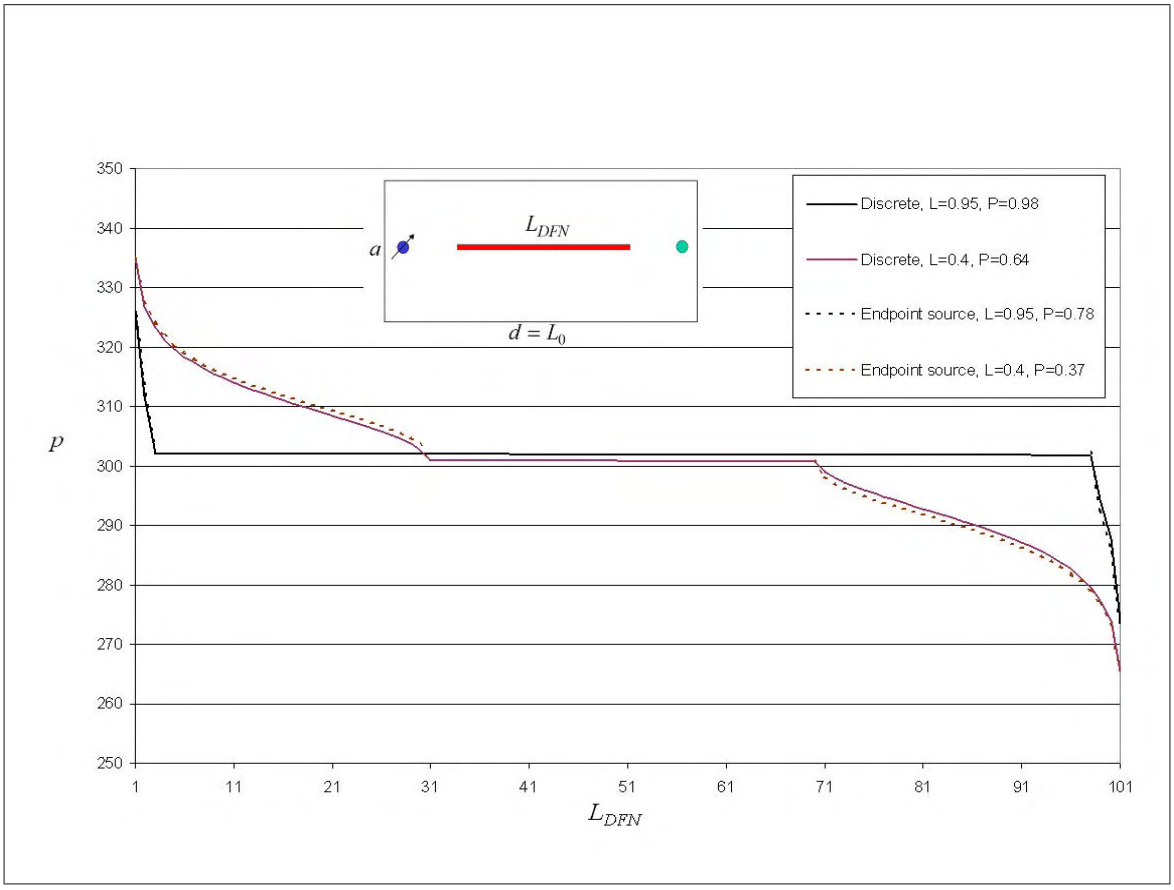

Fig. 8.58: Pressure distribution for isolated endpoint DFN, FCD=100, d/a=2

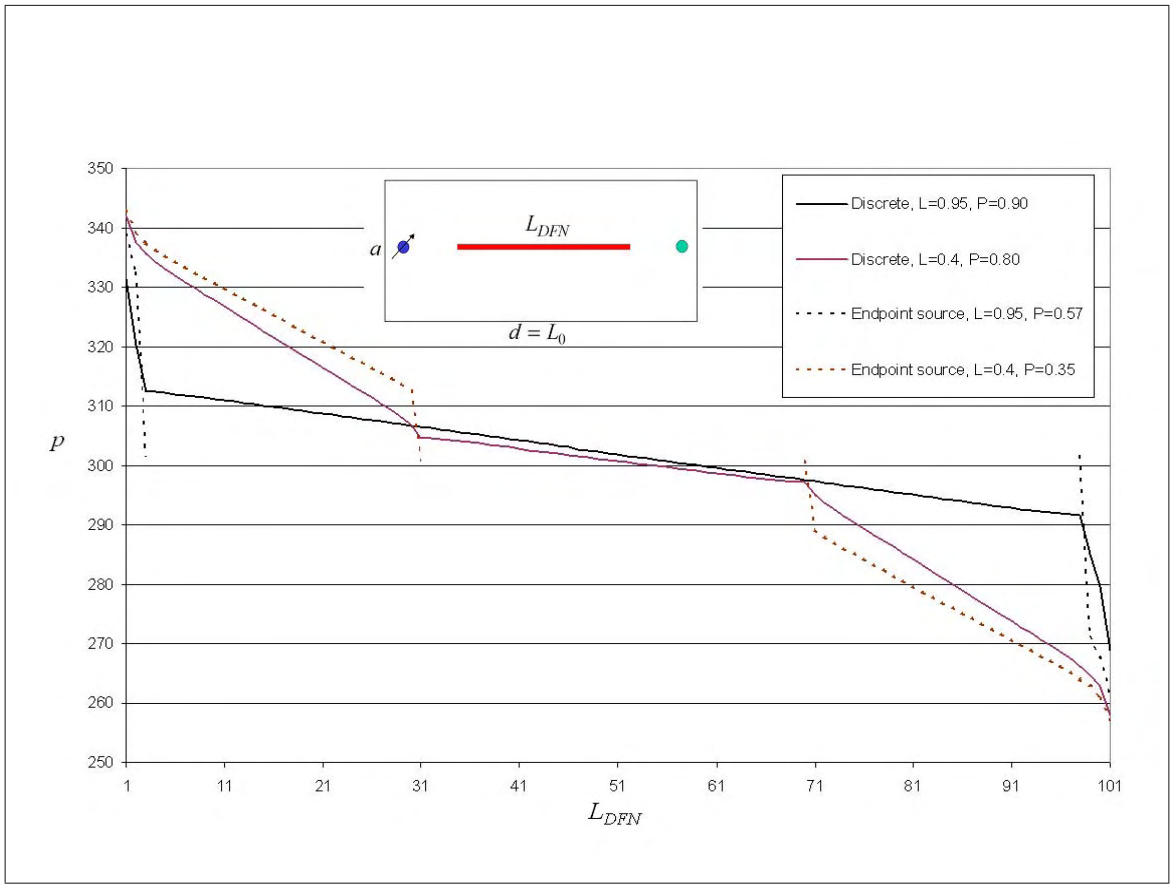

Fig. 8.59: Pressure distribution for isolated endpoint DFN, FCD=1, d/a=10

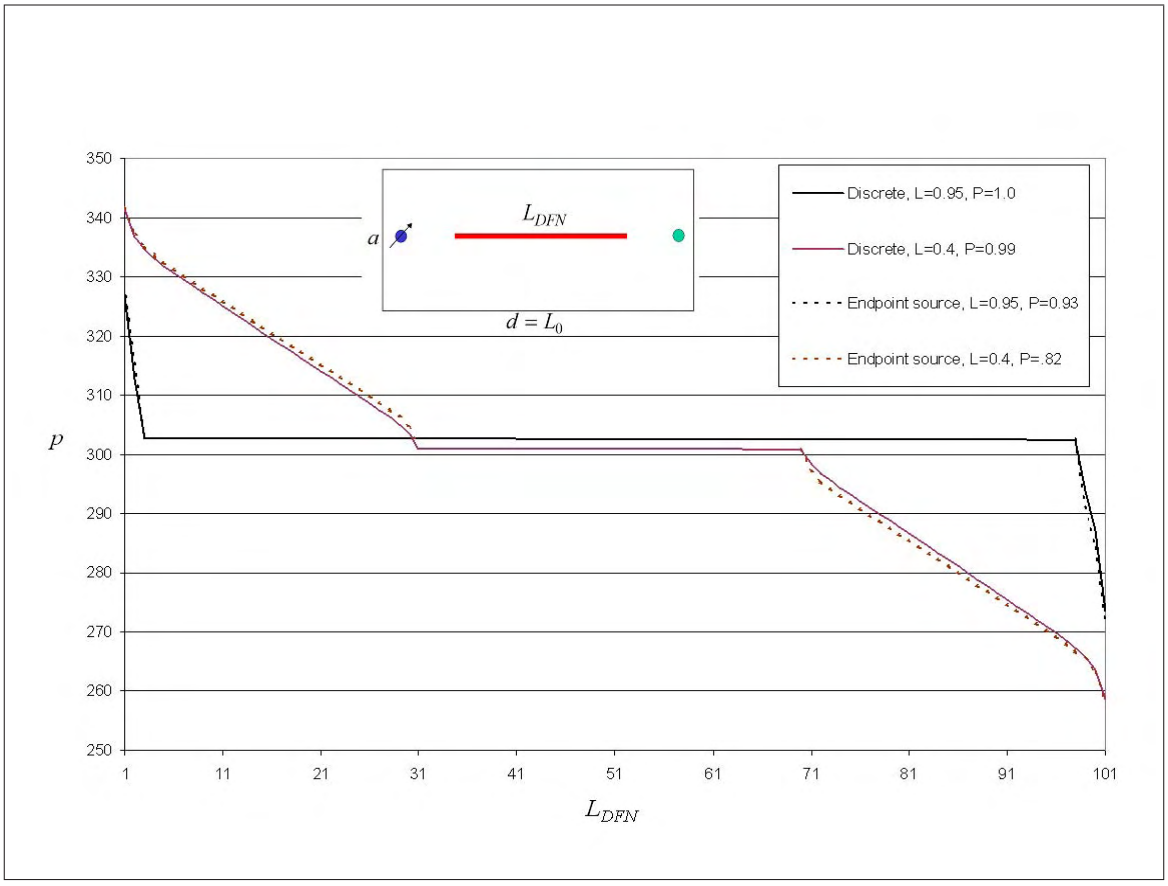

Fig. 8.60: Pressure distribution for isolated endpoint DFN, FCD=100, d/a=10

Chapter 9

The static reservoir model

This chapter describes a static DFN model, developed in this thesis work as an element of the production history matching algorithm. The model, DISCFRAC, is described in detail in this chapter, complete with an implementation guide, using standard GSLIB input formats.

This static DFN model is simple, object -based, and serves our purpose in constructing a complete history matching algorithm that stochastically generates DFN realizations and practically incorporates them into flow simulation using the source model. It is emphasized that this static model is not intrinsic to the algorithm. *Any* static DFN model which includes a facility that transfers DFN maps into source connection maps, may be used in place of DISCFRAC. The static model may be derived from any non-dynamic data, or from a geomechanical model. Alternatively, the DISCFRAC connection mapping algorithm, which is very sound, may be used alone; the static DFN model, no matter the derivation, may be mapped to the object-based model presented here, which will then be subsequently efficiently transferred to a source map.

9.1 DISCFRAC: An object-based static DFN model

Fig. 9.1 presents a *GOCAD* rendering of a realization of DISCFRAC. The model is constructed without a grid; the 3D grid shown is a flow simulation grid, upon which

the DFN model is superimposed. The grid corresponds to that used in the study: $32 \times 12 \times 60$. The vertical exaggeration is approximately 200.

The planar objects represent DFNs, with varying azimuths, plunge, lengths, and vertical thicknesses. There are 28 such networks in this example. One of the networks, colored black, is represented as an intersection of two planes. This network will be examined in more detail. Also shown are production and injection well traces, with well connections marked with small spheres. The well paths and connection locations are plotted as they exist in the flow simulation grid.

The cube markers in Fig. 9.1 indicate the upper and lower extents of the vertical intervals over which flow simulation transmissibility connections are placed. For example, a pair of markers on the end of a plane indicates that transmissibility connections are placed at those locations, as well as all grid blocks in a vertical line between the markers. These connection markers are placed at various points, described in detail in Chapter 7:

1. terminal points of planes,
2. intersection points of planes,
3. points of intersection of planes with the grid boundary,
4. points on the planes near to production or injection wells,
5. points on planes near other DFN planes.

These connections are shown as they are mapped onto the simulation grid, and therefore coincide with simulation blocks.

The planes, in some instances, extend outside the boundary of the flow simulation grid. Transmissibility connections are, however, placed at points where the planes pierce the boundary, and therefore the effective terminal points of the network are at the boundary, and not beyond.

An *ECLIPSE* well file, shown in Fig. 9.2 is generated by the model; this well file is included into the *ECLIPSE* general input file.

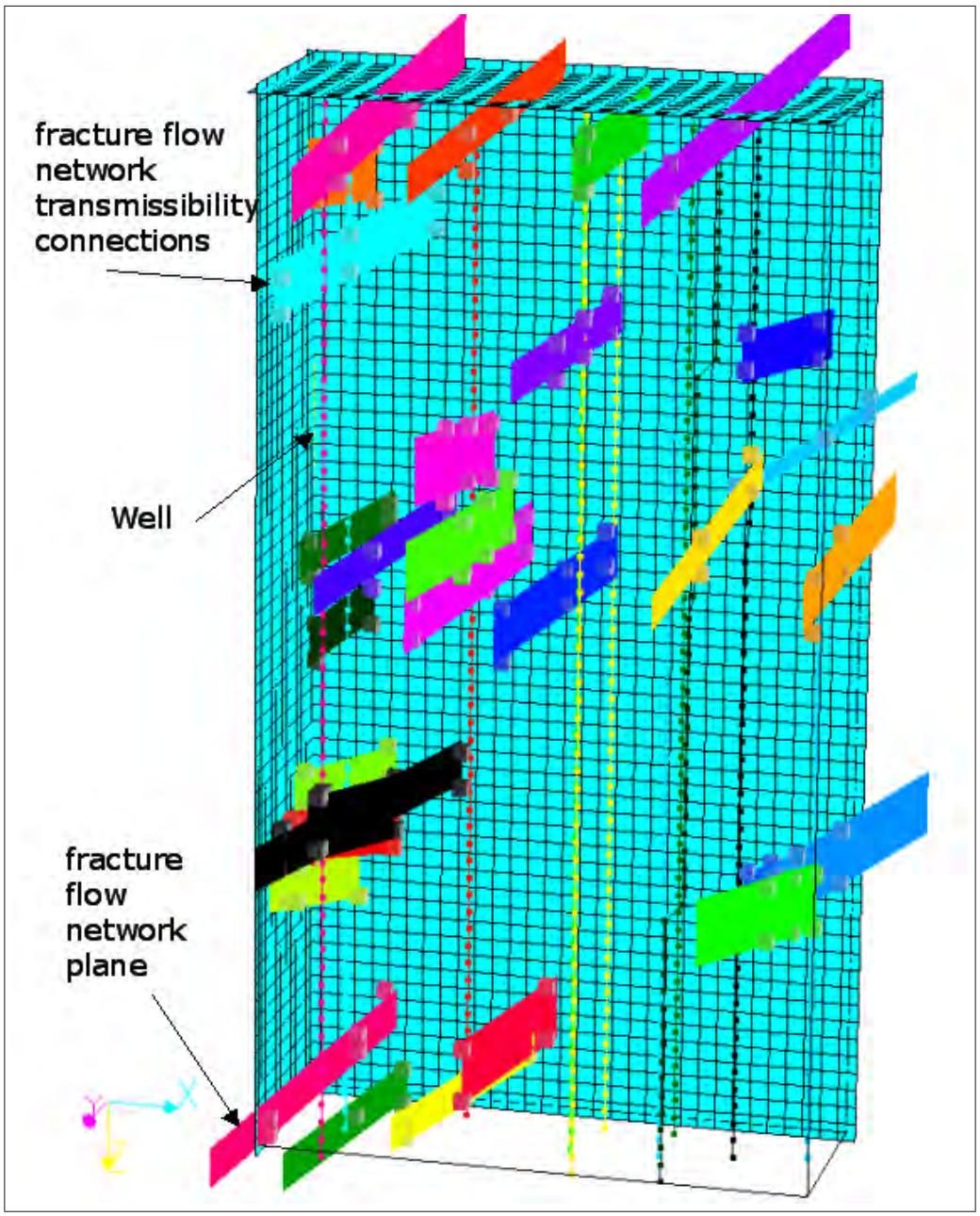

Fig. 9.1: DISCFRAC realization

This feature, generation of a flow simulation well file, is a necessary module for any DFN model, if the source model is chosen to simulate flow through DFNs. Otherwise, the DFN model has no other restrictions.

```
                                        File : ECLIPSE well
WELSPECL
'F     1' 'FRAC' 'LGR1'   2   8 1* 'LIQ' 2* 'STOP' 'YES' /
/
COMPDATL
'F     1' 'LGR1'    2   8   11   13 3*  1.0   3*     'Z'  2.71828183   /
'F     1' 'LGR1'    6   4    7    9 3*  1.0   3*     'Z'  2.71828183   /
'F     1' 'LGR1'    4   6    9   11 3*  1.0   3*     'Z'  2.71828183   /
/
WPIMULTL
'F     1'  12.000000000 /
/
WCONPROD
'F     1'  'OPEN'  'LRAT'  3*  0.  /
```

Fig. 9.2: ECLIPSE well output file

```
                                    Parameters for DISCFRAC
                                    ***********************
START OF PARAMETERS:
regions                             -region file name
data                                -data file name
wells                               -well file name
32  12  60                          -flow simulation grid dimensions; x,y,z
833.33   833.33    4.17             -grid block dimensions (consistent units)
10                                   -total number of fracture networks
4000.    10000.                     -fracture network length range (low high, consistent units)
8.   16.                            -fracture network vertical thickness range (low high, consistent units)
30.    60.                          -fracture network azimuth range (low  high, degrees cc from north )
0.  .25                             -fracture network plunge range (low high,degrees downward from horizontal)
1  1  2                             -x,y,z tolerances(block units) for neighbor networks and wells
fileout                             -output root name for GOCAD files
```

Fig. 9.3: DISCFRAC parameter file

9.1.1 Model input

The parameter file, Fig. 9.3, shows the input for the program *DISCFRAC*, the DFN model. The format of the file follows the *GSLIB*[35] convention, as does all of the input files to be described here. The model computations will be explained in the context of this parameter file.

DISCFRAC distributes planes stochastically within the volume of the 3D flow simulation grid, according to a total number of planes specified by the user, and a regional proportion, also specified by the user. Therefore, within a region defined by the user, the number of fractures will equal the specified region proportion of the total. The region description, as well as the region proportion, is specified in the region file, here named "regions," and shown in Fig. 9.4. Regions are specified using

file : regions

```
Region definition
2
Region number
Region  fracture network proportion
3    0.7000000
```

Fig. 9.4: Region definition file

file : data

```
Super-k data
3
Well number
Z location
Super-k indicator
47   24     0
47   25     1
```

Fig. 9.5: Super-k data file

the flow simulation grid, with a region number and proportion given to each grid block.

As described in Sec. 7.2.5, *DISCFRAC* conditions DFNs to observed flowmeter indications of super-k flow in production or injection well intervals. The super-k data file, here named "data," and shown in Fig. 9.5, specifies the locations of observed super-k, again using the flow simulation grid as a reference.

Production and injection wells are input in the well file, named "wells," in this example, Fig. 9.6. Note that the well coordinates are input using *ECLIPSE* format, which is different from the GEO-EAS format used in *GSLIB*. The *ECLIPSE* format follows the standard flow simulation format, with X increasing East, Y increasing South, and Z increasing down. The input of the well data using this format allows the user to input well coordinates directly from the *ECLIPSE* input data file.

The flow simulation grid dimensions are input next. This input defines the volume within which DFNs will be placed, and allows the mapping of the DFNs connections into the flow simulator.

Flow simulation grid block dimensions are then input, to provide for proper scale for the later specification of DFN dimensions. The units selected for this input must be the same as that for the fracture dimension inputs.

file : wells

```
Production/injection well locations (Eclipse format)
 4
 X
 Y
 Z top
 Z bottom
 Well number
 4      6      1      47
```

Fig. 9.6: Production and injection well data file

The total number of fractures is input. This number, along with the regional proportion input, determines the number of fractures placed in each region.

The next four sets of input specify the ranges of distributions for the random drawing of length, vertical thickness, azimuth, and plunge of DFN planes. The drawing currently occurs on uniform distributions within these ranges. The units of these ranges must be the same as that specified for the flow simulation grid block dimensions.

The tolerances for which connections are placed in proximity to production and injection wells, and other DFN planes, is then input. Fracture network planes which approach wells or other planes within these tolerances, input in flow simulation block units, will have fracture connections generated in the plane, at points nearest to the object of interest.

9.1.2 Model output

Finally, *GOCAD* output files are given the root name as input on the last line of the parameter file. There are four *GOCAD* output files generated for each realization:

1. A *GOCAD* object file containing the plane surfaces of isolated DFNs, that is, those which did not arise from intersections. This file is named simply, **root**.

2. An object file containing the transmissibility connection markers (the cubes in Fig. 9.1). This file is named **root.**wells.

3. An object file containing the plane surfaces DFNs formed from intersections. This file is named **root**.int

4. An object file containing the transmissibility connection markers for the DFNs formed from intersections. This file is named **root.**intwells.

9.1.3 Intersections of planes

Mere intersection of planes does not generate DFN intersections resulting in a single network in hydrostatic equilibrium. Geologically, two DFNs may intersect without forming a single flow conduit, due to the fact that the complexity of fracture systems persist to extremely fine scales, including the scale over which the intersection zone occurs. Assuming hydrostatic equilibrium with every intersection, does not recognize this persistence of complexity. Therefore, when two planes intersect in the model, the occurrence of hydrostatic equilibrium between the two is modeled stochastically from a distribution determined by the geometry of the intersection itself. The probability P that equilibrium occurs is assumed to be proportional to the fraction of intersection length to combined planar thickness length,

$$P = \frac{h_{int}}{h_1 + h_2 - h_{int}}$$

where h_{int} is the length of intersection, and h_1 and h_2 are the thicknesses of the two intersecting planes.

9.1.4 Examples of transmissibility connection placement

Fig. 9.7 shows a view facing west, of the realization presented previously. It is seen that connections are placed where the planes pierce he flow simulation grid boundaries, even though the planes may extend outside the grid.

Fig. 9.8 presents examples of connections arising from planes near wells and planes near each other. Note for example, the green plane and the blue well, and the two orange planes and the two orange wells. An example of a connection arising from nearness to another DFN is the green plane near the purple plane.

Fig. 9.9 presents the DFN formed by an intersection. Here it is seen that the intersection thickness is large relative to the total thickness, so the probability of hydrostatic equilibrium, described in Sec. 9.1.3, is large, resulting in a single DFN.

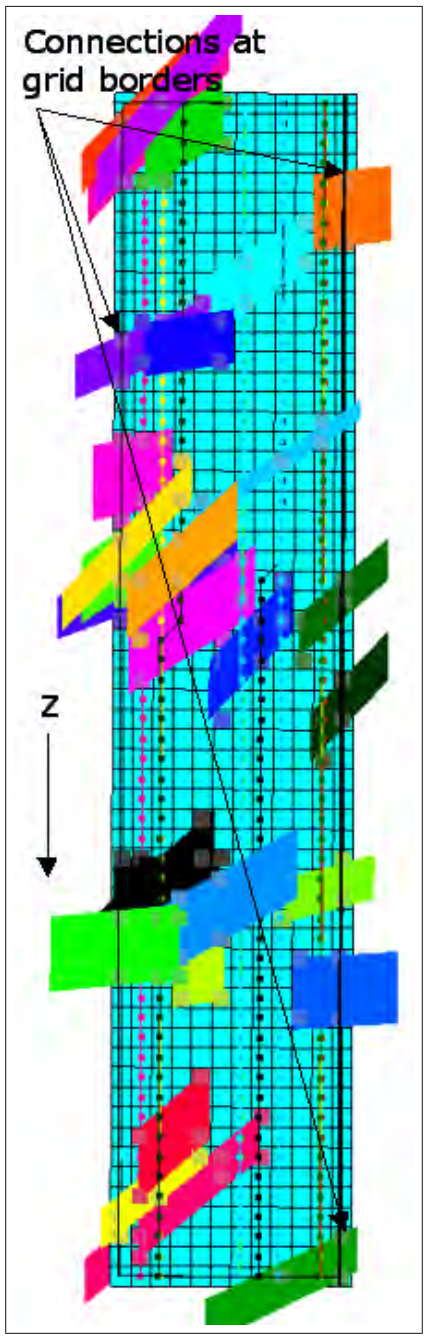

Fig. 9.7: Connections at grid borders

Note the connection markers at the terminal points of the planes. The pair of markers which do not coincide with the edge of the plane extending from left to right, correspond to piercings of the plane with the grid boundary. Note finally the markers

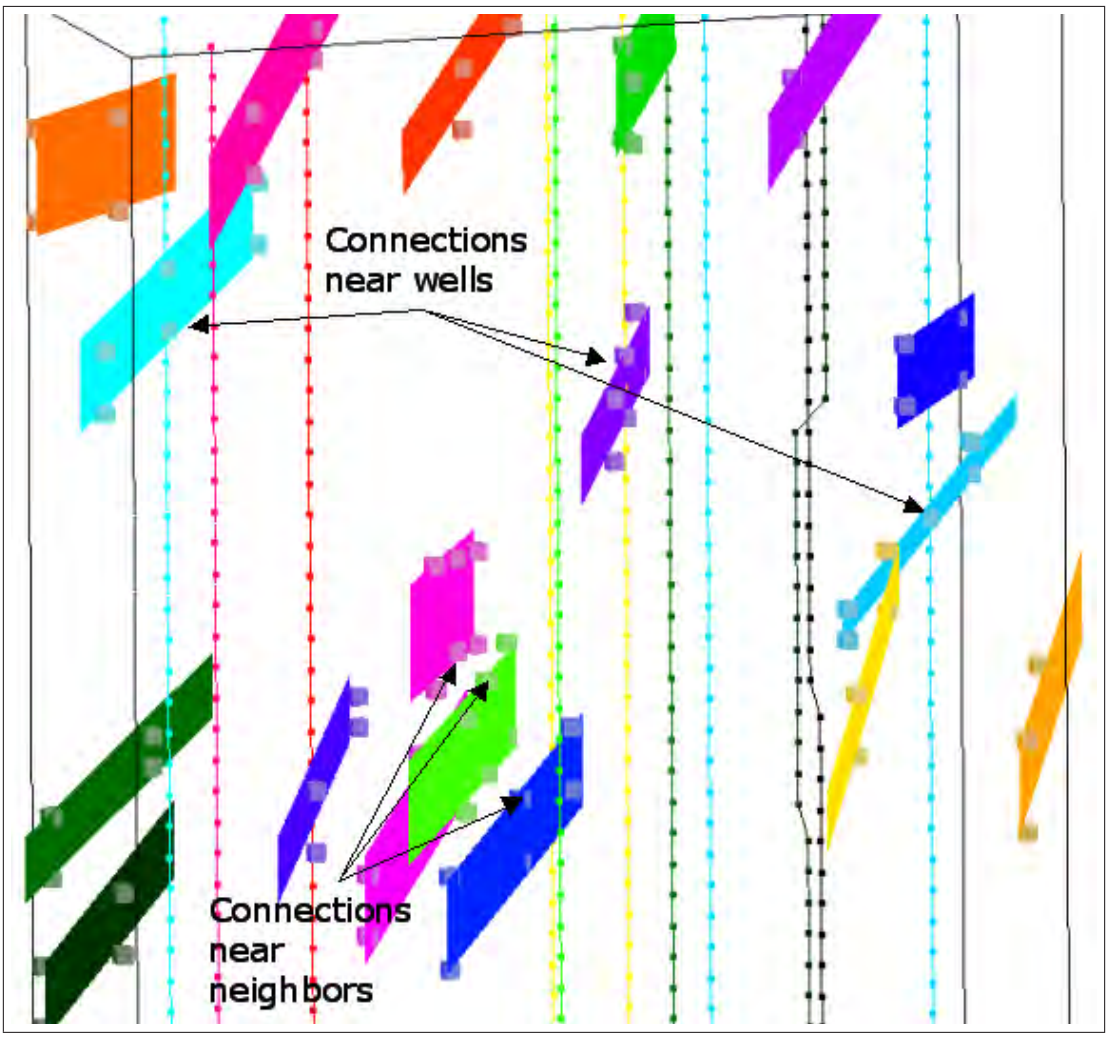

Fig. 9.8: Near-well and near-neighbor connections

coinciding with the green well, and the absence of markers at the intersection. This results from the fact that these two sets of markers occupy the same simulation blocks. The absence of markers on the red well is due to the large distance of the well from the network.

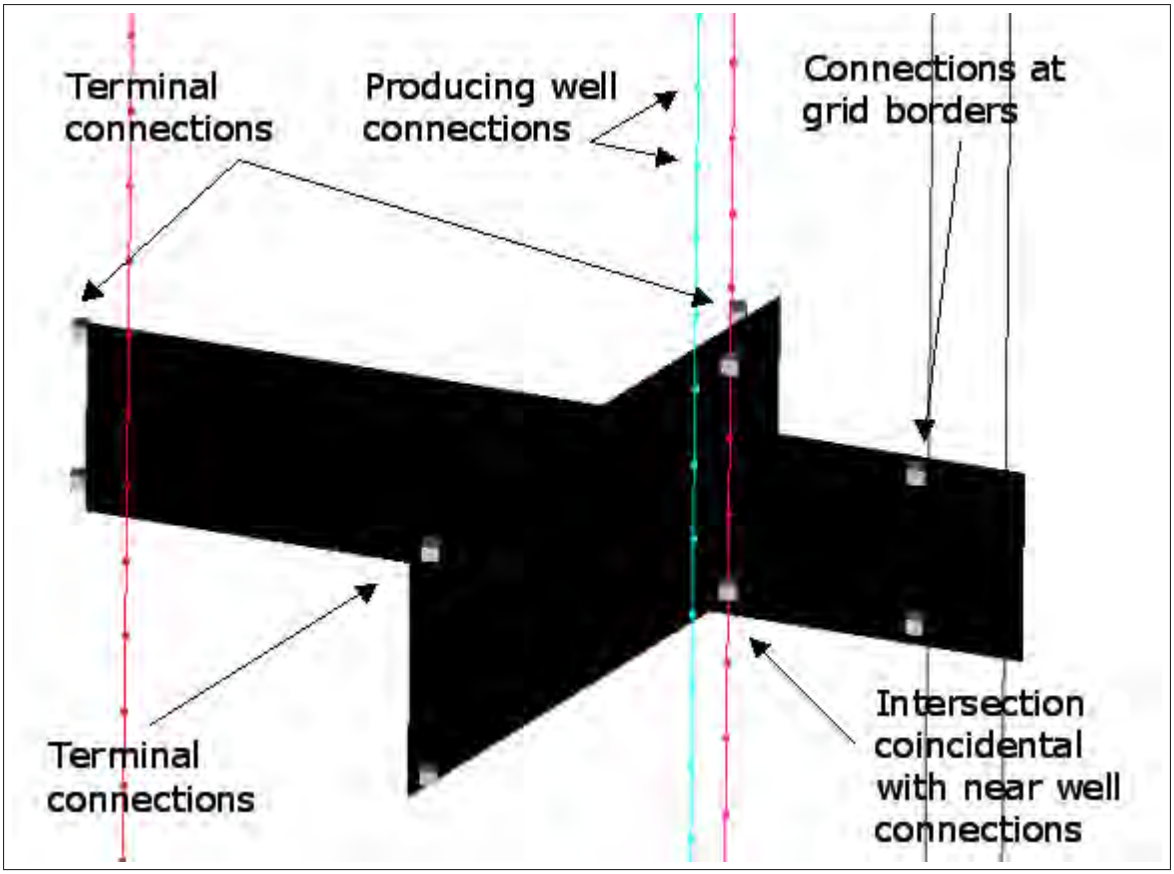

Fig. 9.9: Fracture network generated from an intersection

Chapter 10

Workflow and study area modeling results

We present the reservoir flow effect of the variation of DFN parameters, and a description of our history matching workflow, as applied to the Ghawar study area, in this chapter. We demonstrate the ability of the source model, as generated with our static DFN model, to simulate the flow effects of DFNs on both well performance, and flowmeter performance, relative to that observed in study area wells.

Our general history matching algorithm optimizes DFN parameters through minimization of simulation error relative to flowmeter and well performance data.

It is emphasized that these results are not history matches, but rather results from a DFN parameter sensitivity study. History matching is practically impossible at this point in time, as the DFN static models are not sufficiently constrained by geologic data. Specifically, 3D seismic data is not available currently, although we hope to receive it in the future, at which time practical history matching studies may be performed.

It is further emphasized that our history matching algorithm is a complete tool, in that both, facies, and DFN, perturbation may be performed, toward the minimization of flow simulation error of either, or both, well performance and flowmeter data.

Facies perturbation is performed independently from DFN perturbation; we do not have the capability in this algorithm to perturb them jointly. We acknowledge,

however, that DFNs and facies may correlate well, and that a joint perturbation may be more geologically realistic. This capability may be considered as relevant future work.

The DFN perturbation technique is described in this chapter; the facies perturbation method, probability perturbation,[74] is demonstrated in Appendix F. Facies perturbation was employed in previous studies (Appendix F,Sec. 6.4); we perturb only DFN parameters in this study, as the previous studies ended with the conclusion that facies-only super-k models are incapable of predicting observed super-k flow effects. We therefore investigate the effects of DFN parameters, exclusively, on reservoir flow performance. The facies portion (Sec. 10.2.1) of the reservoir model, is therefore frozen in this sensitivity study.

10.1 Workflow

The results of our sensitivity study demonstrate the variation in the models generated by our workflow, and the variation in the flowmeter and well performance predictions which result from flow simulations on the reservoir models. Parameters which can be perturbed in the algorithm include:

1. DFN density, by region,
2. individual DFN location,
3. DFN azimuthal orientation,
4. DFN length.
5. DFN vertical thickness,
6. DFN declination (plunge).

Generally, DFN connection transmissibility may also be considered an optimization parameter; however, we have chosen not incorporate the ability to perturb this parameter, into our algorithm, as strict values of this parameter are practically defined

for reservoirs in which DFN flow is important. Specifically, the infinite conductivity DFN is, practically, the most reasonable type of DFN to model, as described and developed in Sec. 8.3.3. Therefore, only infinite conductivity DFNs are generated by the static model, and more specifically, only isolated DFNs, those not connected to wells, are generated. As described in Sec. 8.3.3, this type of DFN generates a moderate flow effect on well performance. Thus, the results presented here, although adequately demonstrating the significant flow effects of DFNs, are conservative: even more profound effects, for instance from selecting a subset of DFNs to be strictly of the connecting type, may be generated. However, as recalled from Sec. 8.3.3, the connecting DFN variety is realized under conditions in which water injection wells possess inadvertent hydraulic fractures, which connect to natural DFN systems, or under conditions in which DFNs are known to directly intersect wells, say as inferred from borehole image logs, or from well tests that prove large negative well skin effects. As neither of these conditions are evident in our study area (the data is not available, or simply does not exist), we have chosen to restrict DFN models to the isolated type.

The DFN parameters are perturbed independently. As with the joint perturbation of facies and DFNs, we acknowledge that DFN parameters may also be strongly correlated, and that geological reality may be better maintained with joint perturbations. We again assign this work to future research.

A single facies model is first constructed for the study, and subsequently, each generation of a complete reservoir realization requires the following key steps:

- construction of a DFN realization using the DFN static model,
- generation of a map of connections from the DFN realization,
- imbedding of the connections map and the facies permeability map into the flow simulation grid,
- flow simulation of the combined realization.

The facies portion of the reservoir model is constrained to the following:

- facies data at each well as determined from well logs

- global facies proportions, inferred from well logs

These static facies constraints are honored by the training image algorithm.

The algorithm employs a stochastic simulation, with DFN parameter perturbation achieved with gradual deformation of drawing number sequences[32]. The history matching utilization of the algorithm, not employed in this sensitivity study, optimizes the parameters through minimization of prediction error in production data. In this case the perturbations are performed within a scalar optimization, achieved with the Brent algorithm[36]. Specifically, the production data of interest is flowmeter, and well performance, data. Well performance data (Sec. E.2) consists of flowing well block pressures, assumed to model well 24-hr bulid-up pressures, and oil, gas and water rates. The flow simulation is constrained by total reservoir volume rates, computed by combining observed rates of the three phases at reservoir conditions.

Flow simulation in this study computes 25 years of production from the study area, as well as flowmeter surveys, from eight wells. A total of 19 flowmeter surveys were conducted at various times during the producing history of the study area. We limit the evaluation of flowmeter results to only eight surveys to maintain a reasonable work load. The flowmeter surveys chosen for this study include those which demonstrate the most severe examples of super-k flow, and encompass the entire producing history of the study area.

Flow simulation duration varies from 30 to 120 minutes. The variation in computation time is derived from variation in convergence properties incurred by the source model; this behavior is discussed further in Appendix B. The duration of construction of each reservoir realization, the combined facies / static DFN model, is tens of seconds.

10.1.1 Fracture flow network realizations

We first present an example DFN static model to illustrate the DFN construction portion of the workflow, before proceeding onto the full application of the workflow in the sensitivity study. The example model specifies 3 regions, each with a fixed proportion, or density, of DFNs, out of a total fixed number, in this case, 20. The

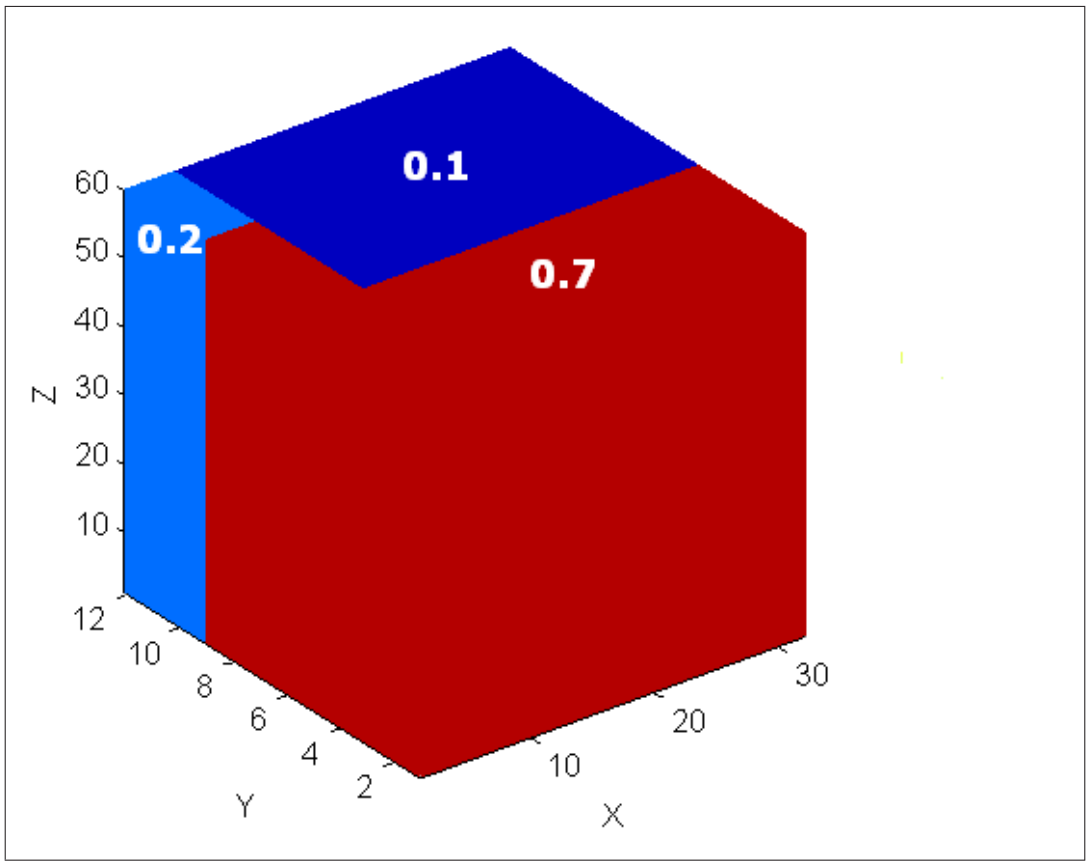

Fig. 10.1: DFN density: red, 0.7, light blue, 0.2, dark blue, 0.1

regions vary only laterally, with the specified network proportion applied to the entire thickness of the reservoir. Generally, however, a region may be defined as any volume in the reservoir, as defined by partitions of the flow simulator grid. The regions must not overlap, however; furthermore, the union of the regions must be the entire flow simulation grid. No data currently is used to constrain regional proportions, as might be accomplished with 3D seismic data; the constraints given here are made only as a demonstration of the region capability. Fig. 10.1 shows the region distribution, chosen arbitrarily, having the following DFN density proportions: red, 0.7, light blue, 0.2, dark blue, 0.1.

DFN parameter ranges are as follows for this example (lengths in ft):

- DFN length range: 1000 - 10000,

- DFN thickness range: 8 - 16,
- DFN azimuth range: 60 - 80^o,
- DFN declination range - 0 - 0.25^o.

The DFN static model is incorporated into the study area flow simulation grid, having dimensions $26,667 \times 10000 \times 250\ ft$ $(8km \times 3km \times 75m)$. Note that the declination range is very small, as the geometry of the reservoir, having a very small vertical aspect relative to the other dimensions, dictates the restriction.

Fig. 10.2 through Fig. 10.6 present five realizations of the model. Here, all DFN parameters are allowed to vary, within the ranges specified.

Shown within the reservoir flow simulation grid, which has a vertical exaggeration of 200, are planes representing DFNs, and markers representing transmissibility connections. The locations of these connection markers are exported to an *ECLIPSE* data input file, as well specification data, so as to enable the well model to simulate flow in the DFNs. Also shown are production and injection wells, represented as curves, also having connection markers. See Chapter 9 for a complete description of the DFN model.

Note in Fig. 10.2 that conditioning of networks to two wells occurs in the model. The well on the west side is an injection well, and on the east, a producing well. The conditioning can be seen in all five realizations.

Finally, Fig. 10.7 is a plan view a static DFN realization, to show that the distribution of networks honors the regional proportions. As expected, the networks are concentrated in the southern half, and in the northwest, and are sparse in the north to northeast.

10.2 The combined facies/DFN model

The reservoir model to be used for flowmeter history matching, incorporates proposed essential elements of the reservoir facies and of the super-k network:

- A grainstone which serves as the connection of the network to the well,

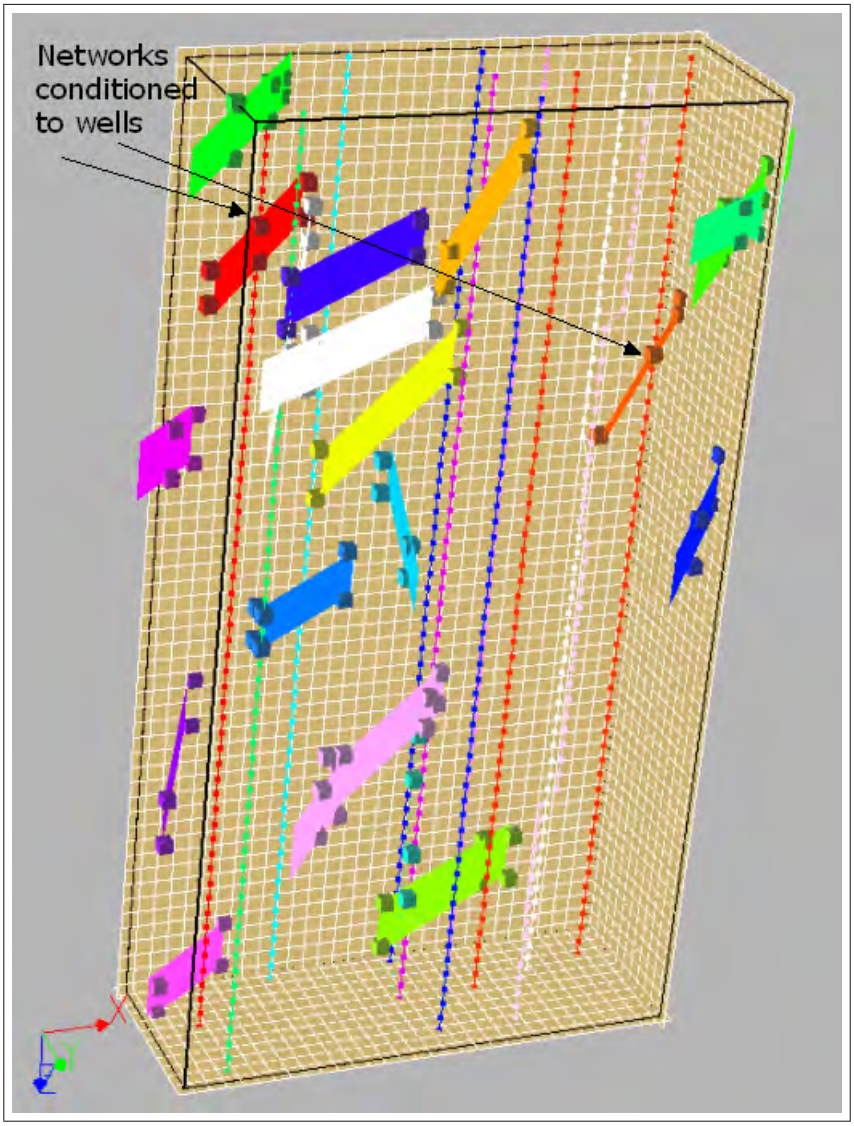

Fig. 10.2: Example static DFN realization

- One or more DFNs which serve as the principle flow conduit of the network,

- A very high permeability facies,

- Background facies, which comprises the complement of the elements described in the three points above.

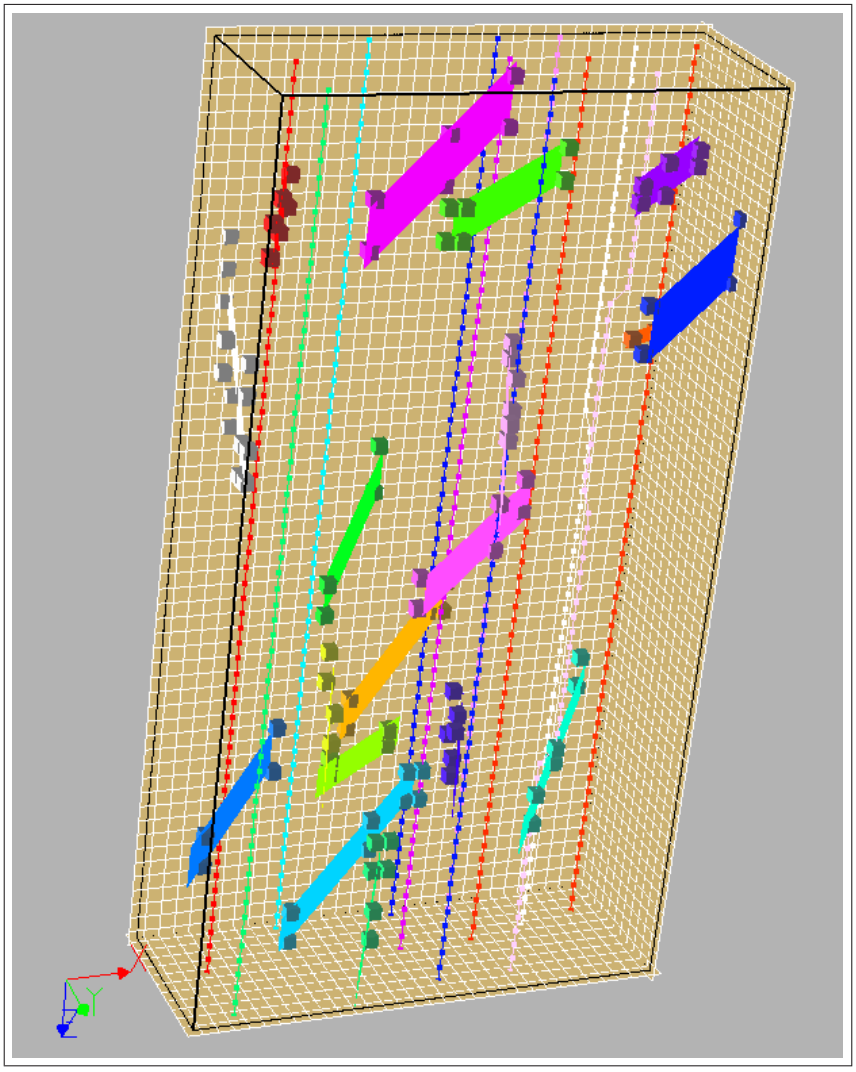

Fig. 10.3: Example static DFN realization

The third element may comprise various Arab-D lithologies, including grainstones, sucrosic dolomites, and leached dolomites, but are characterized specifically by extremely high permeability, in areally limited bodies. We refer to them as "super-k beds," conforming to old terminology which originated in facies-only super-k models. It is a misnomer, as our current super-k model does not expressly incorporate them. We keep the label only for convenience, to differentiate these facies from grainstone facies which serve as super-k network connections to wells, and which do not necessarily possess extremely high permeabilities. We previously included such facies in

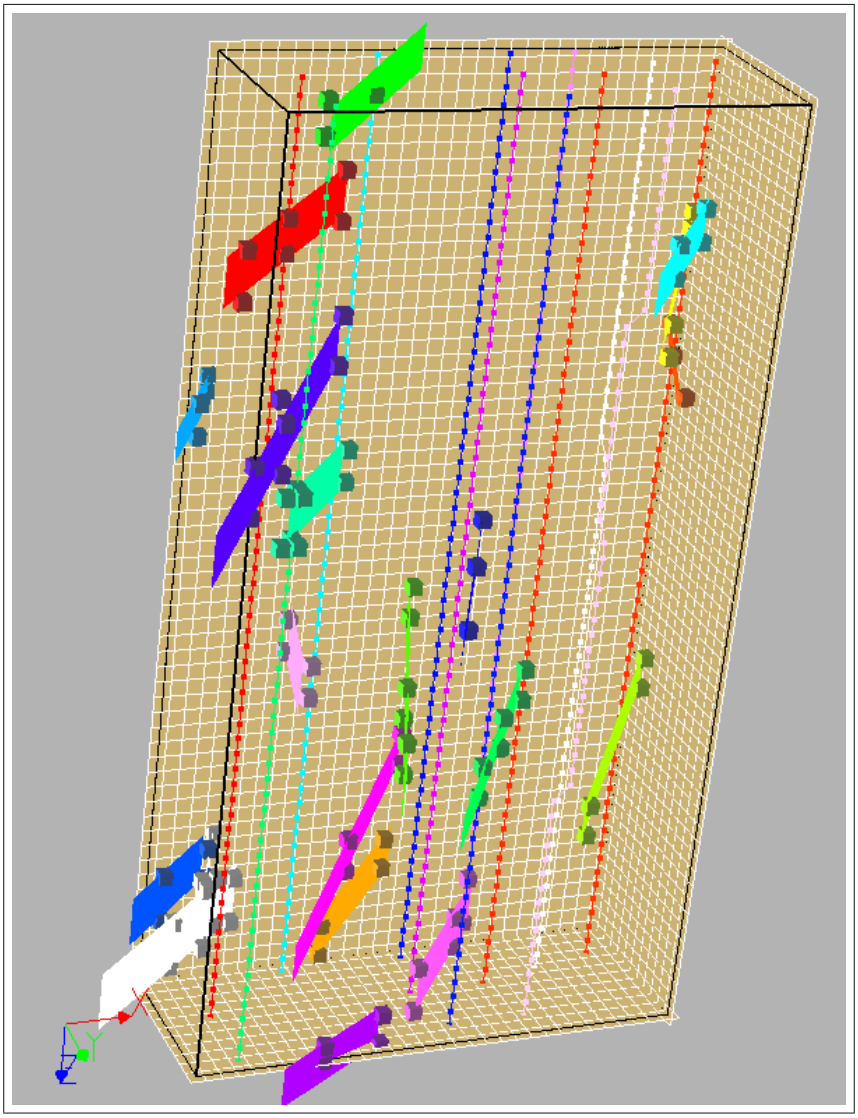

Fig. 10.4: Example static DFN realization

our previous attempts to predict super-k behavior with facies-only reservoir models (Sec. 6.4, Appendix F).

Previous super-k models have also directly associated DFNs, and high permeability beds at the terminal regions of DFNs , away from wells, and shown that this type of system may affect flowmeter performance[30]. The current model does not necessarily associate the two, as we have concluded this association is sufficient to

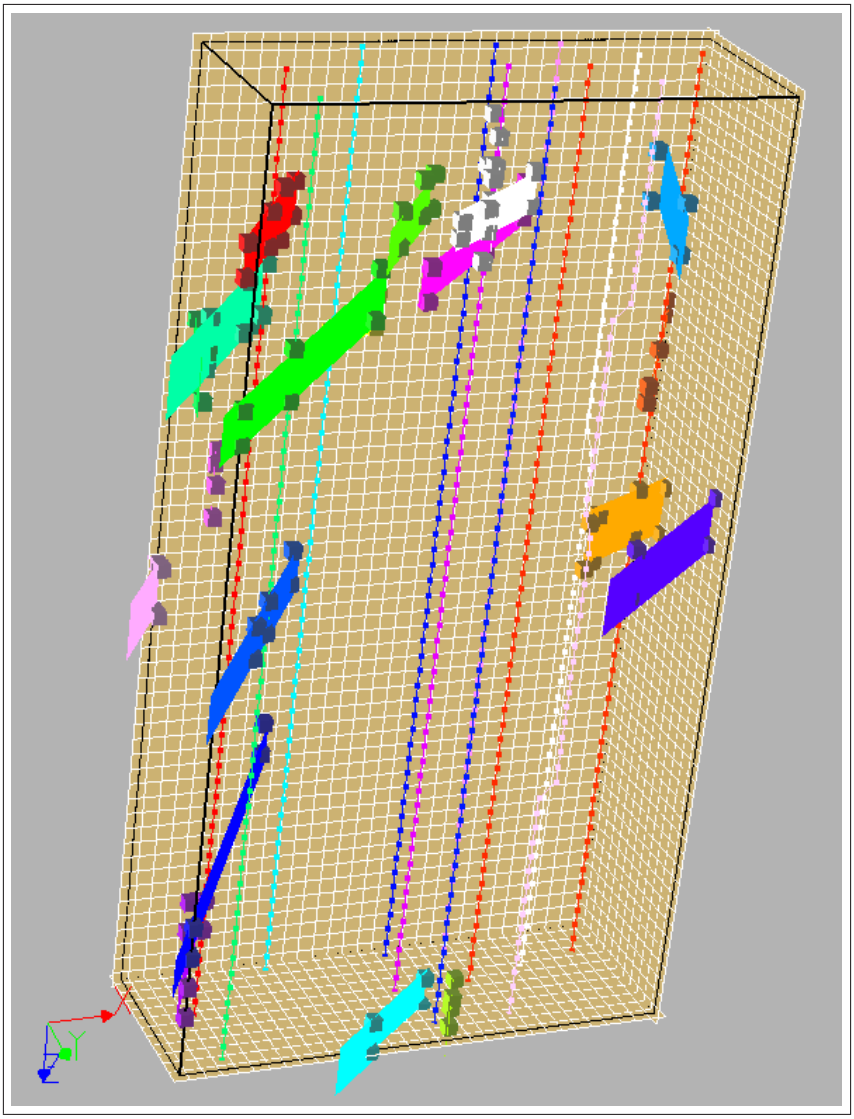

Fig. 10.5: Example static DFN realization

invoke super-k flow, but not strictly required in our study area. Nevertheless, the occurrence of the super-k beds, if not conditioned to DFNs, are ineffectual to flowmeter performance, as shown in Sec. 6.4 and Appendix F. They therefore may be added to the facies model without affecting its efficacy. We reserved this facies component so as to remain constrained by the geology of the Arab-D, which is known to possess super-k facies, in a reasonably small proportion, generally less than 20%.

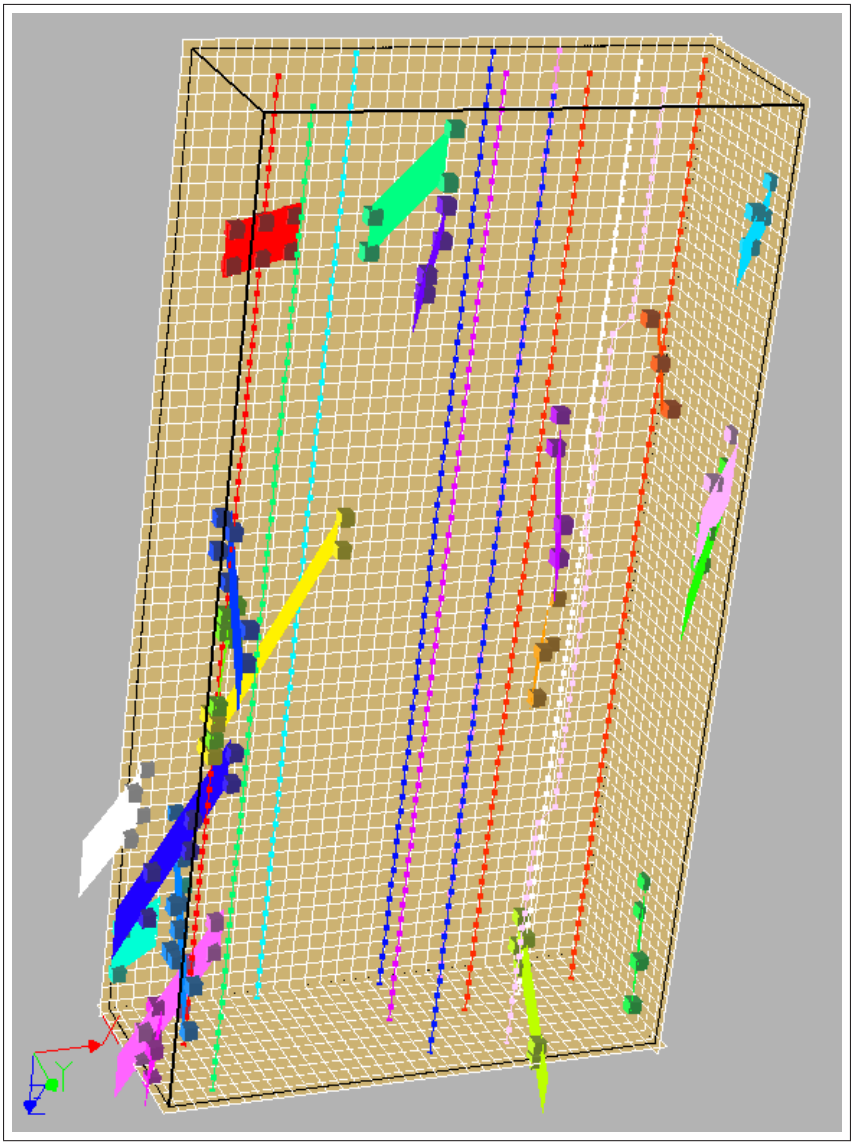

Fig. 10.6: Example static DFN realization

The combined model is composed, therefore, of a facies model, and a DFN model. Realizations of the facies model are generated using multiple point statistics borrowed from training images (Appendix F). The DFN model is incorporated subsequently.

Reservoir simulations were conducted on the Cartesian grid shown in Fig. 10.8. The flow simulation grid is also shown in Fig. 10.8. As mentioned above, both grids are discretized with the same dimensions, 32 x 12 x 60. The flow simulator is an

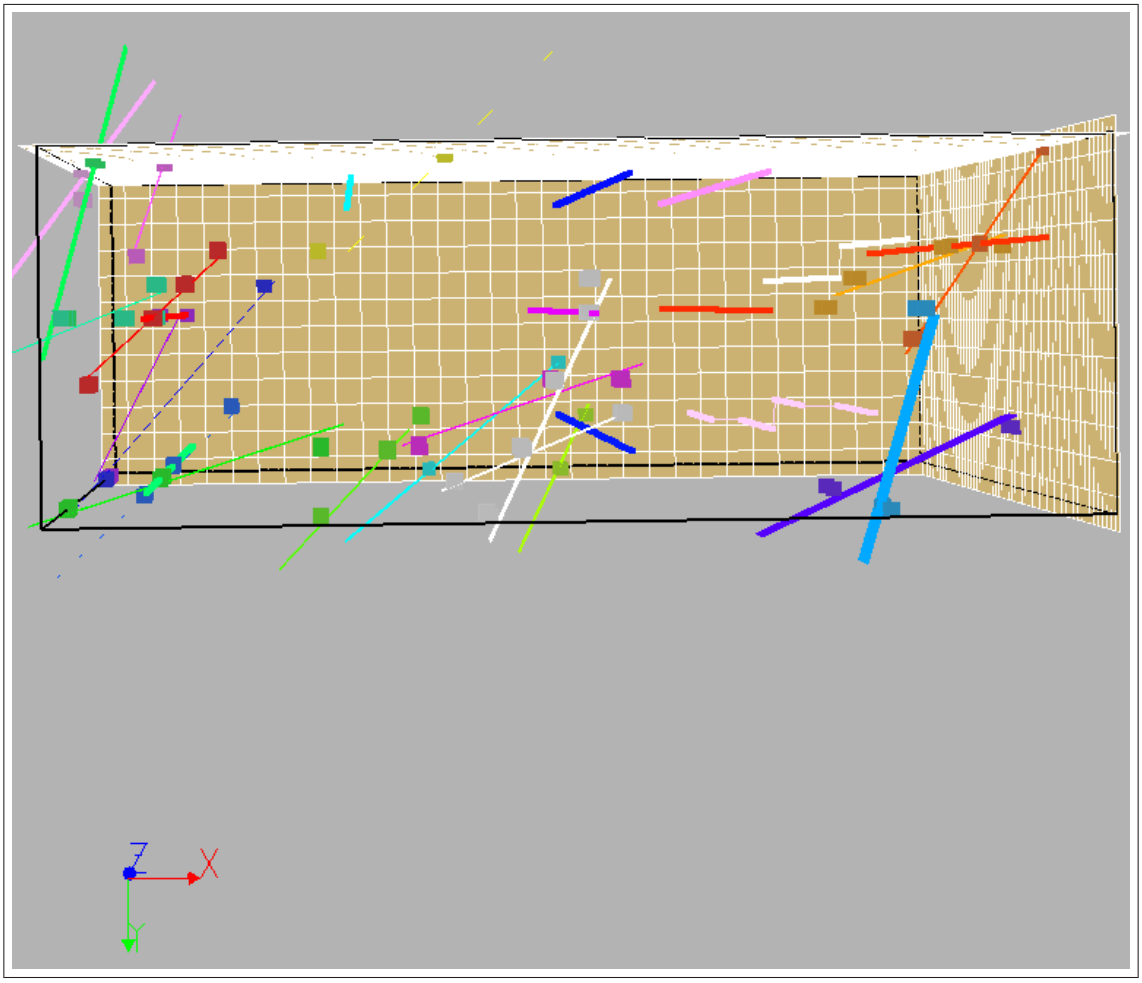

Fig. 10.7: Top view of a realization, showing regional DFN density

ECLIPSE black oil model.

10.2.1 The facies model

The reservoir model is generated from developments in multiple-point (MP) geostatistics. MP geostatistics relies on a so–called training image to represent a proposed geological heterogeneity. A training image depicts, in 3D, the geological model believed to represent the reservoir. Training images need not be constrained to any data; hence, Boolean techniques are well suited to construct them. Little information is available for Ghawar and the study area, about the size and shape of grainstone or

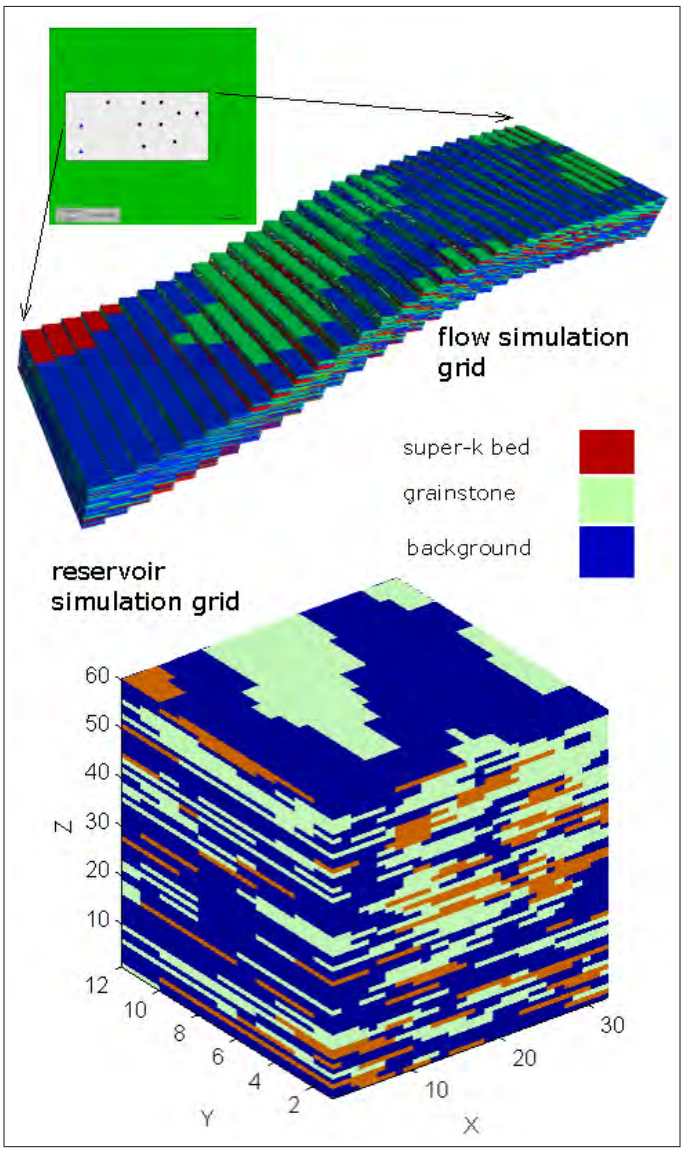

Fig. 10.8: Reservoir and flow simulation grids

super-k bed bodies. Therefore, the training images used in this study contain simple, elliptical shapes.

MP geostatistics is a cell-based technique, and replaces the variogram with the geologically richer, training image. A practical algorithm called SNESIM[31] has been developed that captures geological heterogeneity in terms of MP geostatistics, then anchors the model to measured data such as well log and core data.

The facies model is constructed in two stages, using two separate models. One model is derived from MP geostatistics from a training image of super-k bed distribution. Recall super-k beds may reside with a variety of lithologies. Therefore it was felt that a separate super-k element of the facies model, having a distribution independent of that of grainstone, provided for a more appropriate reservoir model.

The super-k training image is binary and resembles the realization shown in Fig. 10.9. The net-to-gross (N/G), or proportion, of super-k bed is 0.18 in this model. This proportion was provided by SA geologists, and is an estimate of the proportion of the highest permeability volumes in the deposit. The super-k bed element is assigned a permeability of 5000 md.

The second facies model, called the grainstone model, is derived from three training images. Each of the three training images generates a model corresponding to a certain depth interval, with N/G proportions of grainstone given in Fig. 10.9. These proportions were derived from well log analysis of nine wells, and core analysis from one well. The grainstone facies was assigned a permeability of 2000 md. This value was derived from the cored well. The complement of grainstone, previously defined as background, essentially all other facies excluding super-k beds, was assigned a permeability of 300 md, again based on the cored well results.

The facies model is derived from these two models by imbedding the super-k beds into the grainstone model. This model is then kept constant throughout the generation of combined facies\DFN models for this sensitivity study. An example realization of the final facies model is shown in Fig. 10.9.

10.3 DFN parameter sensitivity results

The DFN parameter sensitivity study generated investigations in six major categories: DFN density, location, length, azimuth, declination, and vertical thickness. Results indicate that of these categories, variation in declination realizations has the least effect on either well or flowmeter performance, and the effect of variation in DFN vertical thickness is modest to insignificant. The remaining four categories demonstrate significant ability to effect reservoir flow performance, although not universally. We

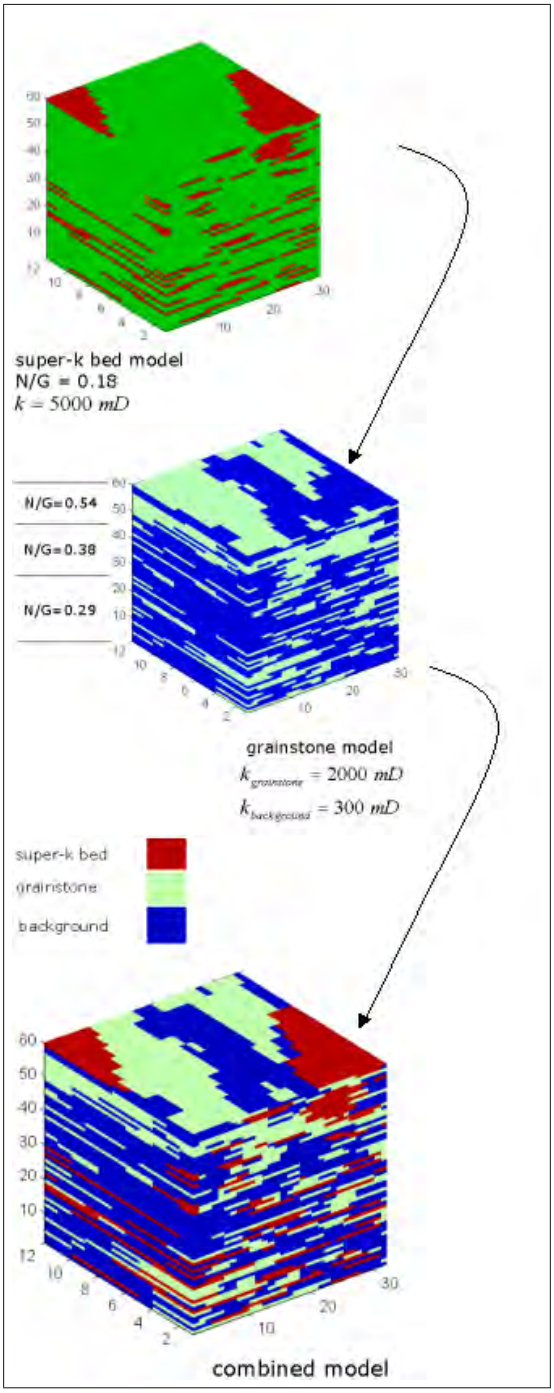

Fig. 10.9: The facies model

will review the effects of each DFN parameter in turn.

Appendix A contains the well performance and flowmeter plots chosen to be extracted from this study. We take the most illustrative examples from that appendix, in describing the most significant effects, or lack thereof, of the various DFN parameters.

10.3.1 DFN regional density

We chose to investigate two DFN region density cases, each comprised of three regions, shown in Fig. 10.10. The regions are vertical partitions of equal volume, dividing the study area volume into thirds. The first case, called Region Case 1, is comprised of the middle region having 80% of the total DFNs, with the remaining DFNs split between the other two regions. The second case, Region Case 2, places 80% of the DFNs in the southern region, with the other two regions splitting the remaining DFNs. This partitioning was based on the distribution of wells in the study area, under the assumption that well performance effects would be distinctly different in the two cases, given such a partition. A DFN region and well map is presented in Fig. 10.11. Note that the areas emphasized by each case, that is the middle and southern regions, are each characterized by the presence of a water injection well. Therefore, increased DFN densities in these two regions should magnify the effect of water injection on the well and flowmeter performance of producing wells in the respective regions.

Ranges of the remaining DFN parameters are as follows for the DFN density region sensitivity evaluation (lengths in ft):

- DFN length range: 6500 - 36000 (approximately 8 to 43 flow simulation grid blocks),
- DFN thickness range: 8 - 16 (approximately 2 to 4 flow simulation grid blocks),
- DFN azimuth range: 85 - 90^o,
- DFN declination range - 0 - 0.25^o.

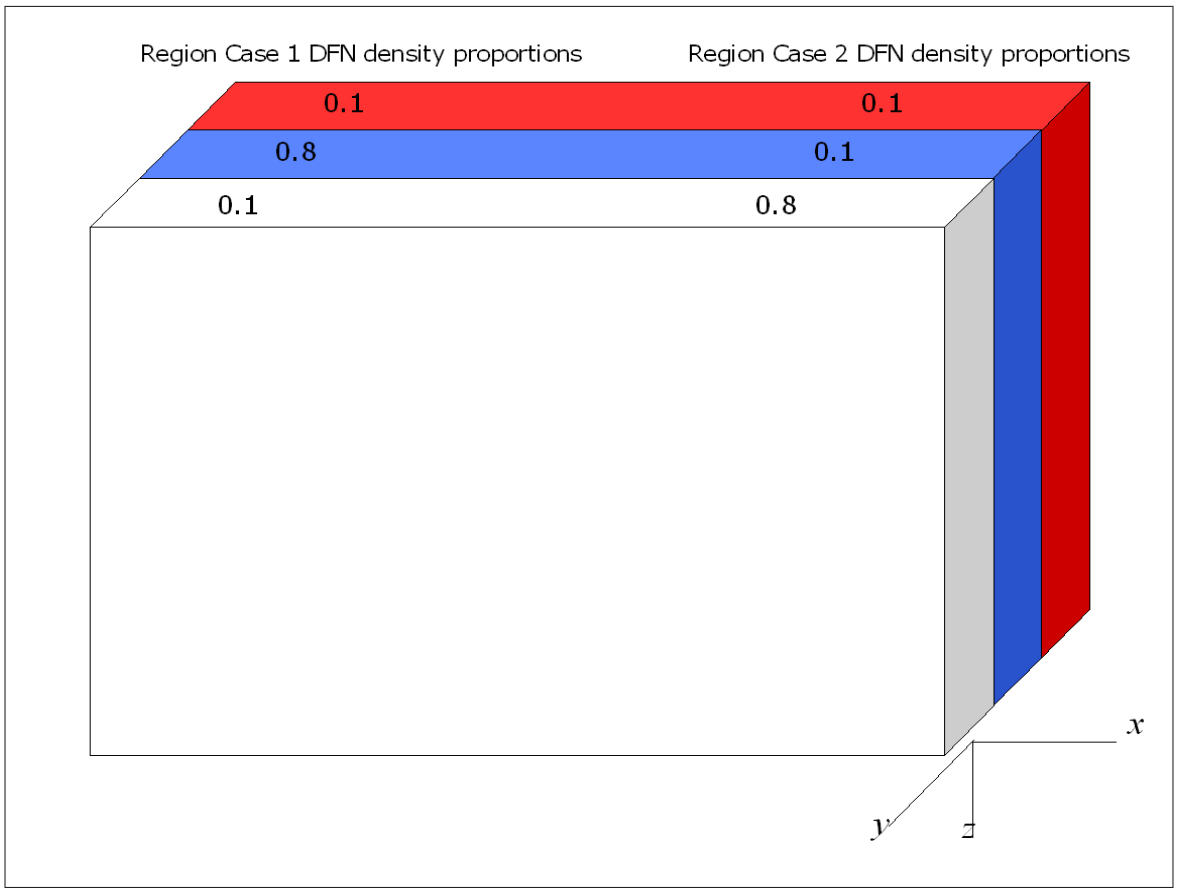

Fig. 10.10: Sensitivity study region partitions

Note that the DFNs applied in these cases are long, so as to affect a large reservoir region, and that they are restricted in azimuth, so as to remain confined to a region. DFN locations are also allowed to vary, while maintaining the specified region density. There are a total of 20 DFNs incorporated into the reservoir model; this total is constant throughout the entire sensitivity study.

Two DFN static model realizations are presented in Fig. 10.12 and Fig. 10.13, in which the DFNs are color coded according to region. The perspective in these figures is from the northwest. Fig. 10.12 presents Region Case 1, where it is seen that the majority of the DFNs are located in the middle, blue, region. Region Case 2, Fig. 10.13, places the majority of DFNs in the southern, white, region.

Fig. 10.14 and Fig. 10.15 are two DFN static model realizations from Case 1 and

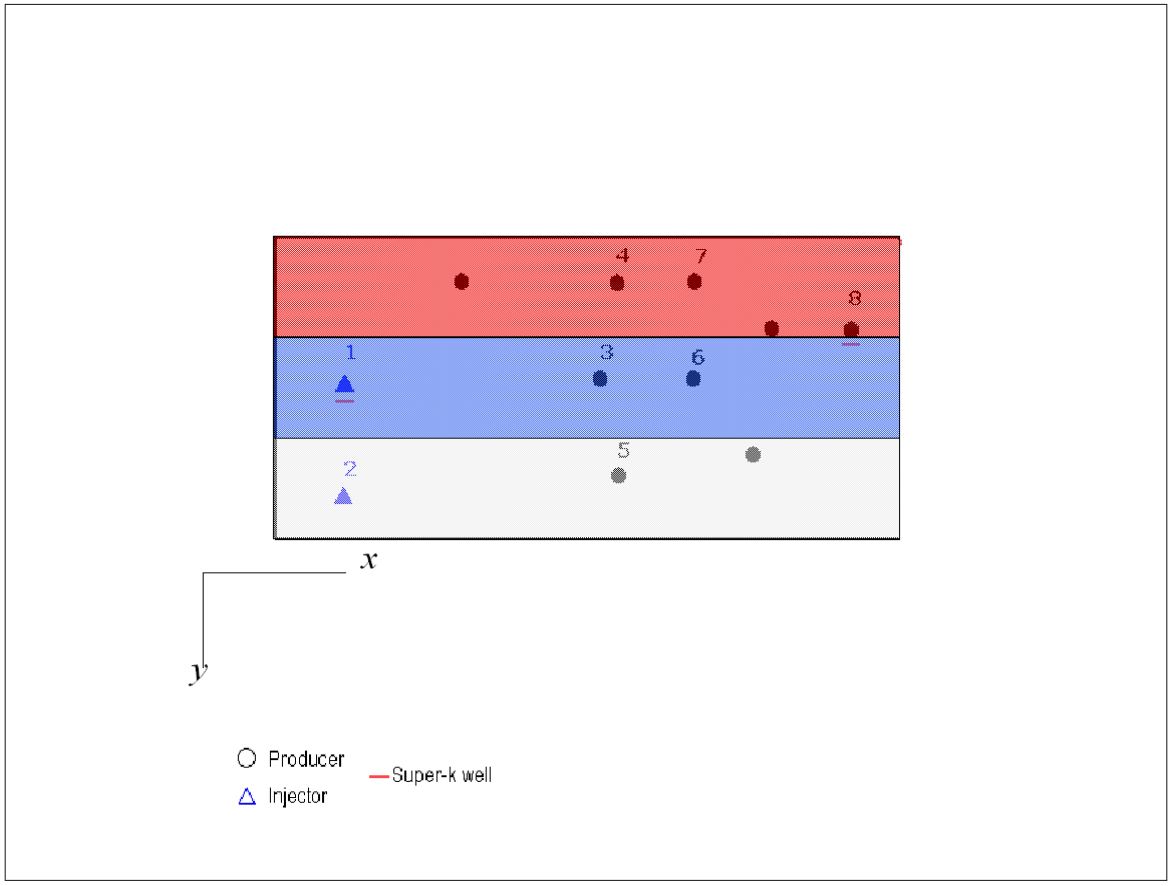

Fig. 10.11: DFN regions relative to study area wells

Case2, respectively, showing the full model, complete with DFN planes and associated source markers. Note that in Fig. 10.12, the majority of the DFNs reside in the middle region, and in Fig. 10.13, the majority lie in the southern region.

Flow performance results - study area water injection wells

The key wells to be presented, demonstrating the effect of the region partitioning, are the two water injection wells and two key producing wells. The remaining well results are presented in Appendix A. Well 1 is a water injection well located in the middle region, and Well 2 is the other water injection well, located in the southern region. Fig. 10.16 and Fig. 10.17 present flowmeter results for Well 1 under the two region cases, Region Case 1, and Region Case 2, respectively. Fig. 10.18 and

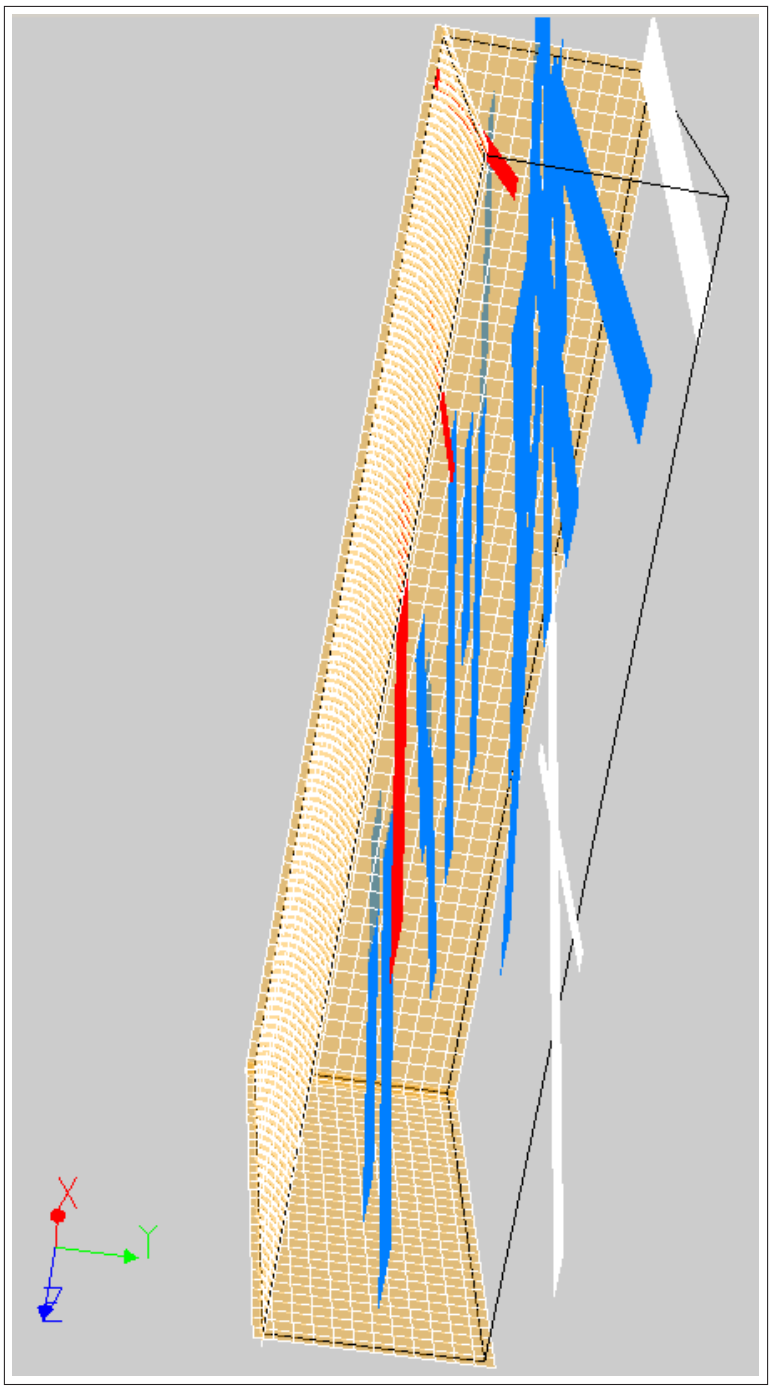

Fig. 10.12: Example DFN distribution Region Case 1

Fig. 10.19 present flowmeter results for Well 2 under the two region cases.

These plots show flow simulation results in blue, and observed data in black. A

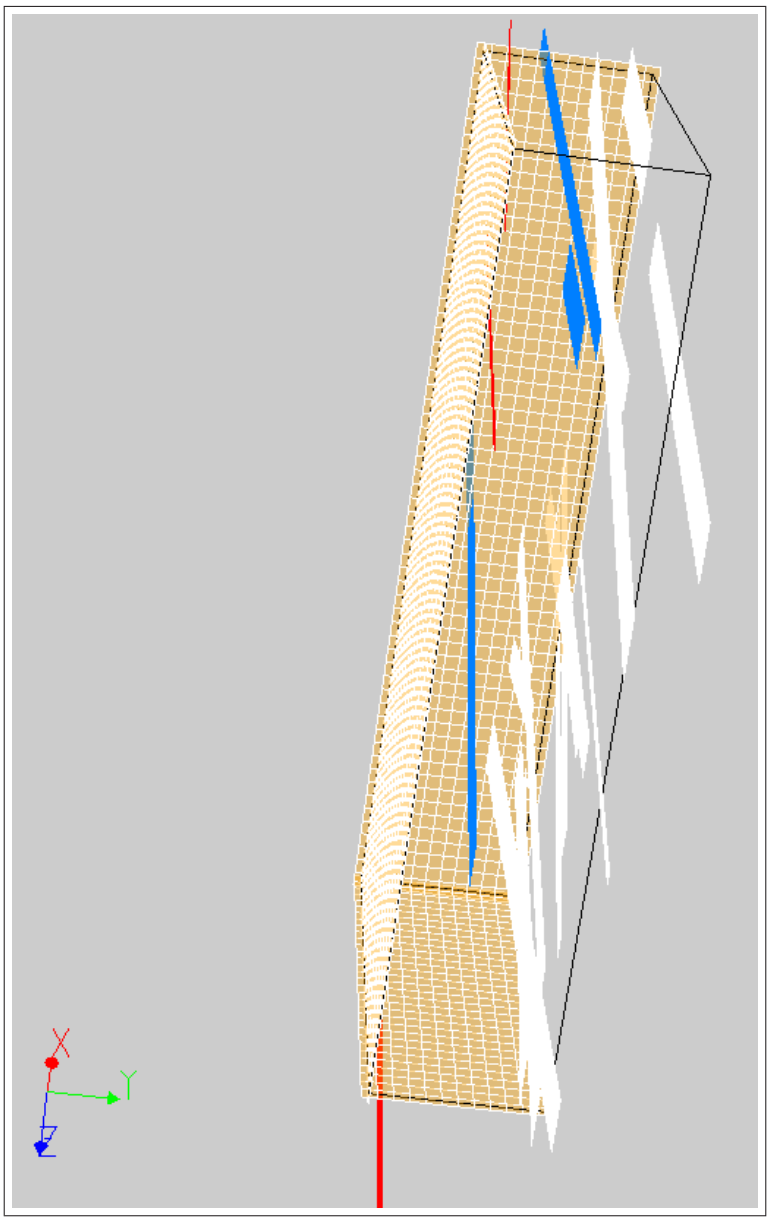

Fig. 10.13: Example DFN distribution Region Case 2

reference case, shown in red, which will be present in all results presented in this chapter, and in Appendix A, represents flow simulation results for a reservoir model in which no DFNs are incorporated, that is, the facies-only reservoir model, which is kept constant throughout all DFN sensitivity evaluations. Inclusion of the results of this model provide for a comparison revealing the effect of DFNs per se, no matter

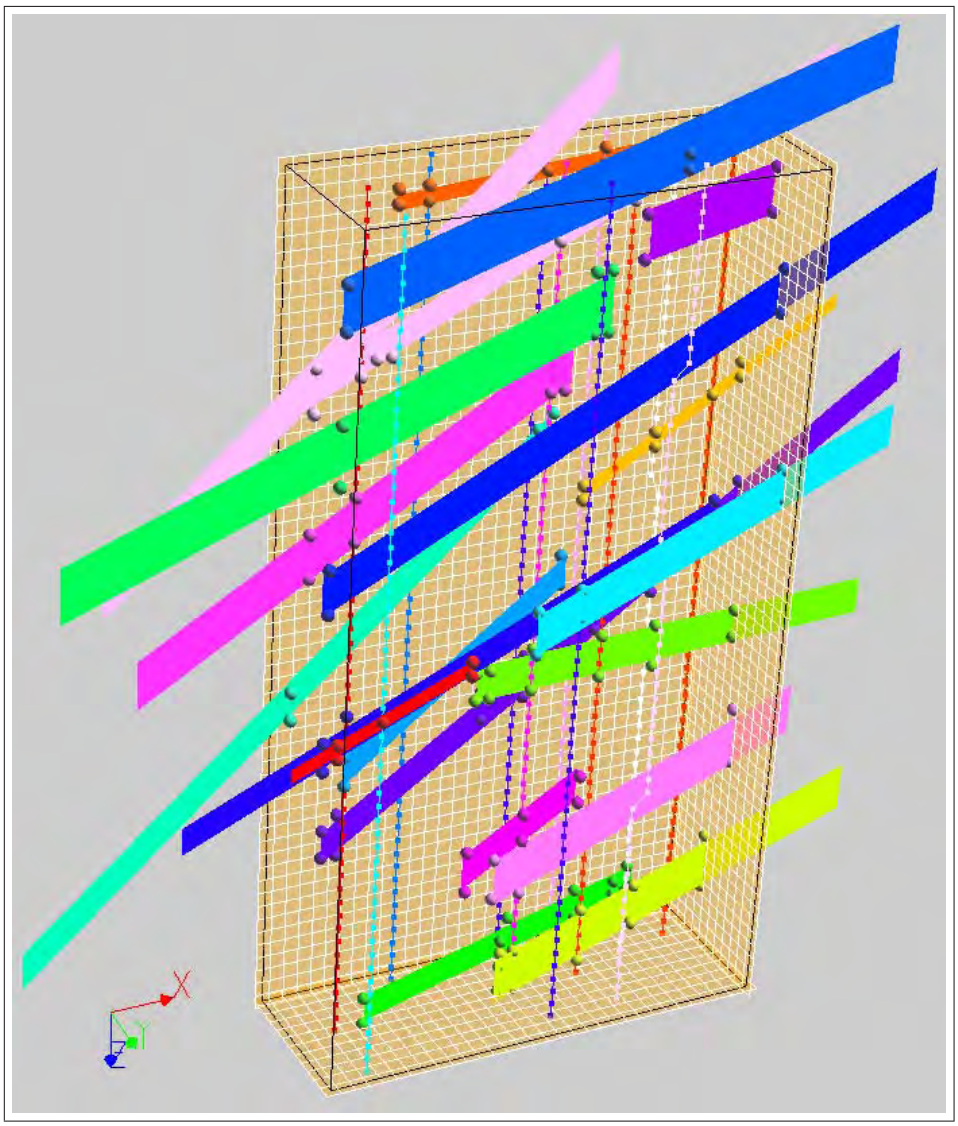

Fig. 10.14: DFN and source connections realization, Region Case 1

the DFN parameter being evaluated.

It must be emphasized that discrepancies exist between observed and simulated data, in all results, both well performance and flowmeter, presented in this sensitivity study, in all DFN parameters evaluated. The intention of the study is not to achieve a history match, but only to demonstrate the flow effects of DFNs. The results of this study will be used to inform a future history matching study. A history match of well performance data was achieved by SA in the original model provided to us, as seen

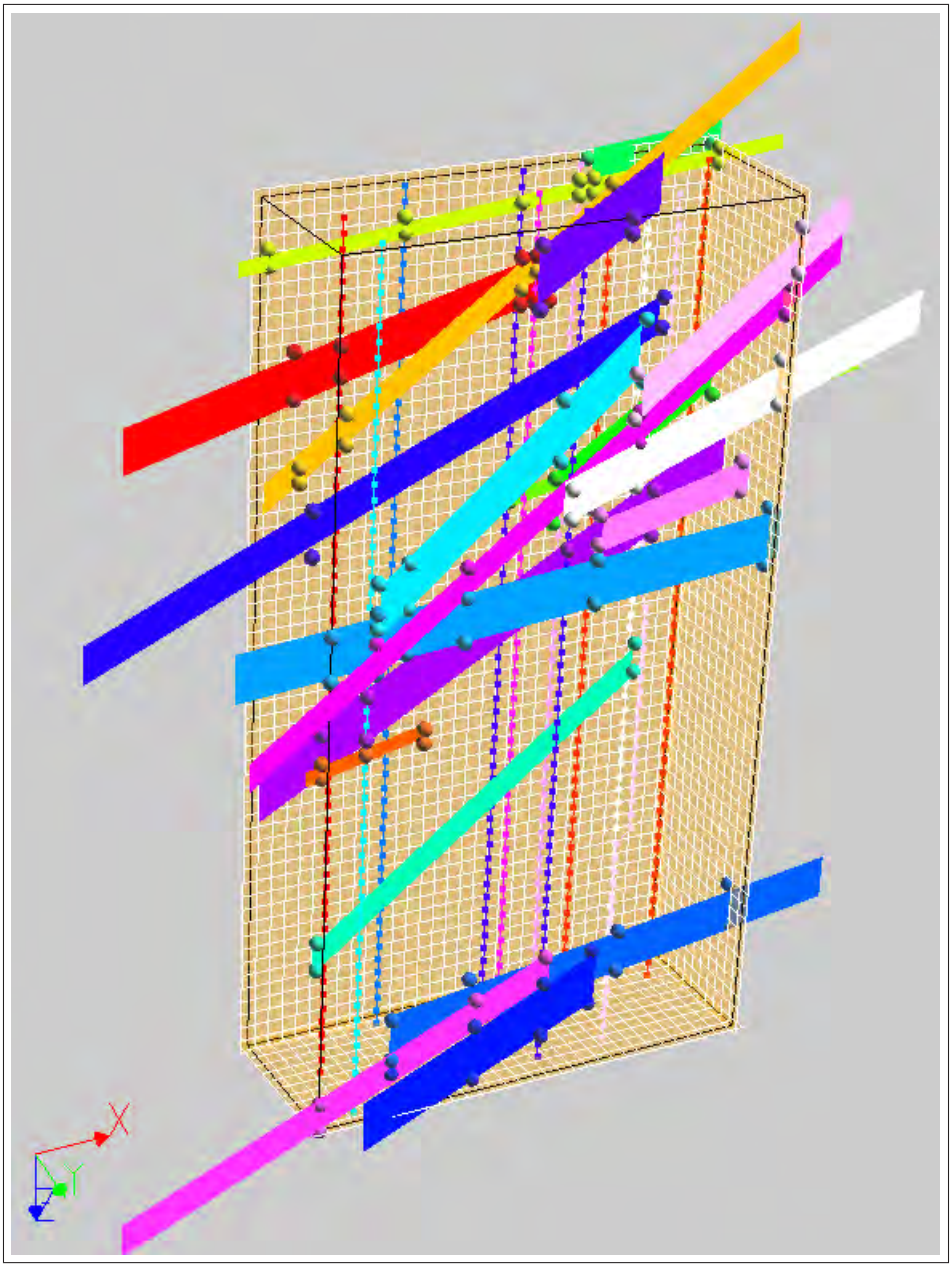

Fig. 10.15: DFN and source connections realization, Region Case 2

in Sec. E.2. Our reservoir model is not merely a modification of that original model, but instead was built from scratch, incorporating the training image concept for the facies portion of the model, and the source model for the DFN portion, and honoring all available hard data. We have not attempted to history match this reservoir

model, but instead have developed a history matching algorithm, to be utilized upon receipt of more data, namely 3D seismic. Thus, the inclusion of observed data in the presentation of our results is done only for reference and completeness, and does not imply history matching attempts.

The flowmeter plots present the liquid flux profile, in $b/d/ft$, over the well. The vertical axis, z, in these plots is measured in flow simulation grid block units; recall the flow simulation grid has a vertical dimension of 60 blocks.

Well 1 is a super-k well, as indicated by the high flux magnitude in the interval $z = 50$ to 53. The flux in this interval approaches -2000 $b/d/ft$. A DFN is therefore conditioned to this interval; that is, the static model places a DFN in those affected well blocks. The DFN is an *isolated* DFN; it does not connect directly with the well. The DFN, as are all DFNs applied in the sensitivity study, is characterized with infinite conductivity (Sec. 8.3.3). Furthermore, all DFNs in the sensitivity study are of the isolated variety, as described previously in Sec. 10.1.

The super-k interval is also conditioned with a grainstone facies, of permeability 2000 md, at the well blocks of the interval. This facies constraint corresponds to the grainstone well connection of our super-k model, as described in Sec. 6.4.3.

Similarly, Well 2 is conditioned with a DFN, at $z = 27$, where the flux approaches -750 $b/d/ft$. Although this flux magnitude is not extreme, the interval was nonetheless conditioned to test the efficacy the DFN source model for this well.

A total of ten realizations are represented by the flow simulation results in blue.

Note first, that DFNs alone, generally increase well injectivity, as expected. The injectivity enhancement is seen in the higher flux magnitudes in the super-k intervals, at which a DFN is conditioned.

Second, note that the injectivity increase is distinctly different for the two cases, with Well 1 experiencing a higher increase in the super-k interval, for Region Case 1, than that in Region Case 2. Note that the reverse is true for Well 2. In fact, no DFN enhancement of injectivity is seen in the conditioned interval $z = 27$, for Region Case 1, while a modest increase is seen in Region Case 2. The fact that injectivity *decreases* slightly for Well 2, in Region Case 1, is due to the elevated productivity of the middle region, and a consequential thieving of productivity from the southern

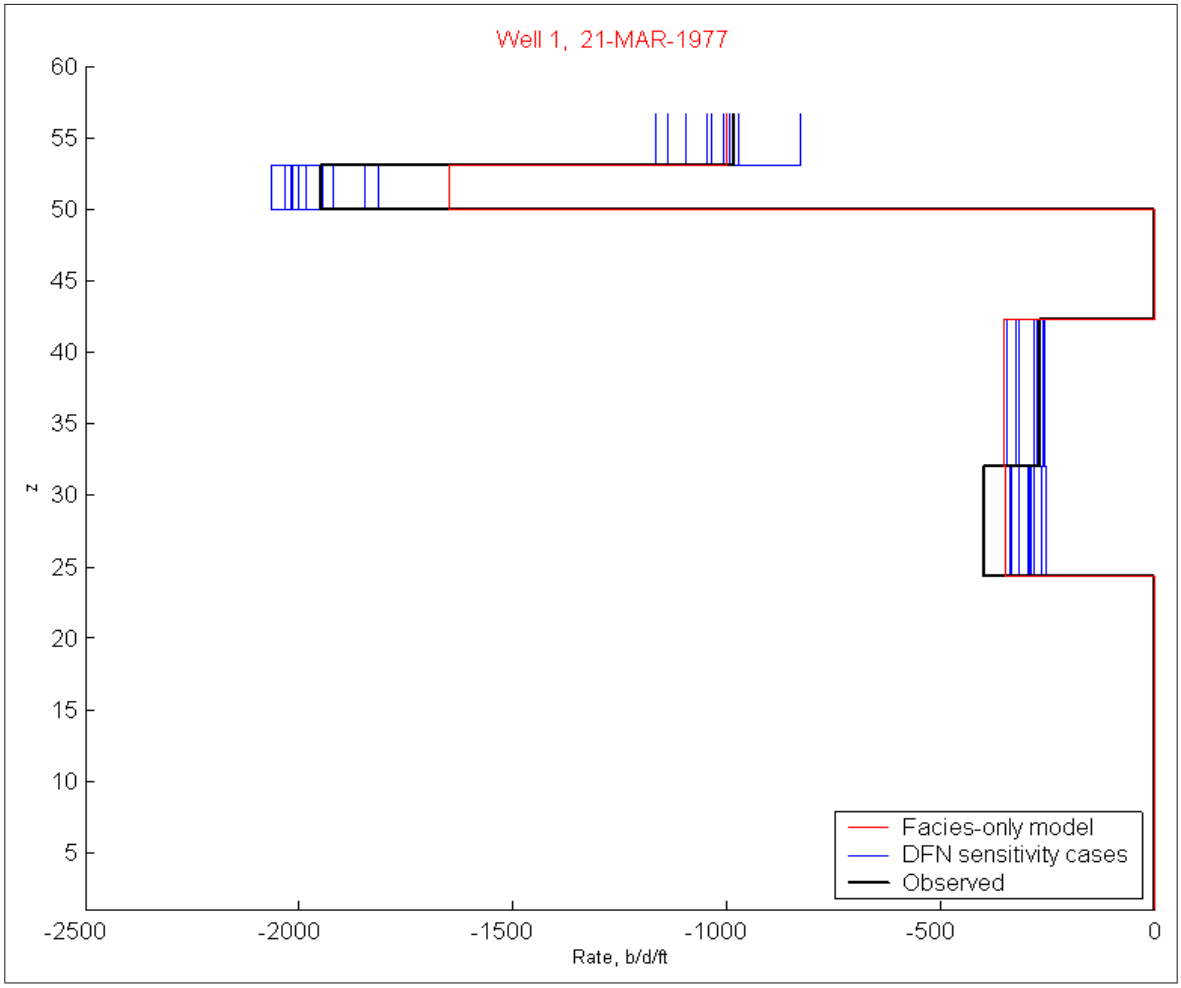

Fig. 10.16: Flowmeter performance under Region Case 1

region. This characteristic theiving of productivity, is seen often, for many wells, throughout our sensitivity study.

Fig. 10.20 and Fig. 10.21 present injection pressures for Well 1 and Well 2, for the two region cases. Here, the flow simulation cases for the facies-only model, in red, and for the ten DFN realizations, in blue, are given, along with observed injection pressures, black circles. This format is constant throughout our presentation of well performance results. Recall the flow simulation results correspond to well block pressures, which are assumed to represent 24-hr shut-in pressures, the observed data.

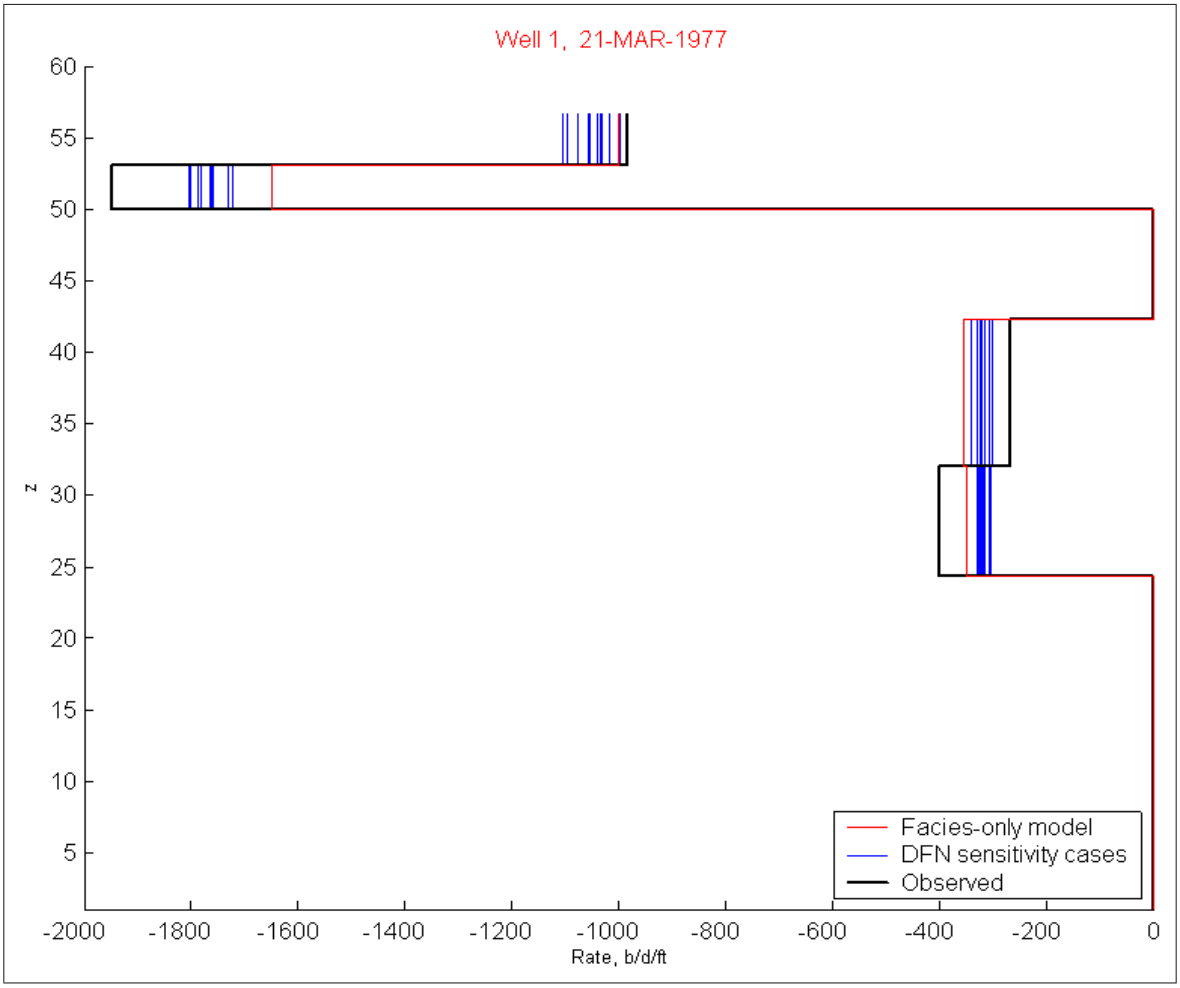

Fig. 10.17: Flowmeter performance under Region Case 2

Note that for both cases, injectivity is increased by the presence of DFNs, evidenced by the generally lower simulated injection pressures, for the DFN models relative to those of the facies-only model. Note also, profoundly, that the pressure results do not distinguish the two region cases. The injectivity increase in either well is not significantly different for the two cases. This result coincides with our early result, using a facies-only super-k model (Appendix F), in which pressure data did not serve well in the spatial distribution characterization of super-k. The pressure response is affected most significantly by both the DFN conditioning at each well, and by the global increase in reservoir productivity brought by DFNs, with regional

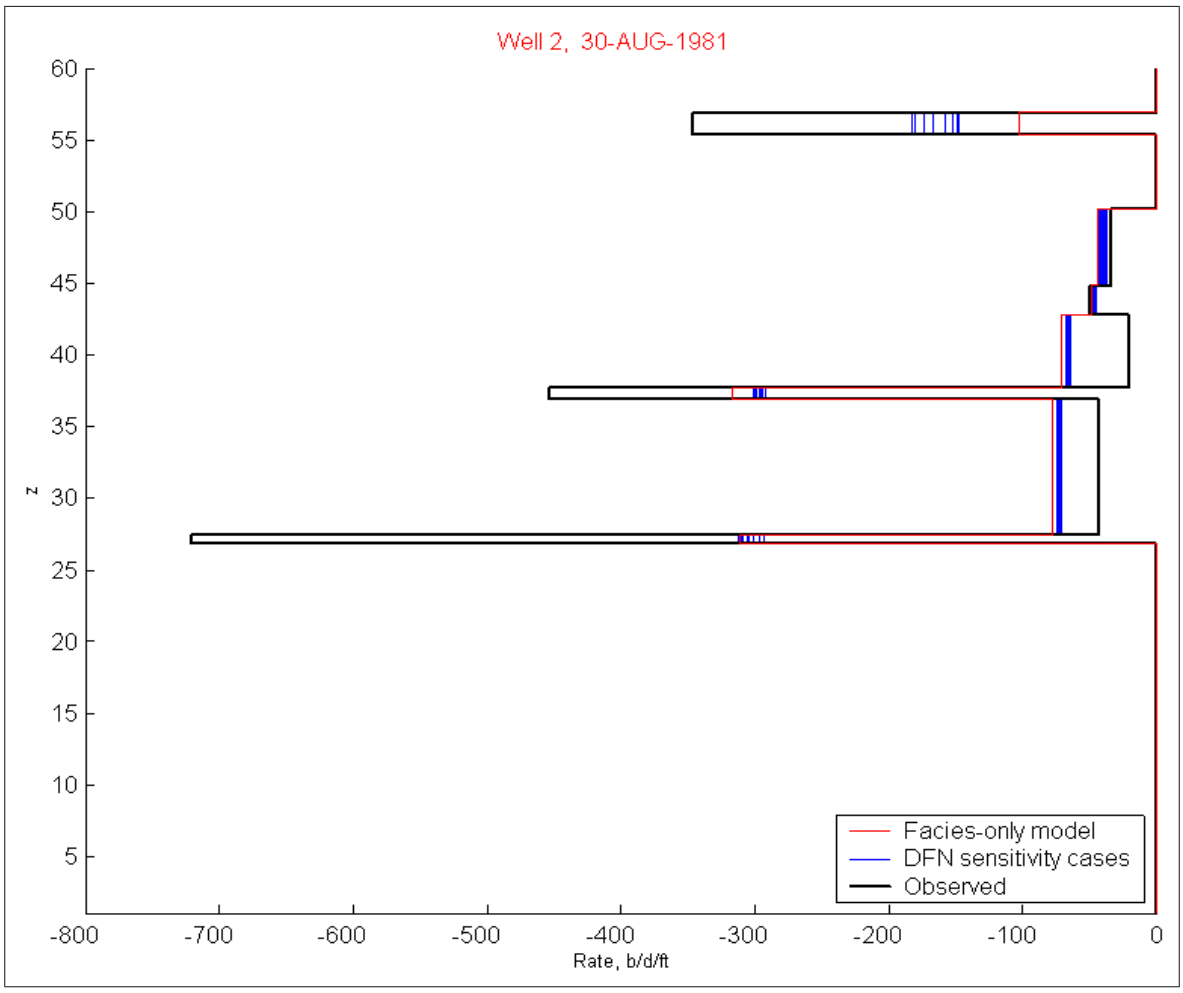

Fig. 10.18: Flowmeter performance under Region Case 1

DFN density variation relatively transparent to well pressure response. This result emphasizes the value of including flowmeter data in the characterization of super-k. The result is generally seen in the pressure response of both injection and production wells, in all sensitivity evaluations.

Note also the fluctuation in the pressure solutions of the DFN realizations in the period year 8 to 15. This interval corresponds to a shut-in period for the study area and surrounding areas, as will be more evident in production plots yet to be presented. The instability of pressure solutions during the area-wide shut-in period is due to computational instability within the DFNs. This topic is discussed in detail

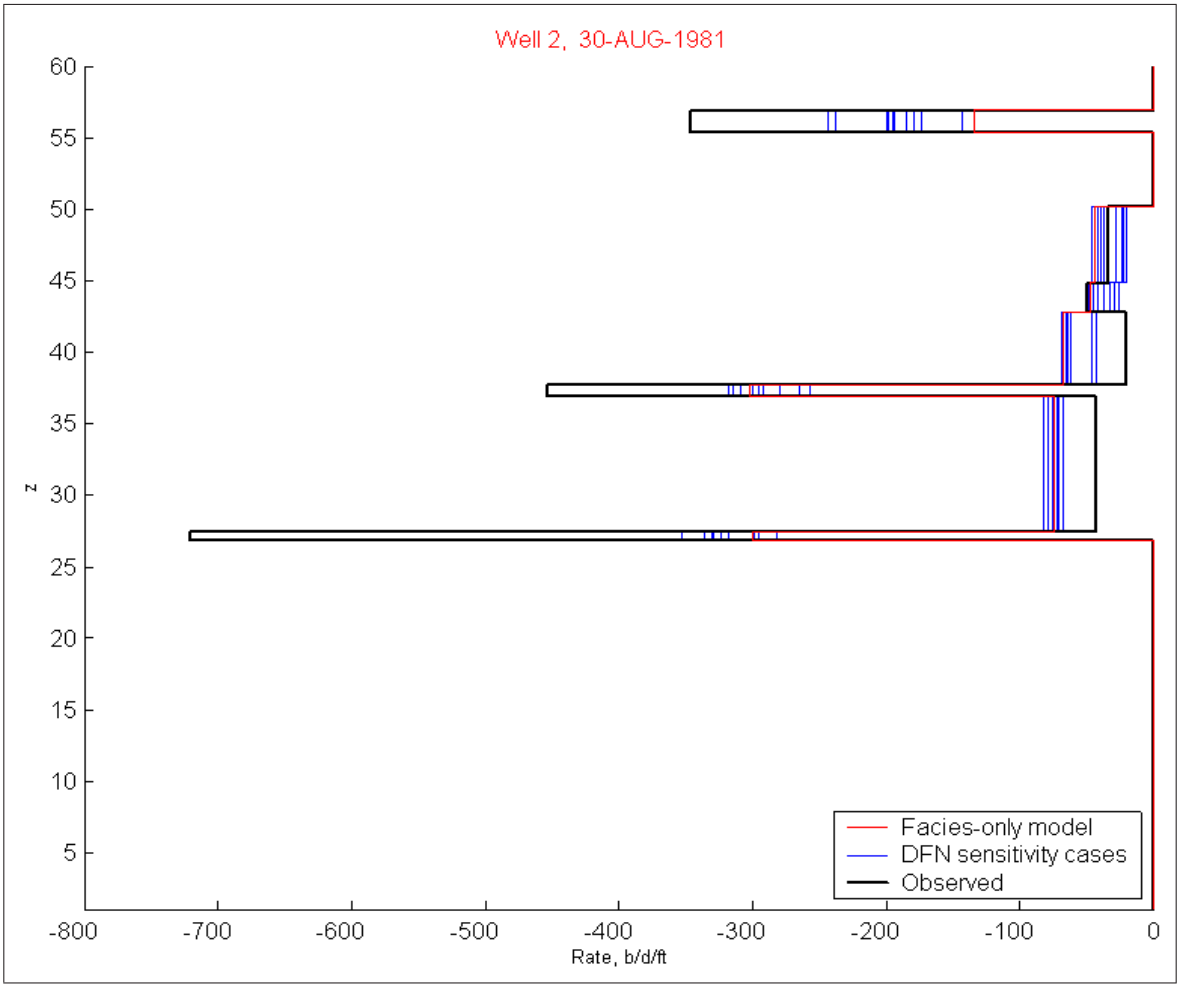

Fig. 10.19: Flowmeter performance under Region Case 2

in Appendix B, more specifically in Sec. B.1. The instability is restricted, in all cases, to the extended shut-in period.

Flow performance results - super-k production well

We next present DFN regional density sensitivity results for a key producing well, Well 8, located in the northeastern corner of the study area. This well is one of two producing wells in the study area with the most extensive production history, and in addition possesses the most prolific super-k interval of any study area well. This interval is seen in the flowmeter results from the two region cases, in Fig. 10.22 and

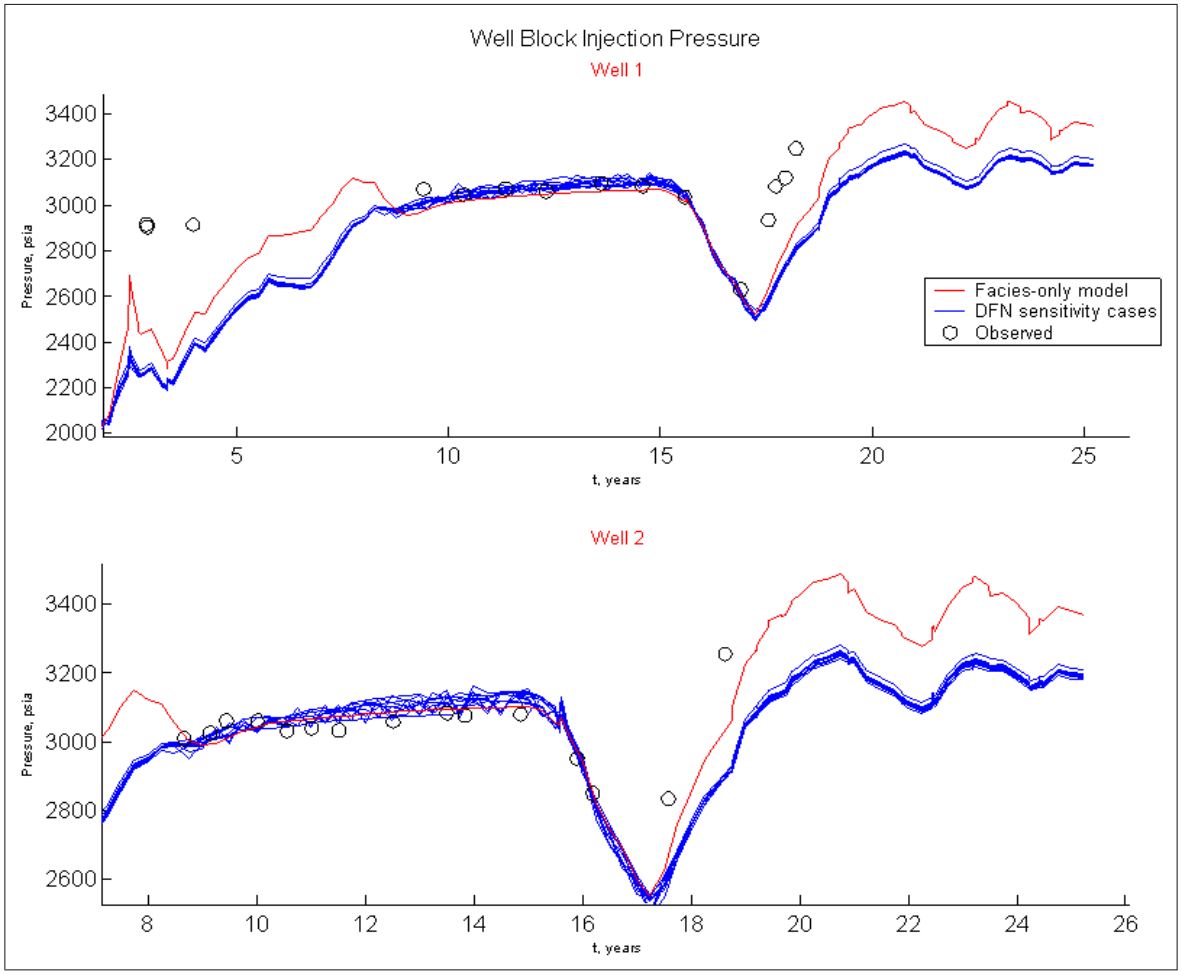

Fig. 10.20: Injection performance under Region Case 1

Fig. 10.23, for Region Case 1, and 2, respectively. The super-k interval is located at $z = 43$, with an astounding flux magnitude exceeding $5000\ b/d/ft$. DFN and grainstone conditioning is enforced at this interval in the reservoir models.

Note that the flowmeter results do not indicate distinguished increases in injectivity at $z = 43$, or any other interval in this well, as was seen in the injection wells. This is probably due to the location of Well 8 in the northern region, which has a low DFN density in both region cases. The restricted azimuth of the DFNs in these cases makes it difficult for the conditioned DFN at the well to intersect other DFNs in the richly populated regions. However, we will demonstrate in the next set of sensitivity cases that exceptions to this general result have been generated.

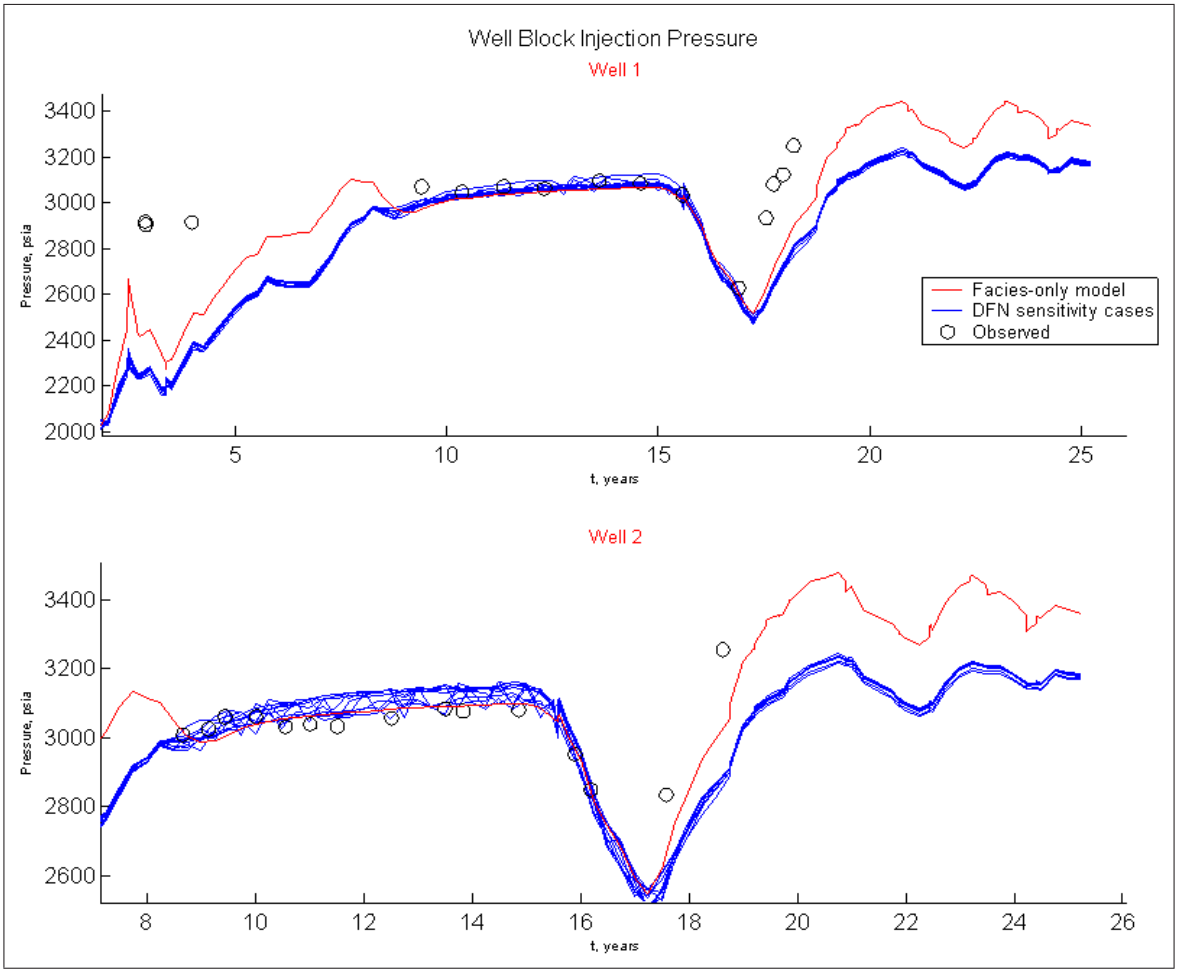

Fig. 10.21: Injection performance under Region Case 2

The effect of regional DFN density differences is, however, seen in Well 8 performance plots, specifically in water cut performance. Fig. 10.24 and Fig. 10.25 show, clockwise, from the upper left plot, well pressure (simulation well block pressure vs. observed 24 hr. shut-in pressures, as in the water injection well results), oil rate, gas rate, and water rate, for the two region cases, respectively. As with previous presentations, the DFN simulation results are the curves in blue, the facies-only simulation is in red, and the observed data are the black circles.

A significant productivity gain attributable to the presence of DFNs is noted for both cases, reflected in the higher producing pressures of the DFN cases, relative to the facies-only simulation results. The productivity gain is higher in Region Case

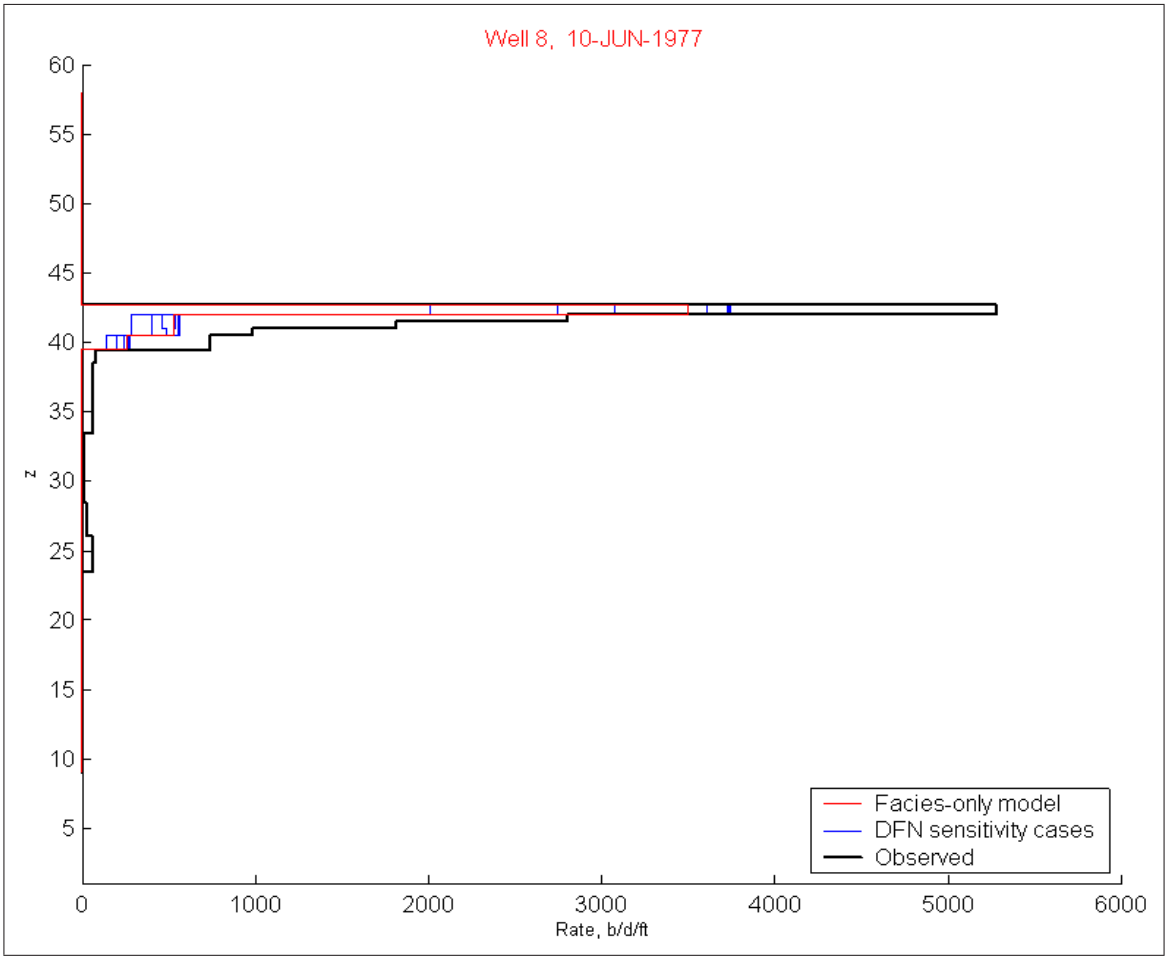

Fig. 10.22: Flowmeter performance - Region Case1

1, as expected due to the proximity of the middle region to Well 8, although the difference between the two cases is not appreciable. Thus, it is doubtful, as was concluded with the water injection wells, that pressure performance may be used to characterize DFN spatial distribution.

Note the area-wide shut-in, seen in the zero production rate period, and the increase in well pressures during this period. Note also the instability in the pressure solution during this period, and the absence of the instability otherwise.

The most evident DFN region density difference in these performance results is seen in the water production plots. Note that the Region Case 1 DFN realizations generate higher water production rates than those in Case 2. Note also, that in

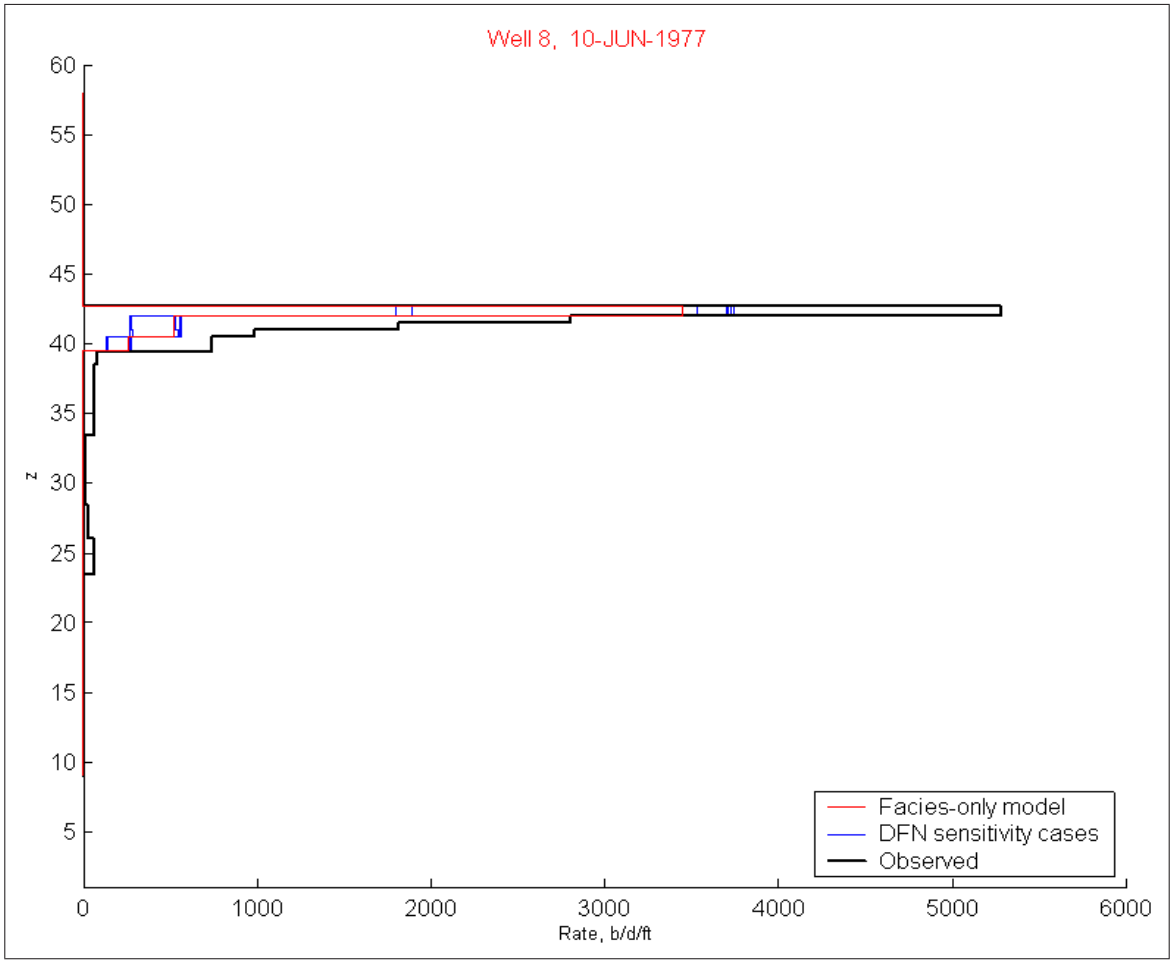

Fig. 10.23: Flowmeter performance - Region Case 2

both cases, water breakthrough occurs almost immediately in the presence of DFNs, whereas the facies-only model delays breakthrough for a much longer period. The efficacy of DFNs in conducting injection water at very high rates, and over great distances, is demonstrated in these results.

10.3.2 Remaining DFN parameter evaluation

The remaining sensitivity cases to be presented are characterized with a single varying DFN parameter, while the remaining DFN parameters are kept constant, over

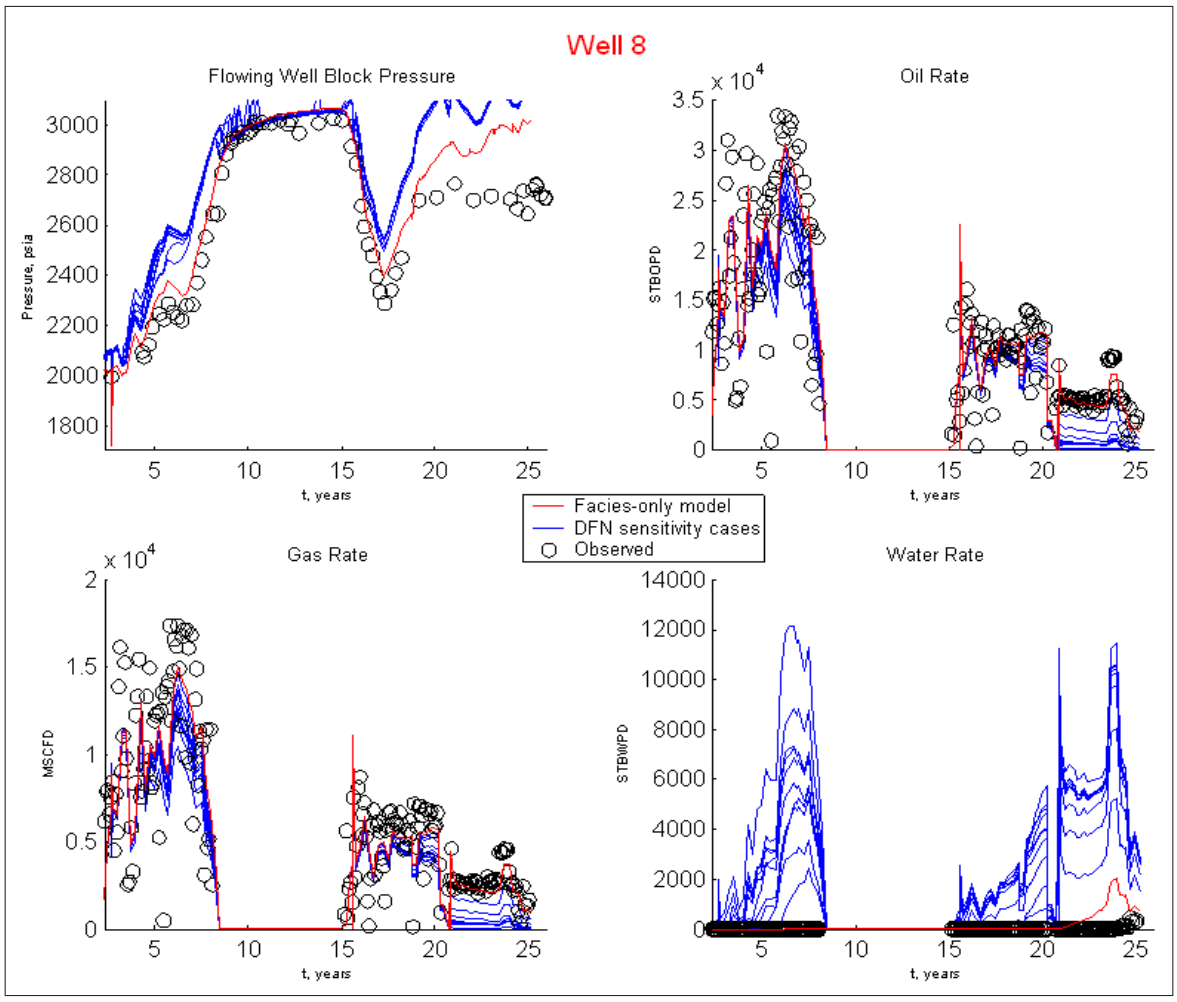

Fig. 10.24: Well performance under Region Case 1

approximately ten realizations. The DFN regional density distribution was that corresponding to Region Case 1, in which 80% of the total number of DFNs are placed in the middle third region, and the remaining DFNs are split between the northern and southern regions. This density distribution is kept constant over all remaining sensitivity cases to be presented.

Each DFN parameter to be evaluated, such as DFN location, presented in the following section, varies over realizations which are independent from each other, that is, each parameter realization is generated from a unique seed. Realizations of the remaining DFN parameters are generated with one seed, common to all realizations.

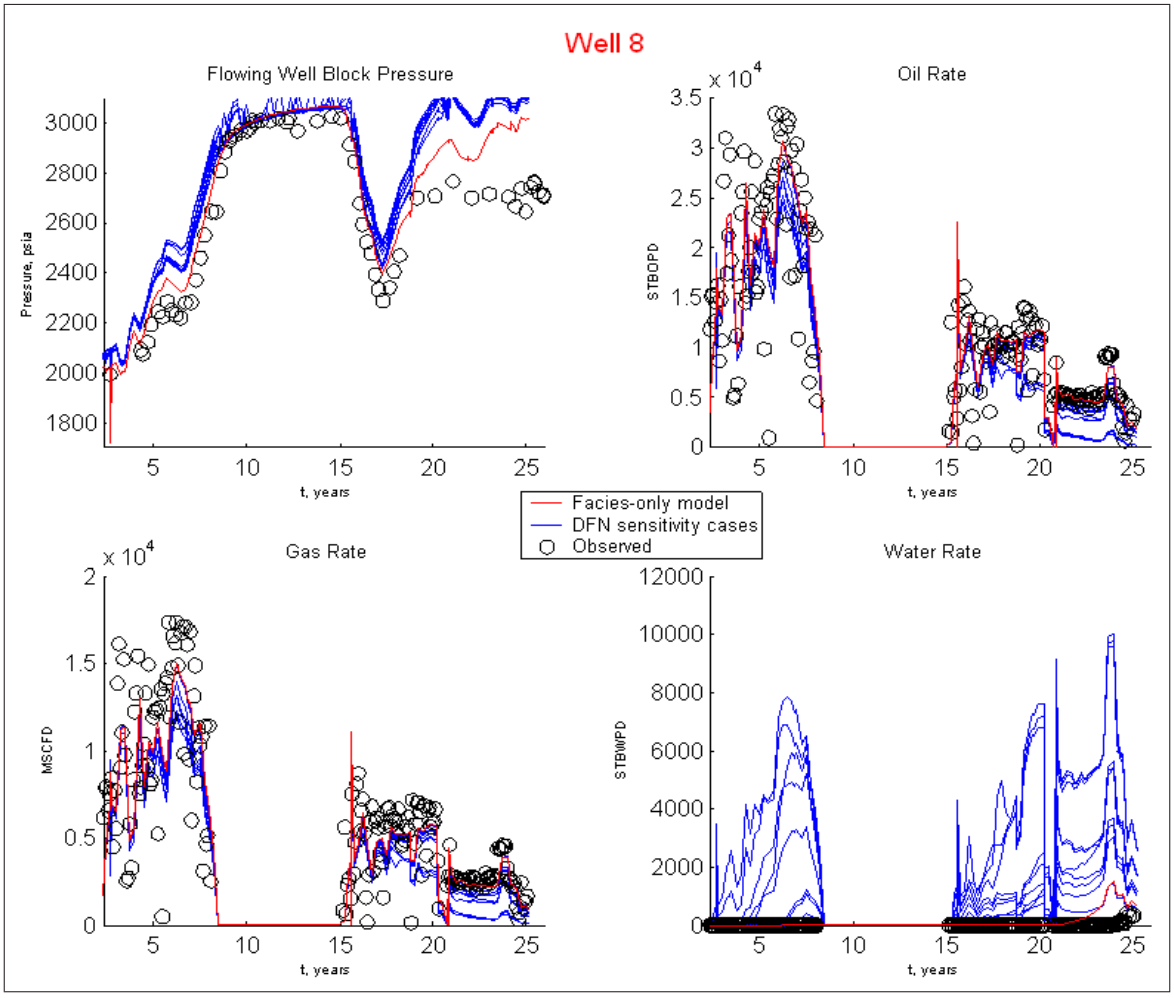

Fig. 10.25: Well performance under Region Case 2

Thus, as the DFN parameter of interest varies in each realization, the remaining parameters remain frozen.

We present flow performance results for two key wells in the study area, the water injection well, Well 1, located at the aquifer on the west side of the study area (Fig. 10.11), and the producing well, Well 8, located in the northeastern corner of the study area. These wells were presented in the previous sections. Other wells of interest, for each DFN parameter evaluation, are presented in Appendix A.

The importance of a DFN parameter may be ascertained, in part, by the amount of variation in flow performance results, induced by the presence of DFNs, over the

realizations. As all other DFN parameters are constant during the evaluation of a given DFN parameter, the variation in flow performance seen from the realizations should be attributable to the variation in the evaluated DFN parameter. The variation in flow performance results, seen in the DFN regional density evaluation, is a cumulative variation, in that all DFN parameters, except DFN density, were allowed to vary between realizations. As was discussed at the beginning of the chapter, some DFN parameters account for the majority of that flow performance variation, while others are relatively insignificant. DFN location, for example, is a parameter that accounts for a significant portion of the variation, as shown in the next section.

DFN location

Fig. 10.26, Fig. 10.27, and Fig. 10.29 indicate significant variation in both flowmeter and well performance results. Most significantly, Fig. 10.27, shows that these realizations generated a single model which produced a simulated flux magnitude of approximately 4800 $b/d/ft$, at $z = 43$, the super-k interval conditioned with a DFN, and a grainstone facies. Fig. 10.28 shows the DFN static model realization corresponding to this high simulated flux at $z = 43$. As is often the case with these sensitivity evaluations, the correspondence between simulated flow performance, and the reservoir model that generated it, is not always a simple one in which reservoir engineering fundamentals, or intuition, provide clarity. Unlike the two-well, one DFN, cases presented in Sec. 8.3.3, in which results are relatively straightforward, the complexity brought by 11 wells and 20 DFNs is not always grasped through fundamentals and intuition. For example, it is seen that the DFN conditioned to Well 8 at $z = 43$ is a relatively short one, apparently not providing the necessary productivity increase, as many realizations and flow simulations have been performed in which longer DFNs, placed at that well interval, were ineffective. Note, however, that two DFNs approach the water injection well, Well 1, at a depth near that of the Well 8 super-k interval, and that both of these DFNs possess relatively substantial lengths. We believe these two DFNs provide the impetus for the productivity gain at the super-k interval at Well 8. Only when DFNs are allowed to vary in position, can a result like this be achieved.

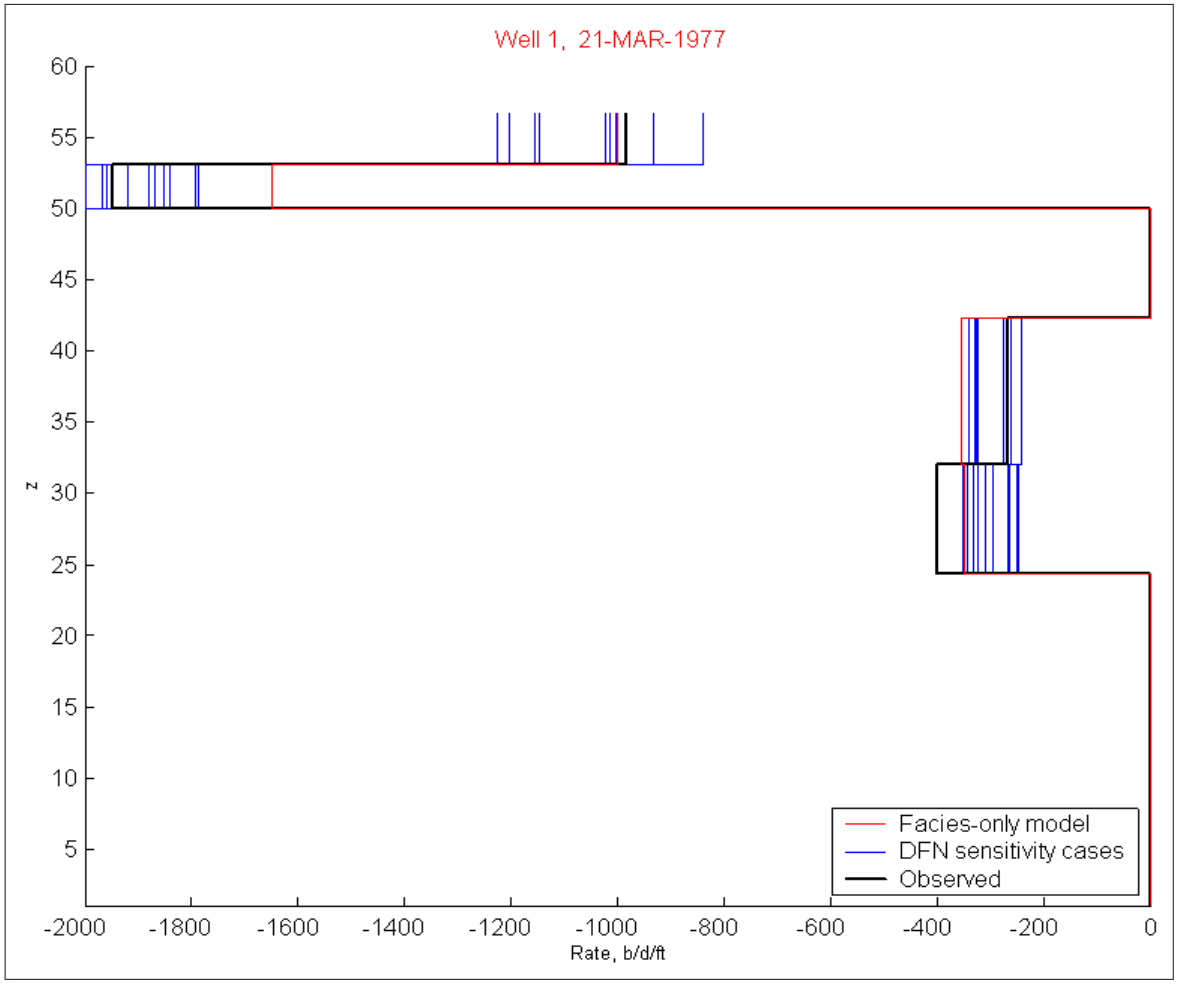

Fig. 10.26: Flowmeter performance under varying DFN locations

Note finally that Well 8 performance results show a significant variation in water production over the realizations.

DFN azimuth

The orientations of the DFNs also prove to be significant parameters, as the flowmeter and flow performance variation is significant among realizations in which only DFN azimuth is allowed to vary.

The azimuth varies from 10^o to 90^o , a wider range than that applicable to the evaluation of the other DFN parameters. Recall that the azimuth range was restricted

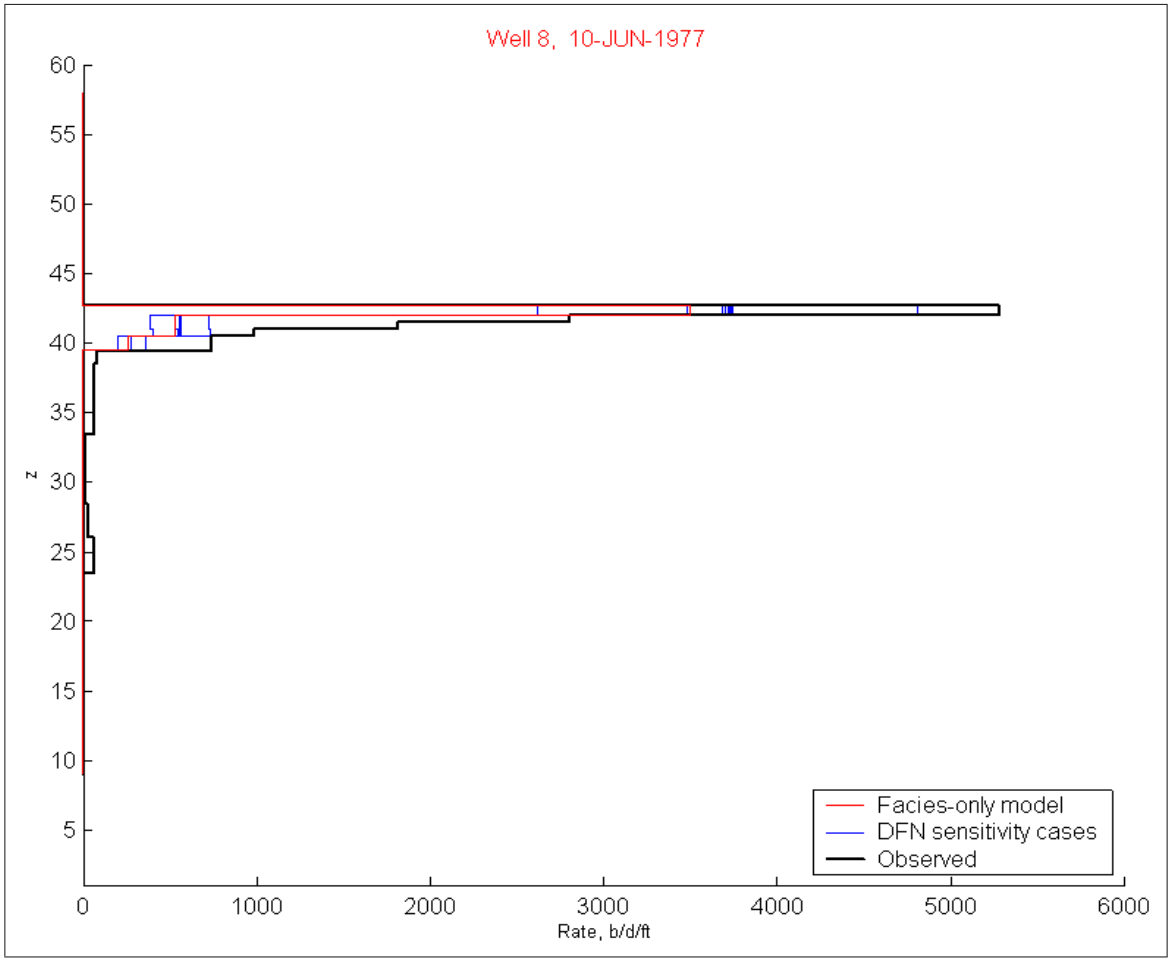

Fig. 10.27: Flowmeter performance under varying DFN locations

so as to limit the flow effect of DFNs to their respective ranges.

Fig. 10.40 is an example realization from the DFN azimuth sensitivity evaluation. Fig. 10.31, Fig. 10.32, and Fig. 10.33 present the flowmeter and well performance results for the two key wells. Note the significant variation in Well 1 super-k flow, and in Well 8 water production.

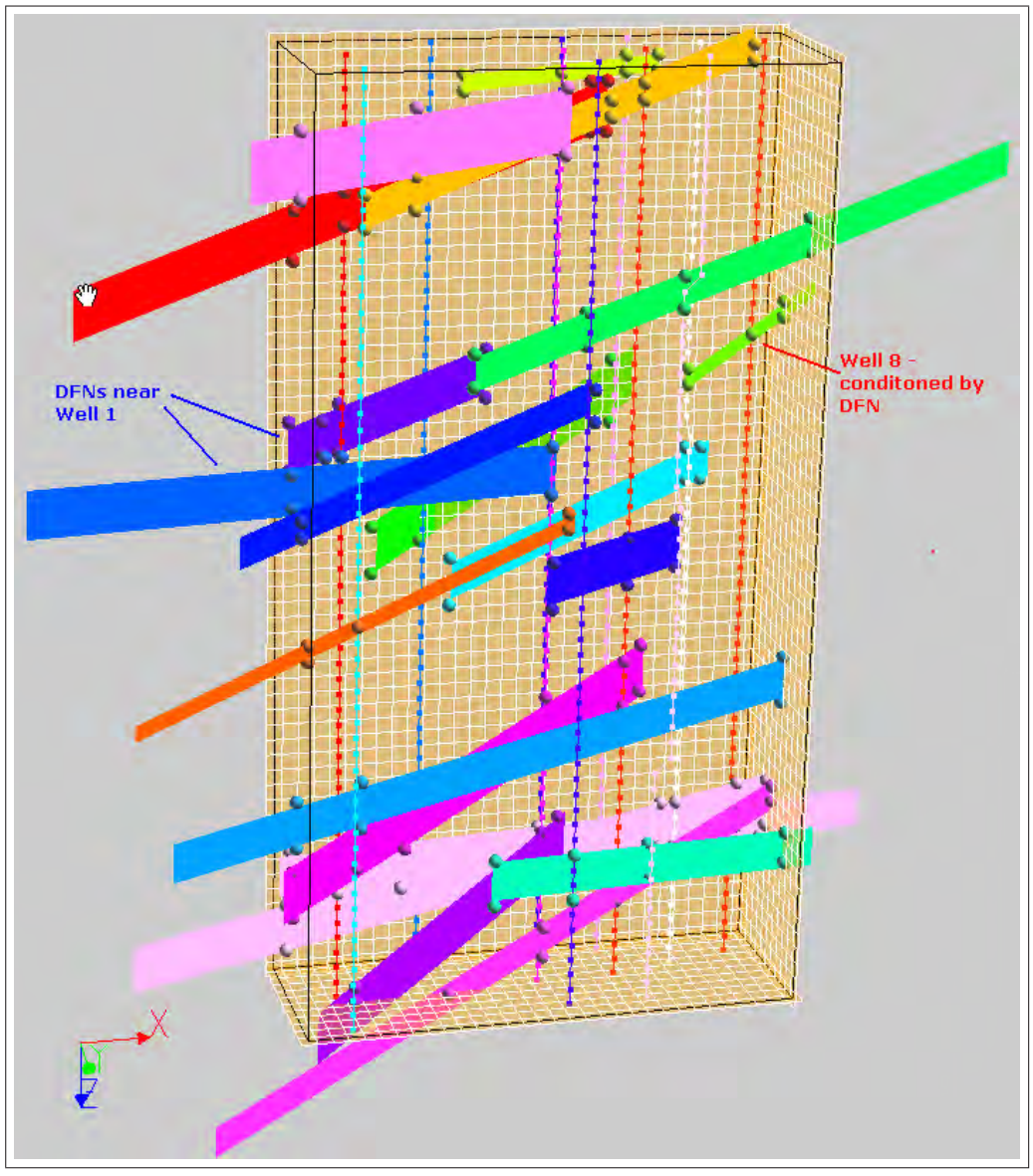

Fig. 10.28: DFN and source connections realization, DFN location sensitivity

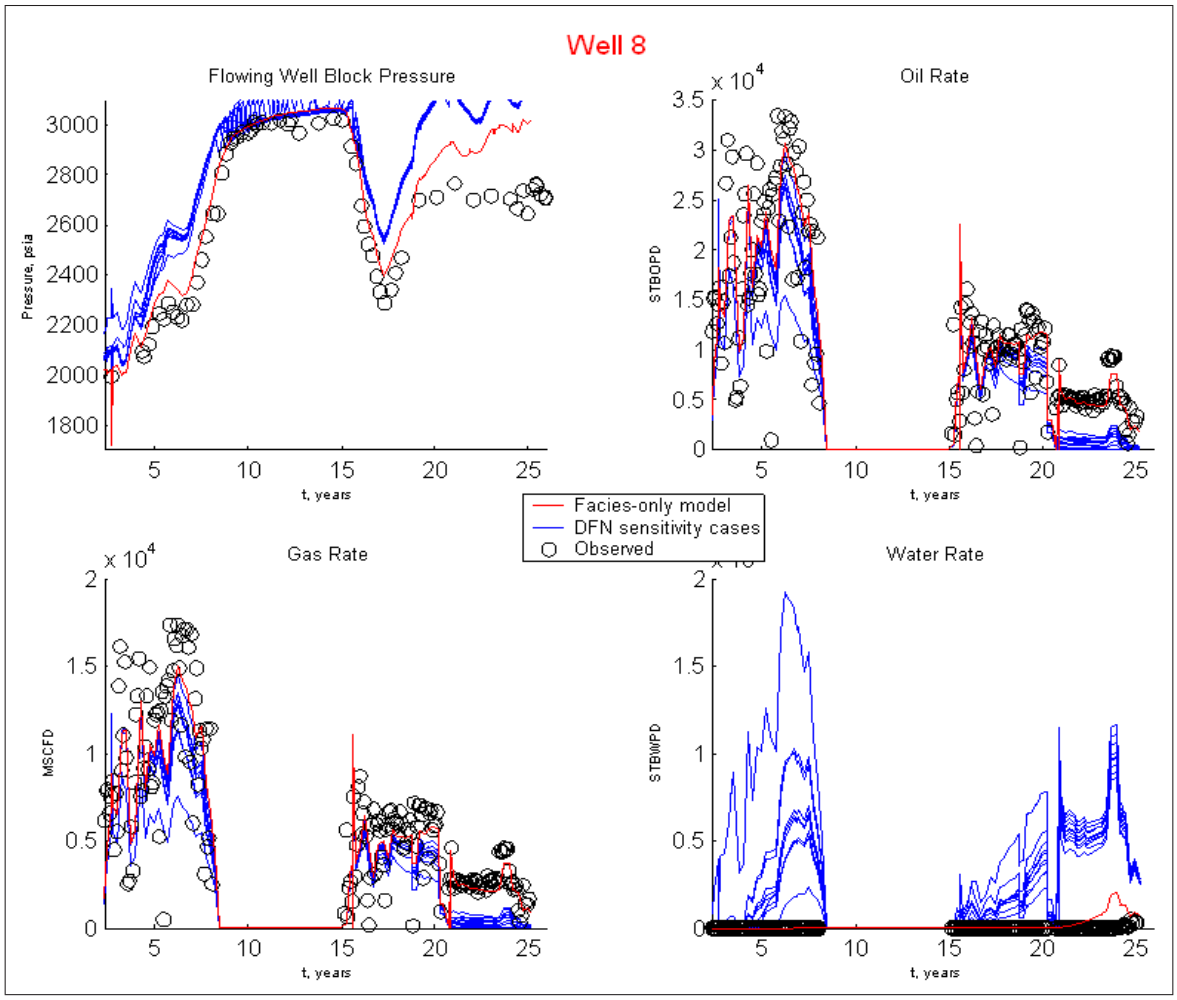

Fig. 10.29: Well performance under varying DFN locations

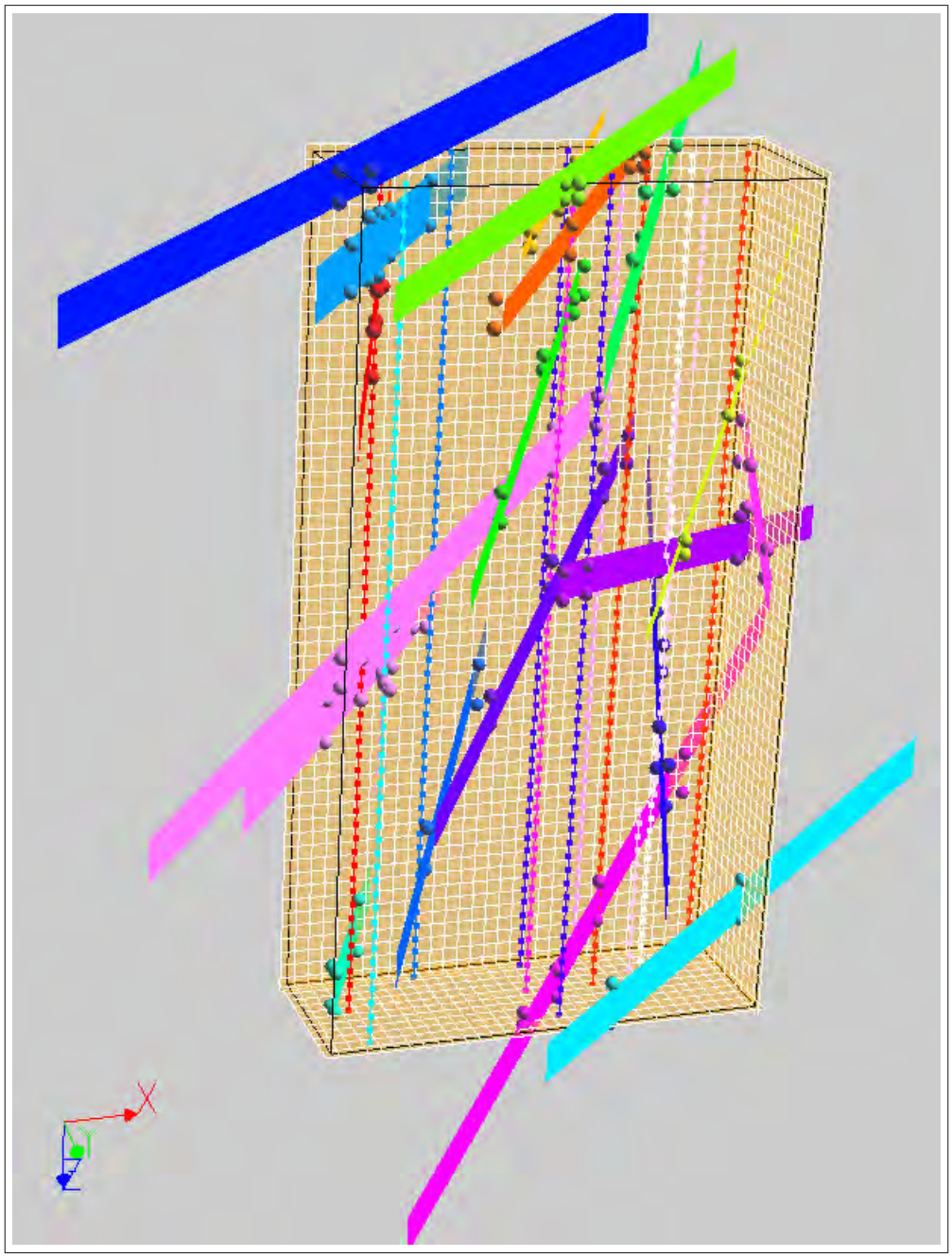

Fig. 10.30: DFN and source connections realization, DFN azimuth sensitivity

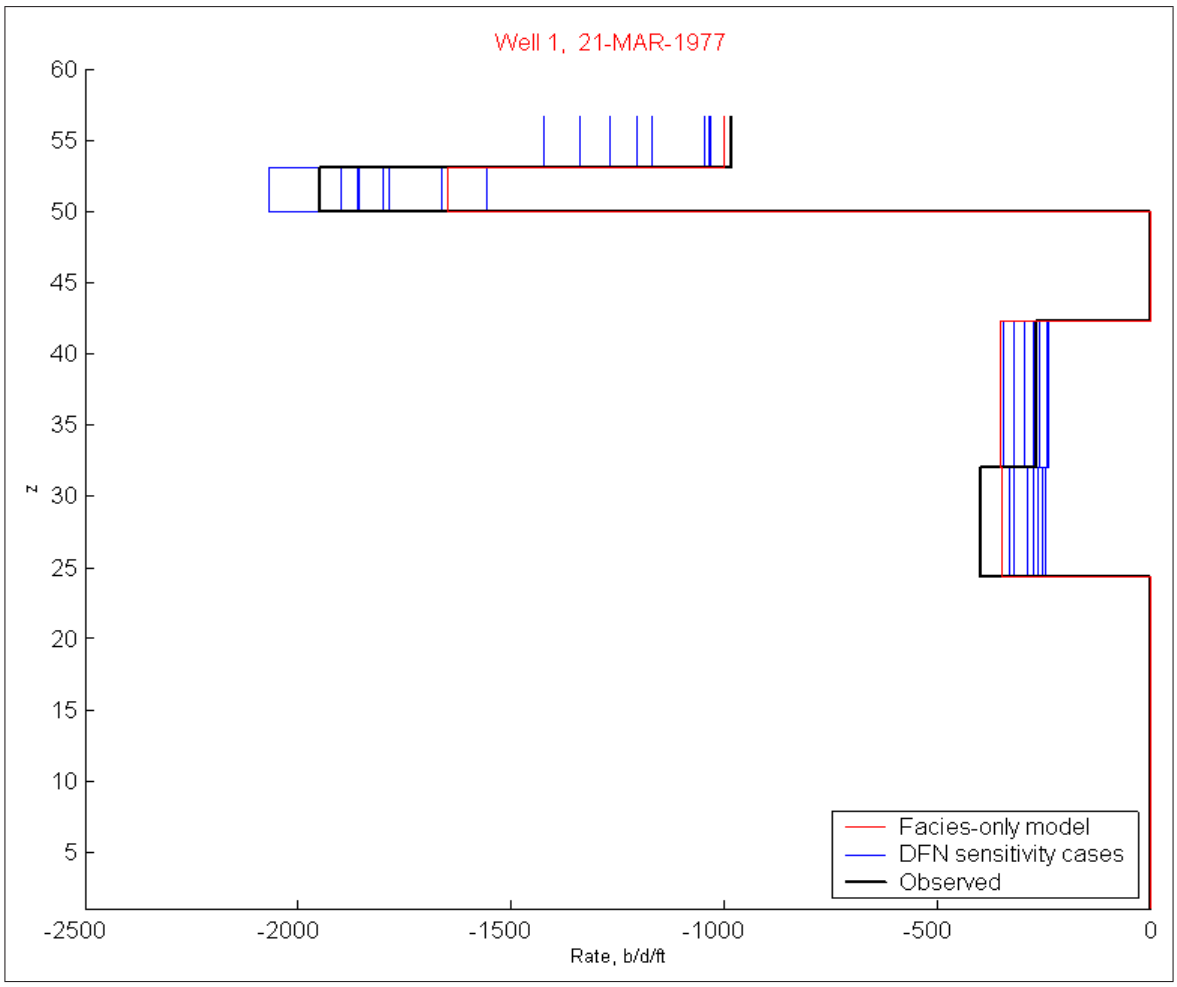

Fig. 10.31: Flowmeter performance under varying DFN azimuth

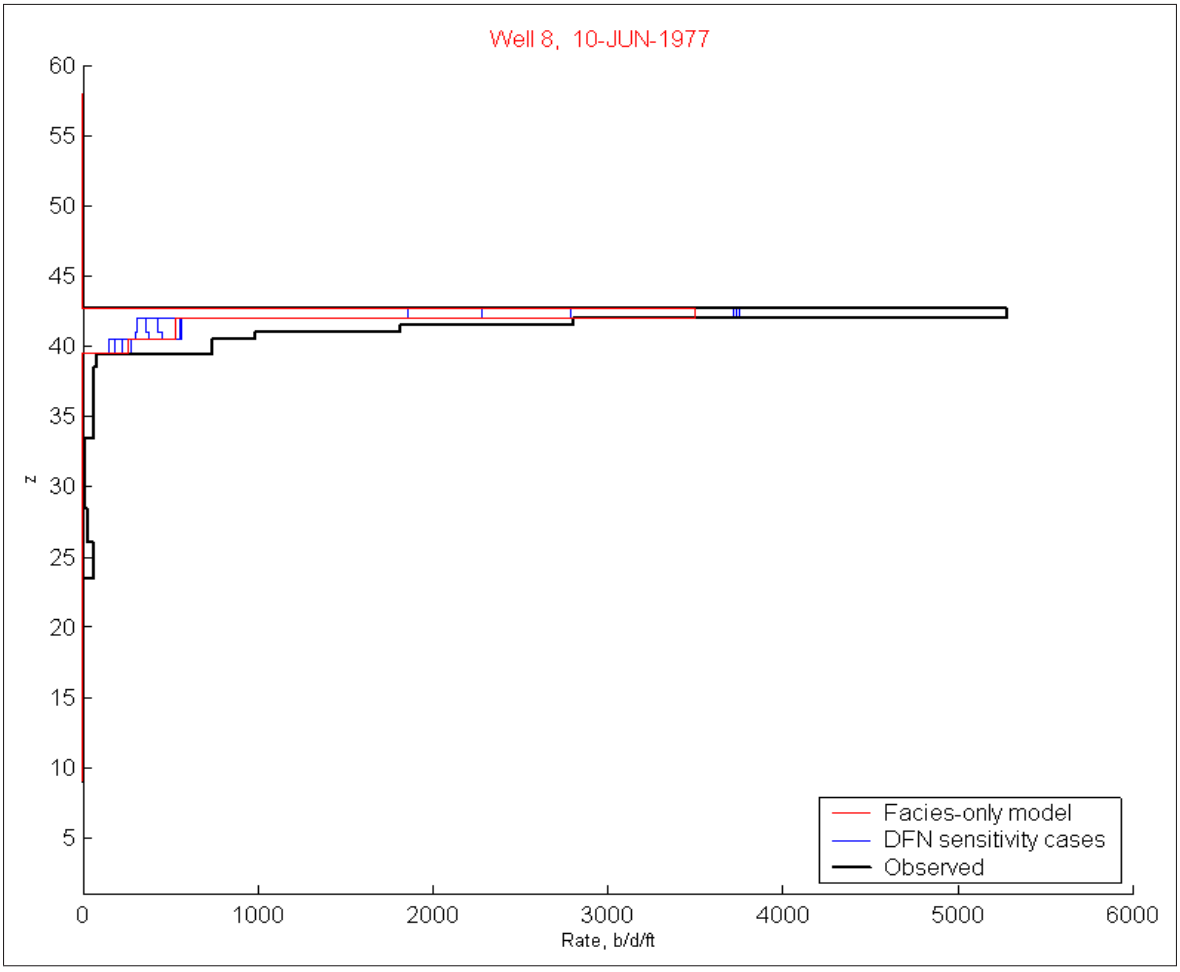

Fig. 10.32: Flowmeter performance under varying DFN azimuth

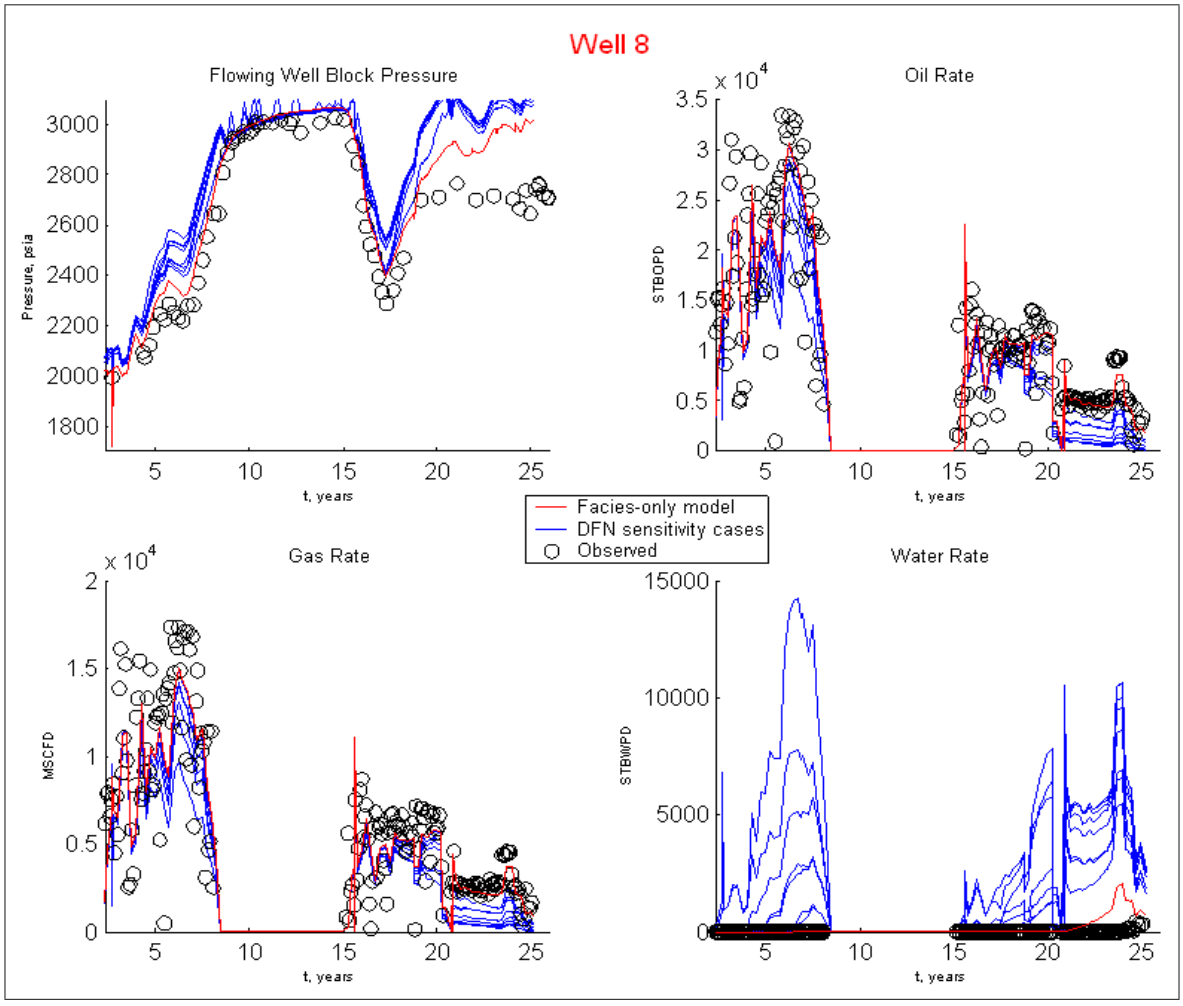

Fig. 10.33: Well performance under varying DFN azimuth

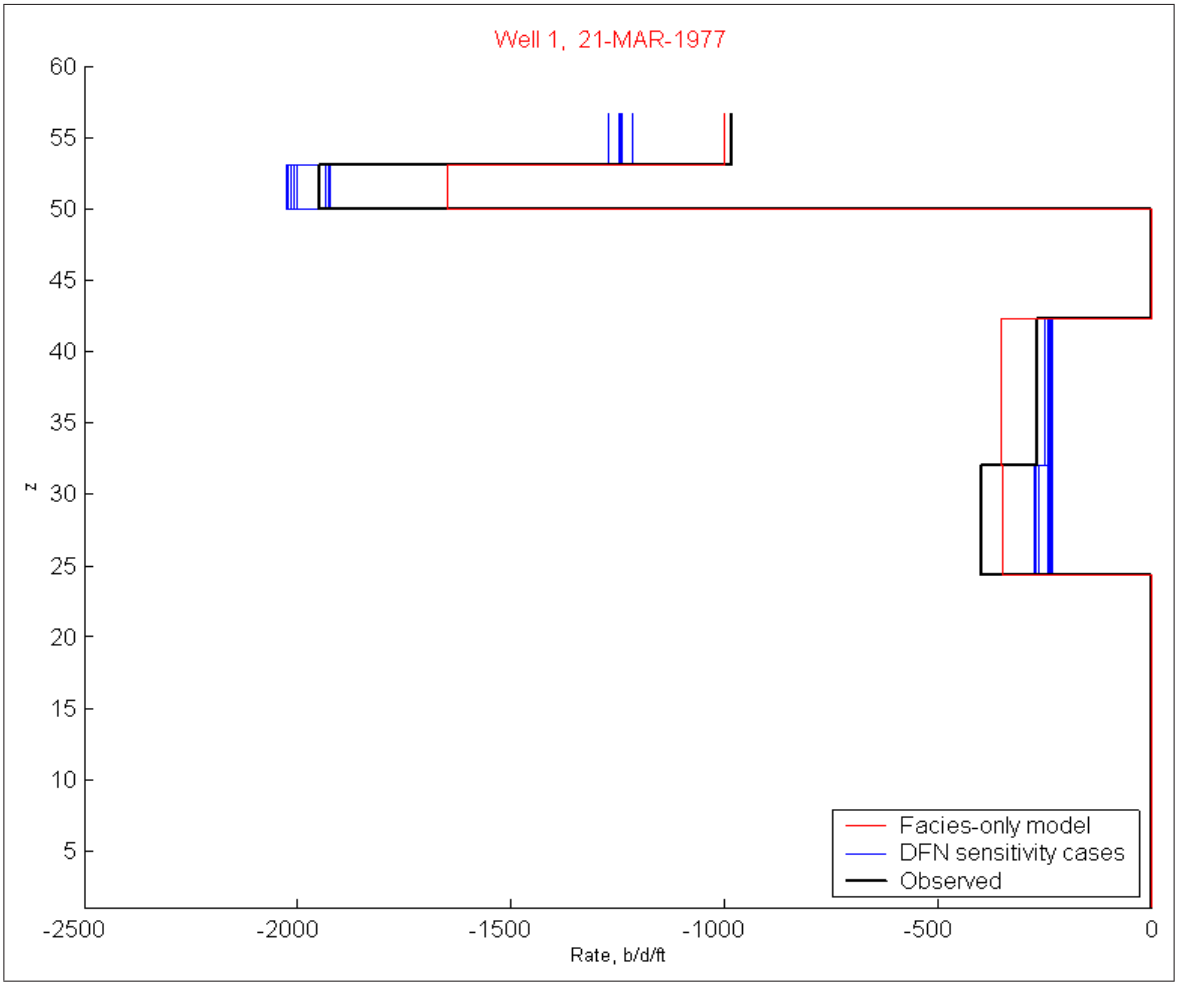

Fig. 10.34: Flowmeter performance under varying DFN length

DFN length

Variation in the length of a DFN has shown a modest effect on the well performance of the two key wells, particularly in Well 8 water production. The DFN length range was that applied in the other DFN parameter evaluations, and so a static model realization is not conspicuous relative to the previous realizations shown.

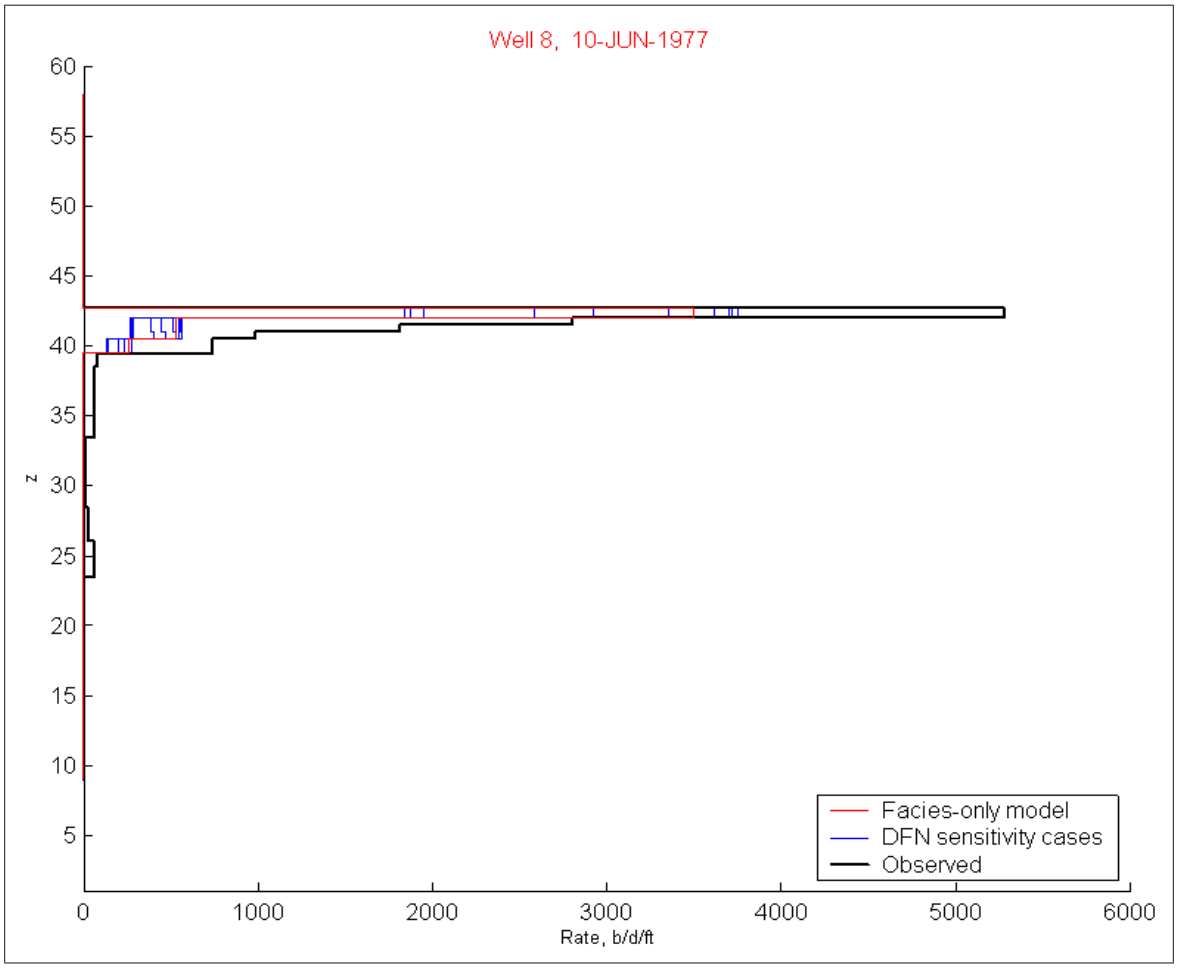

Fig. 10.35: Flowmeter performance under varying DFN length

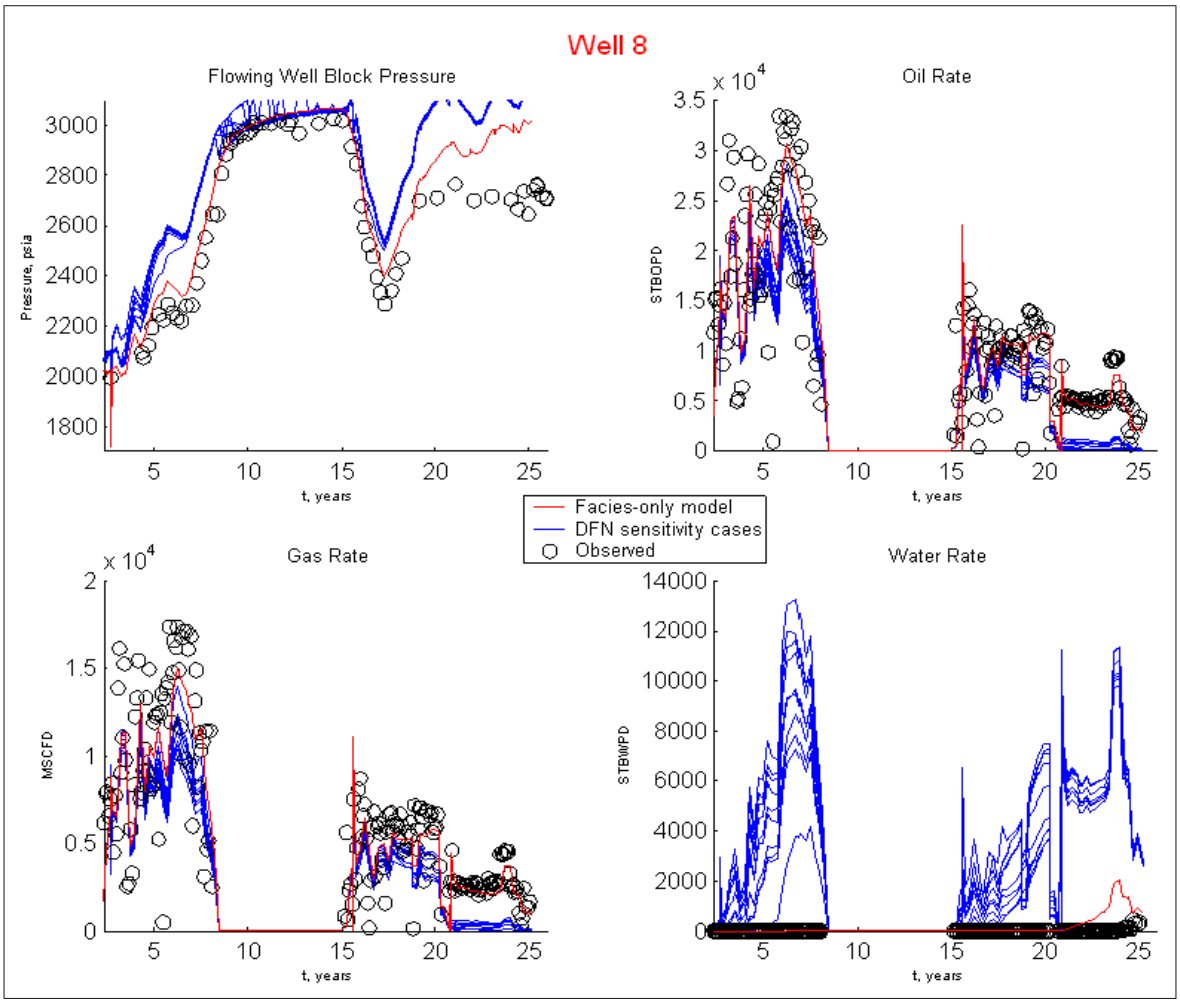

Fig. 10.36: Well performance under varying DFN length

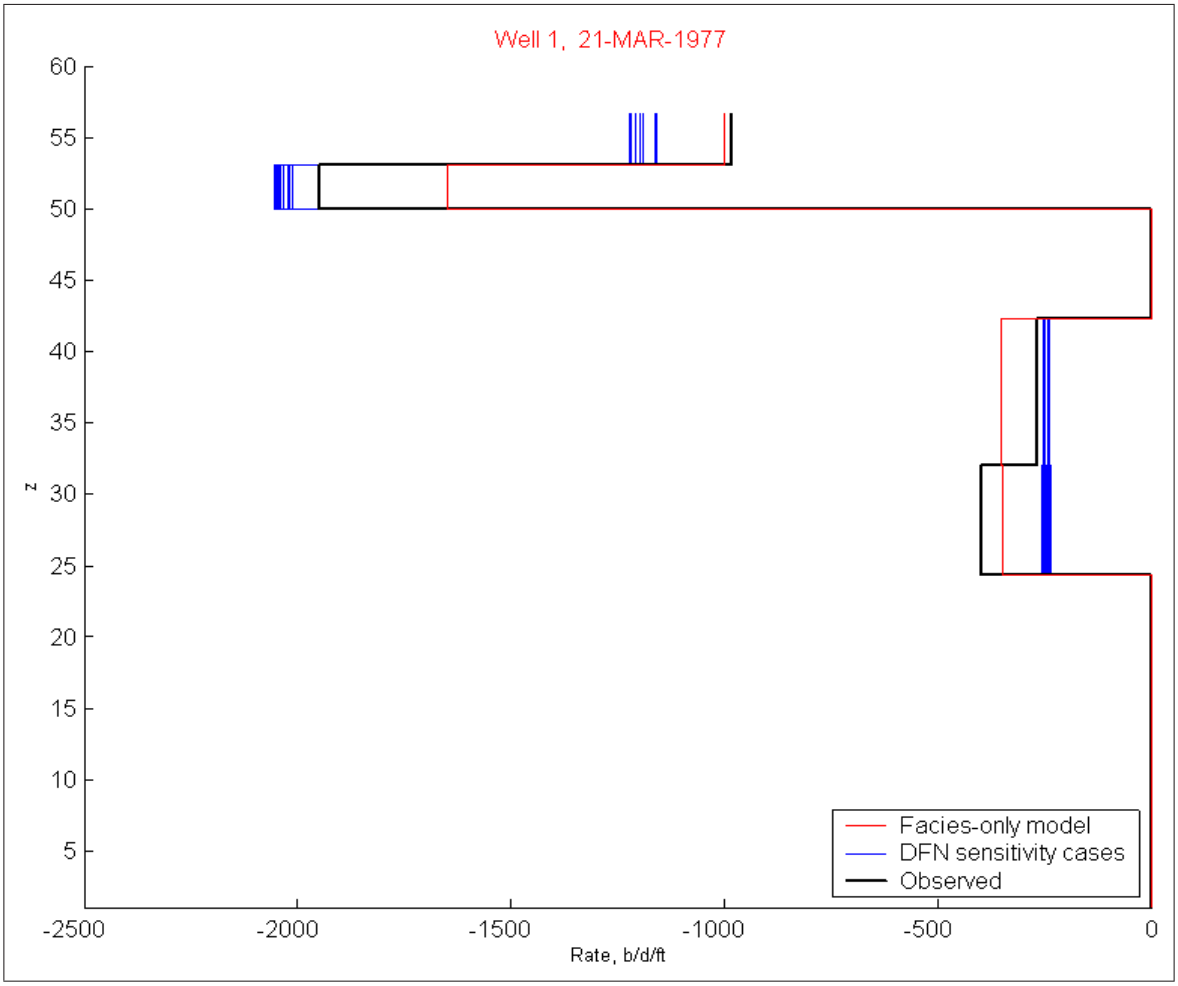

Fig. 10.37: Flowmeter performance under varying DFN plunge

DFN declination and vertical thickness

The most ineffective DFN parameters proved to be DFN declination (plunge) and DFN vertical thickness, as is evident from the remaining flowmeter and well performance plots for the two key wells.

The declination range was not changed for the sensitivity, as the range was fairly extensive. The thickness range was increased, to vary from 8 to 32 ft, from the range which applied to the other DFN evaluations, 8 to 16 ft. Fig. 10.40 presents a realization from the DFN vertical thickness evaluation. It is apparent that thicker DFNs reside in this realization, although the variation in flow performance is minimal.

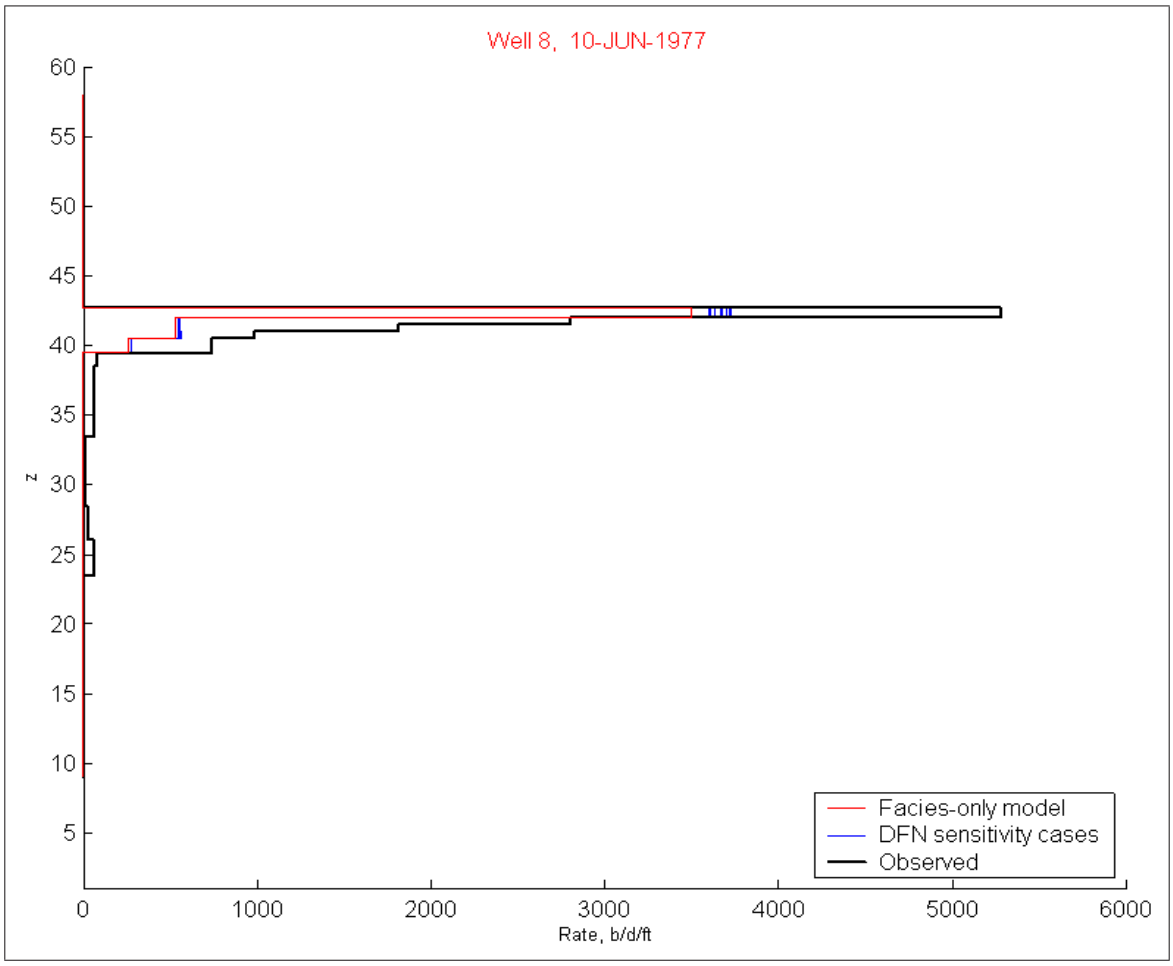

Fig. 10.38: Flowmeter performance under varying DFN plunge

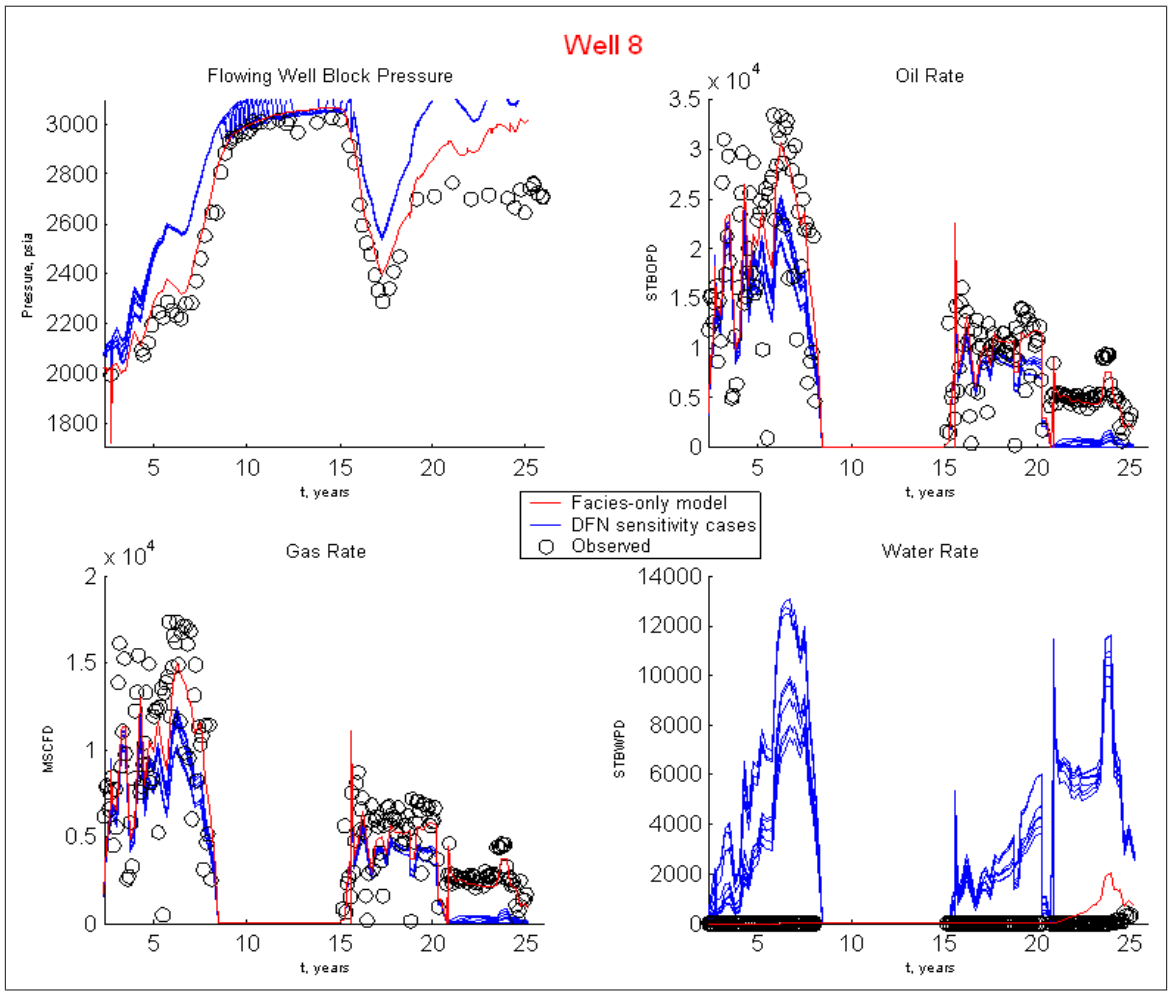

Fig. 10.39: Well performance under varying DFN plunge

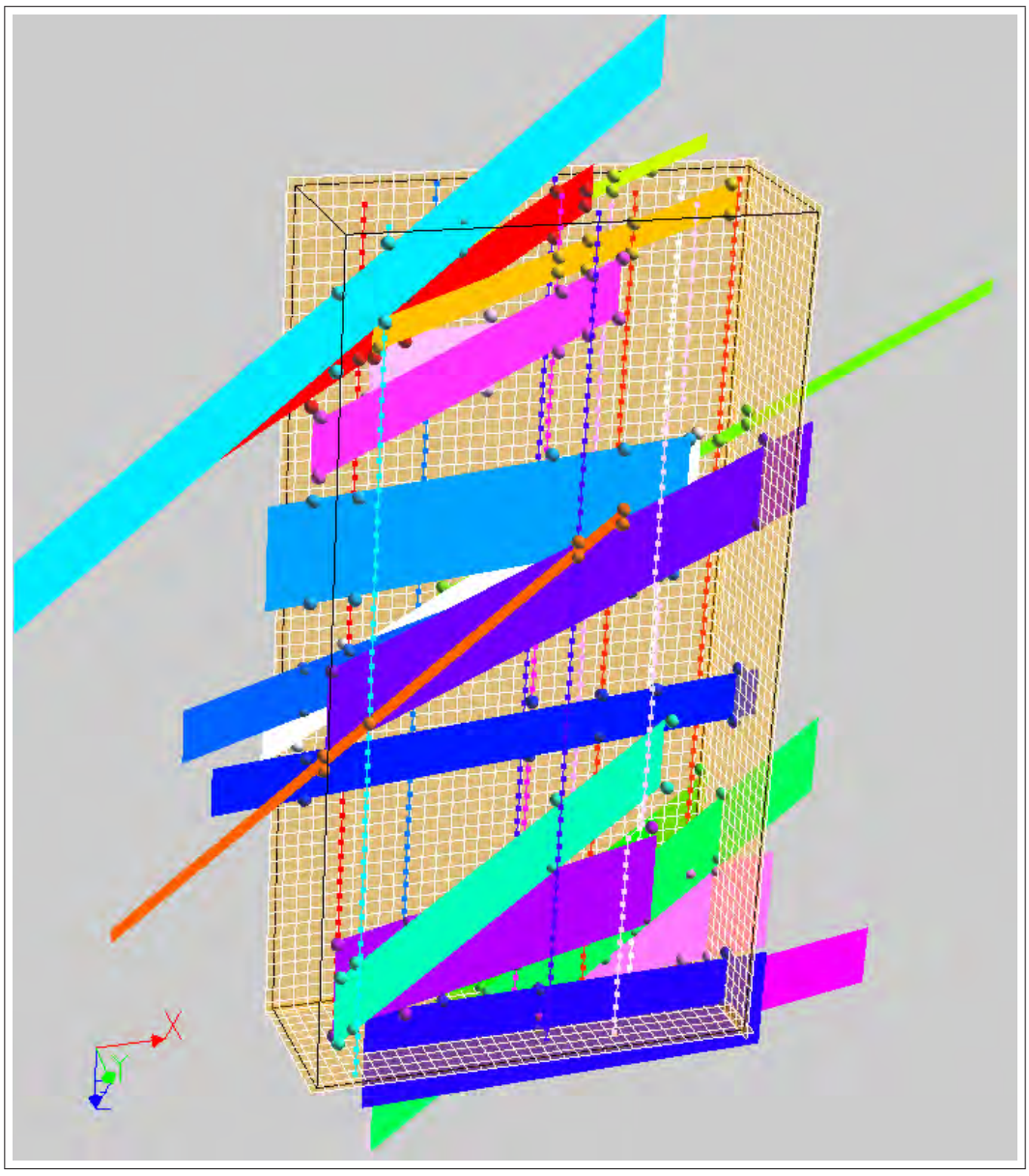

Fig. 10.40: DFN and source connections realization, thickness sensitivity

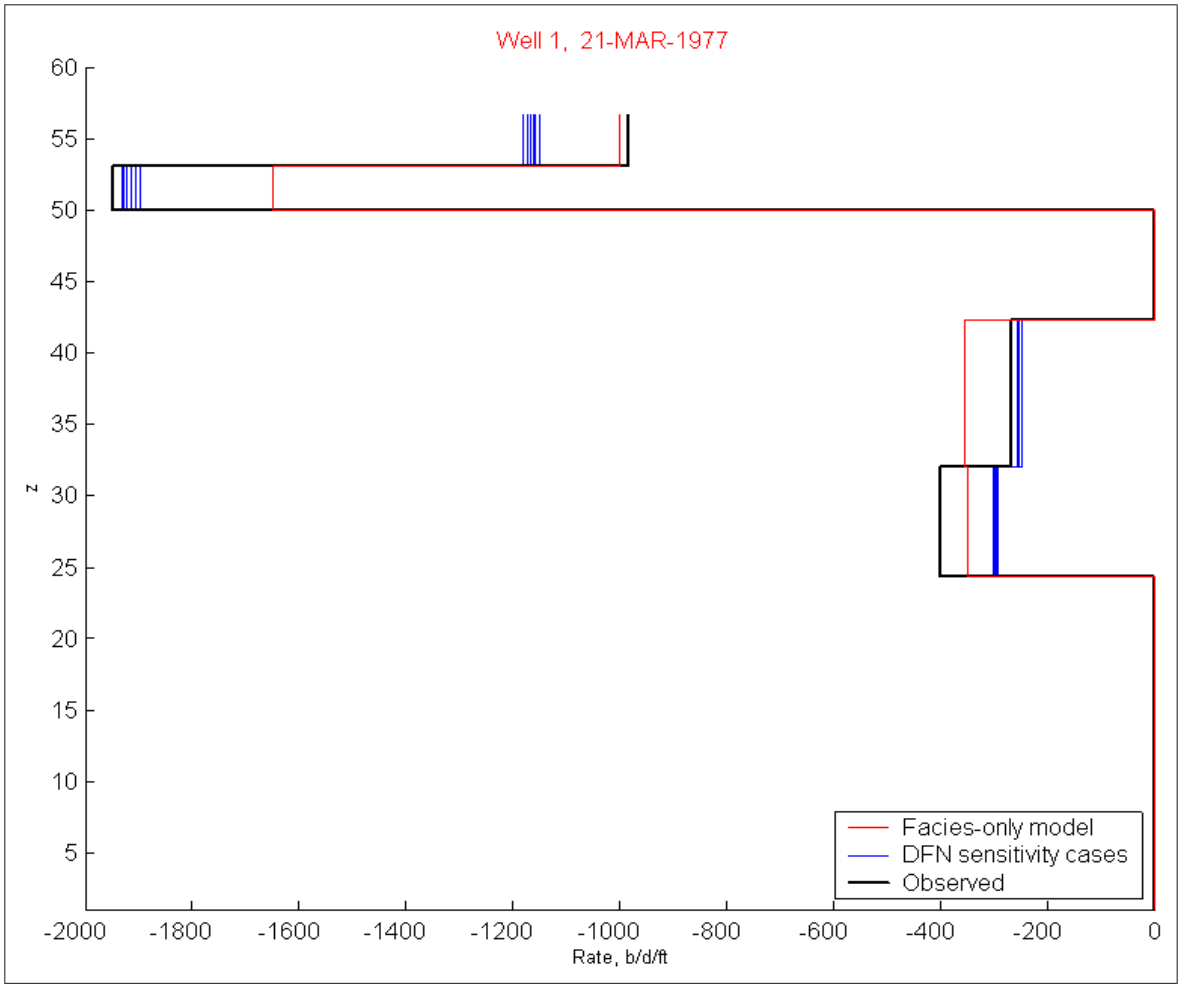

Fig. 10.41: Flowmeter performance under varying DFN thickness

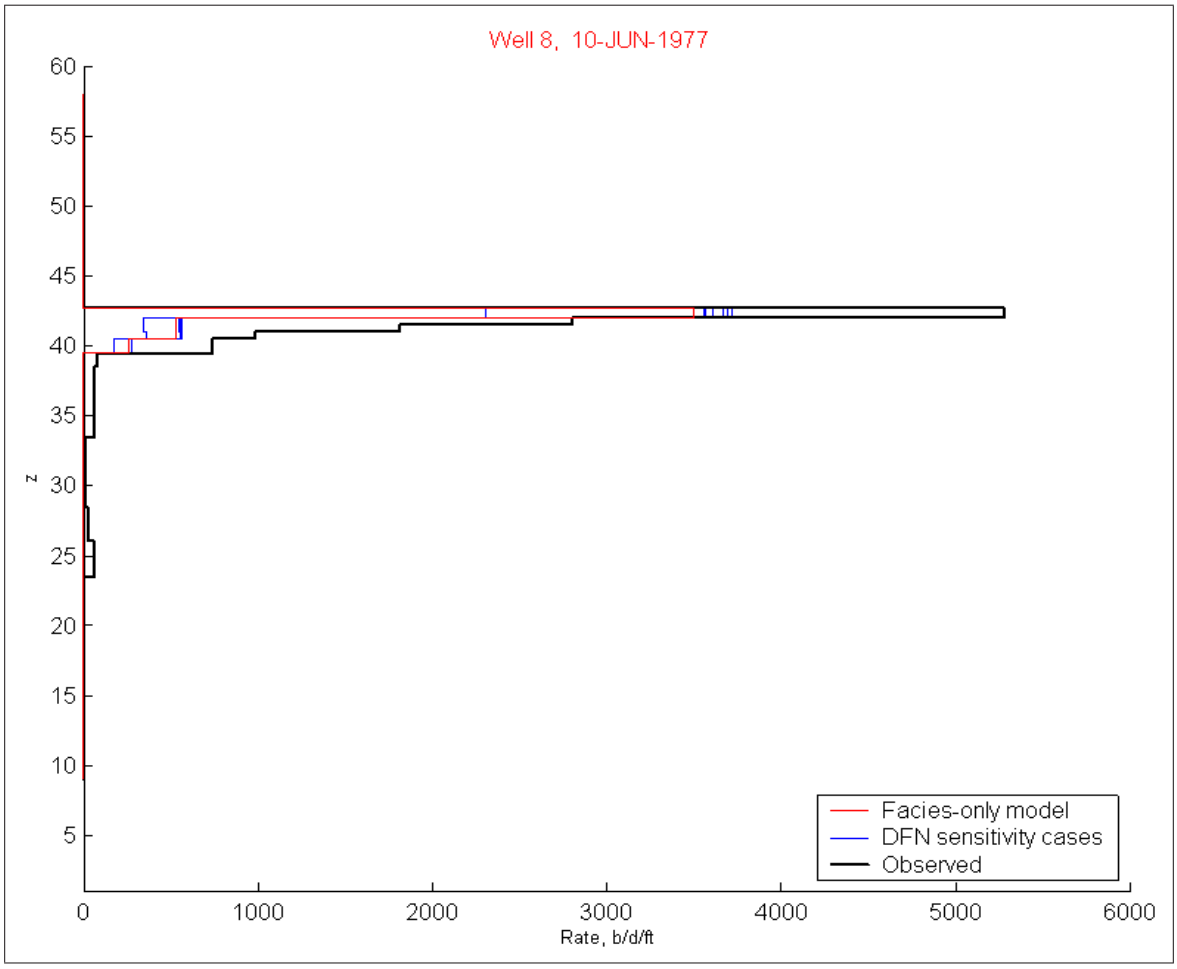

Fig. 10.42: Flowmeter performance under varying DFN thickness

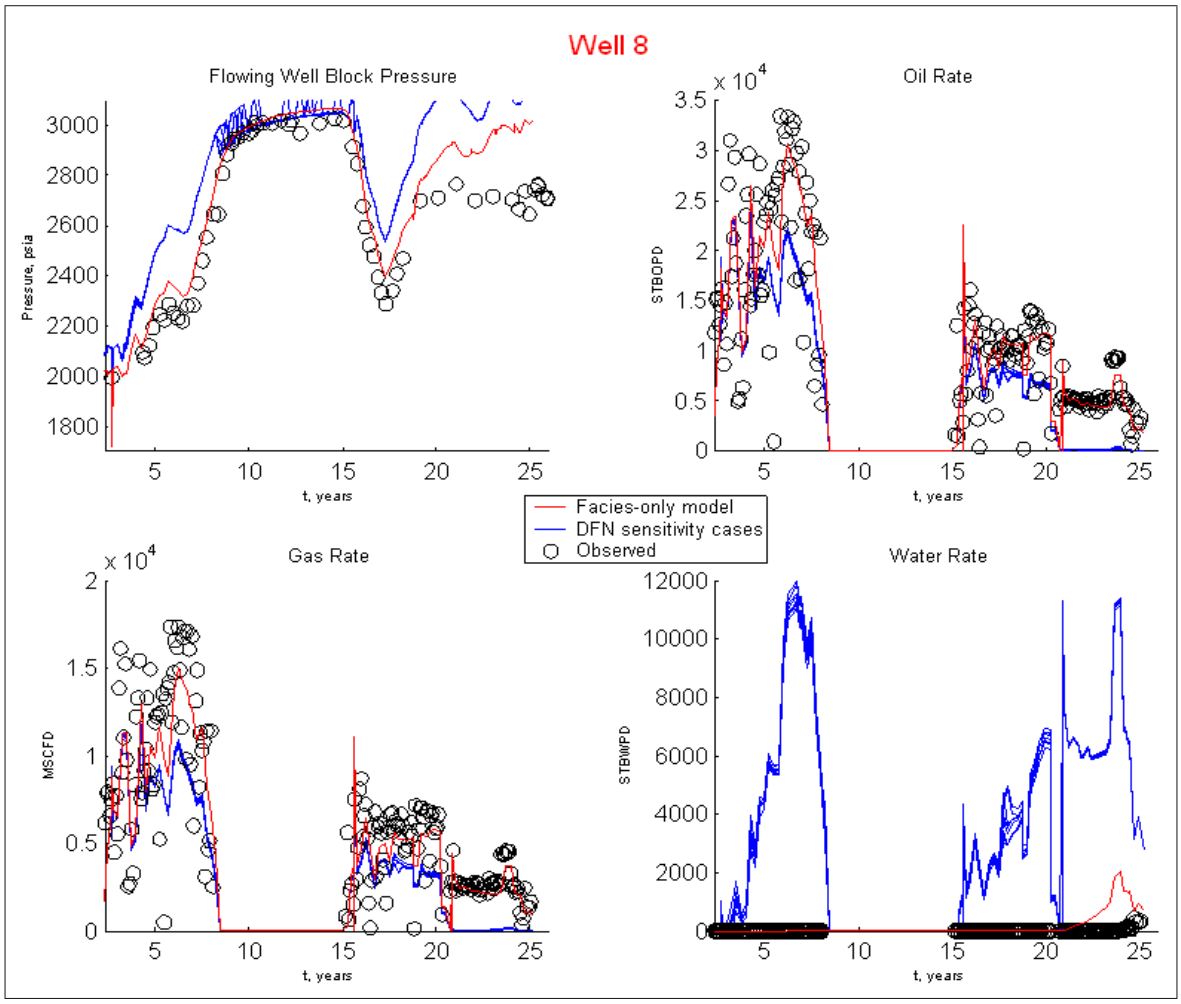

Fig. 10.43: Well performance under varying DFN thickness

APPENDICES

Appendix A

Results of DFN parameter sensitivity tests

This appendix includes an extensive set of the results of the DFN parameter sensitivity study, discussed in detail in Chapter 10. We refer the reader to that chapter for discussions of DFN parameter ranges, as well as details of the sensitivity study in general.

A.1 Regional DFN density sensitivity results

The flowmeter and well performance variations induced by regional DFN density variations is presented for all eight wells in the study area which have performance data. Three of the study area wells have little to no production history.

A.1.1 Flowmeter and well performance of water injection wells

Fig. A.1 through Fig. A.6 present flowmeter and well injection pressure performance results for the two water injection wells (see Fig. 3.2 for study area well locations), under both regional density scenarios.

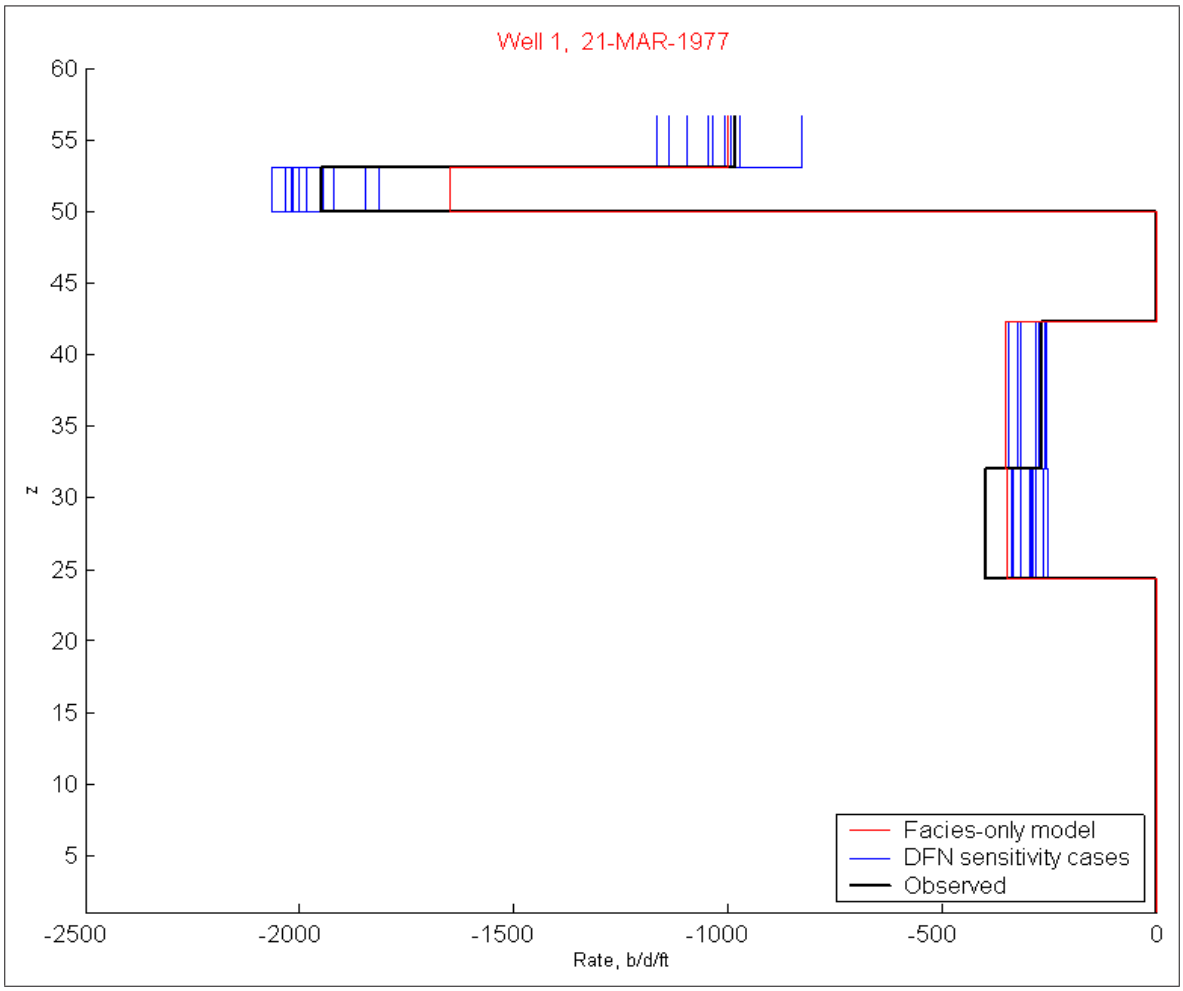

Fig. A.1: Flowmeter performance under Region Case 1

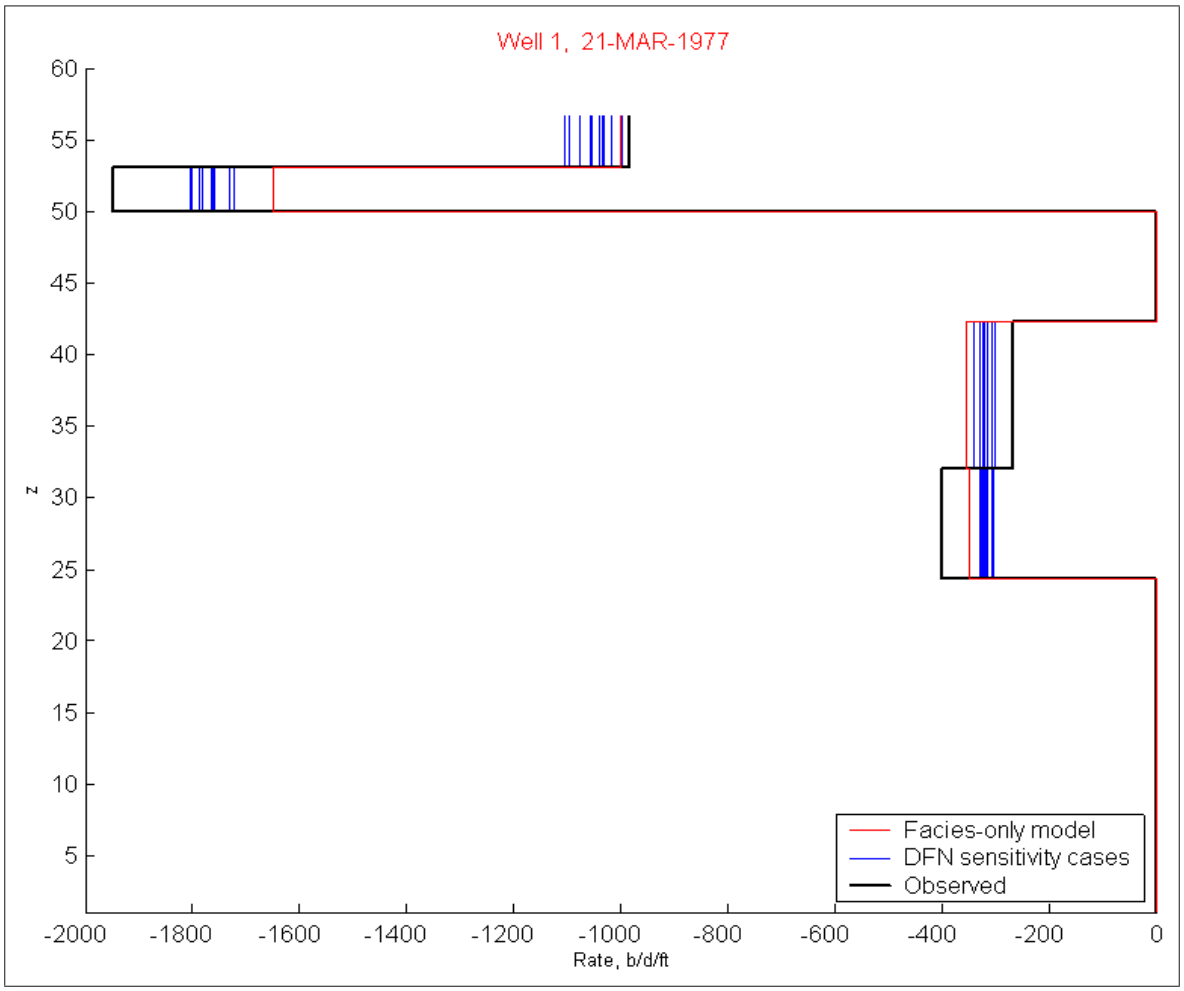

Fig. A.2: Flowmeter performance under Region Case 2

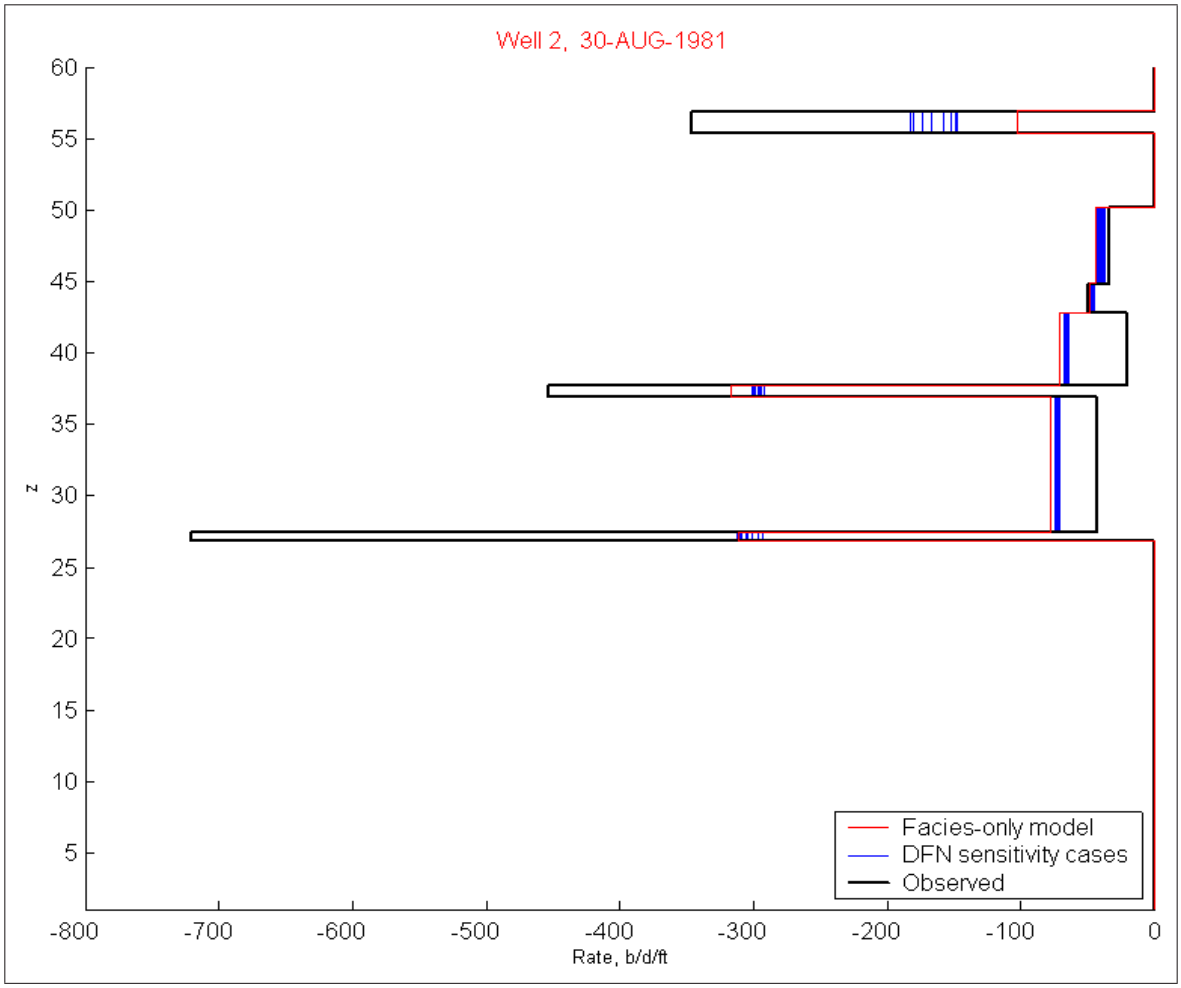

Fig. A.3: Flowmeter performance under Region Case 1

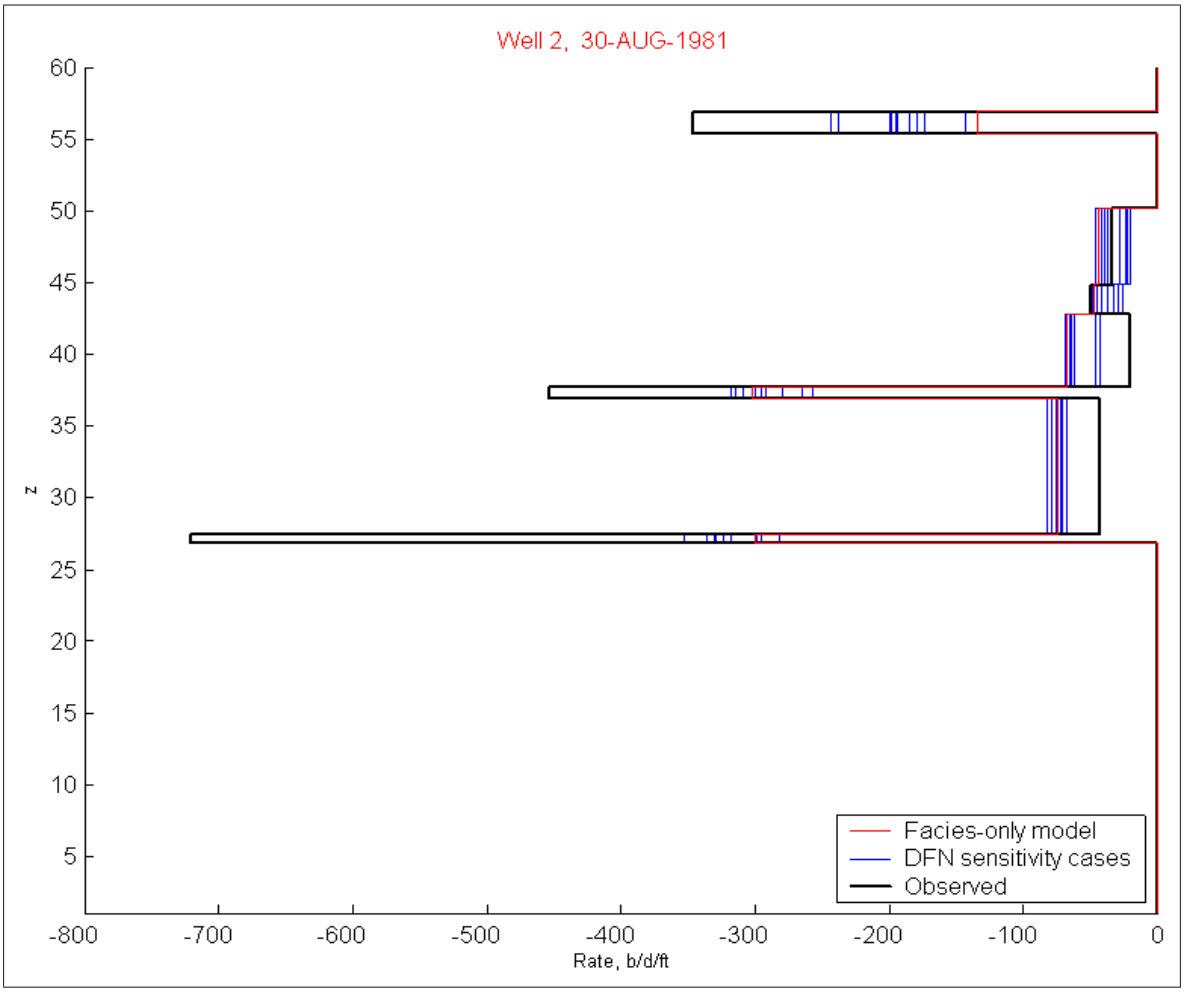

Fig. A.4: Flowmeter performance under Region Case 2

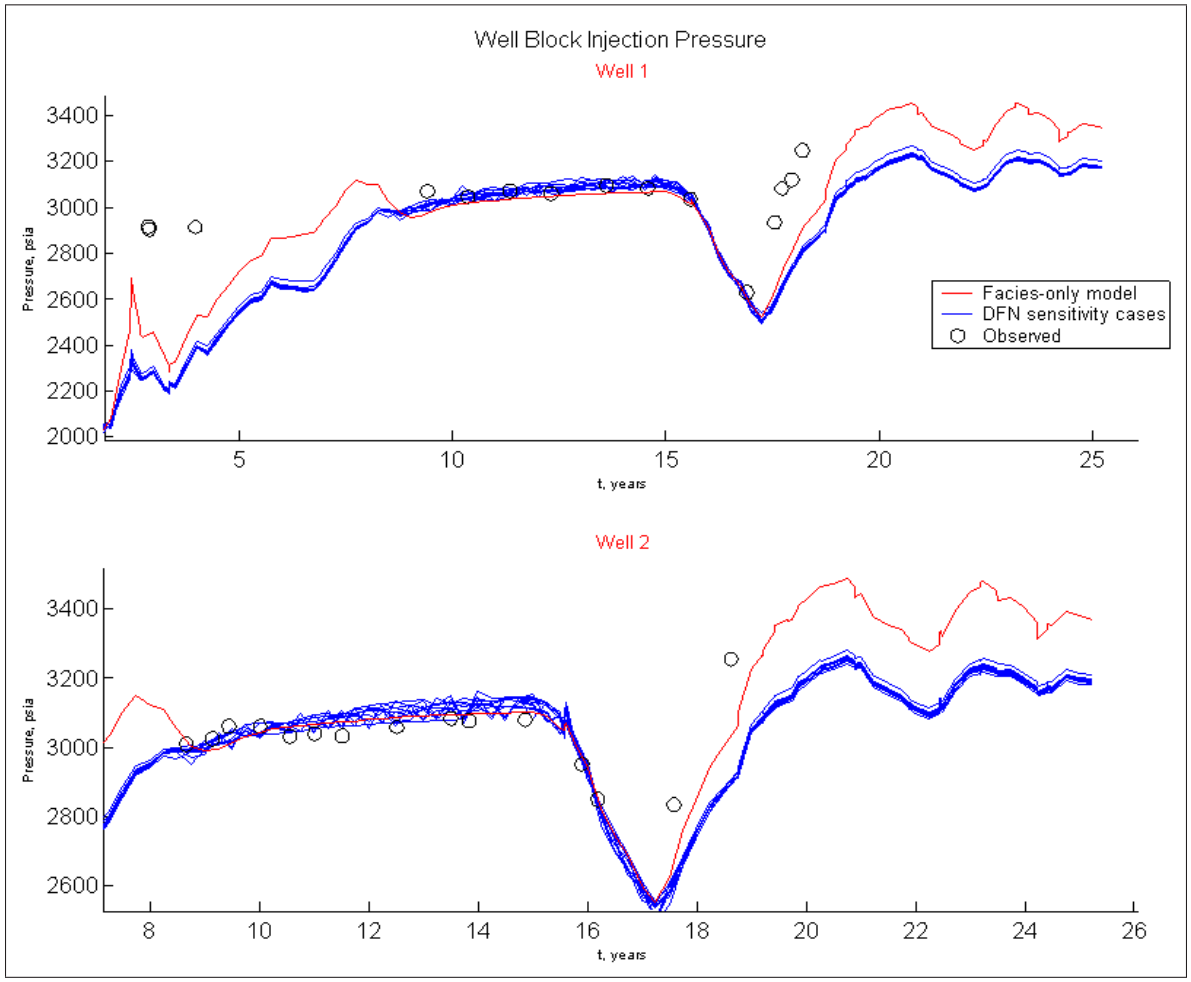

Fig. A.5: Injection performance under Region Case 1

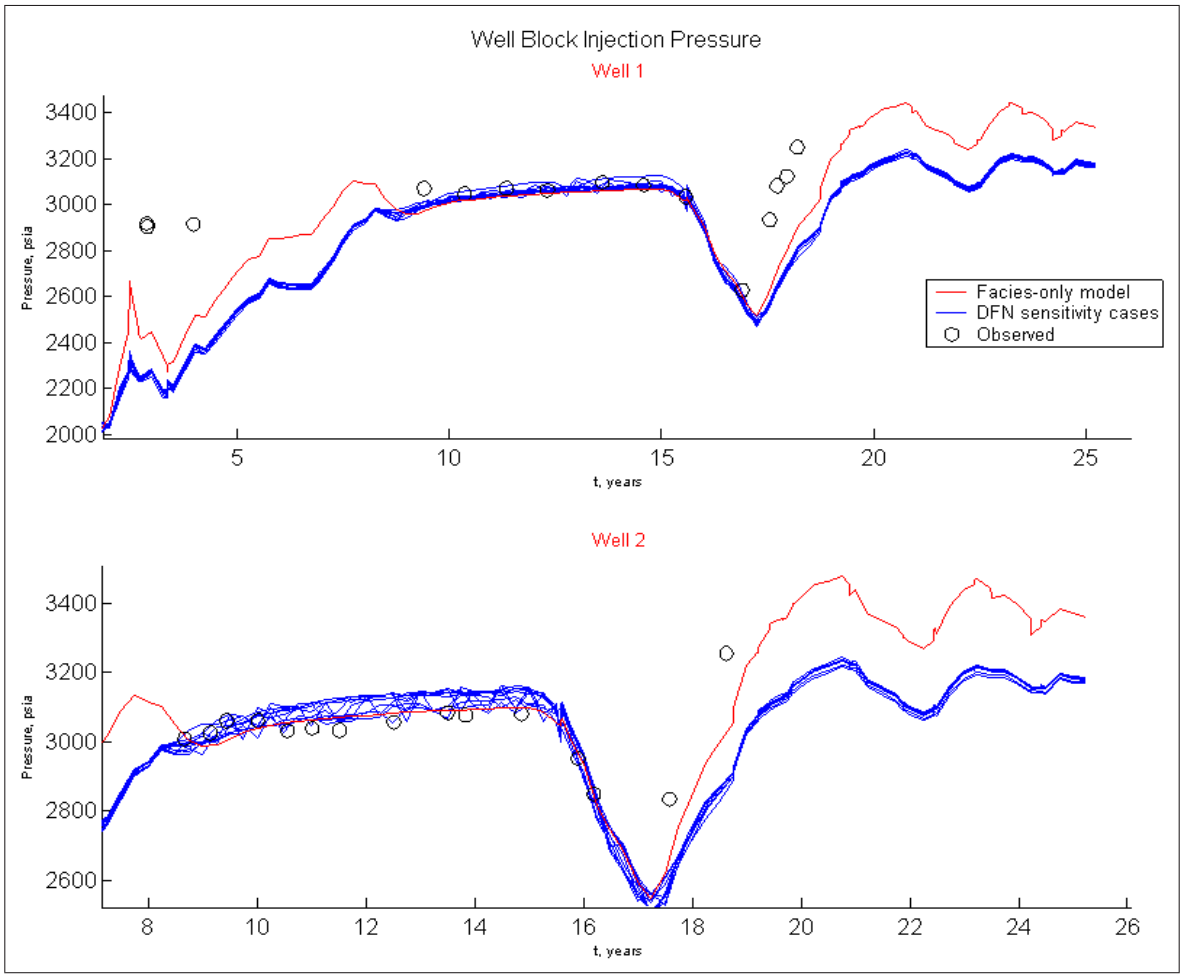

Fig. A.6: Injection performance under Region Case 2

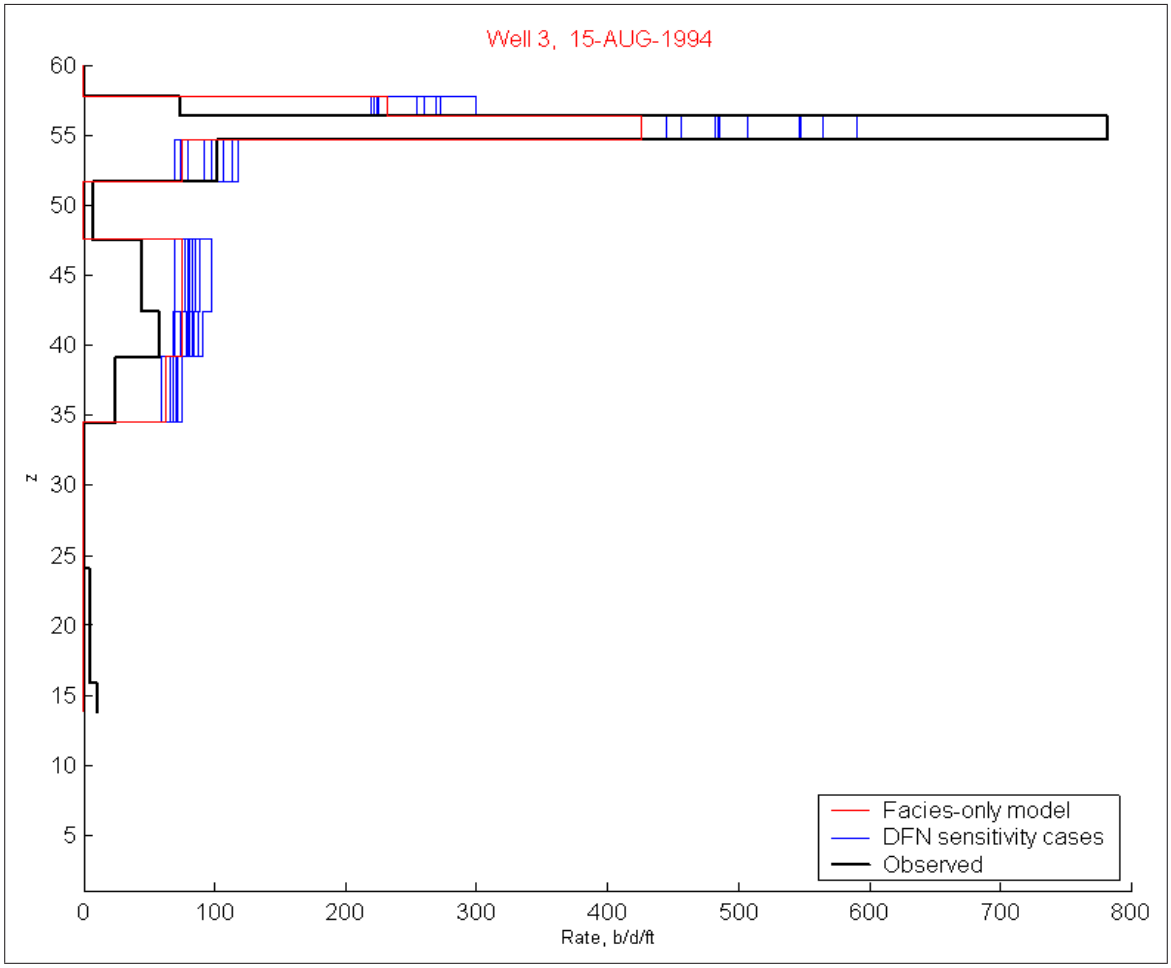

Fig. A.7: Flowmeter performance under Region Case 1

A.1.2 Flowmeter and well performance of producing wells

Fig. A.7 through Fig. A.30 present flowmeter and production well performance results for six study area producing wells (see Fig. 3.2 for study area well locations), under both regional density scenarios.

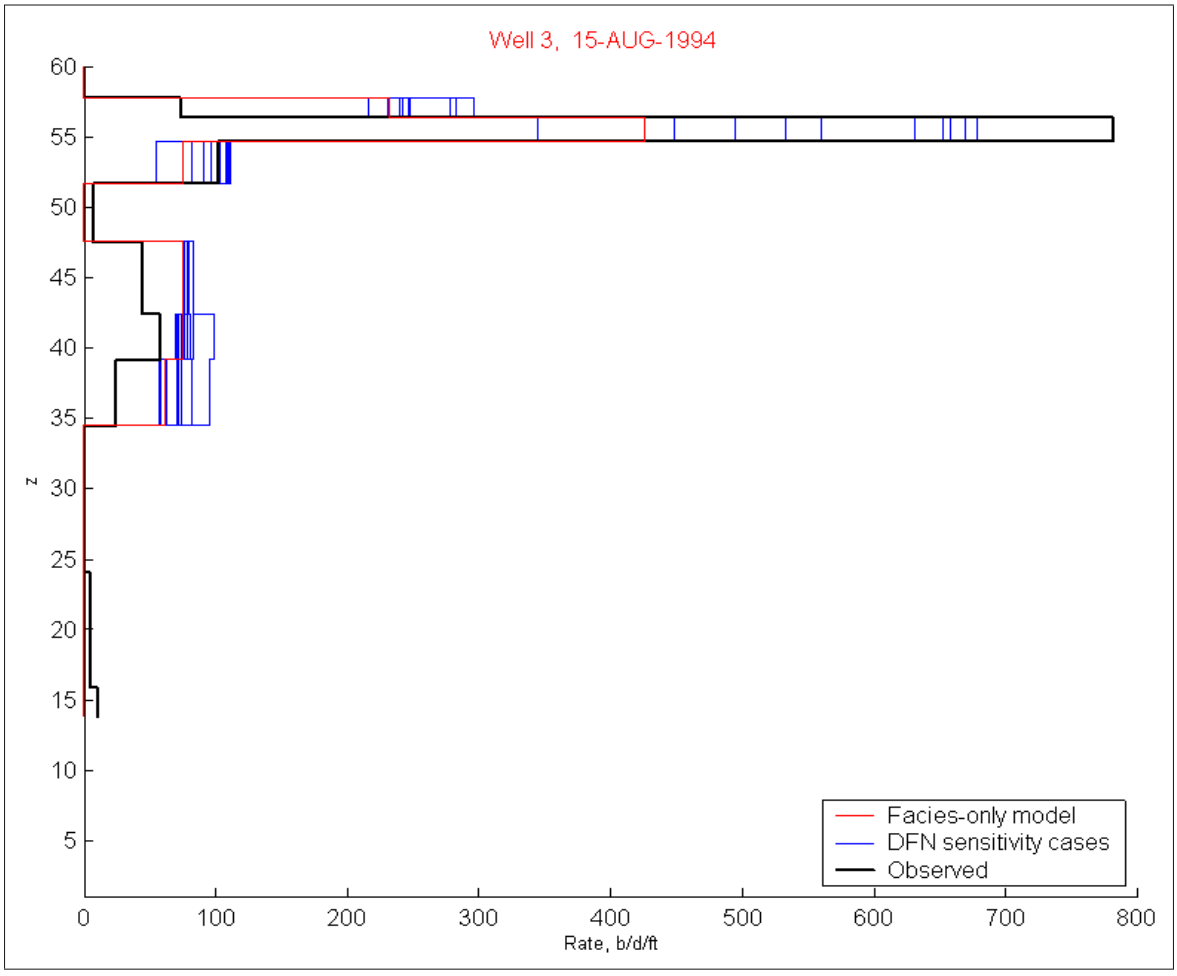

Fig. A.8: Flowmeter performance under Region Case 2

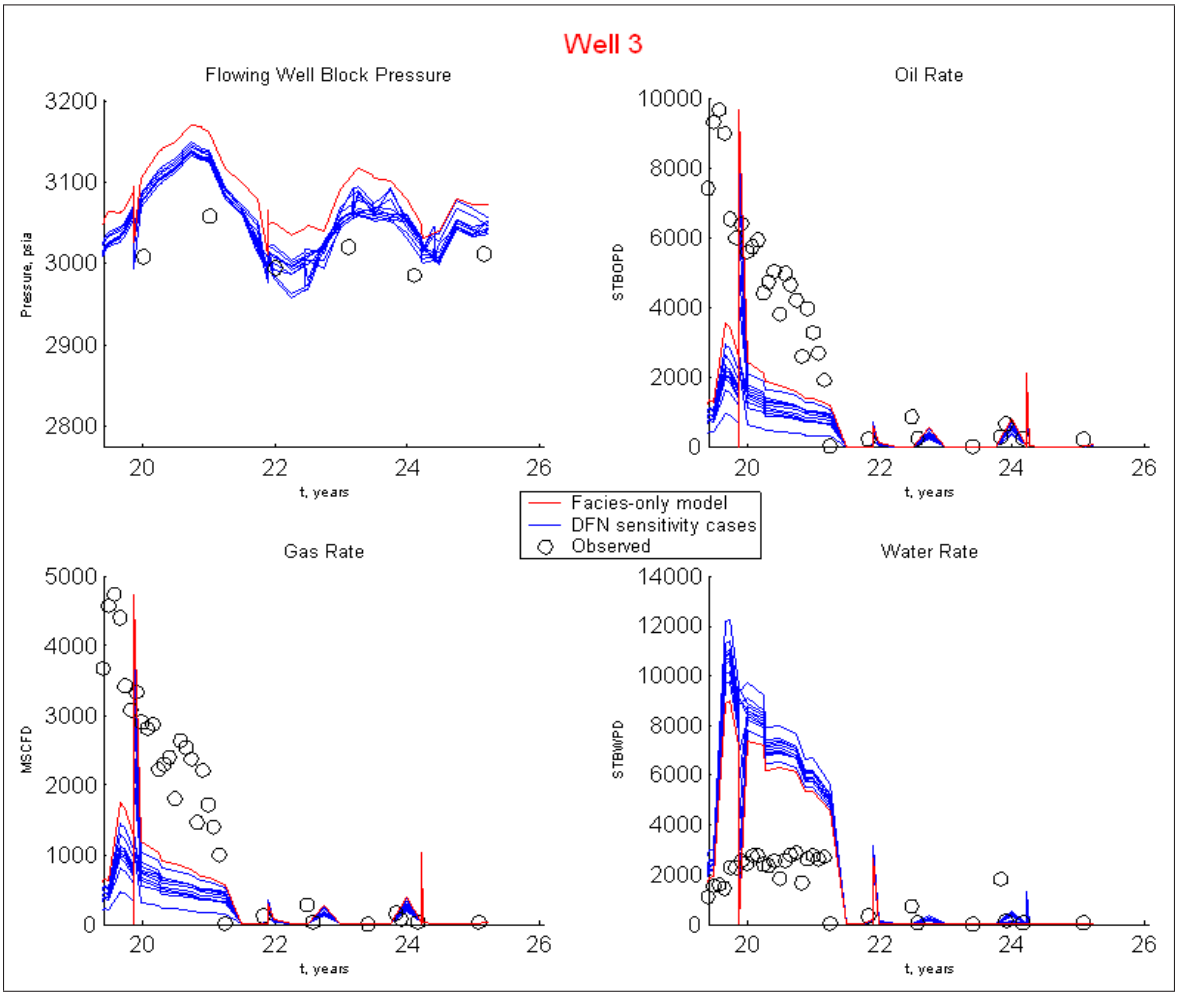

Fig. A.9: Well performance under Region Case 1

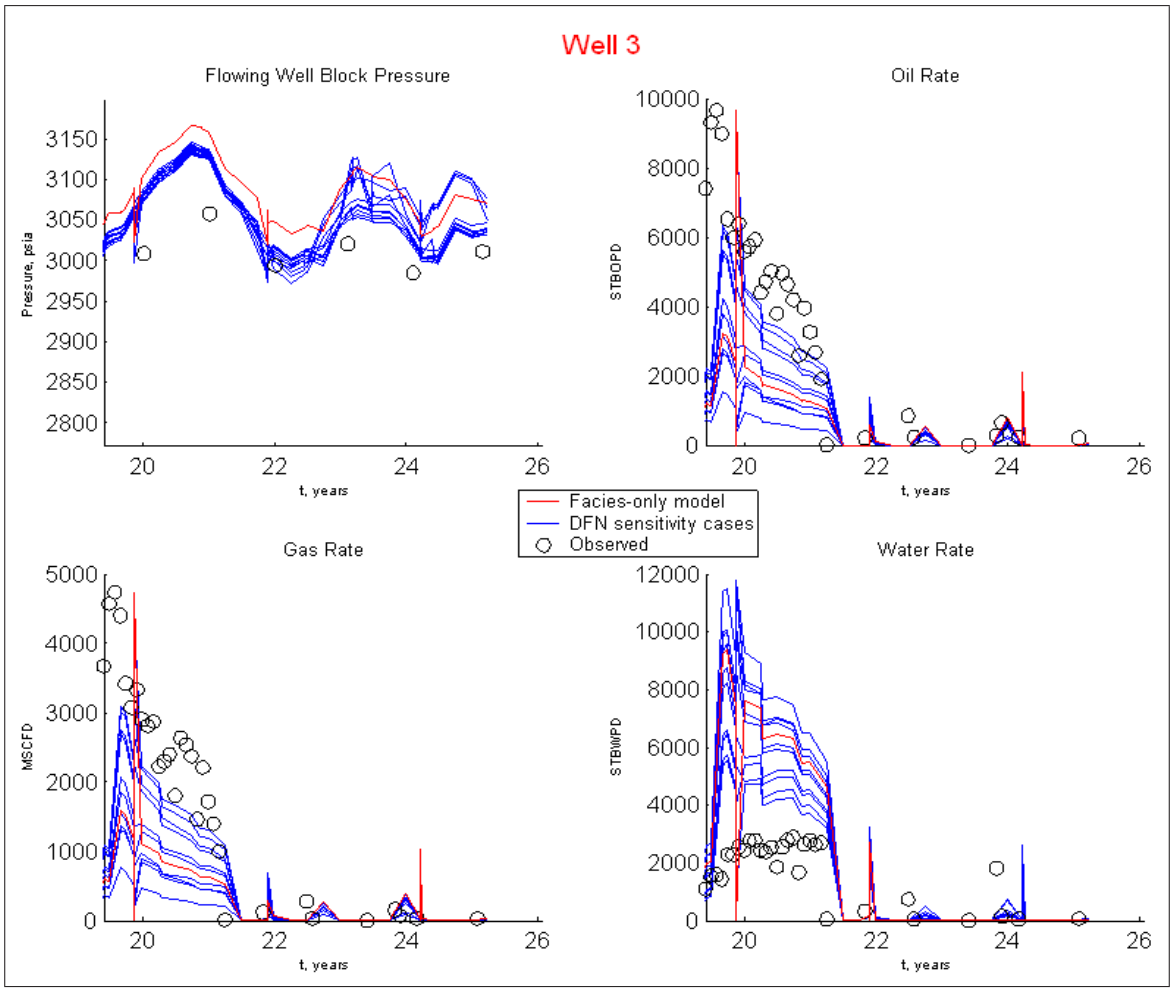

Fig. A.10: Well performance under Region Case 2

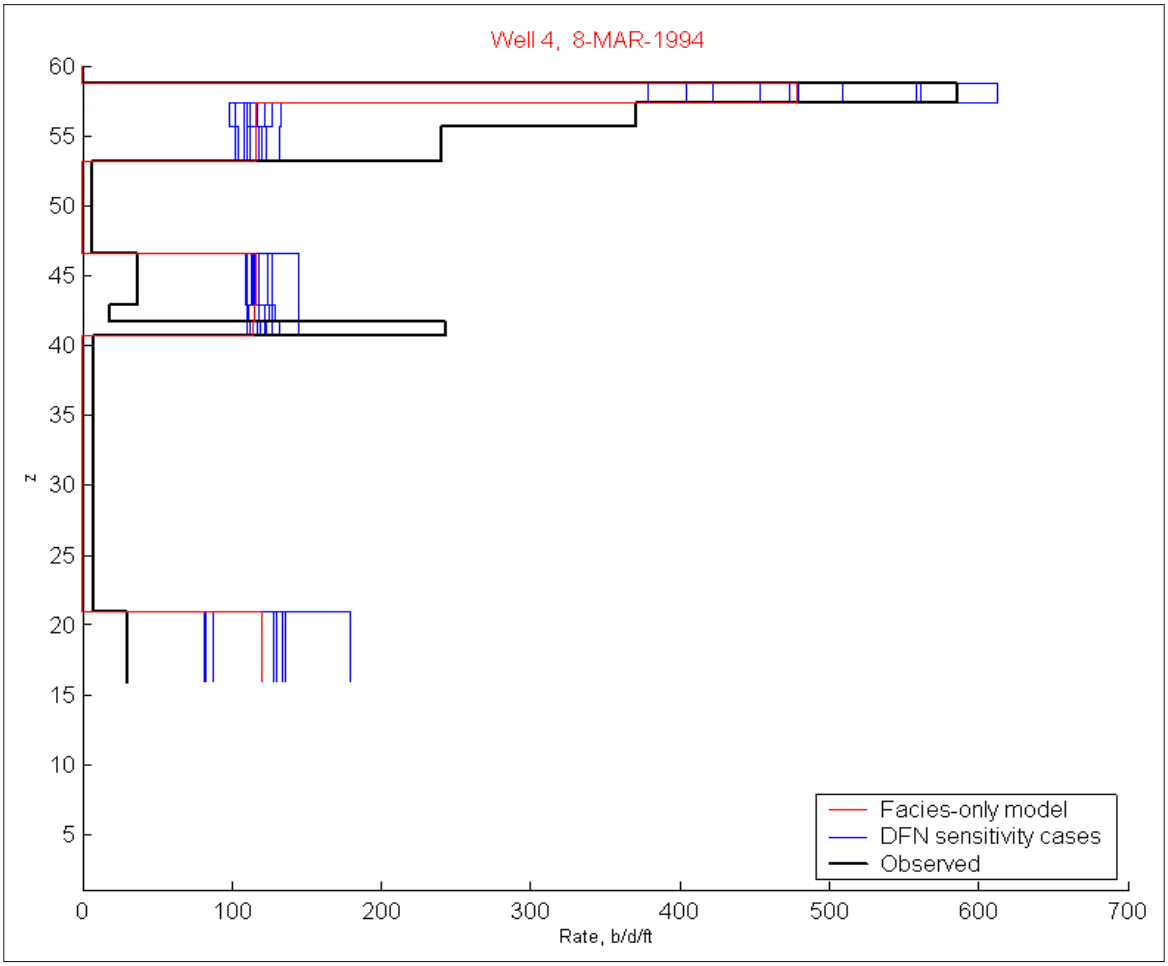

Fig. A.11: Flowmeter performance under Region Case 1

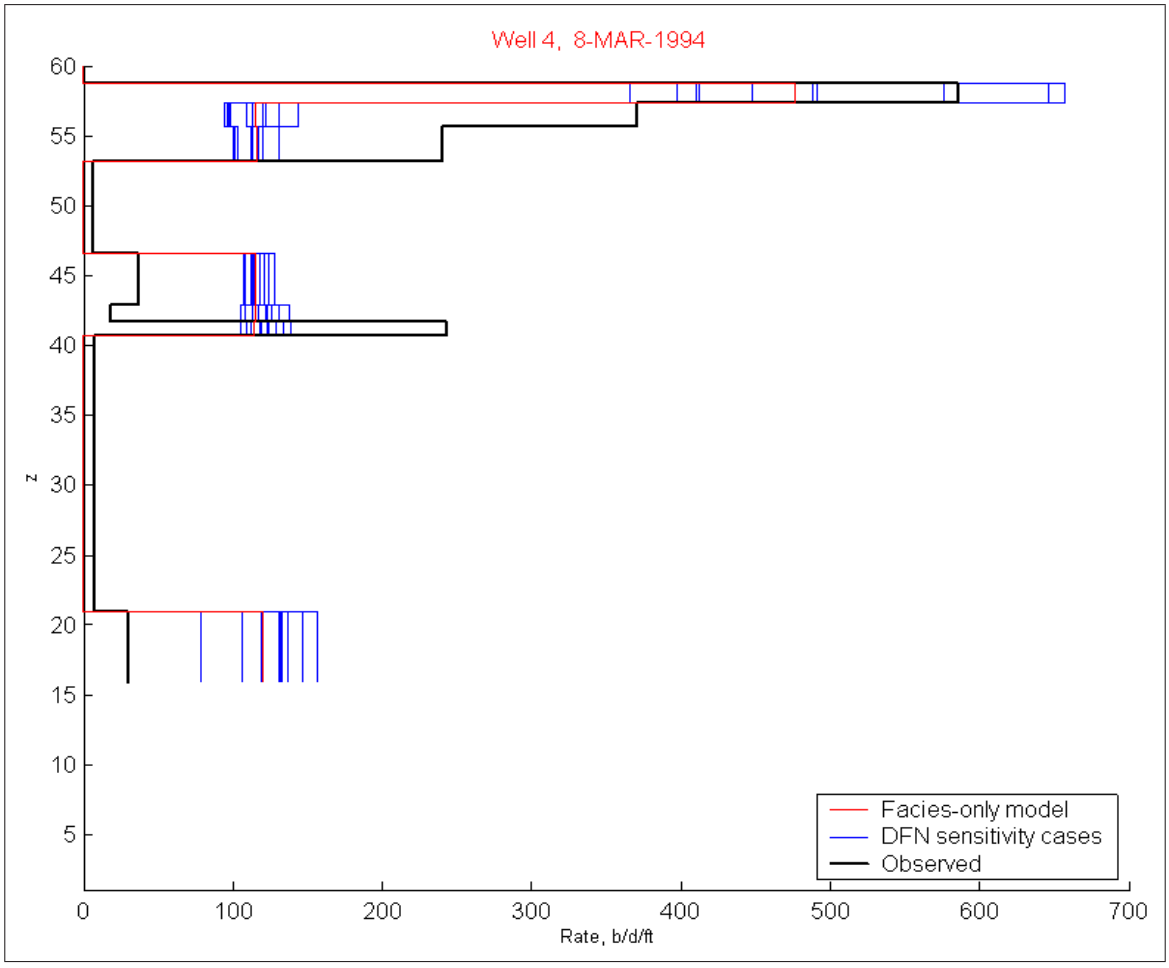

Fig. A.12: Flowmeter performance under Region Case 2

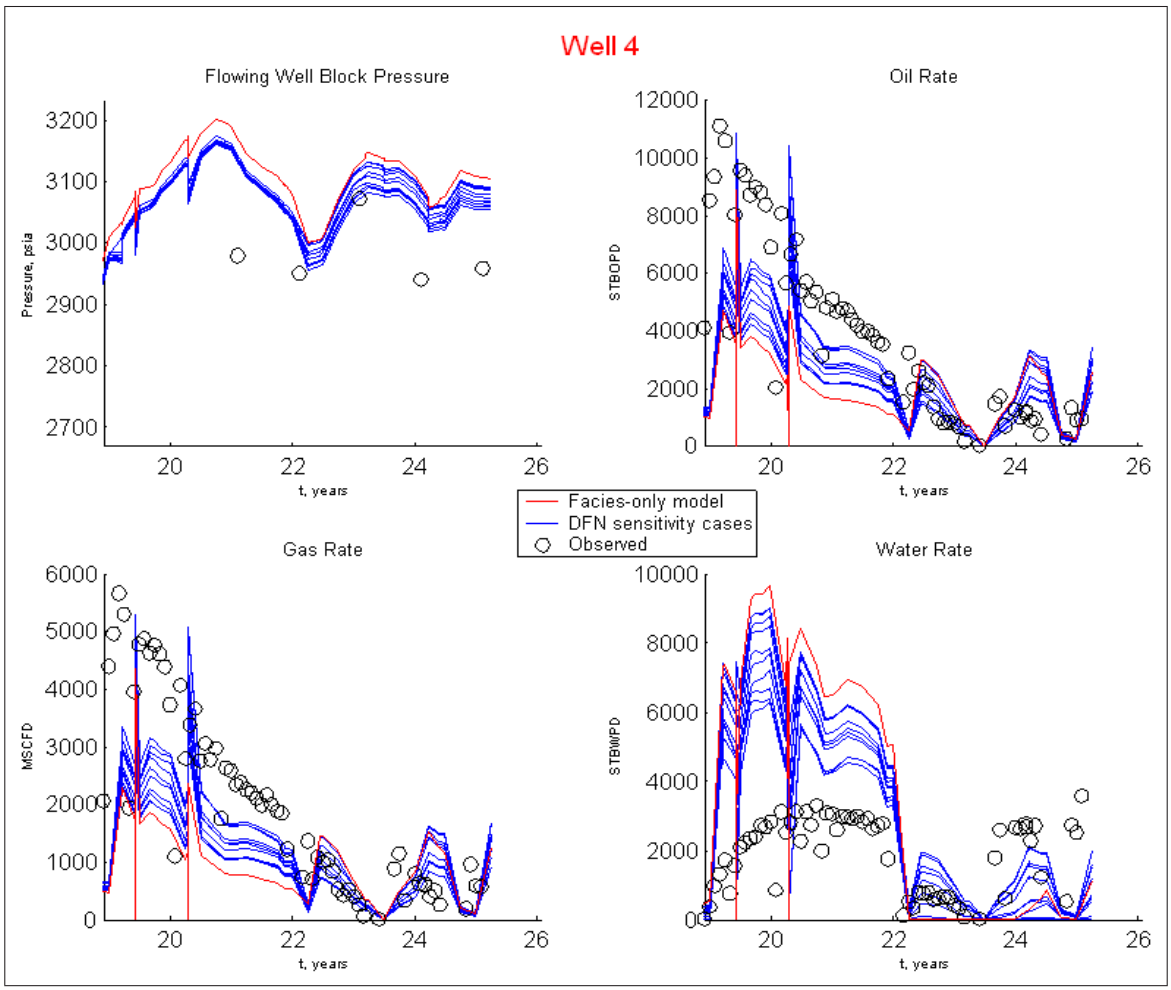

Fig. A.13: Well performance under Region Case 1

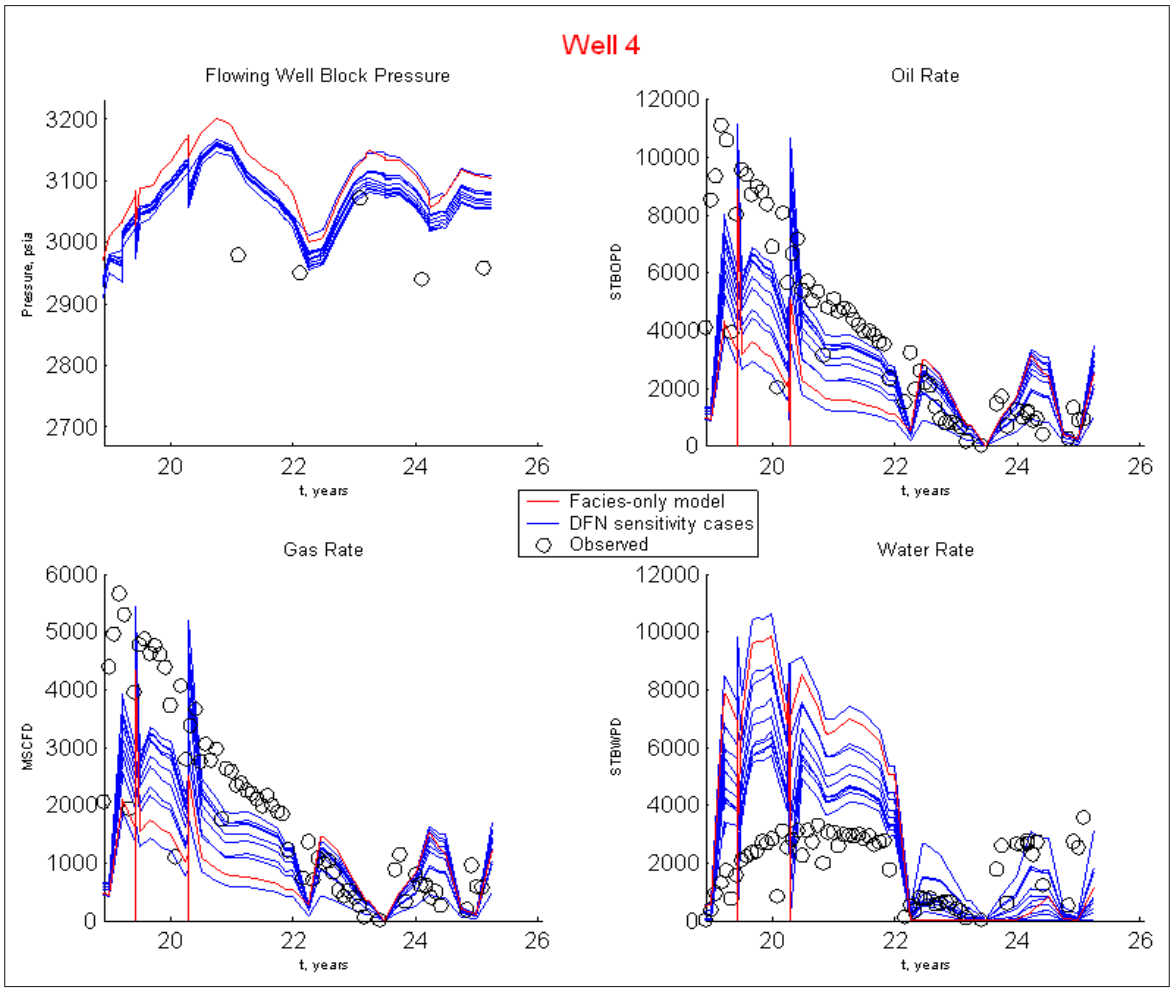

Fig. A.14: Well performance under Region Case 2

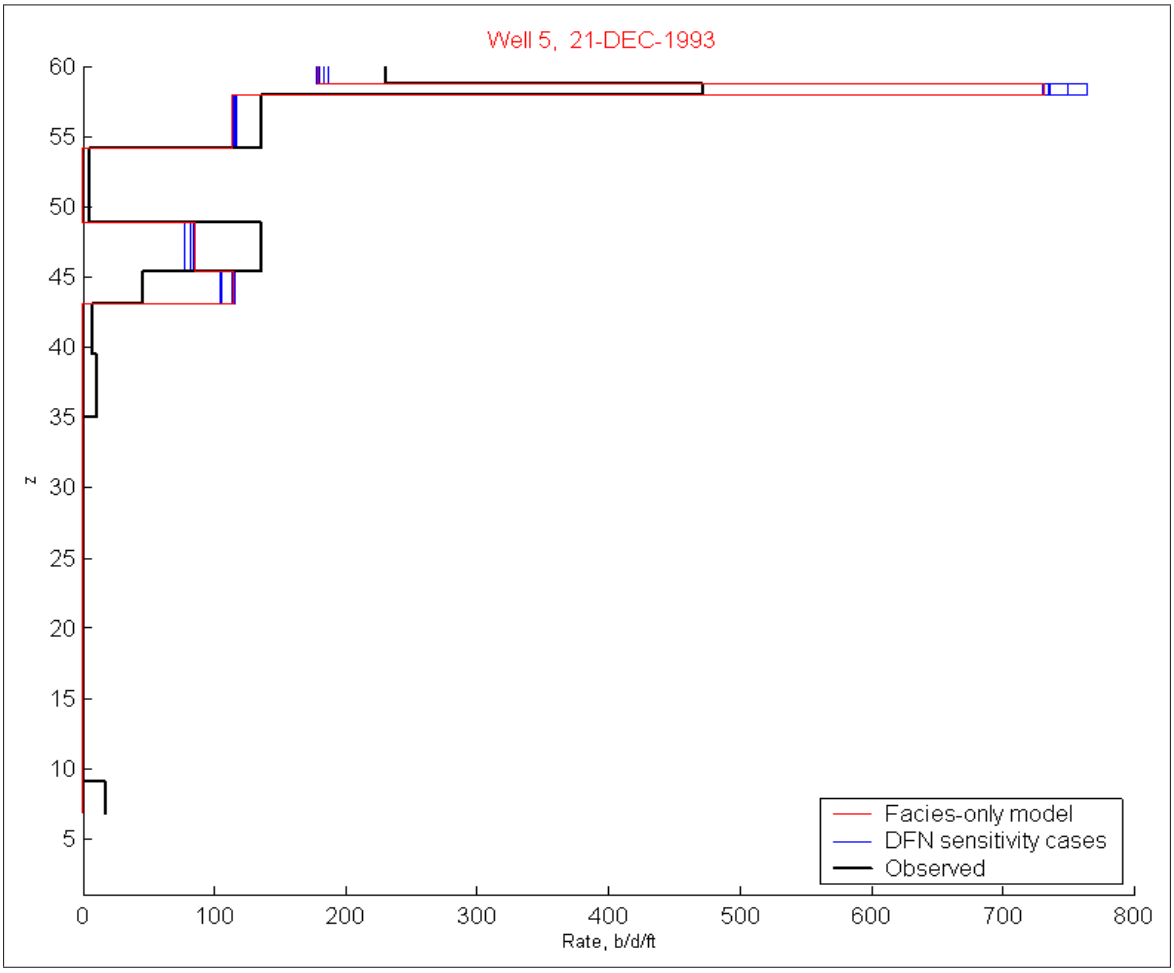

Fig. A.15: Flowmeter performance under Region Case 1

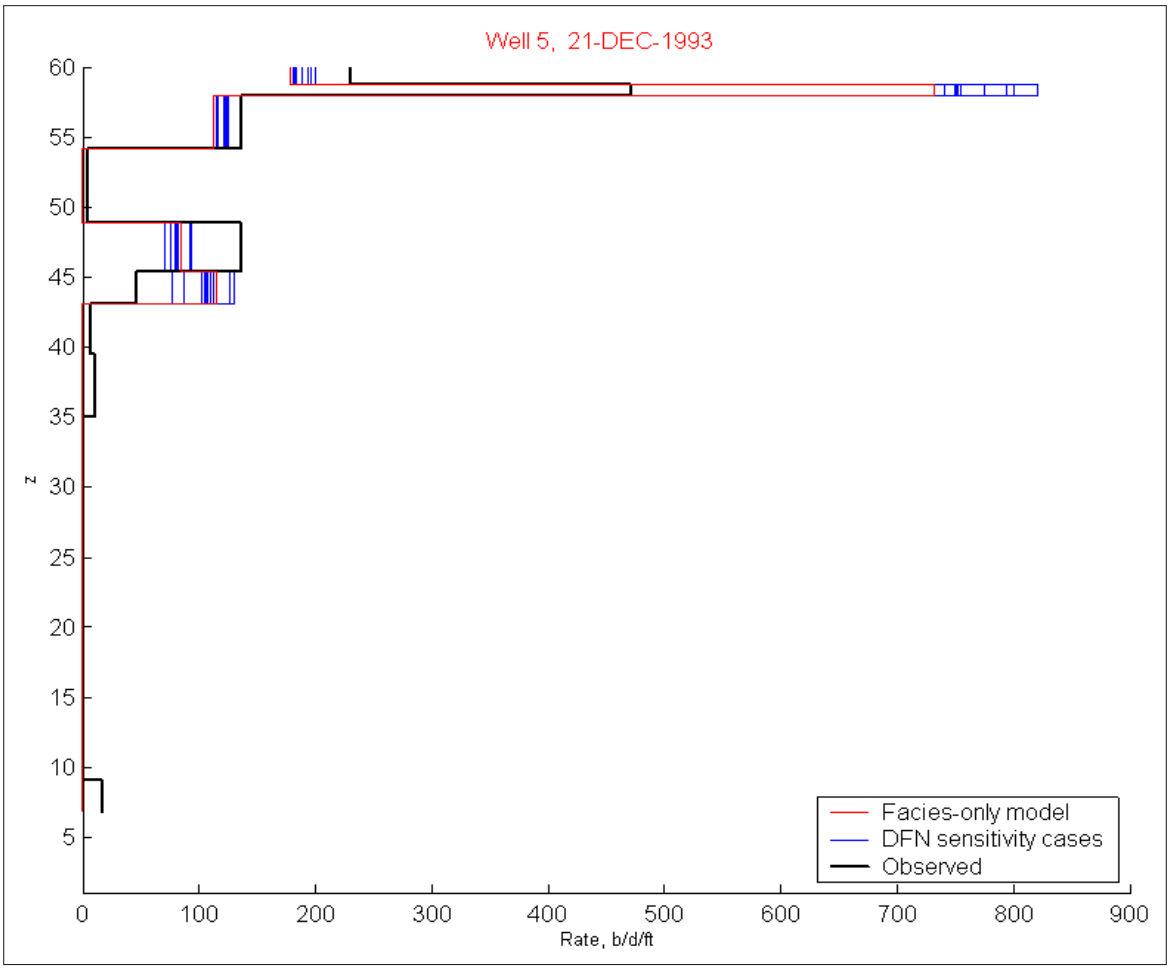

Fig. A.16: Flowmeter performance under Region Case 2

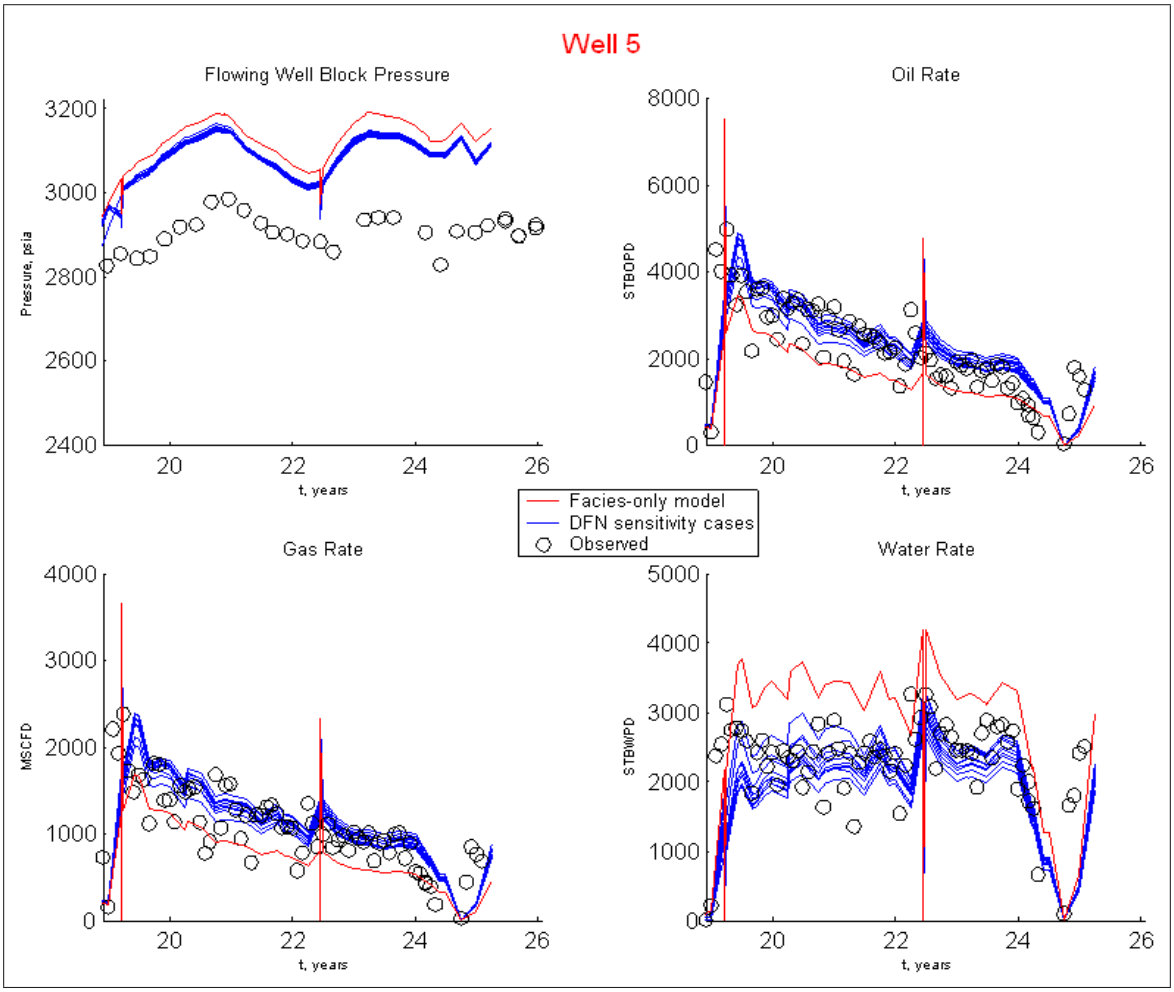

Fig. A.17: Well performance under Region Case 1

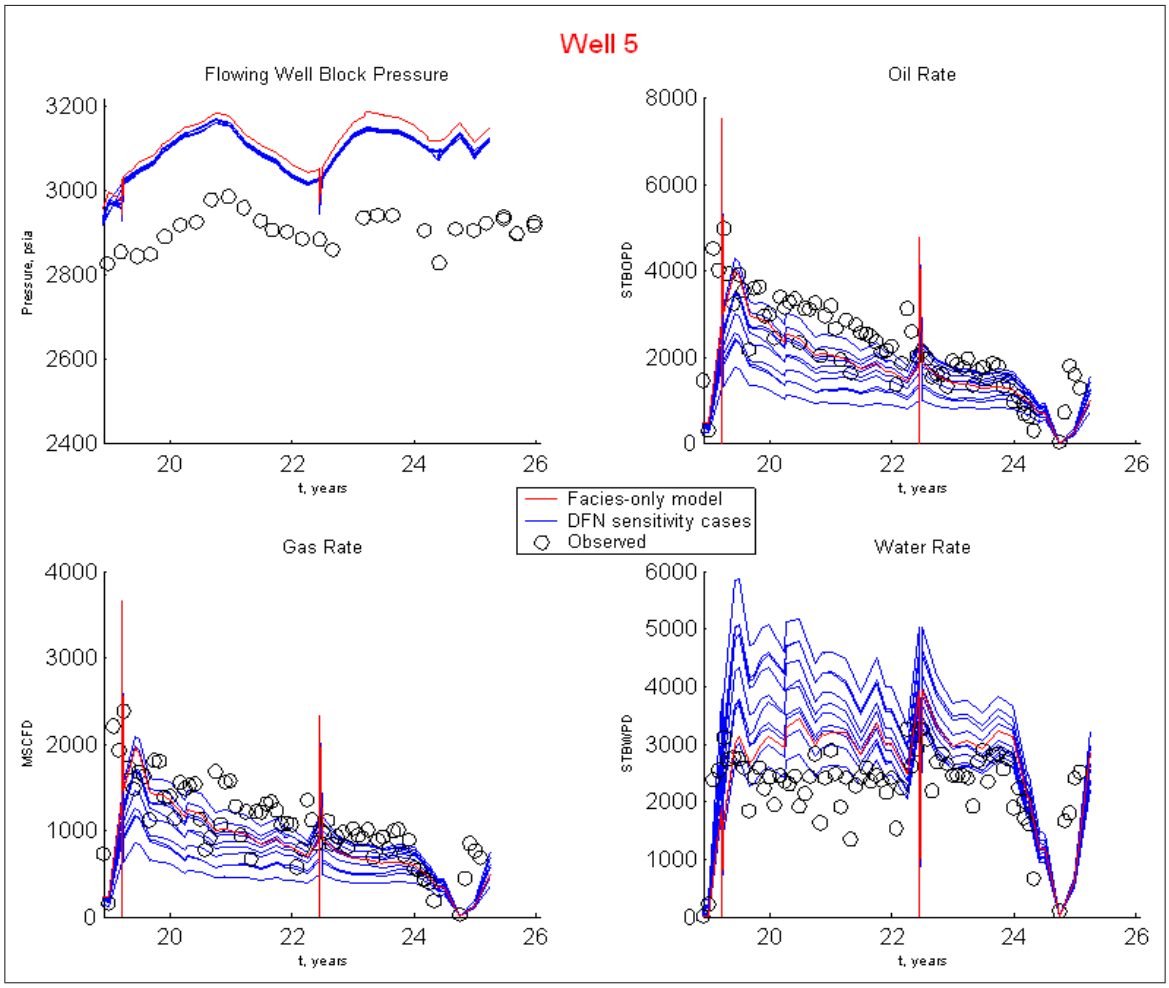

Fig. A.18: Well performance under Region Case 2

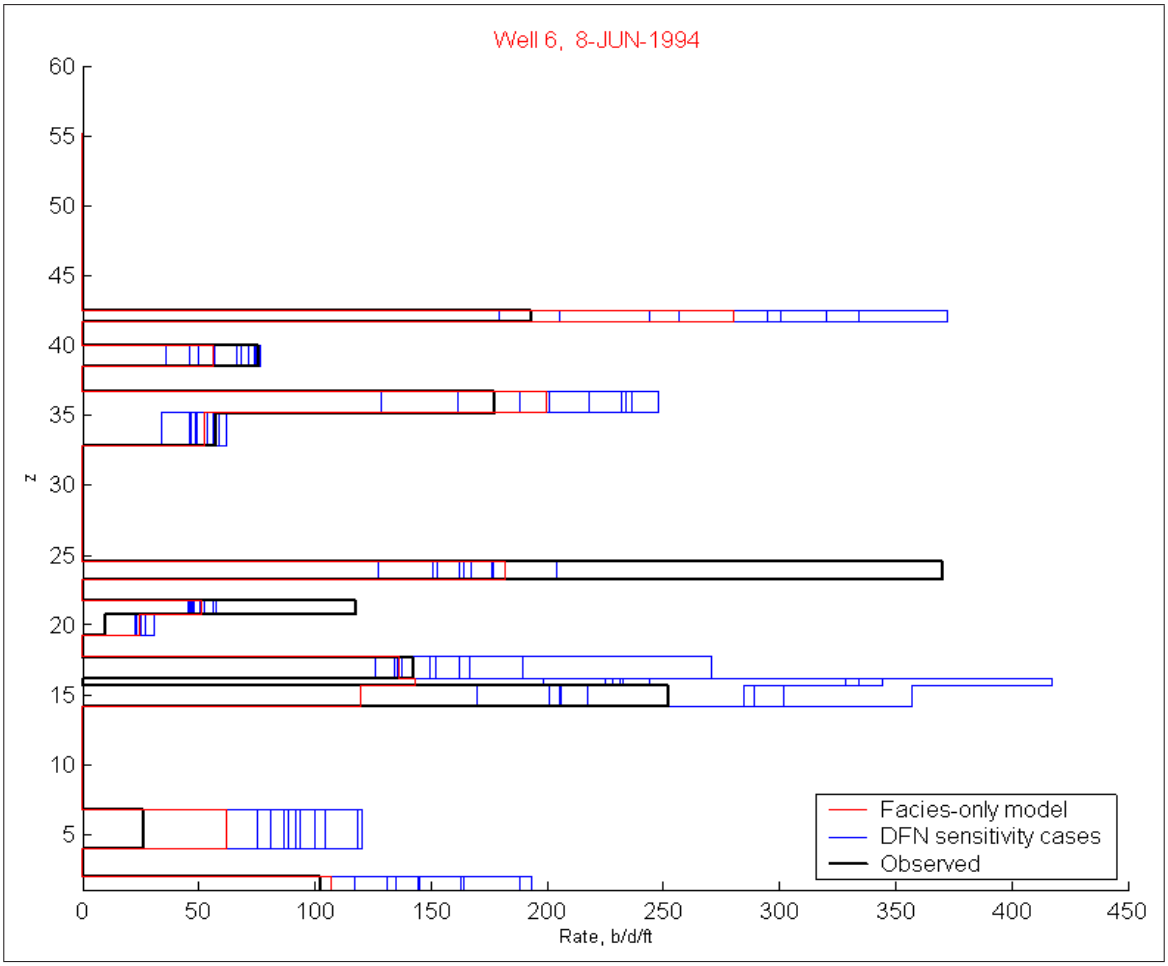

Fig. A.19: Flowmeter performance under Region Case 1

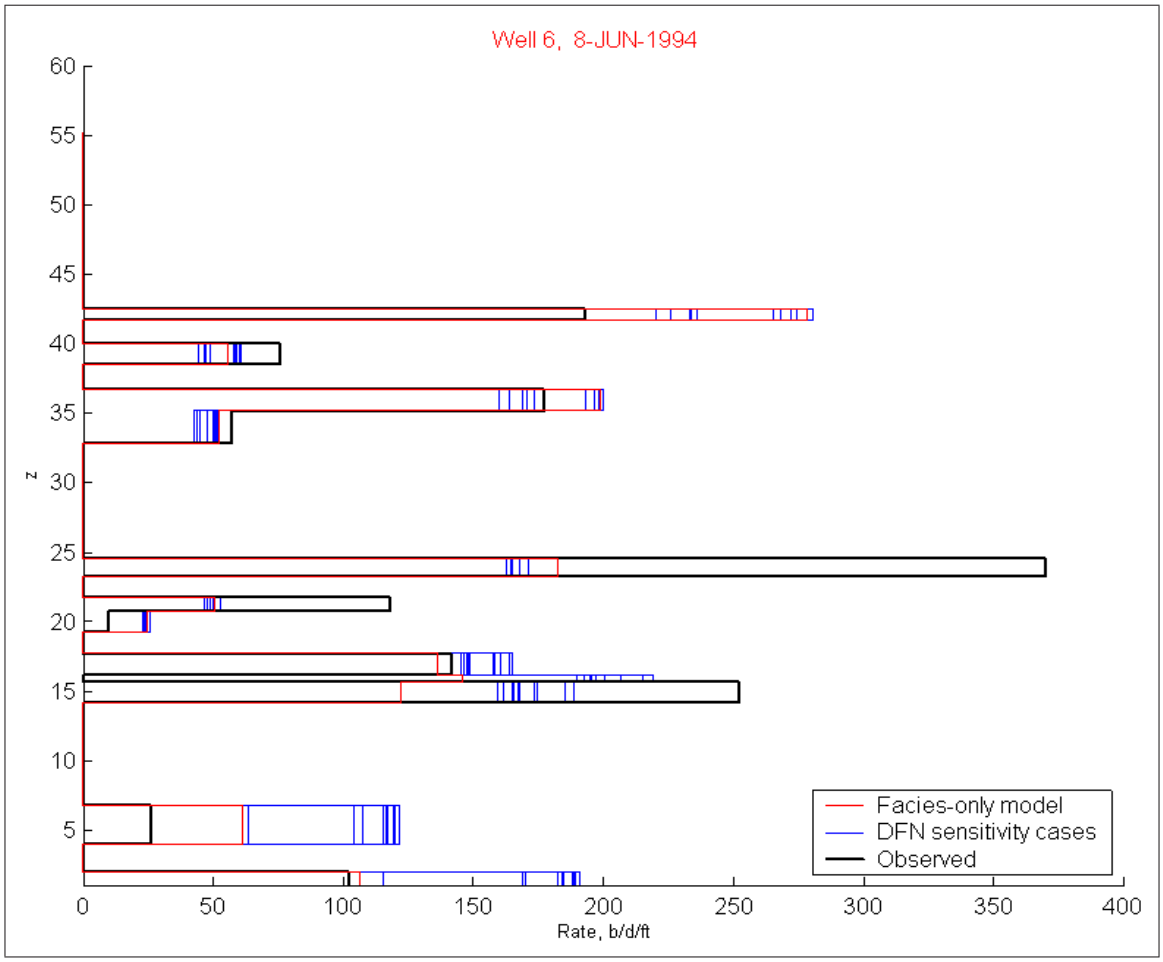

Fig. A.20: Flowmeter performance under Region Case 2

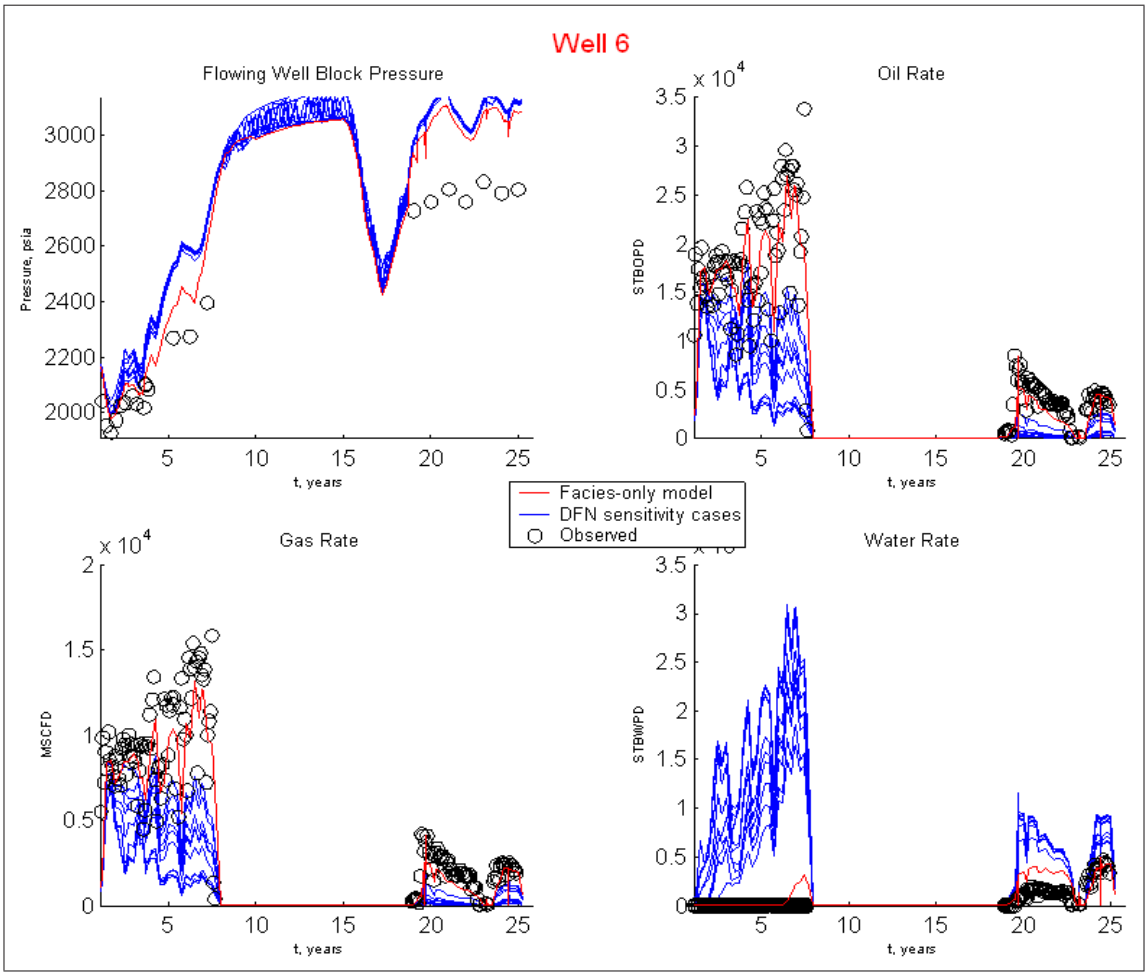

Fig. A.21: Well performance under Region Case 1

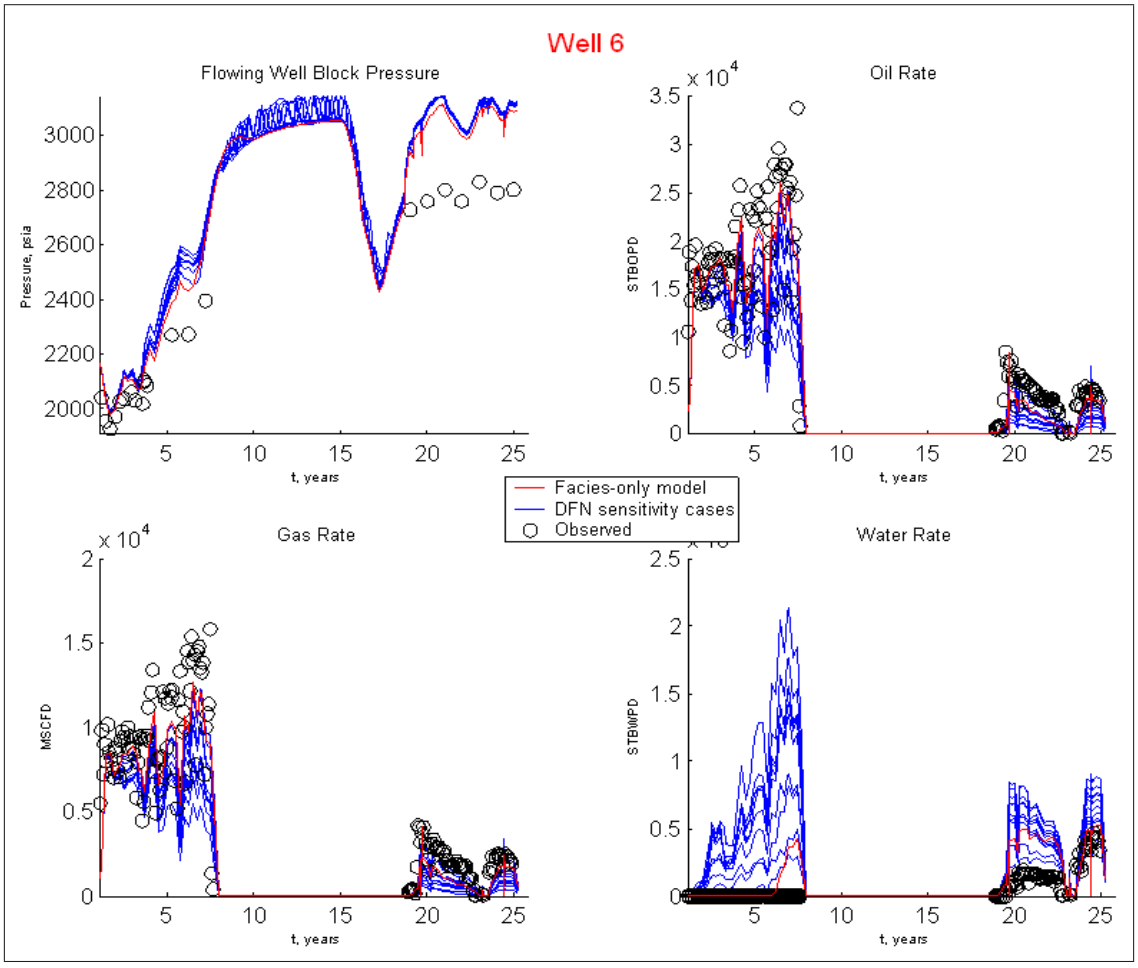

Fig. A.22: Well performance under Region Case 1

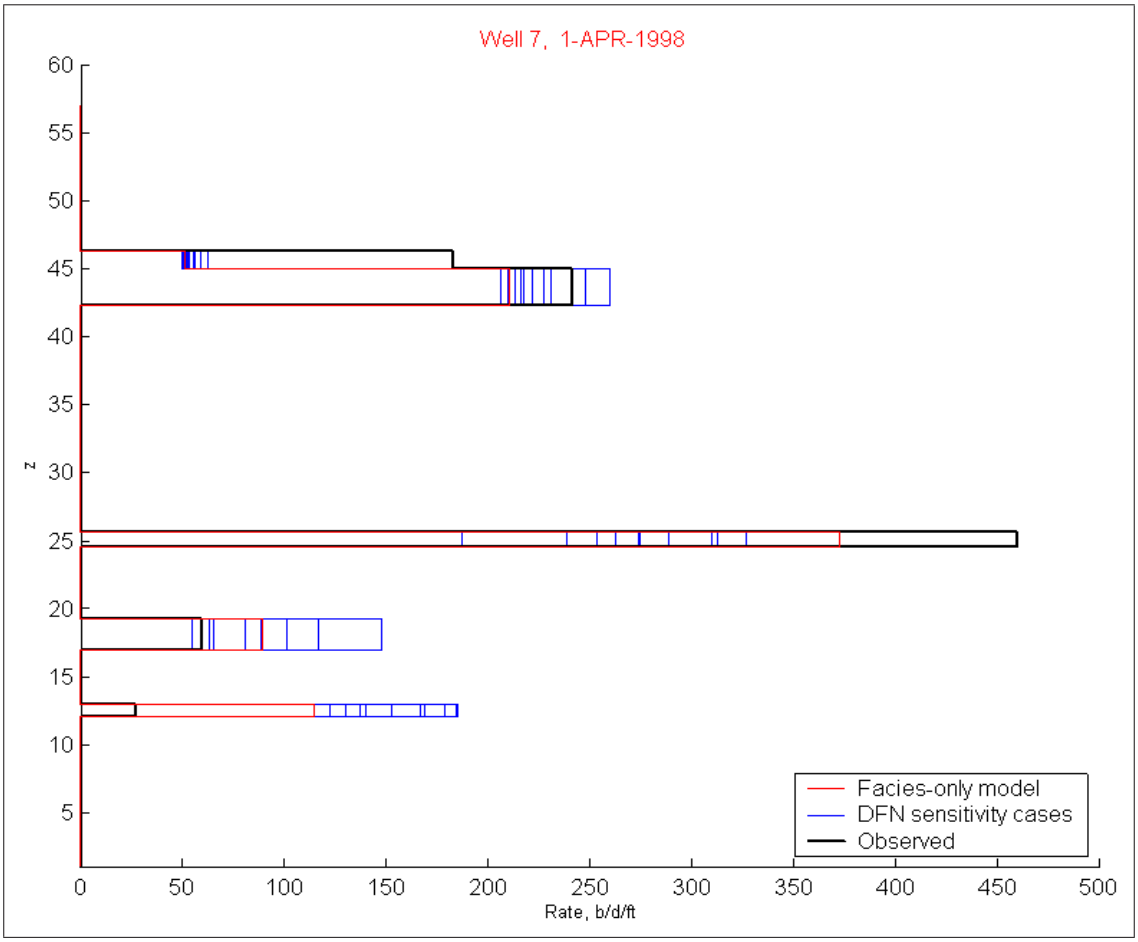

Fig. A.23: Flowmeter performance under Region Case 1

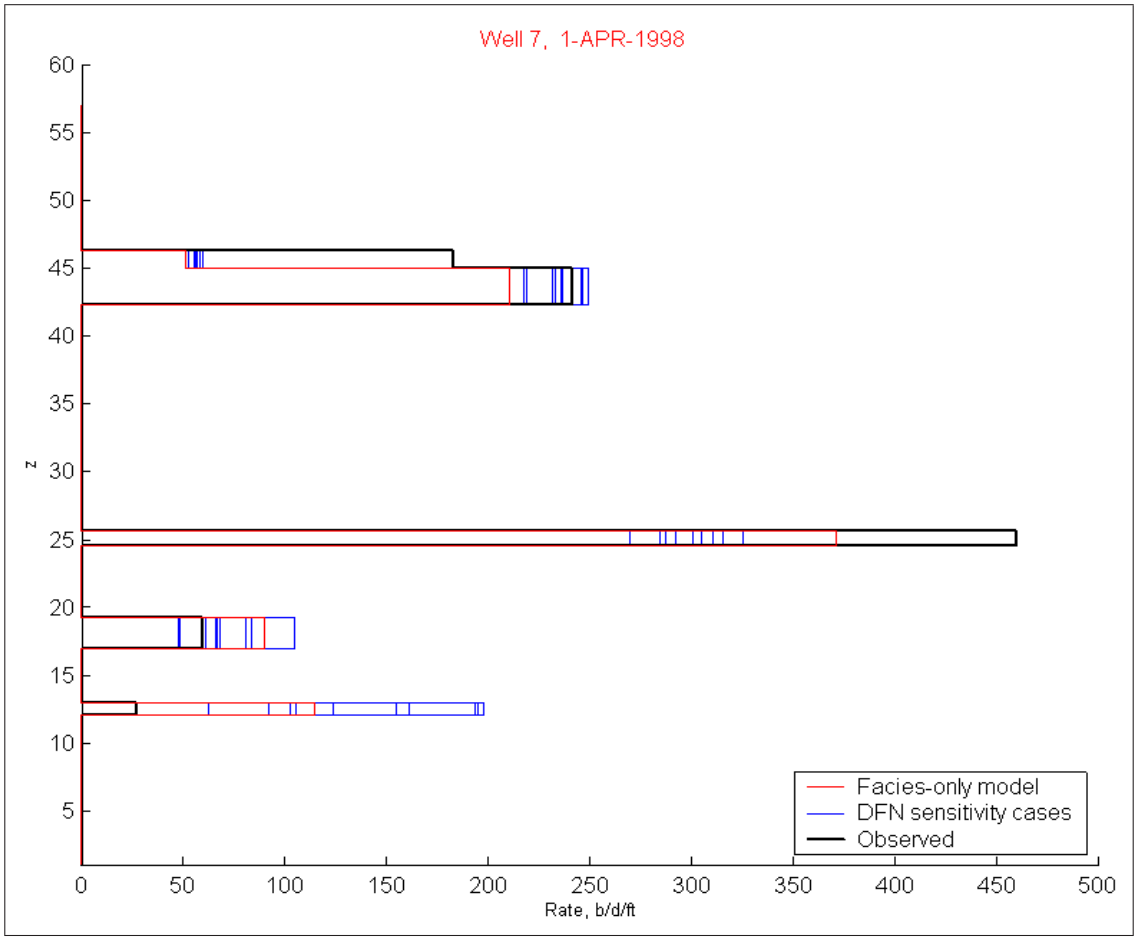

Fig. A.24: Flowmeter performance under Region Case 2

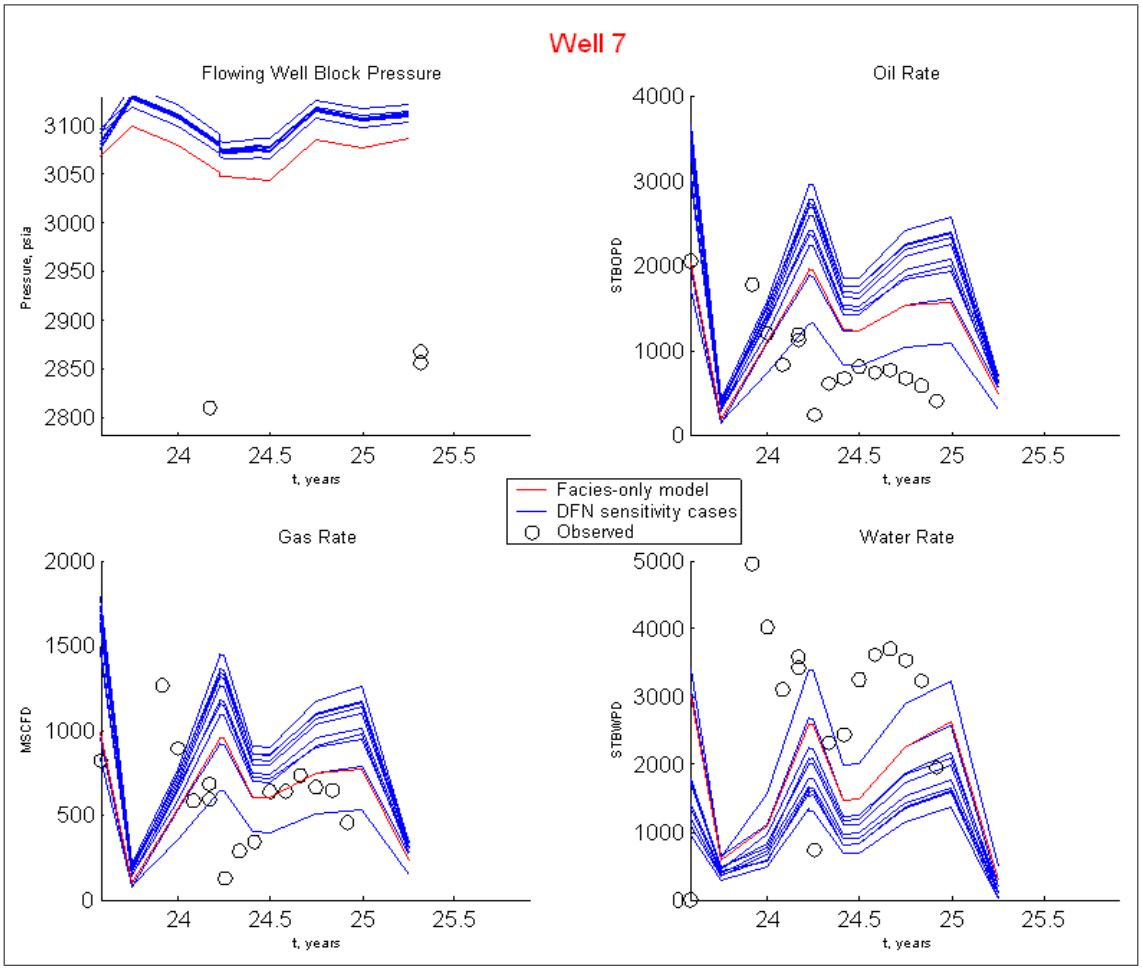

Fig. A.25: Well performance under Region Case 1

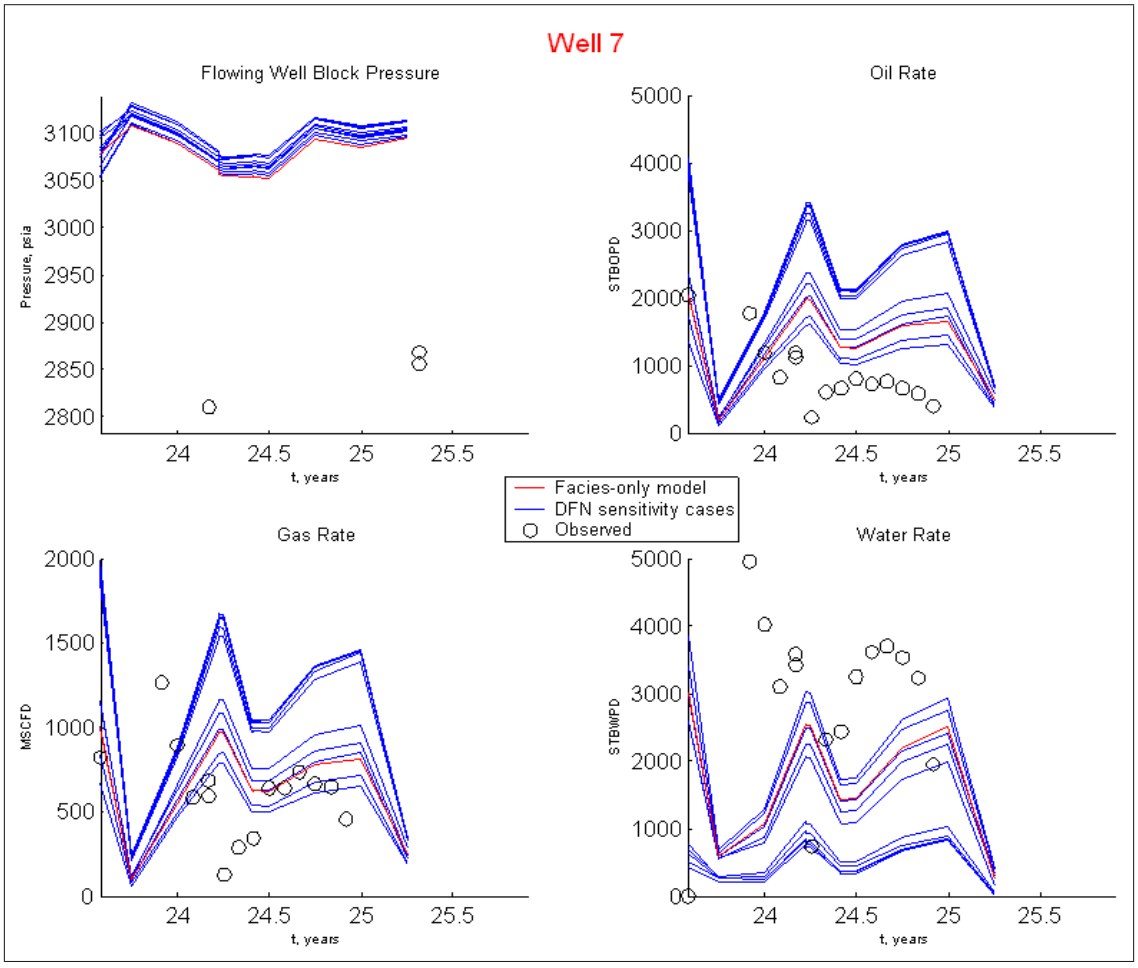

Fig. A.26: Well performance under Region Case 1

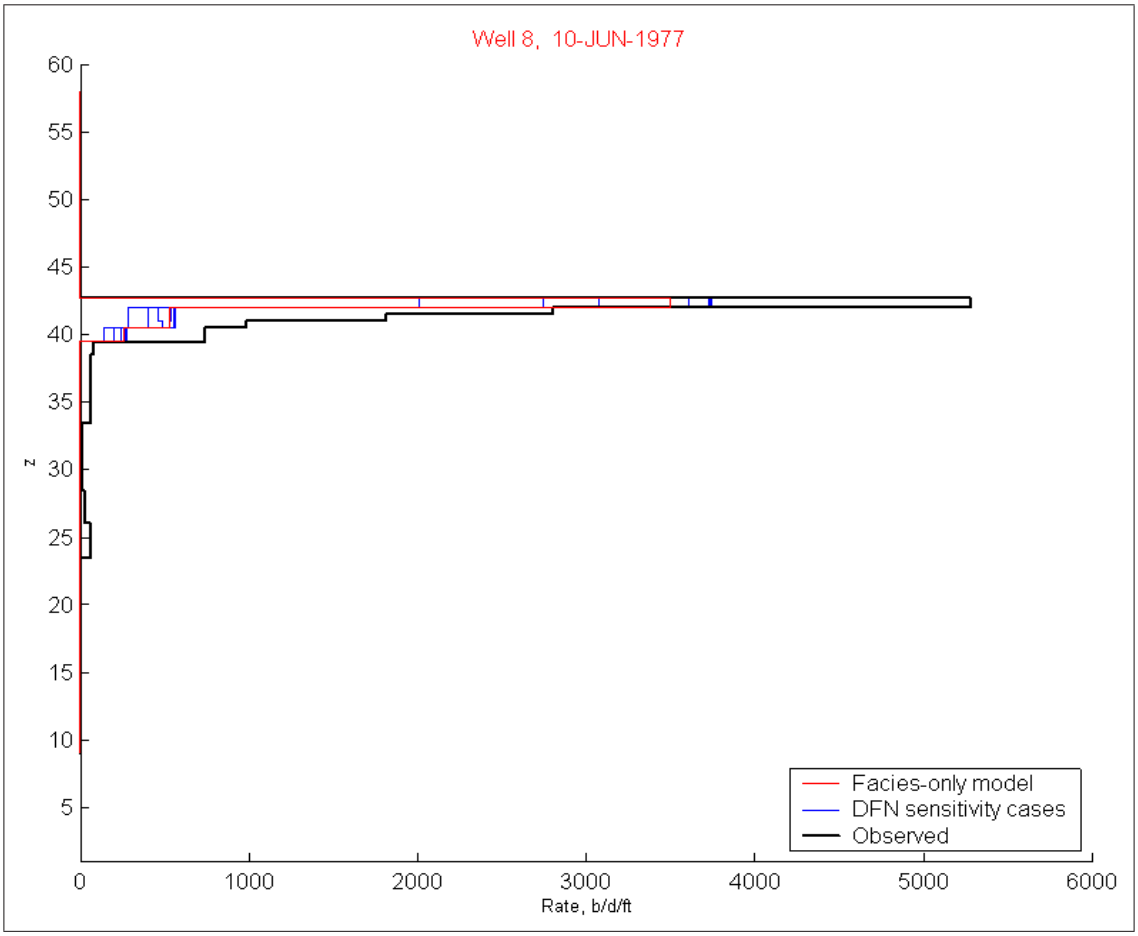

Fig. A.27: Flowmeter performance under DFN conditioning

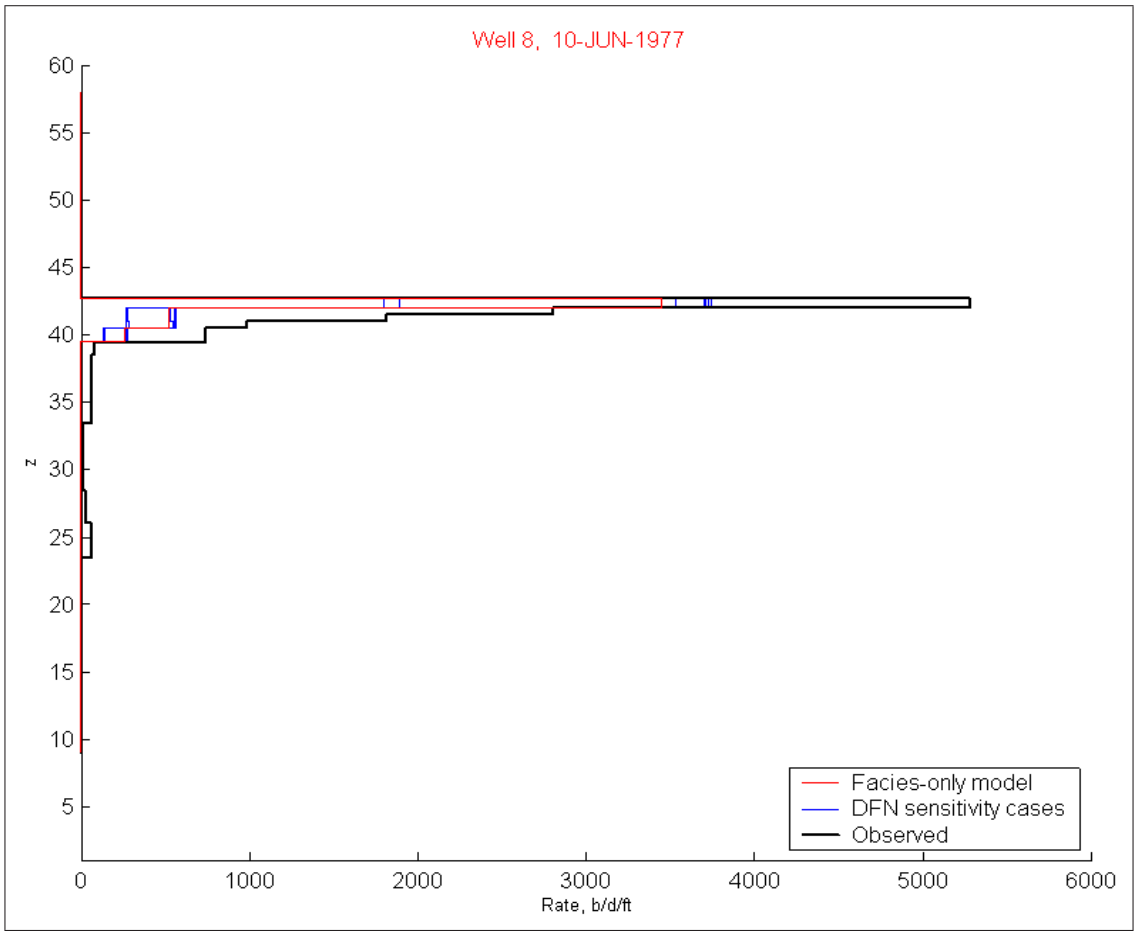

Fig. A.28: Flowmeter performance under DFN conditioning

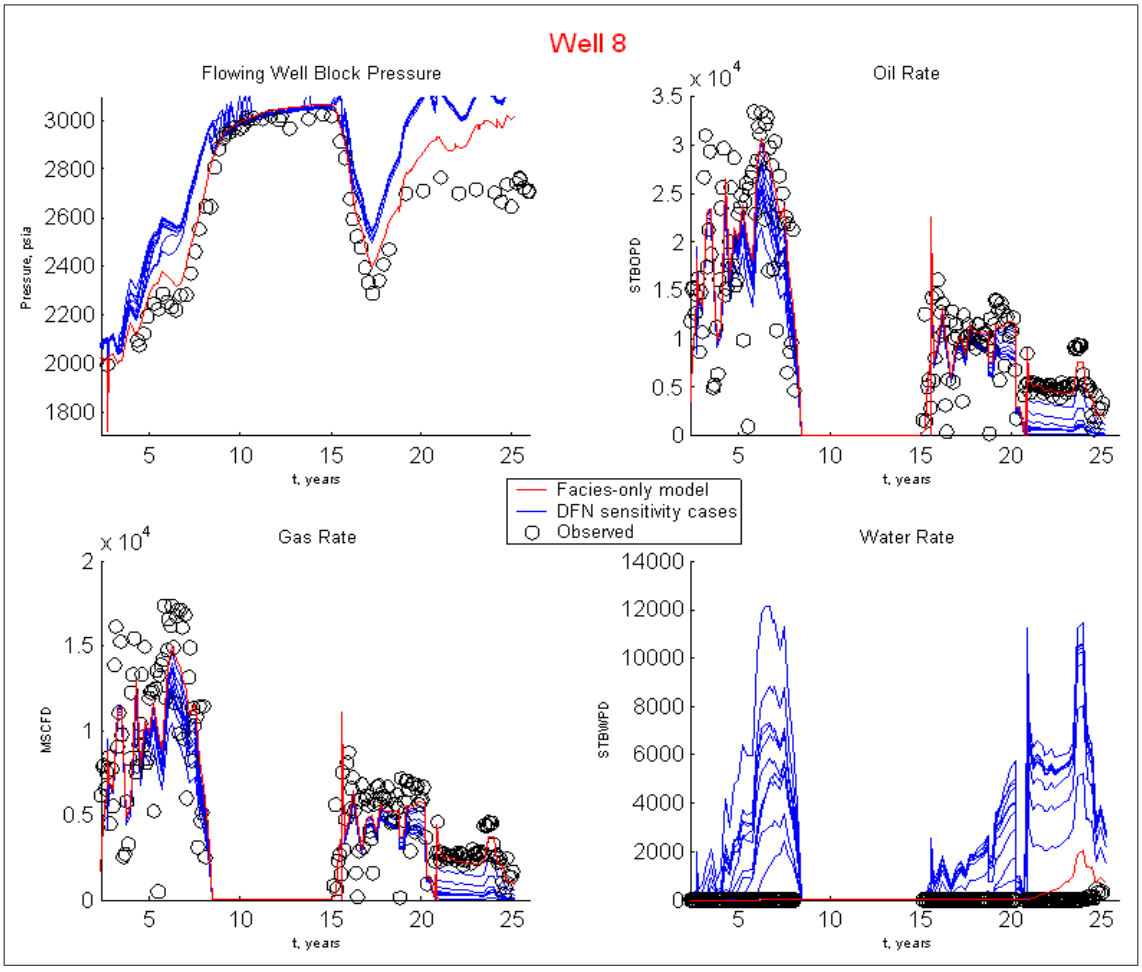

Fig. A.29: Well performance under Region Case 1

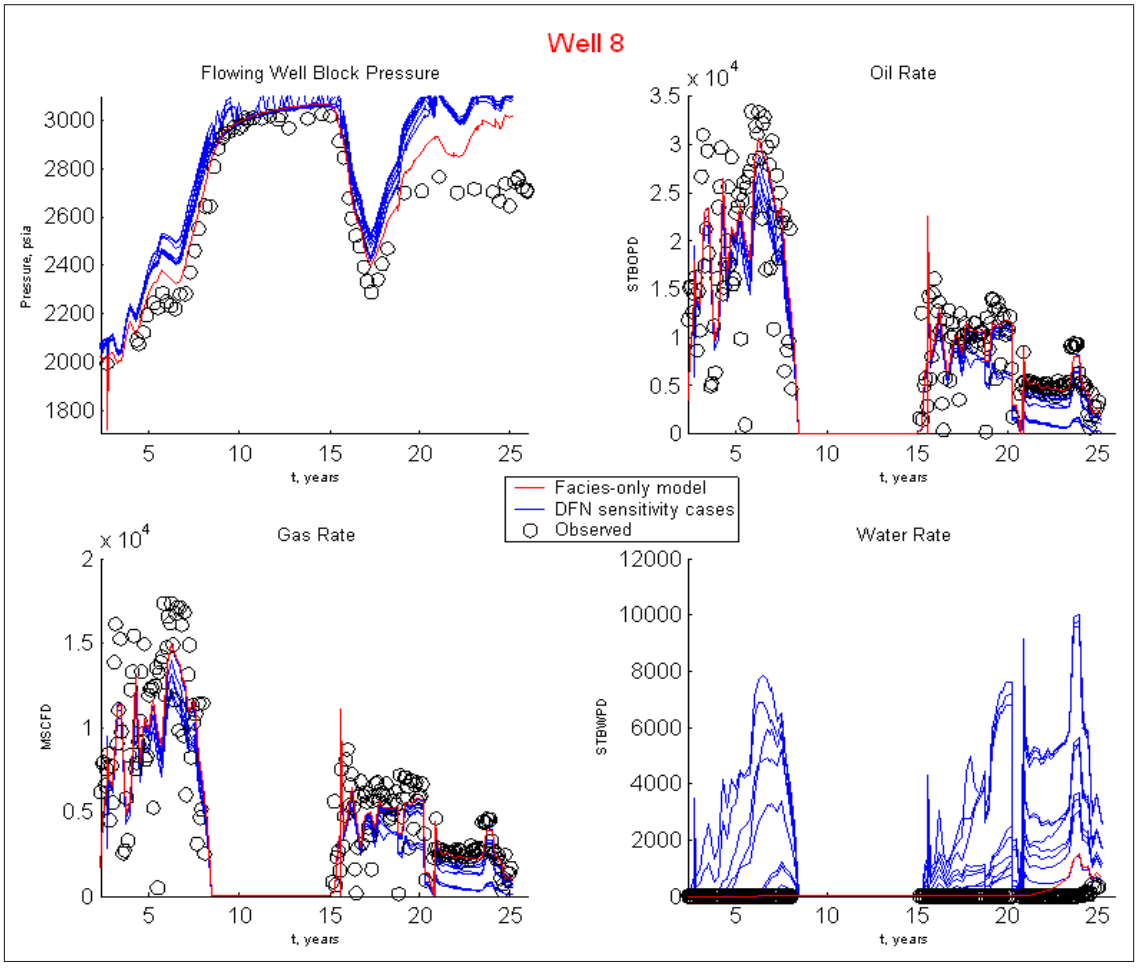

Fig. A.30: Well performance under Region Case 2

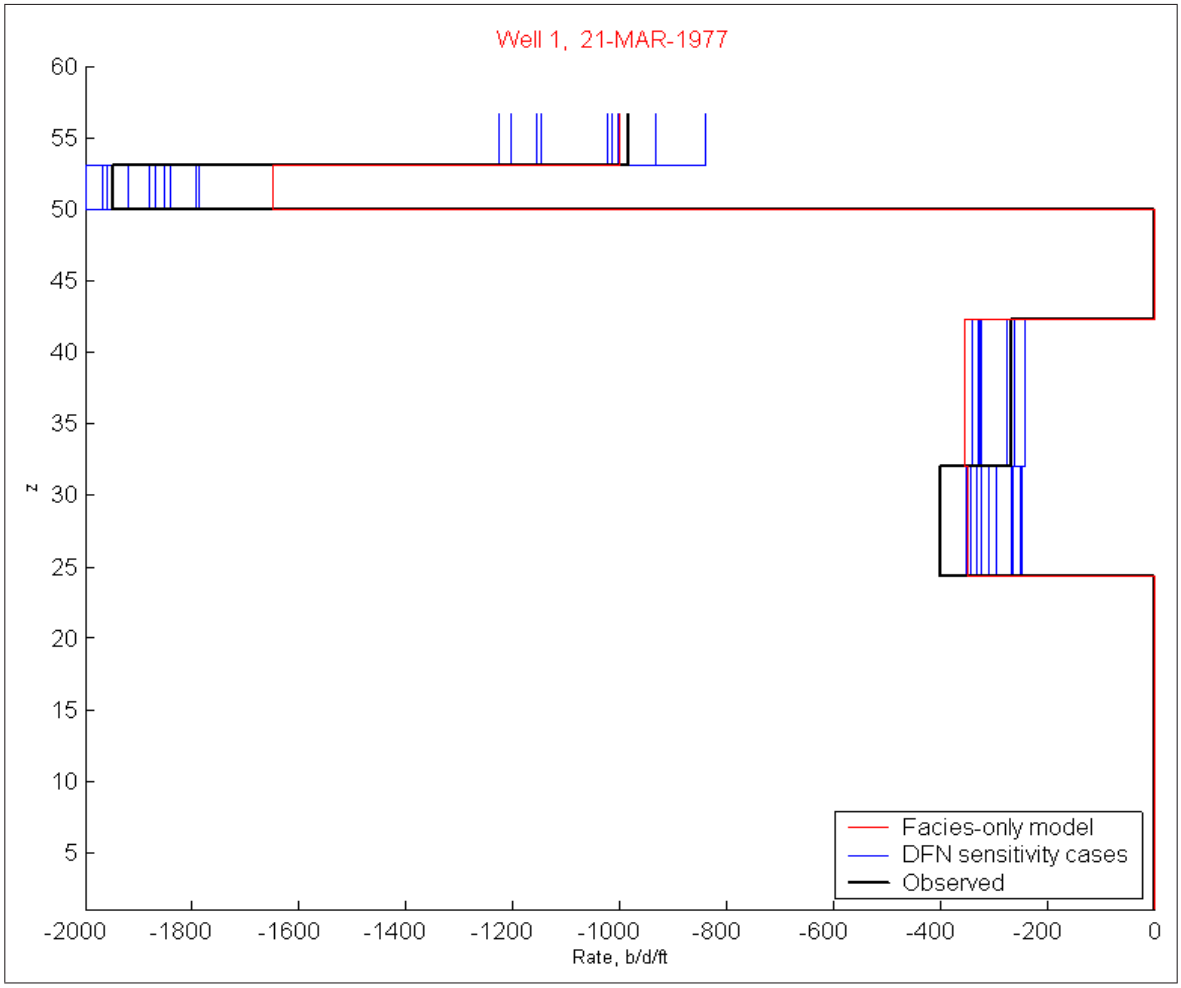

Fig. A.31: Flowmeter performance under varying DFN locations

A.2 Region Case 1 with varying DFN location

Fig. A.31 through Fig. A.39 show performance results of variation in DFN location, for both water injection wells, Well 1 and Well 2, and two key producing wells which have the most extensive production history, Well 8 and Well 6 (see Fig. 3.2 for study area well locations). Finally, Well 3 is also included, as it is the offset well to Well 1, a key water injection well. This water injection well has a prolific super-k interval, as well as does Well 8.

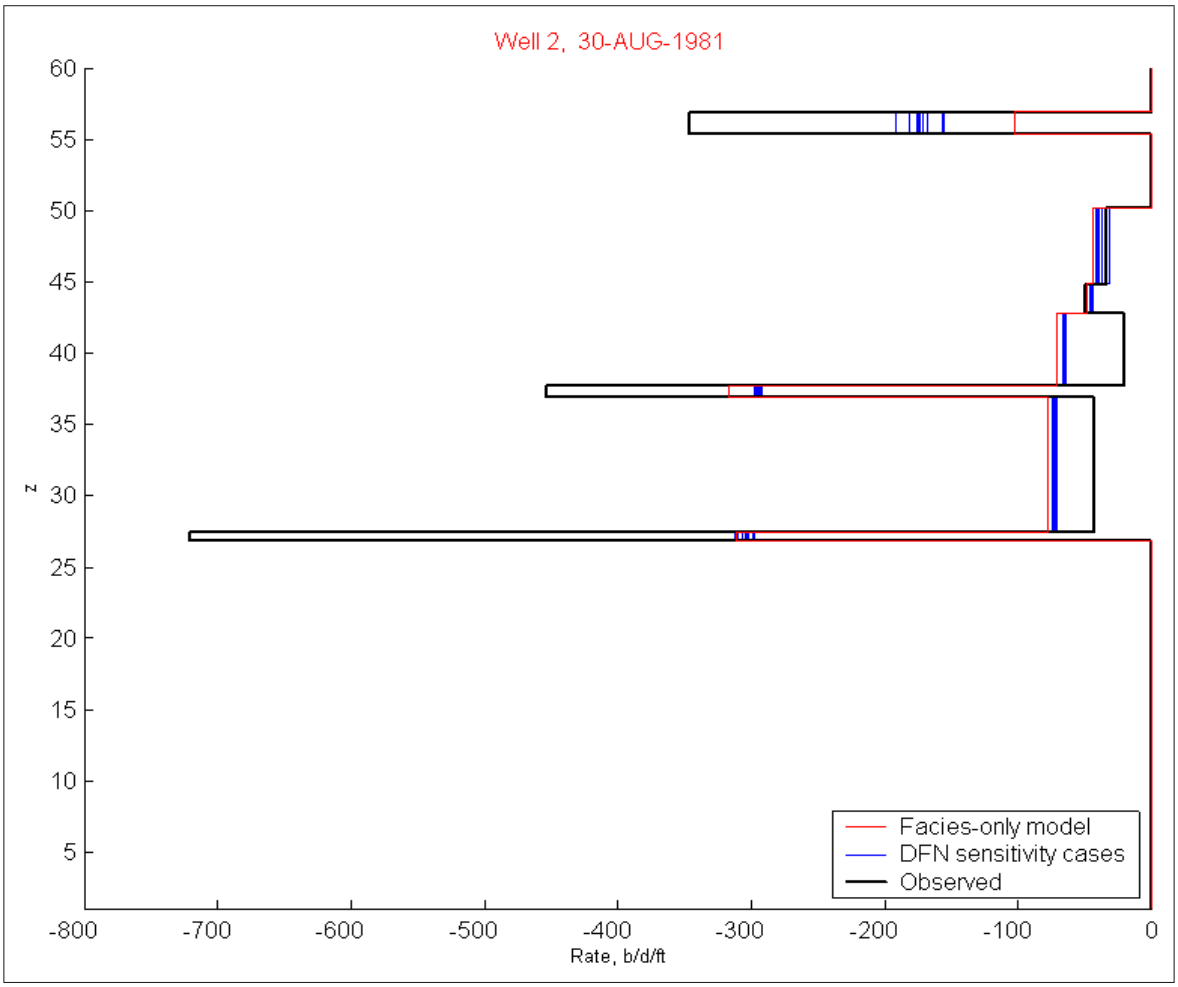

Fig. A.32: Flowmeter performance under varying DFN locations

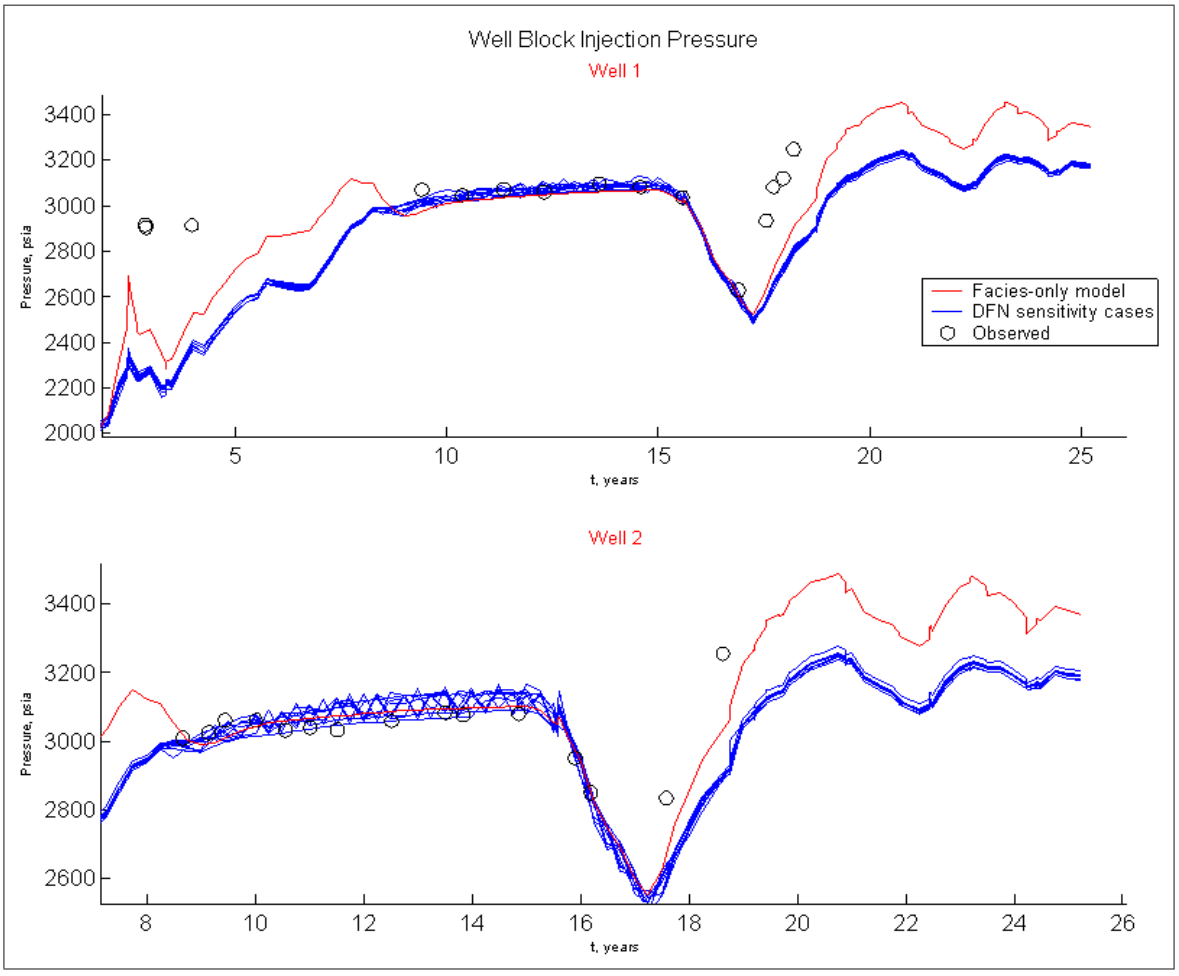

Fig. A.33: Well performance under varying DFN locations

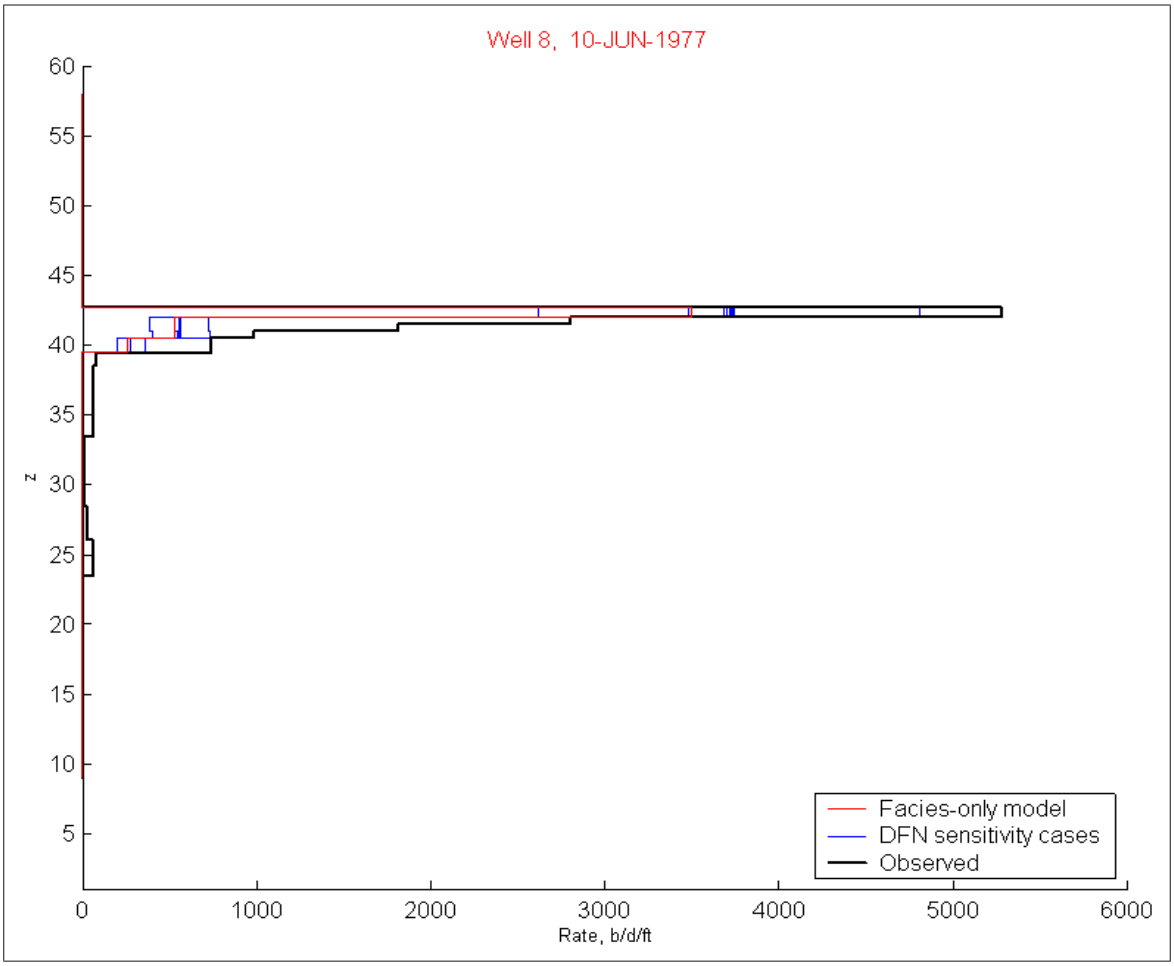

Fig. A.34: Flowmeter performance under varying DFN locations

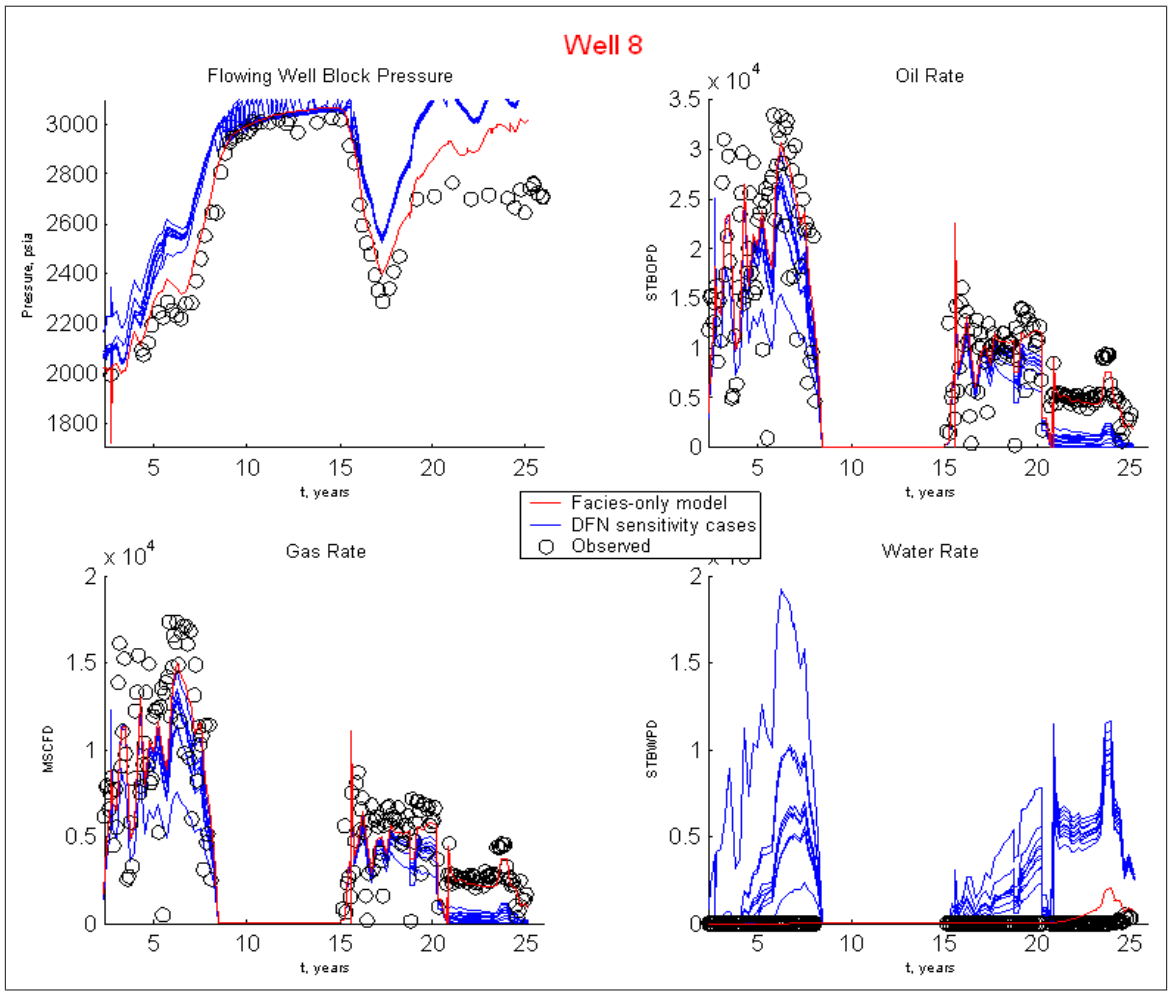

Fig. A.35: Well performance under varying DFN locations

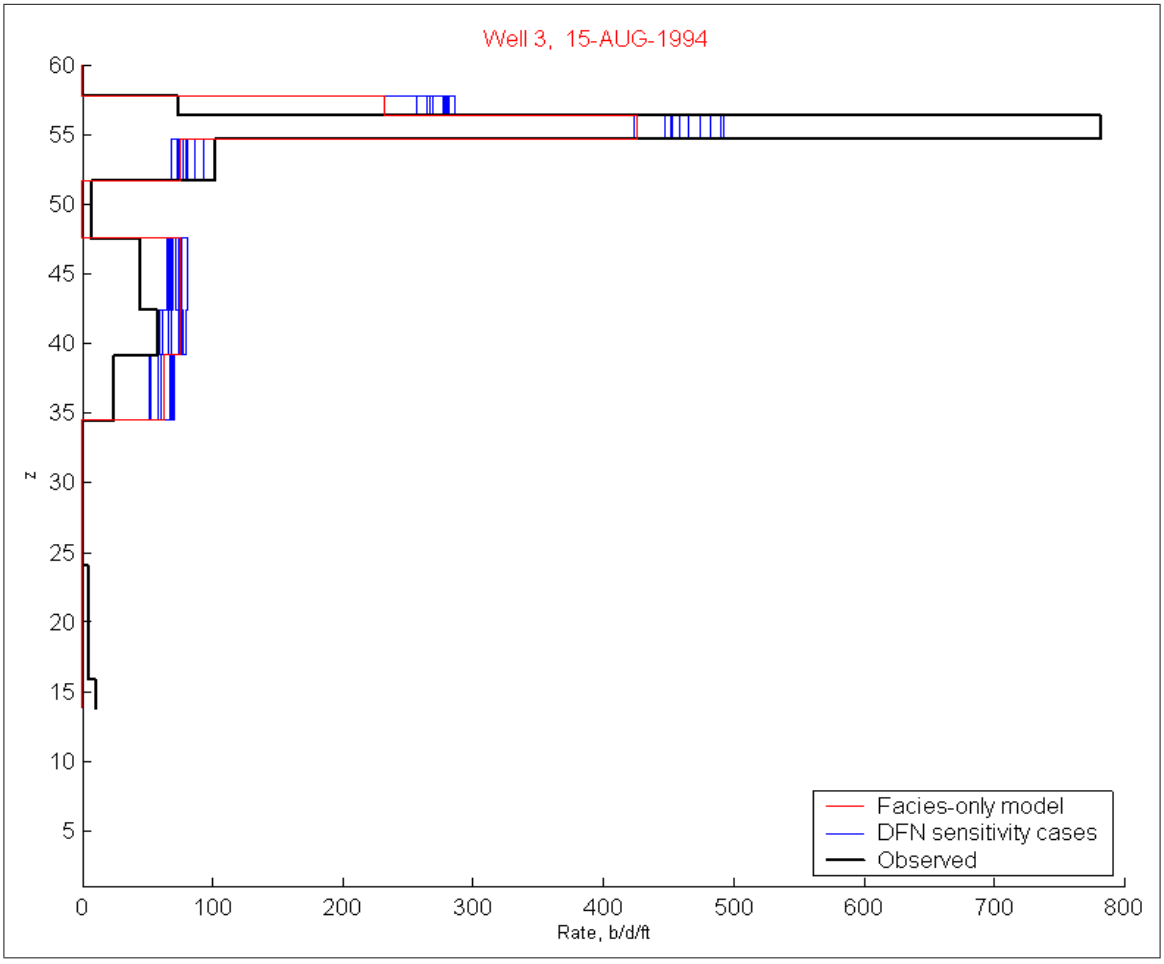

Fig. A.36: Flowmeter performance under varying DFN locations

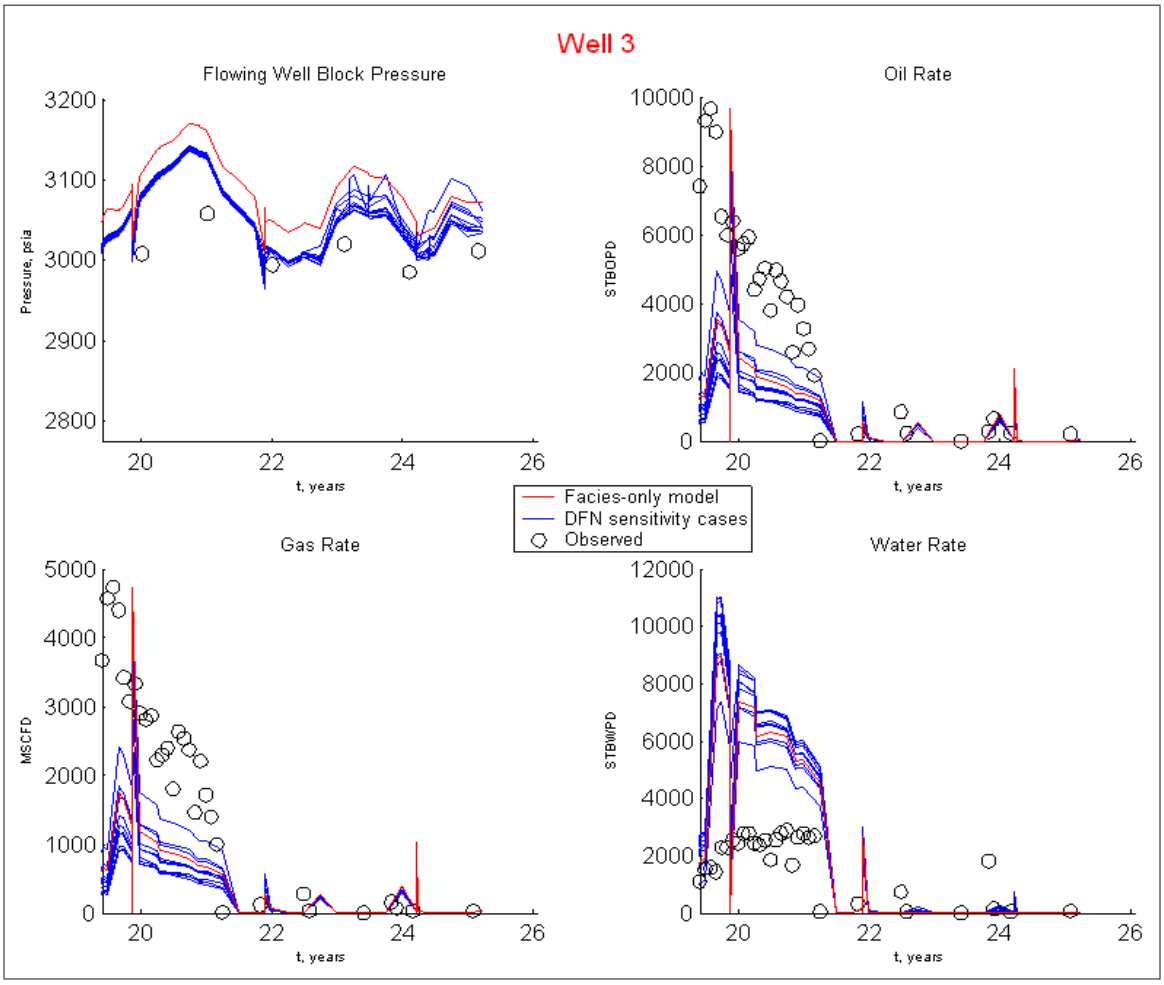

Fig. A.37: Well performance under varying DFN locations

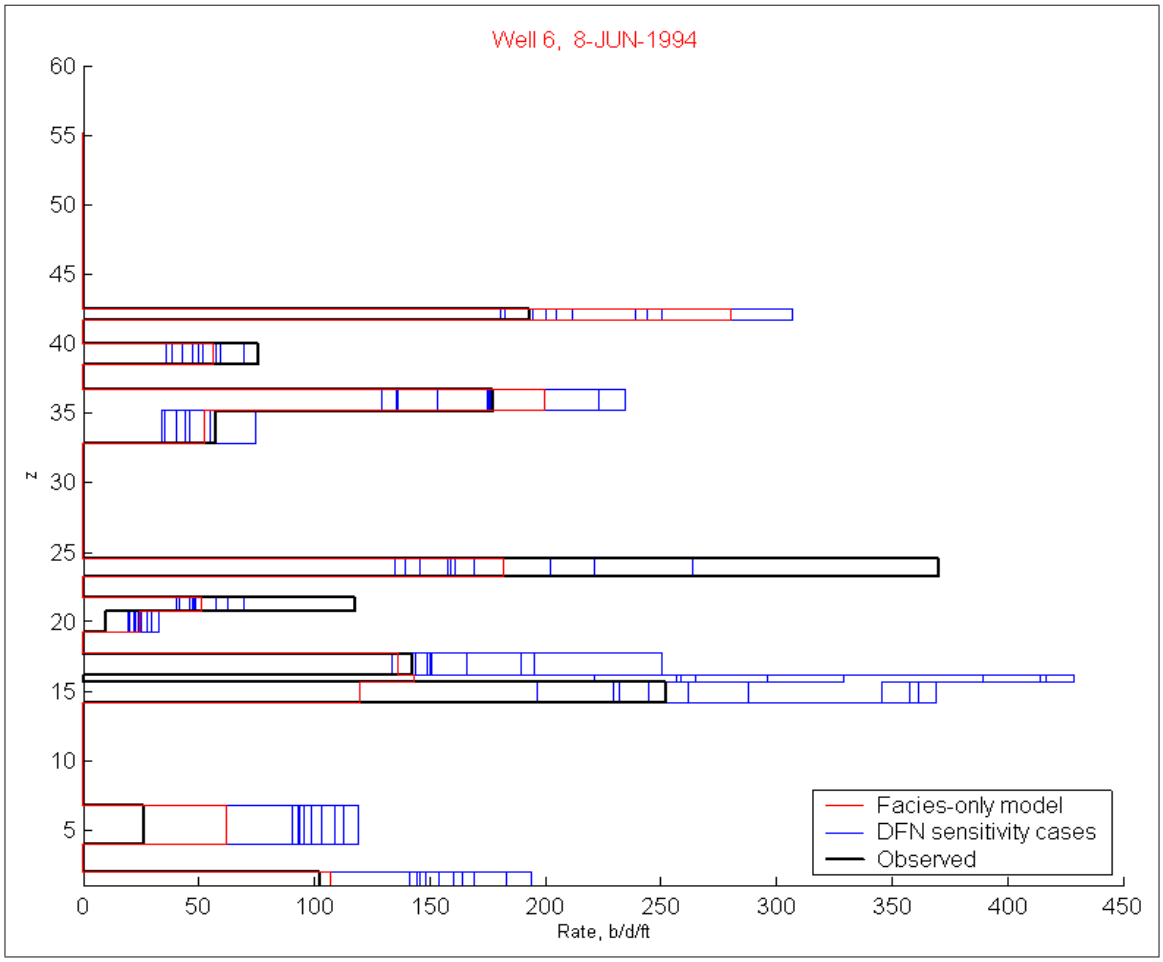

Fig. A.38: Flowmeter performance under varying DFN locations

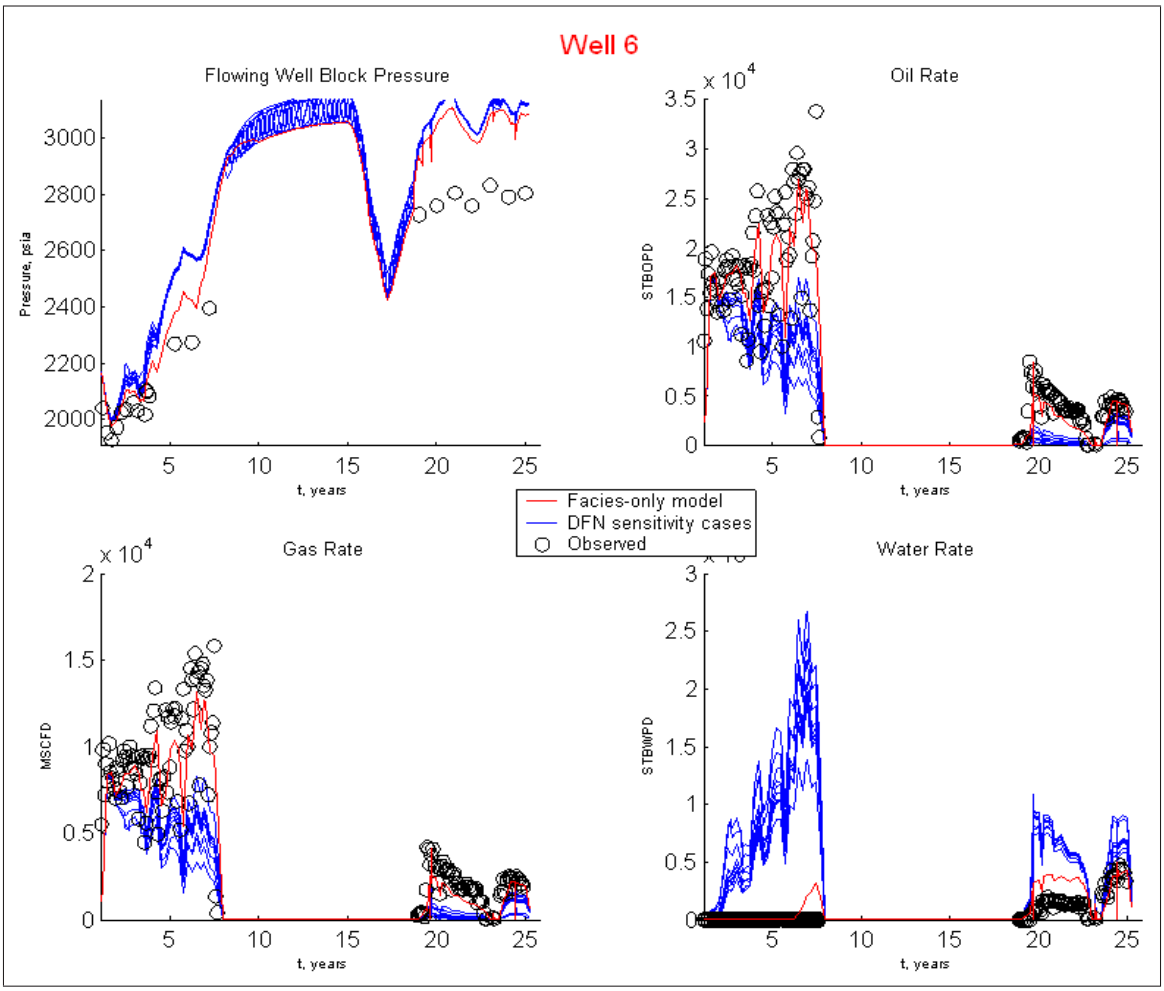

Fig. A.39: Well performance under varying DFN locations

A.3 Region Case 1 case with varying DFN azimuth

Fig. A.40 through Fig. A.48 show performance results of variation in DFN azimuth, for both water injection wells, Well 1 and Well 2, and two key producing wells which have the most extensive production history, Well 8 and Well 6 (see Fig. 3.2 for study area well locations). Finally, Well 3 is also included, as it is the offset well to Well 1, a key water injection well. This water injection well has a prolific super-k interval, as well as does Well 8. The azimuth is drawn from a uniform distribution in the range 10^o to 90^o from North.

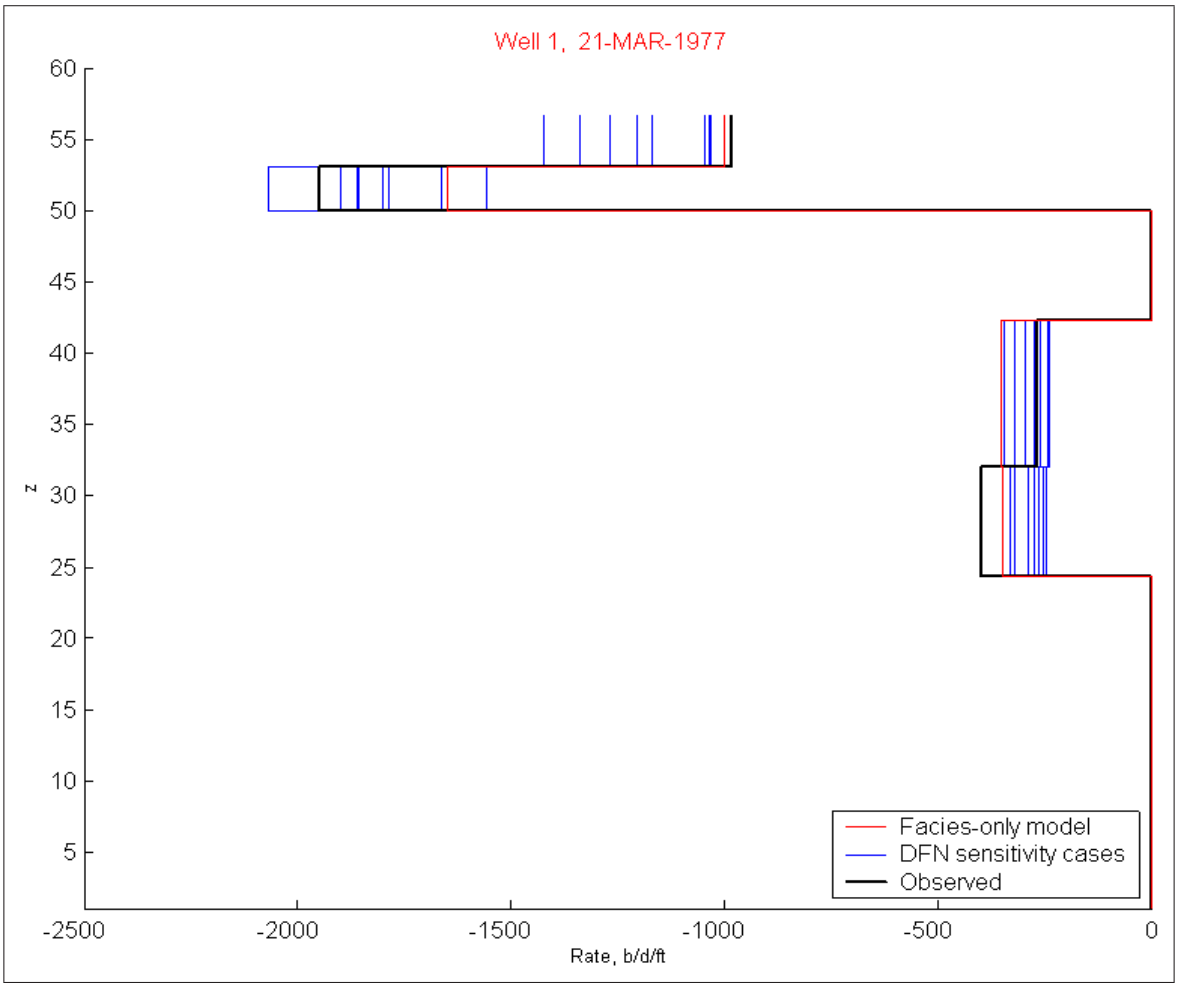

Fig. A.40: Flowmeter performance under varying DFN azimuth

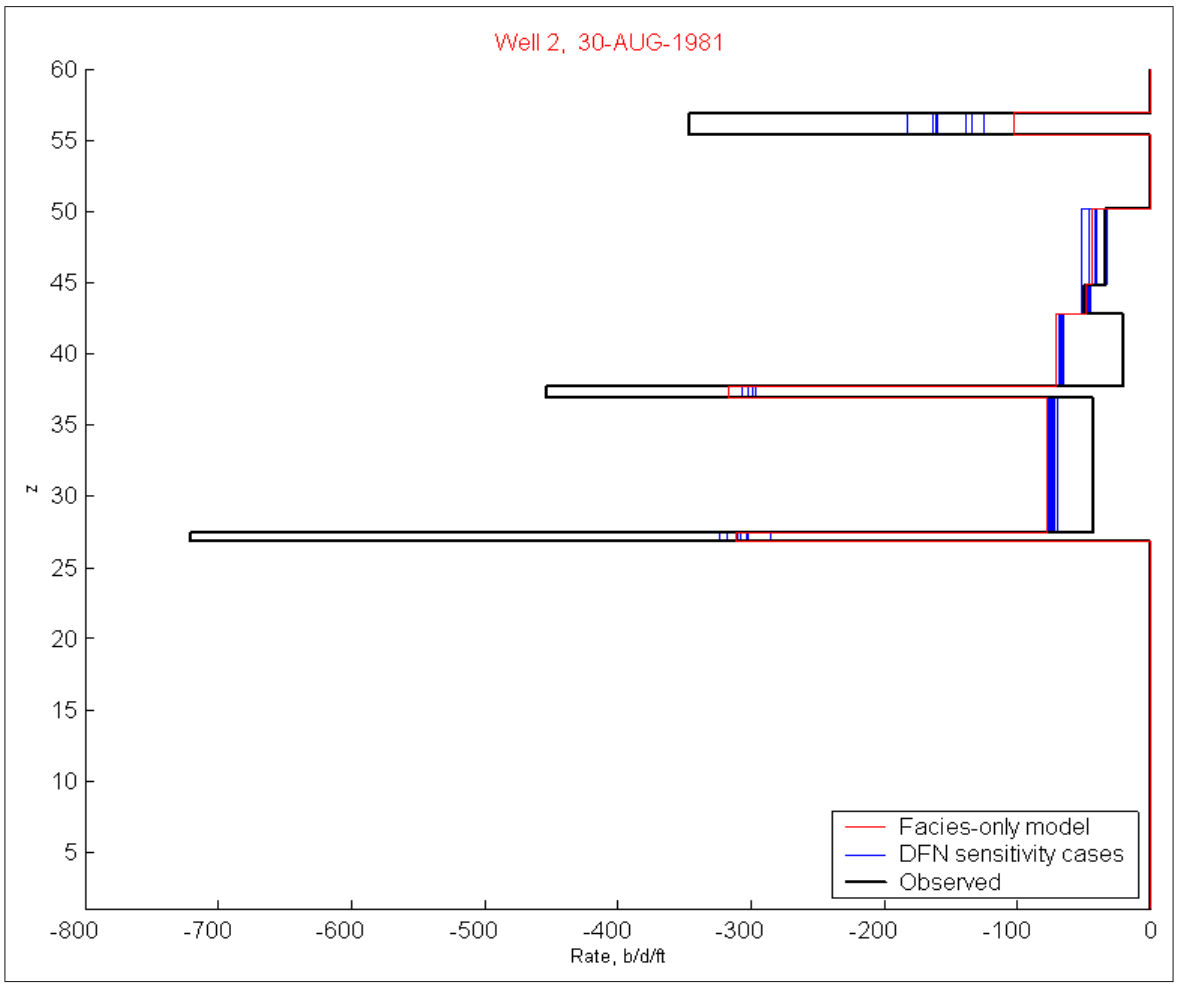

Fig. A.41: Flowmeter performance under varying DFN azimuth

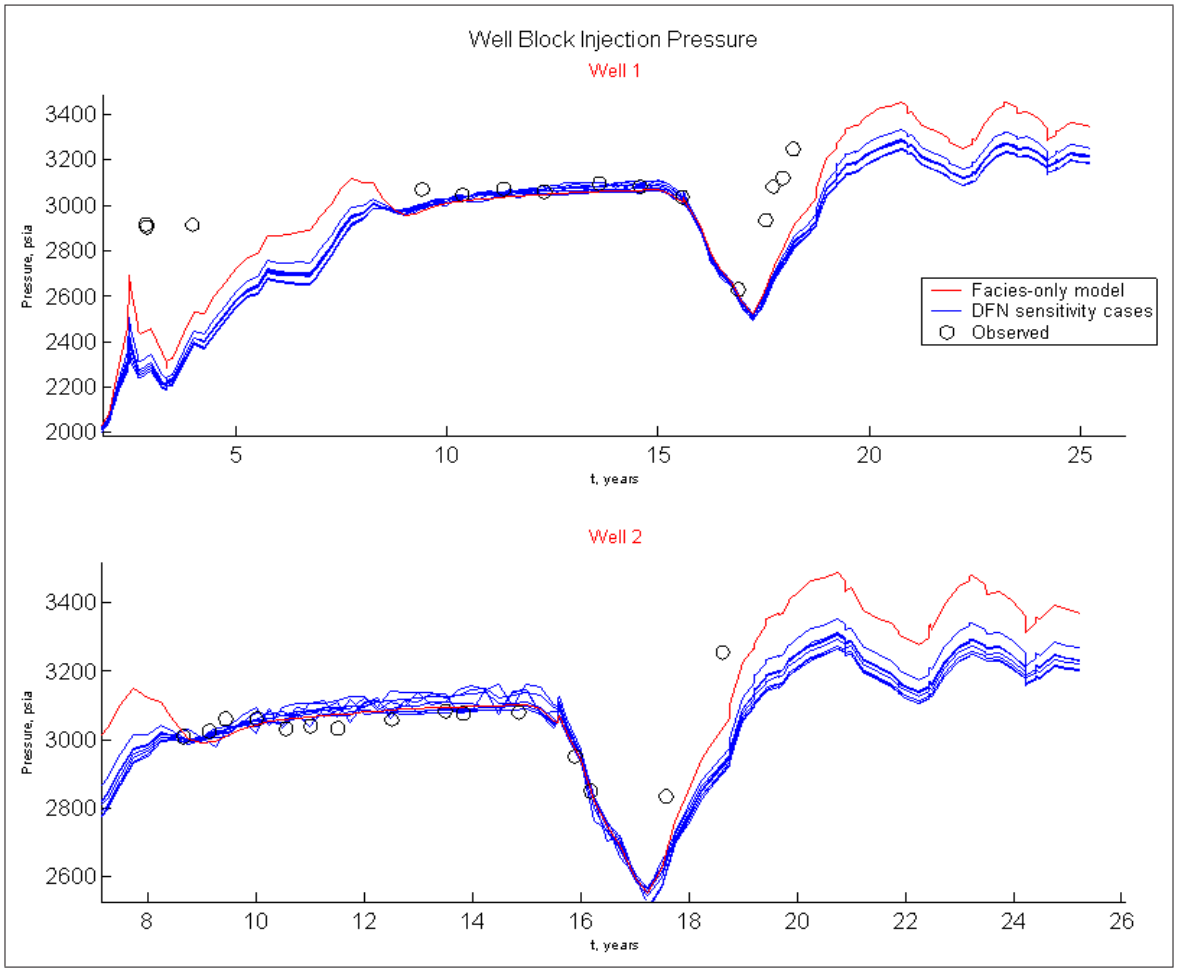

Fig. A.42: Well performance under varying DFN azimuth

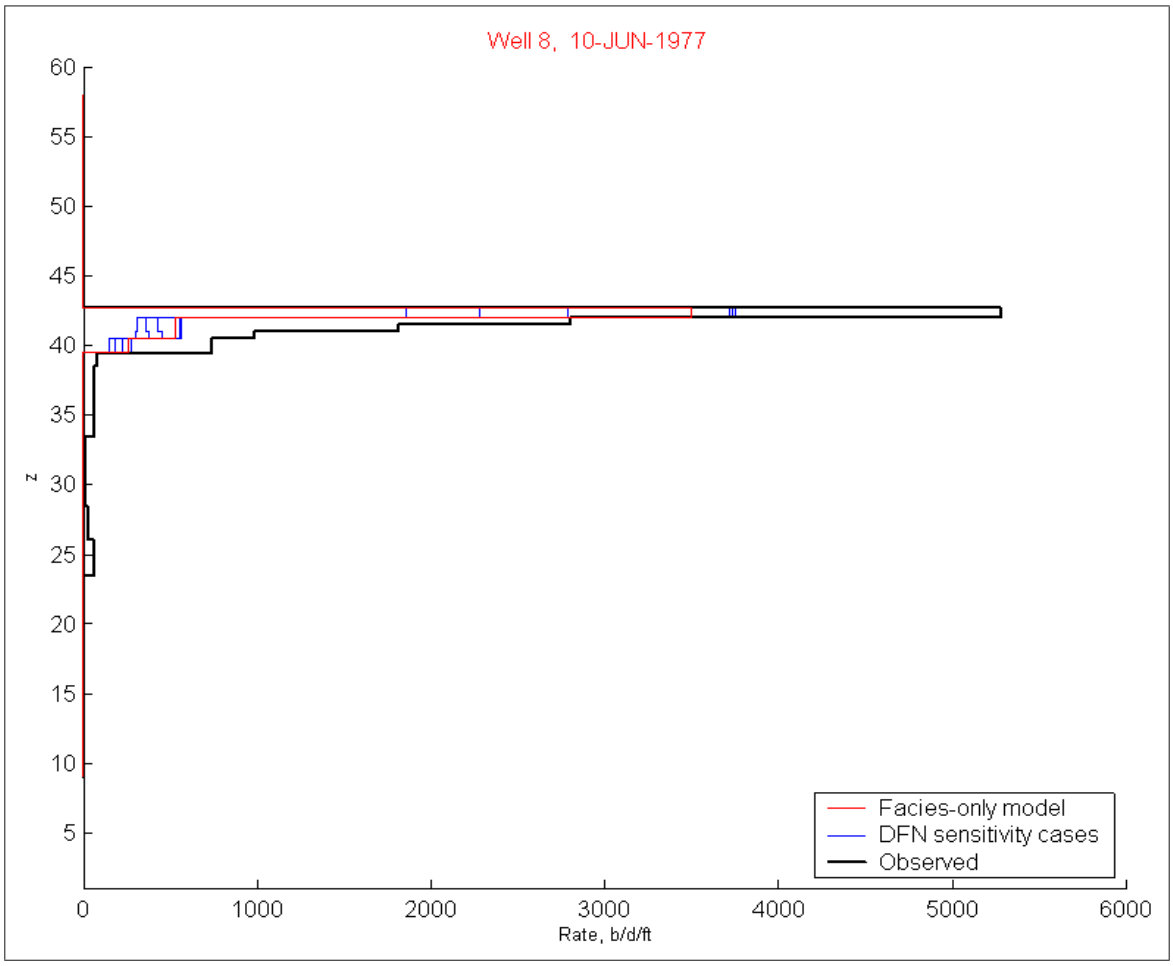

Fig. A.43: Flowmeter performance under varying DFN azimuth

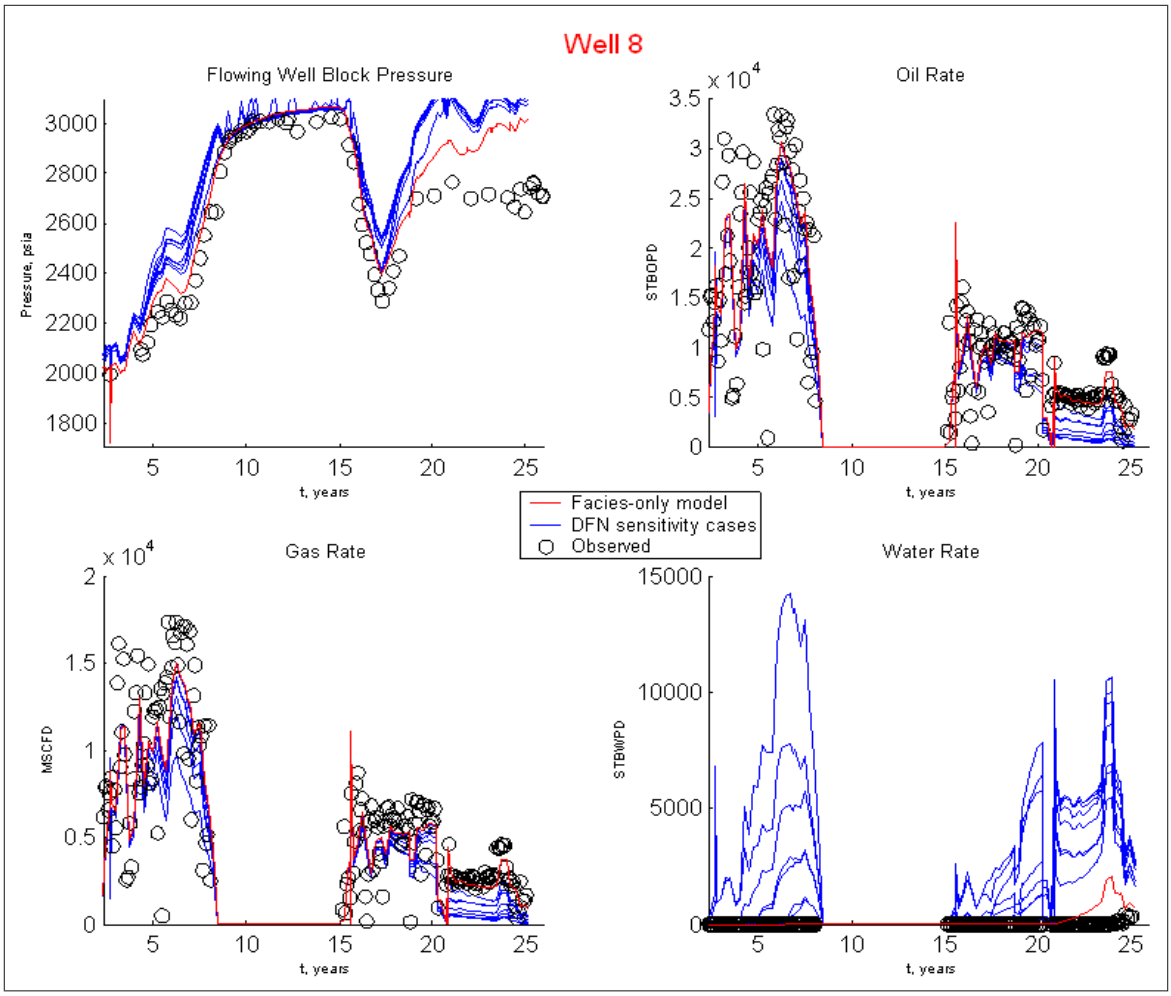

Fig. A.44: Well performance under varying DFN azimuth

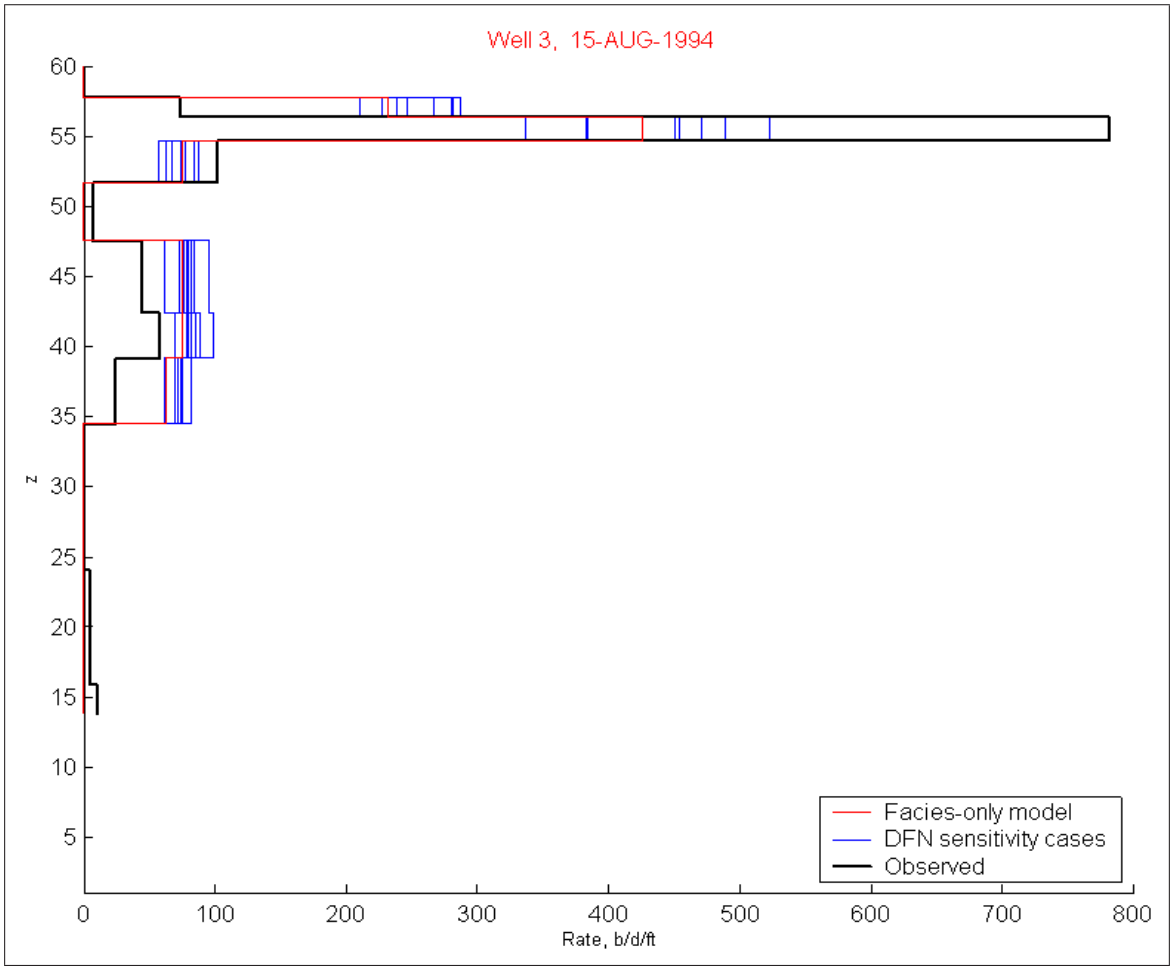

Fig. A.45: Flowmeter performance under varying DFN azimuth

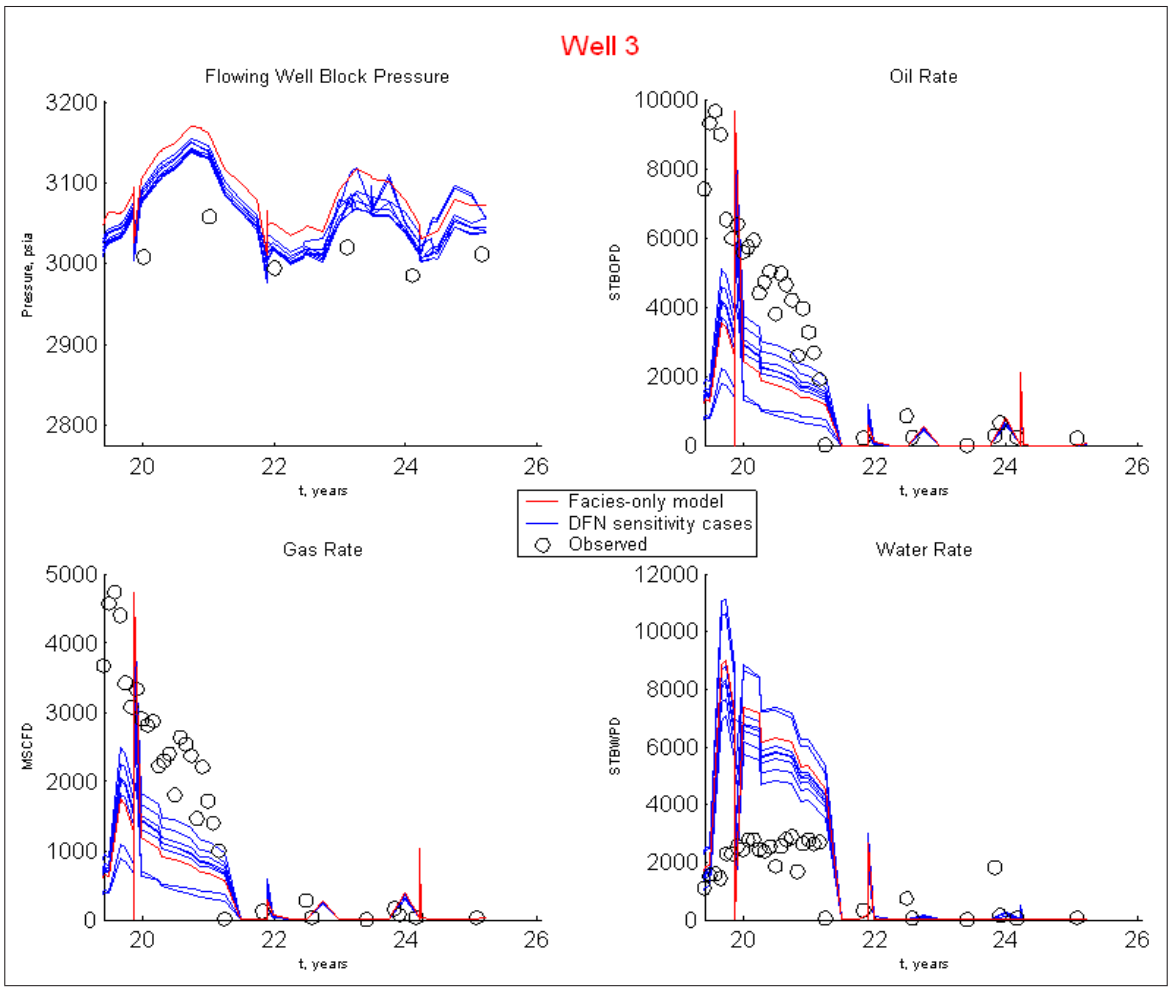

Fig. A.46: Well performance under varying DFN azimuth

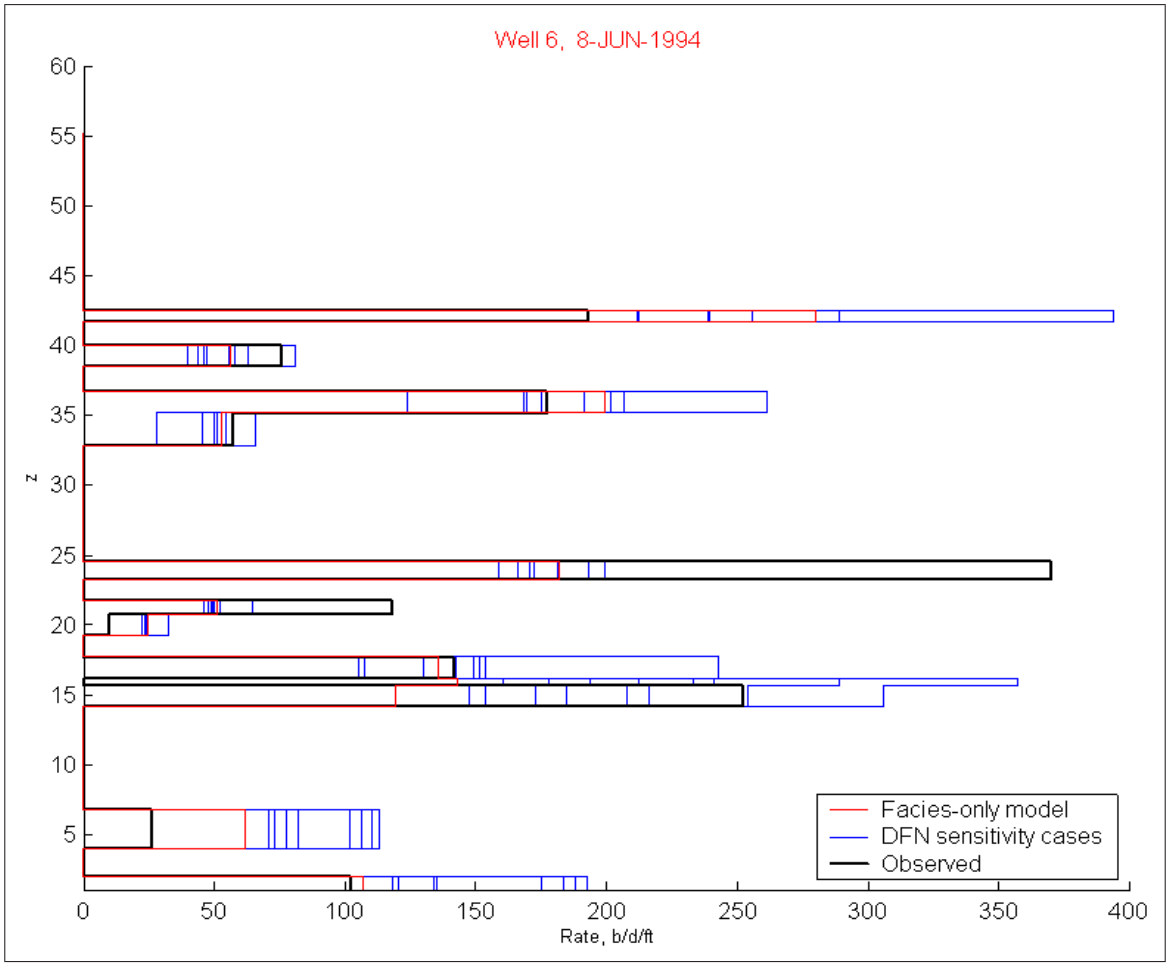

Fig. A.47: Flowmeter performance under varying DFN azimuth

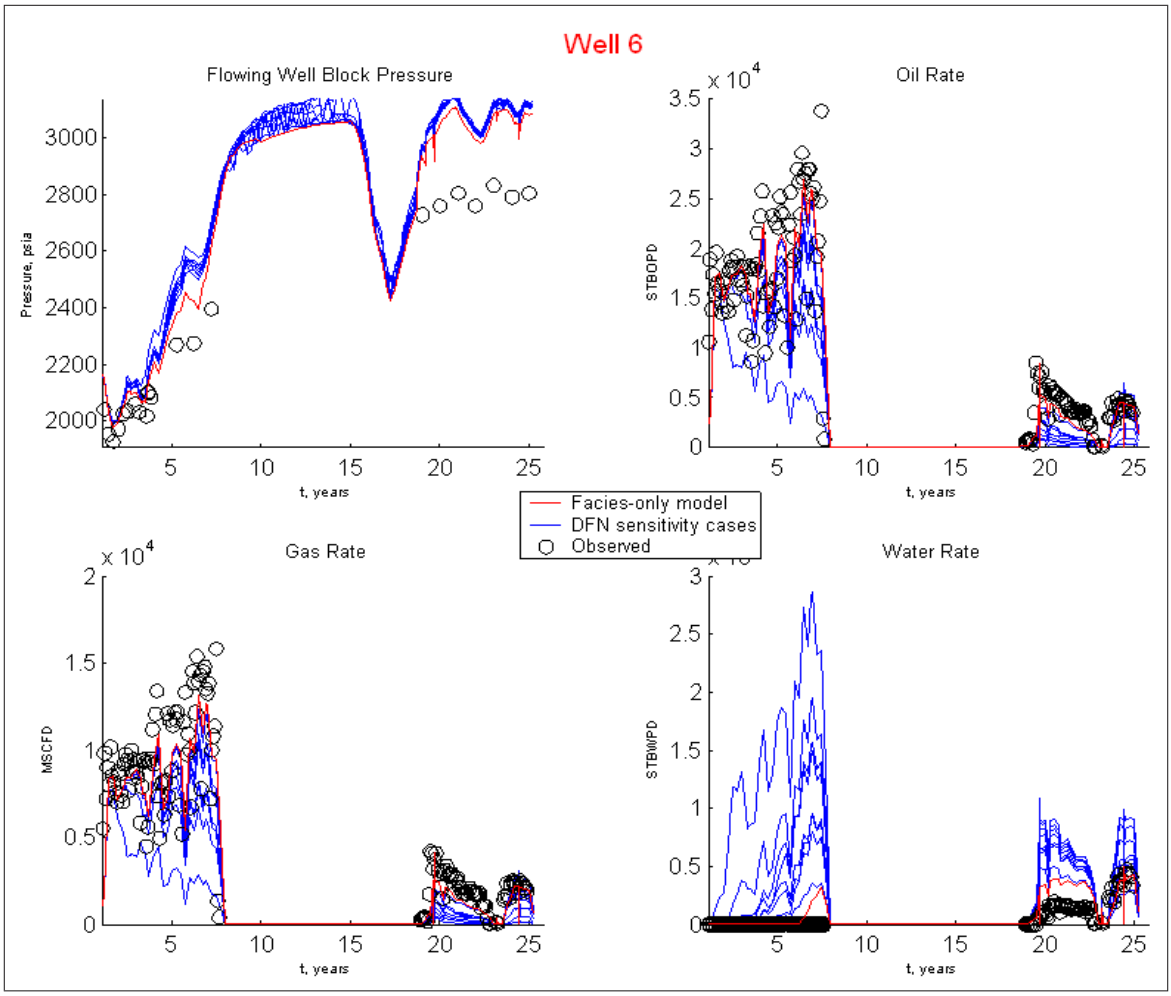

Fig. A.48: Well performance under varying DFN azimuth

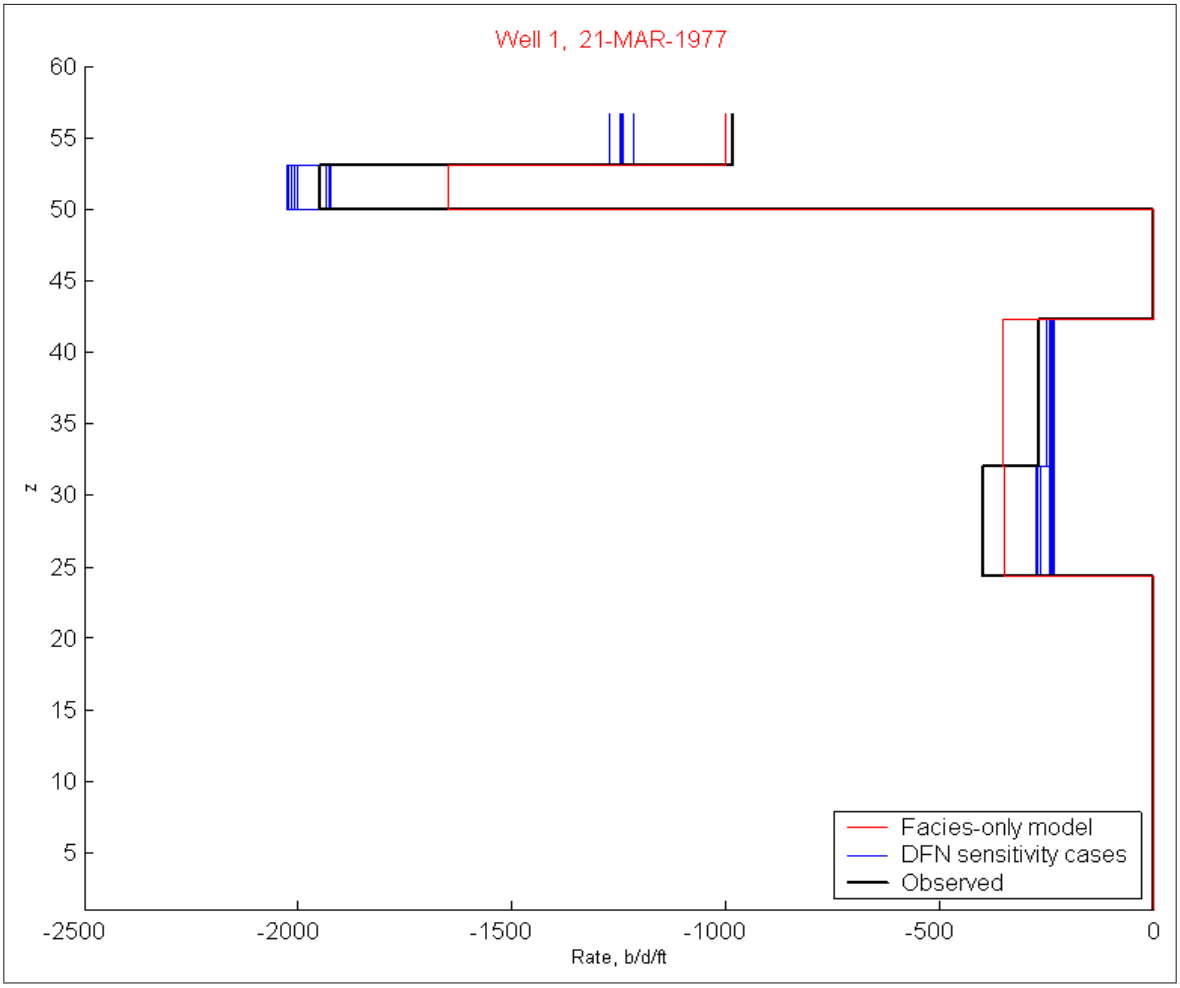

Fig. A.49: Flowmeter performance under varying DFN length

A.4 Region Case 1 with varying DFN length

Fig. A.49 through Fig. A.57 show performance results of variation in DFN length, for both water injection wells, Well 1 and Well 2, and two key producing wells which have the most extensive production history, Well 8 and Well 6 (see Fig. 3.2 for study area well locations). Finally, Well 3 is also included, as it is the offset well to Well 1, a key water injection well. This water injection well has a prolific super-k interval, as well as does Well 8. The length is drawn from a uniform distribution in the range 6500 to 36000 ft (approximately 8 to 43 flow simulation grid blocks).

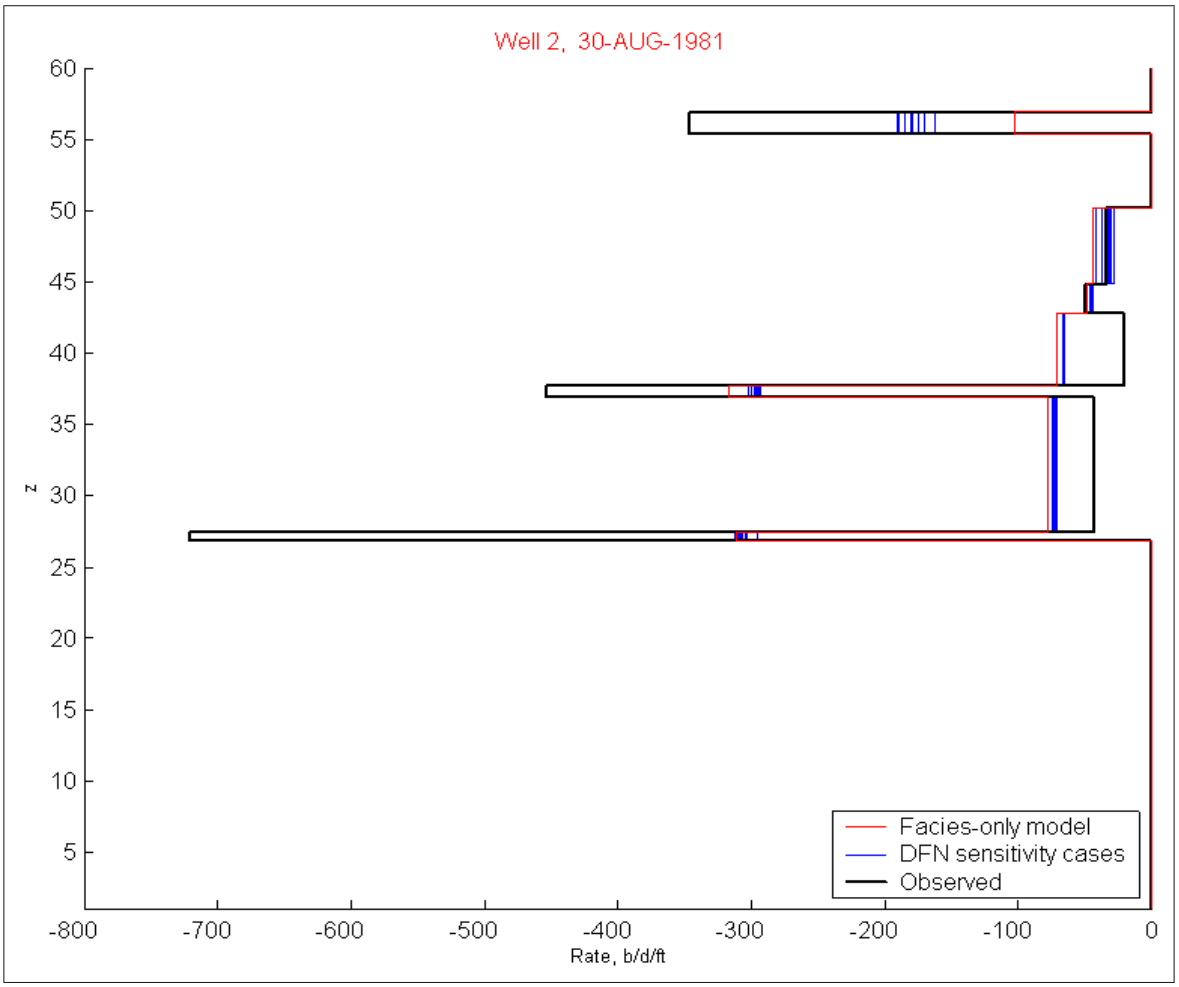

Fig. A.50: Flowmeter performance under varying DFN length

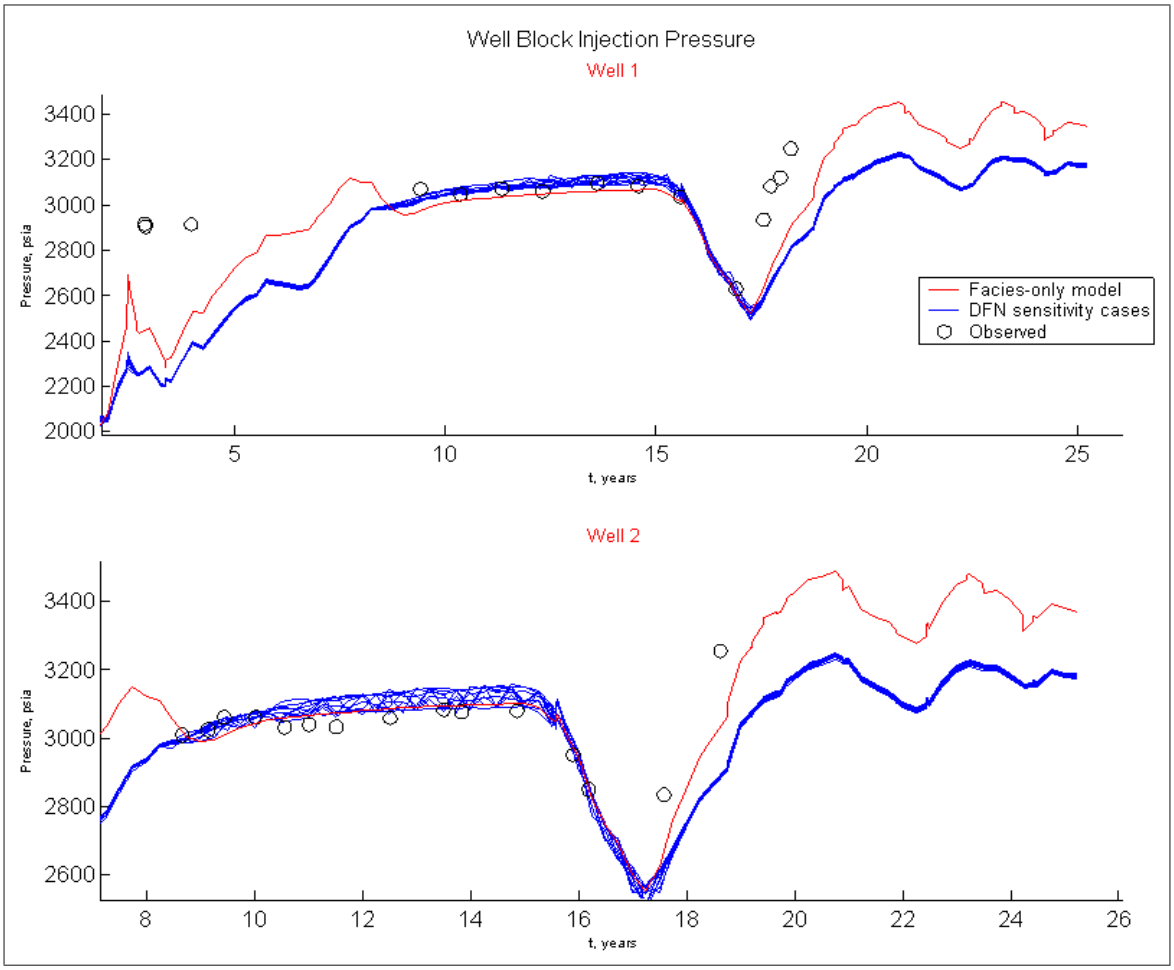

Fig. A.51: Well performance under varying DFN length

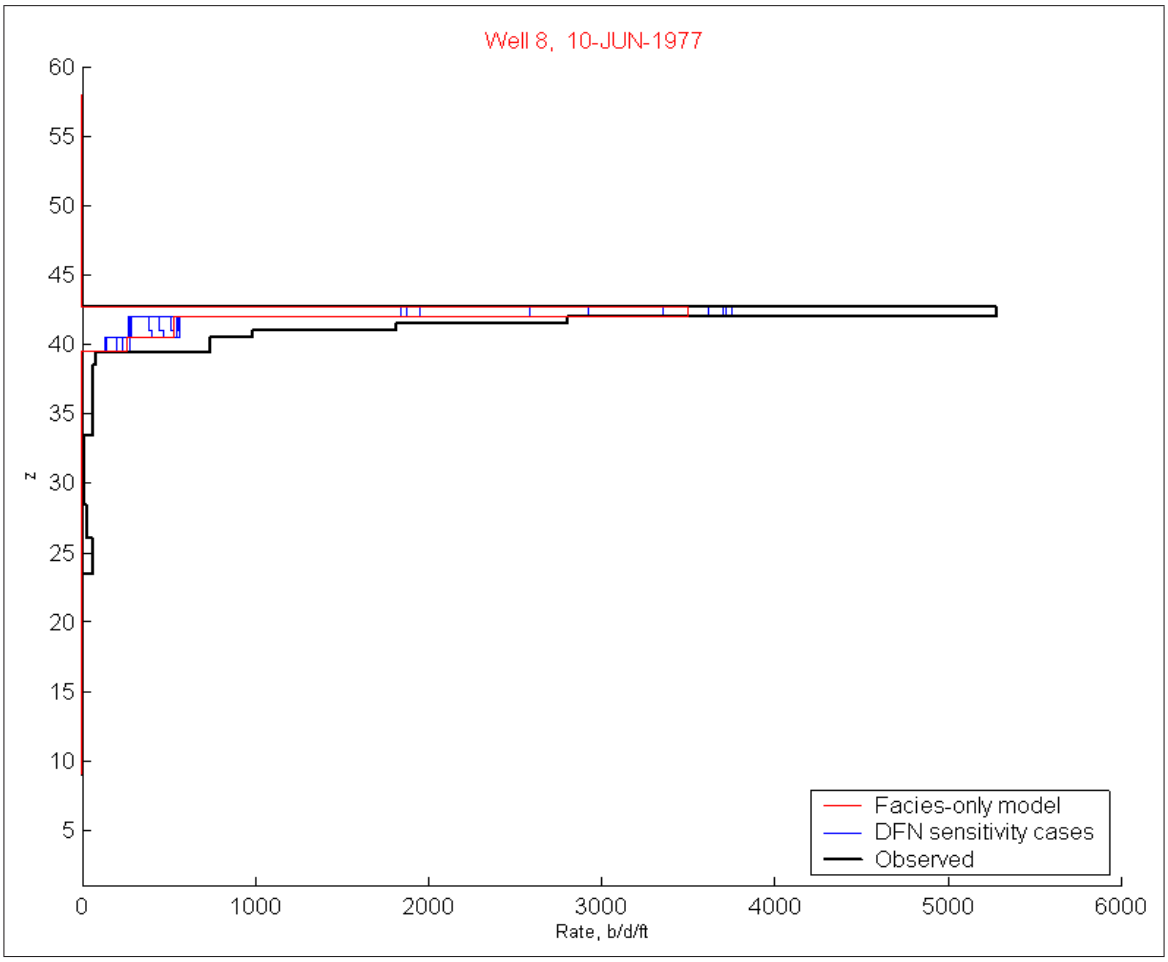

Fig. A.52: Flowmeter performance under varying DFN length

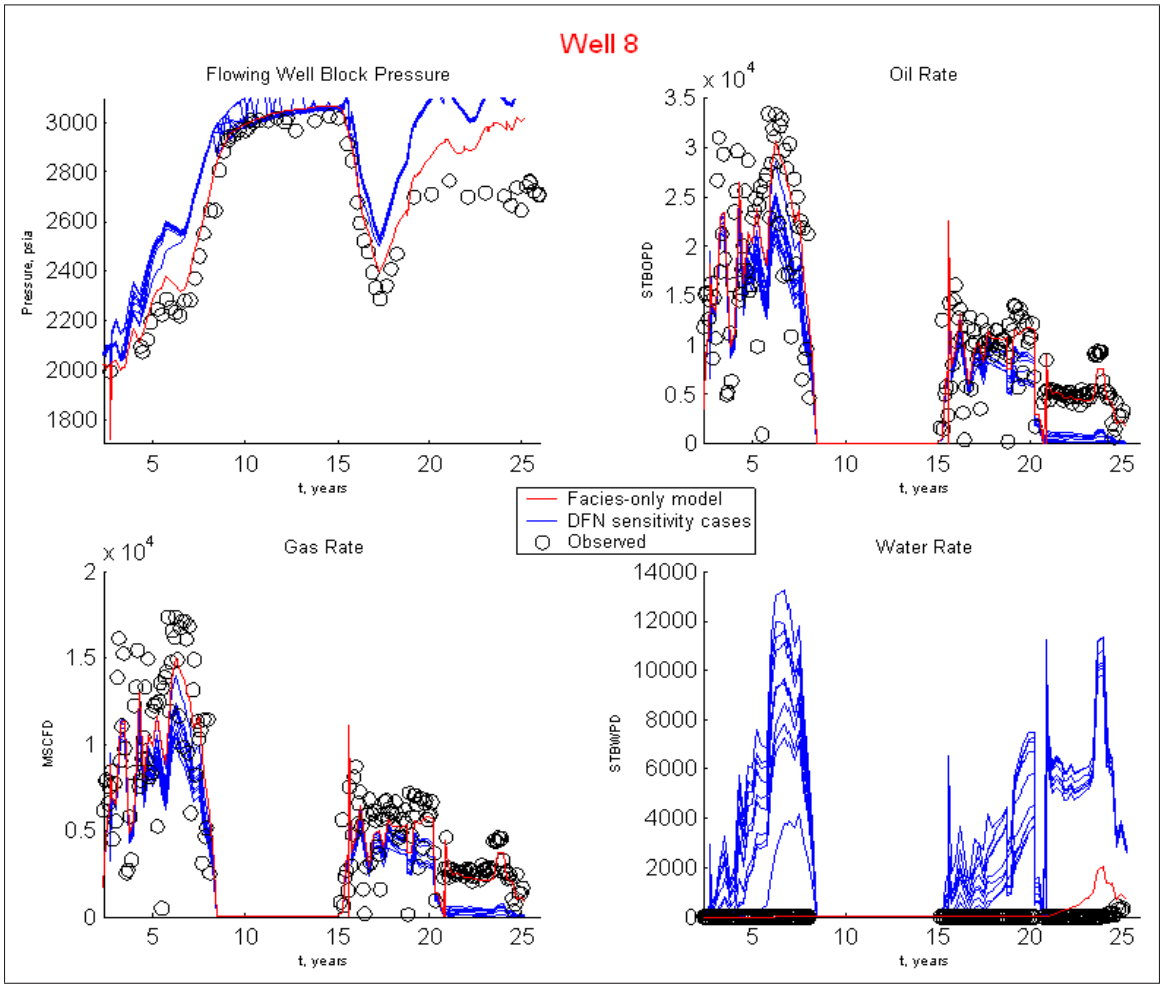

Fig. A.53: Well performance under varying DFN length

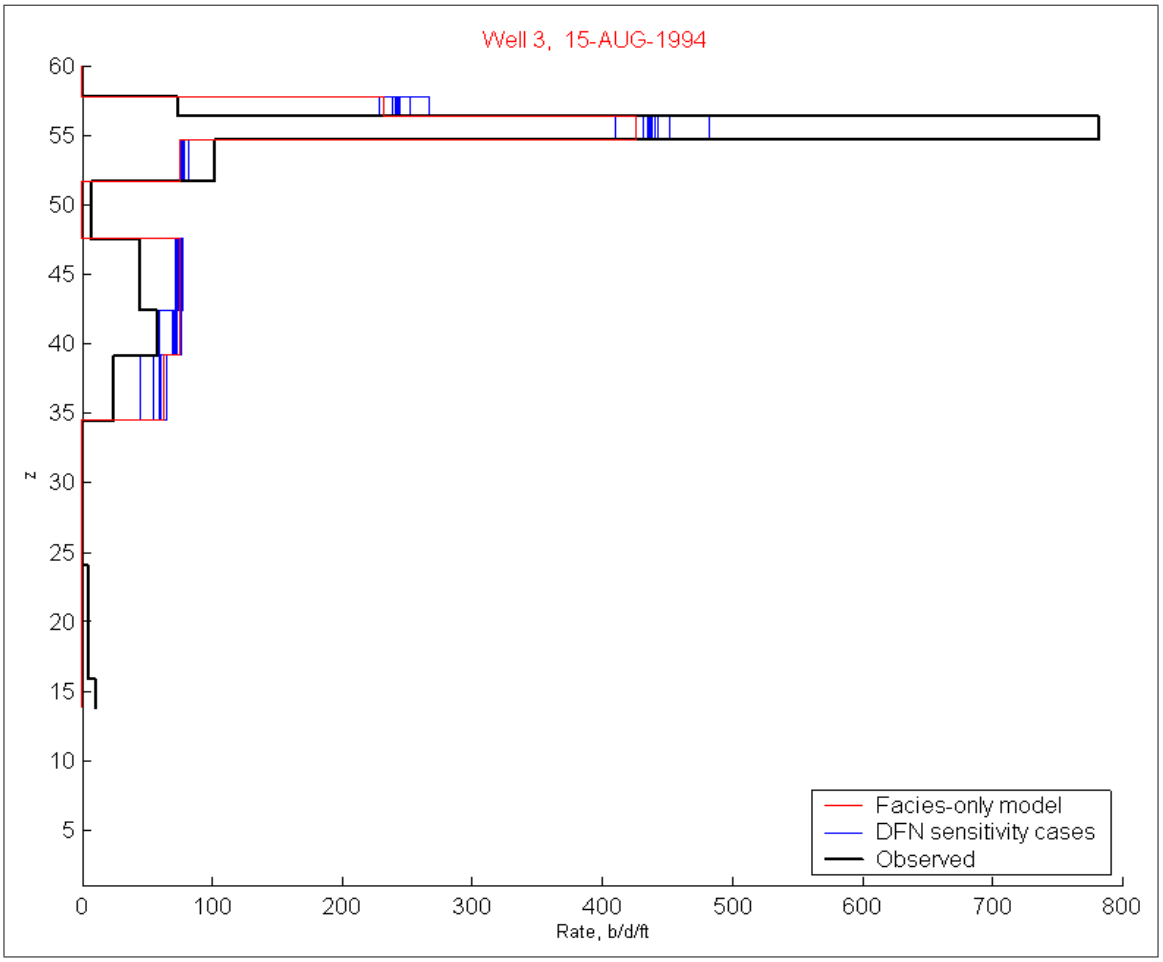

Fig. A.54: Flowmeter performance under varying DFN length

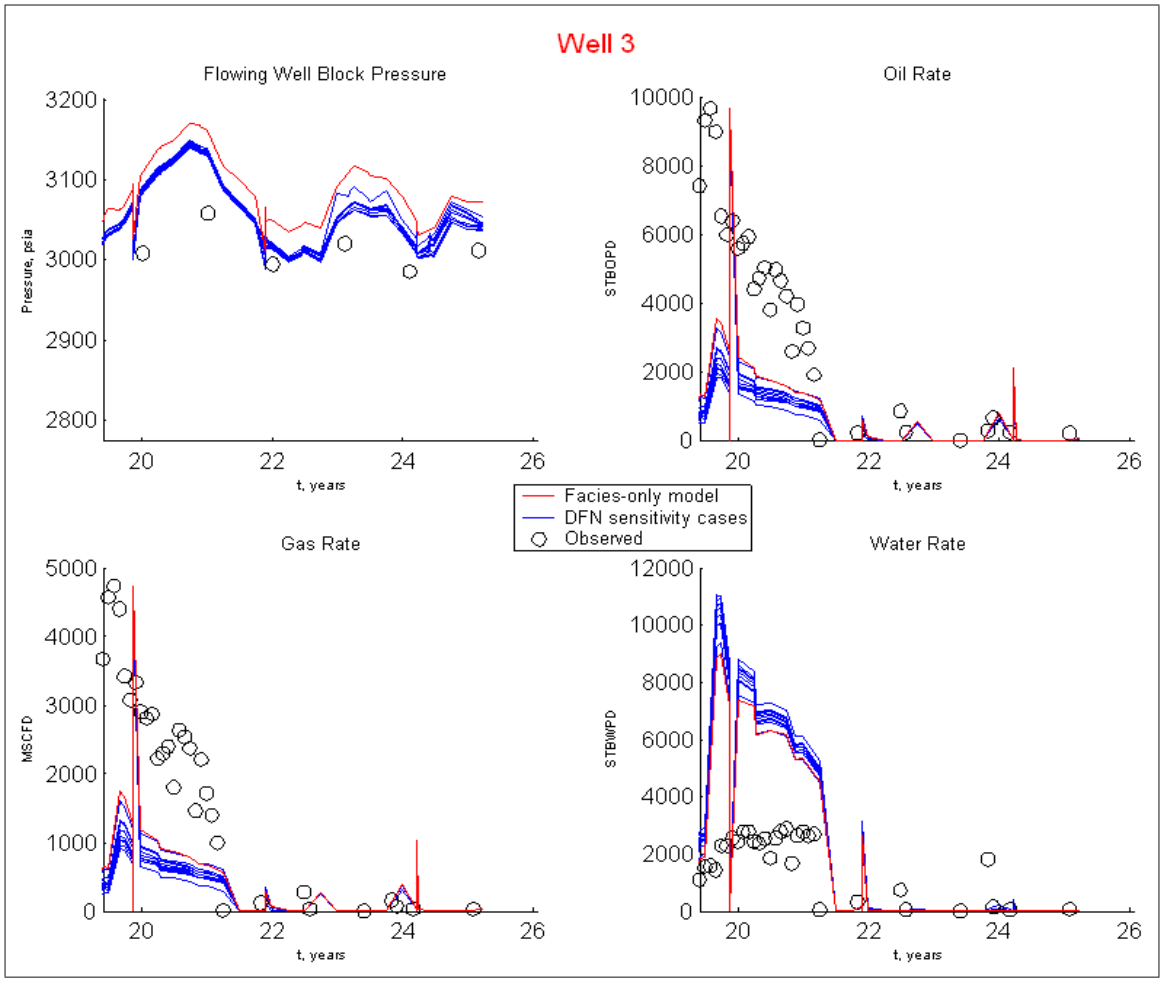

Fig. A.55: Well performance under varying DFN length

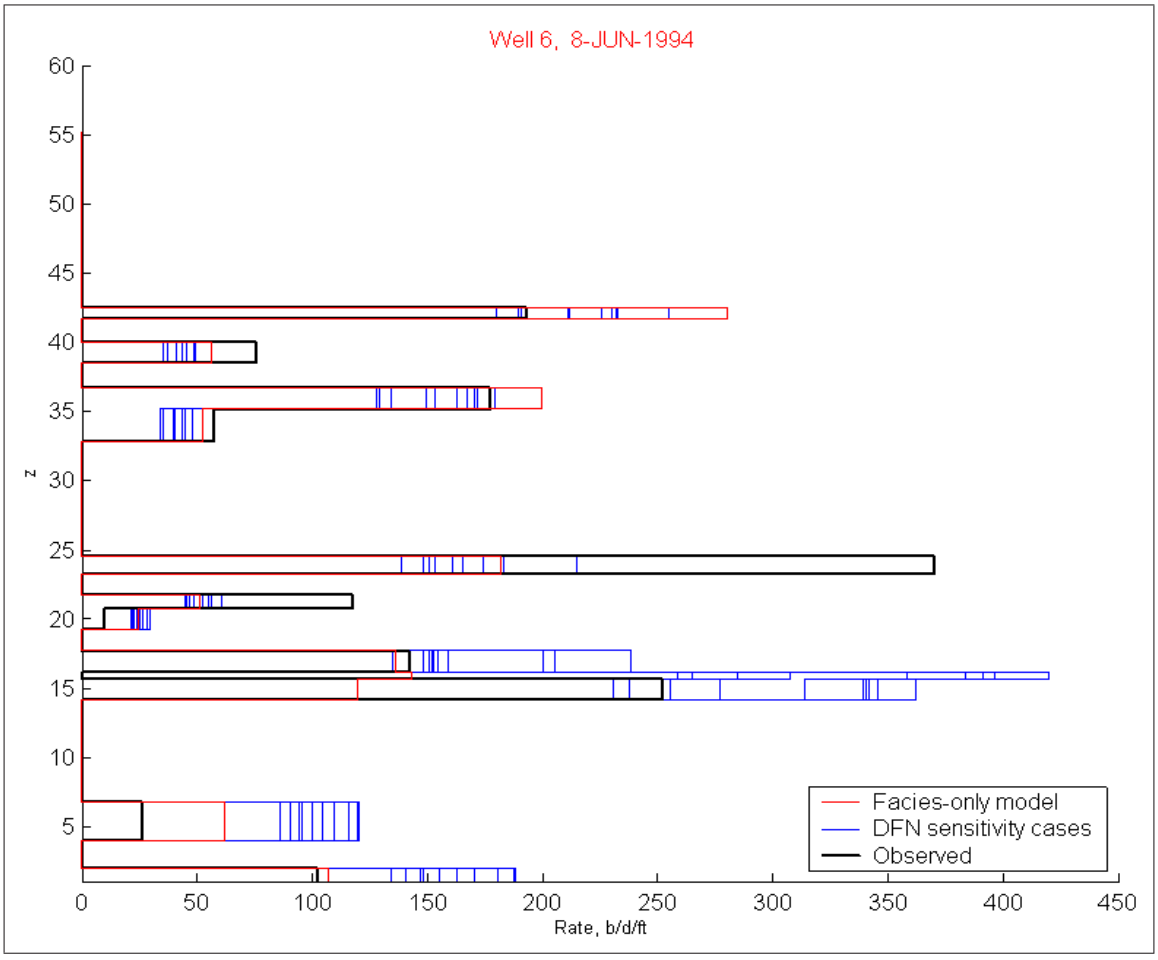

Fig. A.56: Flowmeter performance under varying DFN length

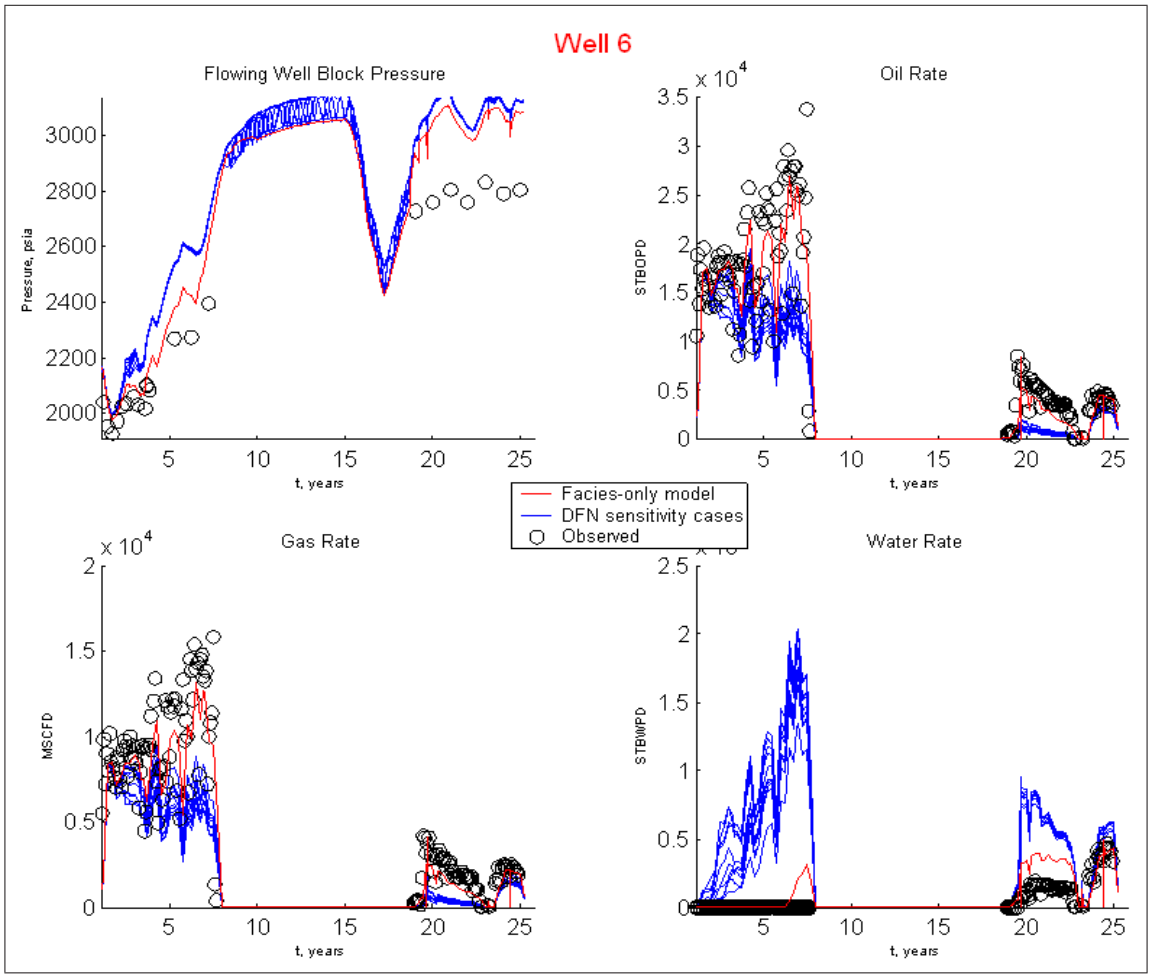

Fig. A.57: Well performance under varying DFN length

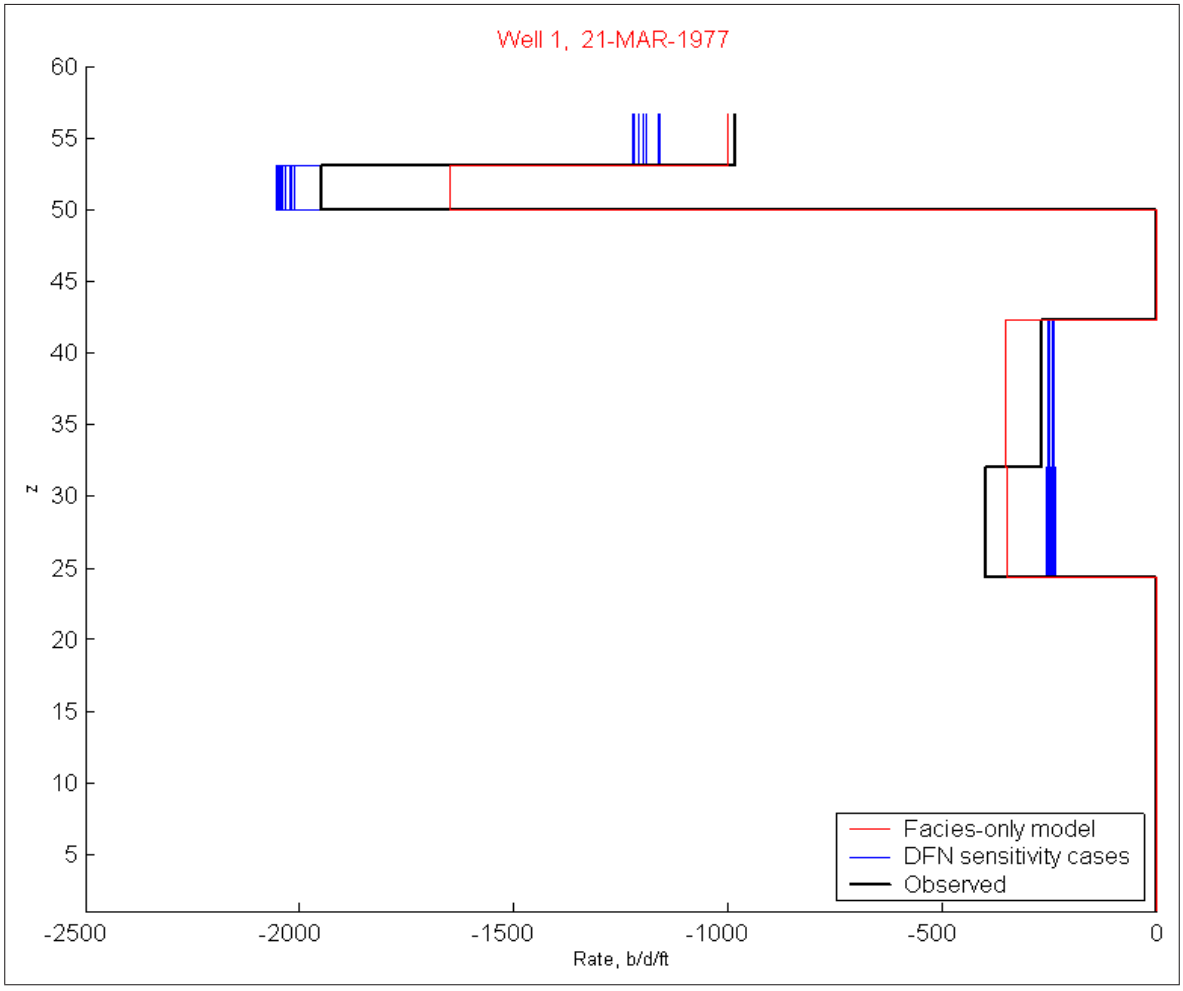

Fig. A.58: Flowmeter performance under varying DFN declination

A.5 Region Case 1 with varying DFN declination

Fig. A.58 through Fig. A.66 show performance results of variation in DFN declination (plunge), for both water injection wells, Well 1 and Well 2, and two key producing wells which have the most extensive production history, Well 8 and Well 6 (see Fig. 3.2 for study area well locations). Finally, Well 3 is also included, as it is the offset well to Well 1, a key water injection well. This water injection well has a prolific super-k interval, as well as does Well 8. The declination is drawn from a uniform distribution in the range 0^o to 0.25^o from horizontal.

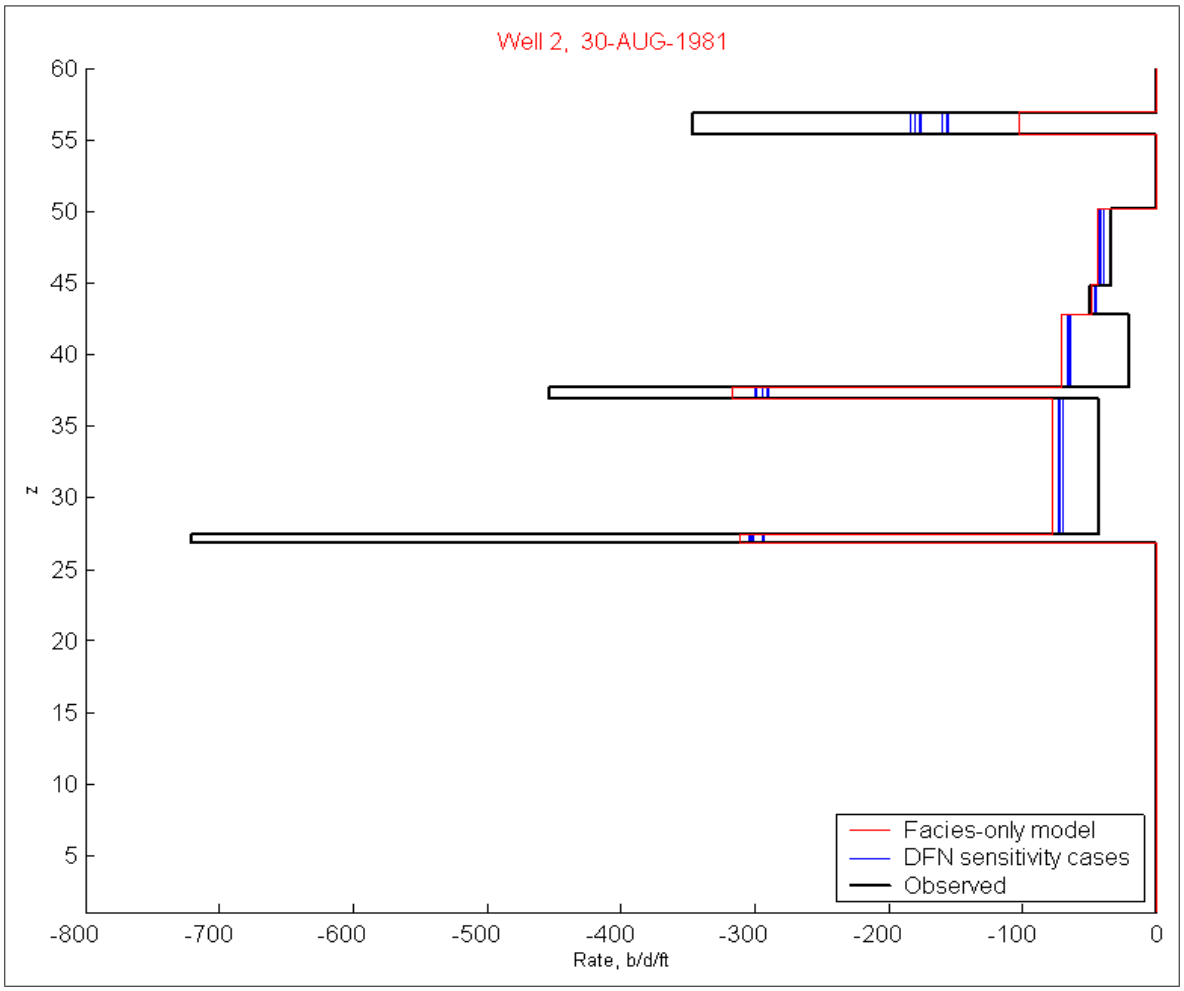

Fig. A.59: Flowmeter performance under varying DFN declination

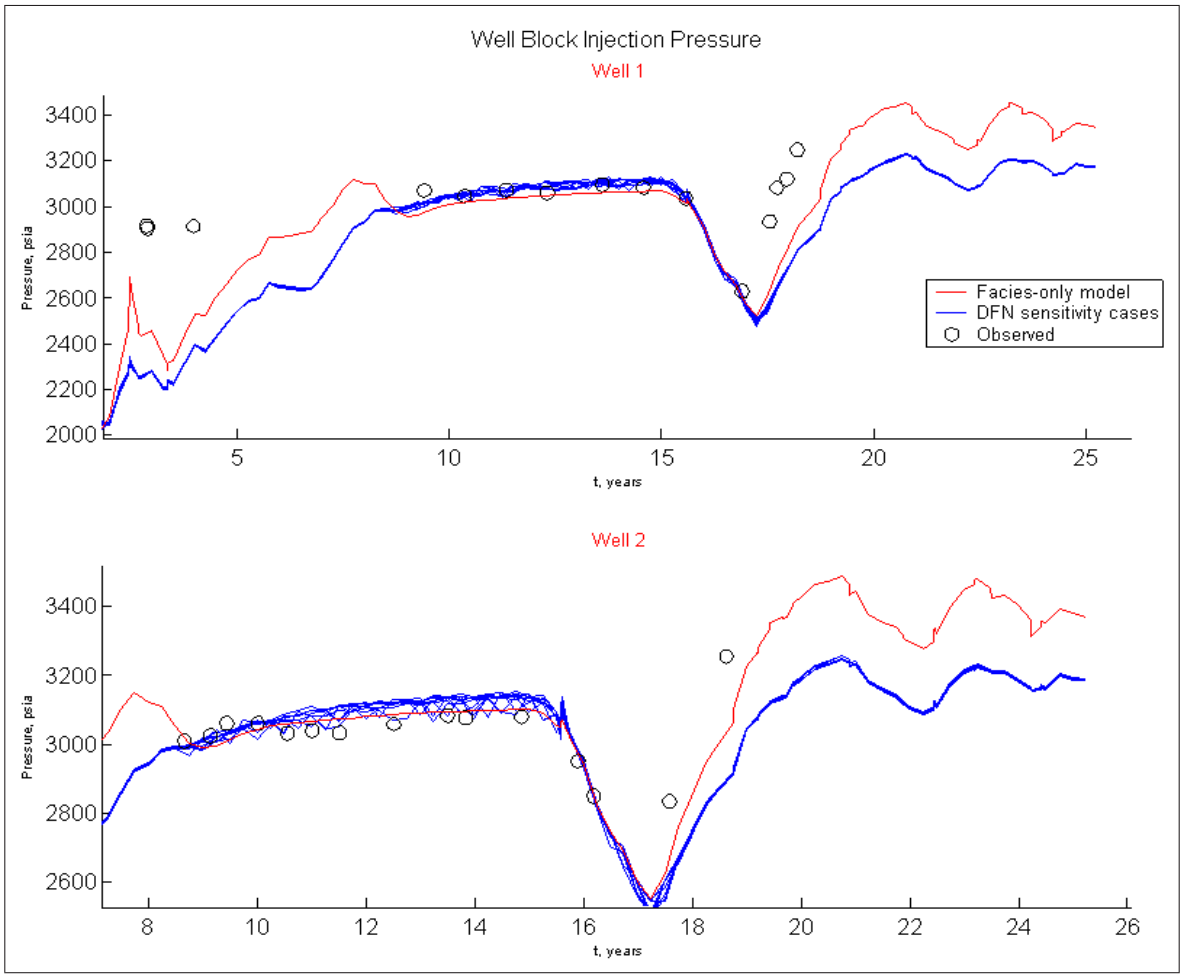

Fig. A.60: Well performance under varying DFN declination

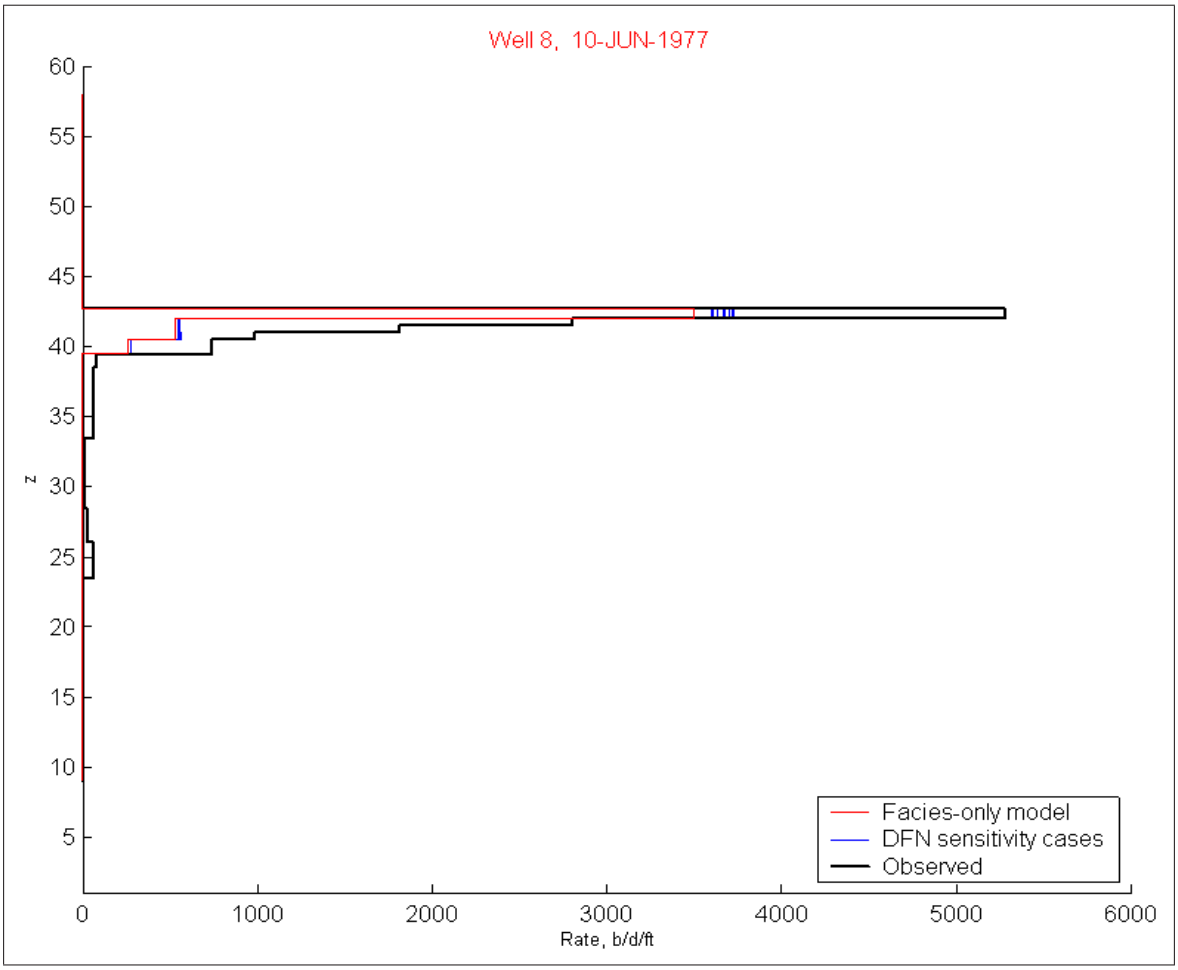

Fig. A.61: Flowmeter performance under varying DFN declination

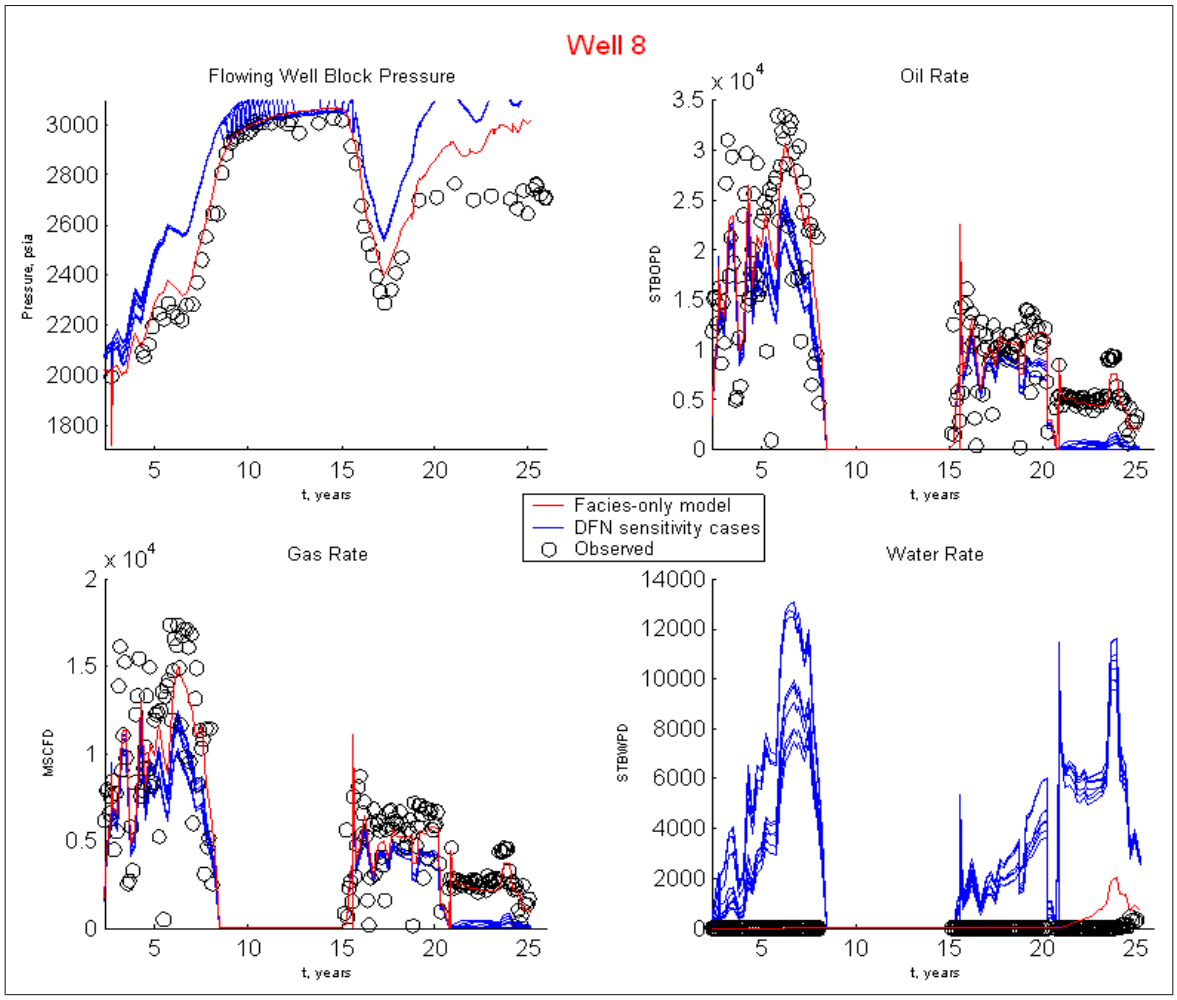

Fig. A.62: Well performance under varying DFN declination

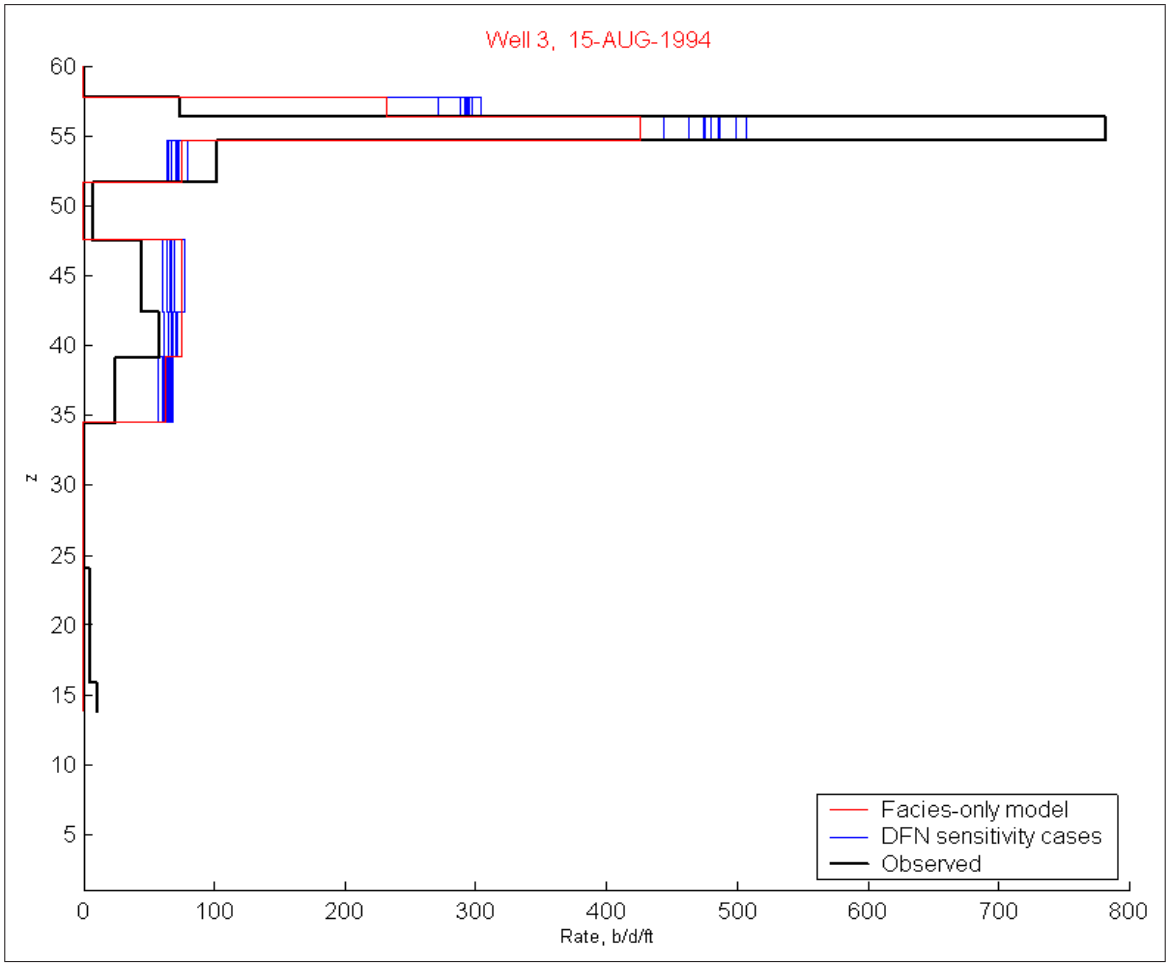

Fig. A.63: Flowmeter performance under varying DFN declination

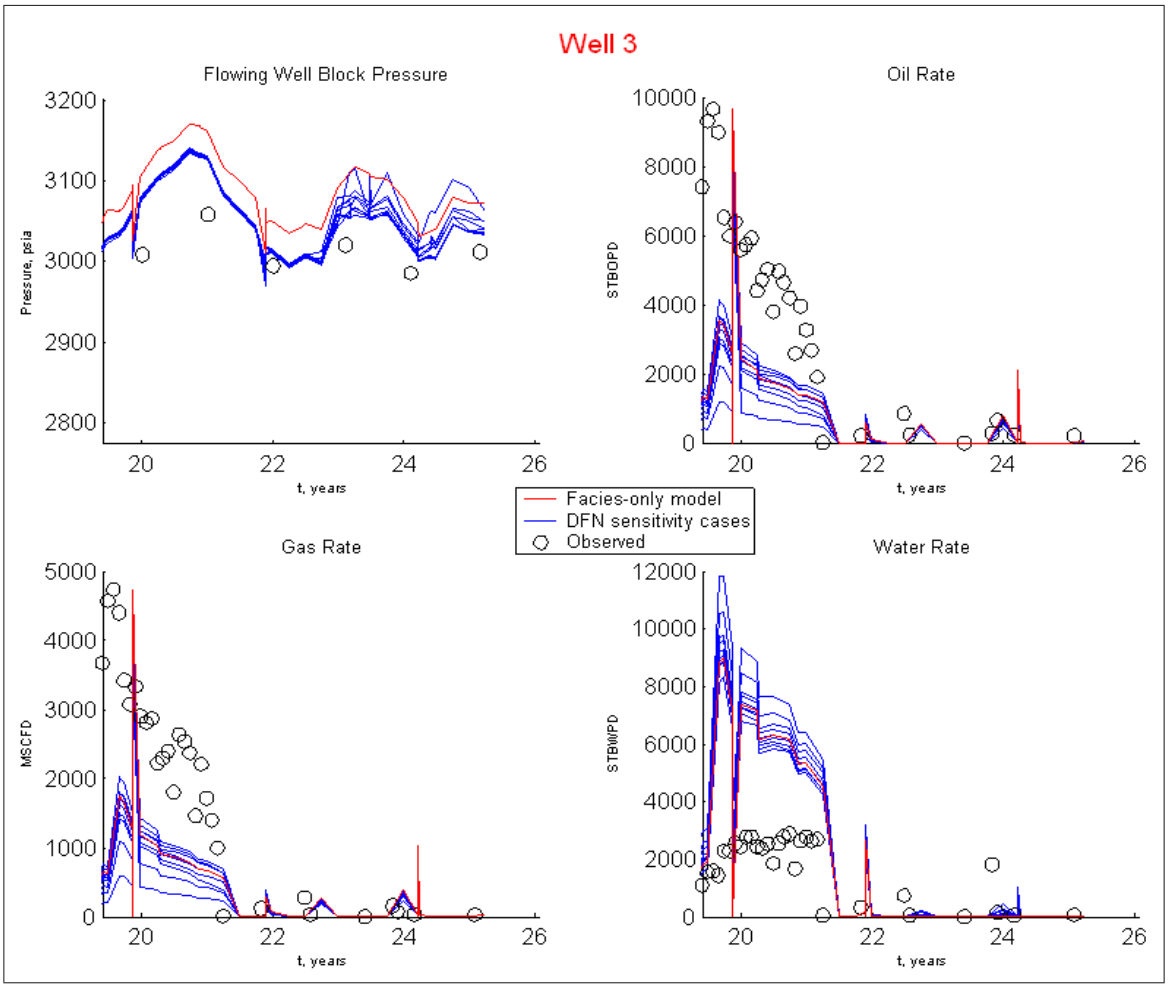

Fig. A.64: Well performance under varying DFN declination

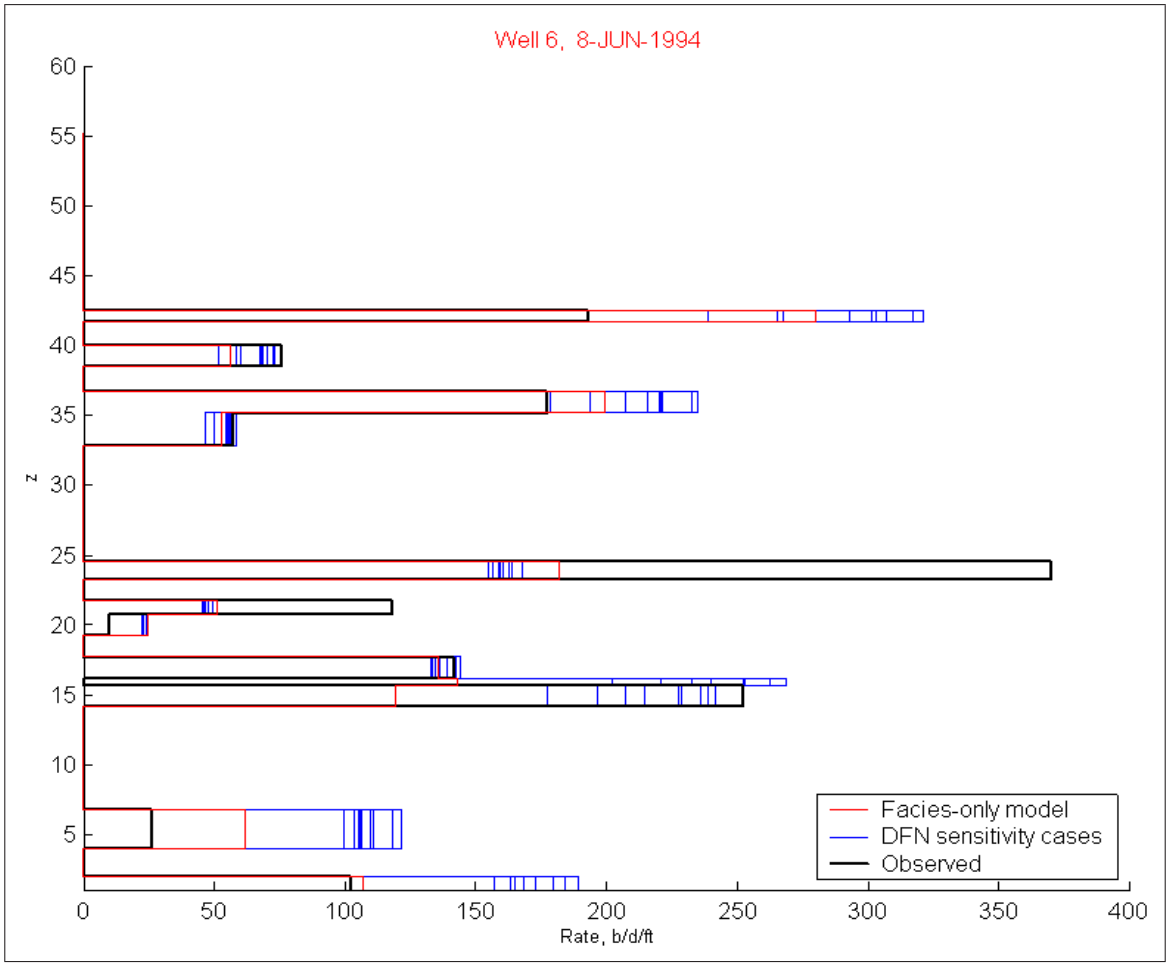

Fig. A.65: Flowmeter performance under varying DFN declination

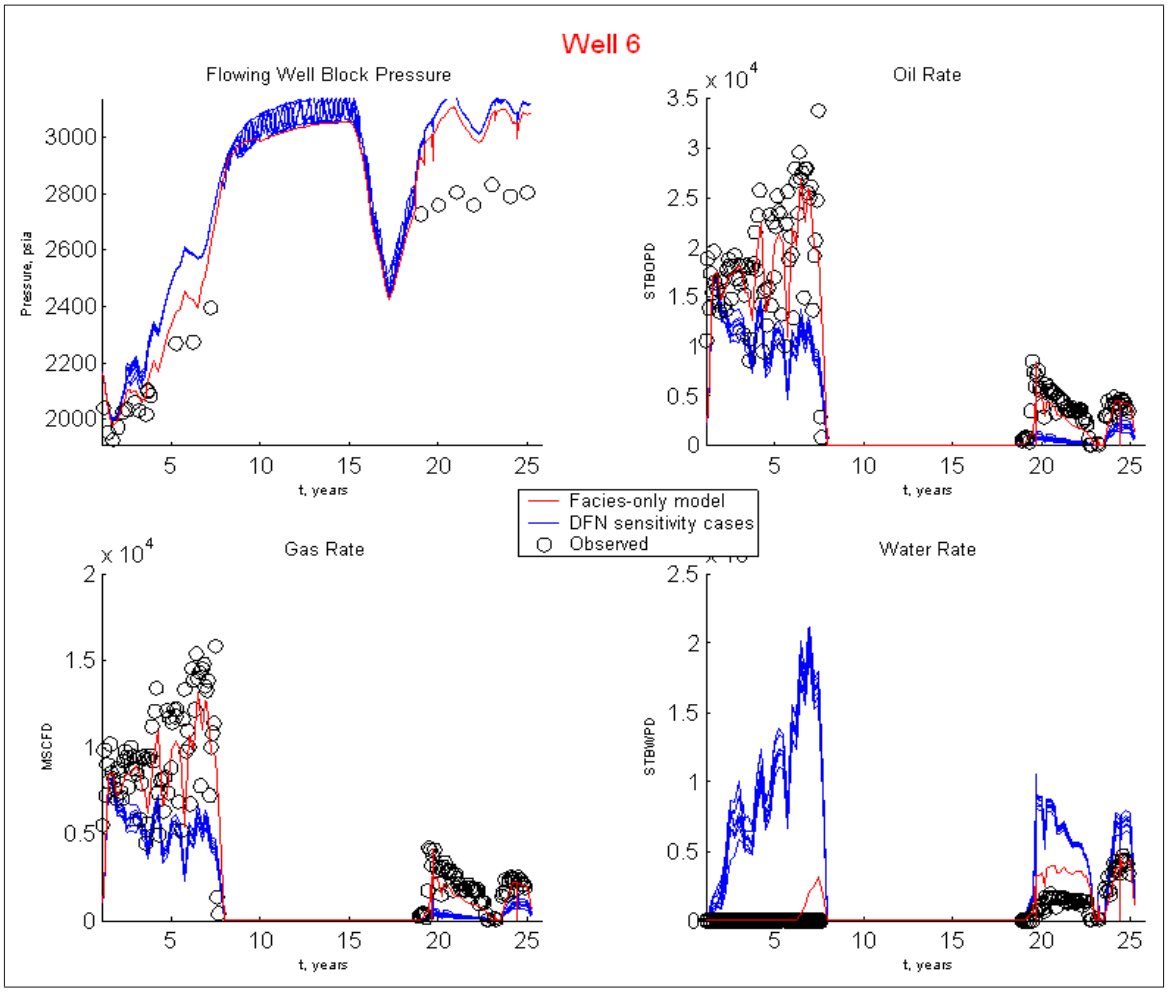

Fig. A.66: Well performance under varying DFN declination

A.6 Region Case 1 with varying DFN vertical thickness

Fig. A.67 through Fig. A.75 show performance results of variation in DFN vertical thickness, for both water injection wells, Well 1 and Well 2, and two key producing wells which have the most extensive production history, Well 8 and Well 6 (see Fig. 3.2 for study area well locations). Finally, Well 3 is also included, as it is the offset well to Well 1, a key water injection well. This water injection well has a prolific super-k interval, as well as does Well 8. The vertical thickness is drawn from a uniform distribution in the range 8 to 32 ft (approximately 2 to 8 flow simulation grid blocks).

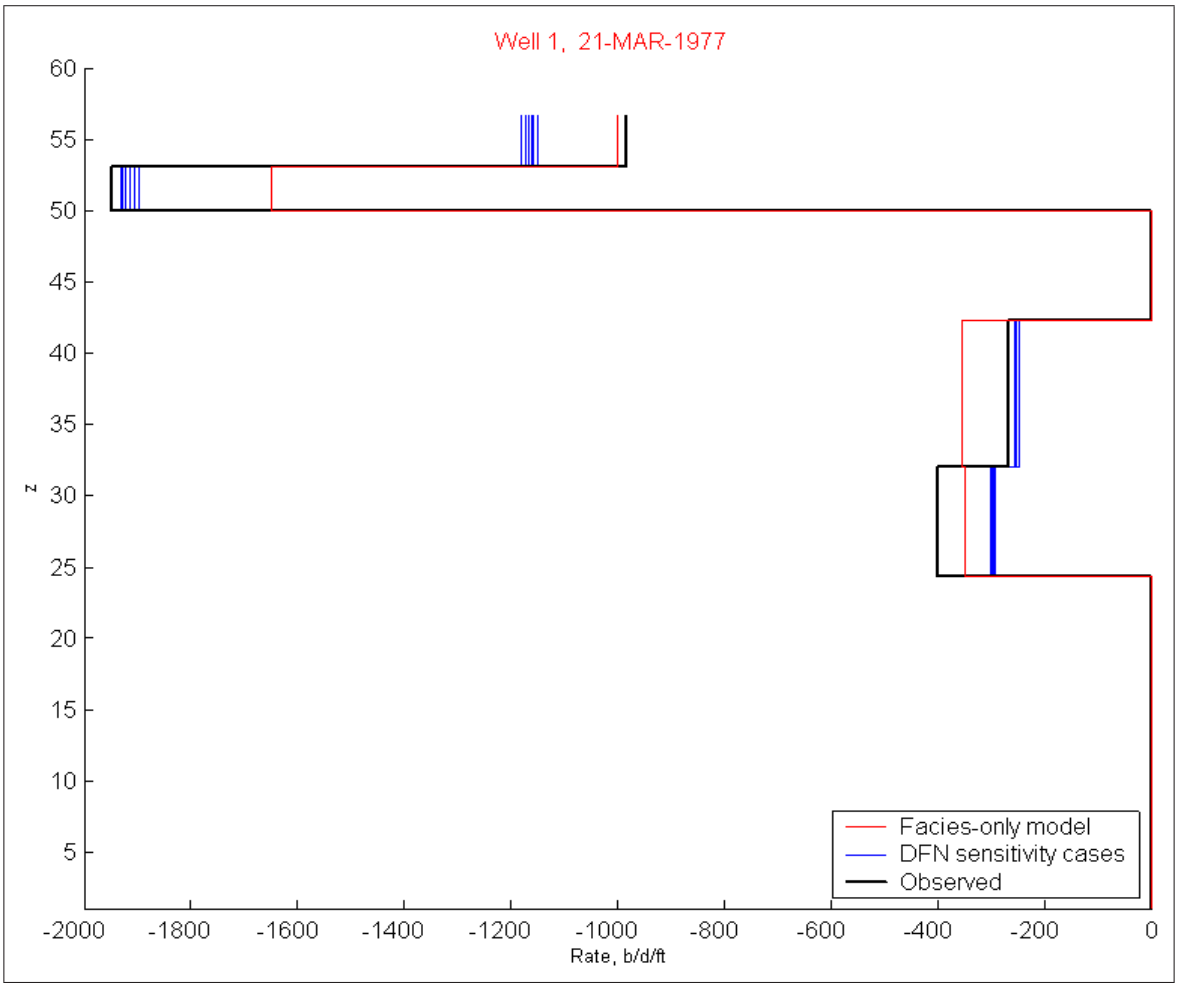

Fig. A.67: Flowmeter performance under varying DFN vertical thickness

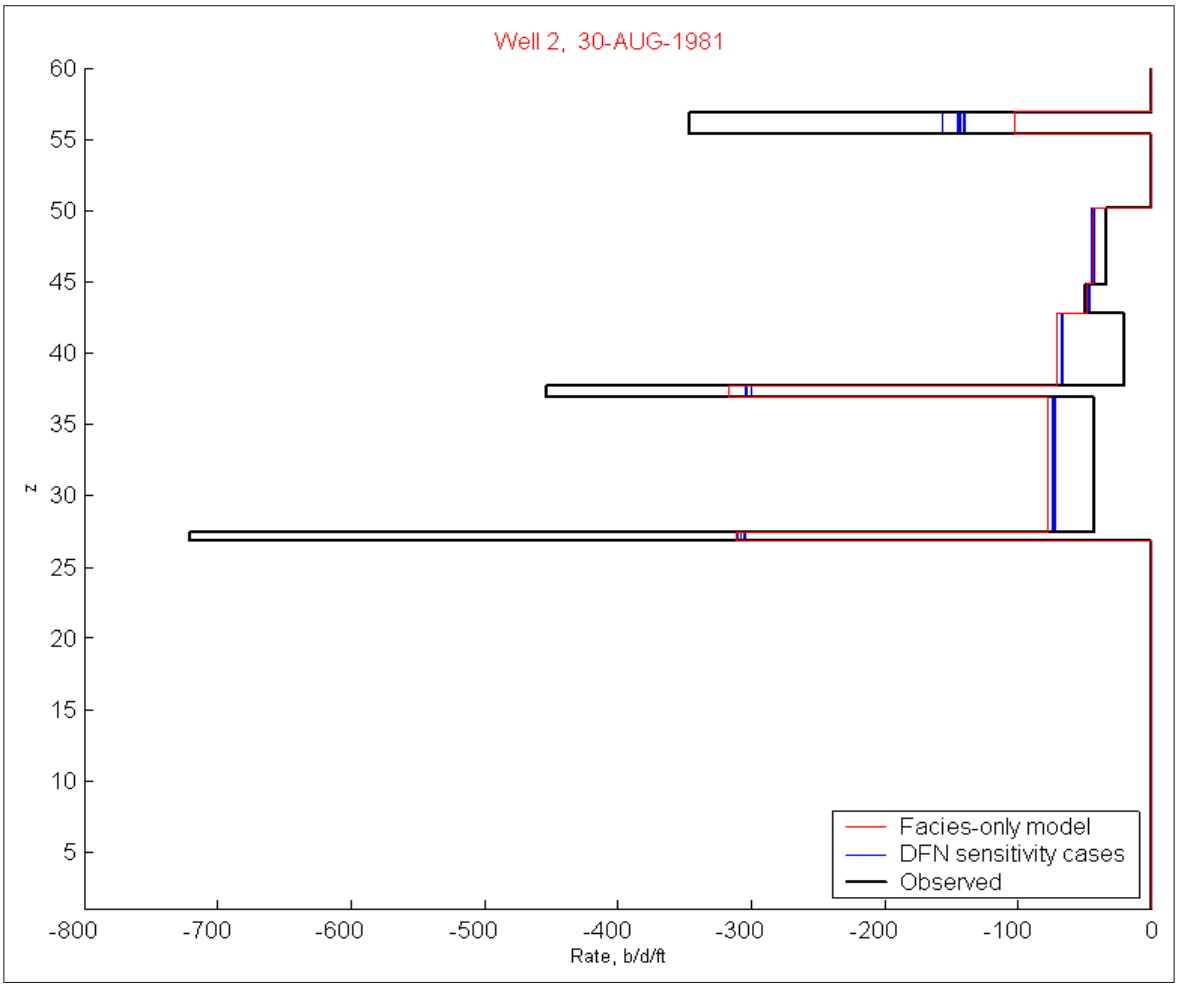

Fig. A.68: Flowmeter performance under varying DFN vertical thickness

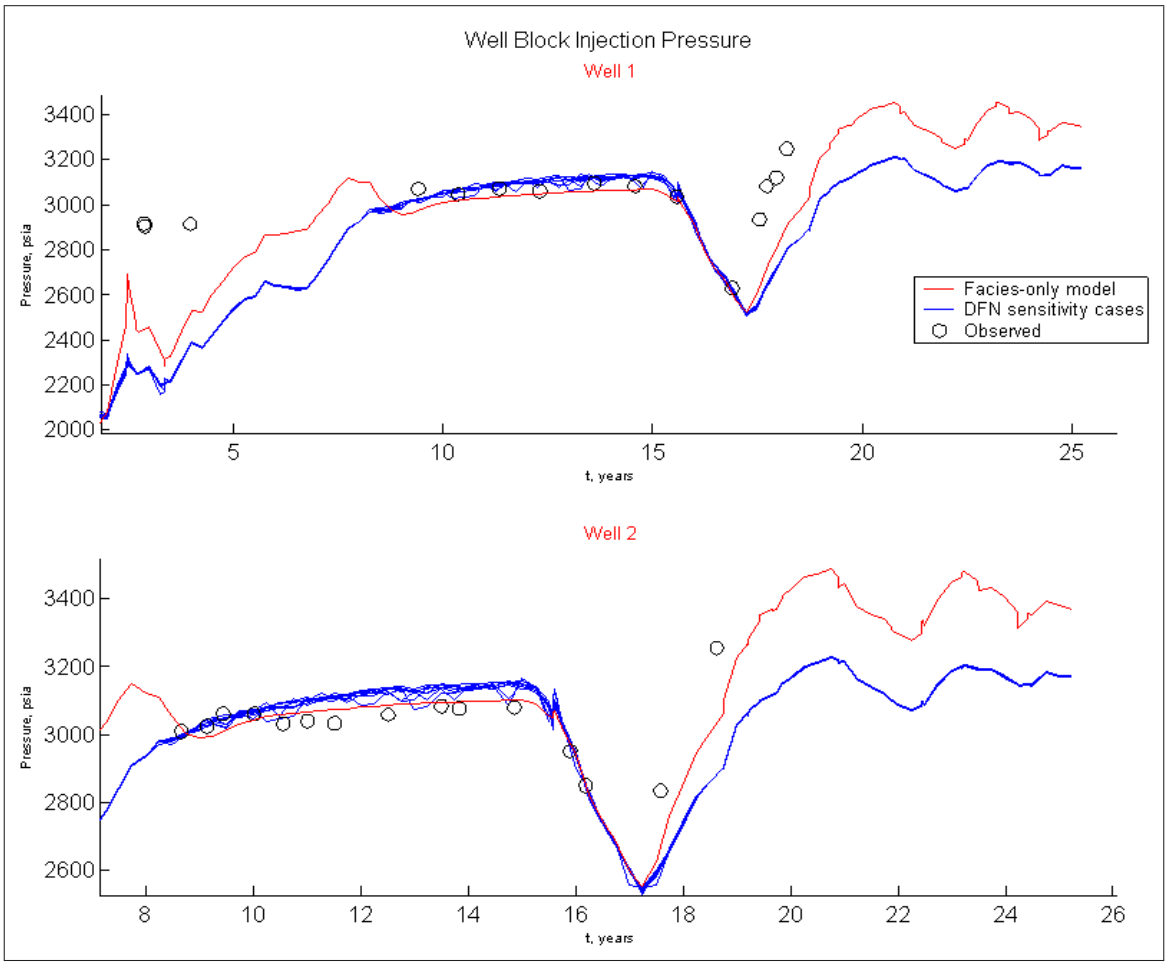

Fig. A.69: Well performance under varying DFN vertical thickness

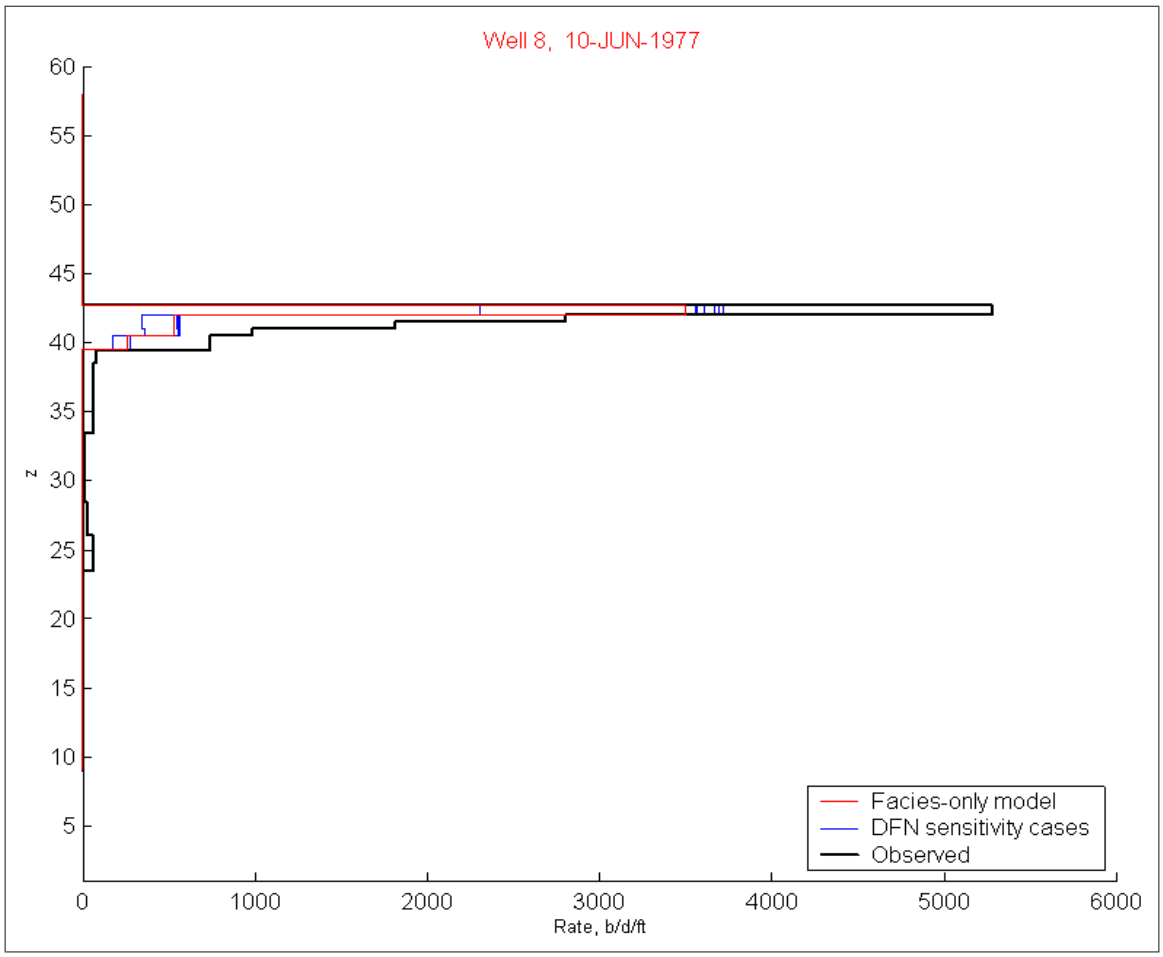

Fig. A.70: Flowmeter performance under varying DFN vertical thickness

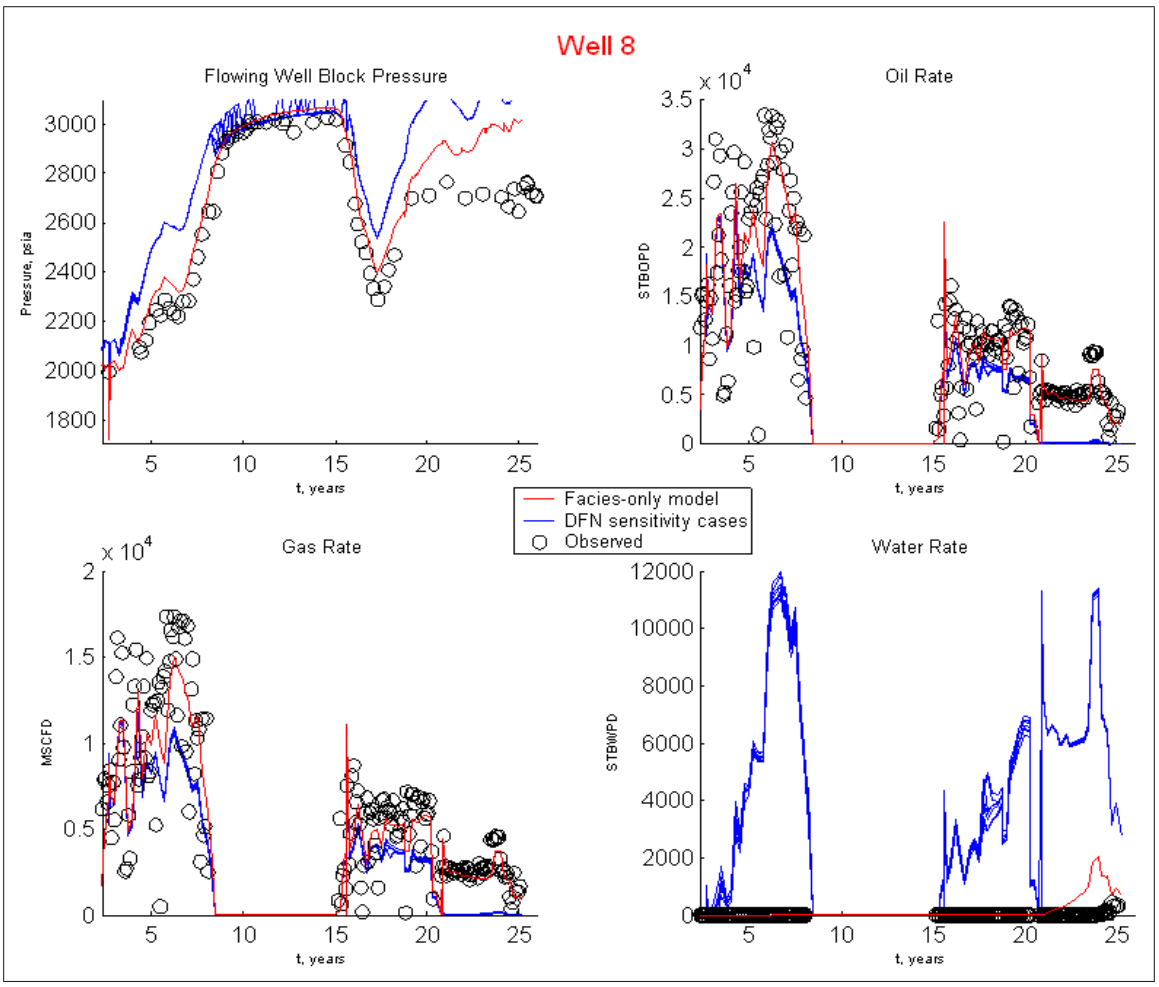

Fig. A.71: Well performance under varying DFN vertical thickness

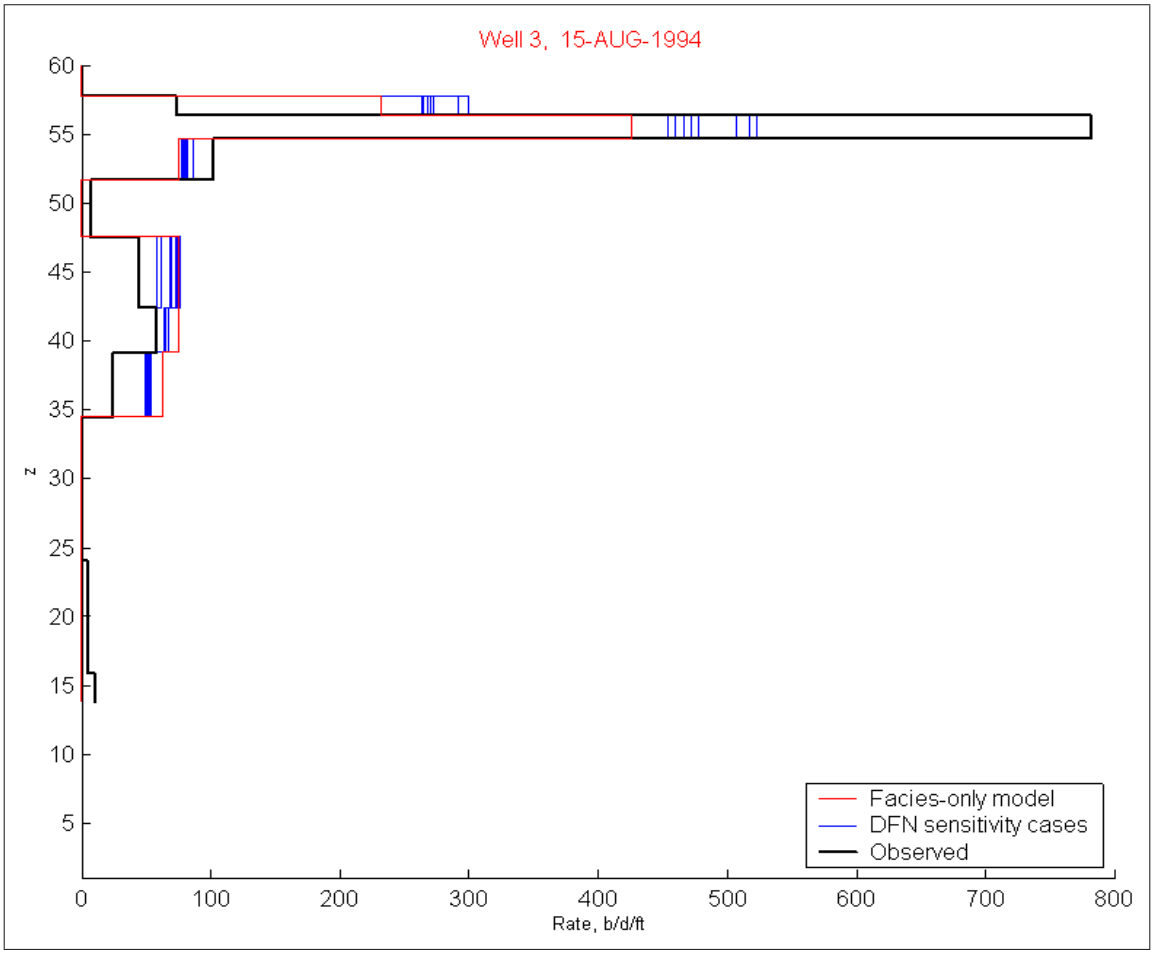

Fig. A.72: Flowmeter performance under varying DFN vertical thickness

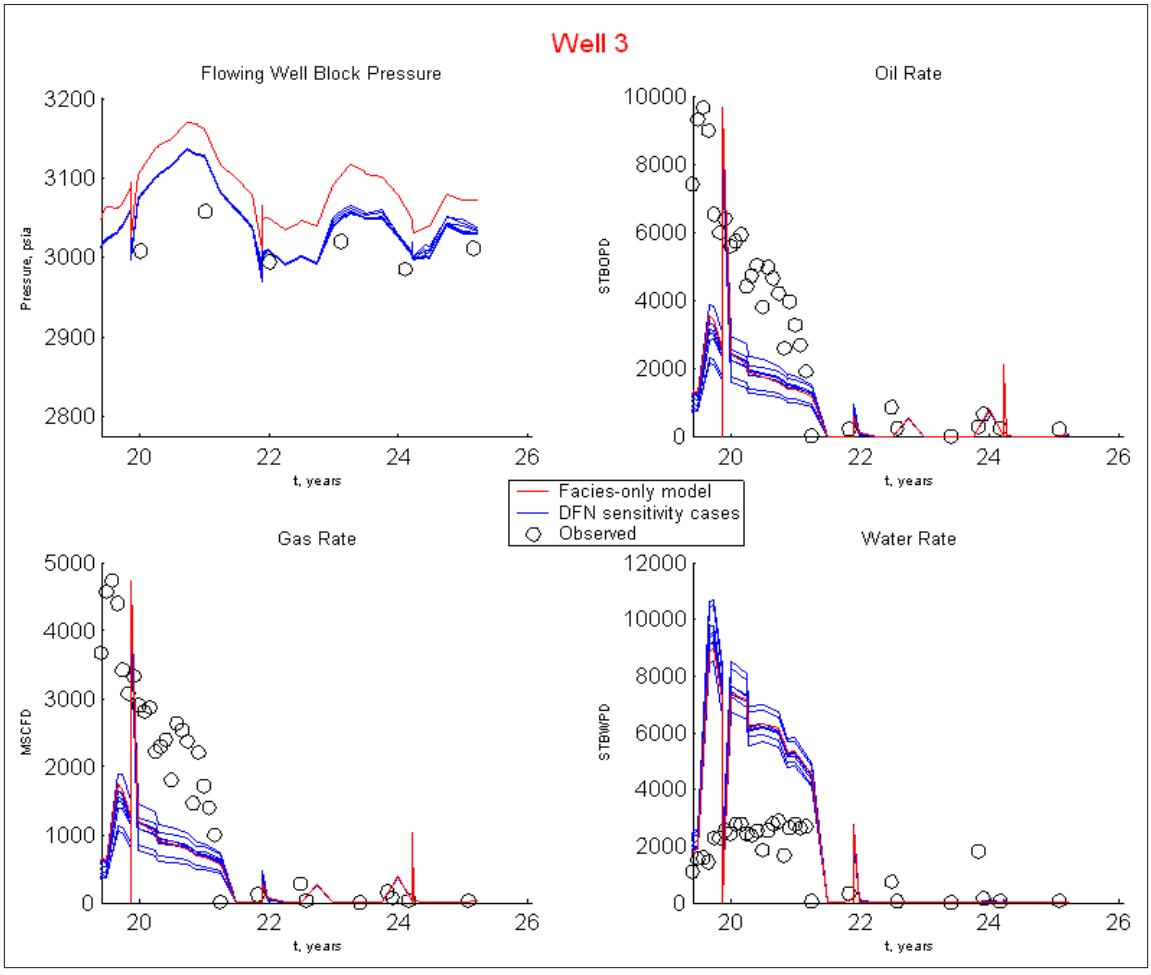

Fig. A.73: Well performance under varying DFN vertical thickness

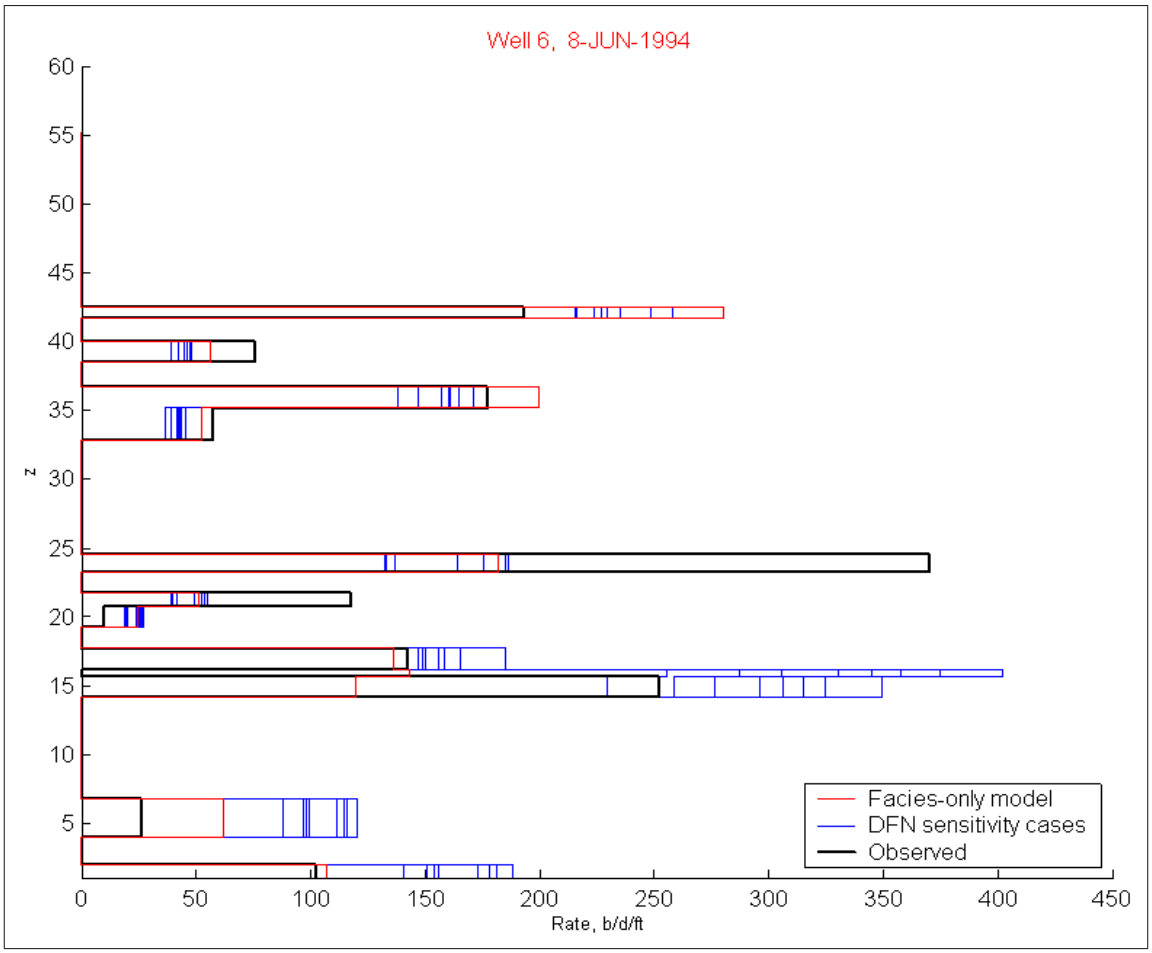

Fig. A.74: Flowmeter performance under varying DFN vertical thickness

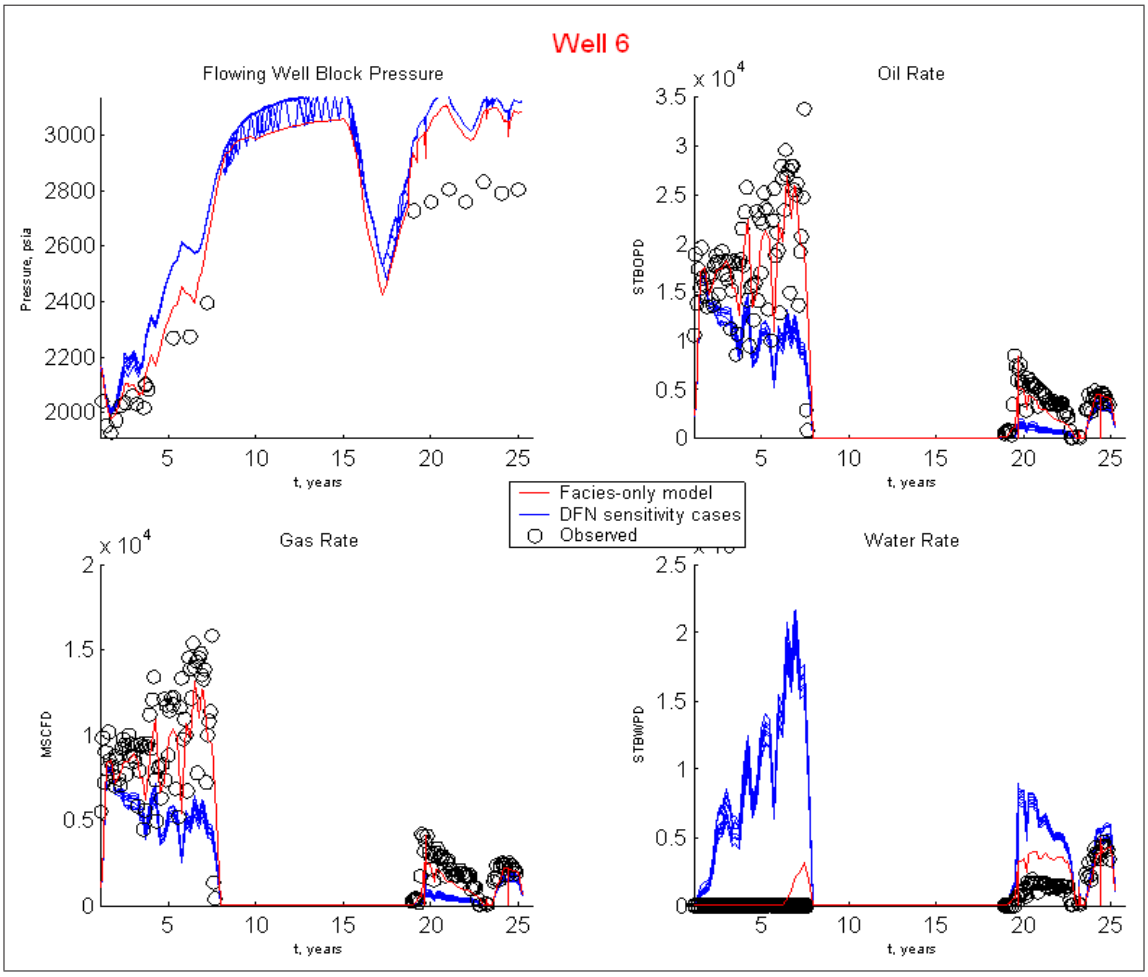

Fig. A.75: Well performance under varying DFN vertical thickness

Appendix B

Source model flow simulation performance

Flow simulations using the source model were made using *ECLIPSE*, on 2-3 GHz, 2GB machines, with the following typical CPU costs:

- 25 year run, no DFNs (facies-only model): ~30 minutes
- 25 year run, 20 DFNs: ~60-120 minutes

The last case is significant in that it may prove to be a benchmark example; given that each DFN describes a flow model possibly composed of a complex fracture network, 20 such networks within the confines of the study area, may prove to be an upper bound. We employ 20 DFNs in our DFN sensitivity study (Chapter 10) The CPU time indicated for this case, one to two hours, is not unreasonable. However, we believe this performance is not optimal, and that it may be improved.

Currently, effort is being directed at further improving the convergence behavior of DFN flow simulations using the source model. This aspect of our research is critical, in that only flow simulations which are reasonably fast may be included in the history matching algorithm, and any plan to extend the method to a larger area requires that the inclusion of DFNs not be overly burdensome to the CPU load.

This appendix summarizes the work done thus far in addressing simulation solution convergence issues.

B.1 Solution instability

Fig. B.1 presents an example of instability which may occur as a result of application of the DFN source model. The well performance of Well 6 is presented. These results are derived from a reservoir model of the study area in which 20 DFNs are incorporated, a few of which intersect various Well 6 blocks. Instability in the pressure solution is demonstrated in the simulated well block pressure, in the upper left plot. Note that the instability occurs only during the shut-in period. Indeed, little to no solution instability occurs outside of the shut-in interval, in all flow simulations performed for this thesis. Furthermore, the character of the instability varies according to DFN length. Fig. B.2 presents the same well performance in the presence of shorter DFNs. Here, 25 realizations are presented. Although the instability persists during the shut-in period in this case, the pressure fluctuation is of a much lower frequency.

The cause of the instability in the pressure solution in Fig. B.1 may be seen in the flow behavior of individual connections in both Well 6 and in a DFN which intersects a series of Well 6 blocks. Fig. B.3 is a plot of liquid flow rate from a Well 6 connection. Note the rate fluctuations during the shut in period, in years 7 to 24, indicating backflow occurring in the well. Although this is not an uncommon occurrence in shut-in wells, due to differential depletion in the layers completed in the well, Fig. B.4 shows that this backflow does not occur when DFNs are not present. Here, the connection rate is plotted for the case in which DFNs are not included in the reservoir model: flow occurs only within reservoir model facies. Note that the connection rate is stable, at zero, during most of the shut-in period, following a monotonic decline immediately after shut-in. Therefore, the instability is due to the presence of DFNs.

The effect of the DFN on pressure and rate instability in Well 6 is derived from instability in simulated connection performance. Fig. B.5 is a plot of rate from a connection in the DFN which intersects the Well 6 block. This connection is located in the same well block that hosts the well connection described in the previous plots. Note that during the shut-in period, this connection demonstrates a general change

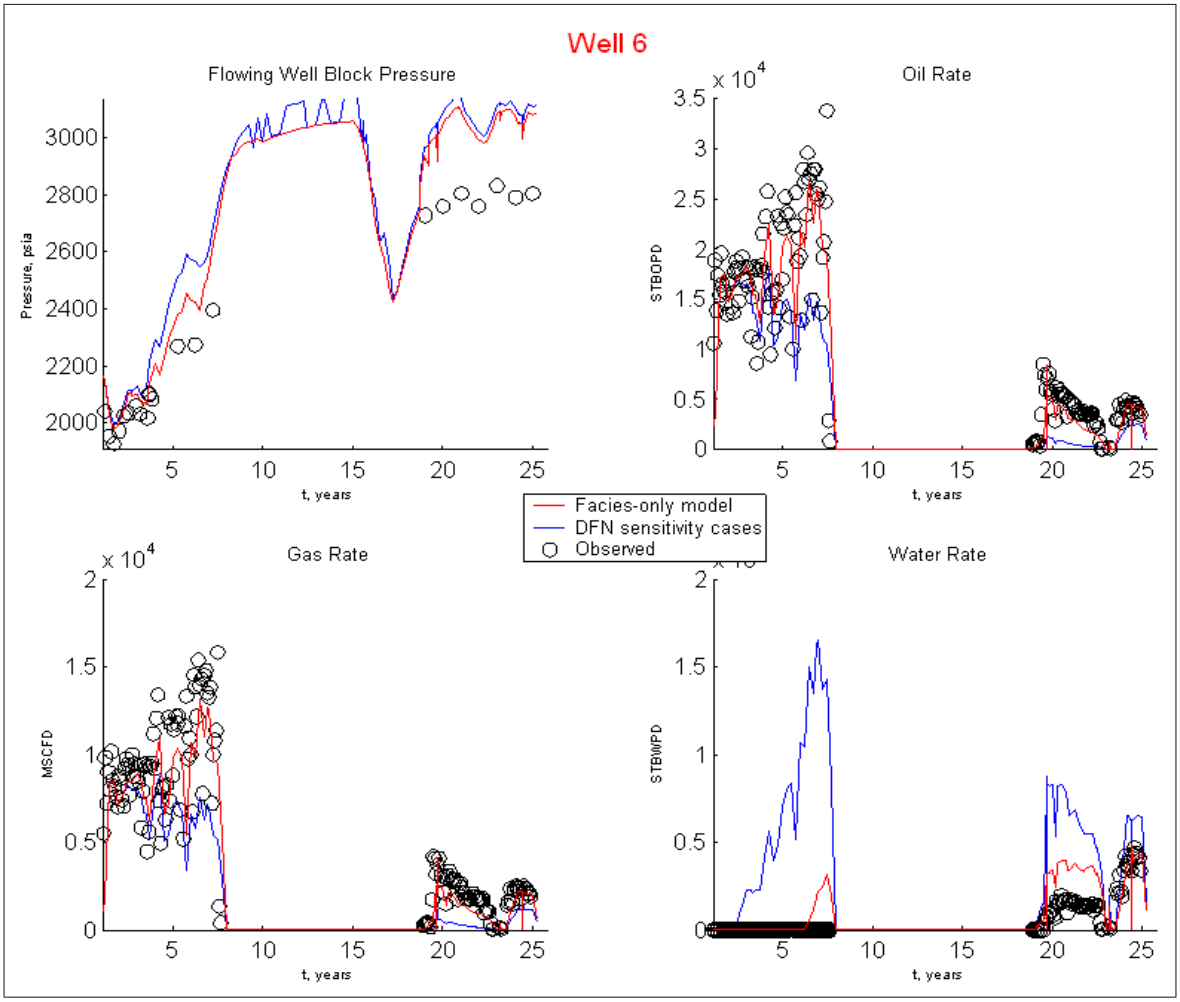

Fig. B.1: Example instability in pressure solution

in flow, from positive (flow into the DFN) to negative (flow from the DFN), reflecting a global difference in reservoir pressure regions intersected by the DFN. However, the rate wildly fluctuates during this general change, as much as 3000 b/d. The block pressure fluctuation associated with this connection rate fluctuation, is seen in the Well 6 plot, Fig. B.1.

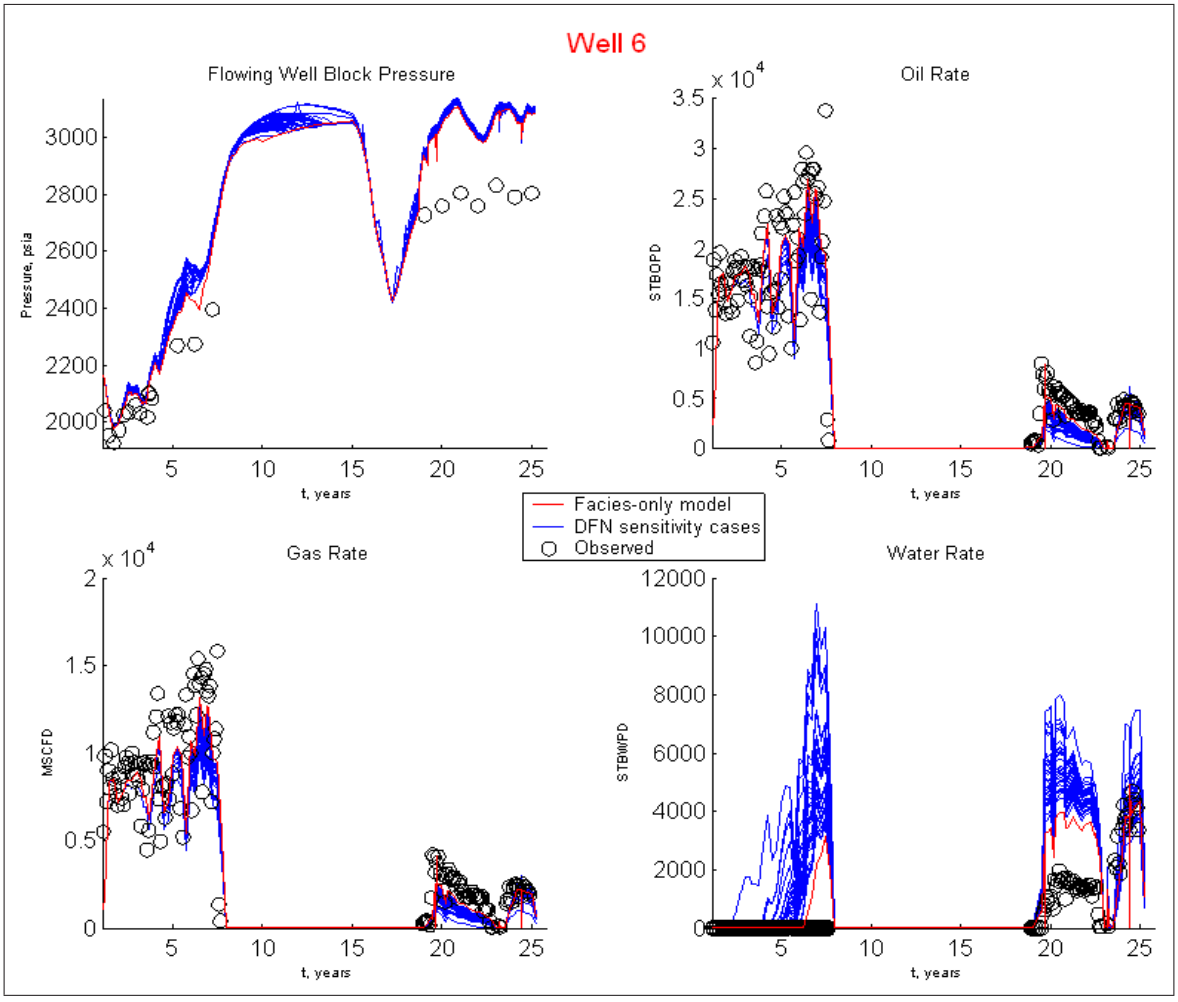

Fig. B.2: Example instability in pressure solution - shorter DFNs

B.2 Convergence improvement

Extensive testing was performed to determine the efficacy of various convergence and timestepping criteria, relative to reduction of CPU cost[1]. A dramatic reduction in CPU time was achieved through careful selection of three performance parameters:

- nonlinear convergence criteria,
- linear convergence error,
- time truncation error.

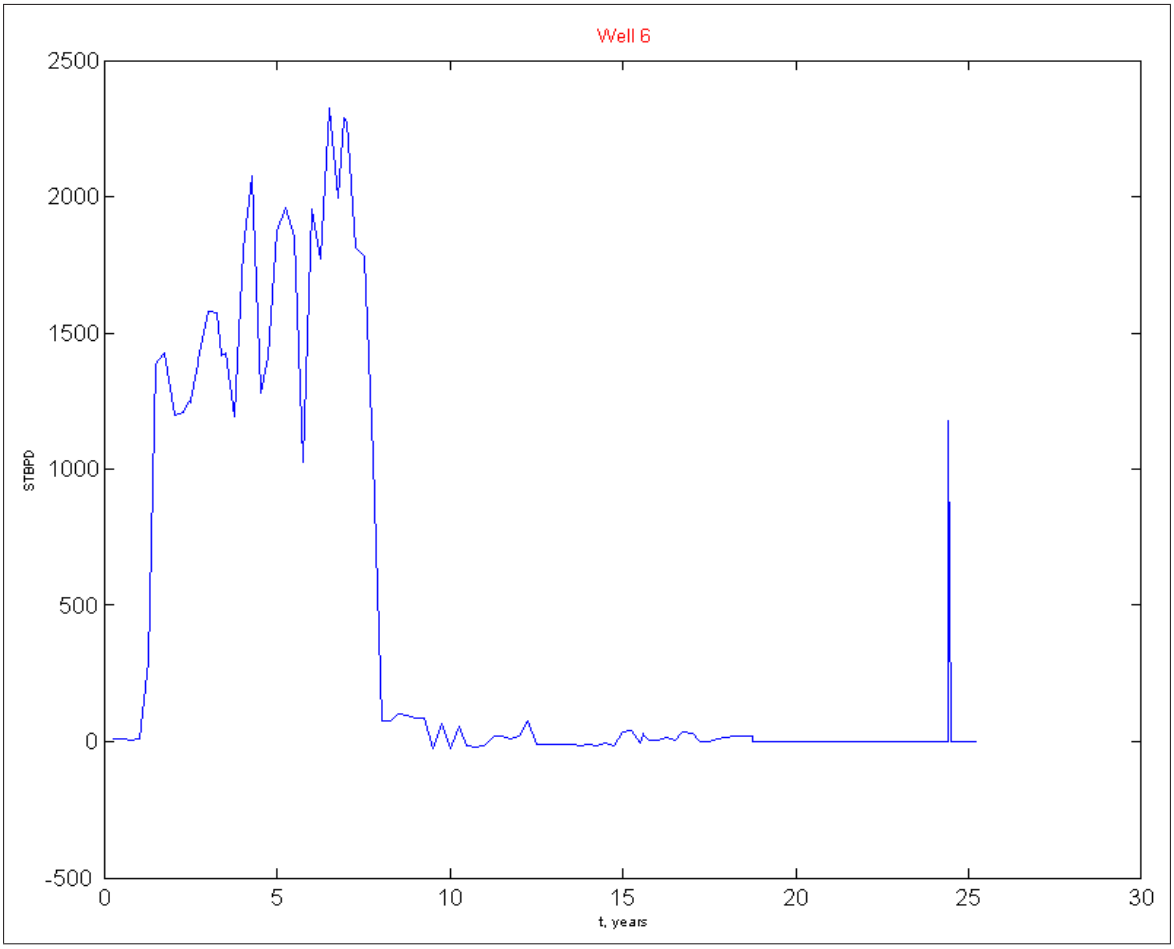

Fig. B.3: Well connection flow profile

The accuracy of the resulting solutions appears to be acceptable, with evaluations currently ongoing. Solution accuracy is addressed in Sec. B.3 and in Appendix C.

B.2.1 Definitions

Solution change criteria are included as nonlinear convergence criteria, in addition to the residual criterion, for determining the solution. A minimum specified change in either pressure solution, or saturation solution, over a nonlinear iteration, will render the system solved, superseding the residual criterion.

Linear convergence error is the criterion for which the iterative solution of the linear system is accepted.

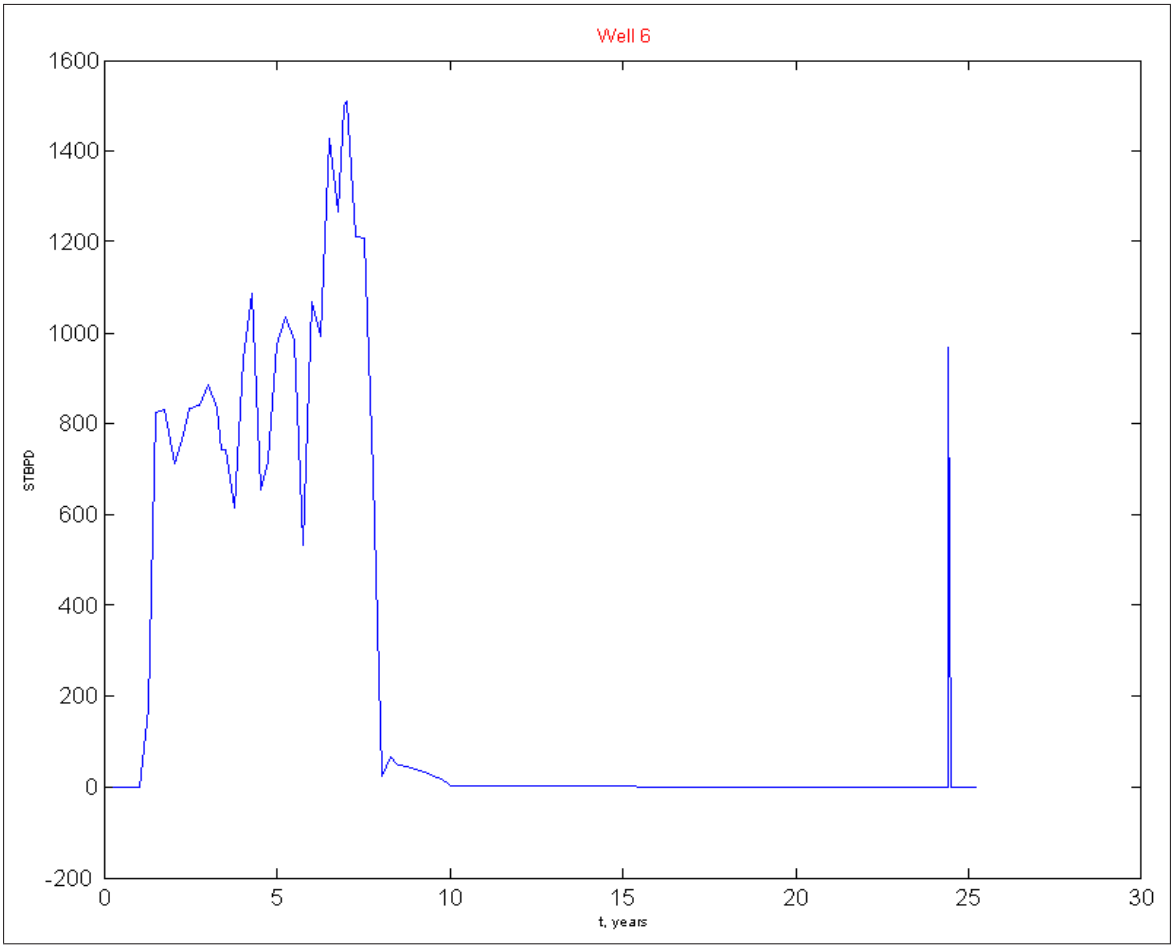

Fig. B.4: Well connection flow profile - no DFN case

Time truncation error, TTE, provides a constraint on timestepping. TTE is defined,

$$TTE = \Delta S - \left(\frac{\Delta S}{\Delta t}\right)_{prev} \Delta t$$

where ΔS is the saturation change over the current time step, Δt is the current time step size, and $(\Delta S/\Delta t)_{prev}$ is the ratio of those quantities from the previous time step. TTE prevents saturation changes, over a time step, from deviating significantly from an established trend. Eclipse sets the maximum allowed TTE to a default value of 0.1. If the computed TTE exceeds the maximum allowed, the time step is reduced and the solution is recalculated.

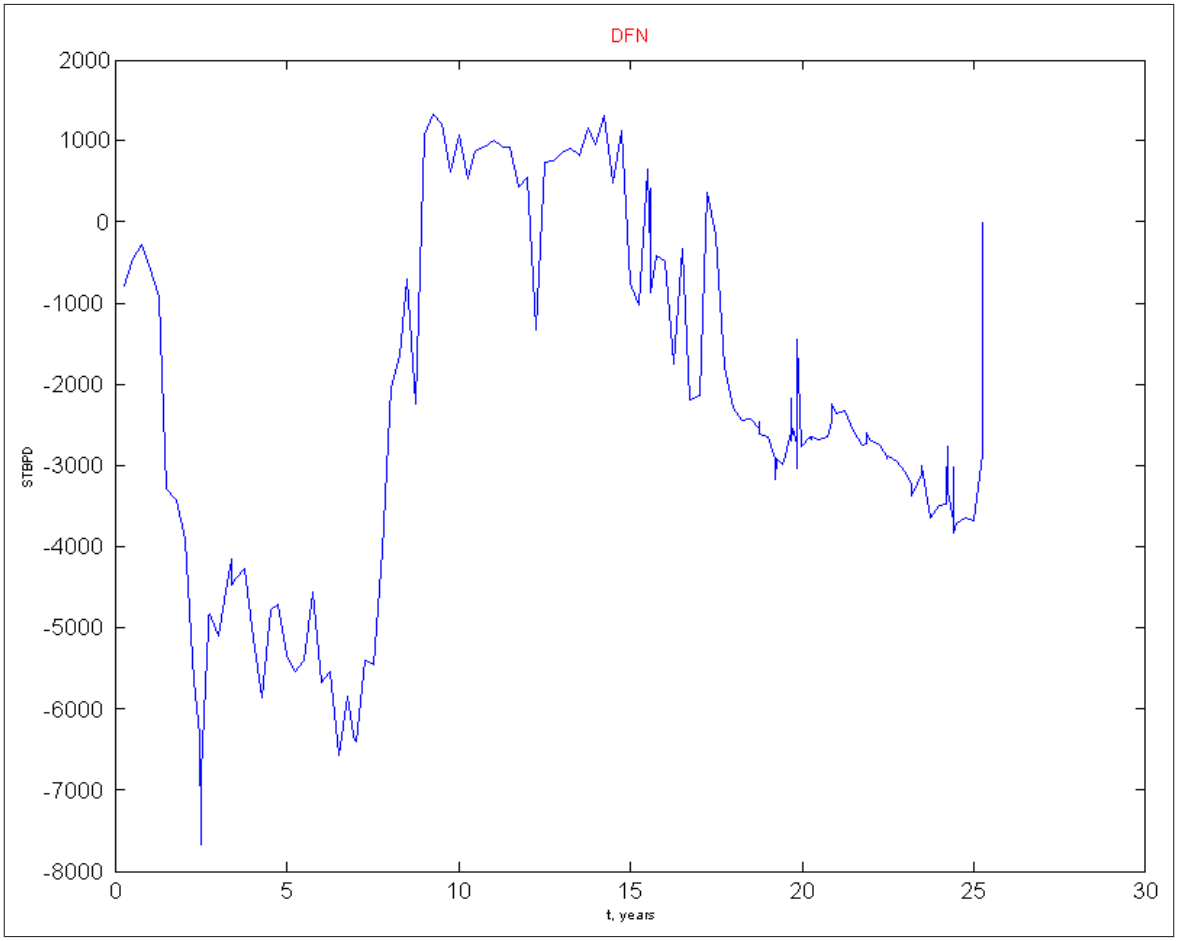

Fig. B.5: Rate instability at a DFN connection

TTE affects DFN problems because fluid fluxes are often large in DFNs, causing large saturation changes in the blocks containing sources. Fluid fluxes increase significantly, relative to conventional fluxes associated with diffusive flow between blocks, if:

- Connection transmissibilities are made large,
- DFN terminal regions are located in significantly different pressure regions of the reservoir.

Table B.1: Source model simulation performance

Case	Lin iter	Non-lin iter	Ratio, lin / non-lin iter	Timesteps	CPU (min)[1]
Base (no DFNs)	7474	2928	2.5	453	25
Default	54475	9923	5.5	2355	119
Modified	31673	3352	9.4	513	49

Table B.2: Individual convergence control components

Case	Lin iter	Non-lin iter	Ratio, lin / non-lin iter	Timesteps	CPU (min)[1]
TTE relaxed	25634	3405	7.5	377	61
LCR	65935	9370	7.0	2277	105
SCC	63072	8172	7.7	2635	101
TTE relaxed + LCR	38871	3956	9.8	443	71
TTE relaxed + SCC	32437	3290	9.9	494	51
LCR + SCC	61387	7876	7.8	2504	95

B.2.2 Results

Table B.1 and Table B.2 summarize the results. The following case definitions apply, with all simulations covering a full, 25 year span, and all simulations, excluding the Base case, having 36 DFNs:

- Base: No DFNs included.
- Default: ECLIPSE default performance criteria used.
- Modified: Solution change criteria (SCC) added to residual convergence criteria, linear convergence criteria restricted (LCR) by factor of 10, and *TTE* relaxed by factor of 10.

The three components comprising the Modified case were analyzed individually and in tandems. Table Table B.2 presents performance results for these cases.

The following findings are distilled from Tables Table B.1 and Table B.2:

- The DFN (Default) case requires 3.4 times more non-linear iterations, and 7.3 times more linear iterations, than the Base case.

- The selected modifications (Modified case) reduce the non-linear iteration ratio relative to the Base case to 1.1. It reduces the linear iteration ratio relative to the Base case to 4.2.
- The increase of the time truncation error, TTE, results in a non-linear iteration ratio of 1.2, and a linear iteration ratio of 3.4, relative to the Base case.
- Introducing pressure and saturation changes as non-linear convergence criteria, results in a non-linear iteration ratio of 2.8, and a linear iteration ratio of 8.4, relative to the Base case.
- Further reduction in simulation time may be obtained with an improvement in linear solution convergence performance. The ratios of linear to non-linear iterations for the DFN cases is significantly higher than that of the Base case. Note also that the ratio is not improved, but indeed worsened, by the modifications.

B.3 The accuracy of the solutions

The accuracy of the solutions derived from the modified performance parameters, is determined by comparing them with the solution obtained from the simulation using the default parameters. The solutions are compared over three types of reservoir performance:

- Well performance solutions, including well block pressure and phase rates
- Flowmeter solutions
- Connection liquid flow rate solutions in the DFNs

Plots of these comparisons, as well as discussion, are presented in Appendix C.

[1] 2 GHz, 2Gb machine

Appendix C

The accuracy of DFN simulation solutions

This appendix presents simulation results for two cases having differing convergence and timestepping criteria. The Default case assumes *Eclipse* criteria considered as default, or applicable for most simulation requirements. The other case employs some modifications to the default criteria, and is designed to decrease simulation time. The cases are discussed in Sec. B.2.

The following sections present simulation results comparisons in an effort to verify that the faster, modified, simulations, yield equivalent solutions to that of the slower, default case.

C.1 Comparisons of well performance data

The following plots show well performance comparisons between the two simulation cases. The simulation results are well block pressures and phase rates. The plots present results for eight wells in which production history is extensive. The remaining three wells in the study area have little or no production history. Also shown are the actual measured data, in circles. However, for purposes of comparing simulation results, these data are irrelevant. That is, this is not a demonstration of a history match, but instead a comparison between two simulations.

Note that the simulation results are nearly identical for most of the well histories. This is a desired result since well performance data are one of two principle history matched data in the algorithm.

Discrepancies between the two simulations are most evident during an extended period of shut-in, from years 8 to 14. During this period, all wells in the study area, as well as surrounding wells, were shut in. These discrepancies can be seen in the plots for wells 1, 2, 6, and 8. Characteristic of the simulated shut-in results for these wells is oscillatory pressures in the Default case, and smoothed results for the Modified case. This lends credence to the contention that the modified simulation results more reasonably model well performance, as during this interval of shut-in, only monotonic pressure behavior would be expected.

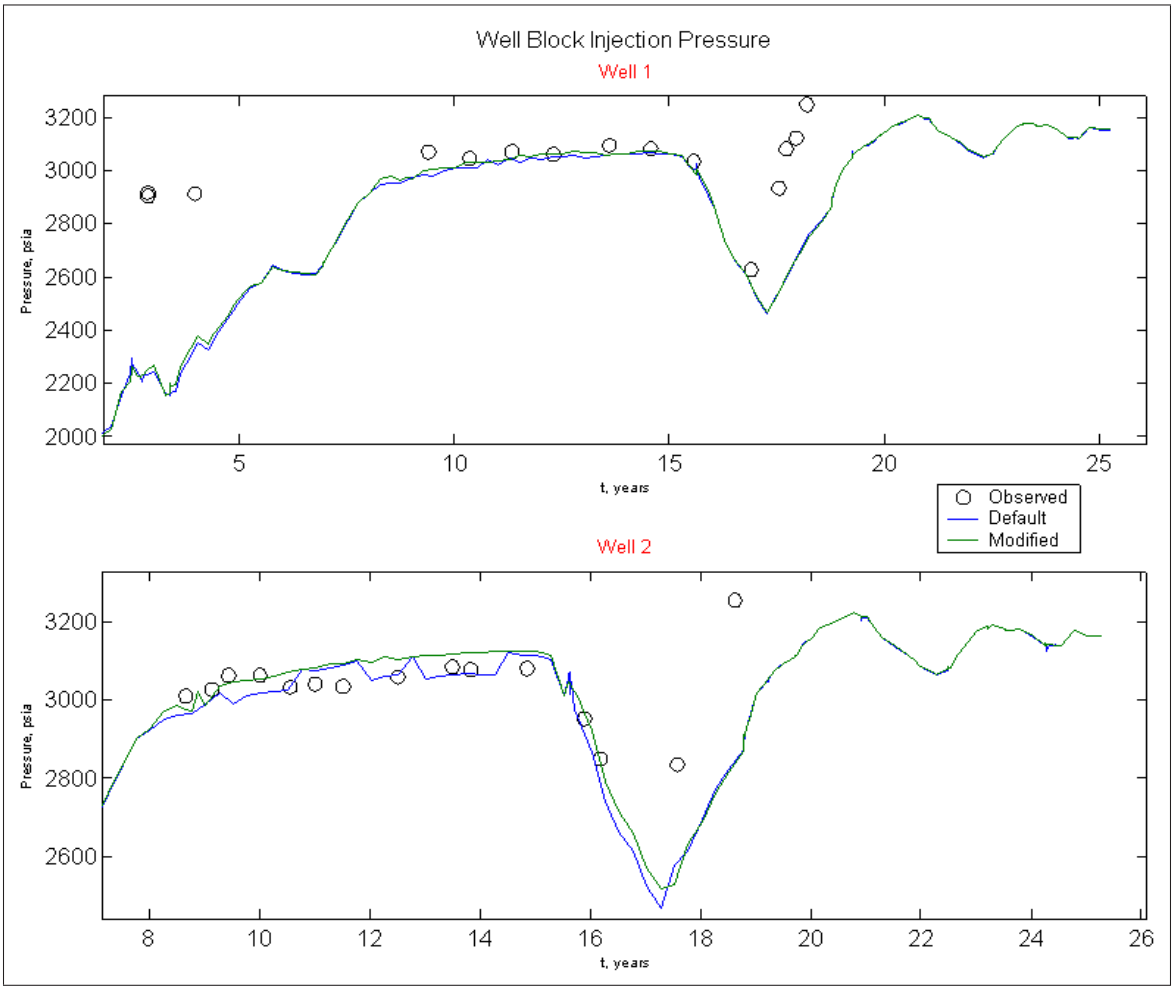

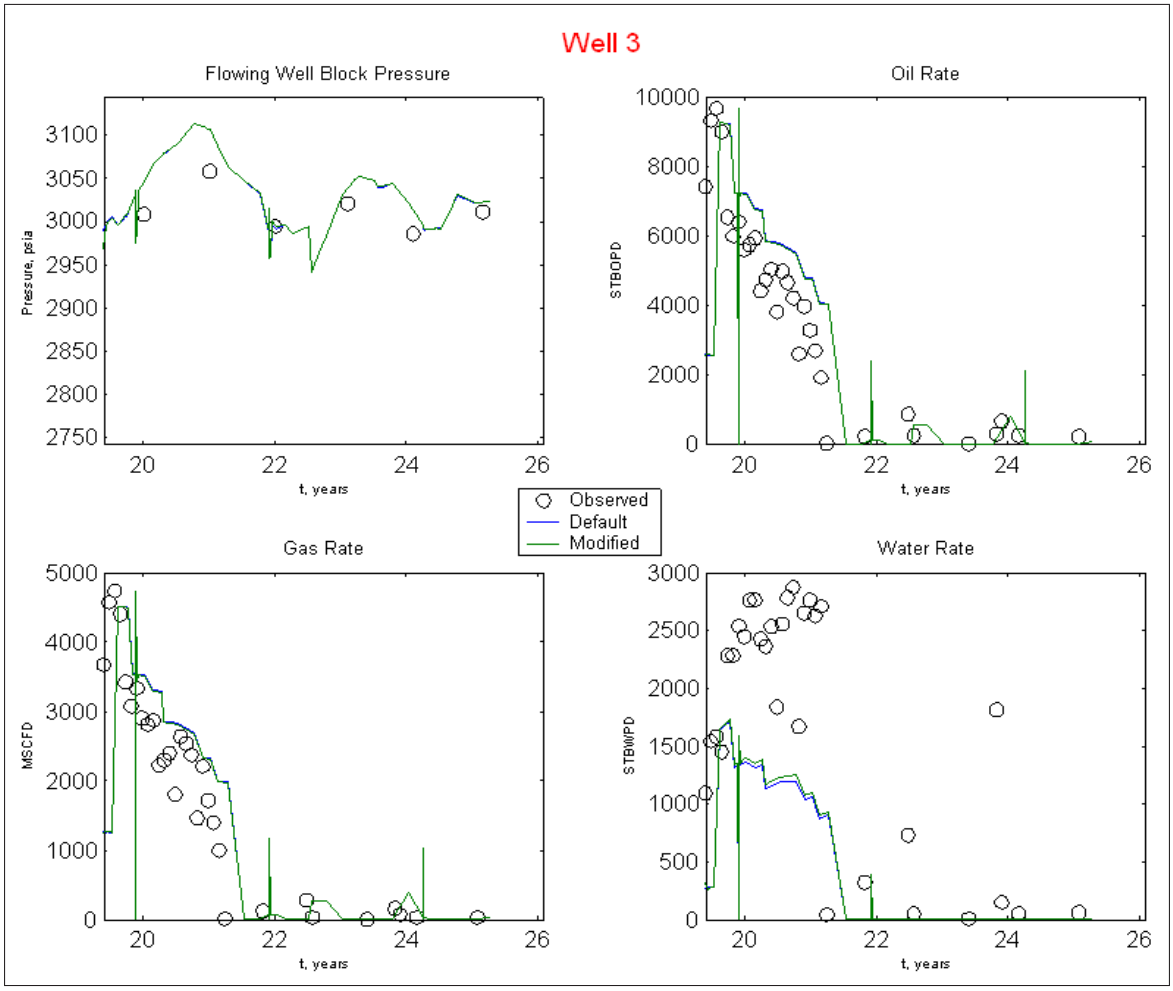
Well 3
Flowing Well Block Pressure
Pressure, psia
t, years
Oil Rate
STBOPD
t, years
Observed
Default
Modified
Gas Rate
MSCFD
t, years
Water Rate
STBW/PD
t, years

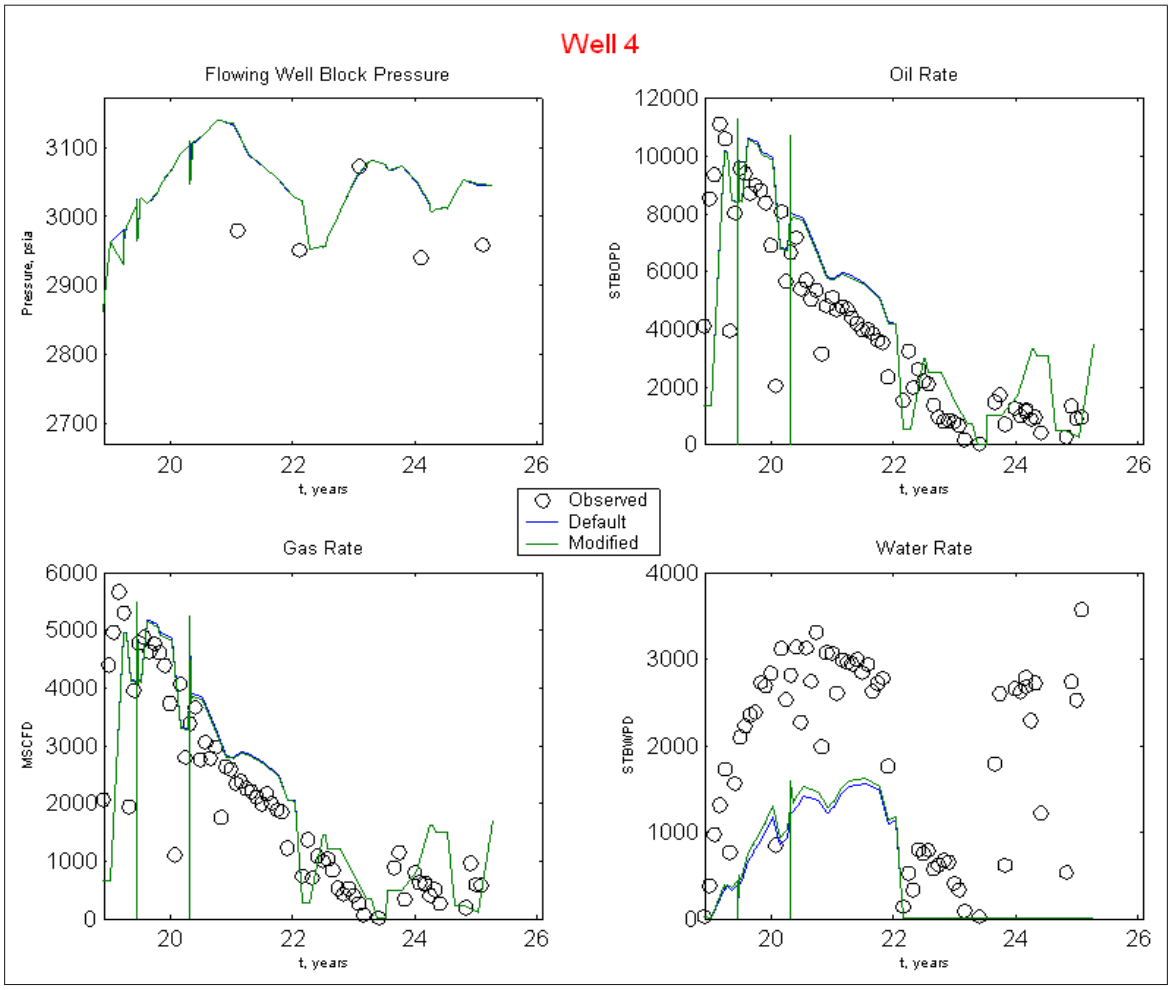
Well 4
Flowing Well Block Pressure
Pressure, psia
3100
3000
2900
2800
2700
20
22
24
26
t, years
Oil Rate
STBOPD
12000
10000
8000
6000
4000
2000
0
Observed
Default
Modified
Gas Rate
MSCFD
6000
5000
4000
3000
2000
1000
0
Water Rate
STBWPD
4000
3000
2000
1000
0

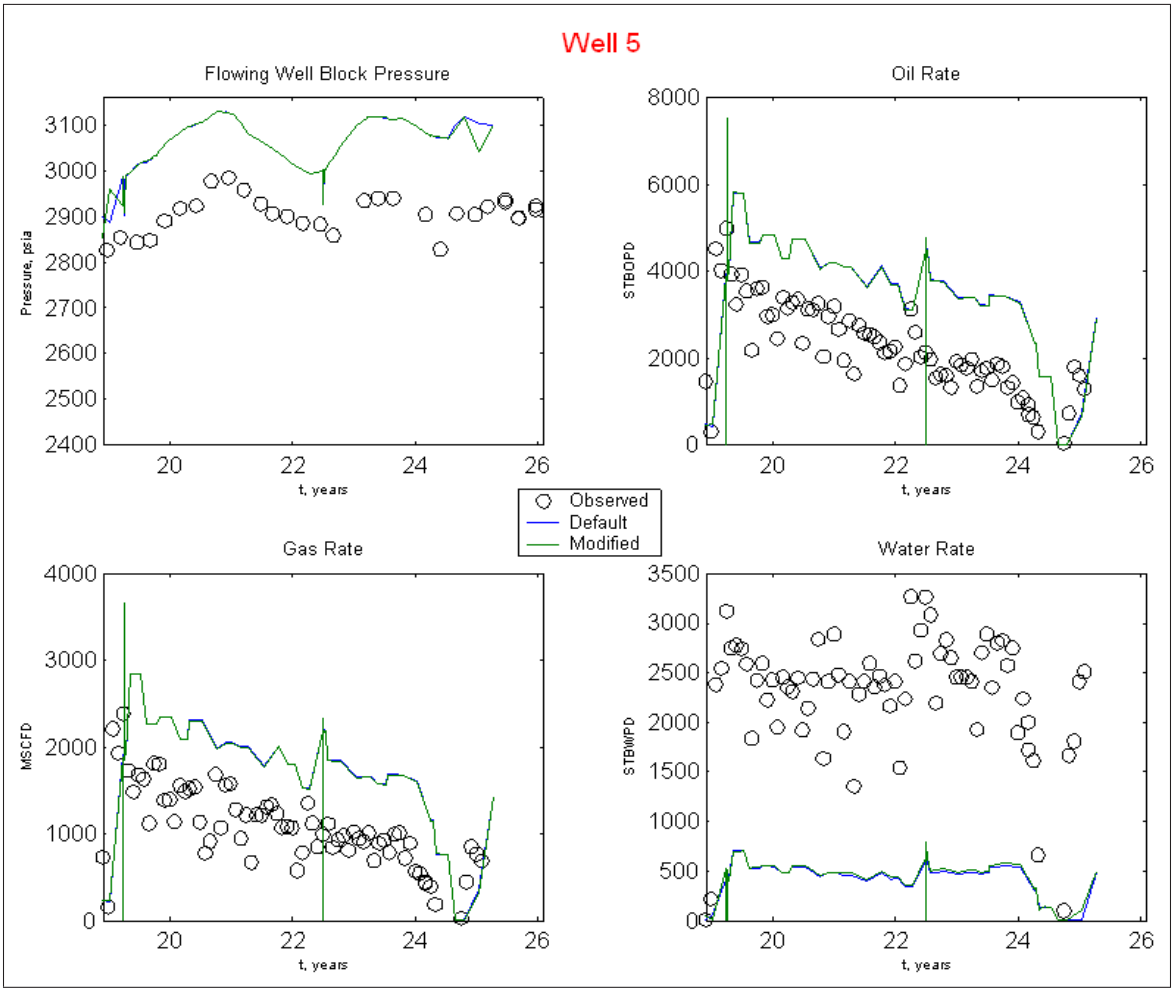
Well 5
Flowing Well Block Pressure
Pressure, psia
t, years
Oil Rate
STBOPD
t, years
Observed
Default
Modified
Gas Rate
MSCFD
t, years
Water Rate
STBWPD
t, years

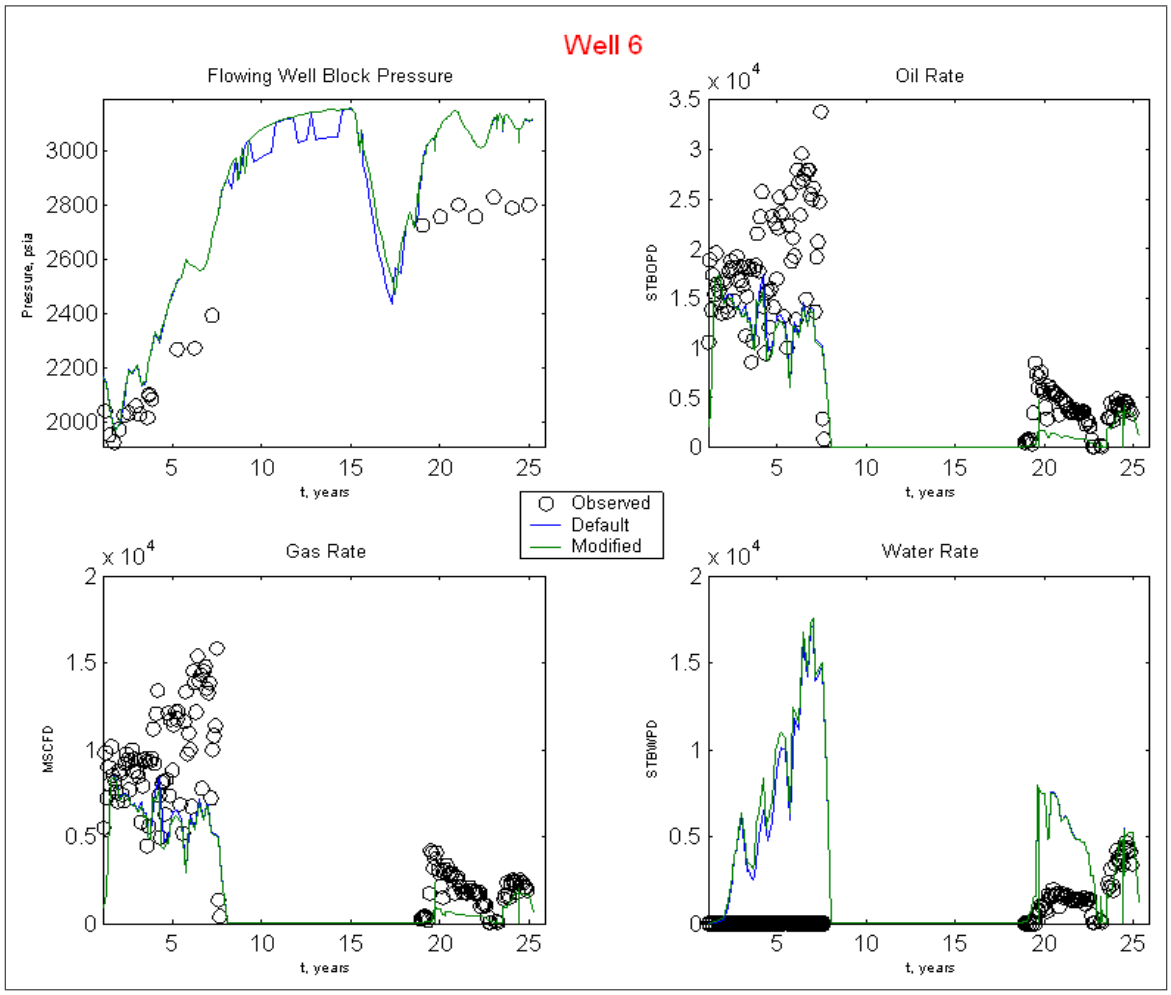
Well 6
Flowing Well Block Pressure
Pressure, psia
t, years
Oil Rate
x 10^4
STBOPD
t, years
Observed
Default
Modified
Gas Rate
x 10^4
MSCFD
t, years
Water Rate
x 10^4
STBWPD
t, years

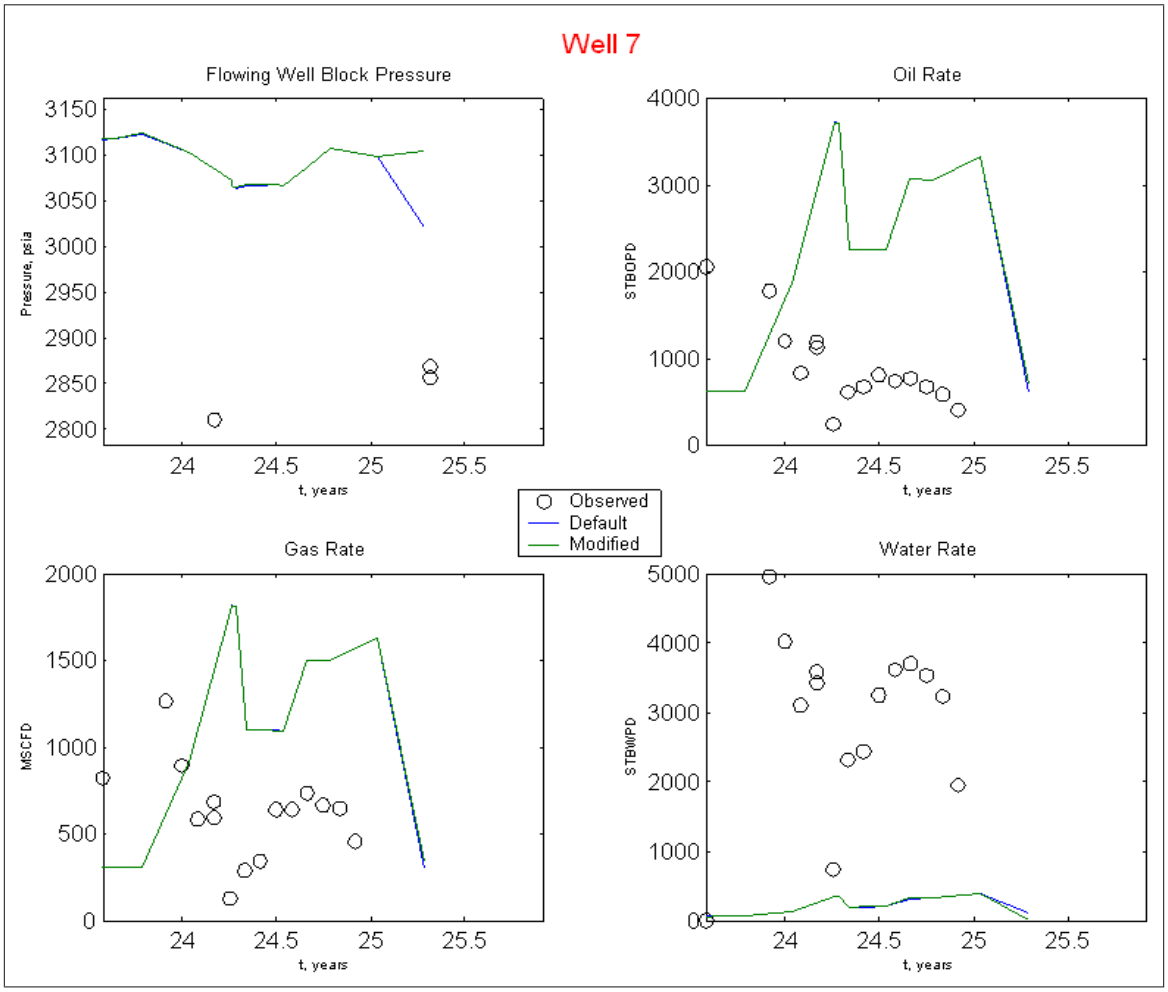
Well 7
Flowing Well Block Pressure
Pressure, psia
t, years
Oil Rate
STBOPD
t, years
Observed
Default
Modified
Gas Rate
MSCFD
t, years
Water Rate
STBWPD
t, years

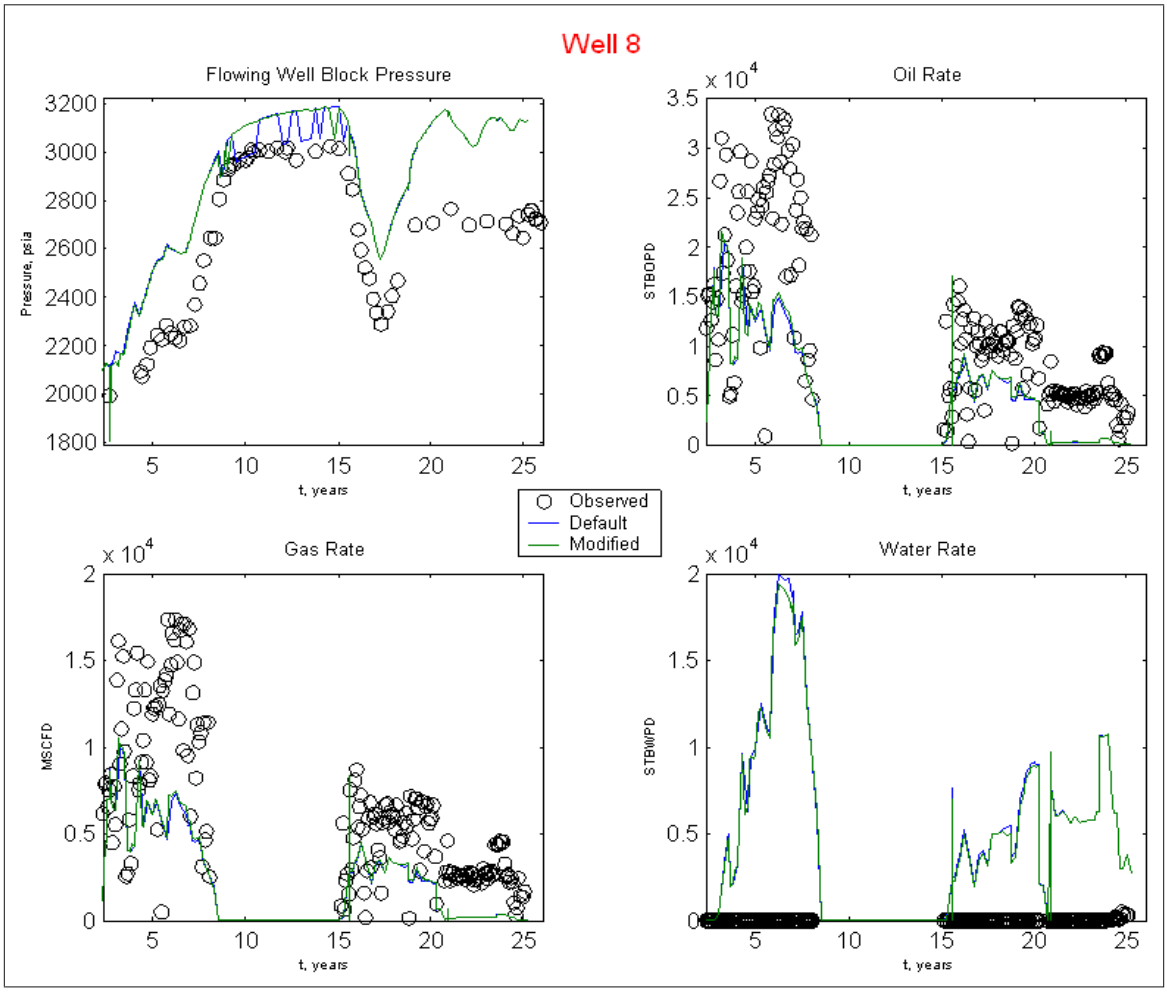
Well 8
Flowing Well Block Pressure
Pressure, psia
t, years
Oil Rate
x 10^4
STBOPD
t, years
Observed
Default
Modified
Gas Rate
x 10^4
MSCFD
t, years
Water Rate
x 10^4
STBWPD
t, years

C.2 Comparisons with flowmeter data

The following plots are flowmeter profiles, taken from all 19 flowmeter surveys conducted in study area wells from 1977 to 1999, comparing the same two simulations as in Sec. C.1, that is, the simulation having default convergence performance parameters, and that having modified parameters.

The simulations compare very favorably in these plots, and in fact, cannot be distinguished in most of the plots.

Here the actual, measured data is in red, and as with the previous plots, is not pertinent here. The comparison between the two simulations, in blue, shows the modified settings case is equivalent to the default settings case. This verification is significant, since flowmeter history is one of the two principle production data that is history matched by the algorithm.

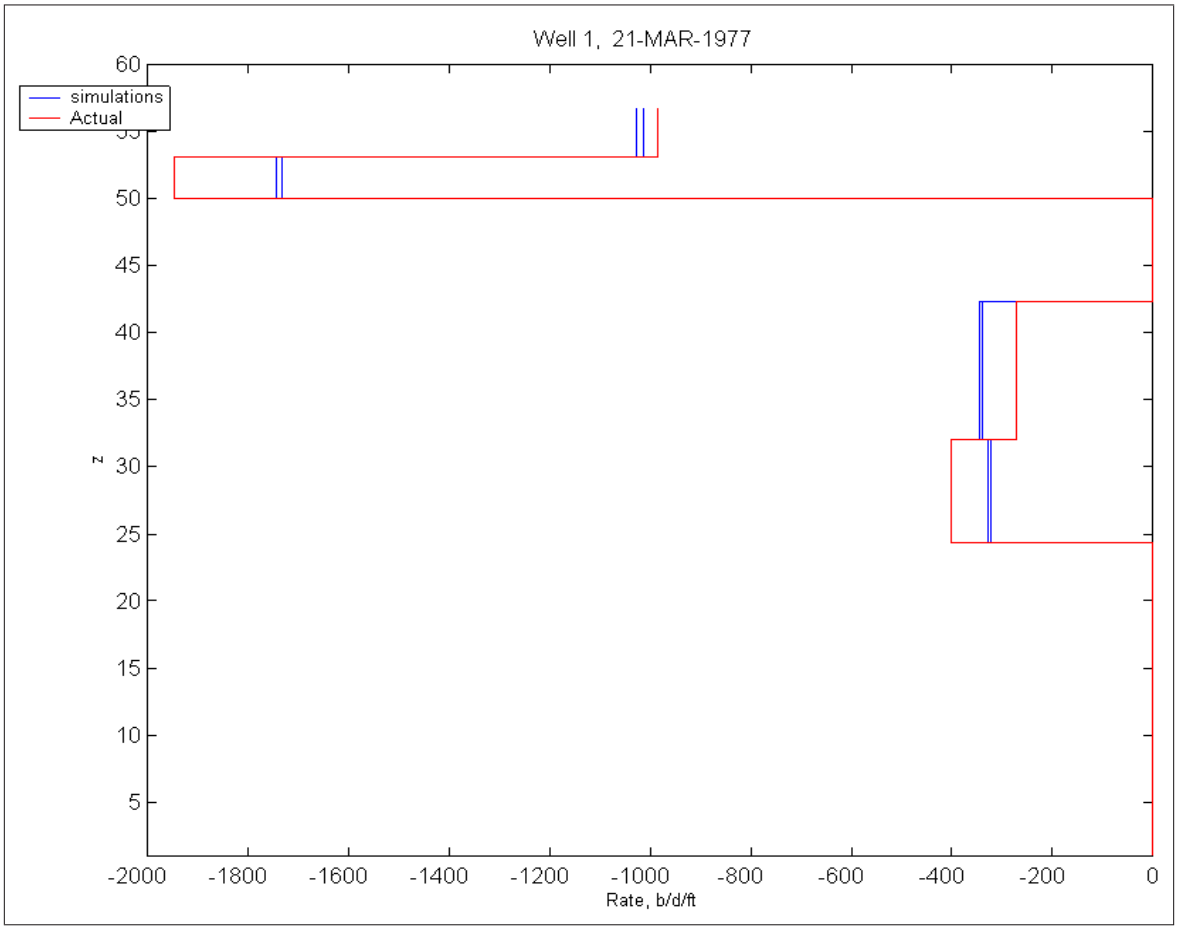
Well 1, 21-MAR-1977
simulations
Actual
60
50
45
40
35
30
25
20
15
10
5
z
-2000
-1800
-1600
-1400
-1200
-1000
-800
-600
-400
-200
0
Rate, b/d/ft

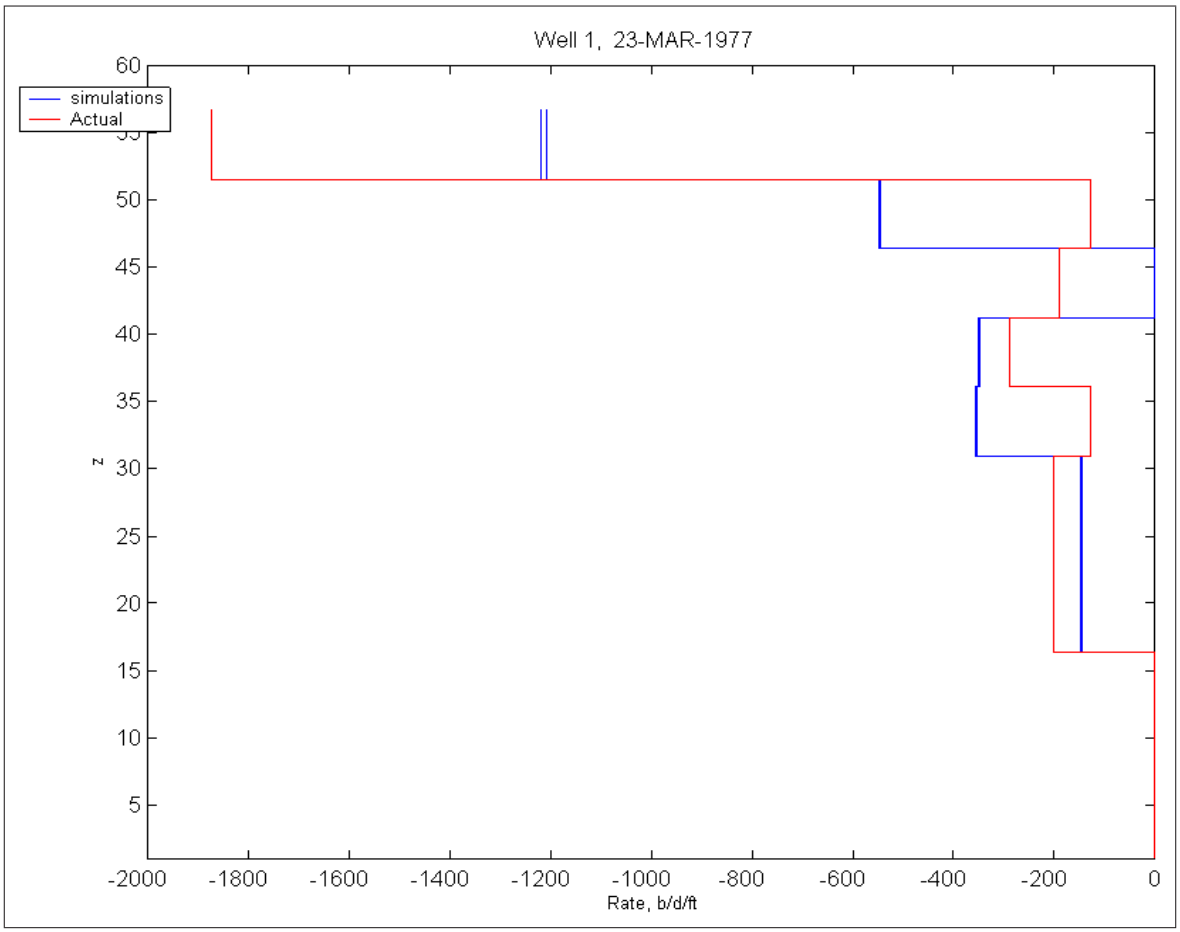
Well 1, 23-MAR-1977
simulations
Actual
60
50
45
40
35
30
25
20
15
10
5
z
-2000
-1800
-1600
-1400
-1200
-1000
-800
-600
-400
-200
0
Rate, b/d/ft

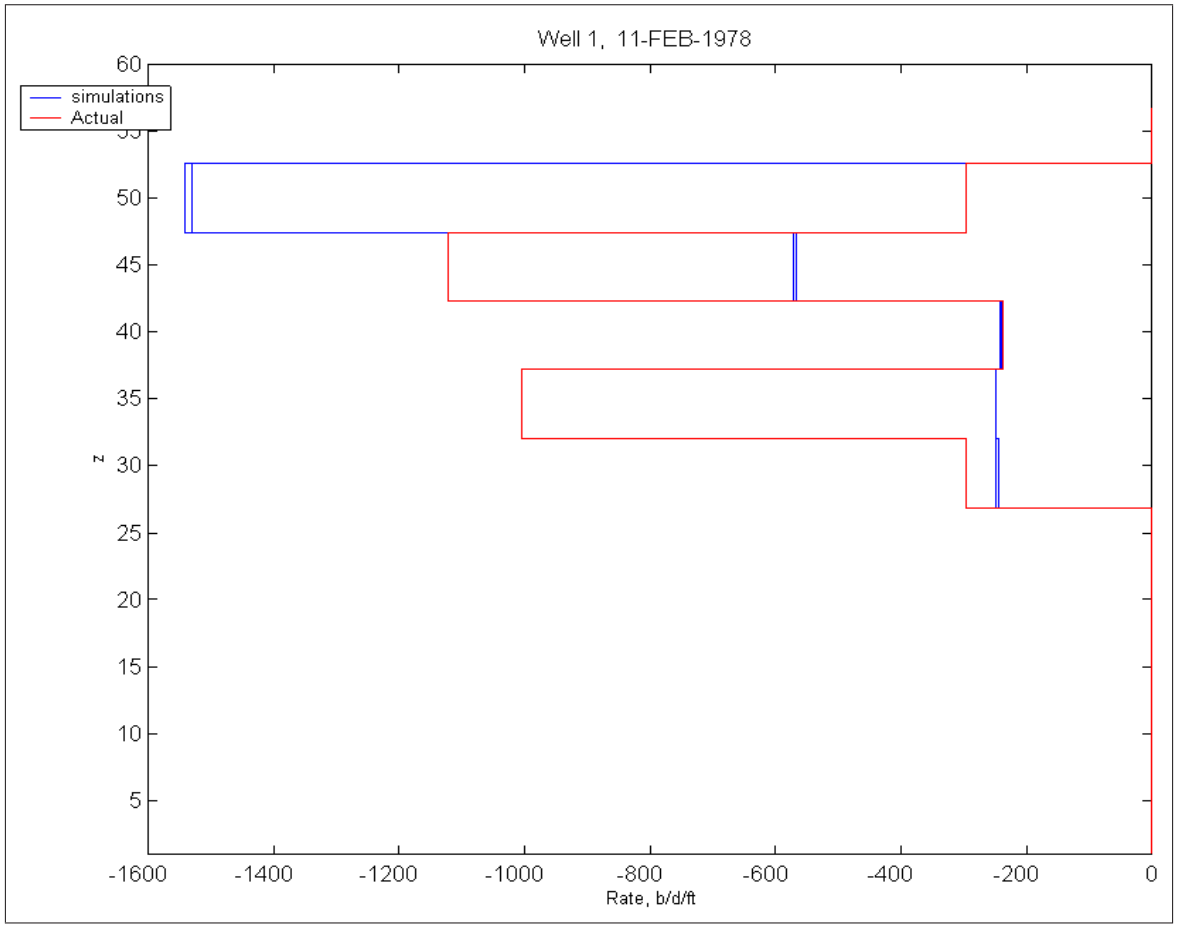
Well 1, 11-FEB-1978
simulations
Actual
60
50
45
40
35
30
25
20
15
10
5
z
-1600
-1400
-1200
-1000
-800
-600
-400
-200
0
Rate, b/d/ft

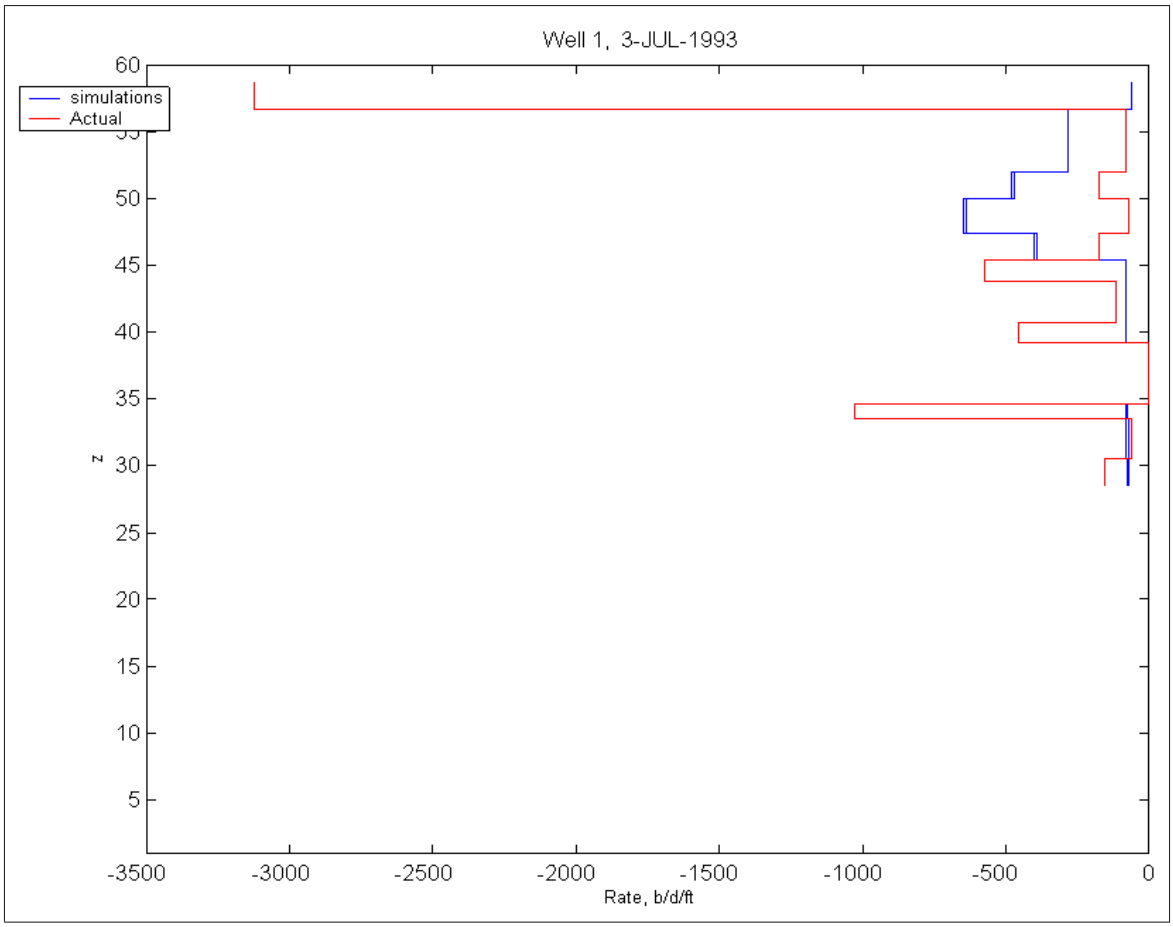
Well 1, 3-JUL-1993
simulations
Actual
60
50
45
40
35
30
25
20
15
10
5
z
-3500
-3000
-2500
-2000
-1500
-1000
-500
0
Rate, b/d/ft

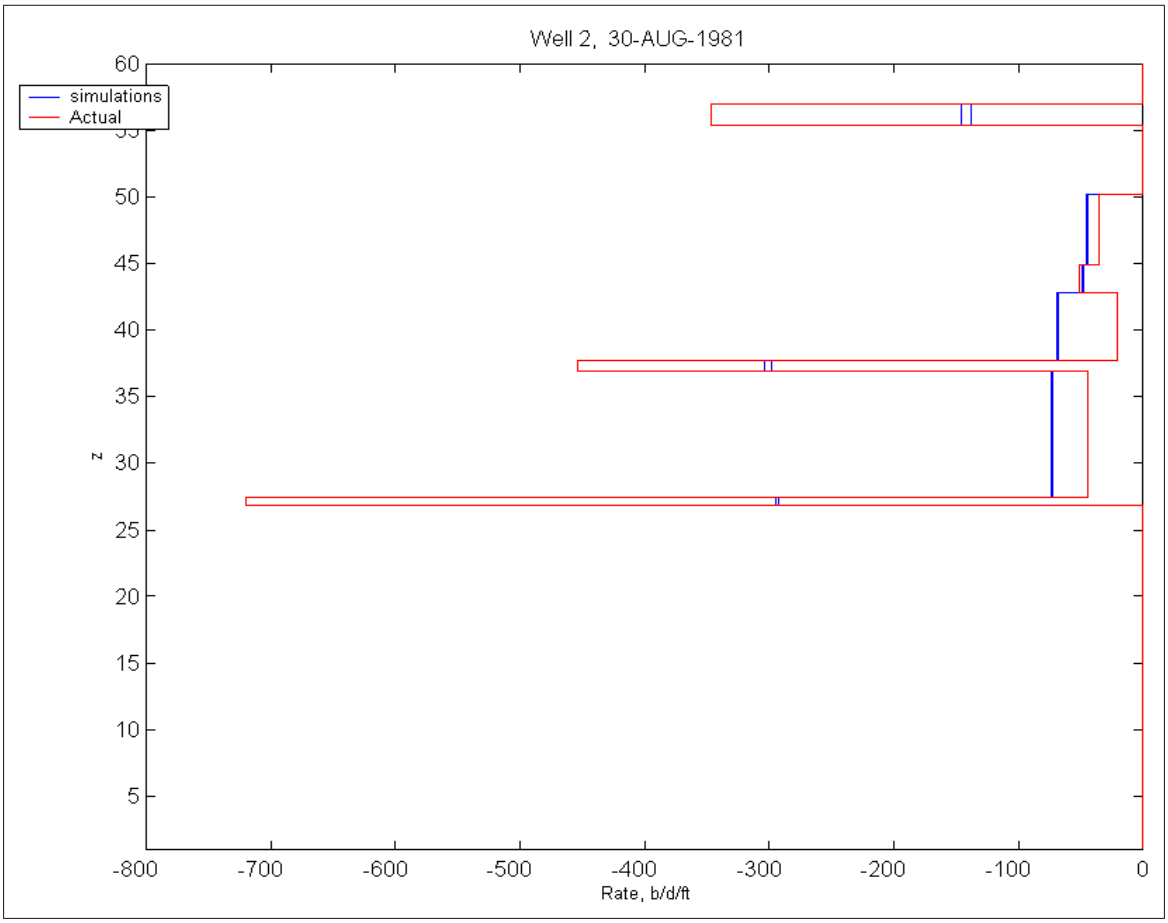
Well 2, 30-AUG-1981
simulations
Actual
60
50
45
40
35
30
25
20
15
10
5
z
-800
-700
-600
-500
-400
-300
-200
-100
0
Rate, b/d/ft

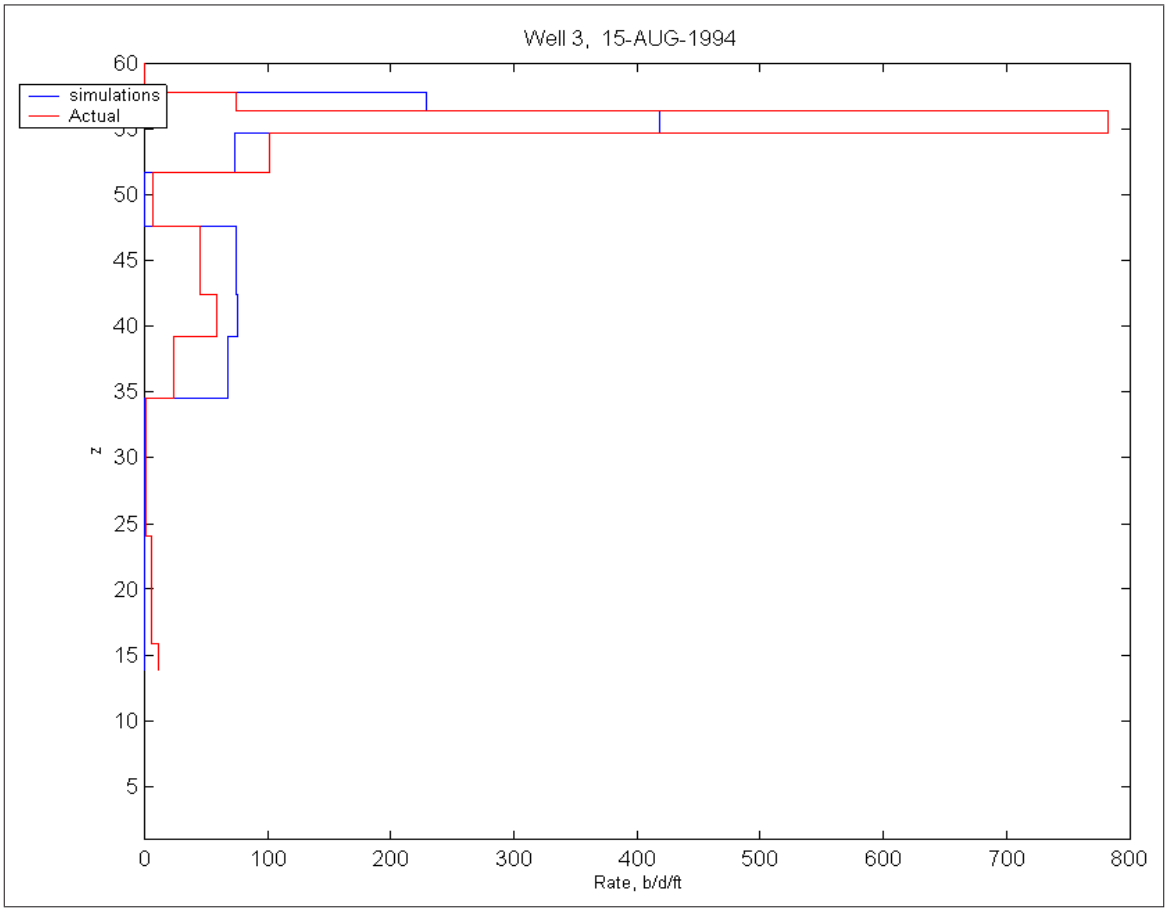
Well 3, 15-AUG-1994
simulations
Actual
z
Rate, b/d/ft
60
50
45
40
35
30
25
20
15
10
5
0
100
200
300
400
500
600
700
800

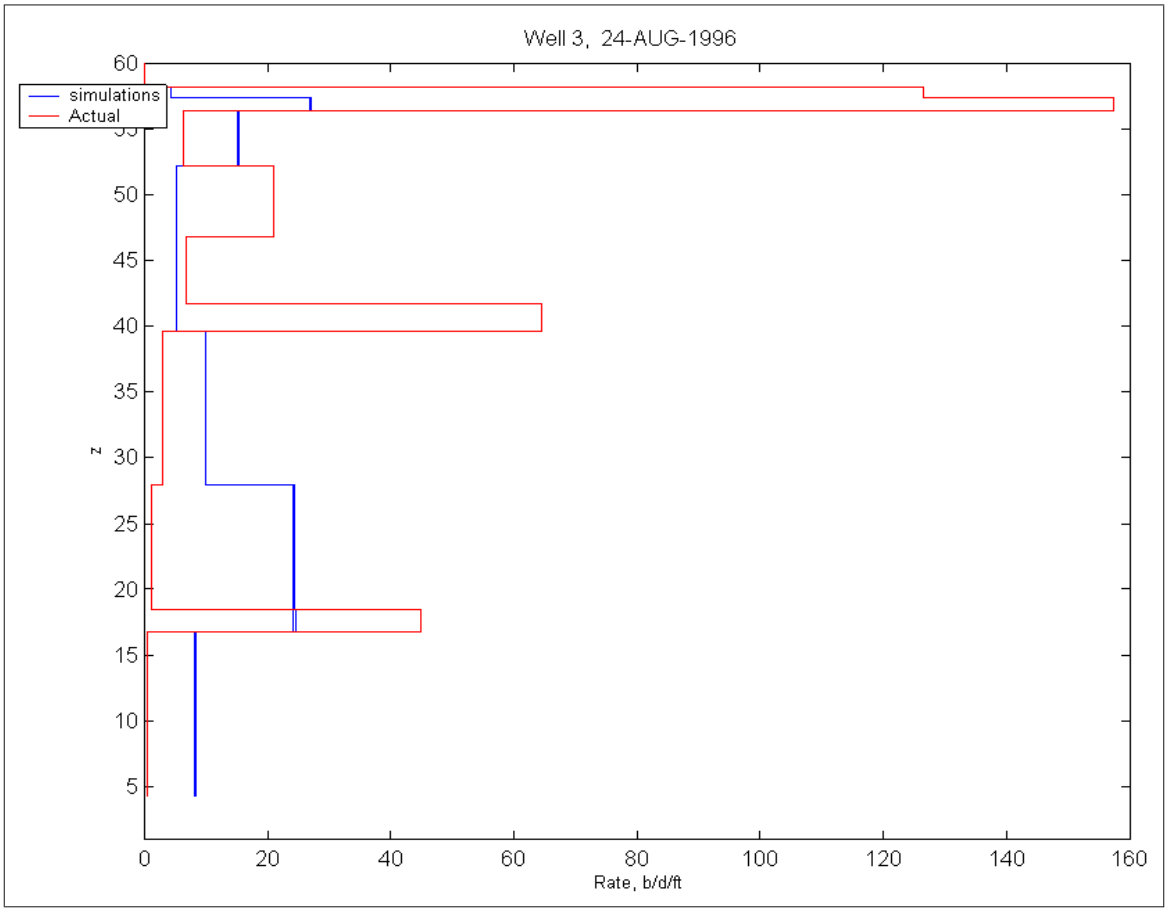
Well 3, 24-AUG-1996
simulations
Actual
z
60
50
45
40
35
30
25
20
15
10
5
0
20
40
60
80
100
120
140
160
Rate, b/d/ft

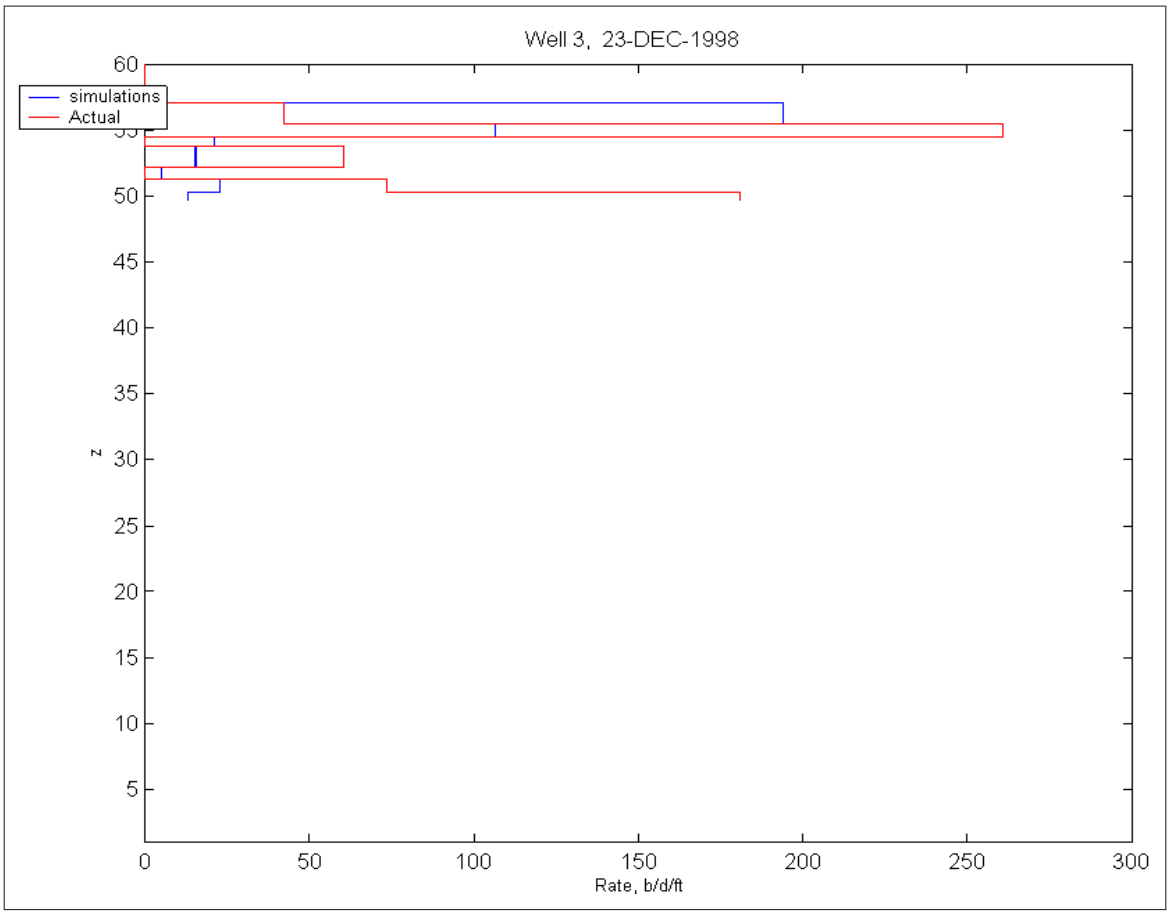
Well 3, 23-DEC-1998
simulations
Actual
z
60
50
45
40
35
30
25
20
15
10
5
0
50
100
150
200
250
300
Rate, b/d/ft

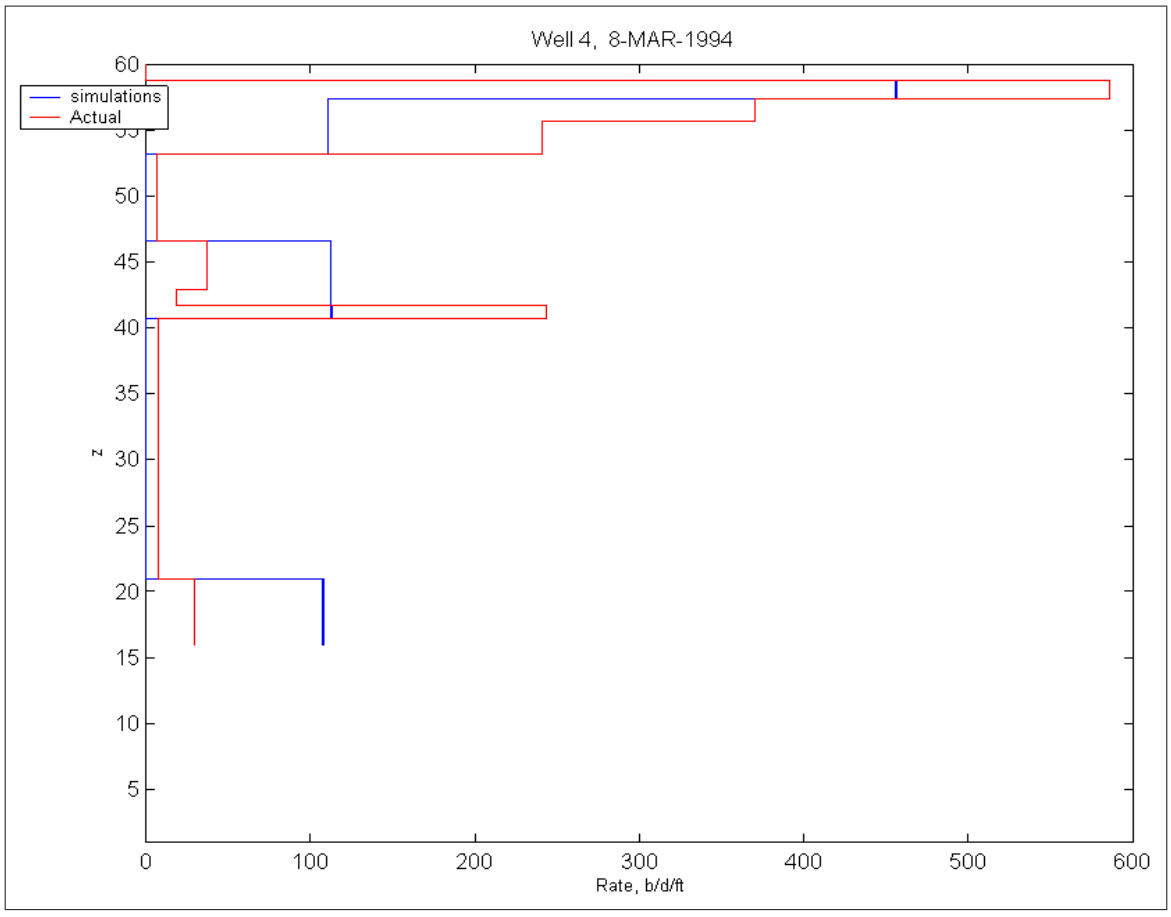
Well 4, 8-MAR-1994
simulations
Actual
z
60
50
45
40
35
30
25
20
15
10
5
0
100
200
300
400
500
600
Rate, b/d/ft

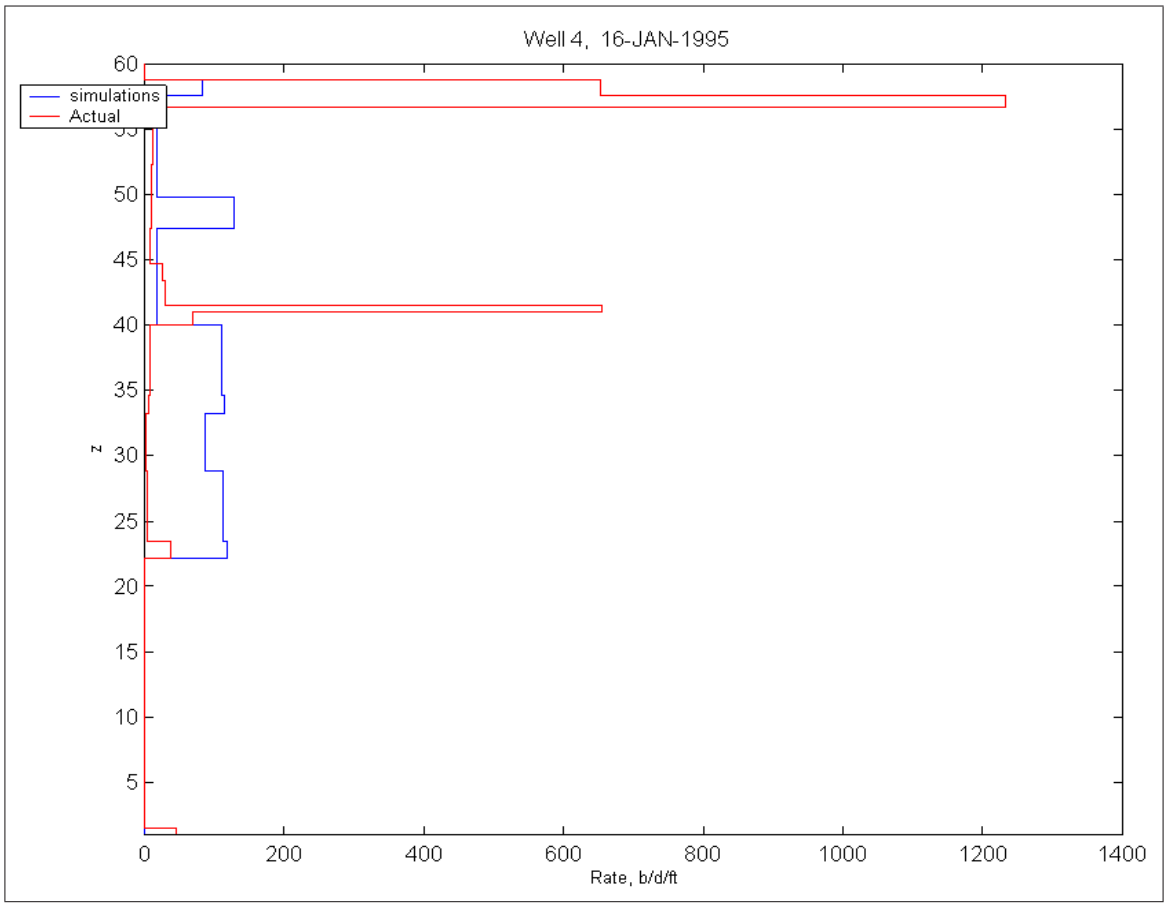
Well 4, 16-JAN-1995
simulations
Actual
z
60
50
45
40
35
30
25
20
15
10
5
0
200
400
600
800
1000
1200
1400
Rate, b/d/ft

C.3 Comparisons of liquid rates in DFN connections

The final comparisons presented here are more interesting than in the previous appendices, in that the accuracy question is more in doubt. These five plots show simulated liquid flow rates vs. time at five connections, among the many connections that comprise the 36 DFNs, through the full history of the study area production. These five examples were chosen as representative of the typical behavior of these comparisons. The two simulations being compared are the same as those compared in the previous two appendices, the simulation having default convergence performance parameters, and that having modified parameters.

Two prevailing characteristics emerge from these plots:

- Although both cases exhibit unrealistic oscillatory behavior, the oscillations in the Modified case are generally attenuated relative to the Default case,
- A low frequency oscillation occurs in both cases, during the period of regional shut-in during years 8 through 14.

Given that study area wells, as well as surrounding wells were shut in during years 8-14, the oscillations, both high frequency and low frequency, are unrealistic. During this period, monotonic flow rates should prevail in the simulations.

This oscillatory simulation behavior gives rise to considerations which may improve the solutions at DFNs, including both linear convergence performance and nonlinear solution improvement.

The attenuated oscillatory behavior of the Modified simulation apparently represents a more realistic performance, and therefore, along with its lower CPU demand, makes it a more desirable DFN model.

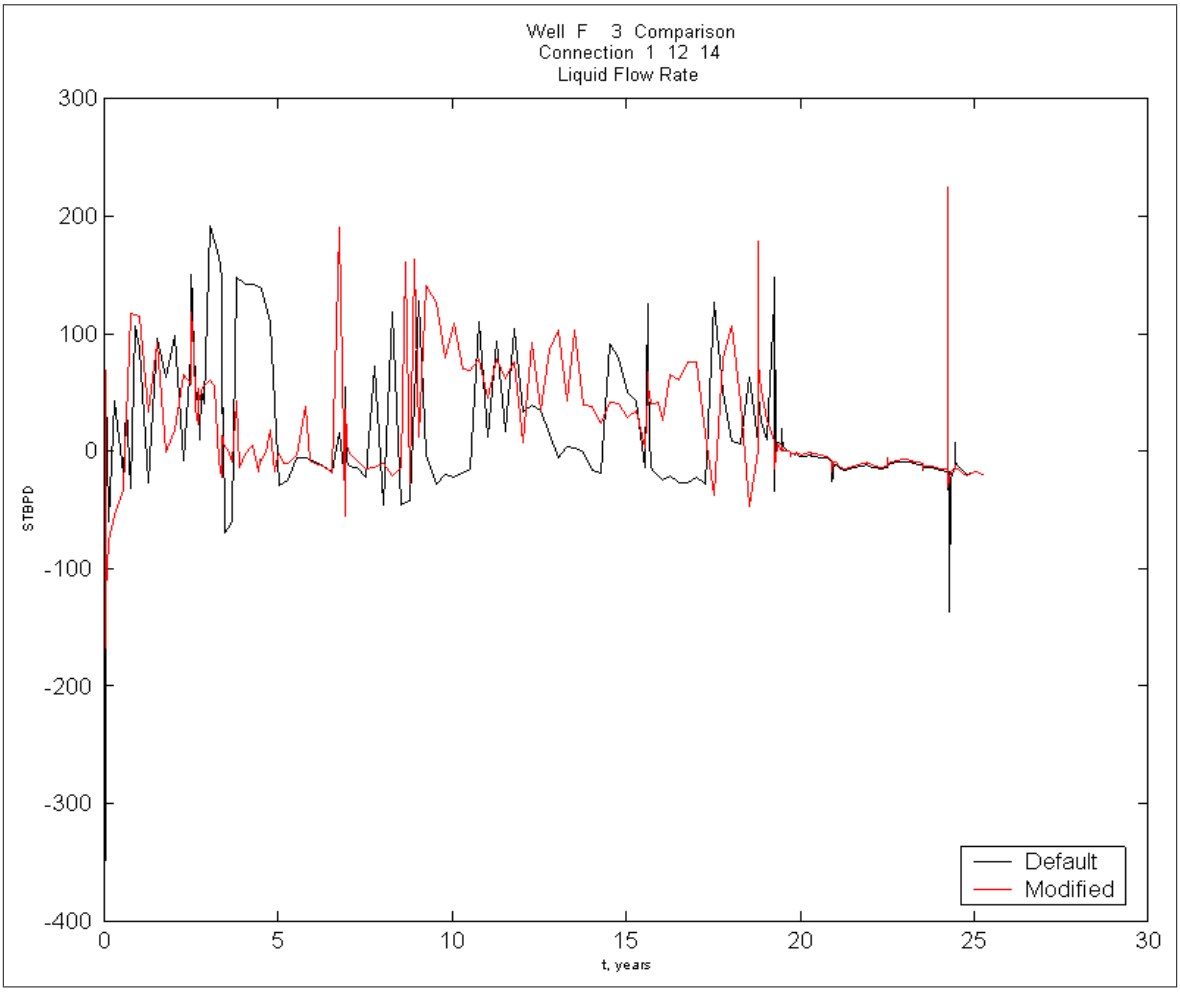
Well F 3 Comparison
Connection 1 12 14
Liquid Flow Rate
300
200
100
0
-100
-200
-300
-400
STBPD
0
5
10
15
20
25
30
t, years
Default
Modified

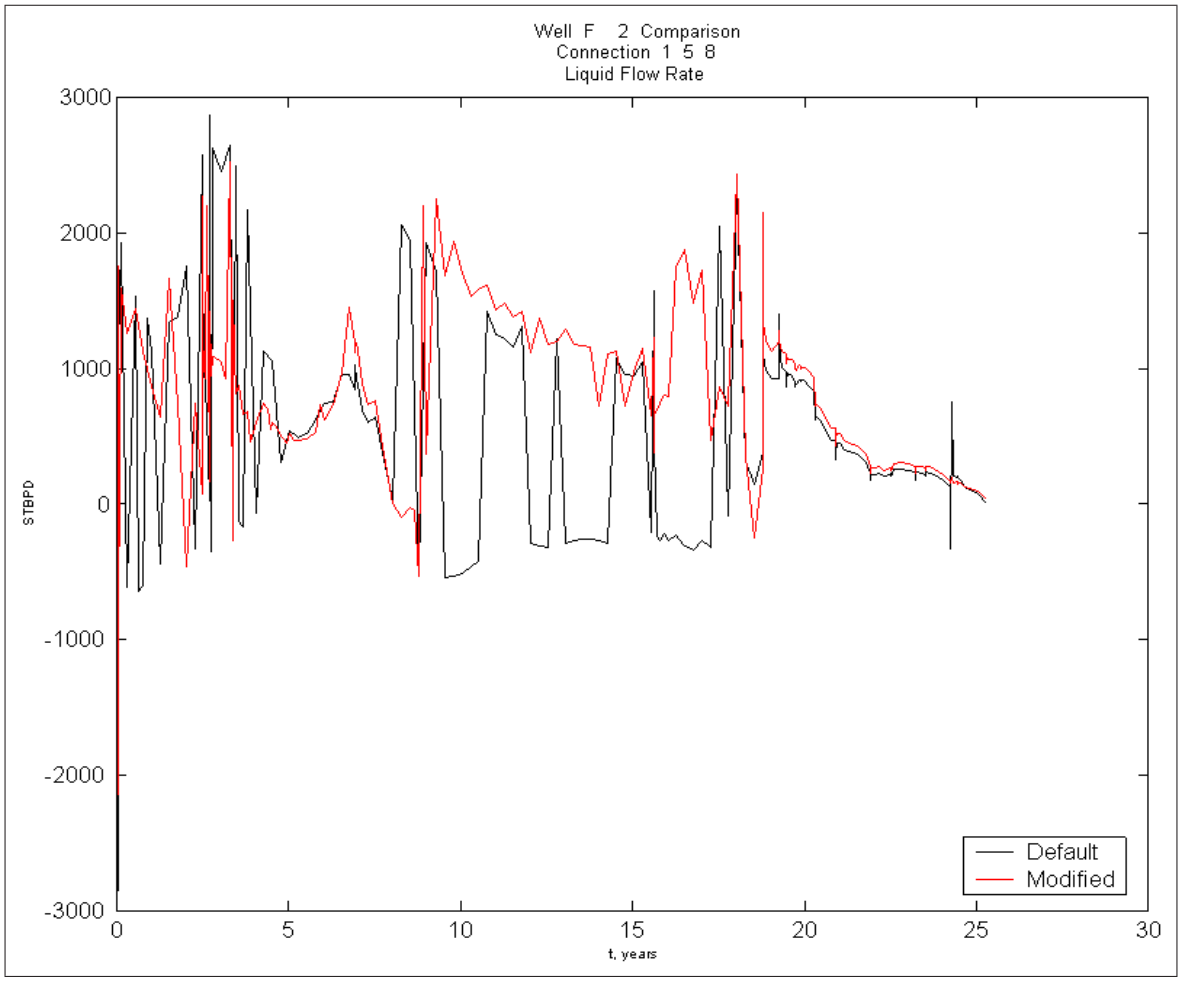
Well F 2 Comparison
Connection 1 5 8
Liquid Flow Rate
3000
2000
1000
0
-1000
-2000
-3000
STBPD
0
5
10
15
20
25
30
t, years
Default
Modified

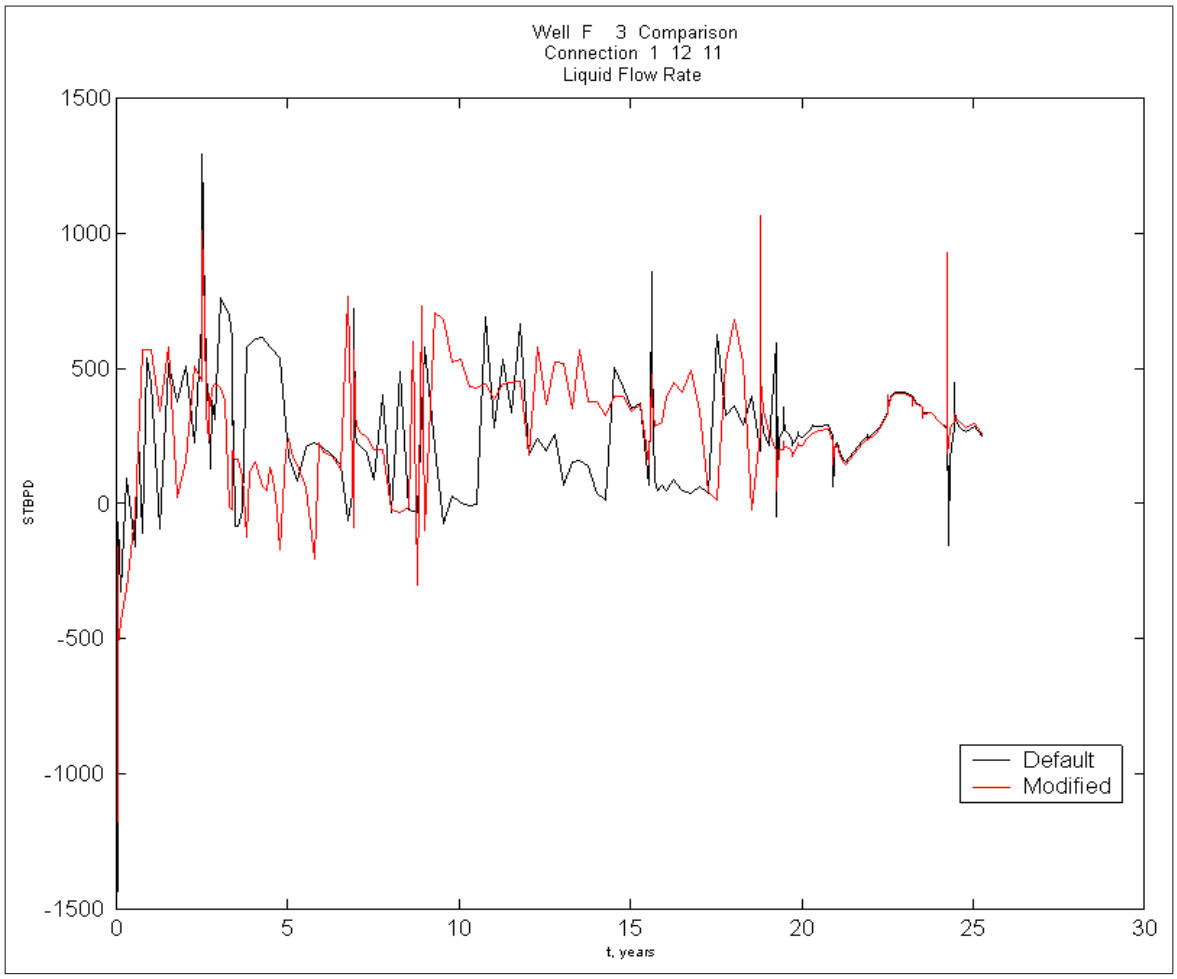
Well F 3 Comparison
Connection 1 12 11
Liquid Flow Rate
1500
1000
500
0
-500
-1000
-1500
STBPD
0
5
10
15
20
25
30
t, years
Default
Modified

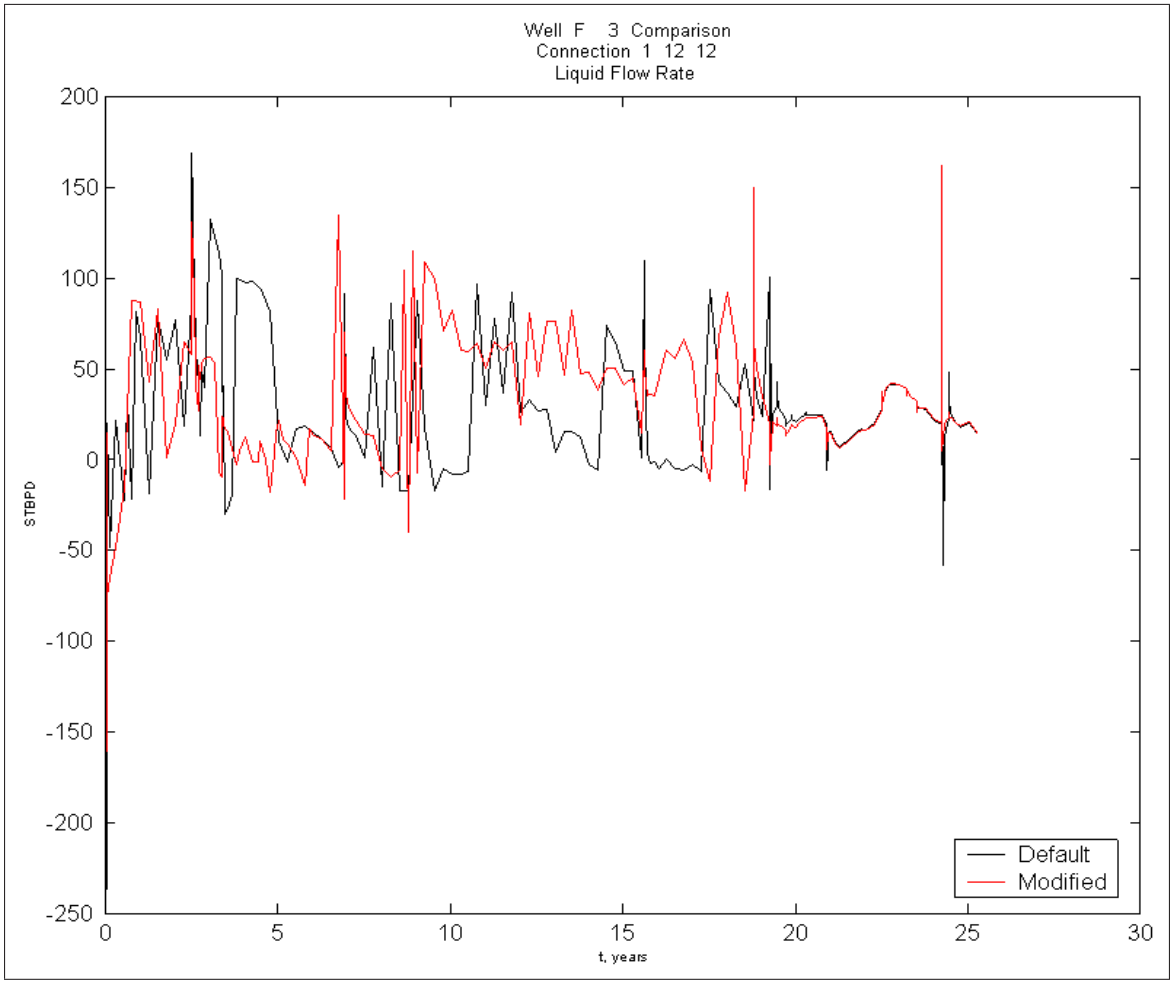
Well F 3 Comparison
Connection 1 12 12
Liquid Flow Rate
STBPD
t, years
Default
Modified
200
150
100
50
0
-50
-100
-150
-200
-250
0
5
10
15
20
25
30

Appendix D

A model for temporal behavior of super-k

Observed super-k behavior at Ghawar, and in particular, in the study area, is, in some instances, time dependent. That is, intervals which exhibit super-k flux magnitudes in a flowmeter survey, may exhibit significantly different flux magnitudes in later, or earlier surveys.

Relative flux magnitudes as evident in flowmeter surveys are rarely caused by changing boundary conditions at Ghawar, as most completions are openhole, extending over the entire productive interval, in both production and injection wells. Thus, any change in injection or production well boundary conditions, affect the entire productive interval, eliminating vertically differential boundary conditions, which, if existing, would affect flowmeter profiles.

An increase in flux magnitude over time may be explained by an increase in the conductivity of the super-k network, perhaps by dilating or extending the DFN. Alternatively, flux magnitudes may increase due to a corresponding decrease in flux in an adjacent interval in the same well.

Flux magnitude decreases in time are more difficult to explain, in that, with the exception of an adjacent interval, in the same well, becoming more conductive, a mechanism for conductivity decrease of a super-k network must be proposed.

Fig. D.1 shows examples of significant super-k flux decrease with time, in two

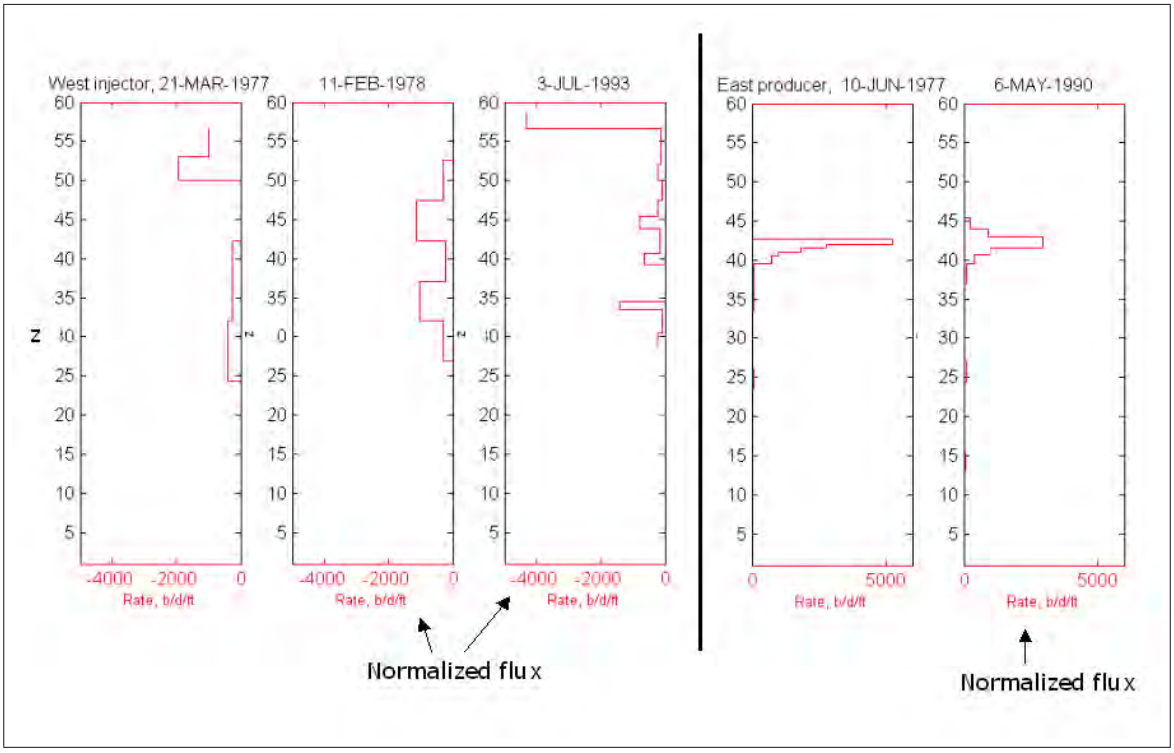

Fig. D.1: Super-k flux decrease with time

wells. These are the west water injection well, and the east producing well.

Super-k flux is observed in the earliest flowmeter profile of the west injector, in 1977, in vertical flow simulation cells 50, 51, and 52, as shown. This flux is then absent in the subsequent surveys, in 1978 and 1993. Correspondingly, a super-k flux is measured in the latest survey in cells 56 and 57. This flux may have arisen because of the decrease in flux at the lower interval, however, the mechanism behind the flux decrease in that interval has been elusive.

Note that the later surveys were normalized for differing total well injection rates. The normalization was performed using the earliest well injection rate as a base. Normalization allows for a valid comparison of flux between the surveys.

Similarly, super-k flux is seen to decrease significantly in the east producer, for surveys taken in 1977 and 1990. Flux in the later survey was normalized relative to the first survey.

Note that the intervals open to injection and production, in both of these wells,

did not change during these time intervals. Therefore, barring unmeasured changes in interval productivity, due to changes in well skin damage, the changes in flux recorded by these flowmeter surveys are not wellbore related.

D.1 2D synthetic example

An investigation to ascertain a possible reservoir performance explanation for super-k flux decrease with time, was conducted by analyzing a 2D synthetic case, in which individual connection rates in injection and producing wells, as well as in DFNs, was computed and analyzed.

This 2D case is extracted directly from the 3D facies model described in Chapter 10, with reservoir properties, pore volumes of production and injection, and reservoir pressures, nearly identical to that of the 3D model and the actual production and pressure history of the study area.

Fig. D.2 presents the synthetic case model, a 2D cross-sectional slice from the east-west center line of the 3D model, which was presented in Fig. 10.8. Both the flow simulation and stratigraphic grids are shown.

One down-dip injection well, and two up-dip producing wells, are placed, as shown, in the 2D model. These well locations are similar to actual, relative, locations, of the most significant wells in the study area. The western producer is called the "near producing well," and the eastern, the "far producing well."

A simple DFN is installed, a single curve connecting two simulation grid blocks, one in a super-k bed, and a well block in the near producing well. Note that although the DFN appears to be dipping down from left to right, in the stratigraphic model, it is actually inclined upward from west to east in the flow simulation model, due to the westerly dip of the study area.

D.1.1 Boundary conditions

Fig. D.3 presents the production / injection constraints on the wells. These constraints mimic the actual depletion, during primary production for the study area, as

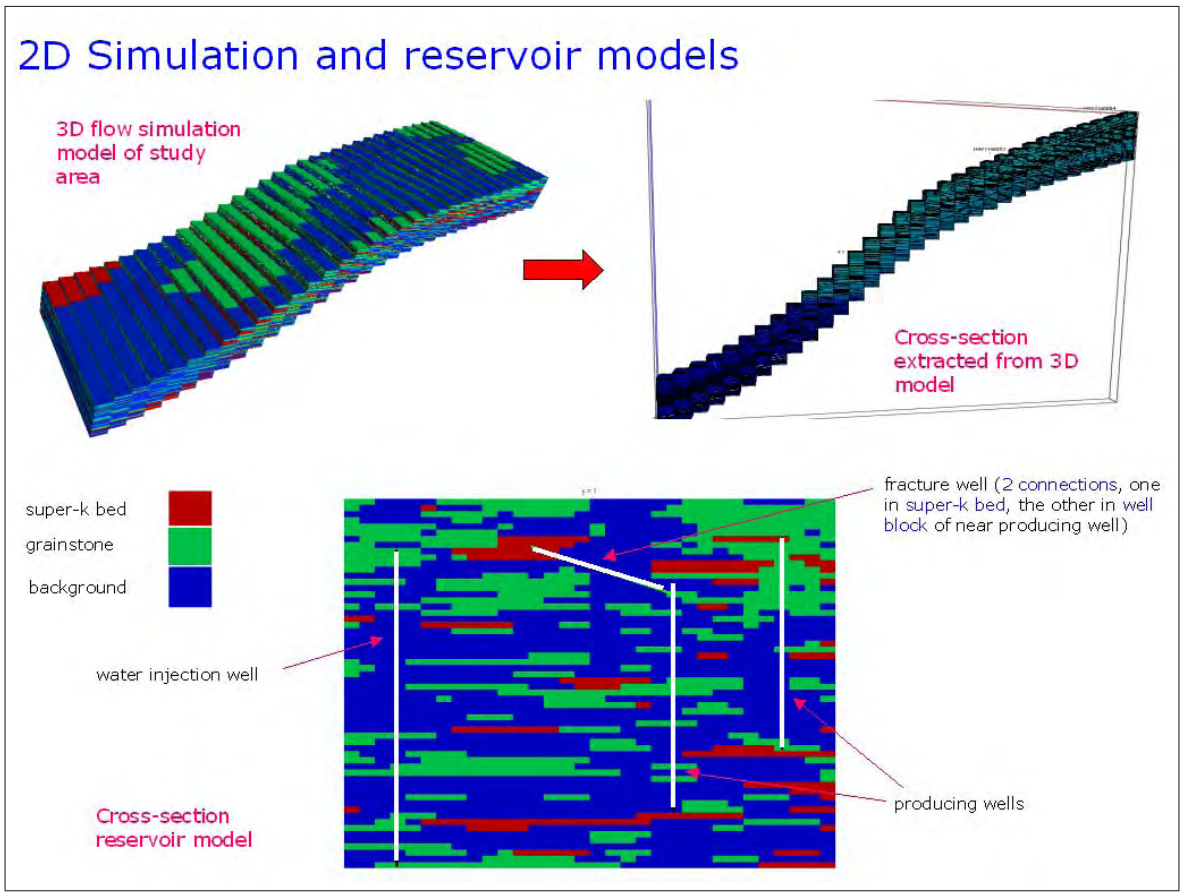

Fig. D.2: Synthetic 2D case

well as the actual pore volumes injected and produced during water injection in the area, during the 60 year production history at Ghawar.

The production constraint on the DFN is necessarily a zero net flow, although backflow, that is, flow between connections, is allowed.

D.1.2 Results

Fig. D.4 and Fig. D.5 presents how time dependency, specifically a decrease in super-k flux, may occur. The four plots in each figure present simulated (with *ECLIPSE*) well connection flow rates vs. time, in the injection well, two producing wells, and the DFN. Note there are only two source transmissibility connections in the DFN.

Fig. D.4 presents total liquid flow rates, and Fig. D.5 presents water flow rates.

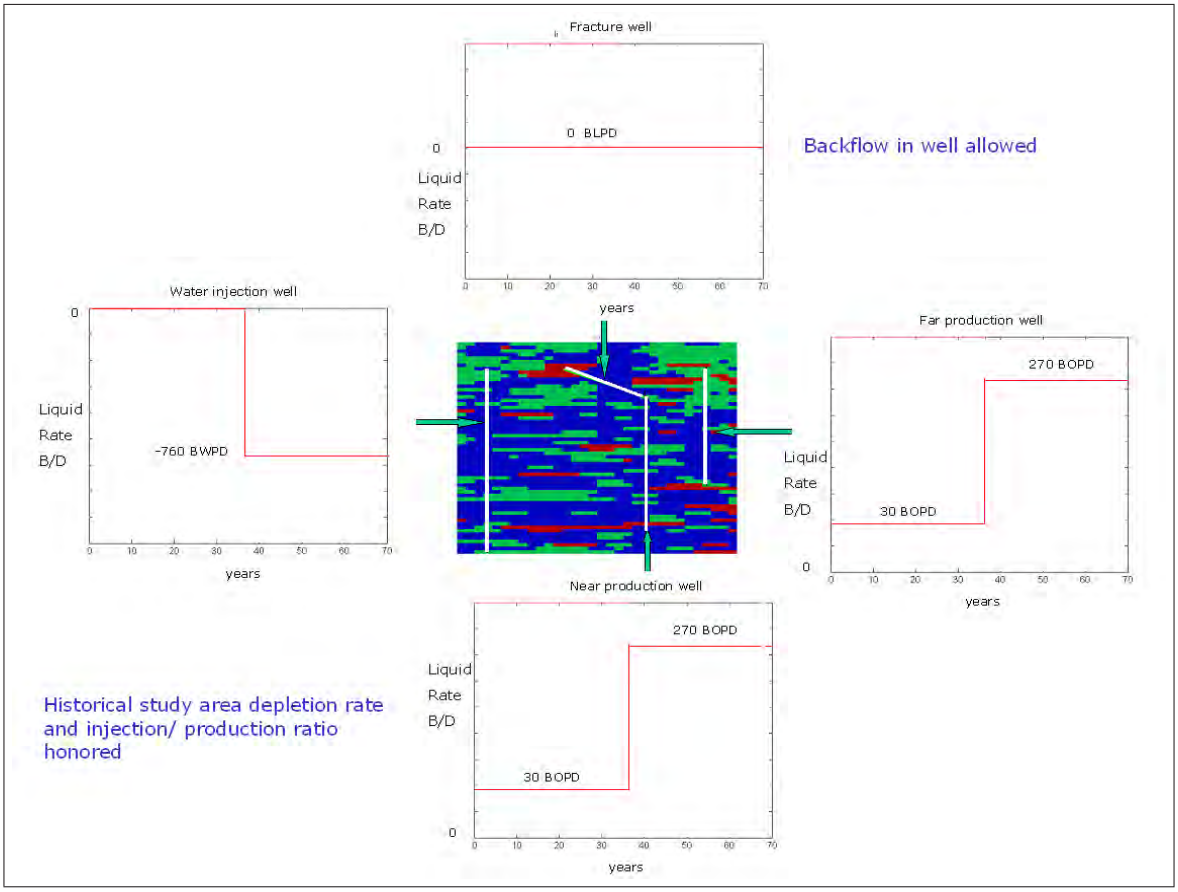

Fig. D.3: Synthetic 2D case boundary conditions

The multiple curves in the plots represent the rate vs. time behavior of the each connection in the subject well. The plots show flow rates from all connections.

Note first the effect of the DFN on the productivity of the near producer. During primary production, the effect is not apparent, by a comparison between the connection rates of the two producers, as they are very similar. However, when water injection begins, the effect of the DFN on the near producer is evident. It is almost instantaneous due to the relative incompressibility of the system, which is essentially gas free. The effect of water injection on the far producer is also evident, as a dramatic increase in rate, although there are significant differences between the two producing well responses.

During water injection, the effect of the DFN's connection to a well block of the

near producer, its increase in the productivity of the well block, is very evident. This solitary, local productivity increase results in an increase in the variation of connection rates in this well, relative to that existing prior to water injection, and as compared to that in the far producer, which, due to its location, is not affected by the DFN.

Although there is also a variation in connection rates in the far producing well, note that the rates are grouped into a few, tight groupings. The post-injection connection rates of the near producer, on the other hand, show a greater spread of rates within any grouping. This is expected well response to a system with highly variable interval productivity. This response may arise even when only one interval with an extreme productivity, high or low, is present.

Most significantly, unlike the rate vs. time behavior of the injector and the far producer, the connection rates in the near producer become time dependent.

Of course, the variation of connection rate in time first occurs, in all wells, as expected, with the onset of water injection. The time dependency of interest, that of connection rates in the near producer, begins not with injection, but only after a delay following injection. Note in Fig. D.5 that, as indicated by the dashed line, the delay coincides precisely with the arrival of water to the western connection, the upstream connection, of the DFN. In fact, prior to this event, the connection rates in both the DFN and near producer, are constant.

Fig. D.4 shows that, following the arrival of water at the DFN, the backflow rate in the network steadily declines until, eventually, it is zero. Fig. D.5 indicates that this period of decline coincides with increasing water production, and therefore water cut, in the DFN. Coincidentally, this decline in DFN backflow rate precisely mimics a decline in rate from the most productive interval in the near producer.

It is concluded, *that the DFN loads up with water and eventually dies, simply due to the fluid density increase concurrent with increasing water cut, and the dip of the reservoir, and that this decline in backflow rate induces a decline in productivity in the interval affected by the DFN, in the near producer.*

The subsequent variation in near producer connection rates is such that as intervals which initially produce at high rates, decline with time, those initially at low rates, are induced to increase with time, so as to maintain a constant total well rate.

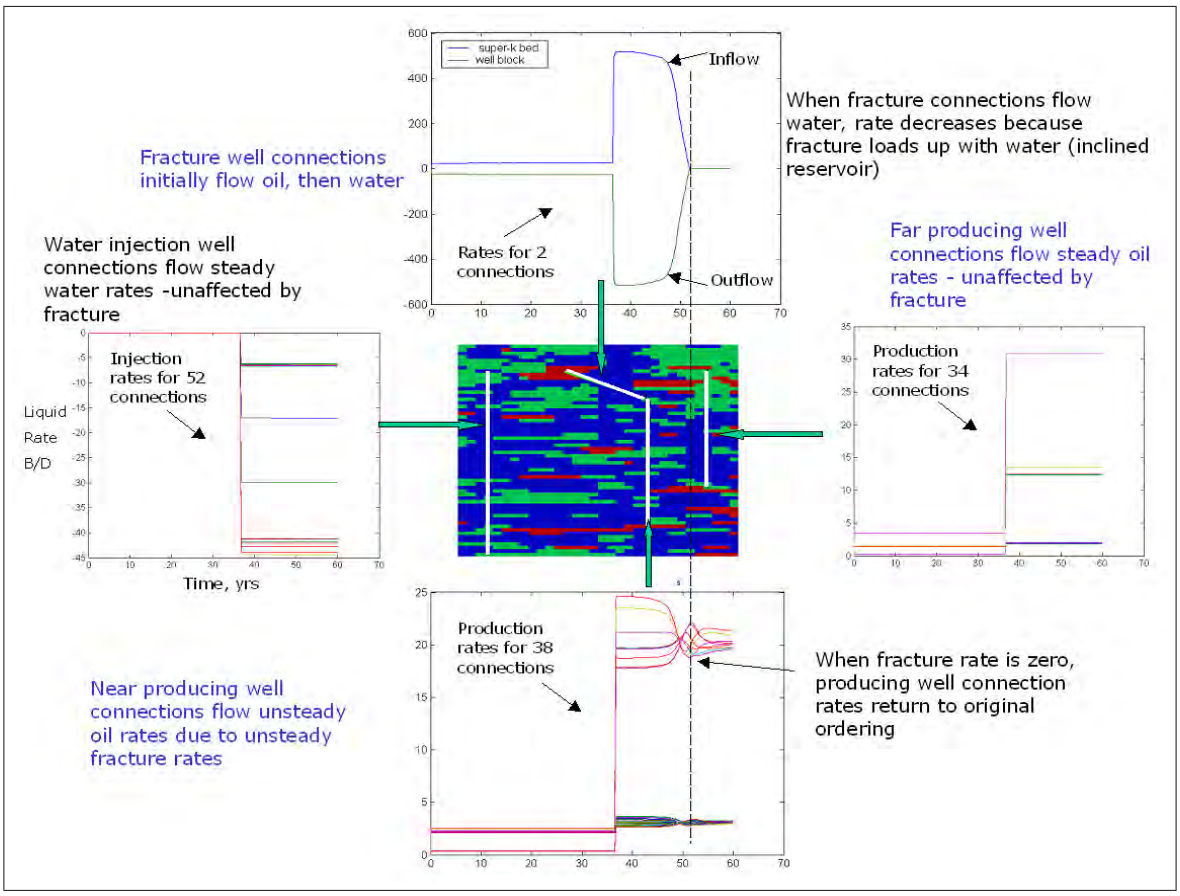

Fig. D.4: Prediction of super-k flux decrease with time

Finally, when the DFN backflow rate is zero, the effect of the DFN is nulled completely, and the connection rates in the near producer tend to converge to a few tight groupings, similar to that of the unaffected, far producer.

Note that the conductivity of the DFN does not effect the injection well, due the distance separating the western end of the DFN and the injection well.

D.1.3 Relative permeability effect

The production wells both produce at nearly 100% oil for the entire life, negating any relative permeability effect on the time dependent rate result. In fact, the relative permeability effect is nonexistent: a linear relative permeability curve, presented in Fig. D.6, such that total mobility, oil and water, is constant, was used in this run.

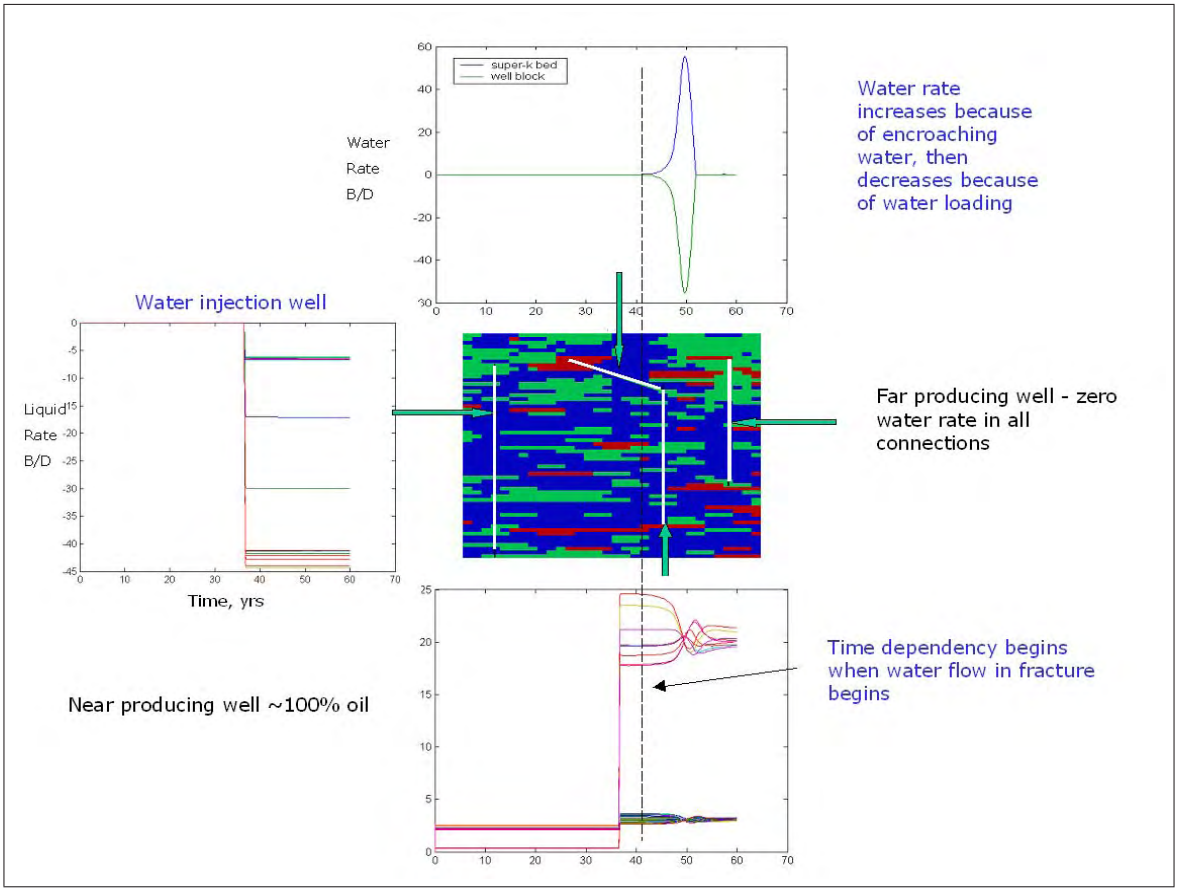

Fig. D.5: Prediction of super-k flux decrease with time

D.2 Summary

The significance of this result is that it was achieved in the first simulation run; no modifications were made to the properties of the 2D extraction model, and no modifications were made to the production and injection constraints, so derived to honor that which was actually observed in the study area, in order to induce this result.

The conditions which may actually induce this result at Ghawar evidently include high permeability reservoir matrix, such that water injection pressures are not sufficiently high, even at prolific injection rates, to overcome water loading of DFNs. The loading of DFNs occurs because they fill with water more quickly than does the

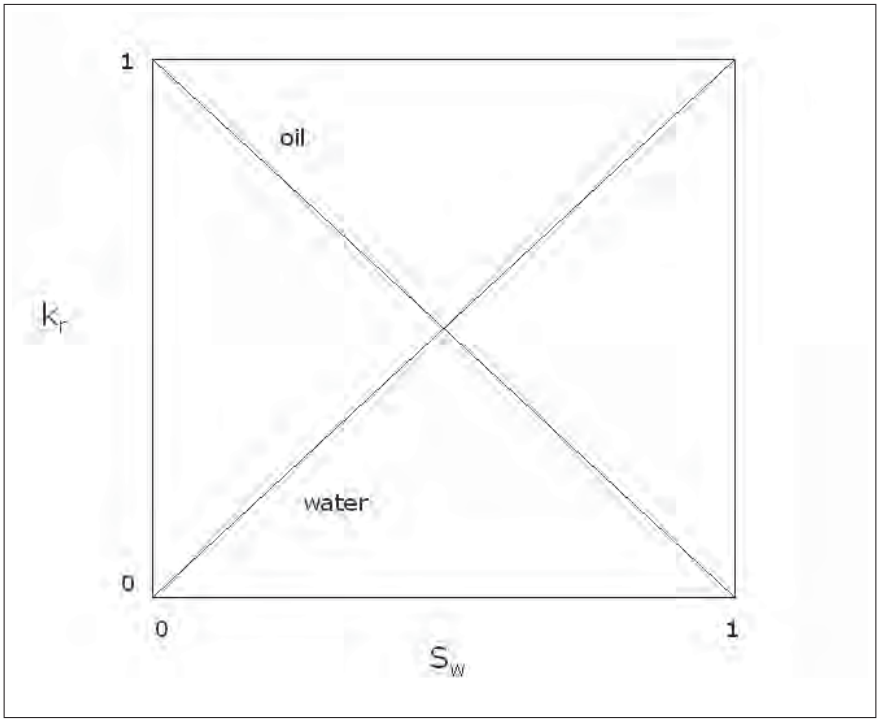

Fig. D.6: Relative permeability for synthetic case

surrounding matrix, while injection pressures are still low, not high enough to prevent the loading. Of course, after the DFN loads up, as water continues to move in the matrix updip, eventually injection pressure becomes high enough to flow water in the DFN again, which will again induce a local productivity increase at the near producer. This productivity increase is then expected to be permanent, given that the fluid in the DFN is at or near 100% water.

In general, this phenomenon may occur in any dipping reservoir, given injection pressures insufficient, early in the water injection operation, to lift water in the DFNs.

Appendix E

Original study area model

SA transmitted an initial flow simulation model, the constituents and flow simulation results of which are also presented in this section. Various modifications of this original model, constructed in the course of thesis work, are described in Appendix F and Chapter 10. The well performance data is presented with simulated performance data from the original model.

E.1 Initial reservoir model

As described in Sec. 3.4, the study area is discretized with a local grid refinement of dimensions 32x12x180. Fig. E.1 presents the study area original permeability map over the local grid refinement. Fig. E.2 is the original porosity map of the study area. The porosity model is Gaussian, conditioned primarily to log and core data, and secondarily to seismic data. The permeability model is derived from $\phi - k$ correlations unique to several reservoir layers. The correlations are calibrated to both well test derived permeability and permeability computed from flowmeter data.

The porosity model is kept intact throughout the characterization process in this study. The permeability model is, however, perturbed during the history matching process.

Note from Fig. E.1, the trend along the X direction, from low to high permeability. This trend is part of a flank to crest transition of permeability increase. This

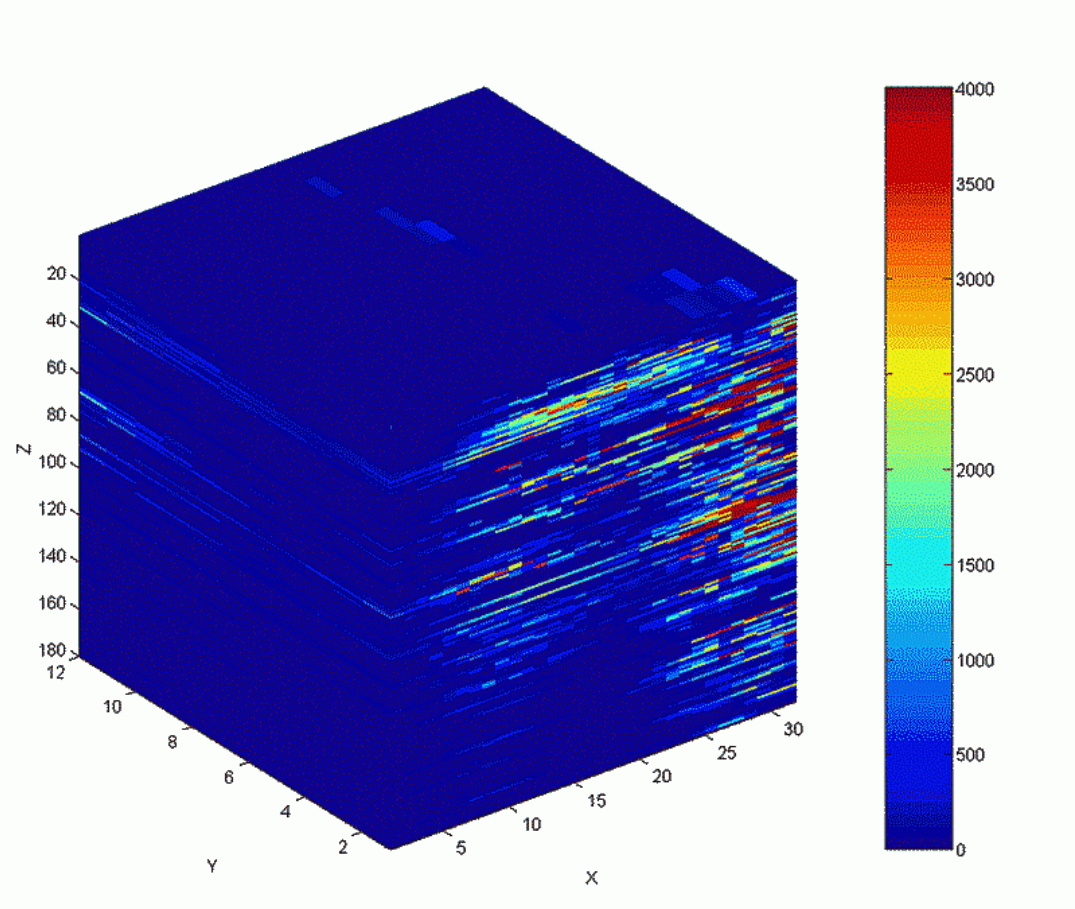

Fig. E.1: Original study area permeability model

transition is observed field wide and is a depositional or deformational characteristic. All subsequent realizations in the history matching algorithm honor, to some degree, this permeability trend.

E.1.1 Initial model statistics

Fig. E.3 shows the distribution of permeability and porosity of the initial model. Note from Fig. E.1 that the maximum plotted permeability is 4000 md; this is approximately the 95% quantile permeability.

The permeability is approximately log normally distributed, and has a mean of 561 md.

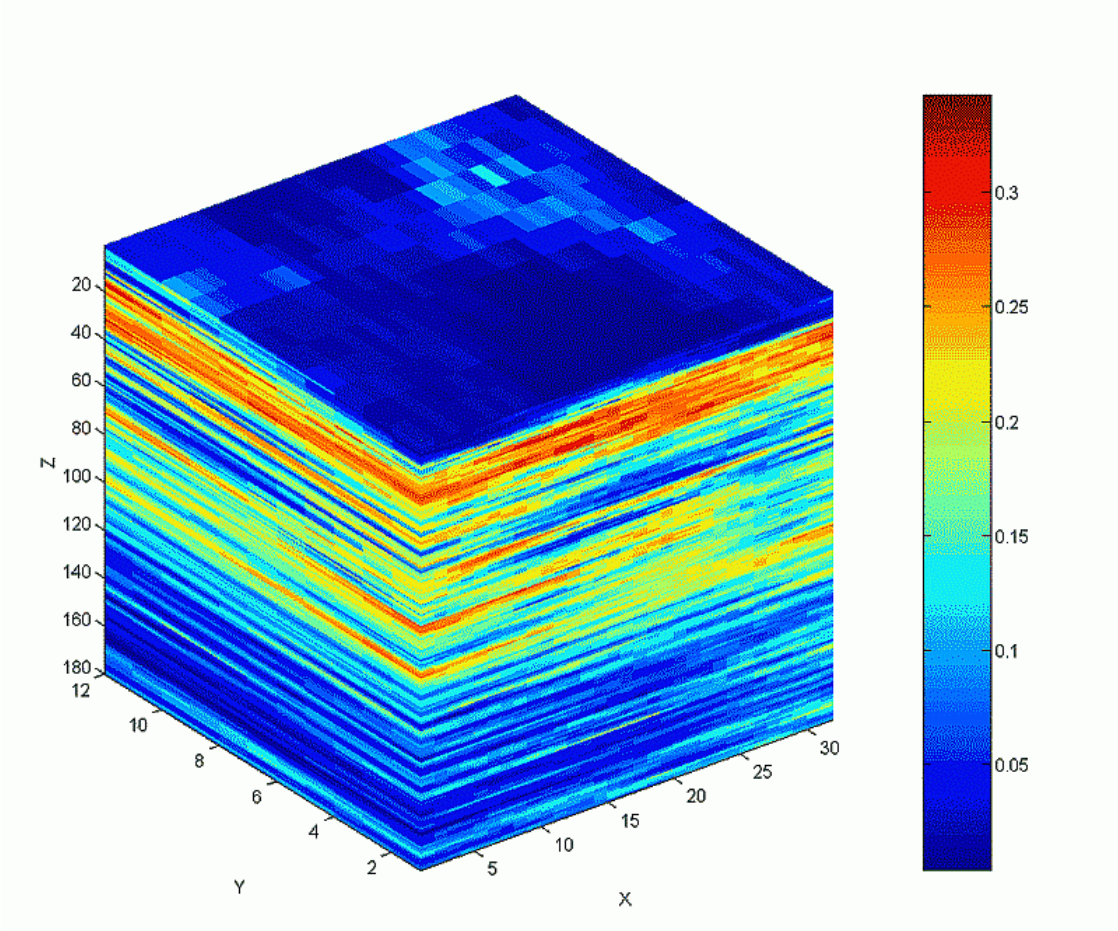

Fig. E.2: Study area porosity model

Fig. E.4 is a plot of the mean areal (x-y area) permeability as it varies in the vertical (z) direction. Note that the areal mean is maximum in the upper portion of the model. This maximum corresponds to the Arab-D zone 2B.

E.2 Well performance data and the initial match

Study area well performance data includes: producing and injection well bottomhole pressures, and oil, gas, and water rates. The measured bottomhole pressures are 24-hr shut-in pressures, which are matched with flowing well block pressures. The 24-hr shut-in pressures have been determined, by SA engineers, to be equivalent to

Fig. E.3: Permeability and porosity distributions of the initial model

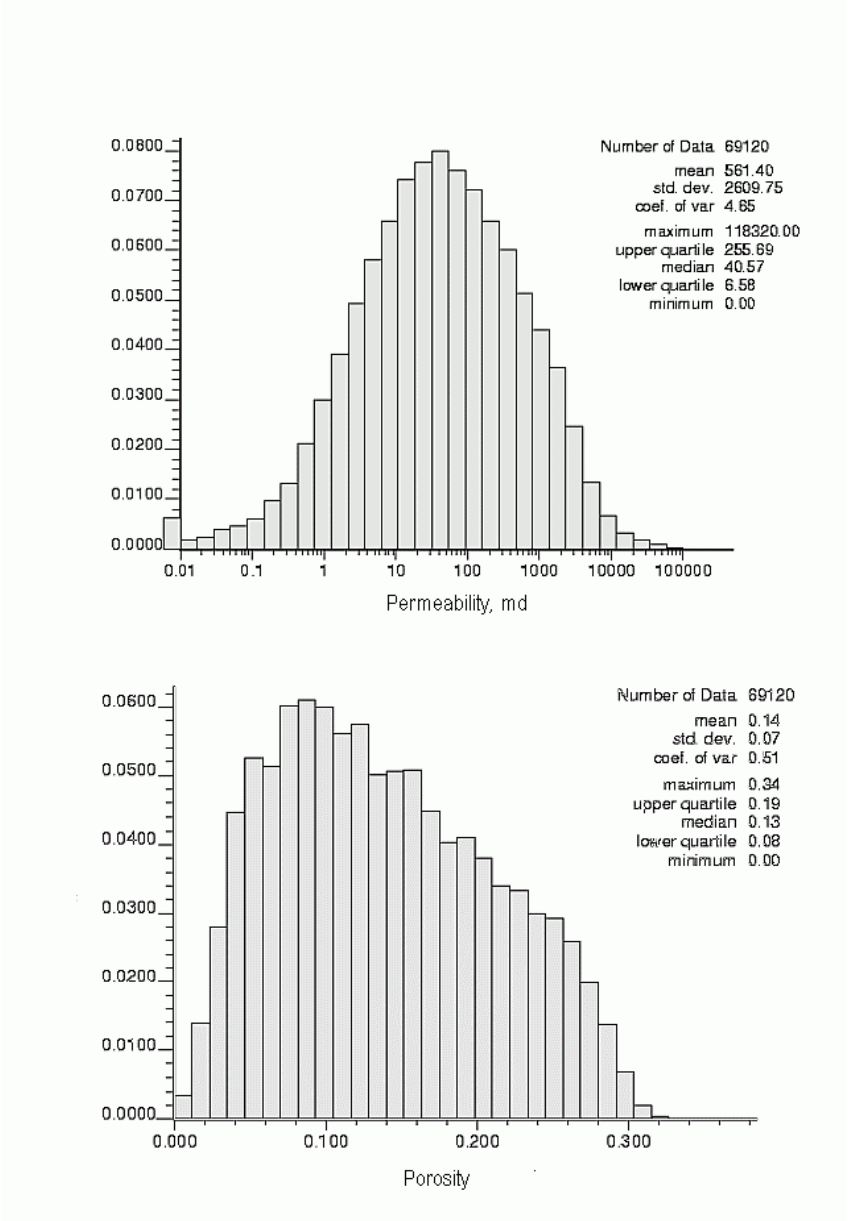

Peaceman pressures [34], and therefore are adequately approximated by well block pressures.

Simulations of well performance for all eleven wells in the study area were made, although only eight of the wells have significant production history, and are presented in this report.

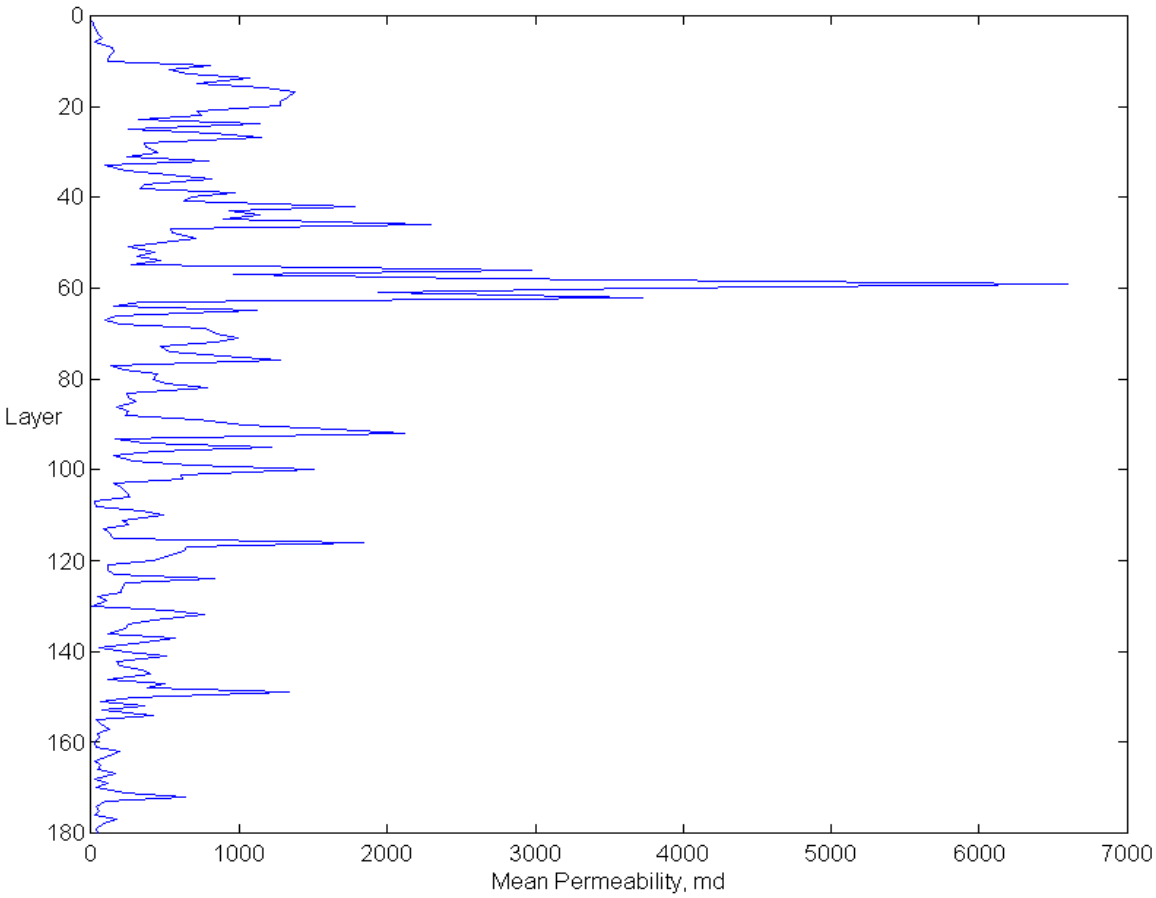

Fig. E.4: Vertical distribution of mean areal permeability of initial model.

Reservoir simulation was performed using the commercial simulator *Eclipse*. A full field, full history matched, Ghawar simulation, using the original reservoir model provided by the operator, was run first in order to record a boundary flux history for the study area. The boundary flux is then assumed to be unaffected by subsequent changes in the study area reservoir characterization, as incurred in the course of history matching. Use of this boundary flux allows for simulation of the study area alone. Also, simulation of the study area proceeds from a restart at 34 years of history, the time of first production from the study area. The production history of the study area is therefore 25 years. Simulation run time for the study area is approximately 1 hour, on a 2 GHz, 2 GB processor.

Flow simulation is conducted under the constraint of reservoir producing rate.

Here, the simulator optimizes the bottomhole flowing pressure to match the total measured bottomhole fluid producing rate. The total measured bottomhole fluid producing rate is the sum of oil, gas, and water rates, converted to reservoir volumes. Therefore, any of the components, oil, gas, and water, taken individually, may not be matched. The degree to which simulated bottomhole pressures agree with measured data is therefore an indication of how well reservoir productivity, and reservoir pore volume, but not necessarily relative phase productivities, are being modeled. This is especially true in moderate to low GOR reservoirs with little well skin damage, which is the case at Ghawar.

Fig. E.5 through Fig. E.11 are plots of measured well performance data, as well as the initial simulation results, for eight wells in the study area. The remaining three wells have little to no production. The eight wells include the two injection wells, Wells 1 and 2, and the two oldest producing wells, Wells 6 and 8. Each of these two producing wells have 25 year production histories. Performance histories of the two injection wells span 18 and 25 years. Four wells which have been associated with Super-k, one injector and three producers, including one of the oldest wells, are also included. These Super-k wells are Wells 1, 3, 4, and 8, and are indicated in Fig. 3.2, underlined in red.

Fig. E.5 presents measured bottomhole transient fall-off pressures and simulated well block pressures. Rate comparisons are not necessary since a single phase, water, is injected, so that simulated and measured well rates are identical. Note that, unfortunately, the measured pressures are generally obtained under inactive injection conditions. The area was shut in during years 8-15 due to low demand (see Fig. E.6 and Fig. E.9). Resumption of injection then lagged an additional 2 years. The measured data prior to 5 years also was obtained under inactive injection conditions. Therefore, well injectivity cannot be computed from the pressure data. However, changes in simulated injectivity upon changes in the reservoir characterization can still be ascertained (Sec. F.3 and Sec. F.4.1).

Fig. E.6 to Fig. E.11 show, in general, a good match of measured bottomhole pressure data. When a mismatch is observed, it is generally due to low simulated productivity. SA attempted to place high permeability layers at wells which exhibited

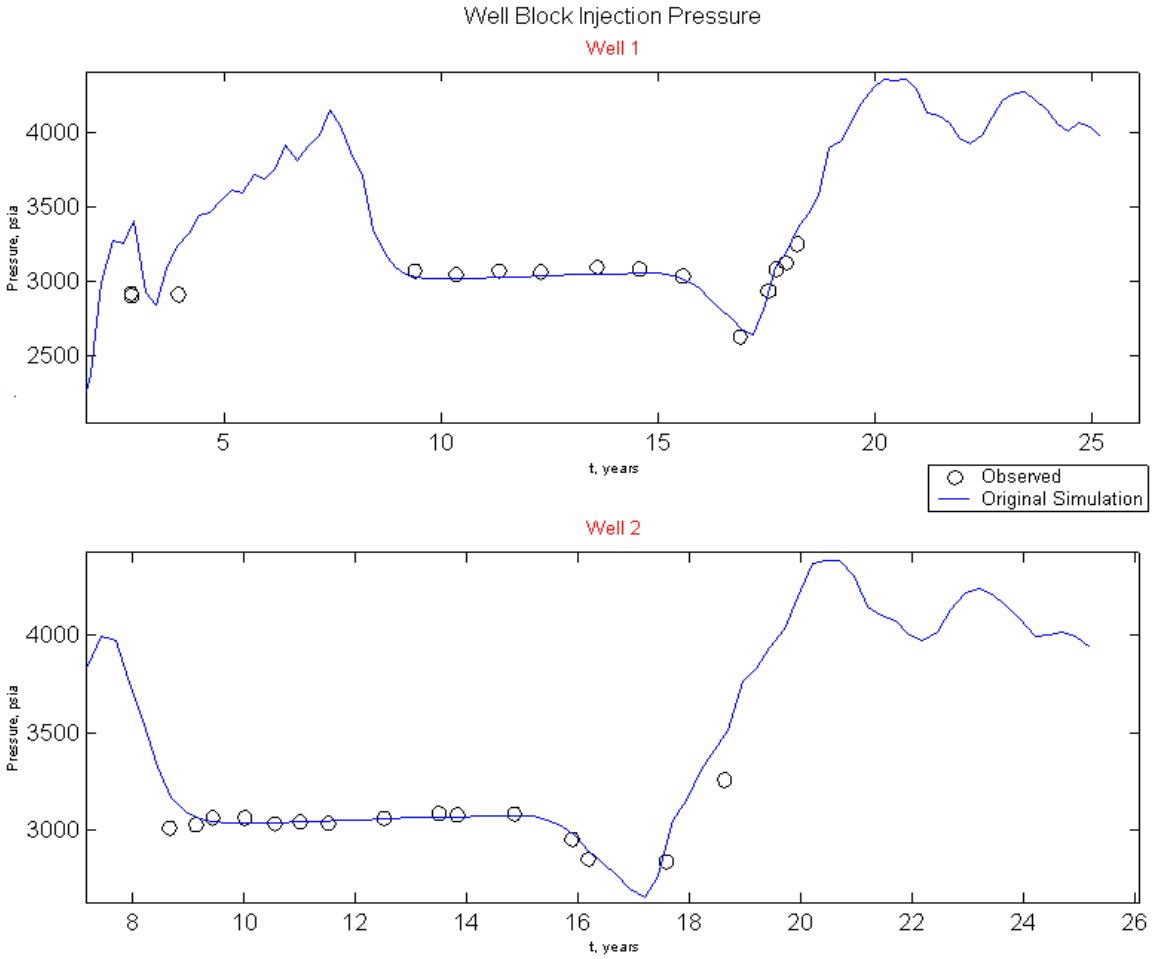

Fig. E.5: Initial match of injection well block pressure

Super-k flow rates, as observed from flowmeter data. The high permeability layers were merged with the background permeability, away from the well (see Sec. E.1).

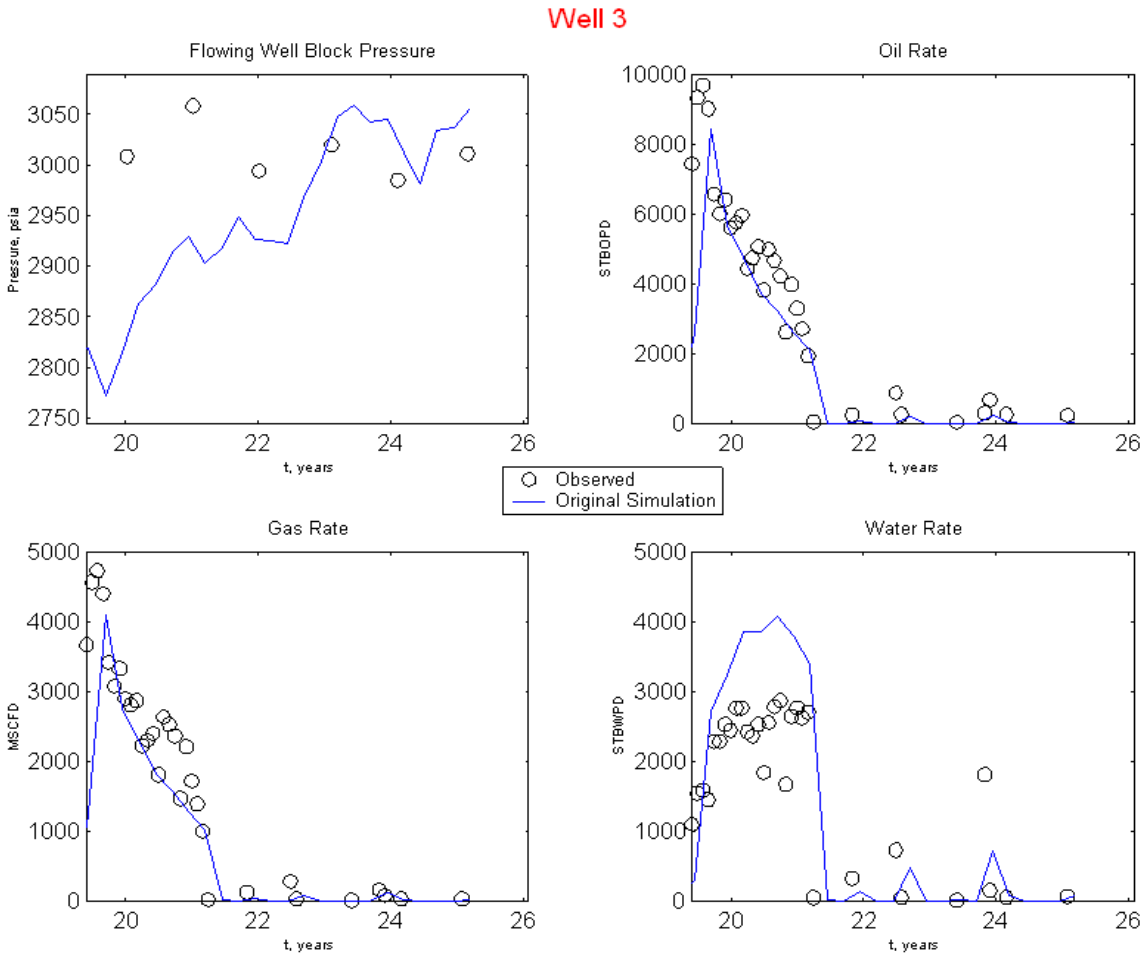

Fig. E.6: Initial match of well performance

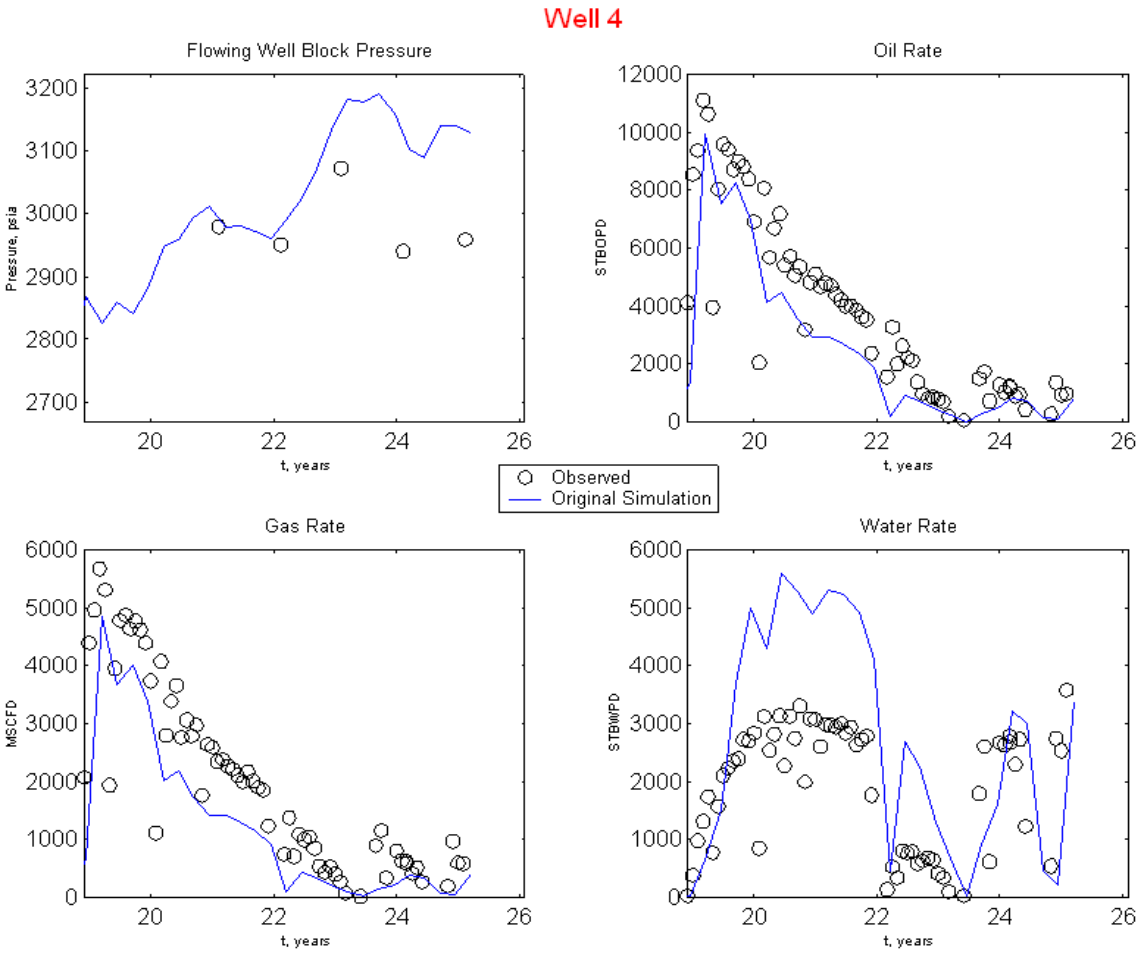

Fig. E.7: Initial match of well performance

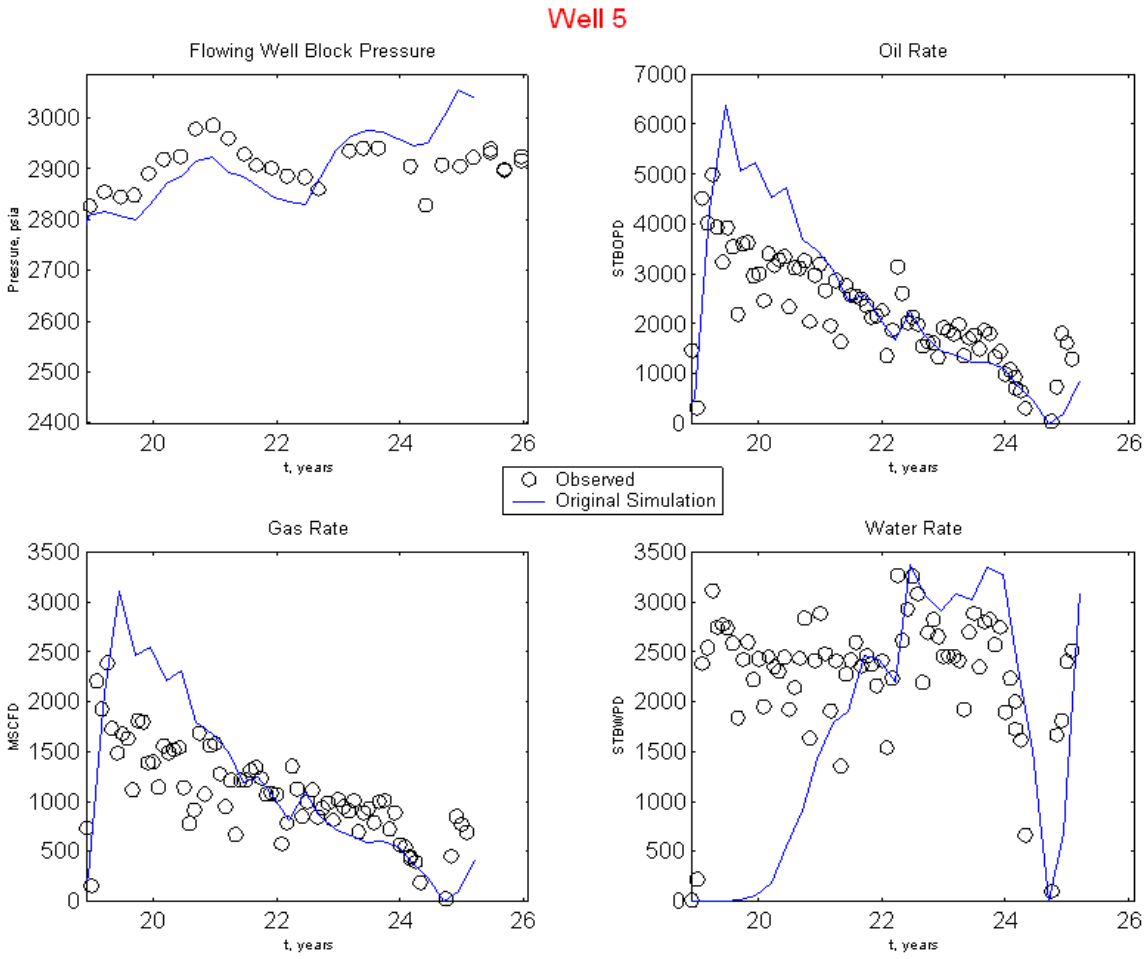

Fig. E.8: Initial match of well performance

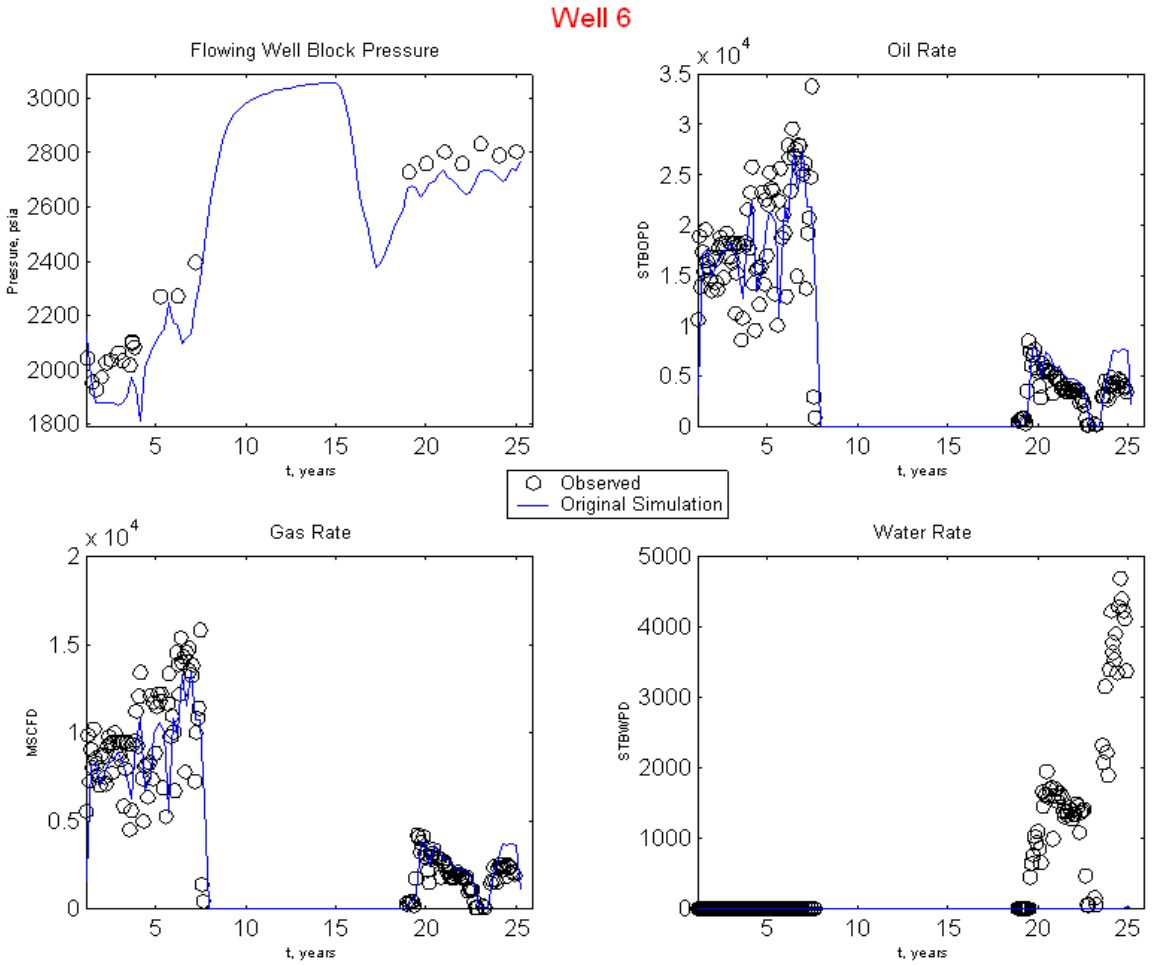

Fig. E.9: Initial match of well performance

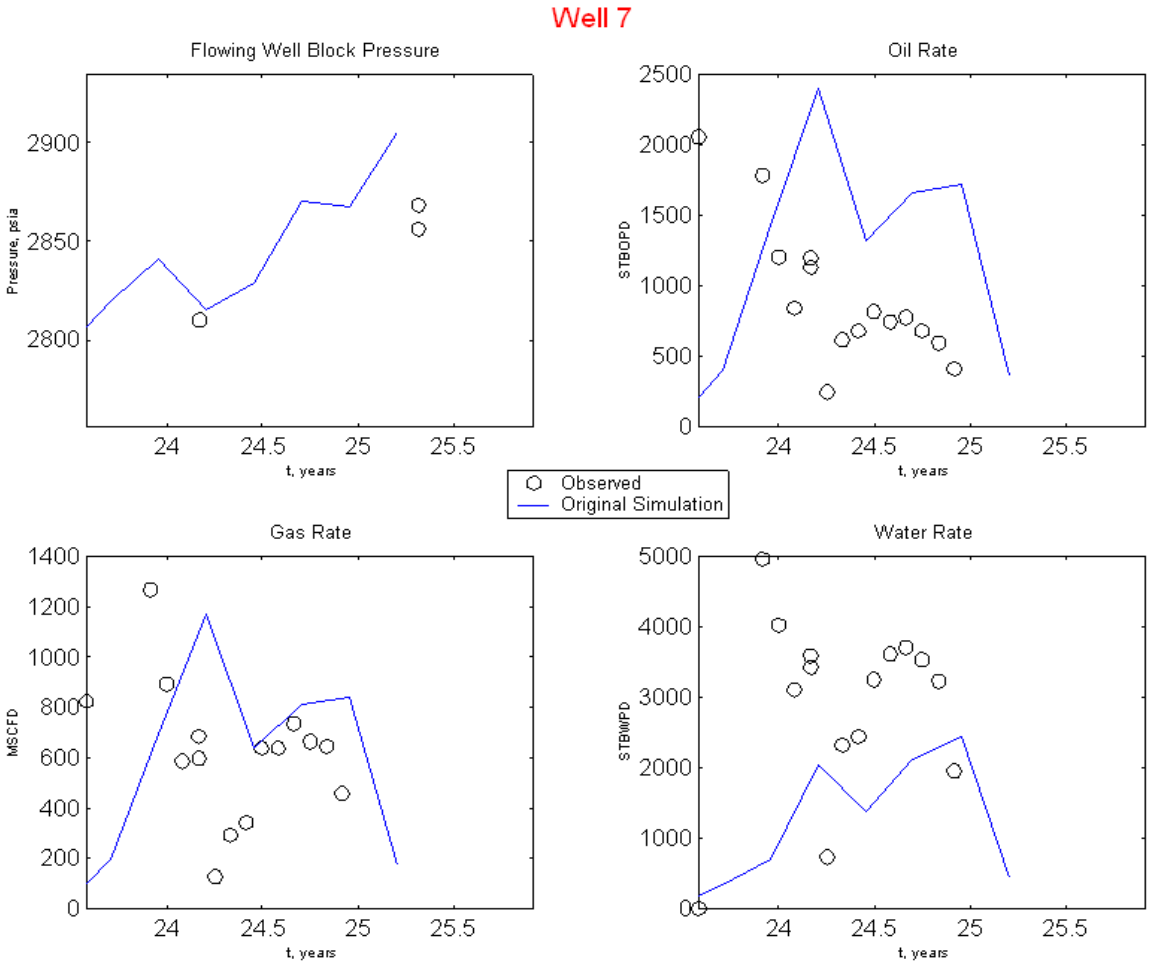

Fig. E.10: Initial match of well performance

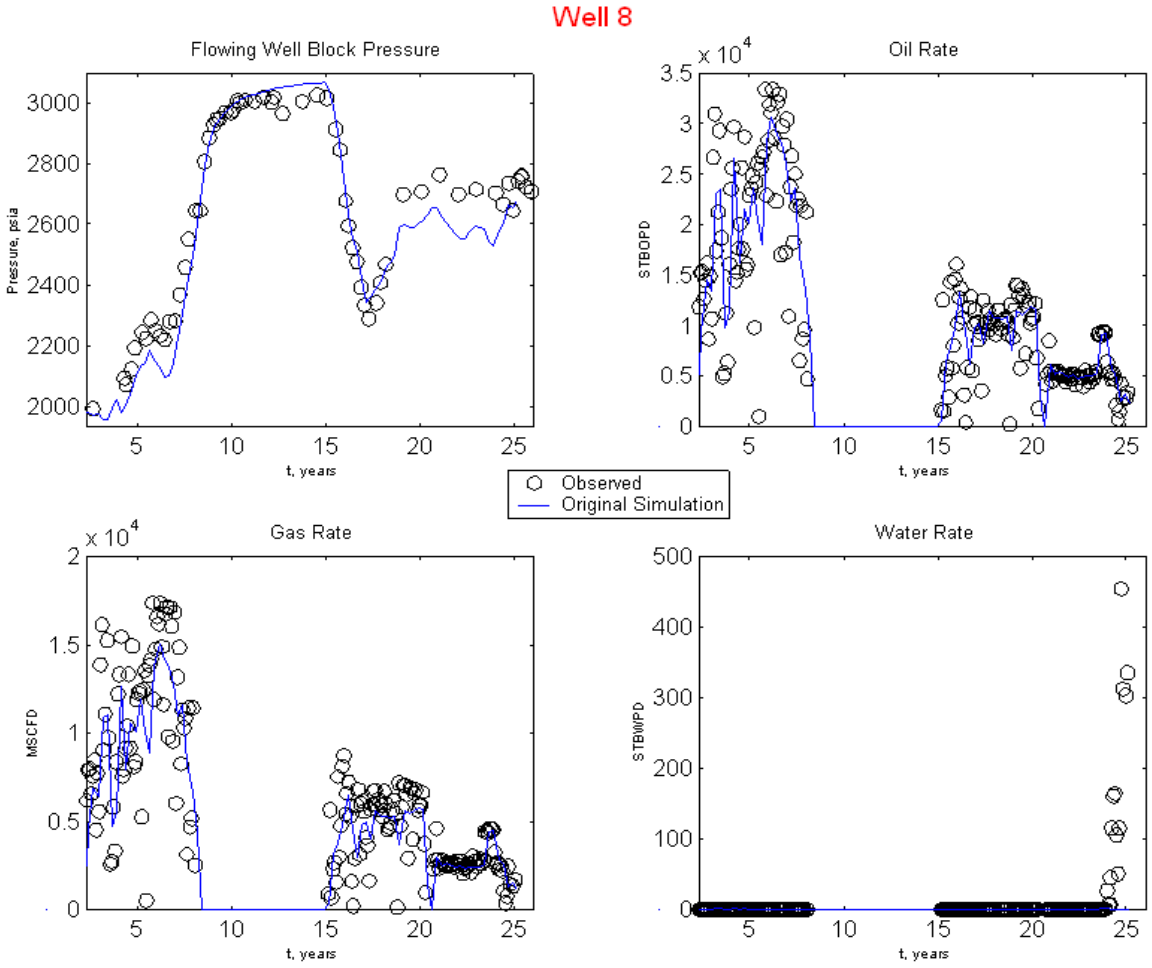

Fig. E.11: Initial match of well performance

Appendix F

A facies only model for super-k

This appendix presents the results of very early studies that were performed to ascertain the flow properties of super-k. Thus the training image-based facies are quite archaic, relative to that presented in Chapter 10, as the facies model has evolved since these initial models were developed.

Nonetheless, the inclusion of these results serves the purpose of demonstrating that high permeability components of a facies only model, which do not intersect wells, cannot significantly affect well performance - well pressure and total well rate vs. time, simply because of radial flow. The same conclusion was made regarding flowmeter data (Sec. 6.4).

Super-k was modeled as a structure that may be composed of various facies, that combined to form a high conductivity network. This model evolved into our DFN-based model. Thus, our initial attempts at modeling super-k involved the use of training images, under the assumption that conceptual models of super-k structures would be provided by Ghawar geologists.

F.1 Super-k training images

Super-k was modeled using three 3-D training images, encompassing the five major Arab-D zones (Fig. 4.6).

The super-k training images are binary. Super-k is modeled as connected high

conductivity bodies, similar to stream channels or grainstone beds. Super-k training images model one or more of the structures displayed in Chapter 6 as a whole, rather than component by component. Super-k comprises about 18% reservoir volume, in accordance with the conceptual models provided by SA. These super-k training images are then used in the program SNESIM [31] to generate unconditioned realizations of super-k spatial distributions. Each of the three divisions were modeled in this fashion independently, with the three models then concatenated to produce a composite 3-D study area realization.

Fig. F.1 presents the three 3D training images. These conceptual models for super-k structures, as well as the zones to which these models apply, were provided by Saudi Aramco geologists. Accordingly, super-k structure in Zone 1 and Zone 2A are modeled under one training image, corresponding predominantly to the dolomite wedge structure (Chapter 6). Super-k in Zone 2B is modeled with a second training image, corresponding to the tempestite bed structure. Finally, Zones 3A and 3B are simulated with a channel structure training image. Super-k in Zones 3A and 3B are not present in the lower portion of the interval, as indicated in Fig. F.1. Super-k flow rates are most prevalent in Zones 2A and 2B in the Arab-D in the region of the study area.

The training images were generated stochastically from given global super-k rock volume proportions. The two training images for Zones 1 through 2B were constructed with the object-based ELLIPSIM [75] program. These were unconditional realizations of ellipsoid bodies. The third training image is an unconditional realization from the program FLUVSIM [76], which simulates channel bodies.

The conceptual models of the super-k represents valuable information which must be honored in the history matching algorithm. The SNESIM algorithm generates numerical models that reproduce the types of structures displayed by the training images.

F.2 The combined permeability realization

SNESIM was used to generate binary realizations according to probabilities derived from the training images. Each of three realizations, derived from the three training images, was generated independently. Fig. F.2 presents the three realizations. The realization for Zones 1 and 2A consists of a grid $32 \times 12 \times 45$. The realization for Zone 2B has a thickness of 60 cells. Finally, the third realization, for Zones 3A and 3B, has a thickness of 75 cells.

Prior to combining the three realizations, tight bounding layers are placed above and below the super-k bodies. A permeability of 1.0×10^{-6} md. is assigned to the tight layers. The bounding layers are one cell thick.

Fig. F.3 is the combined realization for Zones 1 through 3B, including the tight bounding layers, represented by the thin, dark elements. Note that bounding layers are placed only above and below the super-k bodies. Also note that when two or more super-k bodies intersect, the bounding layer is not installed; there are no bounding layers between super-k bodies.

Fig. F.4 is the combined permeability realization. In this realization, the super-k is assigned a permeability of 10000 md., and the background is a SGSIM[77] realization (see following section). The simulated performance of study area wells using this type of permeability model is discussed in Sec. F.4.1.

F.3 Gaussian models

Prior to developing the history matching algorithm, a flow simulation on a permeability realization of a sequential Gaussian simulation was performed. The realization does not include discrete super-k structures. This was done to ascertain the importance of the background, non super-k, elements of the characterizations, on well performance. It was suspected that the estimated small reservoir volume fraction occupied by super-k, 18%, would severely limit its effect on well performance, despite its anomalously high permeability.

The importance of the background permeability was ascertained by increasing

its mean significantly, to approximately that which may be characteristic of super-k. Thus, this model is a simple modification of the original model, in which the mean permeability is increased to super-k levels. The mean was increased by a factor of four, to approximately 2000 md.

This increase in the mean permeability was also prompted from an examination of the original history match, Fig. E.5 through Fig. E.11, which indicated the need to increase the background, non super-k, permeability. This requirement was deduced from the observation that some of the mismatches in which deliverability was underestimated by simulation, occurred in non super-k wells. Also, when occurring in super-k wells, the mismatches occurred under conditions in which the super-k was isolated from production. The best examples of these instances are seen in Wells 6 and 8 in Fig. E.9 and Fig. E.11, resp. Well 6 is a non super-k well, and Well 8 is a super-k well in which production beyond year 19 is derived exclusively from non super-k intervals.

The program SGSIM was used for the simulation. The SGSIM realization was generated using the statistics of the original model, with the mean increased by a factor of four. The model also includes a local varying mean derived from the permeability trend of the original model. Variograms from the initial model were also used for the generation of the SGSIM realization.

Fig. F.5 is the SGSIM realization. Comparing Fig. F.5 and Fig. E.1, note the prevalence of higher permeabilities in the SGSIM realization.

Fig. F.6 to Fig. F.12 present the results of the flow simulation using the SGSIM permeability characterization. The well performance comparisons are taken from the same eight wells as discussed previously (Sec. E.2). Comparison between the simulation results from this model and the original model demonstrates a significantly increased flow capacity for all producing wells with the SGSIM realization. The performance of injection wells, Wells 1 and 2, also demonstrate a significant increase in well injectivity with the SGSIM model.

These well performance comparisons demonstrate the large relative influence of the non super-k portion of the reservoir, and indicate the difficulty in using well performance to characterize super-k.

The mean of the SGSIM model is evidently too high. It was decided however, that further attempts to refine the match, by decreasing the SGSIM mean and generating new realizations and new flow simulations, were not warranted. The effect of super-k on well performance may be ascertained using the SGSIM model as a background permeability model. Also, development of a working history matching algorithm does not depend on the mean permeability of the non super-k element of the reservoir characterization.

F.4 History matching algorithm

The history matching algorithm is derived from the probability perturbation method[74]. The optimization is univariate and performed using the Brent [36] method.

Three SNESIM realizations initialize the algorithm by serving as base maps for the COSNESIM realizations. COSNESIM is based on the SNESIM program, and has an additional algorithm providing for the combination of the probability $P(A|D)$ derived from the base maps and a deformation parameter r_D, with probabilities of type $P(A|B)$ derived from the training image. The combined probability then is used to simulate realizations of binary maps consisting of super-k and non super-k.

The objective function f is the absolute sum difference of observed well flowing pressure, obs, and the simulated well flowing pressure, sim,

$$f = \frac{1}{n}\sum_{i=1}^{n} |obs_i - sim_i|$$

The sum is computed over all measured pressures and all 11 wells.

When the objective function minimum criterion is met, the algorithm terminates. If, on the other hand, the minimum does not satisfy the criterion, then the COSNESIM realizations which provided for the minimum, are used as base maps and the Brent algorithm is restarted.

F.4.1 Results from super-k realizations

Various optimization runs were made in which the super-k permeability was kept constant. All runs retained the SGSIM background distribution of permeability, described in Sec. F.3.

The intent of assigning permeabilities in this way was to gauge the effect on simulated well performance, of super-k *geometries and spatial distribution*. Changes in well performance, compared to the original match, incurred with this permeability model will gauge the effect of essentially 18% of the reservoir having a super-k geometry with a constant permeability.

The first set of results to be presented corresponds to a super-k permeability that is *significantly lower* than the background perm. This case was run because the SGSIM model background permeability is too high, as described in Sec. F.3. Although this case is not realistic, given that super-k permeability is generally higher than the background mean, it was necessary to assign a lower super-k permeability in order to adequately test the history matching algorithm, which, of course, is based on a *minimization* of the objective function.

The permeability assigned to the super-k was 400 md. This is approximately 1/5 of the background permeability mean.

Fig. F.13 to Fig. F.19 present the results of the optimization using the type of model described above, compared to those from the SGSIM model. Note that the match is not significantly improved from that derived from the SGSIM model. Therefore, the modeled super-k geometries have little effect on well performance. This conclusion is reinforced further by the finding that the objective function is not reduced by more than 10% during the optimization. Therefore, the objective function appears to be relatively insensitive to super-k spatial distribution.

During this optimization, the maximum number of Brent iterations was set to 10, and the maximum number of base maps used was 5. Approximately 35 flow simulations were performed.

A further demonstration of the insensitivity of simulated well performance to super-k spatial distribution is presented in Fig. F.20 to Fig. F.26. The permeability model is similar to the first case except that the super-k permeability is assigned

a constant 10000 md. Since the assigned super-k permeability is *higher* than the model background mean, the objective function cannot possibly be decreased with this model. Therefore, this case is not an optimization result, but rather the result of a single flow simulation on one realization. A realization of this model is shown in Fig. F.4. The intent of this case was simply to confirm the small effect of super-k permeability on simulated well performance. The permeability of super-k is approximately five times larger than the mean of the SGSIM background.

The simulated well performance is compared to the simulation results using the SGSIM model. Note that, like the previous case, very little change in well performance is the generated by the super-k model.

The results from these two cases stem from the low fraction of super-k, and therefore from its small influence on mean permeability, despite assignment of super-k permeability that is five times higher, and lower, then the SGSIM mean.

Note that the majority of the production history of the study area is effectively under primary production. This is evidenced by the lack of strong well response to water injection. A waterflood front is not evident in actual production performance except possibly in Fig. E.9. Water injection is essentially providing a repressure response rather than a waterflood response. Well flowing pressure performance is therefore governed primarily by diffusion. Thus, the permeability of bodies comprising a small fraction of the reservoir volume cannot influence significantly well pressure behavior, no matter the magnitude of their permeability, as long as the bodies are not spatially concentrated at wells. Modeled super-k spatial distribution does not concentrate super-k bodies preferentially at wells.

The importance of the super-k reservoir volume fraction is demonstrated in Fig. F.27 to Fig. F.33. Here, the *original* permeability model is embedded with a super-k realization in which the volume fraction was increased from 18% to 50%. The permeability of the super-k is a constant 10000 md. The results are obtained from a single flow simulation; the optimization algorithm was not used since it was desired only to demonstrate the increased volume effect. The results are compared to those from the original permeability model. Note that in all eight wells, flow capacity is significantly

increased with the new permeability model. Indeed, the well performance plots indicate that the 50% fraction is too high, given the super-k permeability of 10000 md. It is evident that a lower volume fraction will improve the match. It's also evident that a volume fraction constrained to 18% may also provide an adequate match, if the super-k permeability was allowed to become an optimization parameter. Recall, however, that non super-k permeability is constrained to that of the original model, in these cases.

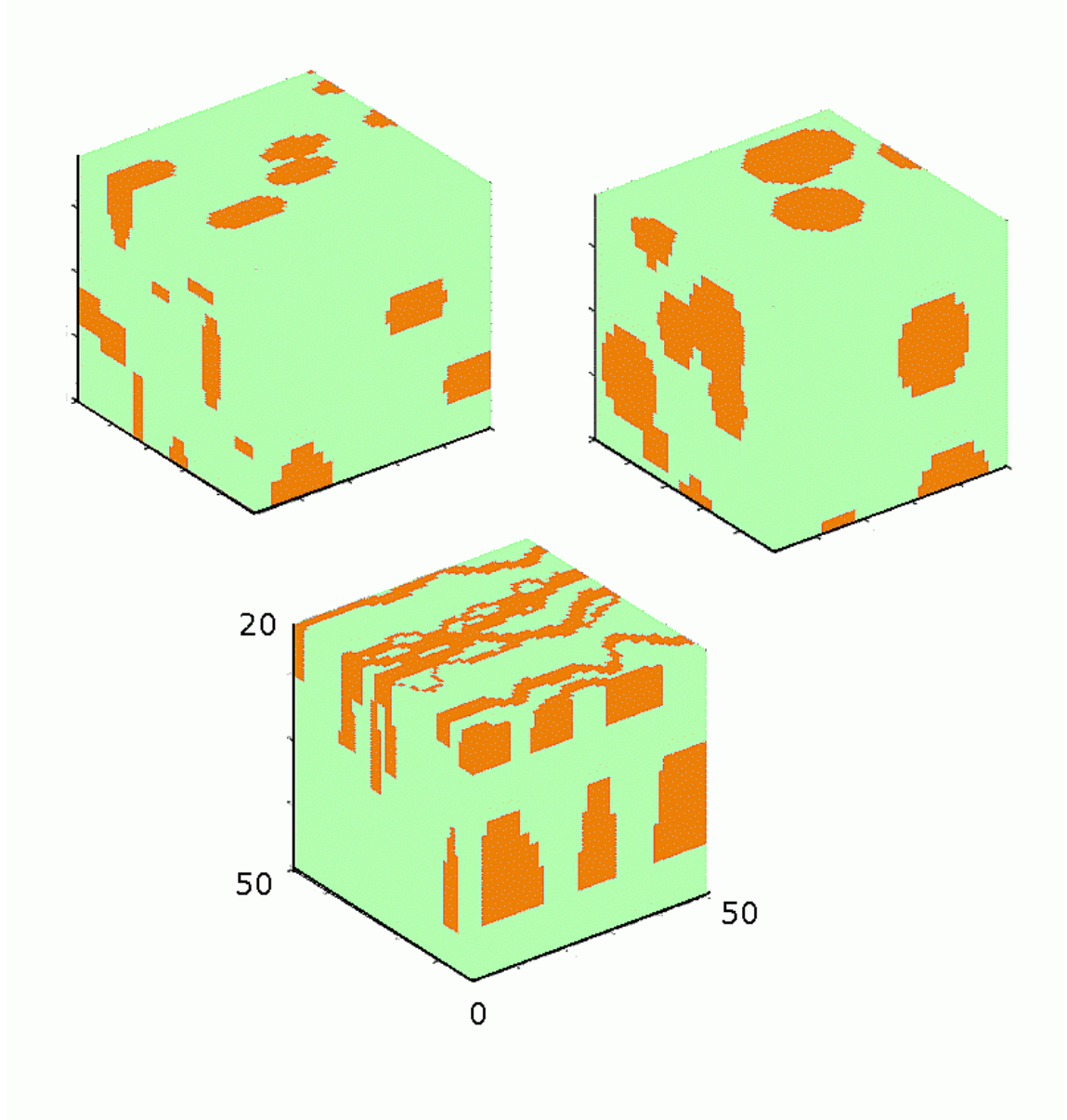

Fig. F.1: Super-k training images

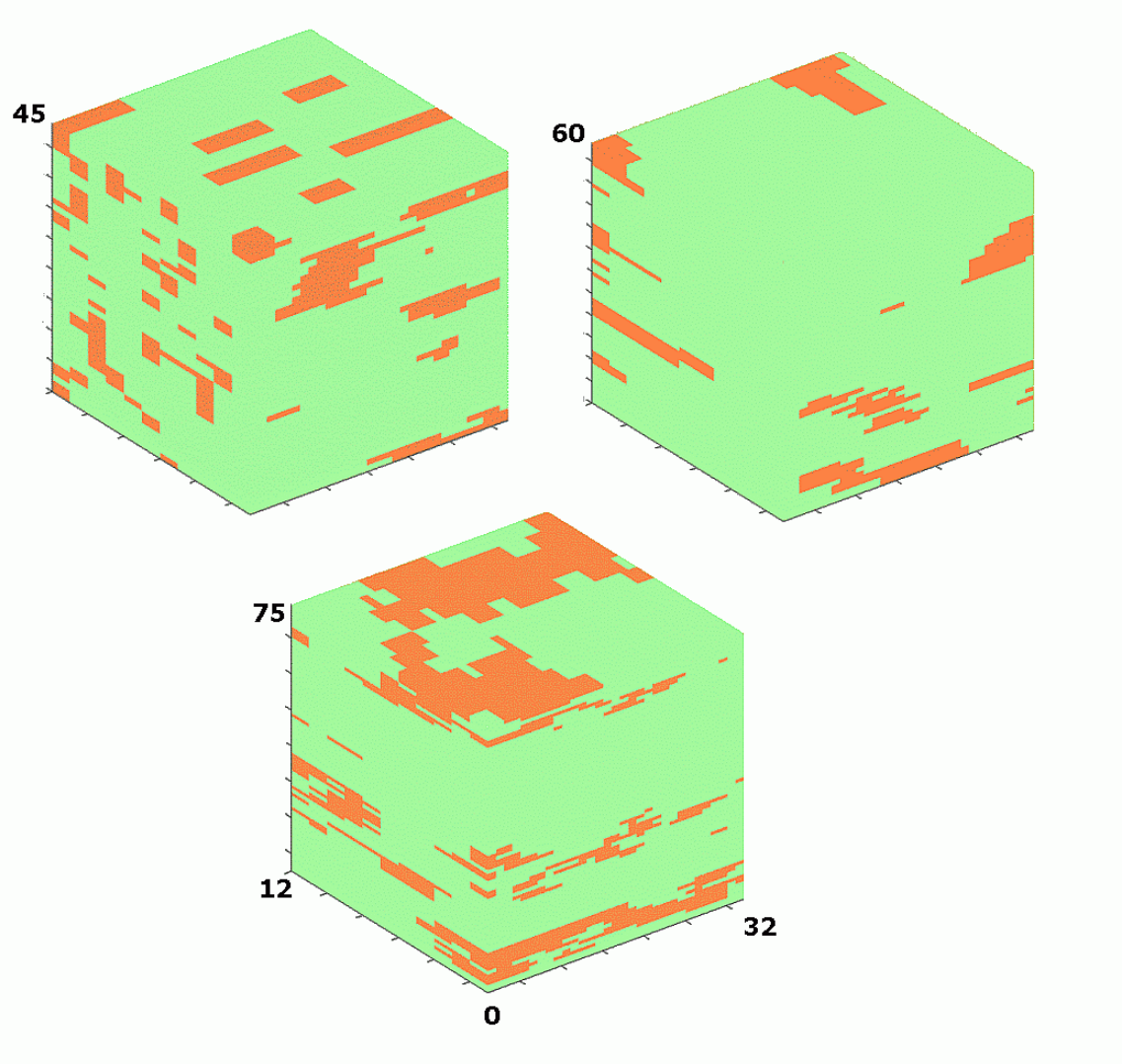

Fig. F.2: Zonal realizations

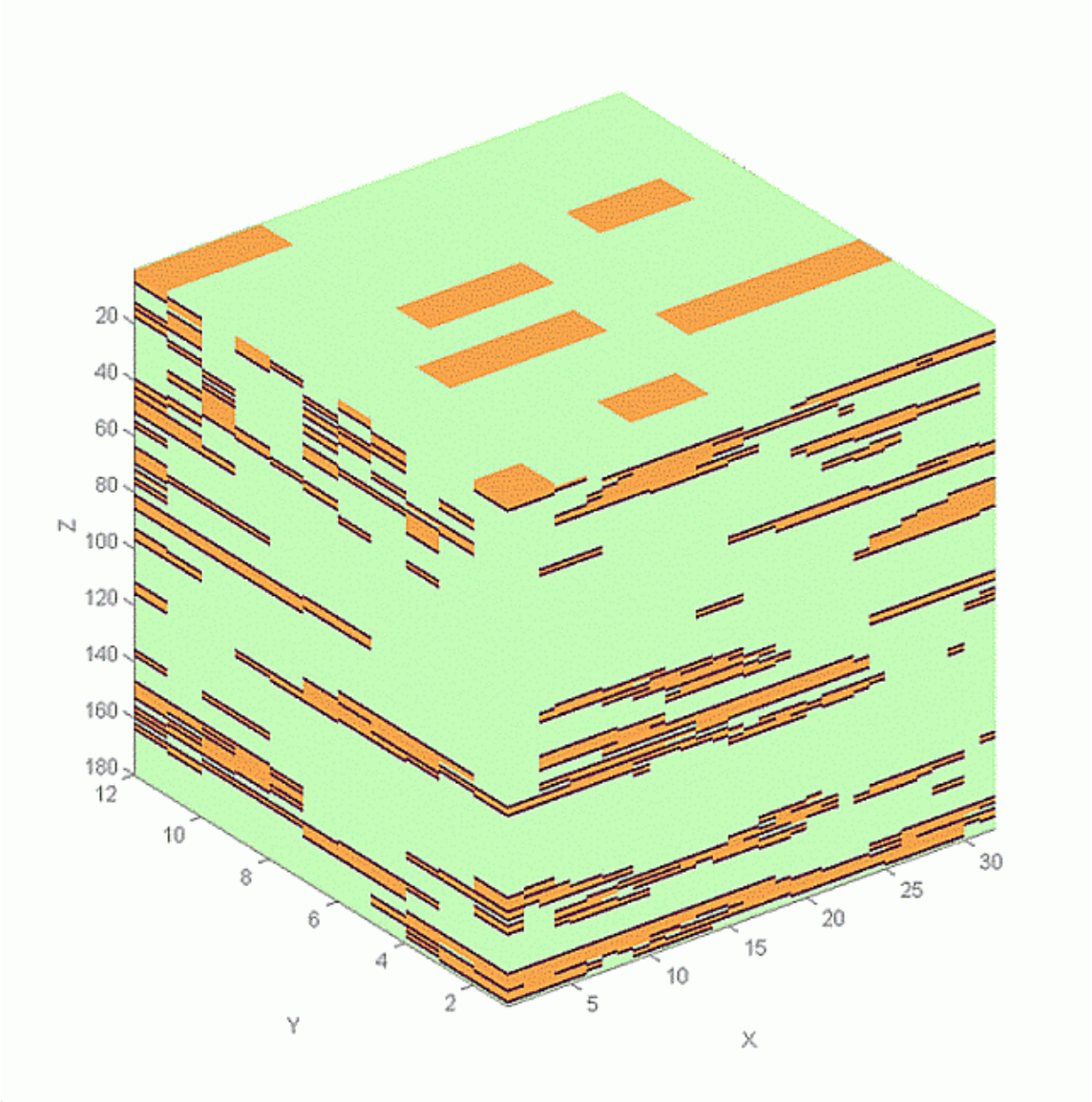

Fig. F.3: Combined zonal realizations

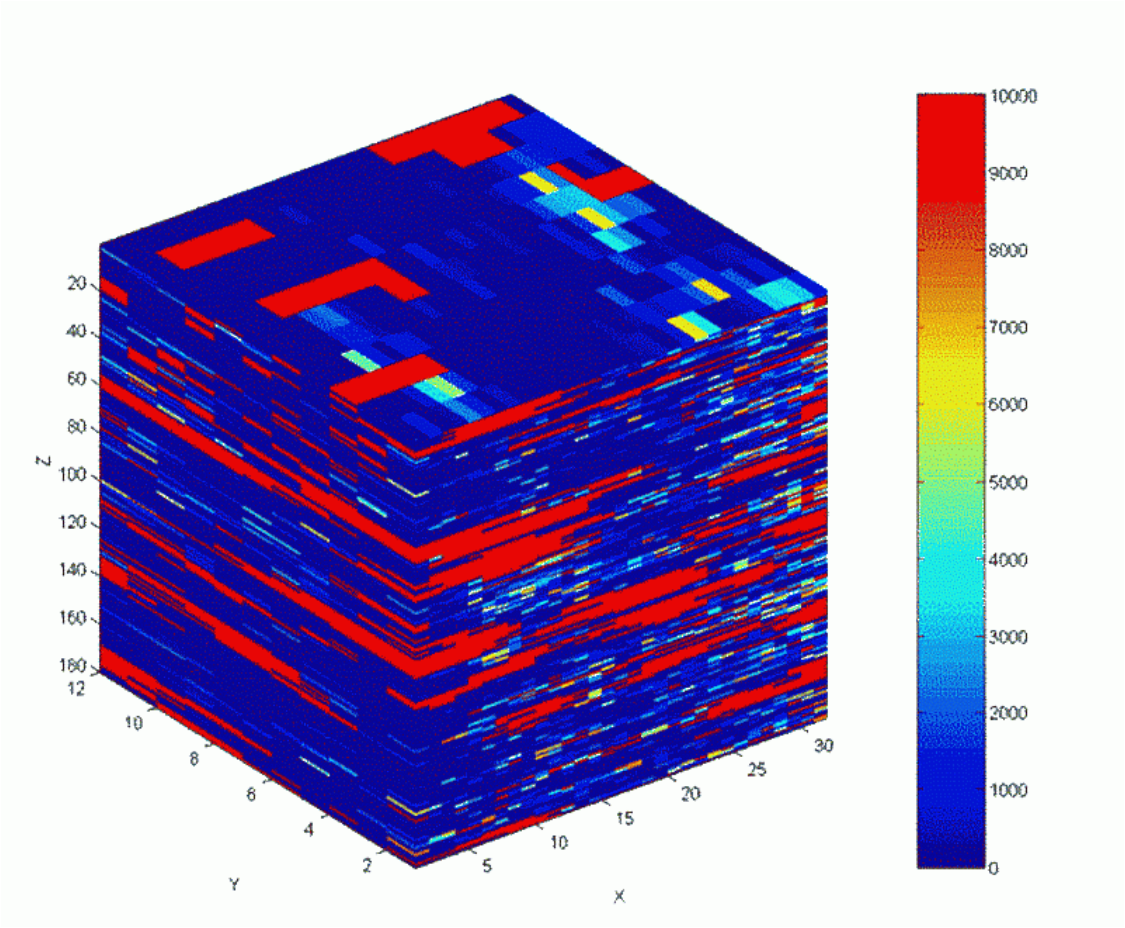

Fig. F.4: Permeability realization

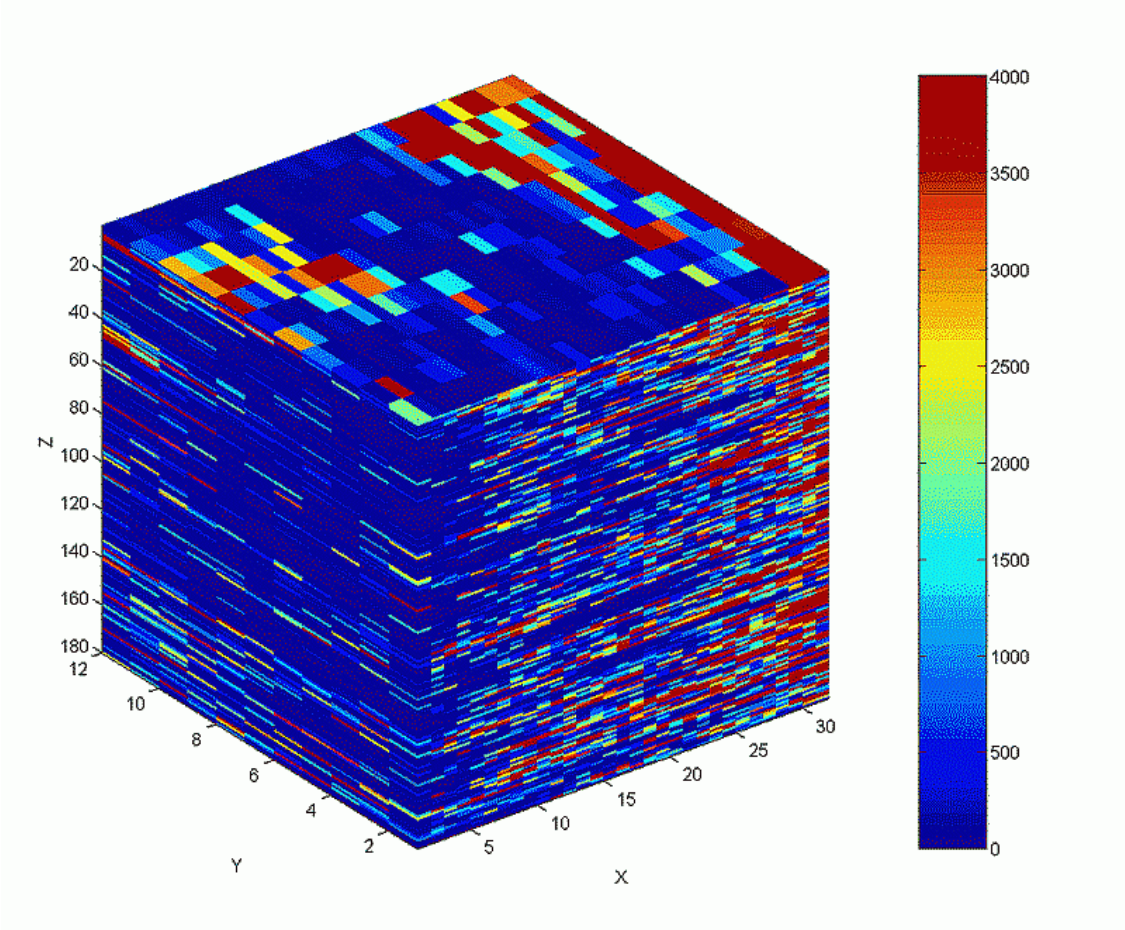

Fig. F.5: SGSIM permeability realization

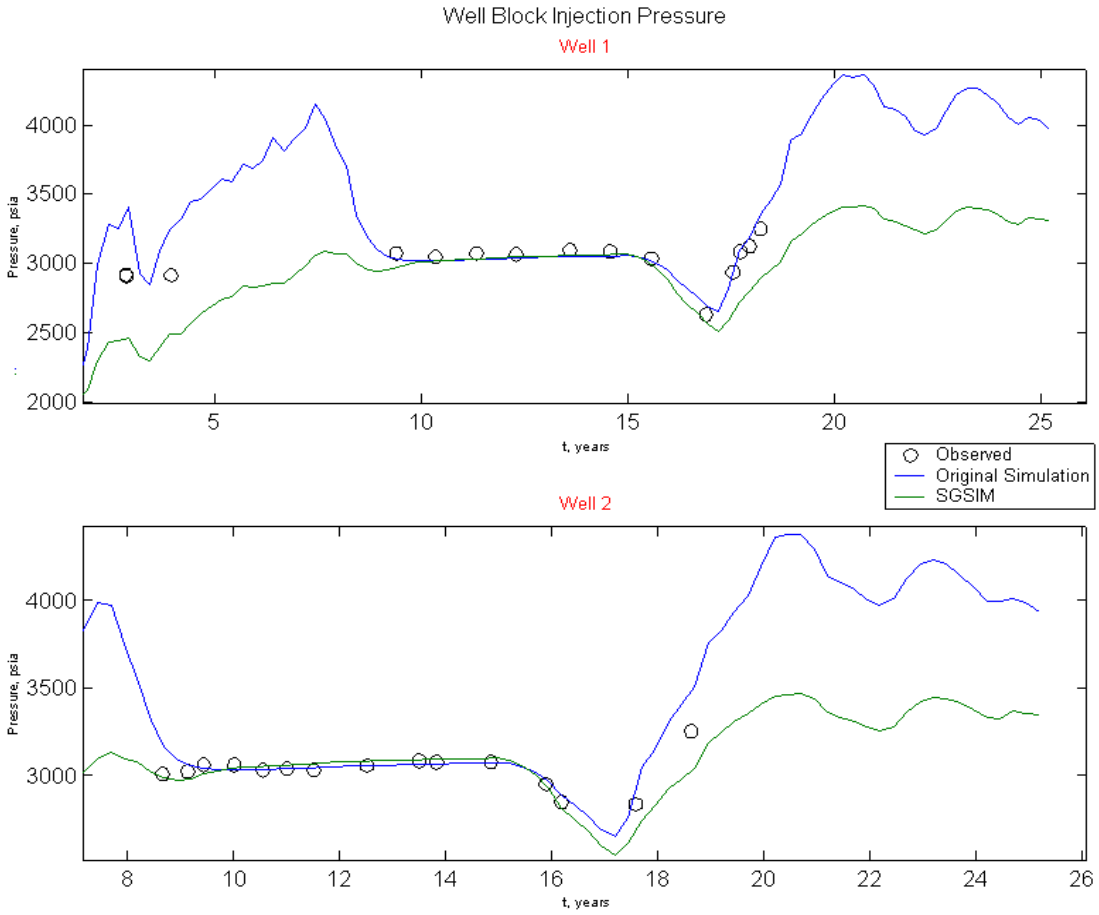

Fig. F.6: Match of SGSIM realization and original model

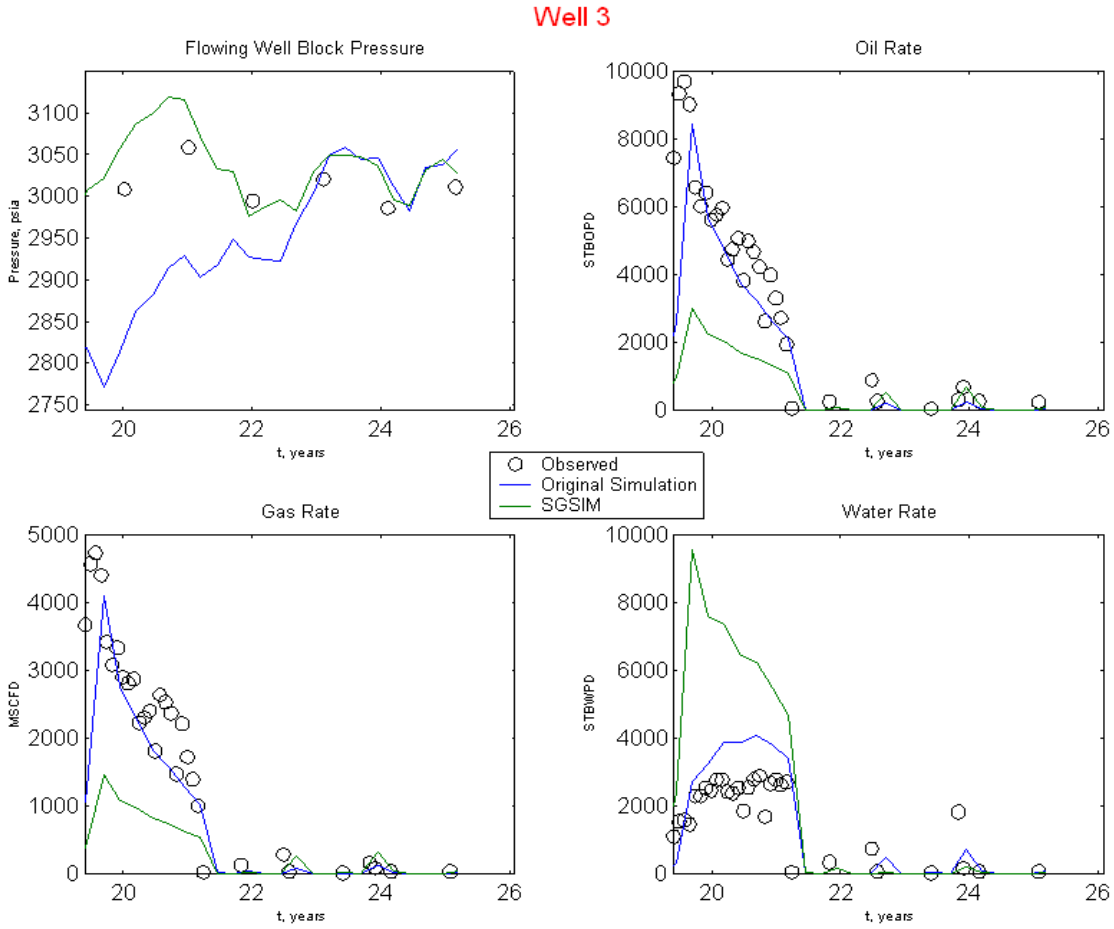

Fig. F.7: Match of SGSIM realization and original model

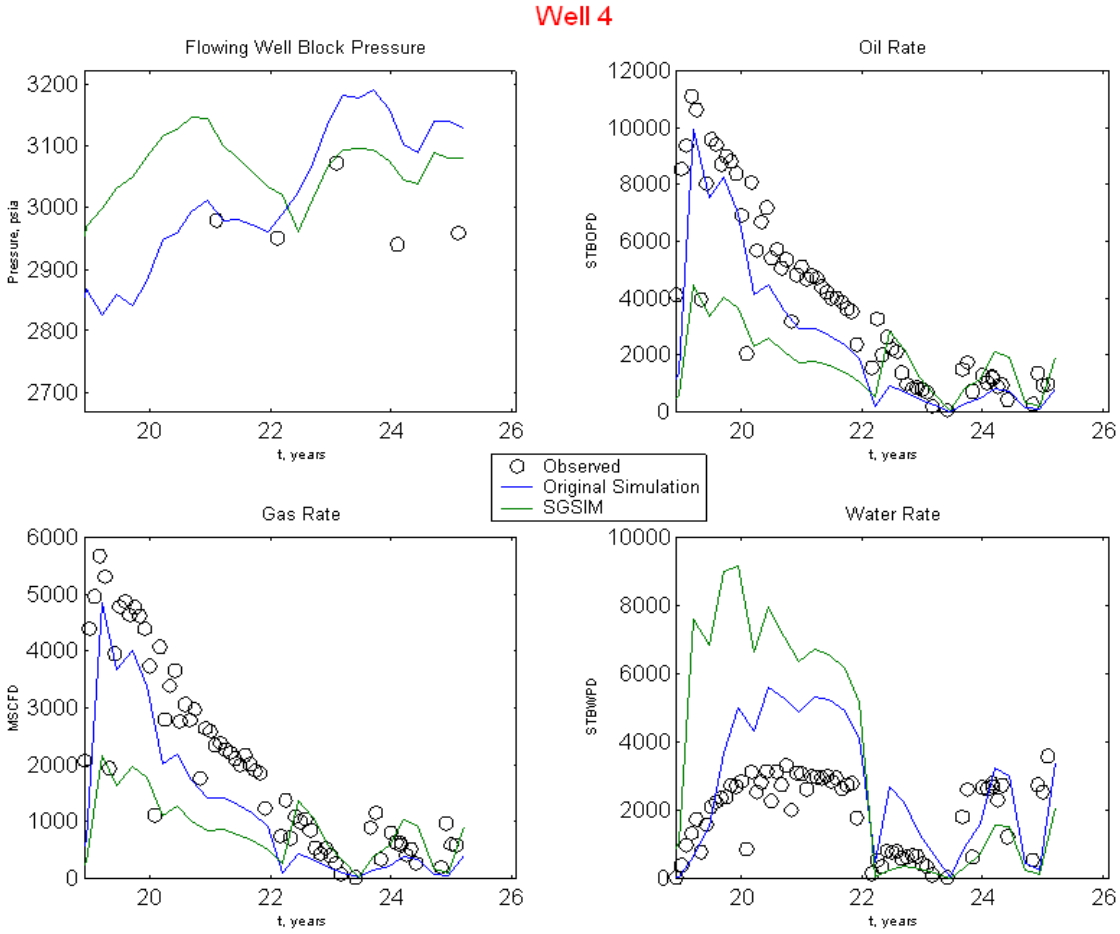

Fig. F.8: Match of SGSIM realization and original model

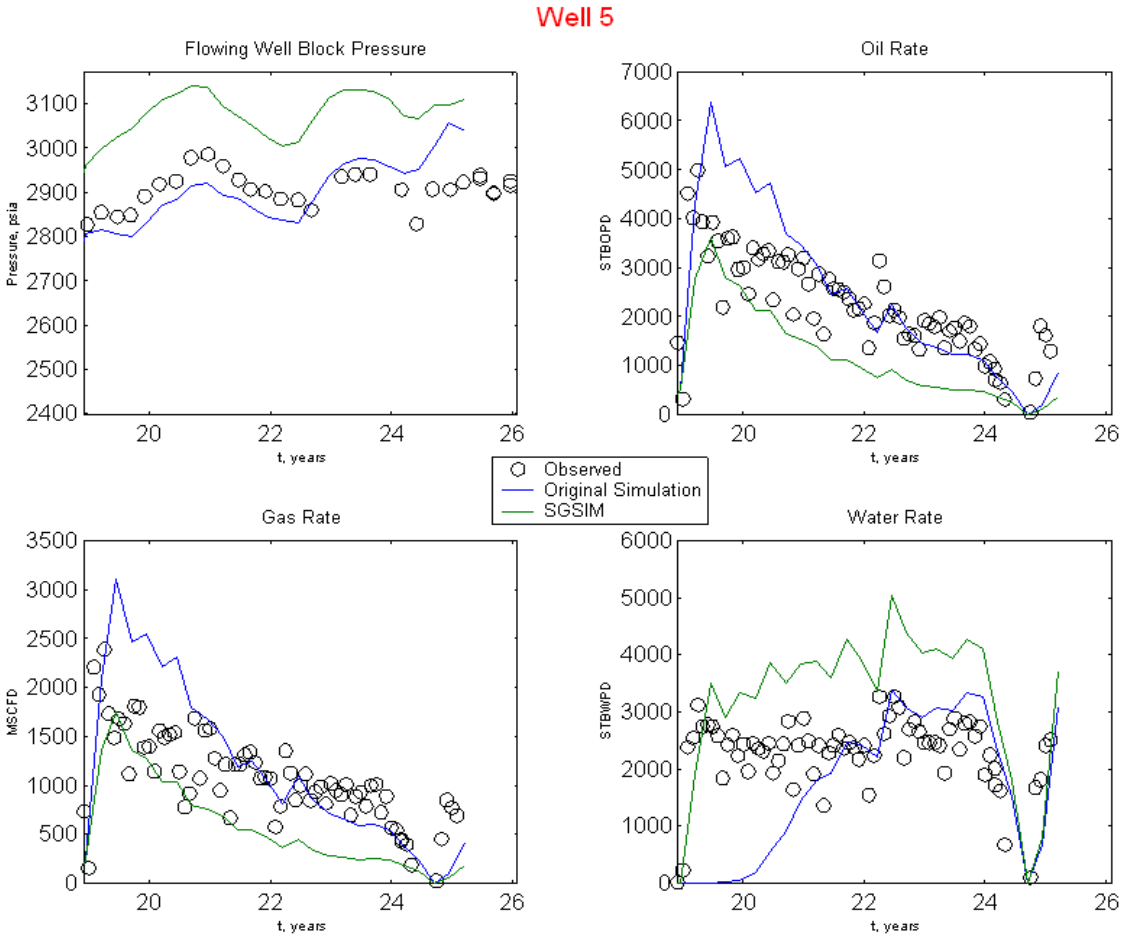

Fig. F.9: Match of SGSIM realization and original model

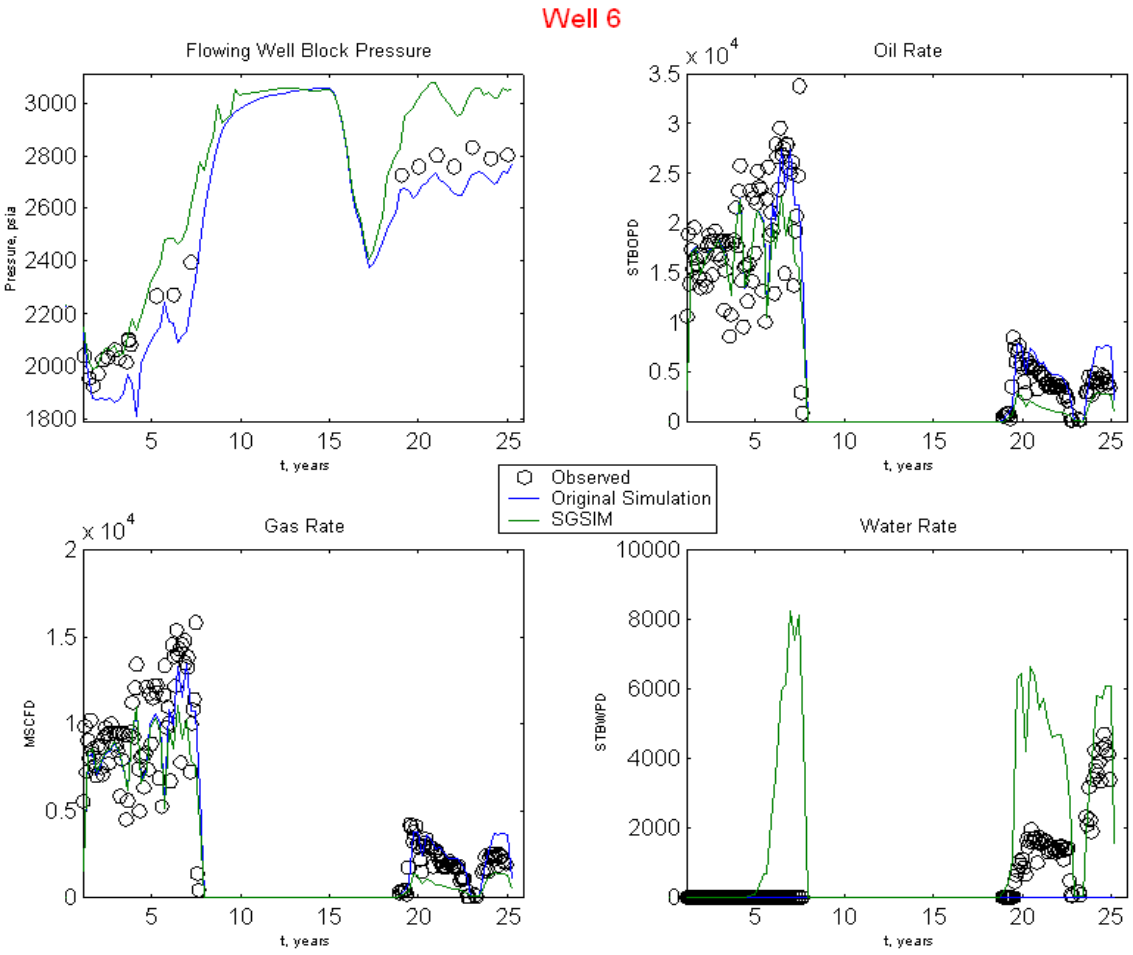

Fig. F.10: Match of SGSIM realization and original model

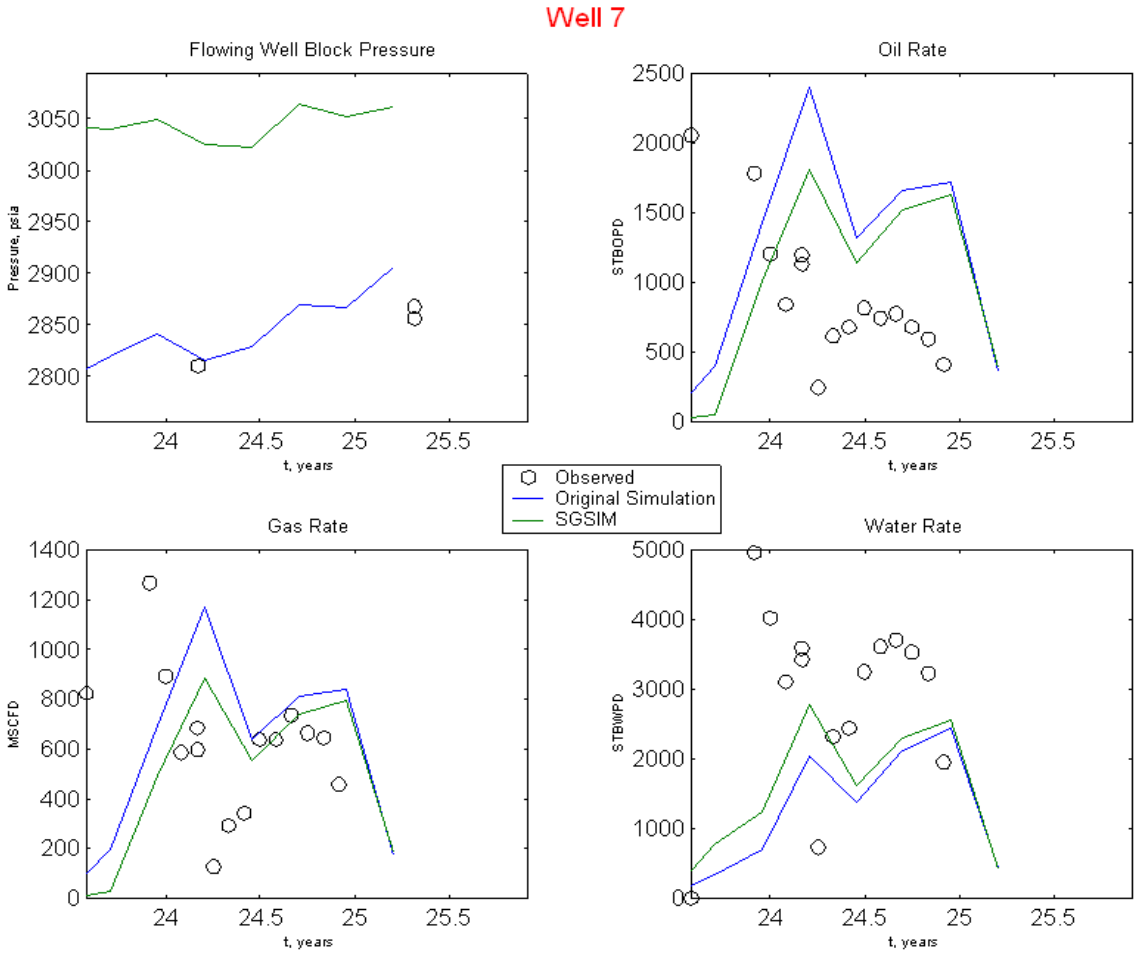

Fig. F.11: Match of SGSIM realization and original model

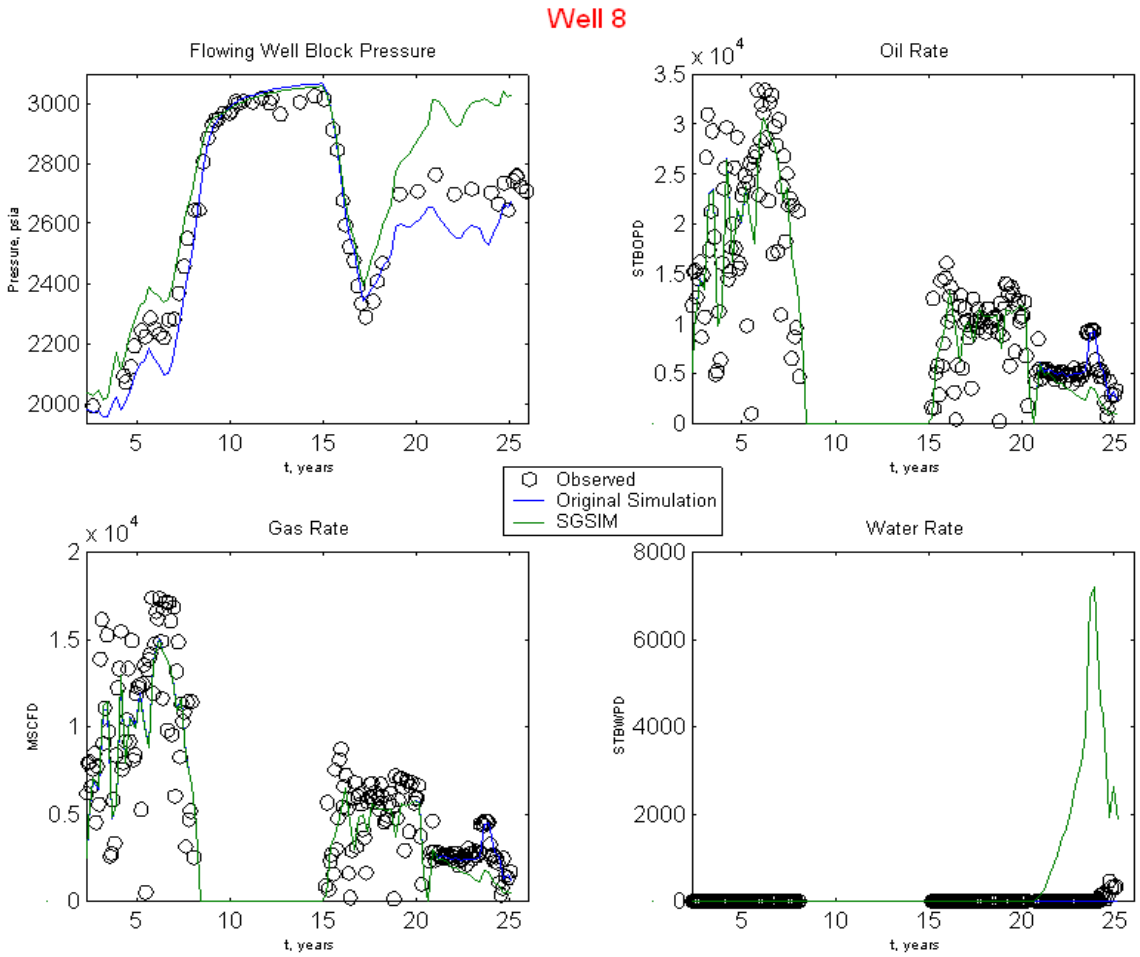

Fig. F.12: Match of SGSIM realization and original model

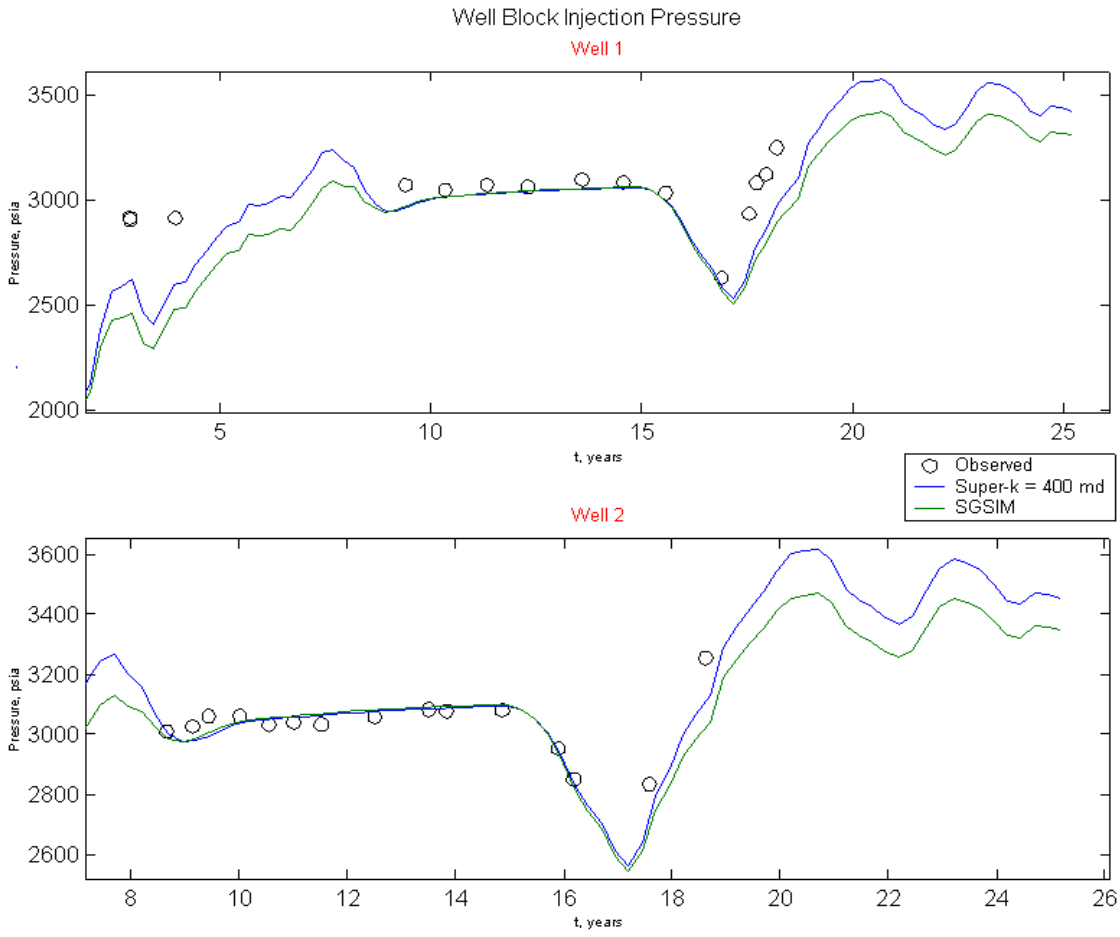

Fig. F.13: Match of super-k model with constant permeability = 400 md.

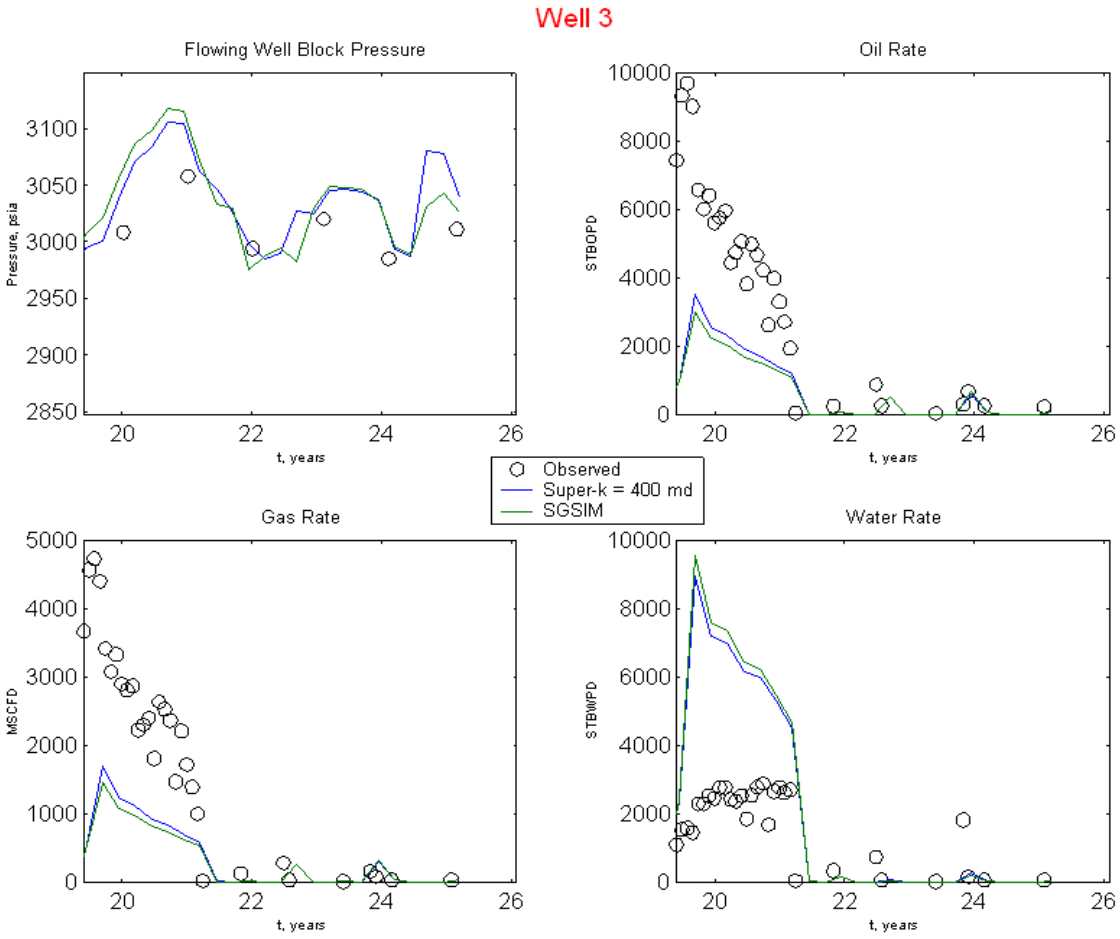

Fig. F.14: Match of super-k model with constant permeability = 400 md.

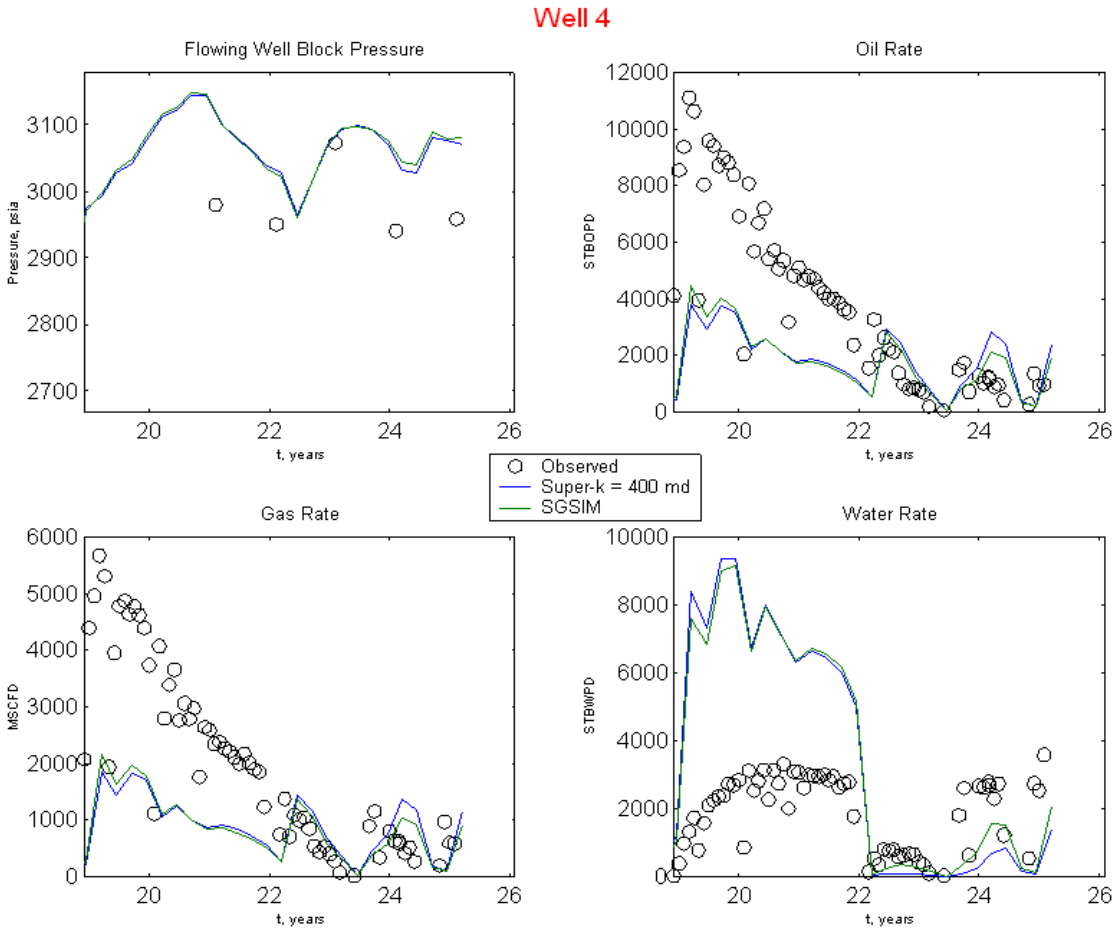

Fig. F.15: Match of super-k model with constant permeability = 400 md.

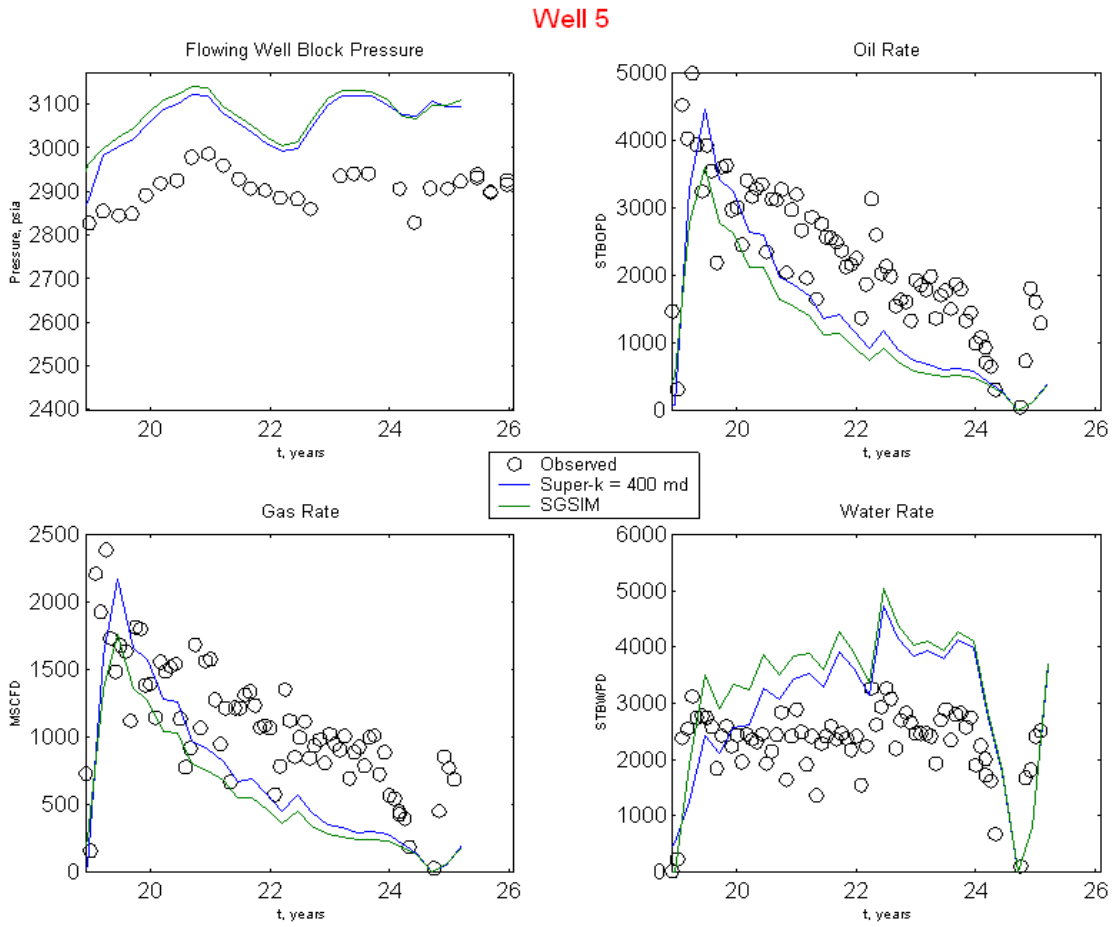

Fig. F.16: Match of super-k model with constant permeability = 400 md.

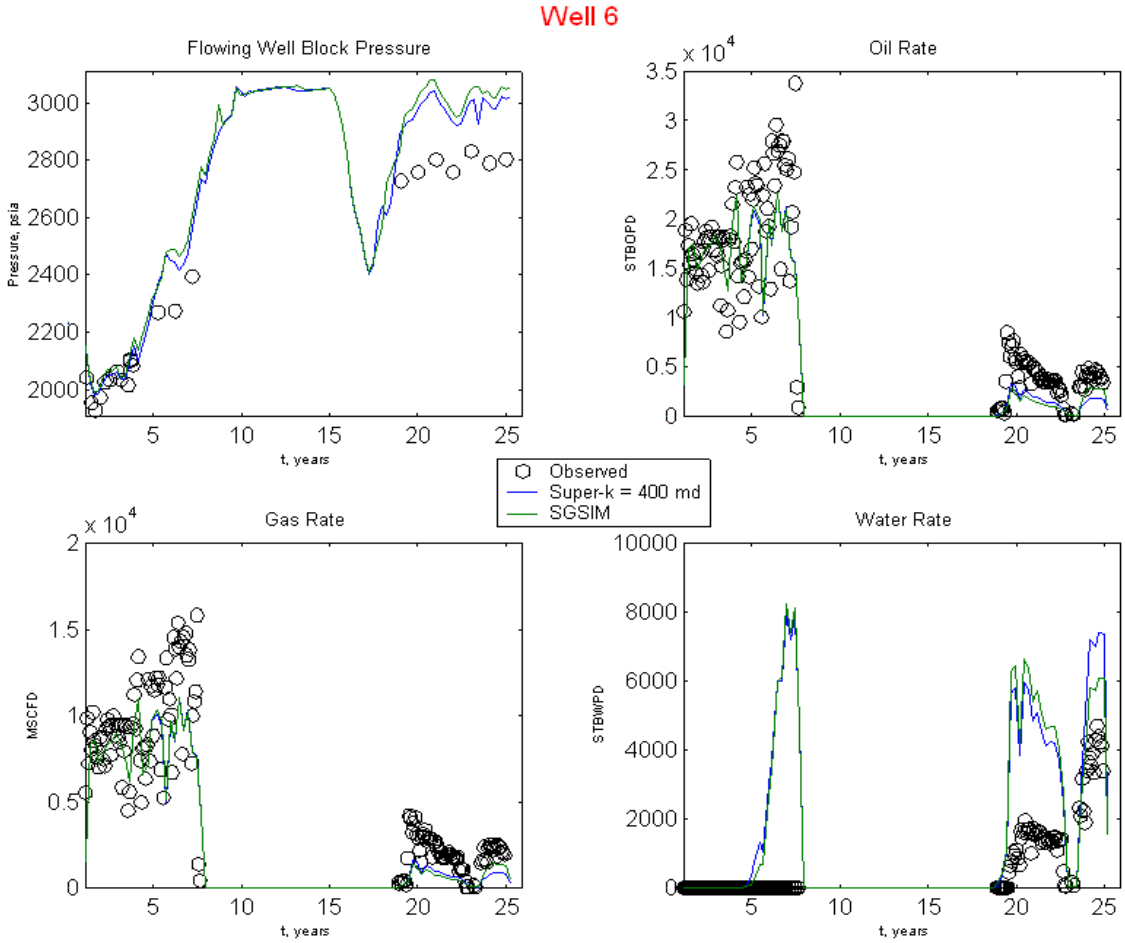

Fig. F.17: Match of super-k model with constant permeability = 400 md.

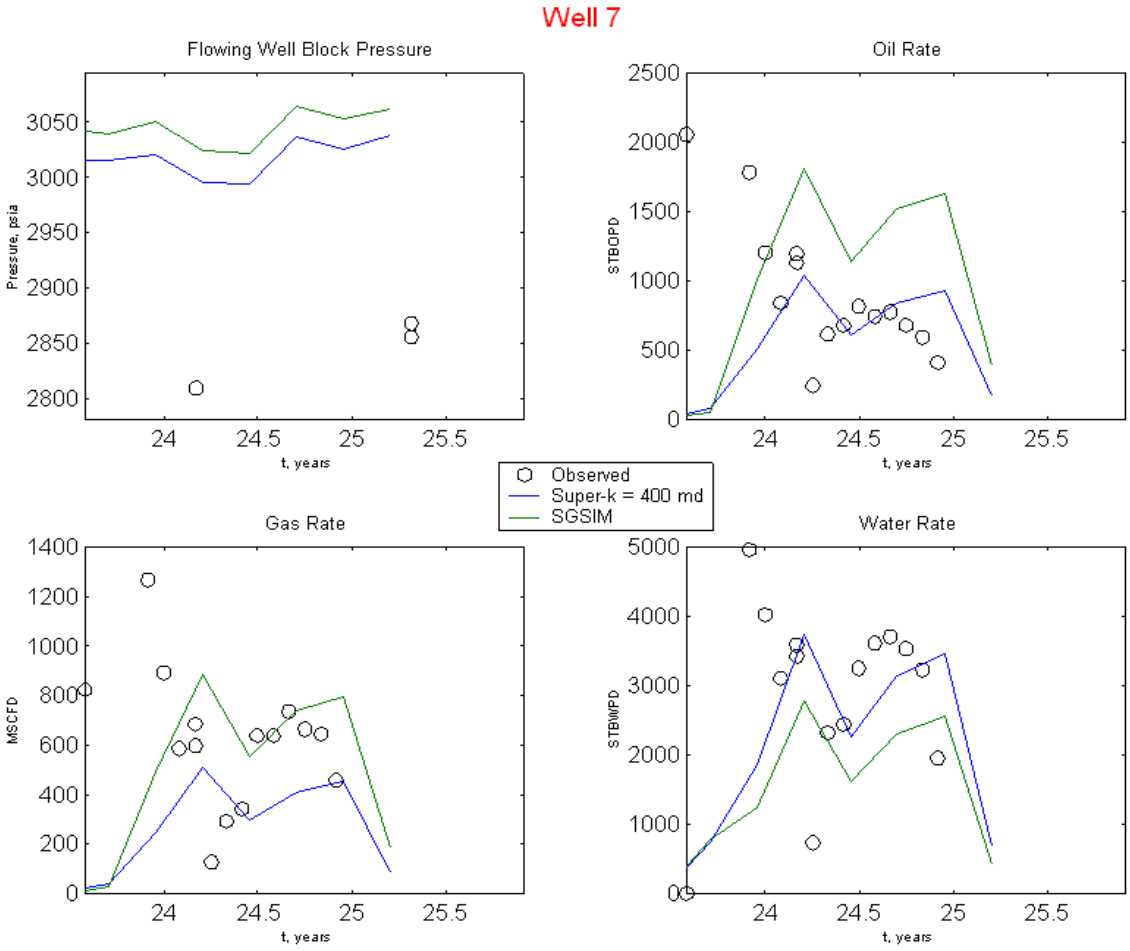

Fig. F.18: Match of super-k model with constant permeability = 400 md.

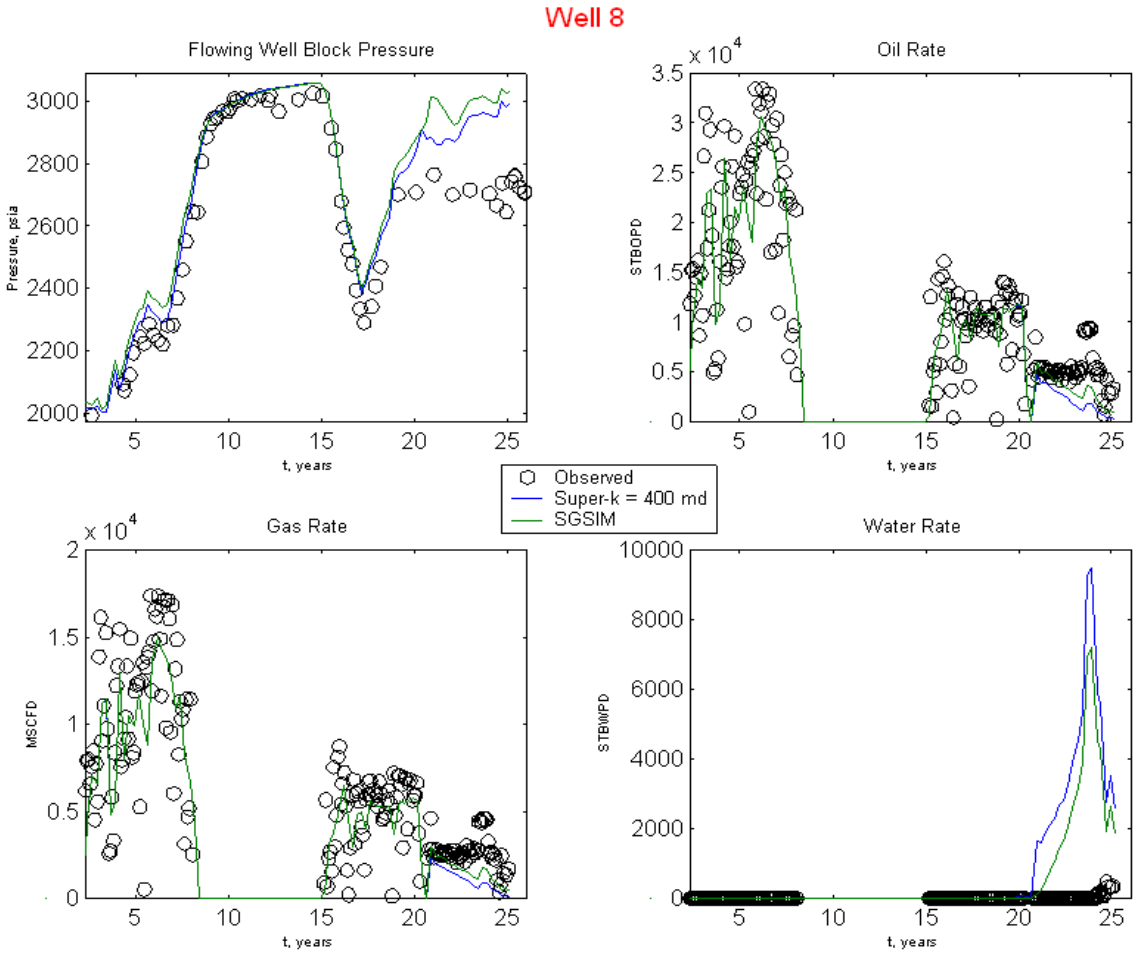

Fig. F.19: Match of super-k model with constant permeability = 400 md.

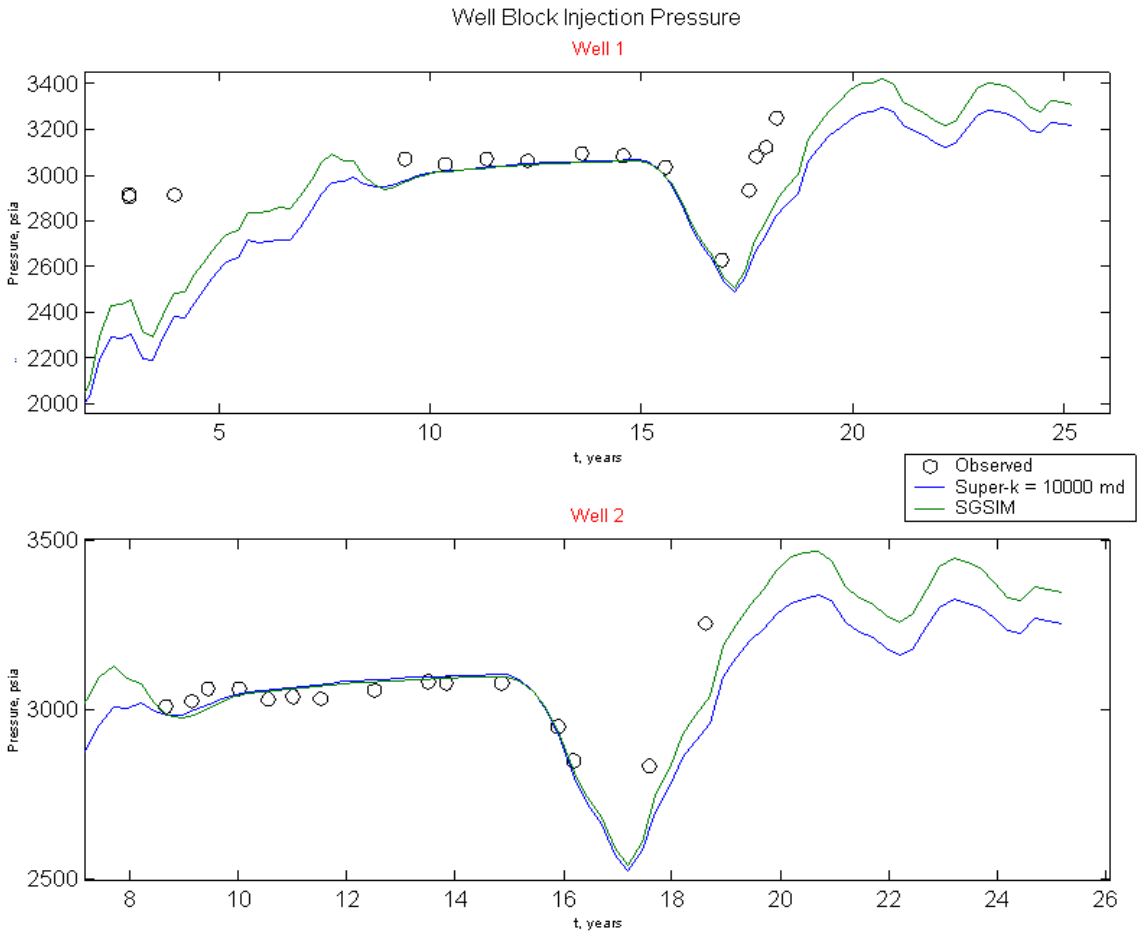

Fig. F.20: Match of super-k model with constant permeability = 10000 md.

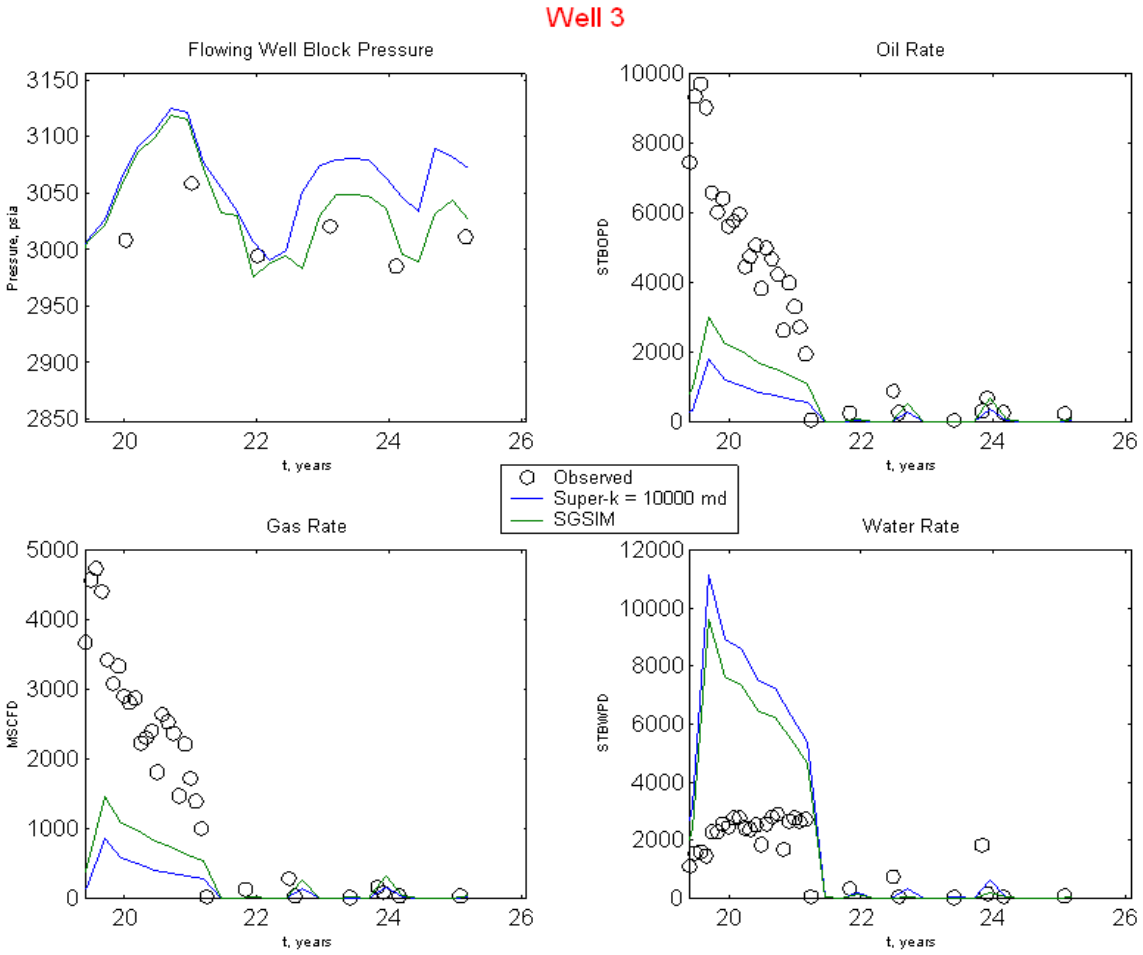

Fig. F.21: Match of super-k model with constant permeability = 10000 md.

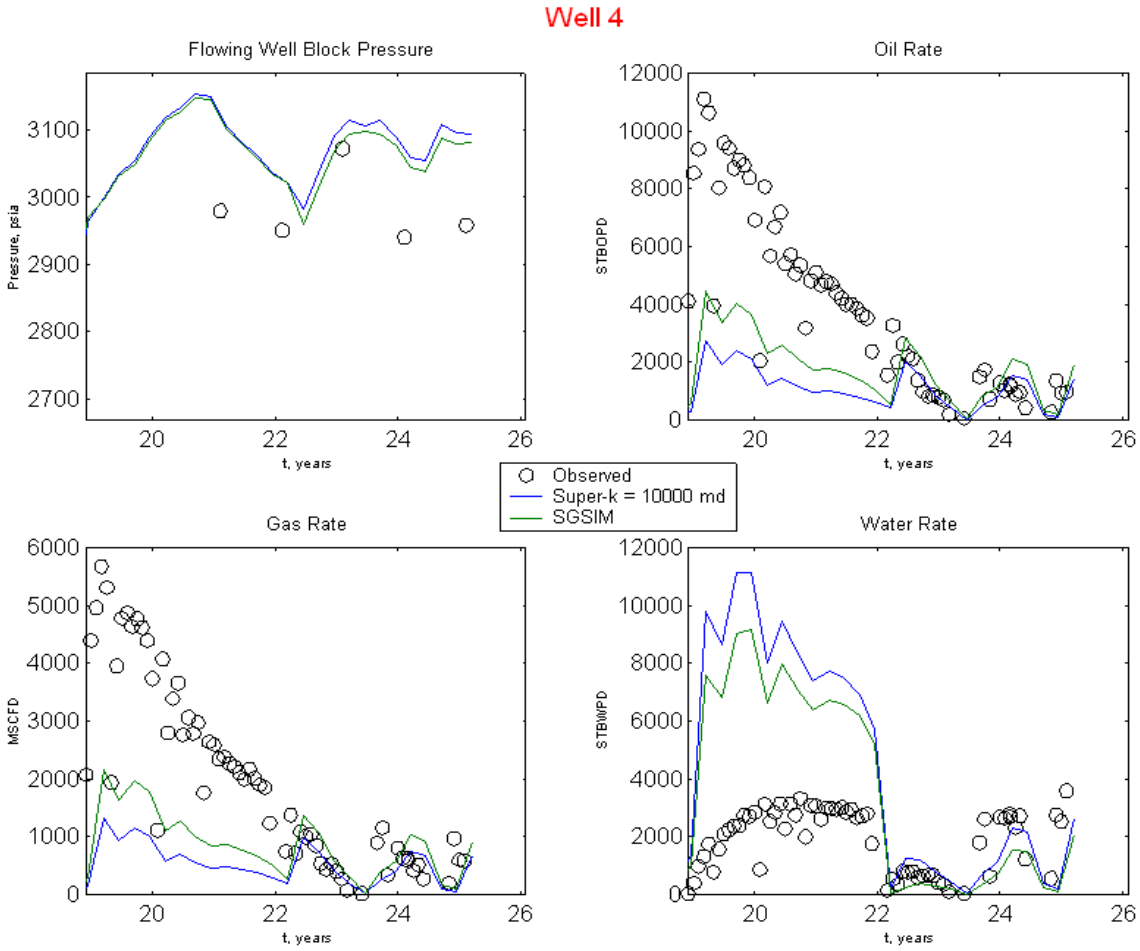

Fig. F.22: Match of super-k model with constant permeability = 10000 md.

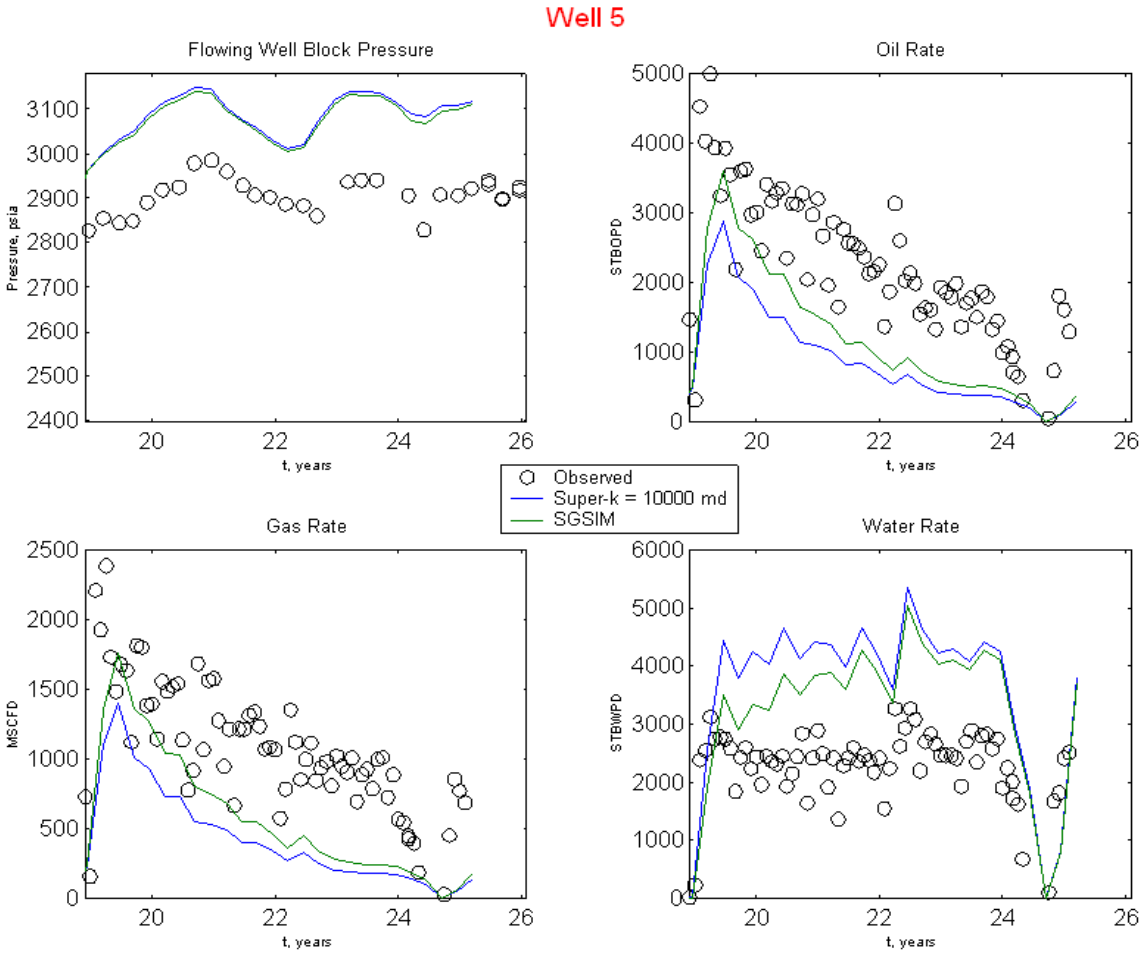

Fig. F.23: Match of super-k model with constant permeability = 10000 md.

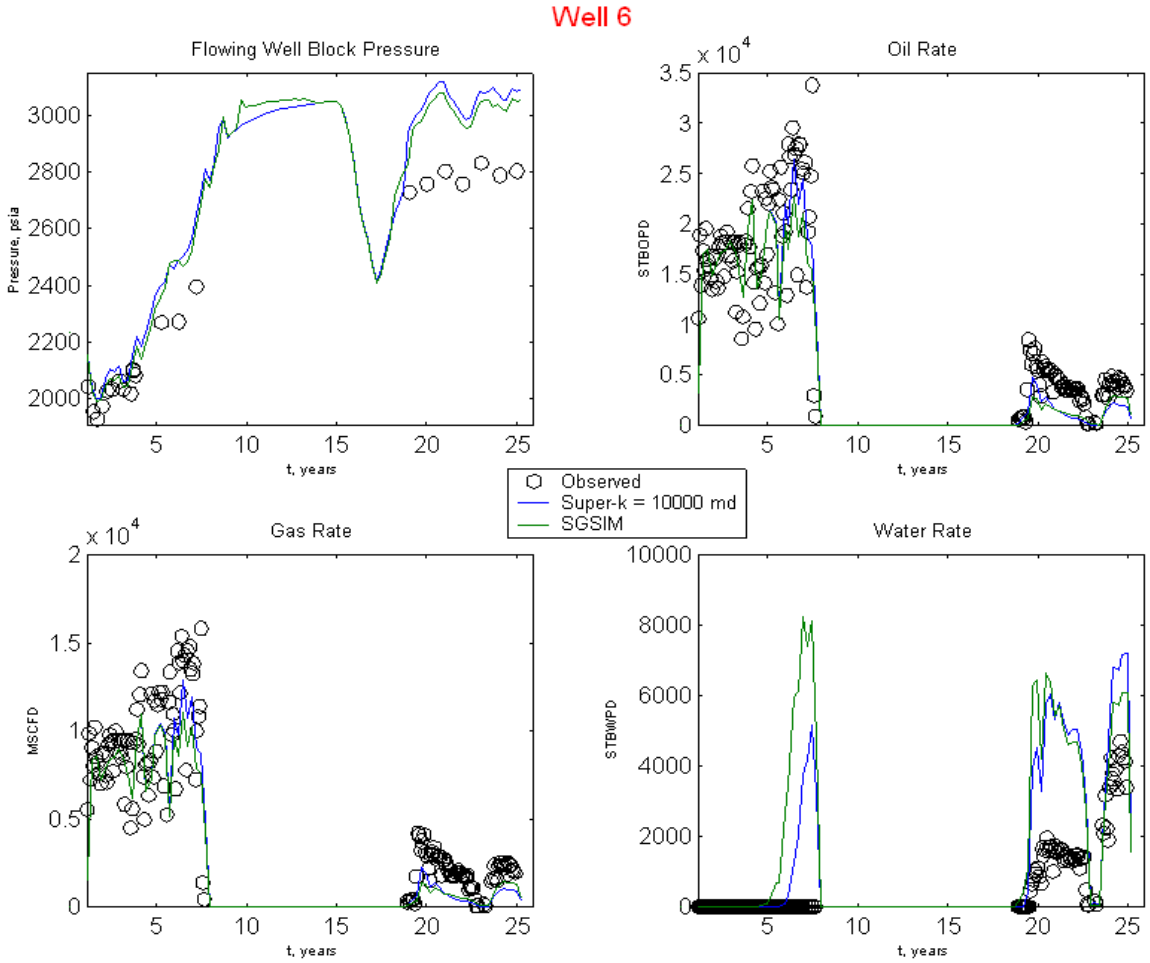

Fig. F.24: Match of super-k model with constant permeability = 10000 md.

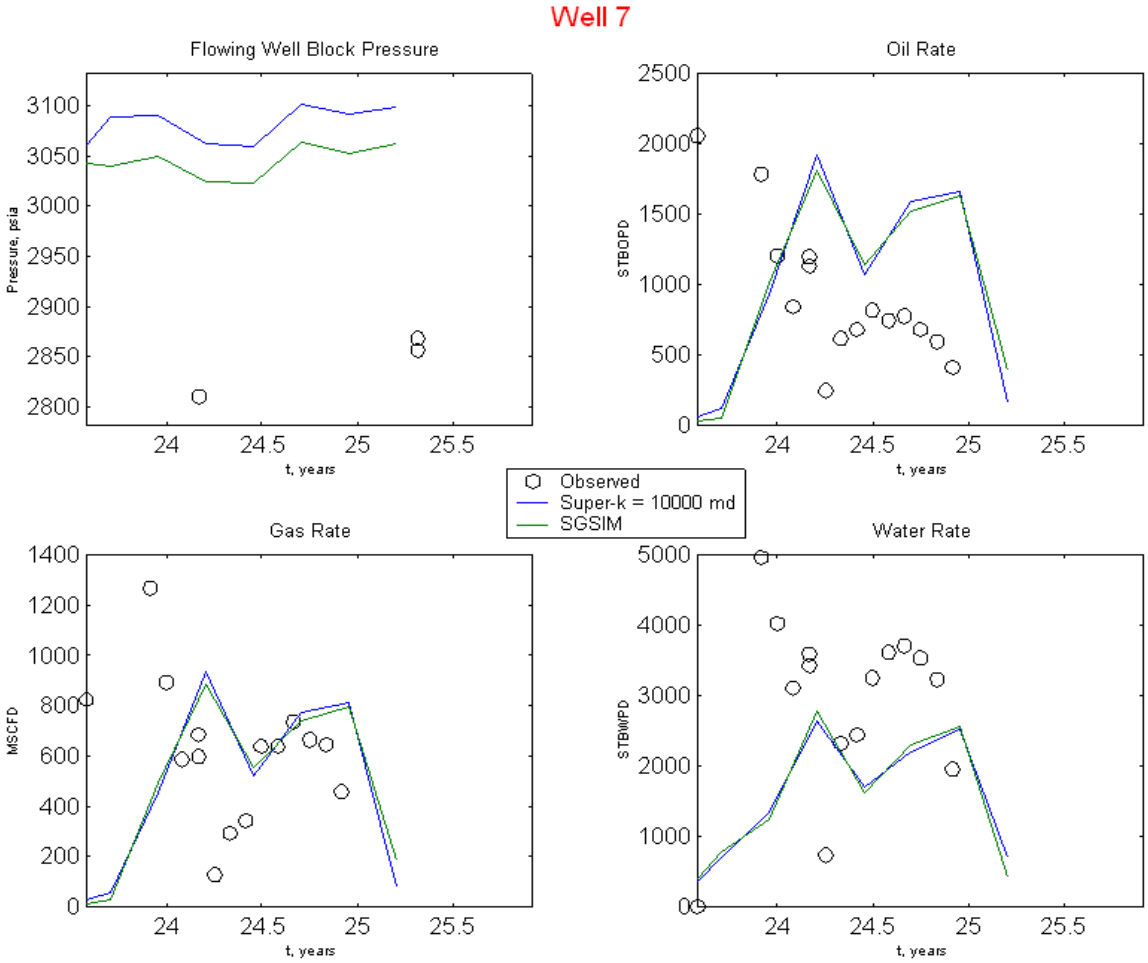

Fig. F.25: Match of super-k model with constant permeability = 10000 md.

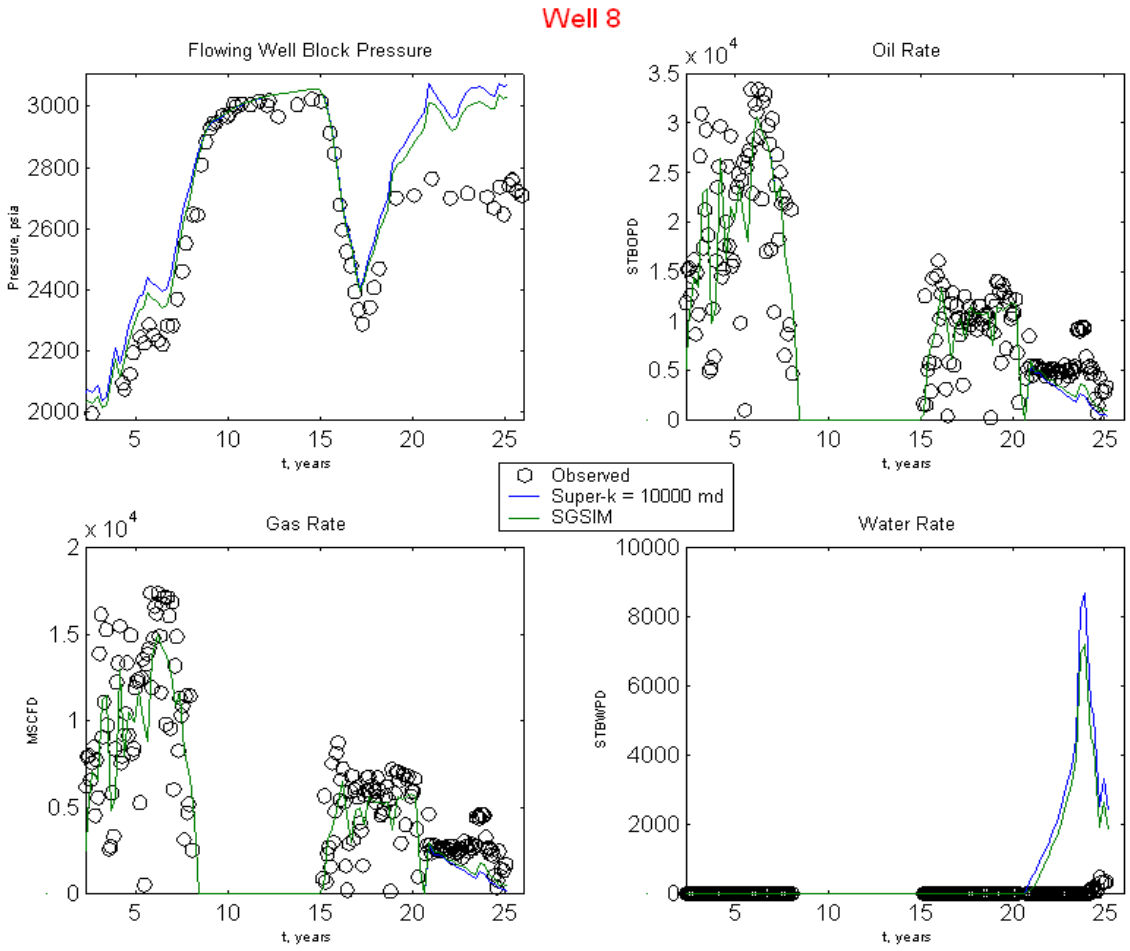

Fig. F.26: Match of super-k model with constant permeability = 10000 md.

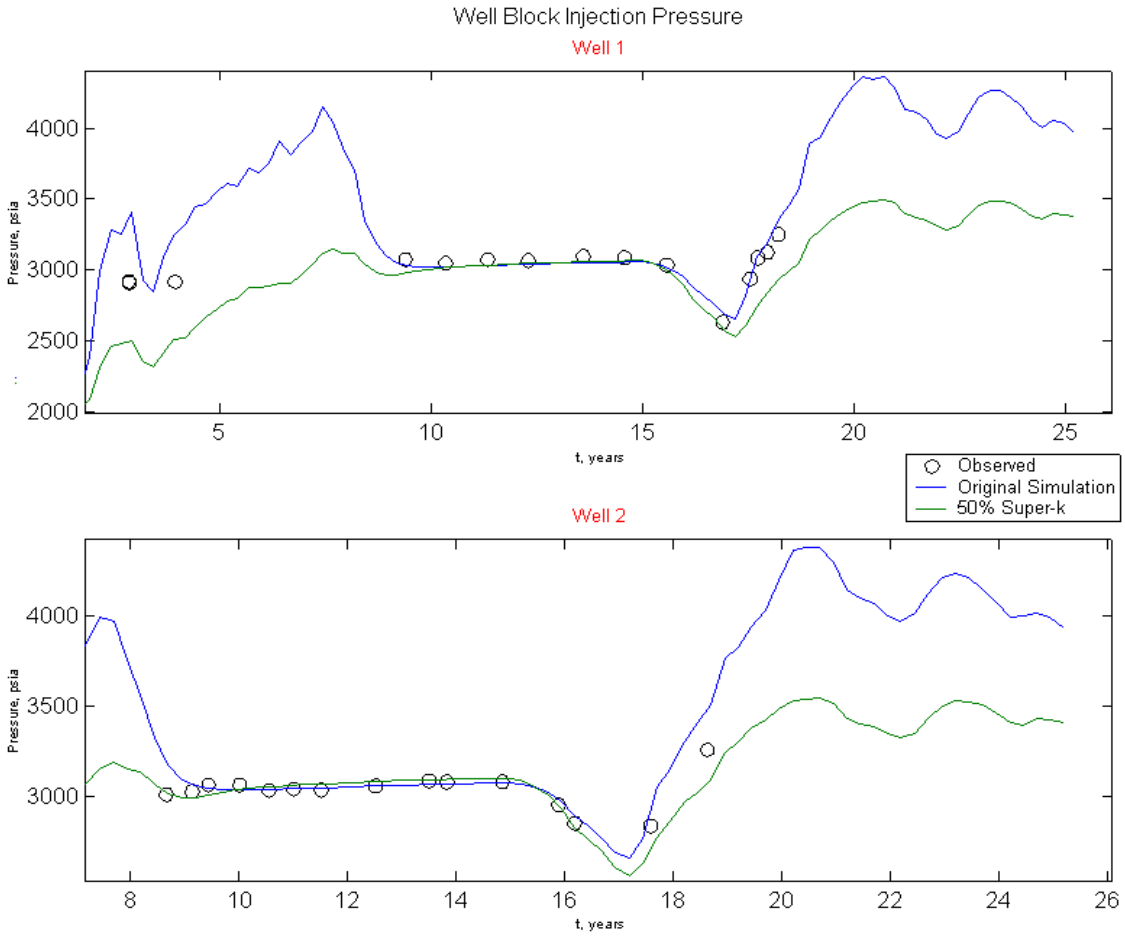

Fig. F.27: Match of 50% super-k model with constant permeability = 10000 md.

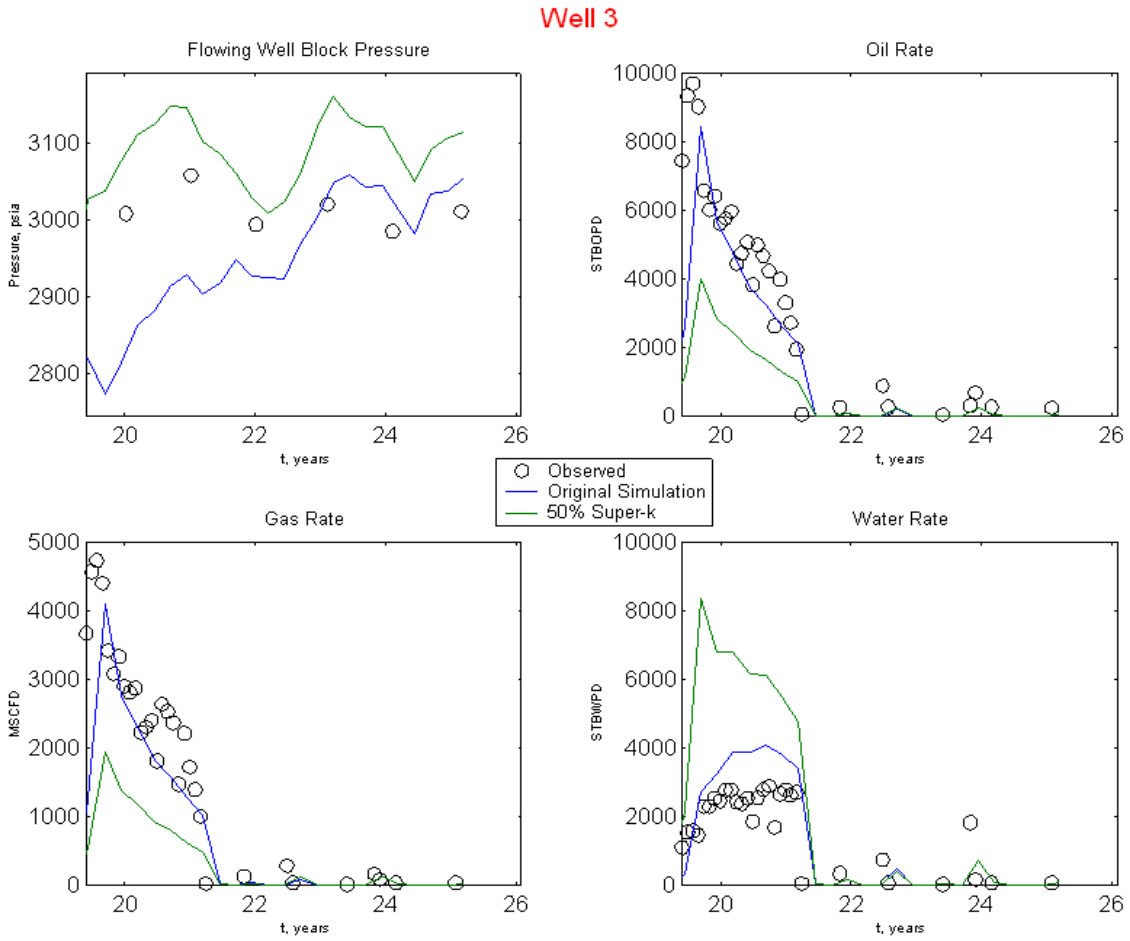

Fig. F.28: Match of 50% super-k model with constant permeability = 10000 md.

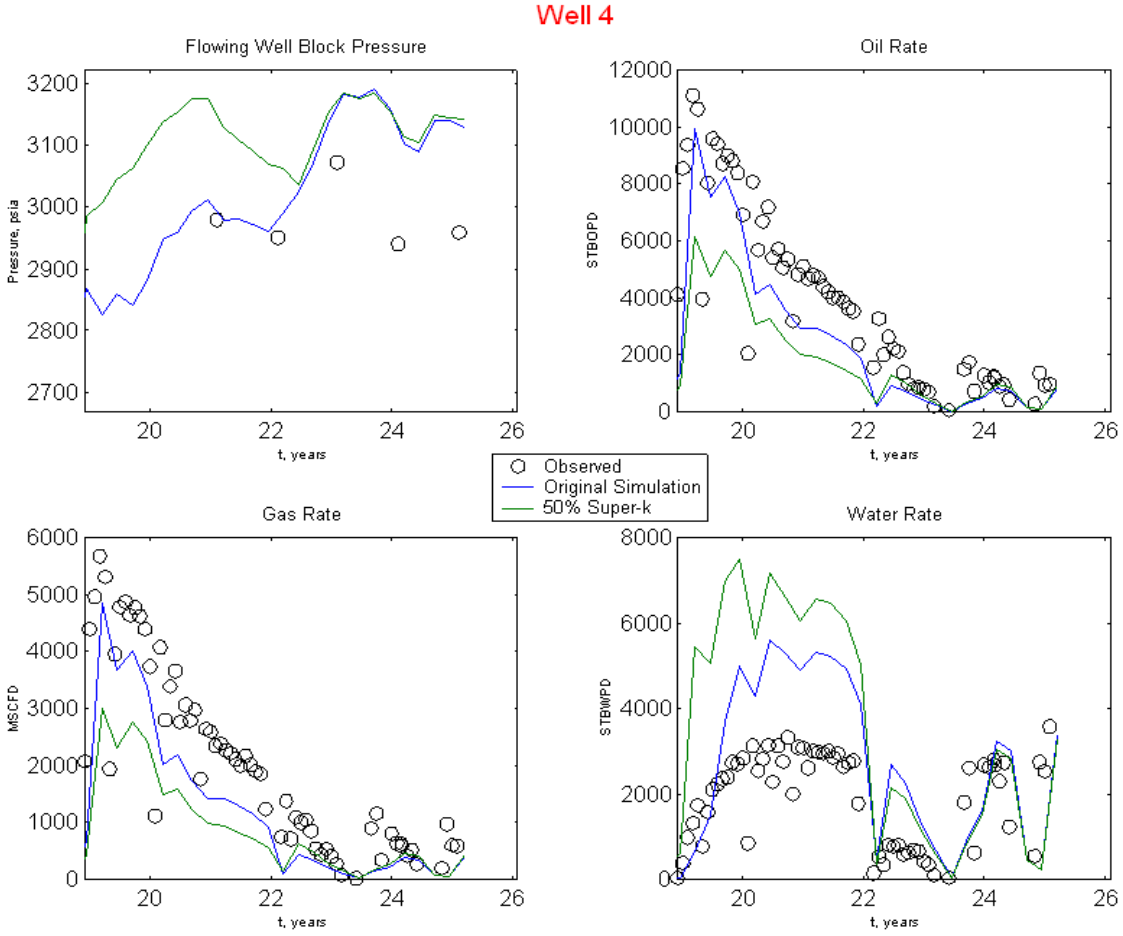

Fig. F.29: Match of 50% super-k model with constant permeability = 10000 md.

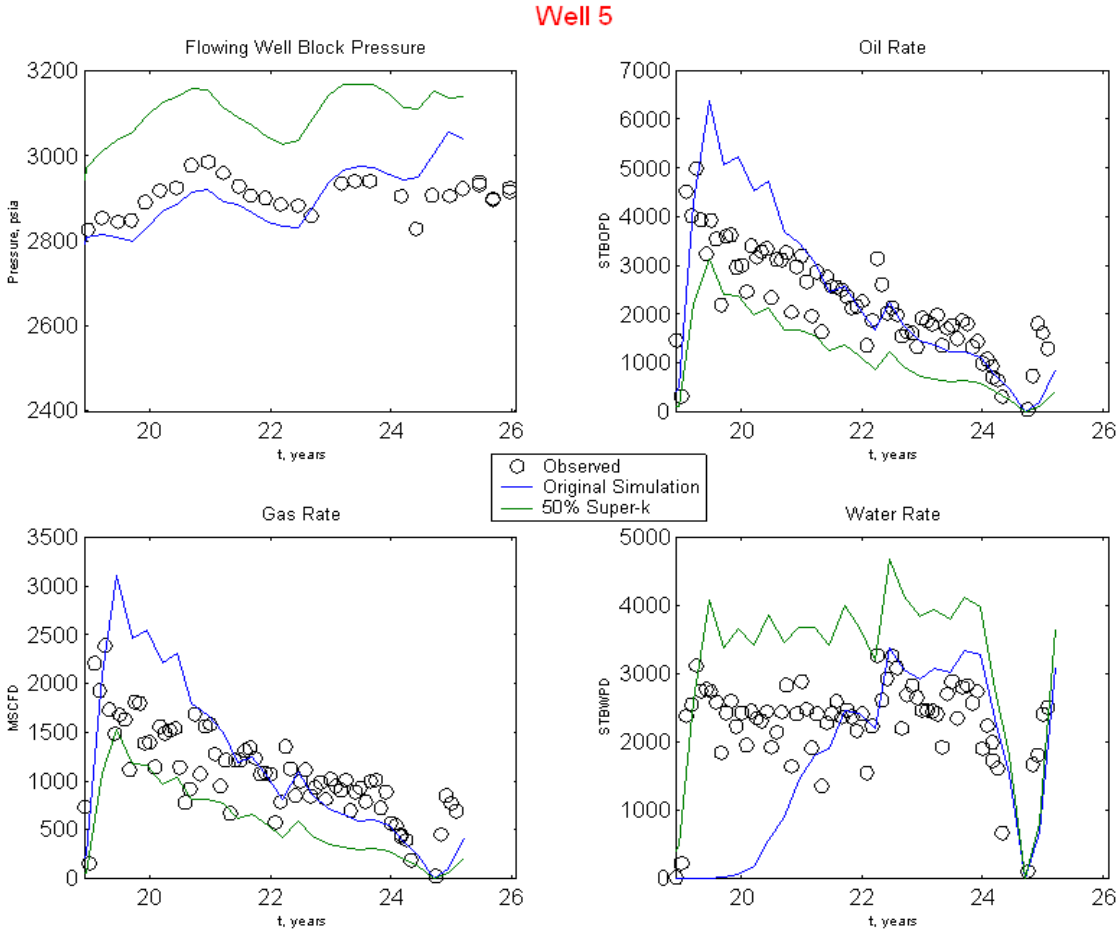

Fig. F.30: Match of 50% super-k model with constant permeability = 10000 md.

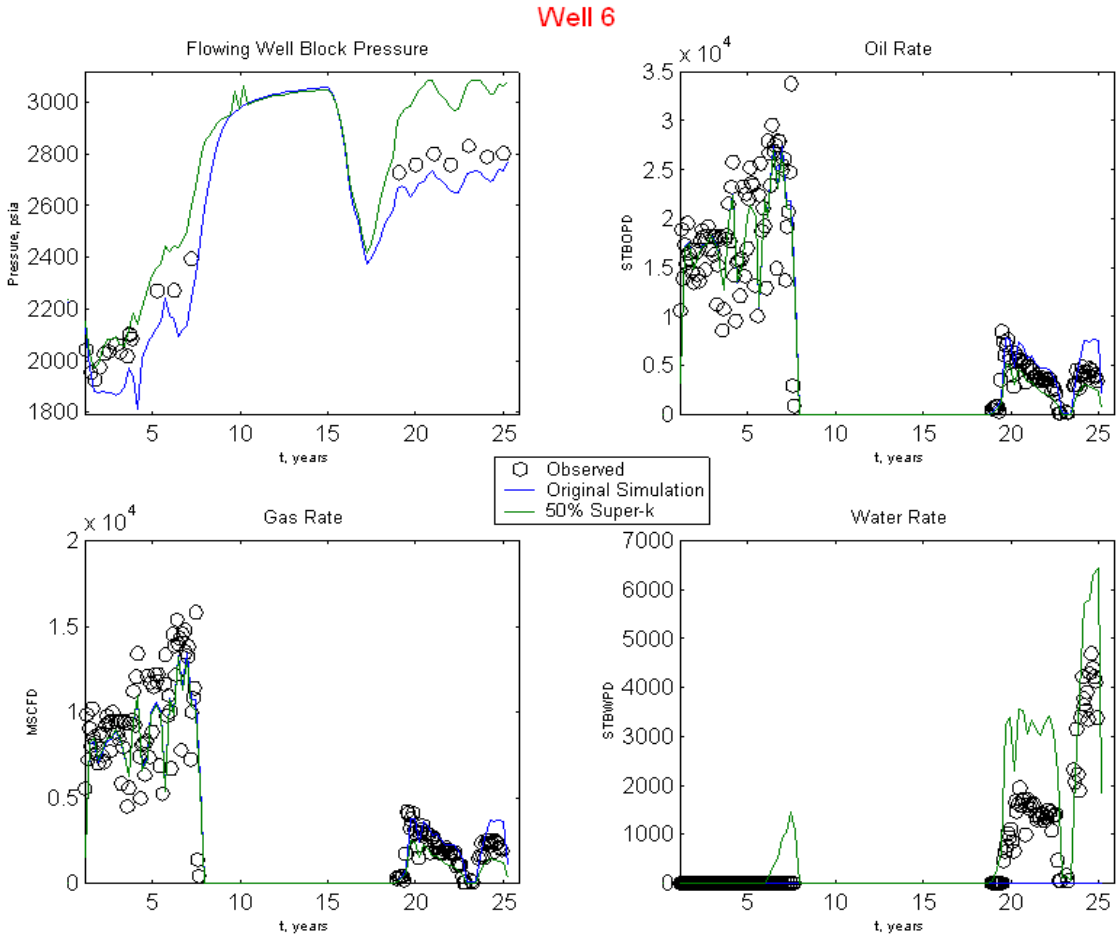

Fig. F.31: Match of 50% super-k model with constant permeability = 10000 md.

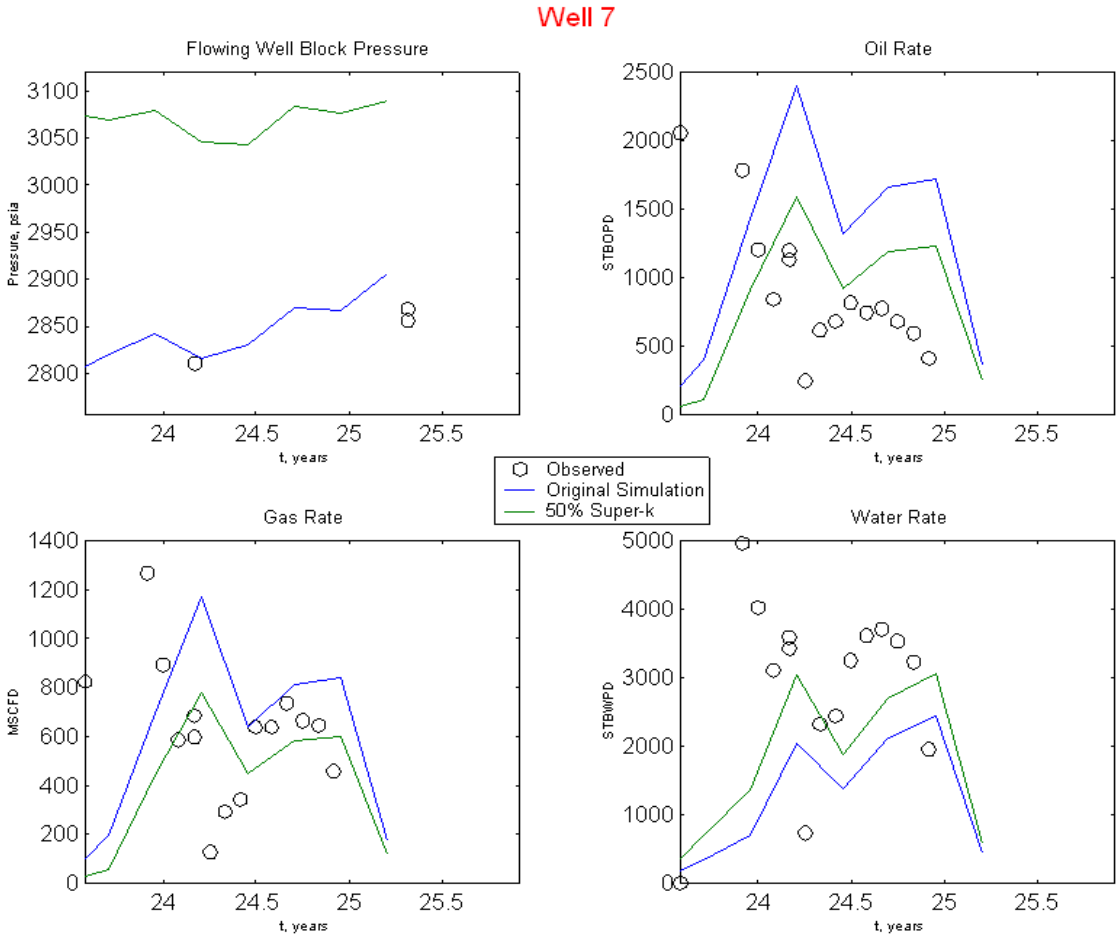

Fig. F.32: Match of 50% super-k model with constant permeability = 10000 md.

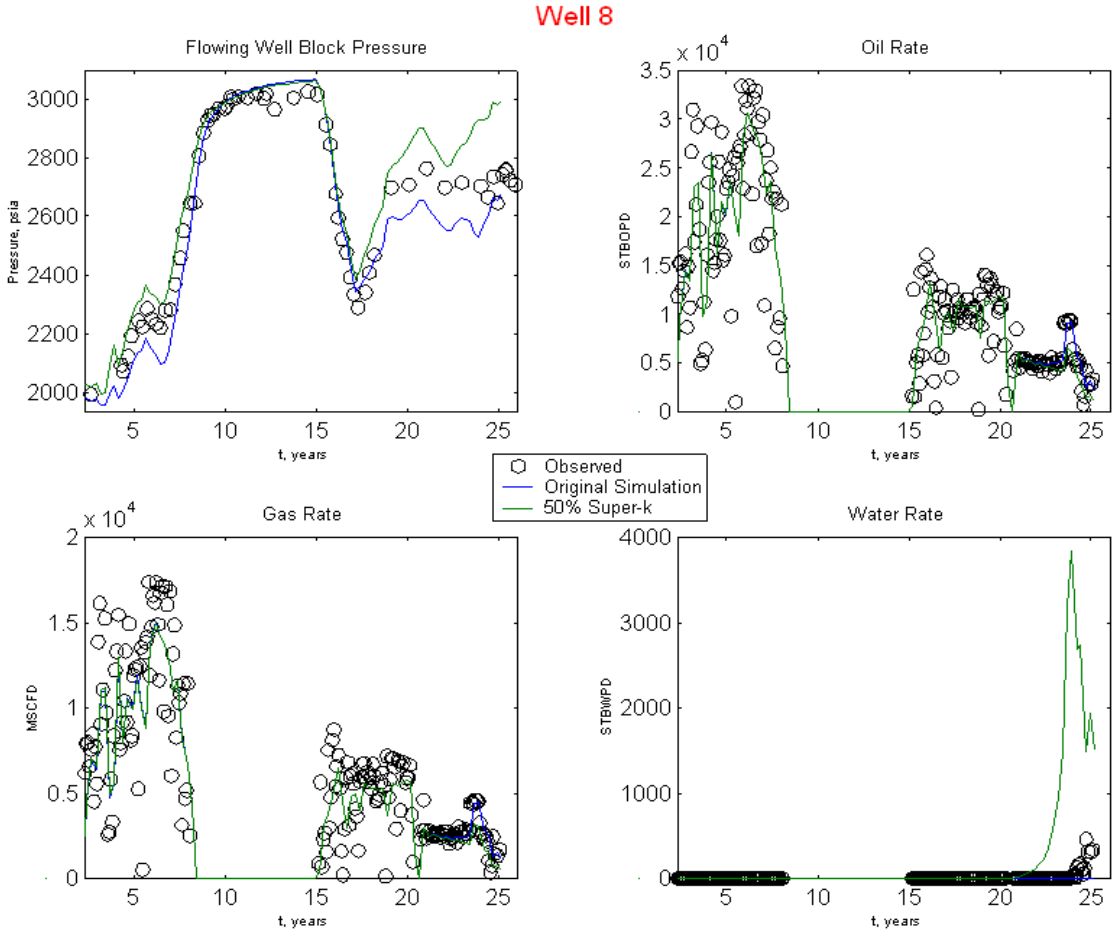

Fig. F.33: Match of 50% super-k model with constant permeability = 10000 md.

Appendix G

Coarsening of the original model

This appendix describes the model coarsening from 180-layers, to 60 layers. The horizontal dimensions in X and Y were not changed. Further, verification of the proper transfer of pore volumes and phase volumes from the fine model to the coarse model, is presented.

The upscaling of pore volumes and phase volumes, incumbent with coarsening in the vertical dimension, followed a simple algorithm, conserving both from the previous model. Porosity was arithmetically averaged over every three cells, since cell bulk volumes change very little over that interval. Water saturations were also arithmetically averaged, after weighting by porosity.

All other changes in the model, such as conversion of well connections, generation of the boundary flux file, and generation of the restart file, were done appropriately so as not to alter simulated production and injection well performance.

Phase volumes and pore volumes were manually checked in simulation output, and determined to be nearly identical.

Further verification of the successful conversion of pore and phase volumes lies in plots of historical well performance. This appendix presents well performance comparisons for eight of the study area wells. These plots compare the 60-layer model, to the 180-layer model, in flowing well block pressure, and the rate constraint imposed on the simulator, reservoir fluid volume rate.

Note that by definition, the rate matches should be, and are, exact. This was

presented to show that all rates were made in the 60-layer model, an indication that minimum flowing bottomhole constraints were not reached, due to lack of pore or phase volumes.

The matches in flowing well block pressures are acceptable, though not exact. This is due to the inexact nature of upscaling the permeability field. The permeabilities were simply arithmetically averaged over every three cells. The upscaling is not pertinent to the model, since the permeability field is modified during the history matching process. However, the upscaling was performed to demonstrate the model results have not significantly changed.

Note that during years 8 - 14, when the study area wells were shut in, that well block pressure matches are exact. This can be seen in wells 1, 2, 6, and 8. This verifies further the correct transfer of pore and phase volumes from the original model to the coarse model.

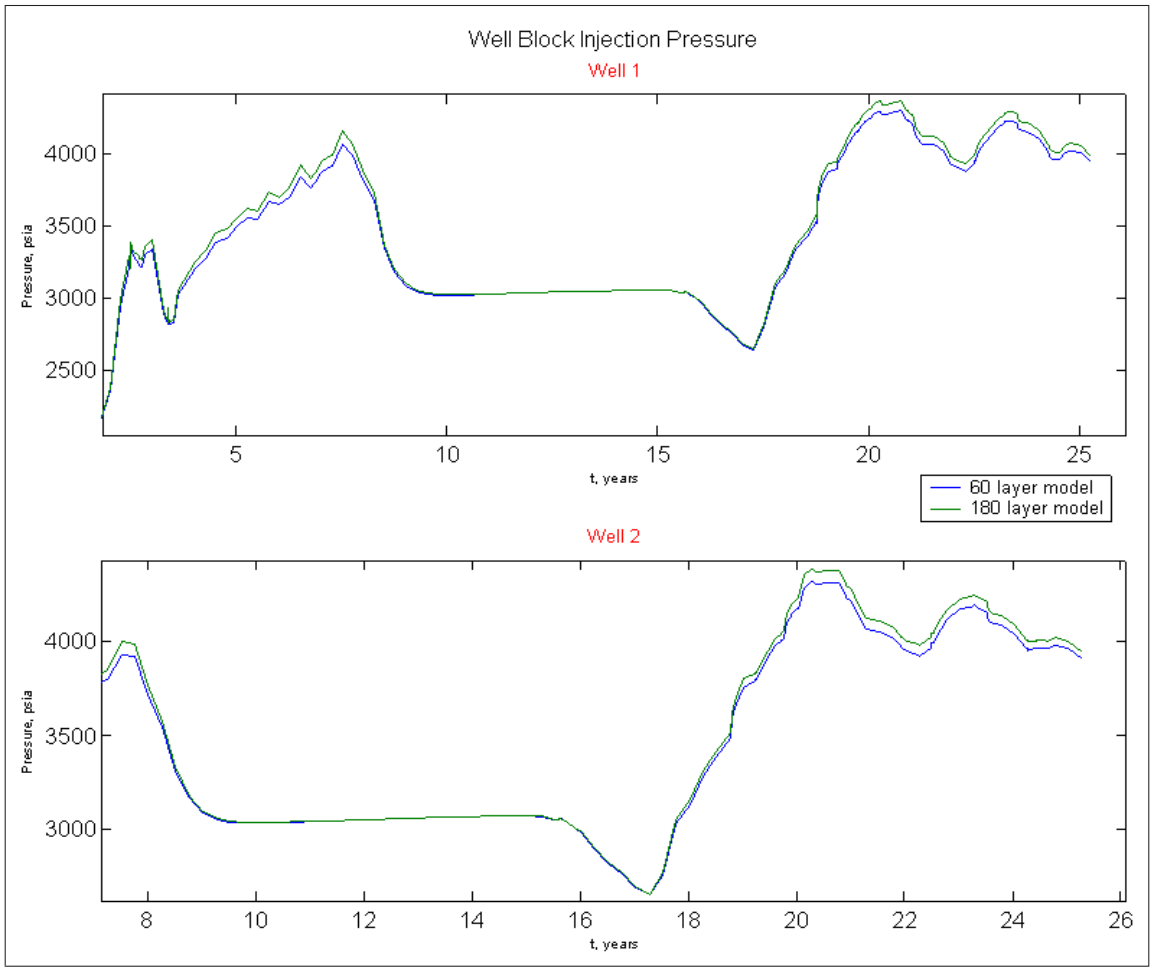
Well Block Injection Pressure
Well 1
Pressure, psia
4000
3500
3000
2500
5
10
15
20
25
t, years
60 layer model
180 layer model
Well 2
Pressure, psia
4000
3500
3000
8
10
12
14
16
18
20
22
24
26
t, years

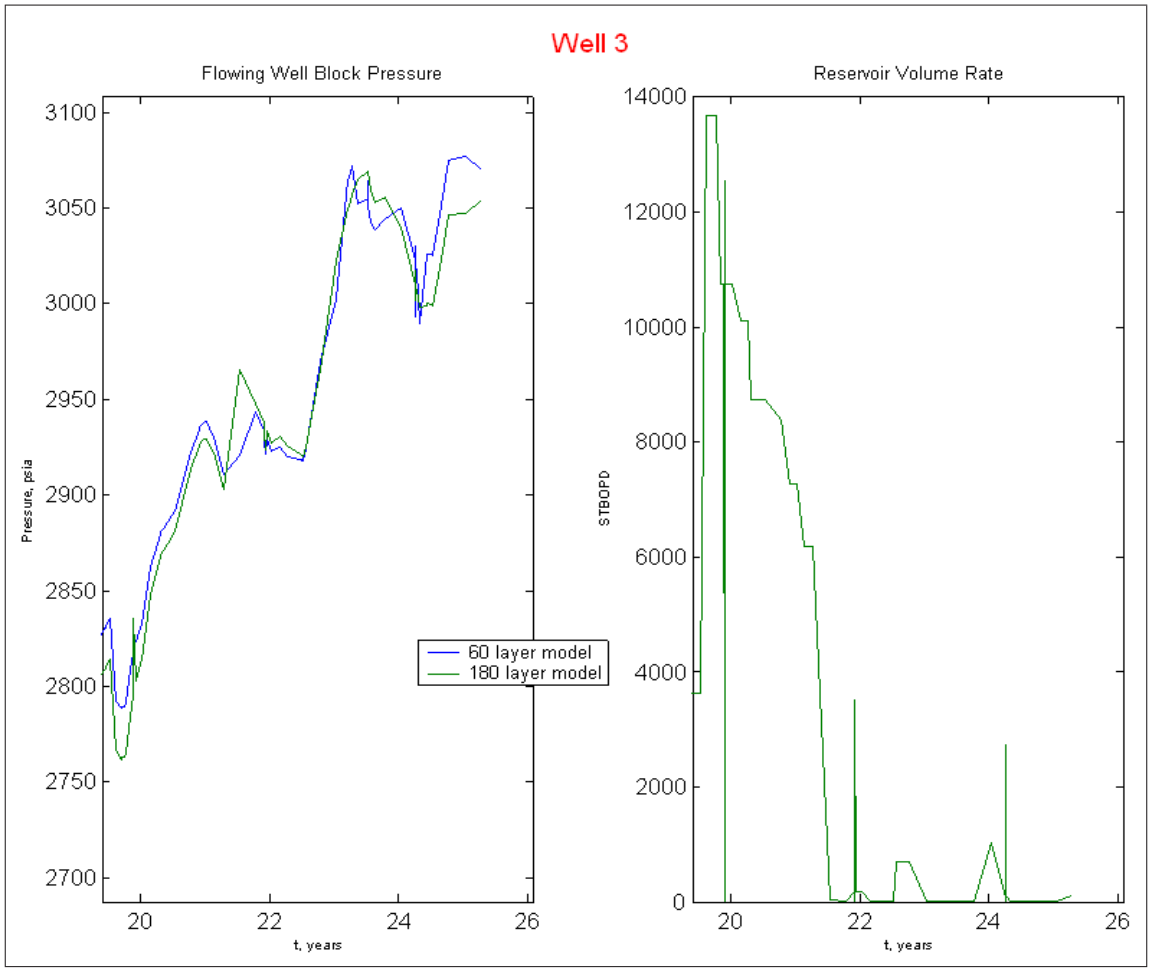
Well 3
Flowing Well Block Pressure
Pressure, psia
t, years
60 layer model
180 layer model
Reservoir Volume Rate
STBOPD
t, years

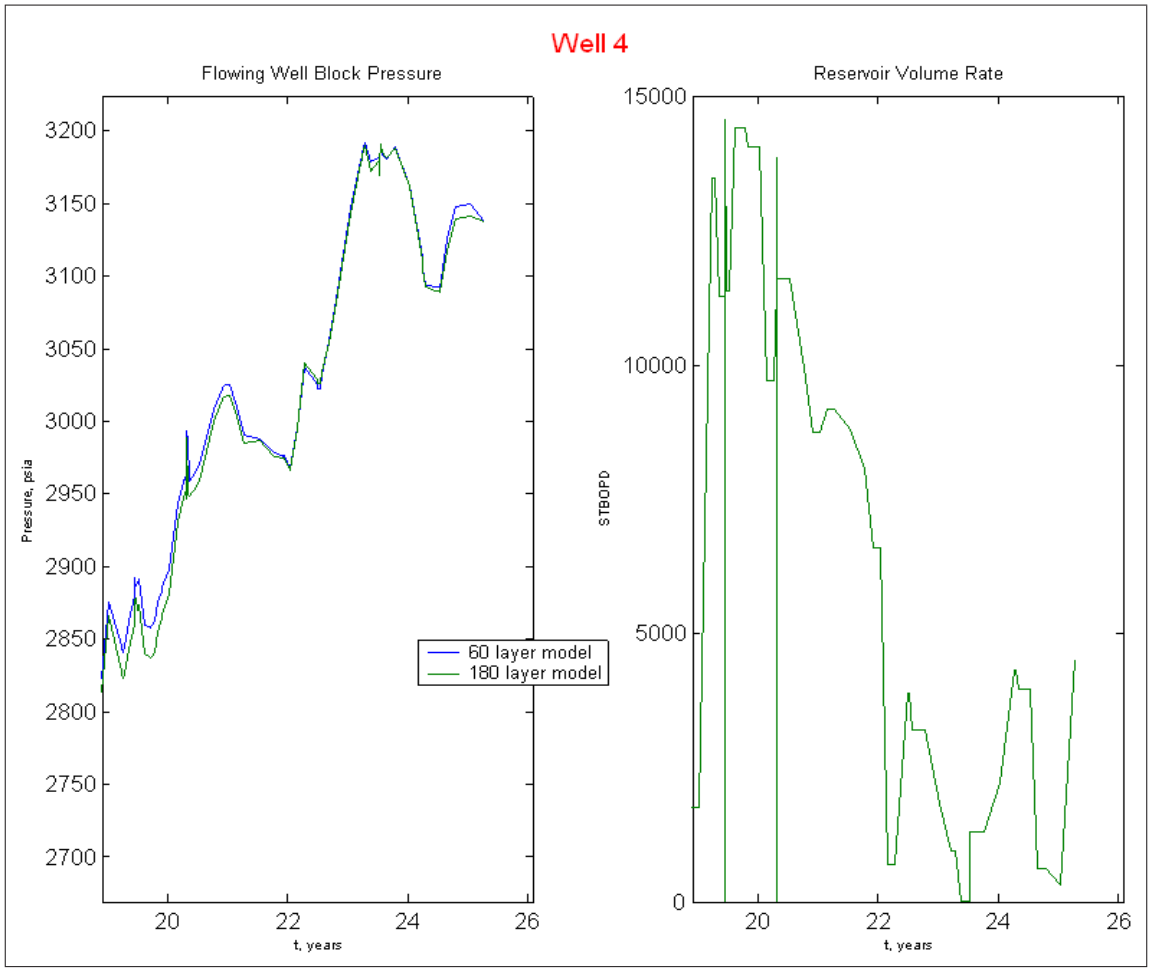
Well 4
Flowing Well Block Pressure
Pressure, psia
3200
3150
3100
3050
3000
2950
2900
2850
2800
2750
2700
20
22
24
26
t, years
60 layer model
180 layer model
Reservoir Volume Rate
STBOPD
15000
10000
5000
0
20
22
24
26
t, years

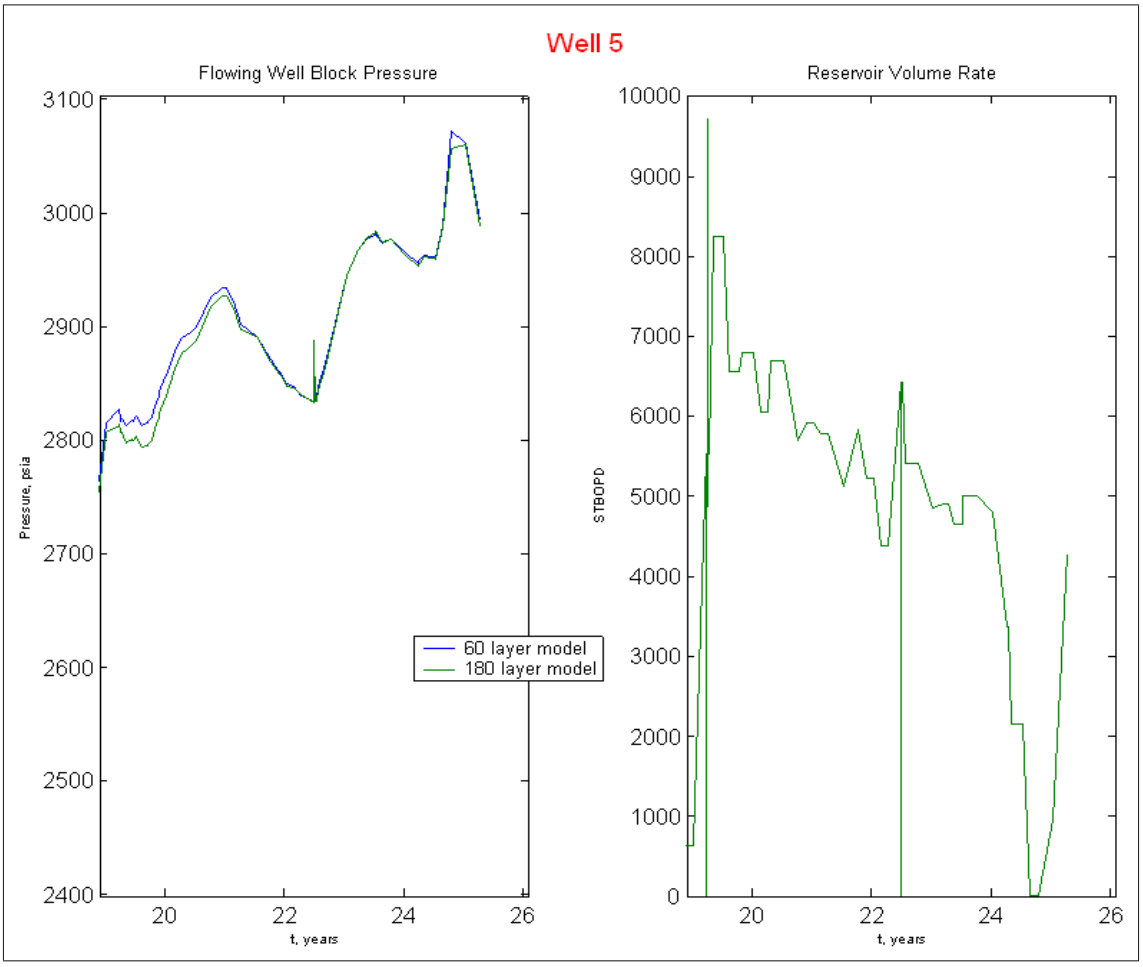
Well 5
Flowing Well Block Pressure
Pressure, psia
t, years
60 layer model
180 layer model
Reservoir Volume Rate
STBOPD
t, years

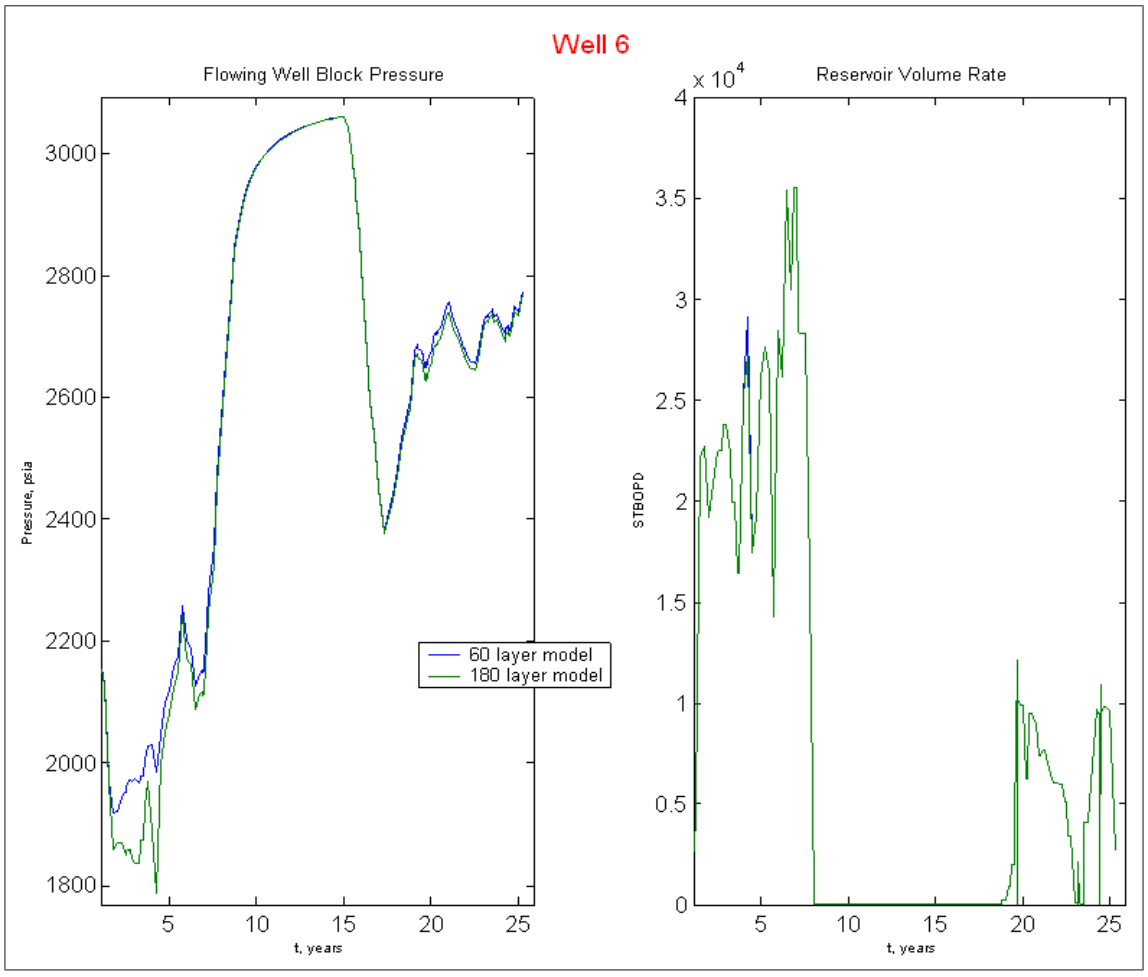
Well 6
Flowing Well Block Pressure
Pressure, psia
3000
2800
2600
2400
2200
2000
1800
5
10
15
20
25
t, years
60 layer model
180 layer model
Reservoir Volume Rate
x 10^4
STBOPD
4
3.5
3
2.5
2
1.5
1
0.5
0
5
10
15
20
25
t, years

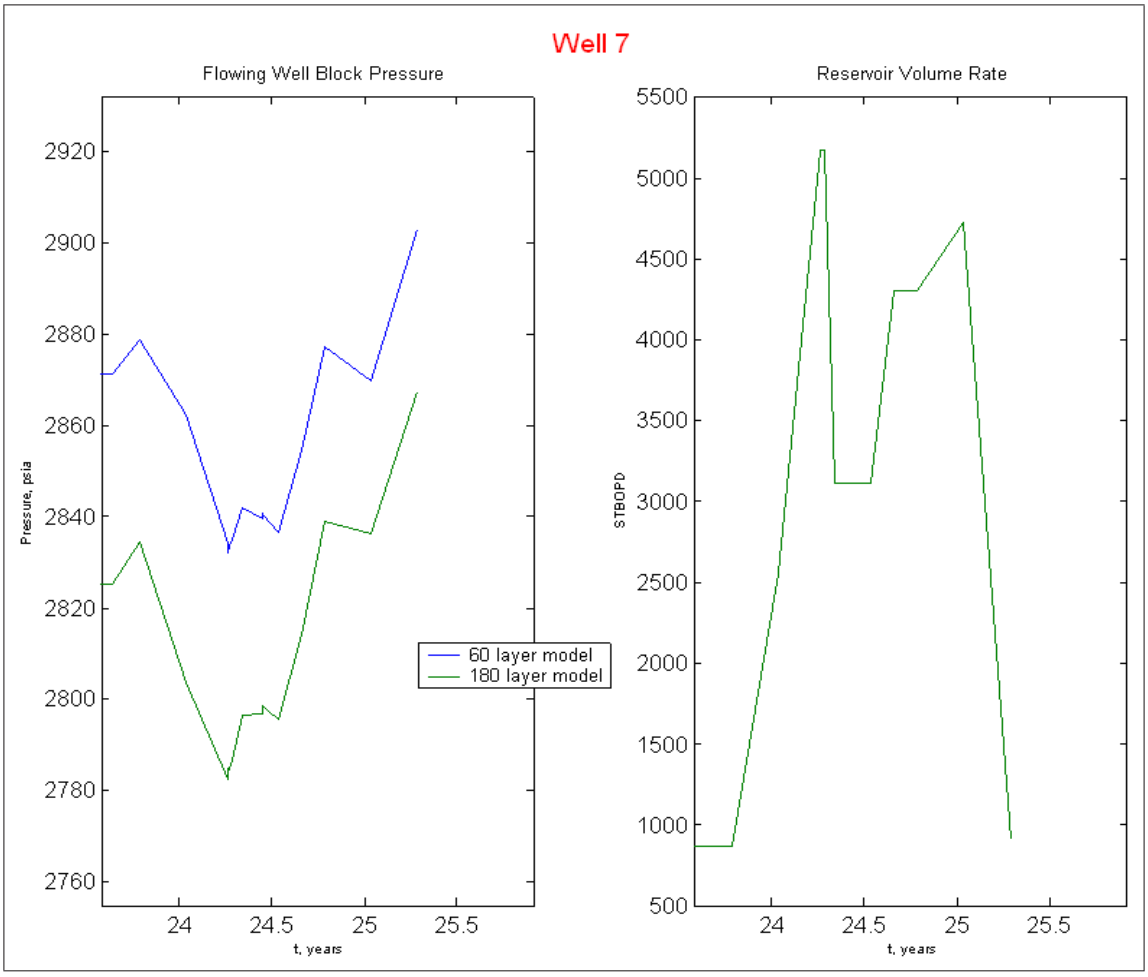
Well 7
Flowing Well Block Pressure
Pressure, psia
2920
2900
2880
2860
2840
2820
2800
2780
2760
24
24.5
25
25.5
t, years
60 layer model
180 layer model
Reservoir Volume Rate
STBOPD
5500
5000
4500
4000
3500
3000
2500
2000
1500
1000
500
24
24.5
25
25.5
t, years

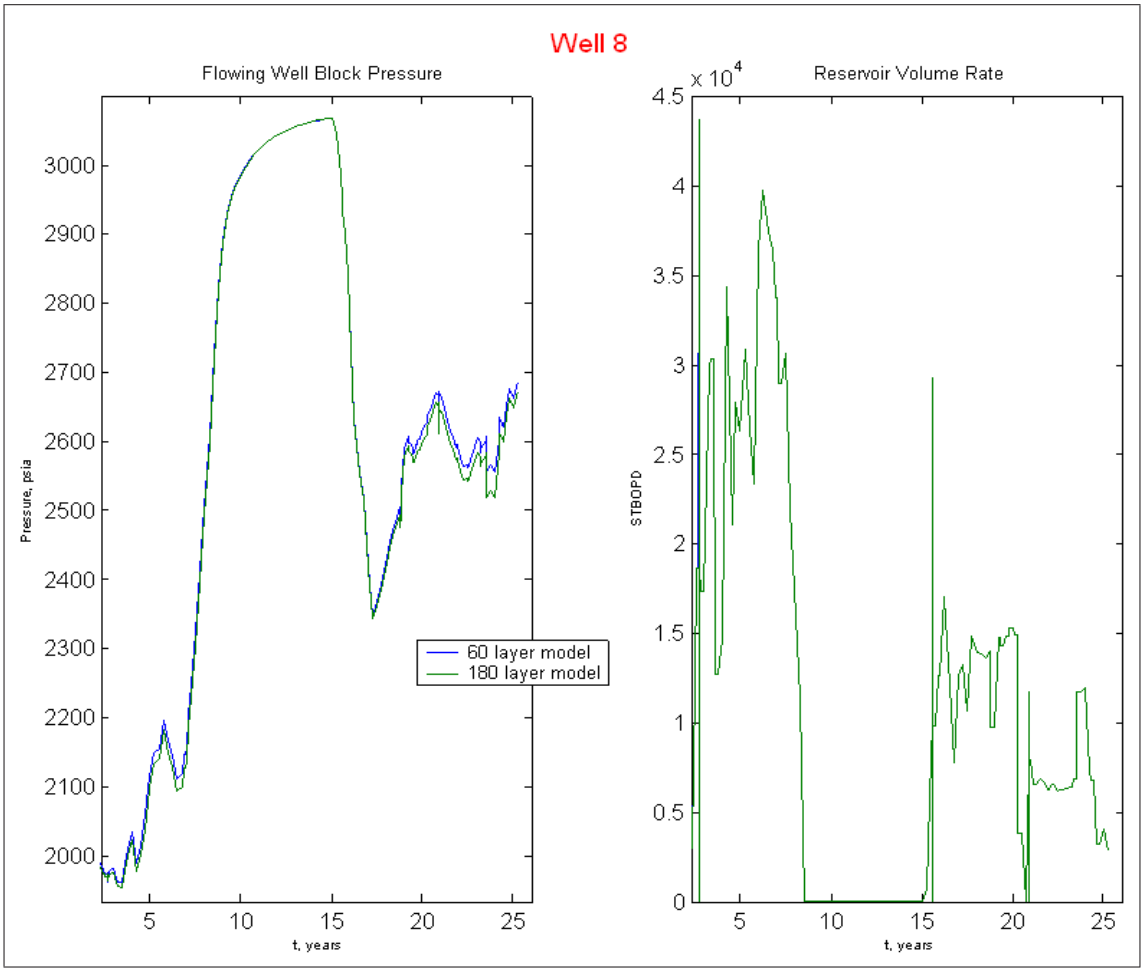
Well 8
Flowing Well Block Pressure
Pressure, psia
t, years
60 layer model
180 layer model
Reservoir Volume Rate
x 10^4
STBOPD
t, years

Bibliography

[1] Liu, J.S., Enwall, R.E., Davis, R.R., Douglas, J.L., Barber, R.M.: "Integration of Engineering Data and Geostatistics in Simulation of a Complex Carbonate Reservoir," paper SPE 25598, presented at the Middle East Oil Technical Conference and Exhibition, Bahrain, April 3-6, 1993

[2] Lee, S.H., Lough, M.F., and Jensen, C.L.: "Hierarchical Modeling of Flow in Naturally Fractured Formations with Multiple Length Scales," Water Resources Research, v.37, no.3, 2001

[3] Voelker, J.: "Geostatistical Characterization of Superpermeability From Flow-Meter Data: Application to Ghawar Field," SCRF Report No. 16, May, 2003

[4] Al-Ali, Z.A., Stenger, B.A.: "A Case History on Integrated Fracture Modeling in a Giant Field," paper SPE 71340, presented at the 2001 SPE ATCE, New Orleans, LA, September 30-October 3

[5] Alexander, David W.: "Impact of 3-D seismic data on reservoir characterization and development, Ghawar Field, Saudi Arabia, " *AAPG Studies in Geology No. 42*, editied by P. Weimer and T. L. Davis, eds., 1996, p.308

[6] Al-Thawad, F., Bin-Akresh, S., Al-Obaid, R.: "Characterization of Fractures/Faults Network from Well Tests; Synergistic Approach," paper SPE 71578, presented at SPE ATCE, New Orleans, LA, 30 september-3 October, 2001

[7] Habiballah, W.A., Hayder, M.E., Khan, M.S., Issa, K.M., Zahrani, S.H., Shaikh, R.A., Uwaiyedh, A.H., Tyraskis, T.P., Baddourah, M.A.:"Parallel Reservoir Simulation Utilizing PC-Clusters in Massive Reservoir Simulation Models," paper SPE 84065, presented at the 2003 ATCE, Denver, CO, October 5-8

[8] Al-Shaalan, T.M., Fung, S.K., Dogru, A.H.: "A Scalable Massively Parallel Dual-Porosity Dual Permeability Simulator for Fractured Reservoirs with Super-K Permeability," paper SPE 84371, presented at the 2003 SPE ATCE, Denver CO, October 5-8

[9] Meyer, Franz O., Price, Rex C., and Al-Raimi, Saleh M.: "Stratigraphic and Petrophysical Characteristics of Cored Arab-D Super-k Intervals, Hawiyah Area, Ghawar Field, Saudi Arabia," *GeoArabia*, v.5, no.3, 2000, p.355

[10] Ahlbrandt, Thomas S.: Project Chief, "U.S. Geological Survey World Petroleum Assessment 2000," U.S. Geological Survey Digital Data Series 60

[11] Blakey, Robert.: Professor, Department of Geology, University of Northern Arizona, website source, http://jan.ucc.nau.edu/~rcb7/mollglobe.html

[12] Wilson, James. L..: "Middle Shelf Environment," AAPG *Memoir 33*, Chapter 7, 1983, edited by Peter A. Scholle, Don G. Bebout, and Clyde H. Moore

[13] Boggs, Sam.: *Principles of Sedimentology and Stratigraphy,* Prentice Hall, New Jersey, 2001

[14] Alnaji, Nassir S..: "Two Carbonate Shelf Margins with Hydrocarbon Potential Compared: Upper Jurassic Formations of Arabian Basin and Guadalupian Formations of Permian Basin of Texas and New Mexico," M.SC. thesis, Department of Geological Sciences, University of South Carolina, 2002

[15] Powers, R. W., L. F. Ramirez, L.f., Redmond, C.D., and Elberg, E.L.,: "Geology of the Arabian Peninsula - Sedimentary Geology of Saudi Arabia," U.S. Geological Survey Professional Paper 560D, 1966, p.127

[16] Wilson, James L.: *Carbonate Facies In Geological History*, Springer-Verlag, New York, N.Y., 1975

[17] Wilson, Augustus O.: "Depositional and Diagenetic Facies in the Jurassic Arab-C and -D Reservoirs, Qatif Field, Saudi Arabia," Chapter 20, *Carbonate Petroleum Reservoirs*, edited by Perry O. Roehl and Phillip W. Choquette, Springer-Verlag, New York, N.Y., 1985

[18] Meyer, Franz O., Price, Rex C.: "A New Arab-D Depositional Model, Ghawar Field, Saudi Arabia," paper SPE 25576 presented at the SPE Middle East Oil Technical Conference, Bahrain, 3-6 April, 1993

[19] Alsharhan, A. S., and Nairn, A. E. M.: *Sedimentary Basins and Petroleum Geology of the Middle East*, Amsterdam, Elsevier, 1997

[20] Murris, R. J.: "Middle East stratigraphic evolution and oil habitat," AAPG *Bulletin*, v. 64, 1980, p.597

[21] Carrigan, W. J., Cole, G. A.,Colling, E. L., and Jones, P. J.: "Geochemistry of the Upper Jurassic Tuwaiq Mountain and Hanifa Formation Petroleum Source Rocks of Eastern Saudi Arabia," in *Petroleum Source Rocks*, edited by B. J. Katz, Springer-Verlag, Berlin, 1995

[22] Mitchell, J.C., Lehmann, J.P., Cantrell, D.L., Al-Jallal, I.A., and Al-Thagafy, M.A.R.: "Lithofacies, diagenesis, and depositional sequence; Arab-D Member, Ghawar field, Saudi Arabia," in *Giant Oil and Gas Fields: A Core Workshop*, edited by J.A. Lamondo and P.M. Harris, Society of Economic Paleontologists and Mineralogists, Tulsa, 1988, p.459

[23] Meyer, Franz O., Price, Rex C., Al-Ghamdi, Ibrahim A., Al-Goba, Ibrahim M., Al-Raimi, Saleh M., Cole, John C.: "Sequential stratigraphy of Outcropping Strata Equivvalent to Arab-D Reservoir, Wadi Nisah, Saudi Arrabia," *GeoArabia (Manama),* v.1, no.3, 1996, p.435

[24] Sharief, Farooq A., Khan, Mohammed S., and Magara, K.: "Outcrop-Subcrop Sequence and diagenesis of Upper Jurassic Arab-Hith Formations, Central Saudi Arabia," Journal of King Abdulaziz University, v.4, 1991, p.105

[25] Parker, Calvin A.: "Geopressures in the Deep Smackover of Mississippi," *JPT,* August, 1973, p.971

[26] Oivanki, Stephen M.: "Paleodepositional Environments in the Upper Jurassic Zuloaga Formation (Smackover), Northeastern Mexico," *Tansactions*, Gulf Coast Association of Geological Societies, v.XXIV, 1974, p.258

[27] Wilson, James L., Ward, William. C., and Finneran, Joseph M.: "Upper Jurassic and Lower Cretaceous Carbonate Platform and Basin Systems, Monterrey-Saltillo Area, Northeast Mexico," Field Guide, Society of Economic Paleontologists and Mineralogists Foundation, Gulf Coast Section, May, 1984

[28] Meyer, Martha G., and Ward, William C.: "Outer-Ramp Limestones of the Zuloaga Formation, Astillero Canyon, Zacatecas, Mexico," *Proccedings*, Third Annual Research Conference, Society of Economic Paleontologists and Mineralogists Foundation, Gulf Coast Section, 1984, p.275

[29] Longoria, Jose F.: "Stratigraphic Studies in the Jurassic of Northeastern Mexico: Evidence for the origin of the Sabinas Basin," *Proccedings*, Third Annual Research Conference, Society of Economic Paleontologists and Mineralogists Foundation, Gulf Coast Section, 1984, p.171

[30] Voelker, J.: "A Characterization of Ghawar Super-k Distribution Through Flowmeter History Updating of Training Image Based Maps," SCRF Report No. 15, May, 2002

[31] Strebelle, Sebastian, Journel, Andre G: “Reservoir Modeling Using Multiple-Point Statistics,” paper SPE 71324 presented at the 2001 SPE Annual Technical Conference and Exhibition, New Orleans, Louisiana, 30 September-3 October

[32] Hu L.Y., Blanc G., and Noetinger B.: "Gradual deformation and iterative calibration of sequential stochastic simulation," Mathematical Geology, vol. 33, no. 6, 2001

[33] Davatzes, N. and Aydin, A.: "The formation of conjugate normal fault systems in folded sandstone by sequential jointing and shearing, Waterpocket monocline, Utah," Journal of Geophysical Research, v. 108, no. B10, 2003

[34] Peaceman, Donald W.: "Interpretation of Well-Block Pressures in Numerical Reservoir Simulation," SPEJ (June,1978) 183-94; Trans., AIME, p.265

[35] Deutsch, Clayton V., and Journel, Andre G.: "GSLIB Geostatistical Software Library and User's Guide," Oxford University Press, 1998, p.21

[36] Brent, Richard P. *Algorithms for Minimization Without Derivatives.* Prentice Hall, Englewood Cliffs, NJ, 1973, Chap. 5.

[37] Karimi-Fard, M: " An efficient discrete fracture model applicable for general purpose reservoir simulators," SPE Journal, 2004

[38] Graham, B., Antonellini M., and Aydin A.: "Formation and growth of normal faults in carbonates within a compressive environment," *Geology*, January, 2003, v. 31, no. 1, 11.

[39] Davis, M.H.: M.Sc. Candidate, Jackson School of Geosciences, University of Texas at Austin, personal correspondence

[40] Cinco-Ley, L.H., Samaniego, F.V., Dominguez, A.N.: "Unsteady-State Flow Behavior for a Well Near a Natural Fracture," paper SPE 6019, presented at the 1976 SPE ATCE, New Orleans, LA, October 3-6

[41] Abbaszadeh, M., Cinco-Ley, H.: "Pressure-Transient Behavior in a Reservoir with a Finite-Conductivity Fault," SPEFE, March, 1995, p.26

[42] Anisur Rahman, N.M., Miller, M.D., Mattar, L.: Analytical Solution of the Transient-Flow Problems for a Well Located Near a Finite Conductivity Fault

in Composite Reservoirs," paper SPE 84295, presented at the 2003 SPE ATCE, Denver, CO, October 3-5

[43] Saudi Aramco Staff: "Ghawar Oil Field, Saudi Arabia," *Bulletin*, American Association of Petroleum Geologists, v.43, no. 2, February, 1959, p.434

[44] Rouser, B.J., Al-Askar, Y.A.:"Monitoring Sweep in Peripheral Waterflood: A Case Hisory," paper SPE 21372, presented at the 1991 SPE Middle East Oil Show, Bahrain, November 16-19

[45] Saner, S., and Sahin, A.: "Lithological and zonal porosity-permeability distributions in the Arab-D Reservoir, Utmaniyah Field, Saudi Arabia," AAPG *Bulletin,* v.83, no. 2, February, 1999, p.230

[46] Al Shahri, A. M., Al Ubaidan, A.A., Kibsgaard, P., Kuchuk, F.: "Monitoring Areal and Vertical Sweep and Reservoir Pressure in the Ghawar Field Using Multiprobe Wireline Formation Tester," paper SPE 48956, presented at the 1998 SPE ATCE, New Orleans, LA, September 27-30

[47] Lake, L.: *Enhanced Oil Recovery*, Prentice Hall, New York, NY, 1988; p. 206; p.216

[48] Brown, J.S., Dubreuil, L.R., Schneider, R.D.: "Seawater Project in Saudi Arabia-Early Experience of Plant Operation, Water Quality and Effect on Injection Well Performance,' paper SPE 7763, presented at the 1979 SPE MIddle East Oil Technology Conference, Bahrain, March 25-29

[49] Bayona, H.J.: "A Review of Well Injectivity Performance in Saudi Arabia's Ghawar Field Seawater Injection Program," paper SPE 25531, presented at the 1993 SPE MIddle East Oil Technical Conference and Exhibition, Bahrain, April 3-6

[50] Azeemuddin, M., Ghori, S.G., Saner, S., Khan, M.N..: "Injection-Induced Hydraulic Fracturing in a Naturally Fractured Carbonate Reservoir: A Case Study from Saudi Arabia," paper SPE 73784, Presented at the 2002 SPE International

Symposium and Exhibition on Formation Damage," Lafayette, LA, February 20-21

[51] Al Shahri, A. M., Al Muraikhi, A.: "A Novel Approach to Characterize Dynamic Interaction Between Super Permeability Layers with Vertical Faults and Their Affect on Flood Front Movement," paper SPE 49275, presented at the 1998 SPE ATCE, New Orleans, LA, September 27-30

[52] Valle, Antonio, Pham, Anthony, Hsueh, P.T., Faulhaber, John: "Development and Use of a Finely Gridded Window Model for a Reservoir Containing Super Permeable Channels," paper SPE 25631 presented at the 1993 SPE Middle East Oil Technical Conference and Exhibition, Bahrain, April 3-6

[53] Valle, A., Faulhaber, J.J., Keith, T.H., Hsueh, P.T.: "Development of an Integrated Reservoir Characterization and Simulation Model for a Heterogeneous Carbonate Reservoir, Arad-D Reservoir, East Flank of Ghawar Field,' paper SPE 37778, presented at the 1997 SPE MIddle East Oil Show, Bahrain, March 15-18

[54] Al-Ajmi, F.A., Al-Shahri, A. M., Sengul, M., Phelps, R.: "Evaluation of Super-k Wells Performance Using Fluid Flow Index in Ghawar Field," paper SPE 68162, presented at the 2001 SPE MIddle East Oil Show, Bahrain, March 17-20

[55] Moore, D.M., "Impact of Super Permeability on Completion and Production Strategies," paper SPE 17974, presented at the 1989 SPE Middle East Oil Technical Conference and Exhibition, Bahrain, March 11-14

[56] Al-Ghamdi, A., BinAkresh, S.A., Bubshait, S.A.: "Characterization of Conductive Faults and Fractures Responsible for Inter-reservoir Communication in the Shedgum Leak Area of the Giant Ghawar Field, Saudi Arabia," paper SPE 81517, presented at the SPE 13th Middle East Oil Show and Conference, Bahrain, June 9-12, 2003

[57] Dogru, A.H., Dreiman, W.T., Hemanthkumar, K., Fung, L.: "Simulation of Super-k Behavior in Ghawar by a Multi-Million Cell Parallel Simulator," paper

SPE 68066, presented at the 2001 SPE Middle East Oil Show, Bahrain, March 17-20

[58] Phelps, R.E., Strauss, J.P.: Capturing Reservoir Behavior by Simulating Vertical Fracture and Super-K Zones in the Ghawar Field," SPEREE, August, 2002. p.333

[59] Cosentino, L., Coury, Y., Daniel, J.M., Manceau, C., Ravenne, C., Van Lingen, P., Cole, J., Sengul, M.:"Integrated Study of a Fractured Middle East Reservoir with Stratiform Super-k Intervals-Part2: Upscaling and Dual Media Simulation," paper SPE 68184, presented at the 2001 SPE Middle East Oil Show, Bahrain, March 17-20

[60] Pham, T.R., Stenger, B.A., Al-Otaibi, U.F., Al-Afaleg, N.I., Al-Ali, Z.A., Sarda, S.: "A Probability Approach to Development of a Large Carbonate Reservoir with Natural Fractures and Stratiform Super-permeabilities," paper SPE 81433, presented at the SPE 13th Middle East Oil Show and Conference, Bahrain, April 5-8, 2003

[61] Sabathier, J.C., Bourbiaux B.J., Cacas, M.C., Sarda, S.: "A New Approach of Fractured Reservoirs, " paper SPE 39825, presented at the 1998 SPE International Petroleum Conference and Exhibition of Mexico, Villahermosa, Mexico, March 3-5

[62] Pham, T.R., Al-Otaibi, U.F., Al-Ali, Z.A., Lawrence, P., Van Lingen, P.: "Logistic Approach in Using an Array of Reservoir Simulation and Probabilistic Models in Developing a Giant Oil Reservoir with Super-Permeability and Natural Fractures," paper SPE 77566, presented at the 2002 SPE ATCE, San Antonio, TX, September 29 - October 2

[63] Croft, G.: http://www.gregcroft.com/ghawar.ivnu

[64] van Lingen, P., Sengul, M., Daniel, J., Cosentino, L.: "Single Medium Simulation of Reservoirs with Conductive Faults and Fractures," paper SPE 68165, presented at the 2001 SPE MIddle East Oil Show, Bahrain, March 17-20

[65] Mezghani, M., van Lingen, P., Cosentino, L., Sengul, M.: "Conditioning Geostatistical Models to Flow Meter Logs," paper SPE 65122, presented at the 2000 SPE European Petroleum Conference, Paris, France, October 24-25

[66] Handford, C.R., Cantrell, D.L., Keith, T.H: "Regional Facies Relationships and Sequence Stratigraphy of a Super-Giant Reservoir (Arab-D Member), Saudi Arabia," pending publication

[67] Huskey, W.L., Crawford, P.B.: Performance of Petroleum Reservoirs Containing Vertical Fractures in the Matrix," *SPEJ*, June 1967, p.221

[68] Prats, M.: "Effect of Vertical Fractures on Reservoir Behavior-Incompressible Fluid Case," *Transactions.*, AIME, v.222, 1961, II-105

[69] Gringarten, A.C., Ramey, H.J.: The Use of Source and Green's Functions in Solving Unsteady-Flow Problems in Reservoirs," *Transactions*, AIME, v. 255, 1973, II-285

[70] Cinco-Ley, L.H., Samaniego, F.V., Dominguez, A.N.: "Transient Pressure Behavior for a Well with a Finite-Conductivity Vertical Fracture," *SPEJ*, August, 1978, p.253

[71] Gill, H.S., Al-Zayer, R.: paper SPE 84293, presented at the 2003 SPE ATCE, Denver, CO, October 5-8

[72] Al-Thawad, F., Agyapong, D., Banerjee, R., Issaka, M.B.: "Pressure Transient Analysis of Horizontal Wells in a Fractured Reservoir; Gridding Between Art and Science," paper SPE 87013, presented at the 2004 Asia Pacific Conference on Integrated Modelling for Asset Management, Kuala Lampur, Malaysia, March 29-30

[73] Voelker, J., Liu, J., Caers, J.: "A Geostatistical Method for Characterizing Superpermeability From Flow-Meter Data: Application to Ghawar Field," paper SPE 84279, presented at the 2003 SPE ATCE, Denver CO, October 5-8

[74] Caers, J.: "History matching under a training image-based geological model constraint," SPE *Journal*, September, 2003, p.218

[75] Deutsch, Clayton V., and Journel, Andre G. *GSLIB Geostatistical Software Library and User's Guide.* Oxford University Press, Oxford, 1998, p.182

[76] Deutsch, Clayton V., and Wang, Libing. Hierarchial Object-Based Stochastic Modeling of Fluvial Reservoirs. *Mathematical Geology*, v.28, no.7, p.857

[77] Deutsch, Clayton V., and Journel, Andre G. *GSLIB Geostatistical Software Library and User's Guide.* Oxford University Press, Oxford, 1998, p.170